2023

14th International Conference on Measurement

May 29 - 31, 2023, Smolenice, Slovakia

Institute of Measurement Science
Slovak Academy of Sciences

MEASUREMENT 2023

The 14th International Conference on Measurement

ORGANIZERS OF THE CONFERENCE

Organizer

Institute of Measurement Science, Slovak Academy of Sciences, Bratislava

Technical sponsorship

IEEE Czechoslovakia Section

IEEE Czechoslovakia Section EMB Chapter

Slovak Metrological Society

Slovak National Committee U.R.S.I.

Slovak Society of Biomedical Engineering and Medical Informatics

MEASUREMENT 2023

Proceedings of the
14th International Conference on Measurement

Congress Center of the Slovak Academy of Sciences
Smolenice Castle, Slovakia
May 29-31, 2023

MEASUREMENT 2023

Editors: Andrej Dvurečenskij, Ján Maňka, Jana Švehlíková, Viktor Witkovský
Cover Design: Ivan Frollo
Publisher: Institute of Measurement Science
Slovak Academy of Sciences
Dúbravská cesta 9
841 04 Bratislava Slovakia

ISBN 978-80-972629-6-9

COMMITTEES

Conference Chairman

J. Maňka, Slovakia

International Program Committee

J. Švehlíková, Slovakia, Chairman
B. Antić, Serbia
I. Bajla, Slovakia
M. Bittera, Slovakia
V. Boháč, Slovakia
K. De Buysser, Belgium
E. Cocherová, Slovakia
I. Frollo, Slovakia
R. Harťanský, Slovakia
P. Jurák, Czech Republic
B. Kessel, Sweden
O. Kochan, Ukraine
R. Köning, Germany
I.C. Lira, Chile
J. Markovič, Slovakia
K. Meigas, Estonia
V. Mlynarik, Austria
V. Novickij, Lithuania
M. Paluš, Czech Republic
K. Roubík, Czech Republic
Y. Serinagaoglu, Turkey
M. Soleimani, United Kingdom
Z. Starčuk, Czech Republic
M. Štork, Czech Republic
S. Takayama, Japan
M. Tyšler, Slovakia
J. Volaufova, USA
G. Wimmer, Slovakia
V. Witkovský, Slovakia
A. Woźniak, Poland
M. Tarata, Romania
P. Tino, United Kingdom
D. Tyler, United Kingdom

Young Investigator Award Jury

Yesim Serinagaoglu-Dogrusoz, Turkey
Laura Bear, France
Jess Tate, USA
Przemysław Otomanski, Poland
Pavel Ripka, Czech Republic
Anna Krakovska, Slovakia
Igor Zakharov, Ukraine

Local Organizing Committee

A. Dvurečenskij, Chairman
E. Gurišová
D. Gogola
M. Chvosteková
J. Jakubík
A. Krafčík
B. Ondrušová
Z. Rošťáková
M. Škrátek
M. Teplan
L. Zelieska

Reviewers

The submitted papers were evaluated by 87 reviewers, members of the International Program Committee and experts in the fields of measurement science and technology. Each paper was scored by two or three reviewers.

Preface

An experiment is a question which science poses to Nature
and a measurement is the recording of Nature's answer.
Max Planck (1858 - 1947)

This conference – MEASUREMENT 2023 – is held in the year of the 70th anniversary of the Institute of Measurement Science and also the whole Slovak Academy of Sciences. After the break in 2021, when due to a pandemic situation, the conference went online, we are glad that it will be held again in person in Smolenice Castle.

We continue with the traditional general topics of the conference - theoretical problems of measurement, measurement of physical quantities, and measurement in biomedicine. Besides the usual keynote lectures, we also continue with the special sessions, first introduced in 2019.

This year, three specific fields were announced for the special sessions, and some speakers were invited to give their talks within:

- Body surface ECG Measurements and Forward and Inverse Problems;
- Connectivity and Causality in EEG or other Biological Signals;
- Low Field MRI vs. High Field MRI - Future Perspectives.

The authors of the Proceedings' papers come from ten countries. We are happy that despite the very difficult situation in Ukraine, our Ukrainian colleagues submitted the results of their work too.

We hope that every reader of the submitted papers will find something new or inspiring for his future work, which is the main goal of the conference.

Ján Maňka, Jana Švehlíková, Andrej Dvurečenskij, Viktor Witkovský

Contents

Body surface ECG Measurements and Forward and Inverse Problems

ISBN 978-80-972629-6-9

Effects of Torso Inhomogeneities on Spontaneous PVC Localization in Potential and Dipole-Based Methods

[1,2]Nika Rasoolzadeh, [3,4]Beata Ondrusova,[1,2]Yesim Serinagaoglu Dogrusoz,[3]Jana Svehlikova

[1]Institute of Applied Mathematics, Middle East Technical University, Ankara, Turkey
[2]Electrical-Electronics Engineering Dept., Middle East Technical University, Ankara, Turkey
[3]Institute of Measurement Science, Slovak Academy of Sciences, Bratislava, Slovakia
[4]Faculty of Electrical Engineering and Information Technology, STU, Bratislava, Slovakia
Email: nika.rasoolzadeh@gmail.com

Abstract. *The use of electrocardiographic imaging for the localization of the undesired premature ventricular contraction needs a torso volume conductor definition. This study aims to investigate the specific effect of lung and blood cavity inhomogeneities on the performance of inverse localization. Two source models were assumed for the inverse solution applied to clinical data; potential on the closed epicardial-endocardial surface and a single dipole. The results showed that the potential-based solution performed better if the presence of at least blood cavities was assumed, while the dipole-based solution was not significantly influenced by the presence of inhomogeneities. The importance of the inhomogeneities in the torso model for the inverse solution also depends on the used model of the equivalent heart generator.*

Keywords: Electrocardiographic Imaging (ECGI), Premature Ventricular Contraction (PVC), Torso Inhomogeneities

1. Introduction

Premature ventricular contraction (PVC) is a form of arrhythmia that occurs when the heartbeat starts from the ventricles earlier than from the sinoatrial (SA) node. Treatment methods such as radiofrequency ablation (RFA) therapy are commonly used to eliminate malfunctioning electrical pathways.

Electrocardiographic imaging (ECGI) is a noninvasive method that inversely reconstructs the cardiac electrical source distributions from body surface potential (BSP) measurements, providing an estimate of the PVC origin. However, the inverse and forward solutions' accuracy depends on the degree of complexity considered in the forward model as well as on the source model. Bear *et al.* have demonstrated that including torso inhomogeneities enhanced the forward computed BSPs [1]. While some studies [2] suggest that there is no significant difference in the inverse solutions obtained from homogeneous and inhomogeneous torso models, another paper has shown that incorporating the lungs in the torso model could enhance the accuracy of the solutions [3].

In this study, we aim to explore the impact of incorporating lung and blood cavities into the heart-torso model on the inverse localization of PVC origins in patients that underwent RFA after the BSP measurement. The inverse problem is solved using a potential-based [4] and dipole-based [4, 5] cardiac source model on the closed Epicardium-Endocardium (EpiEndo) heart surface.

2. Methods

BSPs of ten patients who underwent successful RFA were used for the inverse localization of their PVC origin. Patient-specific torso models, including lungs and heart cavities were created from their CT scans. Two different source models have been used on the EpiEndo surface of the

heart: the dipole-based and potential-based. A detailed description of these models is available in [4].

The solution in terms of the potential-based model uses Tikhonov regularization for finding the inverse problem solutions in terms of potentials on the EpiEndo surface and a spatiotemporal smoothing method to obtain activation time (AT) sequences. The PVC origin is estimated by finding the earliest detected activation time.

The solution by the dipole-based model relies on the premise that the activation area is small enough to be represented by a single dipole in the first 20-30 ms of activation. Therefore, the PVC origin estimate is determined by identifying the dipole position that results in the lowest relative residual error (RRE) between the measured and reconstructed BSP across all time instances in the aforementioned early activation interval and all possible dipole positions.

In this work, lung lobes and heart cavities (atria and ventricles) were considered in the torso model. The conductivity of the lung was assumed four times lower and the conductivity of the blood three times higher than the conductivity of the torso. Then four heart-torso model setups were considered: HT (heart+torso), HBLT (heart+blood+lung+torso), HLT (heart+lung+torso), HBT (heart+blood+torso).

Finally, we compare the PVC origin positions estimated by the two inverse methods with the ablation points (*i.e.* the ground truth) determined by the physician, using the localization error (LE), defined as the Euclidean distance between the two locations.

3. Results

The LE values for all source and torso models for all patients are presented in Fig. 1 as scatter plots. Additionally, the mean and standard deviation of LE values, as well as the median and interquartile range (IQR) of LE values over all patients are given in Table 1. The examples of AT and RRE distribution (maps) on the EpiEndo surface are in Fig. 2 and Fig. 3.

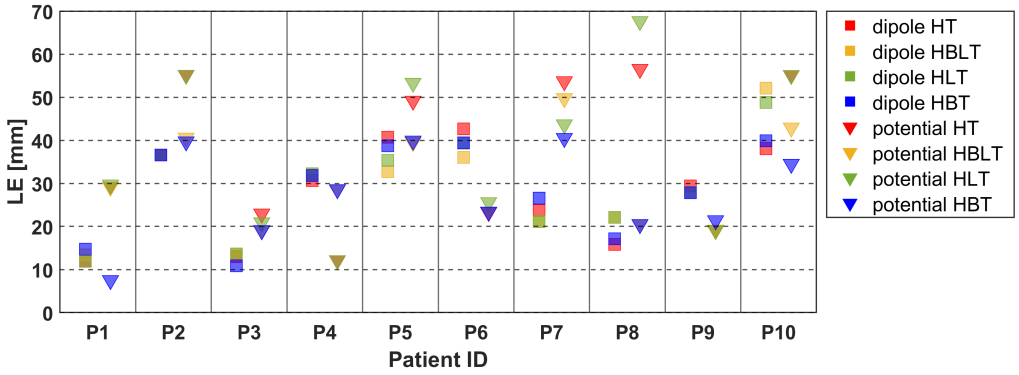

Fig. 1: Potential and dipole-based localization error (mm) for four torso models. Overlapping symbols indicate similar model performance and shared PVC origin estimates for some patients.

Table 1: Statistical measures of localization errors (mm) over all patients for the four torso models with potential and dipole-based methods.

Source Model	Measures	HT	HBT	HLT	HBLT
Potential-based	mean±std	37.6±17.8	27.5±11.0	38.2±19.1	31.3±11.1
	med (IQR)	39.2(31.7)	26.0(17.7)	36.7(32.6)	28.9(19.1)
Dipole-based	mean±std	28.2±11.6	28.4±10.9	28.9±11.8	28.9±11.8
	med (IQR)	30.0(19.9)	29.8(18.7)	30.1(14.9)	30.1(13.8)

ISBN 978-80-972629-6-9

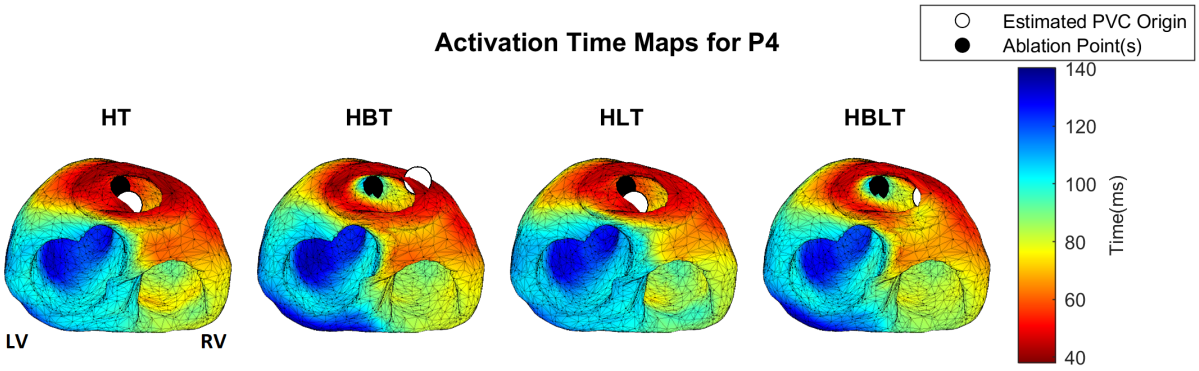

Fig. 2: AT maps of P4 for EpiEndo geometry computed for different heart-torso models, left and right ventricles are shown as LV and RV, respectively. The ablation point is located in anteroseptal right ventricular outflow tract (RVOT).

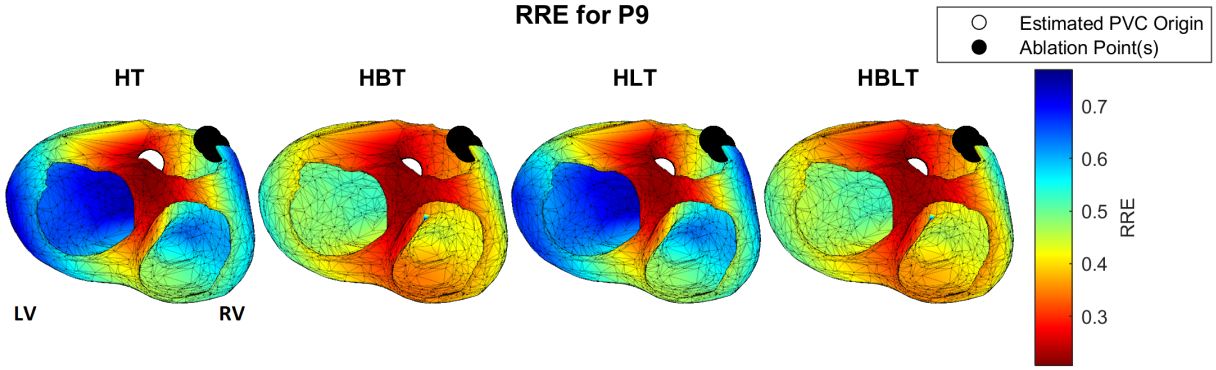

Fig. 3: RRE maps of P9 for EpiEndo geometry computed for different heart-torso models, left and right ventricles are shown as LV and RV, respectively. There are two ablation points located in the anterior RVOT.

4. Discussion

The results for the potential-based method indicate that adding only the lungs to the HT model does not produce significant performance variations, except for P5, which locates PVC origin on the opposite ventricle (LV) of all the other three models indicate (RV). In contrast, adding only the blood cavities in the homogeneous model yields a considerable improvement in outcomes for nearly all patients. It has shown the highest improvement in P1, with a significant 74% reduction in LE from 29.2 to 7.5 mm. The only suboptimal localization when blood cavities are added to the model, as in HBT and HBLT models, is for patient P4. In Fig. 2 PVC origin estimates from all models are located in the right ventricle. However, the HT and HLT models show closer proximity to the ablation points. The combination of lung and blood cavities in the torso model, along with the potential-based model, yielded favorable outcomes similar to the HBT model as can be observed in the mean error and standard deviation values in Table 1. Using the Kruskal-Wallis test, the p-values and non-simultaneous confidence intervals indicate no significant difference or improvement in model performances between HT and HBT, or the other models. The observed differences could be attributed to random variation.

The results obtained through the dipole-based method do not favor any particular torso model, as illustrated in Fig. 1. The comparison of LEs between the HBT and HLT models does not reveal any consistent pattern of improvement between themselves and with respect to

the homogeneous model, as given in Table 1. The performance of HBT is better than HLT for some patients, while for others, the opposite is observed. Similarly, the addition of both lung and blood cavity inhomogeneities to the torso model does not result in significant improvement in the dipole-based method performance to justify the use of a more complex forward model. All the PVC localizations of dipole based method discussed above are consistent with the ablation points except in P9 where the four models locate PVC origin estimate on the septal RVOT, as illustrated in Fig. 3.

5. Conclusions

The influence of the torso model complexity on the inverse localization of PVC origin computed by two different methods for the clinical data was studied. While the inclusion of blood cavities in the torso model using the potential-based method leads to slight improvements in the localization errors, the pairwise comparison tests yield non-significant p-values, suggesting no significant overall improvement across the models. The potential-based method provides information about the ATs on the whole EpiEndo surface. The dipole-based method was not affected by the complexity of the torso model. While it seems more robust, it only estimates the position of the PVC origin and does not provide full information about the activation on the EpiEndo surface.

Therefore, the inhomogeneities in the torso model should also be considered with respect to the used source/forward model.

Acknowledgements

This work was supported jointly by TÜBİTAK (grant no: 120N200) and SAS (grant no: 536057) projects, by the research grant 2/0109/22 from the VEGA Grant Agency, and the grant APVV-19-0531 from the Research and Development Agency in Slovakia. The authors would like to thank Peter Hlivak MD, PhD from the Institute for Cardiovascular Diseases, Bratislava, for assigning the ablation points on the patient's heart models.

References

[1] Bear, L. R., et al. (2015). Forward Problem of Electrocardiography: Is It Solved?. *Circulation. Arrhythmia and electrophysiology*, 8 (3), 677–684.

[2] Ramanathan, C., Rudy, Y. (2001). Electrocardiographic Imaging: II. Effect of Torso Inhomogeneities on Noninvasive Reconstruction of Epicardial Potentials, Electrograms, and Isochrones. *Journal of cardiovascular electrophysiology*, 12(2), 241–252.

[3] van Oosterom A. (2014). A Comparison of Electrocardiographic Imaging Based on Two Source Types. *Europace: European pacing, arrhythmias, and cardiac electrophysiology: journal of the working groups on cardiac pacing, arrhythmias, and cardiac cellular electrophysiology of the European Society of Cardiology*, 16 Suppl 4, iv120–iv128.

[4] Rasoolzadeh, N., Svehlikova, J., Ondrusova, B., Dogrusoz, Y. S. (2022). Variability of Premature Ventricular Contraction Localization with Respect to Source and Forward Model Variation in Clinical Data. *In Proceedings of the Computing in Cardiology Conference*, Tampere, Finland.

[5] Svehlikova, J., Pribilova, A., Zelinka, J., Ondrusova, B., Kromkova, K., Hlivak, P., Hatala, R., Tysler, M. (2022). The Importance of ECG Offset Correction for Premature Ventricular Contraction Origin Localization from Clinical Data. *Measurement Science Review*, 22(6), 246–252.

The Significance of the Torso Electrodes for Selected Cardiac Regions

[1, 2]Beata Ondrusova, [3]Peter Tino, [1]Jana Svehlikova

[1]Institute of Measurement Science, Slovak Academy of Sciences, Bratislava, Slovakia
[2]Faculty of Electrical Engineering and Information Technology, Slovak University of Technology, Bratislava, Slovakia
[3]School of Computer Science, University of Birmingham, Birmingham, UK
Email: beata.ondrusova@savba.sk

Abstract. *The significance of the torso electrodes for the solution of the inverse problem of electrocardiography using a single dipole depends on the position of the true origin of the cardiac activity, i.e., ground truth. However, the ground truth is not known in clinical practice. Therefore, we studied whether similar electrode significances would be computed for the dipole corresponding to the ground truth, the computed inverse solution, and dipoles within the 30 mm radius around the inverse solution. The significance of torso electrodes was computed for 8 datasets of patients with a known position of the ground truth. The significance assessment of torso electrodes was performed using algebraic properties of the transfer matrix computed for the given dipole position. We studied three variants of the significance assessment of torso electrodes and for two of them similar electrode significances were obtained for all positions of dipoles within 30 mm of the inverse solution. For those two variants, the most significant electrodes created a subset of 47 ± 6% and 40 ± 4% from the full set of electrodes. The results suggest that the electrode significances for a given patient can be established from the inverse solution if the inverse solution lies within 30 mm of the ground truth.*

Keywords: Inverse Problem of Electrocardiography, Body Surface Potential Mapping, Lead Selection, Transfer Matrix

1. Introduction

The solution of the inverse problem of electrocardiography is a noninvasive tool that allows localizing the origin of undesired cardiac activity using body surface potentials (BSPs) recorded from multiple sites on the torso (tens to hundreds of electrodes) and using the geometrical properties of the torso captured by CT or MRI scans [1]. The research shows that accurate localization by the inverse solution can be obtained with a subset of electrodes [2], [3].

In our research, we use a full set of electrodes placed evenly on the whole torso to localize the undesired premature ventricular contraction (PVC) by a single dipole. In our previous work, it was shown that using a subset of the most significant electrodes could improve the results and that the significance of the electrodes depends on the true position of the origin of PVC [4].

Using the full set of electrodes, we can assess the position of the PVC origin on the heart with the localization error (LE) from 20 to 30 mm. In this study, we investigated whether the subset of electrodes detected as significant is robust against dipole positioning to within 30 mm distance from the full set inverse solution.

2. Subject and Methods

The pipeline of this study is shown in Figure 1. Each step is described below.

Data

EP Solutions datasets obtained from the EDGAR database (https://www.ecg-imaging.org/edgar-database) containing BSPs recorded in 196 ± 28 torso electrodes and 3D triangulated meshes of the torso and heart of 5 patients were used. Each patient had implanted

pacemaker and the BSPs were recorded when the heart was stimulated by the pacemaker's electrode placed in the right (RV) and/or left ventricle (LV). The stimulation by the pacemaker's electrode imitates the PVC. The position of the pacemaker's electrode represents the ground truth. Eight datasets were used in total as shown in Table 1 [5].

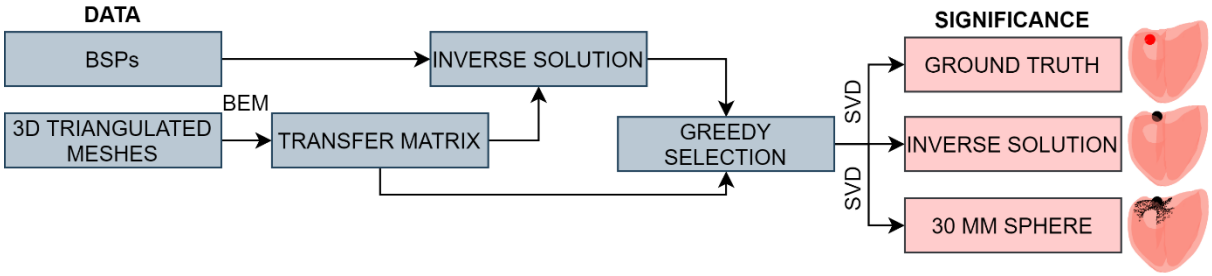

Fig.1. The pipeline of the study.

Inverse solution

Assuming a single dipole cardiac source S_C with 3 orthogonal components, the inverse problem was solved using the equation

$$S_C = T^{+}\varphi_B, \tag{1}$$

where $T \in \mathbb{R}^{N \times Number\ of\ S_C \times 3}$ is a transfer matrix and $\varphi_B \in \mathbb{R}^{N \times 30}$ are the potentials (BSPs) recorded on the torso surface at N electrodes within the first 30 ms of the cardiac cycle. A single dipole cardiac source S_C allows to identify the origin of localized events such as stimulation from the pacemaker's electrode or origin of PVC. The T^{+} denotes the pseudoinverse of the transfer matrix. The boundary element method was used to compute a transfer matrix T for a homogenous volume conductor. The inverse dipole is computed in each node of the heart model. The dipole that best describes the electrical activity was selected based on the criterion of the minimal relative residual error computed between the measured BSP and the BSP computed by the cardiac source S_C in each time instance [1]. The position of such dipole is considered as the PVC origin. The LE was calculated as the Euclidean distance between the ground truth and the dipole corresponding to the inverse solution.

Electrode Significance

The significance of the torso electrodes was assessed from the transfer matrix $T_S \in \mathbb{R}^{N \times 3}$ computed for a specific position of a single dipole on the heart model (ground truth, full-set inverse solution and other predefined positions on the heart model within 30 mm distance). Using a singular value decomposition (SVD), the transfer matrix T_S can be written as

$$T_S = U\Sigma V. \tag{2}$$

Matrices U and V are orthogonal matrices and Σ is a rectangular matrix with singular values $\sigma_1, \sigma_2, \sigma_3$ on its diagonal sorted such as $\sigma_1 > \sigma_2 > \sigma_3$. Three criteria were tested. Criterion A searches for the minimal conditional number (σ_1/σ_3). Criterion B searches for the maximal sum of the singular values $(\sigma_1 + \sigma_2 + \sigma_3)$ and criterion C searches for the maximal multiplication of the singular values $(\sigma_1 * \sigma_2 * \sigma_3)$. First, the combination of 4 electrodes that met the given criteria as best was selected from all possible combinations of 4 electrodes, e.g., 94,966,795 combinations for 220 electrodes. Then the greedy selection was implemented. In each step, one electrode (from the rest of the full set) was added to the formerly selected combination so that the chosen combination fulfilled the criterion as best as possible. The electrodes selected in the preceding steps could not be reselected and were chosen without repetition. The greedy algorithm continued execution until all available electrodes were used [4]. The significance of the electrodes was evaluated for all possible positions of PVC origin

on the heart within 30 mm radius around the position found by the inverse solution. The location patterns of the selected significant electrodes were then analyzed.

3. Results

First, the full-set inverse problem was solved, and the results are shown in Table 1. From all 8 datasets, the average LE was 24.7 ± 3.4 mm.

Further, the surrounding with 30 mm distance was defined around the full-set inverse solution so that the dipole corresponding to the ground truth was within that area. The number of predefined positions of the dipoles within the 30 mm sphere is in Table 1.

Table 1. Summary information about the datasets and the results.

Dataset	Num. of electrodes	LE full set [mm]	Num. of heart nodes	Num. of heart nodes in 30 mm distance	Ratio of significant electrodes [%]		
					A	B	C
024 RV	220	27.8	2100	161	90	45	41
024 LV	220	17.4	2100	119	99	50	39
026 RV	192	28.8	2200	116	80	35	33
026 LV	192	24.7	2200	127	100	42	37
027 RV	229	23.8	1932	236	99	52	42
033 RV	164	22.1	2011	204	74	48	47
033 LV	164	25.8	2011	165	100	46	37
036 RV	177	27.2	1339	263	100	55	42

Then, for each position in the surrounding, the greedy selection of the torso electrodes was implemented. Figure 2 shows the significance of torso electrodes estimated for two dipoles positions (ground truth and the full-set inverse solution) for 024 RV dataset. The initial configuration of the 4 most significant electrodes is shown in black, followed by additional significant electrodes in red, and finally, the least significant in blue spectra. For criteria

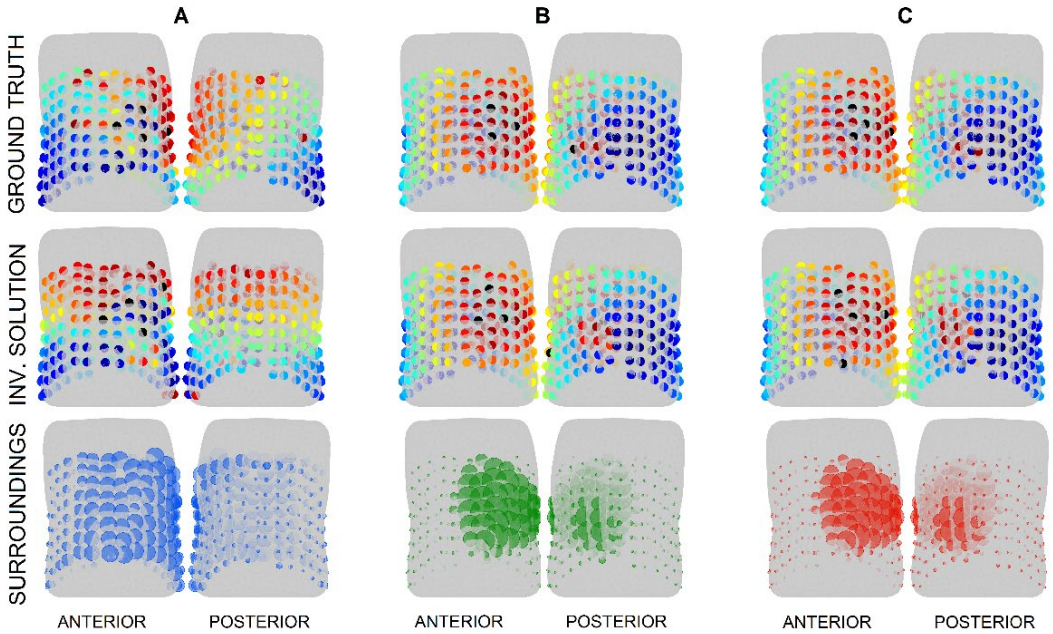

Fig. 2. The significance of the electrodes according to the criteria A, B, C for the dipole corresponding to ground truth (upper panel), the full-set inverse solution (middle panel) and the occurrence of the electrodes sorted by the given criterion (first 15%) for all dipoles within 30 mm distance from the full-set solution (lower panel) for 024 RV dataset.

ISBN 978-80-972629-6-9

B and C, the areas with the most significant electrodes were similar for both dipoles, even if the Euclidean distance of those two dipoles was 27.8 mm.

The electrodes were sorted according to their significance for each position of the dipole in the 30 mm diameter around the inverse solution. Figure 2 (lower panel) shows the positions of the 15% most significant electrodes for all 161 dipoles in the surroundings for 024 RV dataset. The size of the electrode corresponds to its occurrence for all dipoles. For criterion A, 90% of the full-set of electrodes occurred within 15% of the most significant electrodes. For criteria B and C fewer number of electrodes (45% and 41% of all electrodes) occurred within 15% of the most significant electrodes. For 024 RV, the most significant electrodes were primarily placed anteriorly in the left lateral plane. The results for all datasets are summarized in Table 1, last column.

4. Discussion and Conclusions

The significance of the torso electrodes with respect to the inverse localization of the PVC origin using a single dipole was studied for a single dipole position corresponding to the ground truth, inverse solution and for the dipoles not farther than 30 mm from the inverse solution. Three criteria (A-C) derived from the singular values of the transfer matrix were tested. As shown in Table 1, 92.8 ± 9.7% of all torso electrodes were identified among the 15% of the most significant electrodes for criterion A while 47 ± 6% and 40 ± 4% for criteria B and C. Criteria B and C have similar mathematical interpretation and do not omit the second singular value. The results suggest that criteria B and C identify the significance of electrodes given our task better than criterion A because the most significant electrodes remain localized in specific areas and are not scattered throughout the whole chest. This study confirmed that in the future the significance of the torso electrodes could be computed for the dipole corresponding to the full-set inverse solution. The outputs of this study will be consequently used in a two-step inverse solution assuming a single dipole cardiac source. The obtained subset of the most significant electrodes could be used for the second-step inverse computation leading to a more accurate inverse solution.

Acknowledgements

This work was supported by the VEGA Grant Agency under grant number 2/0109/22, by the Slovak Research and Development Agency under grant number APVV-19-0531 and by the Slovak Academy of Sciences under grant number APP0323.

References

[1] J. Svehlikova, M. Teplan, and M. Tysler, “Geometrical constraint of sources in noninvasive localization of premature ventricular contractions,” *J. Electrocardiol.*, vol. 51, no. 3, pp. 370–377, 2018.

[2] F. Gharbalchi No *et al.*, “Reduced leadset selection and performance evaluation in the inverse problem of electrocardiography for reconstructing the ventricularly paced electrograms,” *J. Electrocardiol.*, vol. 60, pp. 44–53, 2020.

[3] L. Parreira *et al.*, “Electrocardiographic imaging (ECGI): What is the minimal number of leads needed to obtain a good spatial resolution?,” *J. Electrocardiol.*, vol. 62, pp. 86–93, Sep. 2020.

[4] B. Ondrusova *et al.*, “Model-Based Relevance of Measuring Electrodes for the Inverse Solution with a Single Dipole,” *Comput. Cardiol. (2010).*, vol. 49, pp. 3–6, 2022.

[5] D. Potyagaylo *et al.*, “ECG adapted fastest route algorithm to localize the ectopic excitation origin in CRT patients,” *Front. Physiol.*, vol. 10, no. MAR, pp. 1–13, 2019.

Electrocardiographic Body Surface Isochrone Maps with Threshold Potential – Variability in Young Healthy Men

Katarína Kozlíková

Institute of Medical Physics, Biophysics, Informatics and Telemedicine,
Faculty of Medicine, Comenius University in Bratislava, Bratislava, Slovak Republic
Email: katarina.kozlikova@fmed.uniba.sk

Abstract. *Body surface isochrone maps with a threshold potential of 0.05 mV were constructed and analysed in 15 healthy young men. These maps are capable of displaying the activation sequence of the heart on the surface of the body. The activation was found to start always on the anterior chest surface and mainly in its upper half. It ended prevailingly on the back chest and mainly in its upper half. The spread of activation (activation sequence) can be regarded as counter-clockwise, covering most of the chest surface area.*

Keywords: Electrocardiography, Isochrone Mapping, Heart Activation

1. Introduction

The electrical activity of the heart can be recorded and analysed in different ways. So far, the full available information achievable in a non-invasive way is possible only by using multi-lead recordings – body surface potential mapping – when a large number of electrodes is distributed over the whole chest, including back. In this case, instead of processing individual curves, images resembling geographical maps are displayed and analysed. These maps can display the distribution of potentials in a selected time step (isopotential maps), areas under the electrocardiographic curves (isointegral maps), or time values that have been pre-defined in connection with some value of the potential on the surface of the chest (isochrone maps).

Based on the definition of the displayed time value, several forms of isochrone maps have been published until now. They can represent the durations of different parts of the electrocardiographic curve, such as the durations of the R wave or the Q wave. They can display the time from the beginning of the QRS complex to the time of the R wave peak or to the time of the minimum of the first derivative (both are often called ventricular activation time maps) [1, 2]. They can display time instants in which the potential exceeded a previously set potential value (isochrone maps with threshold potential) [3].

The goal of this study was to analyse the body surface isochrone maps with a threshold potential of 0.05 mV in young adult volunteers when using the time normalisation of the QRS complex.

2. Subject and Methods

Fifteen men without any known cardiovascular diseases aged (18.8 ± 0.5) years were examined. Unipolar electrocardiograms for body surface potential mapping were registered using the limited 24-lead system after Barr, based on a grid of 10 rows and 15 columns implemented in the mapping system ProCardio as described previously [4]. All data were recorded in supine position during normal expiration at sampling rate 500 Hz and filtered using a Pipberger filter. Linear baselines (zero isoelectric lines) were taken through TP segments in each electrocardiogram. The onset and offset of the QRS complex were established manually from the root mean square signal as the time instants when the signal approached the baseline (around 0.01 mV – 0.02 mV in the root mean square signal) and stopped to decrease for at least three milliseconds when reading the values from the middle of the QRS complex.

Body surface isochrone maps with threshold potential 0.05 mV were constructed showing the first time instant in which the potential on the chest surface exceeded the pre-set threshold value. For time normalization, the QRS complex duration of each subject was divided into 20 equidistant parts. The activation sequence represented by the time steps (21 in total) was analysed in each subject, as well as in the group mean isochrone map.

3. Results

The mean duration of the QRS complex was (89 ± 3) ms. The mean time between two subsequent time steps was (4.5 ± 0.2) ms. The potential values during the QRS complex on the chest ranged from -4.3 mV to 2.8 mV.

When evaluating maps of individual subjects, the very first appearance of the threshold potential 0.05 mV was found in the first time step, that is, at the very beginning of the QRS complex, in 8 of 15 subjects (Fig. 1, bottom right). This area covered 34 % of the anterior chest (all cases together), predominantly in the upper right part from the right midaxillary line to the right parasternal area, partially covering the upper right abdomen, and over the upper left sternum where it differed in shape and position (although within the large one described above), was much smaller and ranged from 1 % to 15 % (7 ± 5) % of the anterior chest surface.

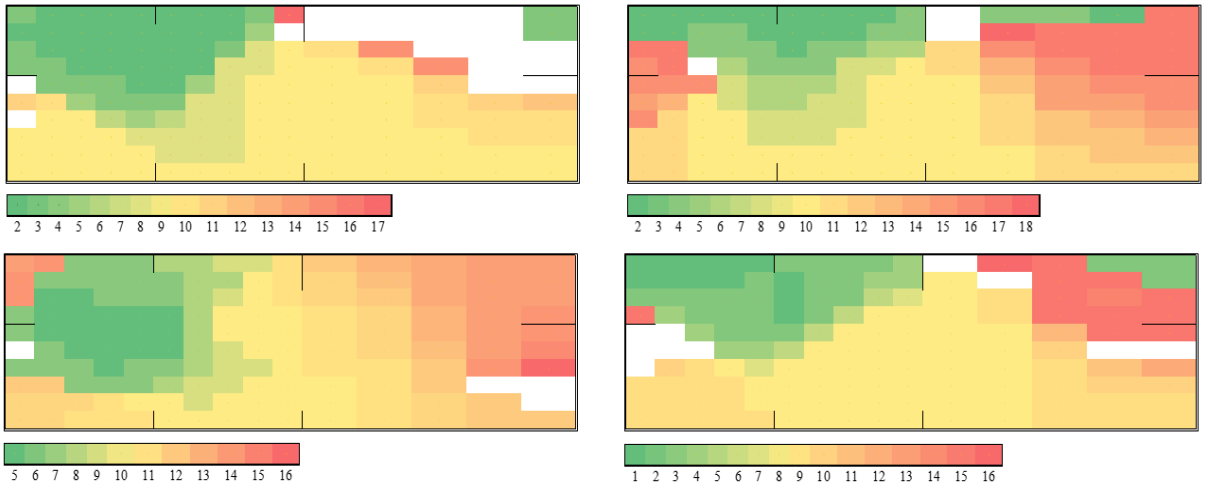

Fig. 1. Examples of QRS body surface isochrone maps with threshold potential of 0.05 mV of 4 different subjects. Each rectangle represents the chest surface enrolled into plane along the midaxillary line. The left half of the rectangle corresponds to the anterior chest, and the right half to the back. The upper edge of the map is at the level of the jugular fossa, the lower edge at the level of the navel. The short horizontal bars indicate the position of the 4th intercostal space. The short vertical bars (from left to right) indicate the positions of the sternum and the left midaxillary line, respectively. The darkest green colour represents the first time step displayed on each map, and the darkest red colour represents the last time step as shown on the scales below each map. White areas represent the parts of the chest where potential remained below the threshold value during the entire QRS complex.

The first appearance of the threshold potential 0.05 mV in the second time step, that is, on average 4.5 ms after the beginning of the QRS complex, was in 4 of 15 subjects (Fig. 1, upper row). This area covered 39 % of the anterior chest (all 4 cases together); in 3 cases starting in the midclavicular area, in 1 case at the level of the 4th – 5th intercostal space. Its size ranged from 14 % to 28 % (21 ± 6) % of the anterior chest surface.

In the remaining 3 subjects, the first appearance of the threshold potential of 0.05 mV was in the 5th and / or 6th time step, that is, at the end of the first quarter of the duration of the QRS complex (Fig. 1, bottom left). It always occurred in the upper half of the anterior chest and

ISBN 978-80-972629-6-9

partially around the right shoulder. Its size ranged from 18 % to 35 % (27 ± 8) % of the anterior chest surface. All "starting" areas are summarised and shown in Fig. 2 (left map).

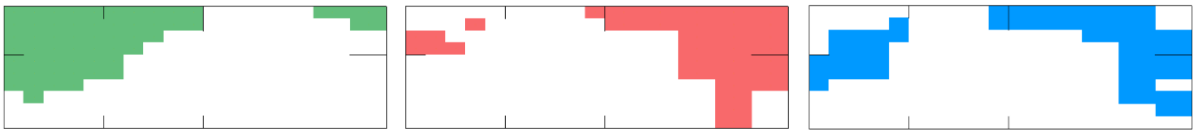

Fig. 2. Areas on the chest surface, where the activation started (left, green areas), ended (middle, red areas), and where the threshold potential was not reached (right, blue areas).

The threshold potential 0.05 mV appeared at latest mainly in the 16th time step (from 13th to 18th), that is 75 % of the QRS duration. These areas, with an overall size of 32 % of the posterior chest, covered the upper back, mainly around the right shoulder slightly extending to the anterior chest, and on the right side of the upper spine (Fig. 1). When considering only the single last time step of the QRS complex, the areas were the smaller, the later they were recorded. Their size in individual subjects represented from 2 % to 22 % (5 ± 6) % of the posterior chest surface (in 10 of 15 subjects it was only 1 grid point).

When considering the last two adjacent time steps, the overall area slightly extended (56 % of the posterior chest), became more compact, and covered the entire right upper back and the area to the right along the entire spine. Additionally, it was slightly extended to the anterior chest. Their size in individual subjects represented from 2 % to 38 % (18 ± 11) % of the posterior chest surface. All "ending" areas are summarised and shown in Fig. 2 (middle map).

In 14 of 15 subjects, there was at least one smaller or larger area on the chest where the potential remained below 0.05 mV throughout the QRS complex. This concerned the back of the left shoulder (up to 8 subjects), the right anterior chest (up to 5 subjects), and the right back (Fig. 2, right map).

The activation of the heart, as represented by the sequence of time steps during the QRS complex, always started in the anterior chest (Fig. 2). When in its upper part, it spread downward, partially rightwards, but prevailingly leftwards. When reaching the left lower back, it turned upward to the right shoulder and ended mainly on the right upper back. When the activation started in the middle right anterior chest, it spread prevailingly leftward to the back, where it continued in a similar way as in previous cases except of one subject where the activation sequence on the back was orientated more downward (Fig. 1 left bottom).

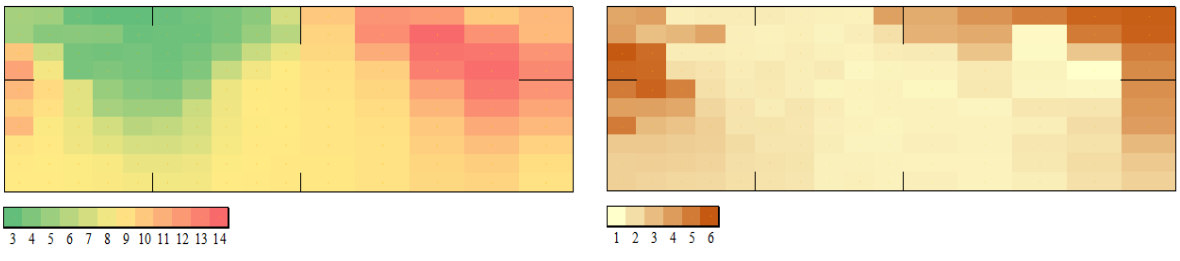

Fig. 3. The group mean QRS body surface isochrone maps with threshold potential 0.05 mV (left – map description as in Fig. 1) and distribution of corresponding standard deviations (right). On the standard deviation map, the darker the area, the greater the variability in time values as expressed in form of time steps (scale below the map).

On the other hand, a kind of activation stop was found in all subjects on the right side of the chest, anterior or posterior. This can also be seen on the mean group map (Fig. 3, left map). The overlap of areas where the activation started and ended in individual subjects is expressed in the map that represents the standard deviations of the time steps (Fig. 3, right map). They varied

from one time step (corresponding to 4.5 ms) on the right middle back to one or two time steps (9 ms) over large area on the left chest (anterior and posterior) up to slightly more than six time steps (27 ms) on the right chest side.

4. Discussion

Body surface isochrone maps with threshold potential can be regarded as an inverse mathematical function of isopotential maps. In principle, they can be constructed for different potential thresholds. In this study, the value of 0.05 mV was selected. In a 12-lead electrocardiogram, this value represents the amplitude of a half-millimetre wave when using the standard voltage calibration of 1 mV / 10 mm. Therefore, it is low enough to display either smaller or more distant activation fronts in the heart but should be high enough to exceed the unavoidable noise of recorded signals. Although the usefulness of body surface isochrone maps with other threshold potential values was published earlier [2, 4], maps of healthy subjects for the value of 0.05 mV were not yet analysed.

5. Conclusions

The beginning of the heart activation in the body surface isochrone maps with the threshold potential of 0.50 mV was always displayed on the anterior chest surface and mainly in its upper half. The later the activation started, the larger the area on the chest it covered and was the more shifted upward and leftward. Regardless of the area and the first time instant, the activation sequence always emerged within the first quarter of the QRS duration.

The end of heart activation in these maps was displayed mainly in the back chest and mainly in its upper half. The later the activation ended, the smaller the area on the chest it covered. It always ended around the last quarter of the QRS duration.

The spread of activation (activation sequence) can be regarded as counter-clockwise, covering most of the chest surface area.

Acknowledgements

The study was supported by the grant KEGA 040UK-4/2022 provided by the Ministry of Education, Science, Research and Sport of the Slovak Republic.

References

[1] Hanashima, K., Ikeda, K., Yamaki, M., Tsuiki, K., Yasui, S. (1988). Clinical-significance of body-surface isochrone maps for predicting ventricular arrhythmias in patients with previous myocardial-infarction. *Japanese Circulation Journal*, 52 (3), 203–210.

[2] Laszki-Szczachor, K., Polak-Jonkisz, D., Zwolinska, D., Makulska, I., Rehan, L., Sobieszczanska, M. (2015). Effects of hemodialysis on ventricular activation time in children with end-stage renal disease. *Hemodialysis International*, 19(1), 115–123.

[3] Kozlíková, K., Hulín, I., Kneppo, P., Polakovič, P. (1992). Body surface isochrone maps with threshold potential in young normal subjects. In *Electrocardiology ´91.* World Scientific, 129–134.

[4] Kozlíková, K., Trnka, M. (2019). Varied onset of heart ventricular depolarization in different age groups of healthy volunteers. *Physiological Research,* 68 (S4), S389–S397.

[5] Kozlíková, K., Hulín, I., Kneppo, P., Tyšler, M., Murín, J., Bulas, J., Bakošová, M., Sapáková, E. (1994). Môžu izochrónne mapy komorovej aktivácie merané na povrchu tela odhaliť infarktové ložisko? *Lékař a technika.* 25(3), 51–56. (in Slovak)

Parameters of Body Surface Potential Maps Reflecting the Dynamics of Ventricular Activation

[1,2]Lukáš Zelieska, [3]Michal Šašov, [3]Peter Hanák, [1]Milan Tyšler

[1]Institute of Measurement Science, Slovak Academy of Sciences, Bratislava, Slovakia
[2] Faculty of Electrical Engineering and Information Technology, Slovak University of Technology, Bratislava, Slovakia
[3]The National Institute for Cardiovascular Diseases, Bratislava, Slovakia
Email: lukas.zelieska@savba.sk

Abstract. *Cardiac resynchronization therapy (CRT) is a medical intervention that involves the use of a specific type of pacemaker to synchronize the ventricular contractions and enhance the pumping function of the failing heart. This study was conducted to investigate specific parameters obtained from body surface potential mapping (BSPM) during spontaneous heart activity that could be used to predict the outcome of CRT and identify possible CRT responders and non-responders. Data from 13 healthy volunteers and 13 patients were collected using ProCardio 8 ECG measuring system with 128 chest electrodes. Selected published parameters based on activation times (AT), ventricular activation times (VAT) and global activation time (GAT) measured on body surface were calculated. A Comparison of the parameters in the groups of healthy subjects and patients showed that most parameters have increased mean values for patients. Increased mean values of the three parameters based on ECG signals mainly reflecting area of septum and right ventricle. The differences in two of them, between responders and non-responders, were found to be statistically significant on significance level $p < 0.05$, which makes them potential indicators of responders and non-responders. The study suggests that selected BSPM-based parameters obtained during spontaneous rhythm have the potential to predict CRT outcome and to distinguish CRT responders and non-responders.*

Keywords: Body Surface Potential Mapping, Electrocardiography, BSPM Derived Parameters, Cardiac Resynchronization Therapy

1. Introduction

Heart failure (HF) is a condition in which the heart is unable to pump enough blood to meet the needs of the body. Currently, HF represents a significant and growing public health problem [1]. HF can occur due to various anatomical or functional disorders that impair the ventricle's ability to effectively fill or eject the blood. Patients who suffer from HF and experience reduced cardiac function often exhibit discoordinate contractions caused by delayed or missing electrical activation. This phenomenon, referred to as dyssynchrony, exacerbates systolic function impairment and chamber inefficiency, leading to increased morbidity and mortality rates.

A medical procedure called cardiac resynchronization therapy (CRT) is utilized to enhance the synchrony of activation of the ventricles and pumping function of the heart. During the therapy, implanted CRT devices with electrodes in the right atrium and both ventricles, which serve to properly timed stimulation of the heart, are used.

The essential criteria for the patient indication for CRT are based on standard 12-lead ECG and echocardiographic measurements. They include the ECG pattern of the left bundle branch block (LBBB), prolongation of the QRS time interval, and left ventricular ejection fraction (LVEF) less than 35%. Restoring left ventricular (LV) electrical and mechanical synchrony through CRT should result in improvement of these parameters [2].

Current research shows that surface ECG potentials recorded by a larger number of electrodes might help in predicting CRT outcomes, in individualised optimisation of CRT device programming and in guiding the LV electrode placement. From the body surface potential

ISBN 978-80-972629-6-9

mapping (BSPM), one would like to extract such BSPM parameters that could serve as suitable indicators of possible responders and measures of the ventricular electrical dyssynchrony. BSPM-based approaches have been studied in numerous clinical studies to develop reliable ventricular activation related parameters for evaluating the CRT effects [3].

The objective of this study is to investigate the parameters obtained from BSPM and to identify which of them could be used to help to predict possible CRT responders and non-responders before the application of the therapy.

2. Subject and Methods

Selected published parameters, derived from BSPM or standard 12-lead ECG, that can be related to local electrical activation times on the heart, were examined. We searched for parameters from BSPM before CRT application that could be used to distinguish responders and non-responders. An overview of the examined parameters is shown in Table 1.

Data to calculate these ventricular activation related BSPM parameters were obtained from 13 healthy volunteers and 13 patients (9 responders, 4 non-responders to CRT). Data acquisition was made using the ProCardio 8 ECG measuring system with 128 chest electrodes. Patient data were acquired in cooperation with The National Institute for Cardiovascular Diseases, Bratislava. All ECG data were processed using standard procedures including filtration, correction of baseline and averaging.

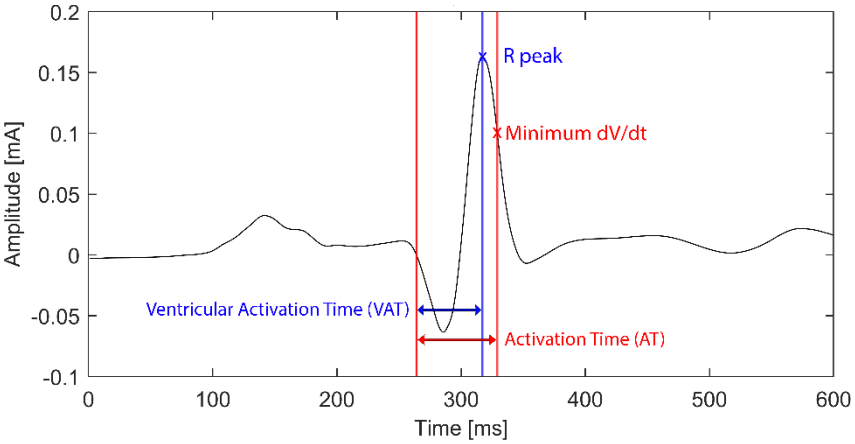

Fig. 1. The duration of AT with marked minimum dV/dt (steepest negative slope of the QRS complex) and VAT with marked R peak.

To obtain BSPM related parameters, first the activation time (AT), ventricular activation time (VAT) and global activation time (GAT) were calculated. In each surface ECG signal, the AT is defined as the time between the QRS complex onset and the steepest negative slope of the QRS complex (Fig. 1.) [4], and the VAT is defined as the time between the QRS complex onset and the R peak, representing the QR interval in the surface ECG (Fig. 1.) [5].

Table 1. Parameters of Ventricular Activation derived from ECG signals obtained during BSPM.

Parameters derived from AT	**Parameter**	**Calculation**
Total Activation Time	TAT	average AT value from all leads
Standard Deviation of Activation Times	SDAT	SD of AT values from all leads
Average Right Thorax Activation Time	RTAT	average AT value from leads 1 –32, 97–128
Average Left Thorax Activation Time	LTAT	average AT value from leads 33 – 96
Maximum of Activation Time	ATmax	maximum AT value from all leads
Minimum of Activation Time	ATmin	minimum AT value from all leads
Left Ventricle Mean Activation Time	mLV	average AT value from leads 57 – 112
Right Ventricle Mean Activation Time	mRV	average AT value from leads 1 – 32
Anterior Septal Area Mean Activation Time	mAS	average AT value from leads 33 – 56
Parameters derived from VAT		
Ventricular Activation Time in V1 – V6	VAT V1 – V6	average of AT from leads 27, 35, 36, 45, 53, 61
Ventricular Activation Time in V1, V2, V3, V4, V5, V6	VAT V1, …, VAT V6	VAT for leads V1 (27), V2 (35), V3 (36), V4 (45), V5 (53), V6 (61) separately

ISBN 978-80-972629-6-9

Based on the data defined by the Selvester diagrams reported by Medvegy et al. [6], we also defined three distinct surface areas related to different parts of the ventricular myocardium (right ventricle – RV, intermediate – AS and left ventricle – LV). Mean AT values from electrodes in these areas were calculated as mRV, mAS and mLV. Finally, GAT is defined as the mean value from those three areas.

3. Results

By comparing the BSPM-derived parameters of patients (responders and non-responders) and healthy subjects (Fig. 2.), it can be seen that most parameters have increased mean values for patients. For ATmin the mean values are similar in all three groups. The parameters VAT V3, mRV and mAS have increased mean values only in non-responders.

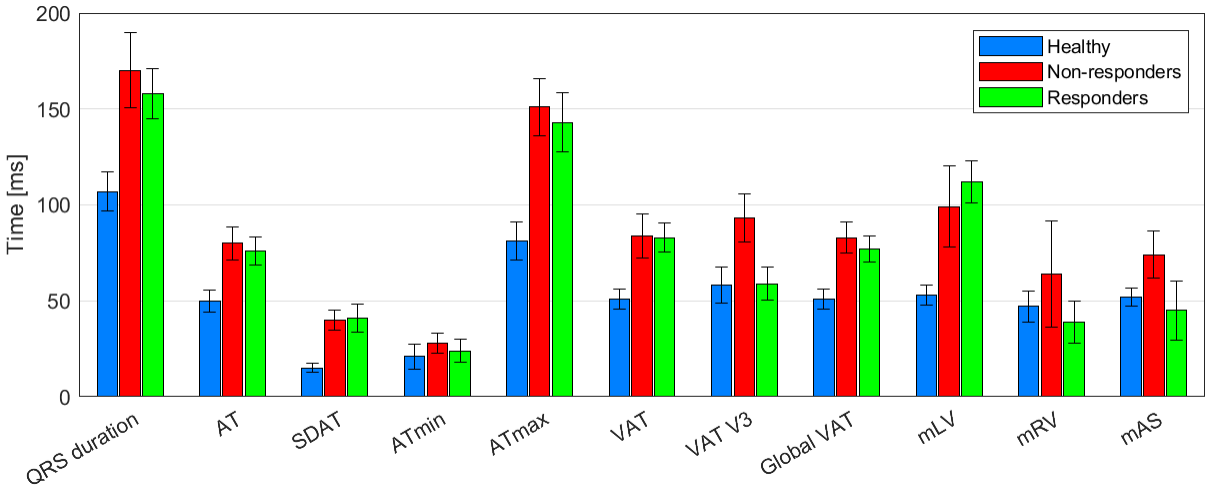

Fig. 2. The comparison of selected parameters of healthy (blue), responders (green) and non-responders (red). The error bars represent the standard deviation of the dataset.

The values of VAT V3 and mAS in responders and non-reponders can not be considered equal (One-way ANOVA test, significance level $p < 0.05$), so they could be used for distinguishing of responders and non-responders. As shown in Fig. 3., the values of non-responders for the VAT V3 parameter are above 76 ms and above 60 ms for the mAS. Both parameters are related to the potentials measured on the middle anterior chest reflecting prevalently the cardiac electrical activity in the septal area.

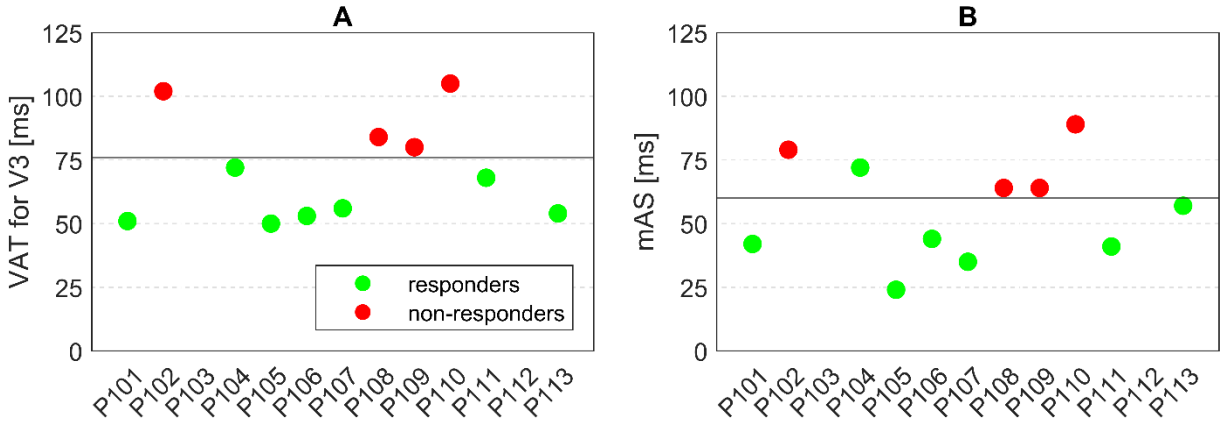

Fig. 3. Parameters VAT V3 and mAS from spontaneous rhythm in patients. A – VAT V3 values, B – mAS values. The threshold value (black horizontal line) for VAT V3 is 76 ms and 60 ms for mAS. The patients P103 and P112 do not have a spontaneous rhythm, as they underwent the AV node ablation procedure.

To exploit the potential of multi-lead ECG, we tried to create modified VAT V3 parameters by adding different combinations of surrounding leads to lead 36. However, it was not possible to distinguish responders from non-responders using this modified VAT V3 parameters.

ISBN 978-80-972629-6-9

4. Discussion and Conclusions

BSPM is a projection of the electrical activity of the heart onto the surface of the human body. Physiological interpretation of parameters obtained from BSPM and their relation to local electrical events in the heart is not trivial because the events are reflected in ECG leads with different weights, depending on their relative position and composition of the body volume conductor.

Our results suggest that using the VAT V3 and mAS parameters might be useful in predicting CRT outcome in individual patients based on BSPM obtained during their spontaneous cardiac activity. The electrical activity, mainly in the right ventricular and septal area reflected in potentials on corresponding parts of the body surface, may be associated with the parameters that can differentiate the patients. Attempted combined parameters calculated from adjacent leads in the vicinity of lead V3 did not help to improve the accuracy of the CRT outcome prediction.

The main limitation of this work is the small group of patients (9 responders, 4 non-responders to CRT). A larger number of responders and non-responders is needed to investigate the behavior of BSPM-derived parameters profoundly.

Other investigated parameters do not seem to be applicable for the differentiation, as the differences are statistically insignificant in our limited number of patients. It might be useful to investigate them on a larger dataset.

Considering the achieved results, it seems that some of the BSPM-derived parameters might be helpful in assessing the degree of ventricular dyssynchrony and predicting the CRT outcome. Other BSPM-derived parameters or their combinations could prove useful for this purpose if larger datasets were available.

Acknowledgements

This work was supported by APVV-19-0531 from the APVV agency and by the VEGA Grant Agency under grant number 2/0109/22. We would like to thank colleagues Jana Švehlíková, Beáta Ondrušová and Ján Zelinka for their help with data acquisition and processing.

References

[1] James, S. L. et al. (2018). Global, regional, and national incidence, prevalence, and years lived with disability for 354 diseases and injuries for 195 countries and territories, 1990 –2017: a systematic analysis for the Global Burden of Disease Study 2017. *The Lancet*, 392(10159),1789-858

[2] Prinzen, F. W., Vernooy, K., Auricchio, A. (2013). Cardiac resynchronization therapy: state-of-the-art of current applications, guidelines, ongoing trials, and areas of controversy. *Circulation*, 128 (22), 2407-2418.

[3] Sedova, K., Repin, K., Donin, G., Van Dam, P., Kautyner, J. (2021). Clinical utility of body surface potential mapping in CRT patients. *Arrhythmia & Electrophysiology Review*, 10 (2), 113-119.

[4] Gage, R. M., et al. (2017). Changes in electrical dyssynchrony by body surface mapping predict left ventricular remodeling in patients with cardiac resynchronization therapy. *Heart Rhythm*., 14 (3), 392-399.

[5] Patel, V. B, Preedz, V. R. (2016). *Biomarkers in Cardiovascular Disease.* Dordrecht: Springer Netherlands.

[6] Medvegy, M., et. al. (2002). Body surface potential mapping: Historical ackground, present possibilities, diagnostic challenges. *Ann Noninvasive Electrocardiol*, 7(2), 139-151.

Theoretical Problems of Measurement
Posters I

ISBN 978-80-972629-6-9

Straight-Line Errors-In-Variables Calibration Model Versus Linear Regression Model

[1]Gejza Wimmer, [2]Viktor Witkovský

[1]Mathematical Institute, Slovak Academy of Sciences, Bratislava, Slovak Republic,
[2]Institute of Measurement Science, Slovak Academy of Sciences, Bratislava, Slovak Republic
Email: wimmer@mat.savba.sk

Abstract. *The aim of this article is to determine the circumstances under which the errors-in-variables regression model, utilized as a straight-line calibration model with measurement errors in both the stimulus and response variables, can be deemed a traditional linear regression model. Additionally, we strive to establish the guidelines for utilizing the locally best linear unbiased estimators (BLUEs) in a secure and optimal manner to estimate the model parameters, their covariance matrix, and confidence intervals for all feasible linear parameter combinations such that these estimators ensure reliable inference.*

Keywords: Linear Calibration Model, Test of Model Linearity, Statistical Inferences in Linearized Model

1. Introduction

Calibration is a critical aspect of measurement science that finds applications in various industrial sectors and services. It involves determining the relationship between the true, error-free values of measured quantities, which are expressed in the units of the measuring instruments used. The process of modeling measurement and subsequent uncertainty analysis is extensively described in basic metrological documents and guidelines, such as JCGM 100:2008 (GUM) [1] and its supplements JCGM 101:2008 (GUM S1) [2] and JCGM 102:2011 (GUM S2) [3]. From a metrological point of view, the straight-line calibration is covered in ISO technical specification 28037:2010 [4].

In this article, we introduce a calibration model that can be represented as a straight-line errors-in-variables (EIV) regression model. From a statistical perspective, this model can be seen as either a nonlinear regression model or a linear regression model with nonlinear parameter constraints. Our primary objective is to determine the conditions under which this model can be considered a conventional linear regression model. This will enable us to estimate the model parameters using the Best Linear Unbiased Estimators (BLUEs) together with the covariance matrix, and under additional normality assumptions, obtain the confidence intervals for any feasible linear combination of parameters. Importantly, the resulting interval estimators ensure reliable statistical inference under the specified conditions.

2. Measurement model for linear comparative calibration

We aim to determine a linear calibration function that expresses the error-free values of response quantities in the units of the measuring instrument $\mathcal{Y}$ as a linear function of the error-free values of stimulus quantities in the units of the measuring instrument $\mathcal{X}$. To simplify the mathematical expressions, we use vector-matrix notation in our investigation. Our analysis is based on the model representing direct measurements in the calibration experiment:

$$\begin{aligned} \boldsymbol{X} &= \boldsymbol{\mu} + \boldsymbol{\epsilon}_x, \\ \boldsymbol{Y} &= \boldsymbol{\nu} + \boldsymbol{\epsilon}_y, \end{aligned} \tag{1}$$

ISBN 978-80-972629-6-9

where $\boldsymbol{X} = (X_1, \ldots, X_m)'$ and $\boldsymbol{Y} = (Y_1, \ldots, Y_m)'$ are random vectors representing the measurements of m objects by the devices $\mathcal{X}$ and $\mathcal{Y}$, respectively. The vectors $\boldsymbol{\mu} = (\mu_1, \ldots, \mu_m)'$ and $\boldsymbol{\nu} = (\nu_1, \ldots, \nu_m)'$ represent the true but unknown values of the measurands expressed in the units of the measuring devices $\mathcal{X}$ and $\mathcal{Y}$, respectively, and are related by the equation

$$\boldsymbol{\nu} = a\mathbf{1} + b\boldsymbol{\mu}, \tag{2}$$

where $\mathbf{1} = (1, \ldots, 1)'$. The parameters a and b represent the intercept and slope, respectively, of the linear calibration function, and are of primary interest. It is important to note that $\boldsymbol{\mu}$, a, and b comprise the complete set of unknown parameters for the straight-line calibration model, and that the relation (2) is nonlinear with respect to these parameters. Furthermore, it is assumed that the measurement errors $\boldsymbol{\epsilon}_x$ and $\boldsymbol{\epsilon}_y$ are zero-mean random vectors that follow a normal distribution. The straight-line EIV calibration model (1) and (2) can be considered as either a linear regression model with nonlinear constraints on its parameters or a nonlinear regression model, that can be expressed as:

$$\begin{pmatrix} \boldsymbol{X} \\ \boldsymbol{Y} \end{pmatrix} \sim N\left(\boldsymbol{f}(\boldsymbol{\mu}, a, b); \boldsymbol{\Sigma}\right), \tag{3}$$

where the expectation and covariance matrix of the observation vector are:

$$\mathcal{E}\begin{pmatrix} \boldsymbol{X} \\ \boldsymbol{Y} \end{pmatrix} = \boldsymbol{f}(\boldsymbol{\mu}, a, b) = \begin{pmatrix} \boldsymbol{\mu} \\ a\mathbf{1} + b\boldsymbol{\mu} \end{pmatrix} \quad \text{and} \quad \mathrm{Cov}\begin{pmatrix} \boldsymbol{X} \\ \boldsymbol{Y} \end{pmatrix} = \boldsymbol{\Sigma} = \begin{pmatrix} \boldsymbol{\Sigma}x & \boldsymbol{\Sigma}xy \\ \boldsymbol{\Sigma}yx & \boldsymbol{\Sigma}y \end{pmatrix}, \tag{4}$$

respectively, with a known positive definite matrix $\boldsymbol{\Sigma}$.

Let $\boldsymbol{\mu}_0$, a_0, and b_0 be appropriately chosen prior values for the model parameters. By denoting $\boldsymbol{\mu} = \boldsymbol{\mu}_0 + \delta\boldsymbol{\mu}$, $a = a_0 + \delta a$, $b = b_0 + \delta b$, and applying the Taylor series expansion, we obtain

$$\boldsymbol{f}(\boldsymbol{\mu}, a, b) = \boldsymbol{f}_0 + \boldsymbol{F}_0(\delta\boldsymbol{\mu}', \delta a, \delta b)' + \frac{1}{2}\boldsymbol{\kappa}_{(\delta\boldsymbol{\mu}, \delta a, \delta b)}, \tag{5}$$

where $\boldsymbol{f}_0 = \boldsymbol{f}(\boldsymbol{\mu}_0, a_0, b_0)$, $\boldsymbol{F}_0 = \boldsymbol{F}(\boldsymbol{\mu}_0, a_0, b_0) = \frac{\partial \boldsymbol{f}(\boldsymbol{\mu}, a, b)}{\partial(\boldsymbol{\mu}', a, b)}\Big|_{(\boldsymbol{\mu}', a, b)' = (\boldsymbol{\mu}_0', a_0, b_0)'}$ is the Jacobian of $\boldsymbol{f}$, and

$$\boldsymbol{\kappa}_{(\delta\boldsymbol{\mu}, \delta a, \delta b)} = \Big((\delta\boldsymbol{\mu}', \delta a, \delta b)\boldsymbol{H}_1\big(\delta\boldsymbol{\mu}\ \delta a\ \delta b\big), \ldots, (\delta\boldsymbol{\mu}', \delta a, \delta b)\boldsymbol{H}_{2m}\big(\delta\boldsymbol{\mu}\ \delta a\ \delta b\big)\Big)', \tag{6}$$

with

$$\boldsymbol{H}_1 = \cdots = \boldsymbol{H}_m = \mathbf{0}_{m+2,m+2}, \quad \boldsymbol{H}_{m+1} = \begin{pmatrix} \mathbf{0}_{m,m} & \mathbf{0} & \boldsymbol{e}_1 \\ \mathbf{0}' & 0 & 0 \\ \boldsymbol{e}_1' & 0 & 0 \end{pmatrix}, \ldots, \boldsymbol{H}_{2m} = \begin{pmatrix} \mathbf{0}_{m,m} & \mathbf{0} & \boldsymbol{e}_m \\ \mathbf{0}' & 0 & 0 \\ \boldsymbol{e}_m' & 0 & 0 \end{pmatrix}, \tag{7}$$

where $\mathbf{0}_{m,m}$ is $(m \times m)$-matrix of zeros, $\mathbf{0}$ is $(m \times 1)$-vector of zeros, and $\boldsymbol{e}_i$ denotes the m-dimensional i-th unit vector, $\boldsymbol{e}_i = (0, \ldots, 0, 1, 0, \ldots, 0)'$. In particular, we get

$$\boldsymbol{f}_0 = \begin{pmatrix} \boldsymbol{\mu}_0 \\ a_0\mathbf{1} + b_0\boldsymbol{\mu}_0 \end{pmatrix}, \quad \boldsymbol{F}_0 = \begin{pmatrix} \boldsymbol{I}_{m,m} & \mathbf{0}_{m,1} & \mathbf{0}_{m,1} \\ b_0\boldsymbol{I}_{m,m} & \mathbf{1}_{m,1} & \boldsymbol{\mu}_0 \end{pmatrix}, \quad \frac{1}{2}\boldsymbol{\kappa}_{(\delta\boldsymbol{\mu}, \delta a, \delta b)} = \begin{pmatrix} \mathbf{0}_{m,1} \\ \delta b\delta\boldsymbol{\mu}. \end{pmatrix} \tag{8}$$

Hence, for any $\boldsymbol{\mu}_0$, a_0, and b_0, the nonlinear model (3) can be written in the following form,

$$\begin{pmatrix} \boldsymbol{X} \\ \boldsymbol{Y} \end{pmatrix} - \begin{pmatrix} \boldsymbol{\mu}_0 \\ a_0\mathbf{1} + b_0\boldsymbol{\mu}_0 \end{pmatrix} \sim N\left(\begin{pmatrix} \boldsymbol{I}_{m,m} & \mathbf{0}_{m,1} & \mathbf{0}_{m,1} \\ b_0\boldsymbol{I}_{m,m} & \mathbf{1}_{m,1} & \boldsymbol{\mu}_0 \end{pmatrix}\begin{pmatrix} \delta\boldsymbol{\mu} \\ \delta a \\ \delta b \end{pmatrix} + \frac{1}{2}\boldsymbol{\kappa}_{(\delta\boldsymbol{\mu}, \delta a, \delta b)}; \boldsymbol{\Sigma}\right). \tag{9}$$

We note that the model (3) is referred to as a *weakly nonlinear model* as the function $\boldsymbol{f}$ can be expressed in the form given by equation (5), which is the Taylor series expansion with terms of order not greater than 2.

ISBN 978-80-972629-6-9

3. Linearity region of the straight-line calibration model

Here, we aim to determine the conditions under which the nonlinear regression model (3) representing the straight-line calibration model can be treated as a conventional linear regression model. To achieve this, we propose testing the significance of the second-order term $\boldsymbol{\kappa}(\delta\boldsymbol{\mu}, \delta a, \delta b)$ in the weakly nonlinear regression model (9). We will test the null hypothesis $H_0 : \boldsymbol{\kappa}(\delta\boldsymbol{\mu}, \delta a, \delta b) = \mathbf{0}$ against the alternative $H_1 : \boldsymbol{\kappa}_{(\delta\boldsymbol{\mu},\delta a,\delta b)} \neq \mathbf{0}$ in model (9). The test statistic and its properties are presented in Theorem 1 and Theorem 2, respectively,

Theorem 1. *Consider the non-linear model (9) with specified prior values of the parameters $\boldsymbol{\mu}_0$, a_0, and b_0. Then the test statistic*

$$R_0^2 = \left[\begin{pmatrix}\boldsymbol{X}\\ \boldsymbol{Y}\end{pmatrix} - \boldsymbol{f}_0\right]' \left(\boldsymbol{\Sigma}^{-1} - \boldsymbol{\Sigma}^{-1}\boldsymbol{F}_0\left(\boldsymbol{F}_0'\boldsymbol{\Sigma}^{-1}\boldsymbol{F}_0\right)^{-1}\boldsymbol{F}_0'\boldsymbol{\Sigma}^{-1}\right)\left[\begin{pmatrix}\boldsymbol{X}\\ \boldsymbol{Y}\end{pmatrix} - \boldsymbol{f}_0\right] \tag{10}$$

has noncentral $\chi^2_{m-2}(\delta)$ distribution with $m-2$ degrees of freedom and the noncentrality parameter specified by

$$\delta = \frac{1}{4}\boldsymbol{\kappa}'_{(\delta\boldsymbol{\mu},\delta a,\delta b)}\left(\boldsymbol{\Sigma}^{-1} - \boldsymbol{\Sigma}^{-1}\boldsymbol{F}_0\left(\boldsymbol{F}_0'\boldsymbol{\Sigma}^{-1}\boldsymbol{F}_0\right)^{-1}\boldsymbol{F}_0'\boldsymbol{\Sigma}^{-1}\right)\boldsymbol{\kappa}_{(\delta\boldsymbol{\mu},\delta a,\delta b)}. \tag{11}$$

Proof of the Theorem 1 can be found, e.g., in [6], p. 171.

Theorem 2. *The test statistics R_0^2 can be equivalently expressed as*

$$R_0^2 = \left[\begin{pmatrix}\boldsymbol{X}\\ \boldsymbol{Y}\end{pmatrix} - \boldsymbol{f}_0 - \boldsymbol{F}_0\begin{pmatrix}\widehat{\delta\boldsymbol{\mu}}\\ \widehat{\delta a}\\ \widehat{\delta b}\end{pmatrix}\right]' \boldsymbol{\Sigma}^{-1}\left[\begin{pmatrix}\boldsymbol{X}\\ \boldsymbol{Y}\end{pmatrix} - \boldsymbol{f}_0 - \boldsymbol{F}_0\begin{pmatrix}\widehat{\delta\boldsymbol{\mu}}\\ \widehat{\delta a}\\ \widehat{\delta b}\end{pmatrix}\right], \tag{12}$$

where $(\widehat{\delta\boldsymbol{\mu}}', \widehat{\delta a}, \widehat{\delta b})'$ is given by

$$\begin{pmatrix}\widehat{\delta\boldsymbol{\mu}}\\ \widehat{\delta a}\\ \widehat{\delta b}\end{pmatrix} = \left(\boldsymbol{F}_0'\boldsymbol{\Sigma}^{-1}\boldsymbol{F}_0\right)^{-1}\boldsymbol{F}_0'\boldsymbol{\Sigma}^{-1}\left[\begin{pmatrix}\boldsymbol{X}\\ \boldsymbol{Y}\end{pmatrix} - \boldsymbol{f}_0\right], \tag{13}$$

with the covariance matrix given by

$$\mathrm{Cov}\left(\widehat{\delta\boldsymbol{\mu}'}, \widehat{\delta a}, \widehat{\delta b}\right)' = \left(\boldsymbol{F}_0'\boldsymbol{\Sigma}^{-1}\boldsymbol{F}_0\right)^{-1}. \tag{14}$$

Proof of the Theorem 2 can be found in [6], p. 171.

The null hypothesis H_0 is rejected if the observed test statistic (10) or (12) is greater than or equal to the $(1-\alpha)$-quantile of the central χ^2 distribution with $m-2$ degrees of freedom, denoted by $\chi^2_{m-2}(0, 1-\alpha)$. The probability of rejecting H_0 is given by

$$\gamma = P\left(\chi^2_{m-2}(\delta) \geq \chi^2_{m-2}(0, 1-\alpha)\right). \tag{15}$$

Based on these results, we can now determine a safe region in the parameter space where the weakly nonlinear model can be approximated by a linear regression model. In order to do so, we need to introduce two additional quantities: δ_{max} and $K^{(int)}(\boldsymbol{\mu}_0, a_0, b_0)$. The value of δ_{max} is defined as the maximum value of the noncentrality parameter for which the following probability holds:

$$P\left(\chi^2_{m-2}(\delta_{max}) \leq \chi^2_{m-2}(0, 1-\alpha)\right) = 1 - (\alpha + \varepsilon), \tag{16}$$

where $\varepsilon > 0$ is a prespecified small probability that defines the acceptable risk. Additionally, we define the Bates-Watts intrinsic curvature of $\boldsymbol{f}$ at the point $(\boldsymbol{\mu}_0', a_0, b_0)'$ as $K^{(int)}(\boldsymbol{\mu}_0, a_0, b_0)$. For more information, we recommend consulting [5].

Theorem 3. *Consider the model (9). If the (unknown) model parameters satisfy the condition*

$$\begin{pmatrix}\delta\boldsymbol{\mu}\\ \delta a\\ \delta b\end{pmatrix} \in \mathcal{L} = \left\{ \begin{pmatrix}\delta\boldsymbol{\mu}\\ \delta a\\ \delta b\end{pmatrix} : \begin{pmatrix}\delta\boldsymbol{\mu}\\ \delta a\\ \delta b\end{pmatrix}' \left(\boldsymbol{F}_0'\boldsymbol{\Sigma}^{-1}\boldsymbol{F}_0\right) \begin{pmatrix}\delta\boldsymbol{\mu}\\ \delta a\\ \delta b\end{pmatrix} \leq \frac{2\sqrt{\delta_{max}}}{K^{(int)}_{(\boldsymbol{\mu}_0,a_0,b_0)}} \right\}, \tag{17}$$

then the term $\frac{1}{2}\boldsymbol{\kappa}(\delta\boldsymbol{\mu},\delta a,\delta b)$ *in (9) can be ignored, and the model can be approximated as a linear regression model.*

We do not provide the proof of Theorem 3 in this paper. However, under its assumptions, model (9) can be simplified and treated as a linear regression model using BLUEs as optimal estimators for the model parameters. The approximate $(1-\omega)$-confidence interval for any linear combination of the model parameters can be constructed using the formula:

$$\mathrm{CI} = \left\langle \boldsymbol{p}'(\widehat{\delta\boldsymbol{\mu}'},\widehat{\delta a},\widehat{\delta b})' - u_{1-\frac{\omega}{2}}\sqrt{\boldsymbol{p}'\left(\boldsymbol{F}_0'\boldsymbol{\Sigma}^{-1}\boldsymbol{F}_0\right)\boldsymbol{p}}, \boldsymbol{p}'(\widehat{\delta\boldsymbol{\mu}'},\widehat{\delta a},\widehat{\delta b})' + u_{1-\frac{\omega}{2}}\sqrt{\boldsymbol{p}'\left(\boldsymbol{F}_0'\boldsymbol{\Sigma}^{-1}\boldsymbol{F}_0\right)\boldsymbol{p}} \right\rangle, \tag{18}$$

where $\boldsymbol{p}\in\mathbb{R}^{m+2}$ and $u_{1-\frac{\omega}{2}}$ is the $(1-\frac{\omega}{2})$-quantile of the standard normal distribution. This interval has a coverage probability of the true value $\boldsymbol{p}'(\delta\boldsymbol{\mu}',\delta a,\delta b)'$ greater than $(1-\omega)\times(1-\alpha-\varepsilon)$.

4. Discussion

In summary, the *linearity region* of the straight-line calibration model is influenced by the selection of $\boldsymbol{\mu}_0$, a_0, and b_0. In cases where the null hypothesis H_0 is rejected for these parameters, we recommend utilizing the Weighted Total Least Squares (WTLS) method for parameter estimation and covariance matrix determination, following the law of propagation of uncertainty as described in GUM [1]. The Monte Carlo method can be used as an alternative approach.

Acknowledgements

The project was supported by the Slovak Research and Development Agency, project APVV-21-0216, project SK-CZ-RD-21-0109, project APVV-21-0195, by the Scientific Grant Agency of the Ministry of Education of the Slovak Republic and the Slovak Academy of Sciences, project VEGA 2/0096/21, project VEGA 2/0023/22, and by the Operational Programme Integrated Infrastructure, project 313011BWH2, co-financed by the European Regional Development Fund.

References

[1] JCGM 100:2008 (GUM) (2008). Evaluation of measurement data – Guide to the expression of uncertainty in measurement (GUM 1995 with minor corrections), ISO, BIPM, IEC, IFCC, ILAC, IUPAC, IUPAP and OIML.

[2] JCGM 101:2008 (GUM S1) (2008). Evaluation of measurement data – Supplement 1 to the Guide to the expression of uncertainty in measurement – Propagation of distributions using a Monte Carlo method. ISO, BIPM, IEC, IFCC, ILAC, IUPAC, IUPAP and OIML.

[3] JCGM 102:2011 (GUM S2) (2011). Evaluation of measurement data – Supplement 2 to the Guide to the expression of uncertainty in measurement – Extension to any number of output quantities. ISO, BIPM, IEC, IFCC, ILAC, IUPAC, IUPAP and OIML.

[4] TS 28037:2010 (ISO/TS) (2010). Determination and use of straight-line calibration functions. ISO.

[5] Kubáček L., Tesaříková, E. (2008). *Weakly Nonlinear Regression Models*. Olomouc.

[6] Rao, C. R., Mitra, S. K. (1971). *Generalized Inverse of Matrices and Its Applications*. John Wiley & Sons, New York, London, Sydney, Toronto.

Algorithm for GUM-Compliant Uncertainty Matrix in Straight-Line Calibration

[1]Gejza Wimmer, [2]Gejza Wimmer

[1]Institute of Measurement Science, Slovak Academy of Sciences, Bratislava, Slovak Republic,
[2]Mathematical Institute, Slovak Academy of Sciences, Bratislava, Slovak Republic
Email: umerwimm@savba.sk

Abstract. *The model of linear calibration can be considered as a straight-line errors-in-variables regression model. Through the eyes of statistics is this model weather a nonlinear regression model or, equivalently, as a linear regression model with nonlinear constraints on parameters. In case we cannot consider this model as a linear regression model, it is suggested for parameter estimation to apply the weighted total least squares (WTLS) method and determine the uncertainty matrix by applying the law of propagation of uncertainty (LPU) as it is stated in GUM. Here we describe in detail this LPU uncertainty matrix.*

Keywords: Linear Calibration Model, LPU Matrix of Uncertainties

1. Model of Linear Calibration

We consider the most simple, however, from a practical point of view the most frequently used type of comparative calibration, the linear calibration. The calibration function, which expresses the relationship between the true (error-less) values of the measured quantities expressed in units of the used measuring instruments, say $\mathcal{X}$ and $\mathcal{Y}$, respectively, is assumed to be a linear function. We describe the calibration model and the WTLS (weight total least squares) based measurement model, which is in considered case multivariate, non-linear and expressed in implicit form. According to basic metrological documents [1], and its Supplements [2], [3], and in many other documents the WTLS based measurement model requires iterative procedures to obtain the estimates of model parameters (see. e.g. [4]). According to aforementioned basic metrological regulations we evaluate the uncertainties of measurands by applying the (linear) law of propagation of uncertainty (LPU) to the model input quantities to output quantities. We consider the following setup of the calibration experiment where the measured quantities are represented by a set of m suitable chosen objects (measurands), say $V_1, \ldots, V_m$, such that their true values μ_i, $i = 1, \ldots, m$, expressed in units of the instrument $\mathcal{X}$, span the required calibration range. The true values of the quantities $V_1, \ldots, V_m$, expressed in units of the instrument $\mathcal{Y}$, are ν_i, $i = 1, \ldots, m$. Vector of measurements with the instrument $\mathcal{X}$ is $\boldsymbol{X} = (X_1, X_2, ..., X_m)'$. Its realization (the measured values) is $\boldsymbol{x} = (x_1, x_2, ..., x_m)'$. Vector of measurements with the instrument $\mathcal{Y}$ is $\boldsymbol{Y} = (Y_1, Y_2, ..., Y_m)'$, and its realization is $\boldsymbol{y} = (y_1, y_2, ..., y_m)'$. Considered calibration model representing direct measurements in the calibration experiment is:

$$\begin{aligned} \boldsymbol{X} &= \boldsymbol{\mu} + \boldsymbol{\epsilon}_x, \\ \boldsymbol{Y} &= \boldsymbol{\nu} + \boldsymbol{\epsilon}_y. \end{aligned} \tag{1}$$

The vectors $\boldsymbol{\mu} = (\mu_1, \ldots, \mu_m)'$ and $\boldsymbol{\nu} = (\nu_1, \ldots, \nu_m)'$ represent the true but unknown values of the measurands expressed in the units of the measuring devices $\mathcal{X}$ and $\mathcal{Y}$, respectively, and are related by the equation

$$\boldsymbol{\nu} = a\mathbf{1} + b\boldsymbol{\mu}, \tag{2}$$

where $\mathbf{1} = (1, \ldots, 1)'$ and $\boldsymbol{\epsilon}_x$, $\boldsymbol{\epsilon}_y$ are measurement errors. The parameters a and b represent the intercept and slope, respectively, of the linear calibration function, and are of primary interest. Note that the relation (2) is nonlinear in parameters.

ISBN 978-80-972629-6-9

So we receive that the model of calibration (1) and (2) could be specified by the nonlinear regression model expressed as:

$$\begin{pmatrix} \boldsymbol{X} \\ \boldsymbol{Y} \end{pmatrix} \sim (\boldsymbol{f}(\boldsymbol{\mu}, a, b); \boldsymbol{\Sigma}), \tag{3}$$

where the expectation and covariance matrix of the observation vector are:

$$\mathcal{E}\begin{pmatrix} \boldsymbol{X} \\ \boldsymbol{Y} \end{pmatrix} = \boldsymbol{f}(\boldsymbol{\mu}, a, b) = \begin{pmatrix} \boldsymbol{\mu} \\ a\mathbf{1} + b\boldsymbol{\mu} \end{pmatrix} \quad \text{and} \quad \mathrm{Cov}\begin{pmatrix} \boldsymbol{X} \\ \boldsymbol{Y} \end{pmatrix} = \boldsymbol{\Sigma} = \begin{pmatrix} \boldsymbol{\Sigma}x & \boldsymbol{\Sigma}xy \\ \boldsymbol{\Sigma}yx & \boldsymbol{\Sigma}y \end{pmatrix}, \tag{4}$$

respectively, with a known positive definite matrix $\boldsymbol{\Sigma}$.

2. Parameter Estimation and Evaluating Uncertainties Associated With Model Parameters

Let us denote

$$\boldsymbol{\Sigma}^{-1}_{2m,2m} = \begin{pmatrix} \sigma^*_{1,1} & \dots & \sigma^*_{1,m} & \sigma^*_{1,m+1} & \dots & \sigma^*_{1,2m} \\ \vdots & & \vdots & \vdots & & \vdots \\ \sigma^*_{m,1} & \dots & \sigma^*_{m,m} & \sigma^*_{m,m+1} & \dots & \sigma^*_{m,2m} \\ \sigma^*_{m+1,1} & \dots & \sigma^*_{m+1,m} & \sigma^*_{m+1,m+1} & \dots & \sigma^*_{m+1,2m} \\ \vdots & & \vdots & \vdots & & \vdots \\ \sigma^*_{2m,1} & \dots & \sigma^*_{2m,m} & \sigma^*_{2m,m+1} & \dots & \sigma^*_{2m,2m} \end{pmatrix}.$$

According to [3] realizations of estimators $\widehat{a}, \widehat{b}, \widehat{\mu_1}, \widehat{\mu_2}, \dots, \widehat{\mu_m}$ based on WTLS method (i.e. the estimates) are such values $\widehat{a}^{real}, \widehat{b}^{real}, \widehat{\mu_1}^{real}, \widehat{\mu_2}^{real}, \dots, \widehat{\mu_m}^{real}$ for which it holds

$$\{\widehat{a}^{real}, \widehat{b}^{real}, \widehat{\mu_1}^{real}, \widehat{\mu_2}^{real}, \dots, \widehat{\mu_m}^{real}\} = argmin_{a,b,\mu_1,\mu_2,\dots,\mu_m} \begin{pmatrix} x_1-\mu_1 \\ \vdots \\ x_m-\mu_m \\ y_1-a-b\mu_1 \\ \vdots \\ y_m-a-b\mu_m \end{pmatrix}' \boldsymbol{\Sigma}^{-1} \begin{pmatrix} x_1-\mu_1 \\ \vdots \\ x_m-\mu_m \\ y_1-a-b\mu_1 \\ \vdots \\ y_m-a-b\mu_m \end{pmatrix} = \tag{5}$$

$$= argmin_{a,b,\mu_1,\mu_2,\dots,\mu_m} Q(\boldsymbol{x}, \boldsymbol{y}). \tag{6}$$

According to LPU (law of propagation of uncertainty) are the uncertainties propagated according to linearized measurement model (see e.g. [3], Section 6.2). As our model is not linear, the uncertainties obtained using LPU are essentially only approximations of the true uncertainties. Estimates $\widehat{a}^{real}, \widehat{b}^{real}, \widehat{\mu_1}^{real}, \widehat{\mu_2}^{real}, \dots, \widehat{\mu_m}^{real}$ calculated by the WTLS method are given in (5). We obtain them as the solution of $m+2$ implicit equations

$$\left.\frac{\partial Q(\boldsymbol{x},\boldsymbol{y})}{\partial(\boldsymbol{\mu}', a, b)}\right|_{\mu_1=\widehat{\mu_1}^{real},\dots,\mu_m=\widehat{\mu_m}^{real},a=\widehat{a}^{real},b=\widehat{b}^{real}} = \mathbf{0}. \tag{7}$$

The covariance matrix of $(\widehat{\mu_1}, \widehat{\mu_2}, \dots, \widehat{\mu_m}, \widehat{a}, \widehat{b})'$ according to LPU (see e.g. [4]) is

$$\boldsymbol{\Sigma}^{LPU}(\widehat{\mu_1}, \dots, \widehat{\mu_m}, \widehat{a}, \widehat{b}) = \boldsymbol{A}^{-1}_{\boldsymbol{\mu},a,b} \boldsymbol{A}_{\boldsymbol{x},\boldsymbol{y}} \boldsymbol{\Sigma} \boldsymbol{A}'_{\boldsymbol{x},\boldsymbol{y}} \left(\boldsymbol{A}^{-1}_{\boldsymbol{\mu},a,b}\right)', \tag{8}$$

where

$$\boldsymbol{A}_{\boldsymbol{\mu},a,b} = \begin{pmatrix} \left.\frac{\partial^2 Q(\boldsymbol{x},\boldsymbol{y})}{\partial\mu_1\partial\mu_1}\right|_{\mu_1=\widehat{\mu_1}^{real},\dots,a=\widehat{a}^{real},b=\widehat{b}^{real}} & \cdots & \left.\frac{\partial^2 Q(\boldsymbol{x},\boldsymbol{y})}{\partial\mu_1\partial b}\right|_{\mu_1=\widehat{\mu_1}^{real},\dots,a=\widehat{a}^{real},b=\widehat{b}^{real}} \\ \vdots & & \vdots \\ \left.\frac{\partial^2 Q(\boldsymbol{x},\boldsymbol{y})}{\partial b\partial\mu_1}\right|_{\mu_1=\widehat{\mu_1}^{real},\dots,a=\widehat{a}^{real},b=\widehat{b}^{real}} & \cdots & \left.\frac{\partial^2 Q(\boldsymbol{x},\boldsymbol{y})}{\partial b\partial b}\right|_{\mu_1=\widehat{\mu_1}^{real},\dots,a=\widehat{a}^{real},b=\widehat{b}^{real}} \end{pmatrix}, \tag{9}$$

ISBN 978-80-972629-6-9

$$\boldsymbol{A}_{\boldsymbol{x},\boldsymbol{y}} = \begin{pmatrix} \frac{\partial^2 Q(\boldsymbol{x},\boldsymbol{y})}{\partial \mu_1 \partial x_1}\Big|_{\boldsymbol{\mu}=\widehat{\boldsymbol{\mu}}^{real},a=\widehat{a},b=\widehat{b}} & \cdots & \frac{\partial^2 Q(\boldsymbol{x},\boldsymbol{y})}{\partial \mu_1 \partial x_m}\Big|_{\boldsymbol{\mu}=\widehat{\boldsymbol{\mu}}^{real},a=\widehat{a},b=\widehat{b}} & \vdots \\ \frac{\partial^2 Q(\boldsymbol{x},\boldsymbol{y})}{\partial \mu_2 \partial x_1}\Big|_{\boldsymbol{\mu}=\widehat{\boldsymbol{\mu}}^{real},a=\widehat{a},b=\widehat{b}} & \cdots & \frac{\partial^2 Q(\boldsymbol{x},\boldsymbol{y})}{\partial \mu_2 \partial x_m}\Big|_{\boldsymbol{\mu}=\widehat{\boldsymbol{\mu}}^{real},a=\widehat{a},b=\widehat{b}} & \vdots \\ \vdots & & \vdots & \vdots \\ \frac{\partial^2 Q(\boldsymbol{x},\boldsymbol{y})}{\partial b \partial x_1}\Big|_{\boldsymbol{\mu}=\widehat{\boldsymbol{\mu}}^{real},a=\widehat{a},b=\widehat{b}} & \cdots & \frac{\partial^2 Q(\boldsymbol{x},\boldsymbol{y})}{\partial b \partial x_m}\Big|_{\boldsymbol{\mu}=\widehat{\boldsymbol{\mu}}^{real},a=\widehat{a},b=\widehat{b}} & \vdots \end{pmatrix}$$

$$\begin{pmatrix} \vdots & \frac{\partial^2 Q(\boldsymbol{x},\boldsymbol{y})}{\partial \mu_1 \partial y_1}\Big|_{\boldsymbol{\mu}=\widehat{\boldsymbol{\mu}}^{real},a=\widehat{a},b=\widehat{b}} & \cdots & \frac{\partial^2 Q(\boldsymbol{x},\boldsymbol{y})}{\partial \mu_1 \partial y_m}\Big|_{\boldsymbol{\mu}=\widehat{\boldsymbol{\mu}}^{real},a=\widehat{a},b=\widehat{b}} \\ \vdots & \frac{\partial^2 Q(\boldsymbol{x},\boldsymbol{y})}{\partial \mu_2 \partial y_1}\Big|_{\boldsymbol{\mu}=\widehat{\boldsymbol{\mu}}^{real},a=\widehat{a},b=\widehat{b}} & \cdots & \frac{\partial^2 Q(\boldsymbol{x},\boldsymbol{y})}{\partial \mu_2 \partial y_m}\Big|_{\boldsymbol{\mu}=\widehat{\boldsymbol{\mu}}^{real},a=\widehat{a},b=\widehat{b}} \\ \vdots & \vdots & & \vdots \\ \vdots & \frac{\partial^2 Q(\boldsymbol{x},\boldsymbol{y})}{\partial b \partial y_1}\Big|_{\boldsymbol{\mu}=\widehat{\boldsymbol{\mu}}^{real},a=\widehat{a},b=\widehat{b}} & \cdots & \frac{\partial^2 Q(\boldsymbol{x},\boldsymbol{y})}{\partial b \partial y_m}\Big|_{\boldsymbol{\mu}=\widehat{\boldsymbol{\mu}}^{real},a=\widehat{a},b=\widehat{b}} \end{pmatrix}. \quad (10)$$

It holds for $i = 1,...,m$

$$\frac{\partial Q(\boldsymbol{x},\boldsymbol{y})}{\partial \mu_i} = -2\Big\{(x_1-\mu_1)\sigma^*_{i,1} + \ldots + (x_m-\mu_m)\sigma^*_{i,m} + b(x_1-\mu_1)\sigma^*_{m+i,1} + \ldots b(x_m-\mu_m)\sigma^*_{m+i,m} + \\ +(y_1-a-b\mu_1)\sigma^*_{i,m+1} + \ldots + (y_m-a-b\mu_m)\sigma^*_{i,2m} + \\ +b(y_1-a-b\mu_1)\sigma^*_{m+i,m+1} + \ldots + b(y_m-a-b\mu_m)\sigma^*_{m+i,2m}\Big\} \quad (11)$$

and also

$$\frac{\partial Q(\boldsymbol{x},\boldsymbol{y})}{\partial a} = -2\Big\{(x_1-\mu_1)(\sigma^*_{1,m+1} + \ldots + \sigma^*_{1,2m}) + (x_2-\mu_2)(\sigma^*_{2,m+1} + \ldots + \sigma^*_{2,2m}) + \ldots + \\ +(x_m-\mu_m)(\sigma^*_{m,m+1} + \ldots + \sigma^*_{m,2m}) + (y_1-a-b\mu_1)(\sigma^*_{m+1,m+1} + \ldots + \sigma^*_{m+1,2m}) + \\ +(y_2-a-b\mu_2)(\sigma^*_{m+2,m+1} + \ldots + \sigma^*_{m+2,2m}) + \ldots + (y_m-a-b\mu_m)(\sigma^*_{2m,m+1} + \ldots + \sigma^*_{2m,2m})\Big\}, \quad (12)$$

$$\frac{\partial Q(\boldsymbol{x},\boldsymbol{y})}{\partial b} = -2\{(x_1-\mu_1)(\mu_1\sigma^*_{1,m+1} + \mu_2\sigma^*_{2,m+2} + \ldots + \mu_m\sigma^*_{1,2m}) + \\ + \ldots + (x_m-\mu_m)(\mu_1\sigma^*_{m,m+1} + \mu_2\sigma^*_{m,m+2} + \ldots + \mu_m\sigma^*_{m,2m}) + \\ +(y_1-a-b\mu_1)(\mu_1\sigma^*_{m+1,m+1} + \mu_2\sigma^*_{m+1,m+2} + \ldots + \mu_m\sigma^*_{m+1,2m}) + \\ + \ldots + (y_m-a-b\mu_m)(\mu_1\sigma^*_{2m,m+1} + \mu_2\sigma^*_{2m,m+2} + \ldots + \mu_m\sigma^*_{2m,2m})\Big\}, \quad (13)$$

$$\frac{\partial^2 Q(\boldsymbol{x},\boldsymbol{y})}{\partial \mu_i \partial \mu_j} = 2(\sigma^*_{i,j} + b\sigma^*_{m+i,j} + b\sigma^*_{i,m+j} + b^2\sigma^*_{m+i,m+j}), \quad i,j = 1,2,...,m, \quad (14)$$

$$\frac{\partial^2 Q(\boldsymbol{x},\boldsymbol{y})}{\partial \mu_i \partial a} = 2(\sigma^*_{i,m+1} + \ldots + \sigma^*_{i,2m} + b\sigma^*_{m+i,m+1} + \ldots + b\sigma^*_{m+i,2m}), \quad i = 1,2,...,m, \quad (15)$$

$$\frac{\partial^2 Q(\boldsymbol{x},\boldsymbol{y})}{\partial \mu_i \partial b} = 2\Big\{(x_1-\mu_1)\sigma^*_{m+i,1} + \ldots + (x_m-\mu_m)\sigma^*_{m+i,m} + \\ +(y_1-a-b\mu_1)\sigma^*_{m+i,m+1} + \ldots + (y_m-a-b\mu_m)\sigma^*_{m+i,2m}\Big\} + \\ +2\Big\{\mu_1\sigma^*_{i,m+1} + \ldots + \mu_m\sigma^*_{i,2m} + b\mu_1\sigma^*_{m+i,m+1} + \ldots + b\mu_m\sigma^*_{m+i,2m}\Big\}, \quad i = 1,2,...,m, \quad (16)$$

$$\frac{\partial^2 Q(\boldsymbol{x},\boldsymbol{y})}{\partial a^2} = 2\Big\{(\sigma^*_{m+1,m+1} + \ldots + \sigma^*_{m+1,2m}) + ... + (\sigma^*_{2m,m+1} + \ldots + \sigma^*_{2m,2m})\Big\}, \quad (17)$$

$$\frac{\partial^2 Q(\boldsymbol{x},\boldsymbol{y})}{\partial b^2} = 2\Big\{\mu_1(\mu_1\sigma^*_{m+1,m+1} + \mu_2\sigma^*_{m+1,m+2} \ldots + \mu_m\sigma^*_{m+1,2m}) + \mu_2(\mu_1\sigma^*_{m+2,m+1} + \ldots + \mu_m\sigma^*_{m+2,2m}) + ... \\ +\mu_m(\mu_1\sigma^*_{2m,m+1} + \ldots + \mu_m\sigma^*_{2m,2m}). \quad (18)$$

$$\frac{\partial^2 Q(\boldsymbol{x},\boldsymbol{y})}{\partial a \partial b} = 2\{\mu_1(\sigma^*_{m+1,m+1} + \ldots + \sigma^*_{m+1,2m} + \ldots + \mu_m(\sigma^*_{2m,m+1} + ... + \sigma^*_{2m,2m})\}, \tag{19}$$

$$\frac{\partial^2 Q}{\partial \mu_i \partial x_j} = -2\left\{\sigma^*_{i,j} + b\sigma^*_{m+i,j}\right\}, \quad i,j = 1,2,...,m, \tag{20}$$

$$\frac{\partial^2 Q(\boldsymbol{x},\boldsymbol{y})}{\partial \mu_i \partial y_j} = -2\left\{\sigma^*_{i,m+j} + b\sigma^*_{m+i,m+j}\right\}, \quad i,j = 1,2,...,m, \tag{21}$$

$$\frac{\partial^2 Q(\boldsymbol{x},\boldsymbol{y})}{\partial a \partial x_j} = -2\left\{\sigma^*_{j,m+1} + \sigma^*_{j,m+2} + \ldots + \sigma^*_{j,2m}\right\}, \quad j = 1,2,...,m, \tag{22}$$

$$\frac{\partial^2 Q(\boldsymbol{x},\boldsymbol{y})}{\partial b \partial x_j} = -2\left\{\mu_1\sigma^*_{j,m+1} + \mu_2\sigma^*_{j,m+2} + \ldots + \mu_m\sigma^*_{j,2m}\right\}, \quad j = 1,2,...,m, \tag{23}$$

$$\frac{\partial^2 Q(\boldsymbol{x},\boldsymbol{y})}{\partial b \partial y_j} = -2\left\{\mu_1\sigma^*_{m+j,m+1} + \mu_2\sigma^*_{m+j,m+2} + \ldots + \mu_m\sigma^*_{m+j,2m}\right\}, \quad j = 1,2,...,m, \tag{24}$$

$$\frac{\partial^2 Q(\boldsymbol{x},\boldsymbol{y})}{\partial a \partial y_j} = -2\left\{\sigma^*_{m+j,m+1} + \sigma^*_{m+j,m+2} + \ldots + \sigma^*_{m+j,2m}\right\}, \quad j = 1,2,...,m, \tag{25}$$

3. Conclusions

In the contribution are obtained explicit formulas for LPU covariance matrix, i.e. uncertainties of parameter estimators in straight-line errors-in-variables regression model (model of linear calibration) obtained by WTLS method. The estimates obtained by the WTLS method we obtain as a solution to equations (7) iteratively. LPU covariance matrix can be obtained also using complicated matrix derivations from (8) where

$$\boldsymbol{A}_{\boldsymbol{\mu},a,b} = \frac{\partial^2 Q(\boldsymbol{x},\boldsymbol{y})}{\partial(\boldsymbol{\mu}',a,b)'\partial(\boldsymbol{\mu}',a,b)}, \quad \boldsymbol{A}_{\boldsymbol{x},\boldsymbol{y}} = \left(\frac{\partial^2 Q(\boldsymbol{x},\boldsymbol{y})}{\partial(\boldsymbol{\mu}',a,b)'\partial\boldsymbol{x}'} : \frac{\partial^2 Q(\boldsymbol{x},\boldsymbol{y})}{\partial(\boldsymbol{\mu}',a,b)'\partial\boldsymbol{y}'}\right).$$

The MATLAB code for computing $\boldsymbol{\Sigma}^{LPU}(\widehat{\mu_1},...,\widehat{\mu_m},\widehat{a},\widehat{b})$ can you find at `https://github.com/dzibo7/Measurement_conference_2023`.

Acknowledgements

The project was supported by the Slovak Research and Development Agency, project APVV-21-0216, project SK-CZ-RD-21-0109, project APVV-21-0195, by the Scientific Grant Agency VEGA, projects VEGA 2/0096/21, and by the Operational Programme Integrated Infrastructure, project 313011BWH2, co-financed by the European Regional Development Fund.

References

[1] JCGM 100:2008 (GUM) (2008). Evaluation of measurement data – Guide to the expression of uncertainty in measurement (GUM 1995 with minor corrections), ISO, BIPM, IEC, IFCC, ILAC, IUPAC, IUPAP and OIML.

[2] JCGM 101:2008 (GUM S1) (2008). Evaluation of measurement data – Supplement 1 to the Guide to the expression of uncertainty in measurement – Propagation of distributions using a Monte Carlo method. ISO, BIPM, IEC, IFCC, ILAC, IUPAC, IUPAP and OIML.

[3] JCGM 102:2011 (GUM S2) (2011). Evaluation of measurement data – Supplement 2 to the Guide to the expression of uncertainty in measurement – Extension to any number of output quantities. ISO, BIPM, IEC, IFCC, ILAC, IUPAC, IUPAP and OIML.

[4] Klauenberg, K. et al. (2022).*The GUM perspective on straight-line errors-in-variables regression*. Measurement 187, 110340.

The Control of a Prepackages by a Truncated Sequential Sampling Plan

[1]Palenčár Jakub, [2]Kováčiková Anna, [1]Palenčár Rudolf

[1]Slovak University of Technology in Bratislava, Faculty of Mechanical Engineering, Bratislava, Slovakia
[2]Slovak Metrological Inspectorate, Bratislava, Slovakia
Email: jakub.palencar@stuba.sk

Abstract: *This article provides a suggestion for a truncated sequential sampling plan for the statistical control of the actual content of products in prepackages and the process of how they are created. In its summary, this article briefly compares reference sampling plans and suggested sampling plans, specifically the standards of their reliability and effectiveness from the point of view of customer guarantees.*

Keywords: Prepackage, Statistical Control, Sampling Plan, Truncated Sequential Sampling Plan

1. Introduction

The ability to control the actual product quantity in prepackages is inevitable for securing fair commerce, maintaining competitive markets, and protecting the consumers from insufficiently filled prepackages, which do not meet the regulatory requirements [6]. Considering the current large-scale production, it is impossible to check every single unit of prepackage in the lot, thus it is appropriate to use statistical methods as an effective tool to evaluate the results of the measurements within the control, either during the packaging or during the control performed by the inspection authorities [7]. In this article, we will discuss the suggestion of a new sampling plan to improve the quality and effectiveness of control of prepackages - the truncated sequential sampling plan.

2. Control the Contents of the Prepackage

The statistical control of the prepackage is performed on a sample or sampling [4, 7] and consists of two parts: the control of the actual content of each prepackage in the sample and the control, at which the average actual content of the prepackage in the sample is determined [2, 4, 7]. In this article, we will discuss more in detail the new method of control of actual content of each prepackage in a sample – the truncated sequential sampling plan.

3. The Control of Actual Content of Each Prepackage in the Sample

As with each statistical control of the actual content of each prepackage in the sample not all prepackages are checked, only some randomly selected (but representative) prepackages, the findings about the quality of the whole lot are inferred based on the control of a small number of elements n (the scope of the sampling). This statistical approach inherently introduces a certain risk of incorrectly rejecting a “good lot” (i.e. a correct lot fulfilling the criteria). This risk is referred to as a “producer’s risk” (PR) - and we mark it α. On the other hand, there is also a certain risk of incorrectly accepting a "bad lot" (i.e. an incorrect lot not fulfilling the criteria). This risk is called a "consumer's risk" (CR) - and we mark it β [6]. The rule by which we evaluate the quality of the lot based on an acceptance sampling is called the sampling plan. Based on the legal regulations [4, 7] are used single sampling plans and double sampling plans.

4. Sequential Sampling Plan of Each Prepackage

Sequential sampling is the extension of the concept of double and multiple sampling, with the difference that the scope of the samplings equals 1. Similarly, to double and multiple sampling plans the decision is made from one of three options (to accept the lot, reject the lot or continue with sampling), however, in this case, the decision is made after the control of each single product, where it is not possible to determine the total number of controlled products [1]. The limits of this approach, however, are difficulties with planning the number of tests, because we don't know in advance when the sampling finishes. Considering this it is possible to use a truncated sequential sampling plan, with which the advantages of planning a single sampling plan are possible to combine with the economic advantages of a sequential sampling plan. The basis of this method is the following:

i. the control is planned based on the single sampling plan, where we set the maximum number of controlled prepackages n_0, as well as the acceptance number c,
ii. we set the sequential sampling plan of separate prepackages and start the control based on this sequential sampling plan,
iii. if the sampling with a sequential sampling plan for $n \leq n_0$, we end the control according to the single sampling plan [5].

Table 1 briefly shows the conditions the sampling plans must meet according to OIML R 87 and Directive 76/211/EHS [2, 4].

Table 1. Pre-defined parameters of sampling plans

P_1	P_2	α	β
0.025	0.09	0.05	0.10

where

α producer's risk,
β consumer's risk,
P_1 allowed ratio of defective prepackages connected to the manufacturer's risk α,
P_2 non-allowed ratio of defective prepackages connected to consumer's risk β.

5. Single Sampling Plan

With the single sampling plan for the use of a truncated sequential sampling plan, we first determine the range of sampling n, acceptance criterion c. Two variants of single sampling plans were found by calculations for the use of the truncated sequential sampling plan (see Table 2), and these are within the considered allowed deviations (±15 %) according to [2, 4].

Table 2. Parameters of the variants of a single sampling plan for the parameters α = 0.05 and β = 0.10

	P_1	P_2	α	β	n	c
1st variant	0.025	0.0857	0.05	0.1	106	5
2nd variant	0.025	0.0975	0.05	0.1	80	4

6. Truncated Sequential Sampling Plan of Each Prepackage

In connection to the previous chapter, where we determined the single sampling plans for the application of the truncated sequential sampling plan, we will create two variants of such

sampling plans in this segment of the article. The pre-defined parameters of these two variants of truncated sequential sampling plans are the same as the parameters of the variants of the single sampling plan stated in Table 2 without parameter *c*. The obtained parameters from the relations [5] for both variants of the truncated sequential sampling plans are stated in Table 3.

Table 3. Parameters of truncated sequential sampling plan

	m'	m''	$n_{\min,A}$	$n_{\min,R}$
1st variant	-1.897+0.047n	2.236+0.047n	38	3
2nd variant	-1.5701+0.051n	2.016+0.051n	32	3

In Table 3 are stated the next parameters: $n_{\min,A}$ as the minimum number of consecutive good prepackages for acceptance, $n_{\min,R}$ as the minimum number of consecutive defective prepackages for rejection, m' as acceptance criteria and m'' as rejection criteria. With the truncated sequential sampling plans stated in Table 3, up to the control of 37th (in case of 2nd variant up to the 31st) product, we can only decide on the rejection of the lot, where only the rejection criteria m'' are stated. After the control of 38th (in case of 2nd variant up to the 32nd) prepackage, if at this point there are 0 defective units, we accept the lot; if at this point the number of defective products is between m' and m'', i.e., for example, one defective prepackage, we continue with the control up to such a number of prepackages, where this value would meet the acceptance criterion m'. If the value increases above the rejection criterion, we reject the lot. With control of each prepackage the decision is made about accepting or rejecting the lot, this happens at the latest at the 106th controlled prepackage (in the case of the 2nd variant up to the 80th), when the control is stopped based on the respective single sampling plan.

In principle, this sampling plan with its predefined parameters and principles of its operation (the decision about the lot is made after the control of each unit) is of the highest quality compared to the other sampling plans. It is exactly such a plan, which can quickly reveal a low-quality lot and reject it e.g. at the control of third prepackage. For the other sampling plans (single and double sampling plans) it is necessary to complete the control within the lot. Only after that, the decision about the lot can be made so the truncated sequential sampling plan compared to the other sampling plans offers great savings (e.g. in comparison to the control of 50 or 80 units - see Table 4).

Table 4. Comparison parameters of sampling plans [3, own]

Sampling plan	Number in lot	P_2 for risk β = 0.10	$n_{\min,A}$	$n_{\min,R}$
Single	whatever the number (≥100)	0.181	20	20
Double	100 – 500	0.136	30	30
	501 – 3 200	0.112	50	50
	3201 – 10 000	0.0875	80	80
Single/truncated sequential	≥80	0.0975	32	3
	≥106	0.0857	38	3

The advantage of single and double sampling plans is their simplicity and predictability at the time of control planning. This comes at the expense of consumer protection. The result is the finding that the ratio of defective products with the three reference sampling plans exceeds the 10 % limit. In general, the reference sampling plans do not offer satisfactory consumer protection.

ISBN 978-80-972629-6-9

Sequential sampling plans offer time savings which are not at the expense of quality, and they can relatively quickly offer the result for the rejection of a very bad lot, where already after three consecutively controlled prepackages, we can decide on the rejection of the lot. This advantage of truncated sequential sampling plans in the sensitivity to the quality of the lot works the other way around as well if the lot is a very good one, the decision about the acceptance of the lot can be made after the control of the 32nd prepackage (or 38th prepackage).

The researched sampling plans, which have a higher guarantee of consumer protection, can seem more complicated for application. However, it is necessary to keep in mind the interests and protection of the consumer, which is also the main goal of the control of prepackages. The truncated sequential sampling plan can thus be a more appropriate sampling plan than the single, or double sampling plans. The truncated sequential sampling plans appear highly effective, especially for high-quality lots and include sufficient consumer guarantees.

7. Conclusion

The article focuses on the prepackages, specifically the control of the actual content of each prepackage. In the article, the legally allowed statistical methods for the control of the actual content of prepackages are described. Usually, these legal reference plans are executed by a single sampling plan or a double sampling plan. The article further describes the suggestion of a new sampling plan: the sequential sampling plan and the truncated sampling plan with specific instructions for implementation and use in practice. The herein-stated results and suggested sampling plans can be appropriate variants of sampling plans for implementation into the current legislature in the area of control of prepackages.

Acknowledgements

This work was supported by the Slovak University of Technology in Bratislava, projects APVV-21-0216, APVV-21-0125 and by projects VEGA 1/0687/21, and VEGA /0675/22.

References

[1] STN ISO 8422 (2009). Sequential sampling plans for inspection by attributes (Preberacie plány postupným výberom pri kontrole porovnávaním. Slovenská technická norma.).

[2] OIML R 87 INTERNATIONAL RECOMMENDATION Edition 2016 (E) Quantity of product in prepackages.

[3] Palenčar, R. (2009). Štatistické metódy pre spotrebiteľsky balené výrobky. [Statistical inspection of prepackages]. *Metrológia a skúšobníctvo*. 2/2009, 3 – 17. ISSN 1335-2768.

[4] Council Directive 76/211/EEC of 20 January 1976 on the approximation of the laws of the Member States relating to the making-up by weight or by volume of certain prepackaged products.

[5] Šor, J.B. (1965). *Štatistické metódy analýzy a kontroly jakosti a spolehlivosti*. [Statistical Methods of Analysis and Quality Control and Reliability]. Prague: SNTL.

[6] Vaterhaus, H.-P., Matsumoto, T., Tanaka, H. (2017). Controlling the quantity of prepackages using OIML R 87. In *OIML Bulletin*. ISSN 0473-2812, LVIII, no. 3, 13-18.

[7] Decree of the Slovak Office of Standards, Metrology and Testing No 188/2018 Coll. on prepackages and bottles used as measuring container and on the requirements for checking the quantity of product in pre-packages and on the requirements for checking the actual volume of the bottle used as measuring container, and amending Decree No 433/2019 Coll.

How Aphasia Influences Written and Spoken Texts

Daniel Petriľak, Mária Markošová

Department of Applied Informatics, Faculty of Mathematics,
Physics and Informatics Comenius University, Bratislava, Slovakia
Email: petrilak3@uniba.sk

Abstract. *Aphasia is disorder of the brain influencing language processing which occurs after the brain damage (such as stroke or brain tumor). People with aphasia have problems in communication in both spoken and written language. Their abilities to understand conversations or written sentences are strongly affected too. In this paper we analyze both written and spoken texts with a help of the graph theoretical, statistics and linguistics methods. We compare several statistical measures and other properties in texts, written or spoken, by people with and without aphasia.*

Keywords: Aphasia, Graph Theory, Linguistic Theory, Word Network

1. Introduction

Aphasia is a brain disorder which often occurs after the stroke, but it might be a result of the brain tumor as well [4], [1].There are several patterns of aphasia which manifest themselves by different ways. For example, in Broca's type of aphasia, the patient understands well other people, but struggles with his own speech. He creates short sentences and even omit some words. Patients with Comprehensive or Wernike aphasia speak fluently, create rather complex sentences, but they do not have sense. They even develop their own incorrect words, making their speech even hard to understand. The most difficult is so called global aphasia, combining both types mentioned above.

Each text can be transformed into word network by different methods. We use position of words in the text to develop a word network. Here words are nodes and each node is connected with his closest neighbors in text, one to the right and one to the left with undirected edge (position of the word, left or right, is not reflected in the graph topology). Dots, comas ...etc are omitted. Each network, and the word network is not an exception, is a graph and as such can be analyzed by graph theoretical methods [2]. We use standard graph statistics such as number of nodes, edges, degree, degree distribution, clusterization coefficient, density, diameter and avg. shortest path. We also calculate number of loops in text (two identical words after each other), but we do not include them into the graph. From the less known methods we used graphlets. Graphlets extend concept of the degree and therefore are able to describe local graph structure in more details [3]. On the other hand we use standard linguistic statistical analysis of our texts too [1]. We calculate number of words and sentences, length of sentences, number of pronouns, prepositions and conjunctions. Also we calculate ratios of these word types.

2. Subject and Methods

In this paper we split our research into two groups. First, we examine written texts by the authors Paul West and Dominik Dán. The first author, Paul West, was born in the UK in 1930. In 2003 he suffered a stroke leading to global aphasia. Two of the analysed books were written before the accident (The Rat Man of Paris - RMP (1983) and The Place in Flowers Where Pollen Rests - PIF (1988)), one after the accident as a therapeutical effort (The shadow factory - SF (2008)). We also elaborated four books (Uzol (2012), Červený kapitán (2007), V tieni (2020)

and KÍbko zmijí (2020)) of author Dominik Dán written in different period of his life to show to which extend is the author's style stable in time. We do not compare books written in different languages, but only books written by the same author.
Second, we examine spoken texts of people with and without aphasia, where all the texts are tied to the same story. These texts were given to us in a framework of our cooperation with Department of linguistics of Pedagogical Faculty Comenius University in Bratislava [1].
We compare graph properties and linguistic properties of the data mentioned above. We have chosen these methods, because they are able to provide novel inside into the language. Graph theoretical methods were already used to study language properties, but there are still plenty of open problems, which are not solved yet.
In the word web, word is a node and thus number of nodes, independently of aphasia, shows how rich the vocabulary of certain person is. Other properties such as number of edges and node degree depend on the number of nodes. Clusterization coefficient and the graph density reflect local interconnections around certain nodes. In the language this property reflects the importance of the word in the text, namely whether it is a hub or not. It also shows how important is the word neighborhood. Diameter of language graph tells us how well the author creates sentences as a sequence of unique words. This can be possibly affected by aphasia. Potential loops in word web might be result of aphasia, therefore we calculate this property as well (we omit them in graphlet analysis). We calculate two up to five node graphlets to get the information about local connectivity in the graph. We used non-lemmatized texts, because for example in the speach of the patient with Broca aphasia mainly root of the words are used and this differences cannot be seen in lemmatized text.
Standard linguistic analyses consists of number of word, sentences, length of sentences etc... calculation. We also measure number of prepositions, conjunctions and pronouns because in Broca aphasia usage of words of these word types is decreasing [1].

3. Results

In Table 1 we provide results of written texts analyses, which contains some differences.

Table 1: Results of graph and linguistics analyses of P.West and D.Dán texts. The values in bold in the table are differences between networks, which we will describe.

	RMP	PIF	**SF**	Uzol	Červený kapitán	KÍbko zmijí	V tieni
Number of nodes	5749	4764	5407	5893	5706	5355	5977
Diameter	**10**	**9**	**7**	10	11	11	10
Loops	10	27	16	29	22	38	30
Avg. length of sentences	13.21	16.93	21.30	10.98	9.99	8.16	8.27
Number of pronouns	**5260**	**5396**	**5088**	1523	1597	1564	1515
Number of prepositions	**793**	**893**	**706**	1525	1427	1526	1491
Size of text	29996	29556	30091	16959	17059	17059	17029

Table 1 shows, that number of nodes are different among West's texts and also the number of nodes are different among Dán's texts. It is not connected to aphasia, but more to the author's

ISBN 978-80-972629-6-9

style, richness of his vocabulary and also amount of direct speech in the text (in which authors have tendency to utilize language of an ordinary people).
Diameters of word webs are significantly different, namely 42.85% difference between word webs of SF and RMP and 28.57% difference between SF and PIF. Difference between RMP and PIF is 11.11%, which shows, that aphasia really have influence on the word web diameter. We assume this is due to the author's decreased ability to form sequences with correct words. Author uses the same vocabulary, but more carefully and more often with the same words. To compare, diameters of Dán´s networks are quite similar and the maximum difference is 10%.
From the previous studies of aphasia [1] we supposed that the number of loops will be the highest in SF, but it is not correct. The reason is, that in PIF author uses direct speech massively. It is a known fact, that the spoken language contains loops more often [1]. Average length of sentences is the highest in SF. We assume, that this is due to the text correction done by the writer Diane Ackerman, author´s wife. In general, it is known, that patients with aphasia are more prone to make sentences with fewer words [1]. Unfortunately, we were not able to gain uncorrected version of SF book.
We also observe differences in the number of pronouns and prepositions. The highest difference in prepositions is 26.48% and pronouns 6.05% between SF and PIF. Between RMP and PIF the difference is 12.61% in prepositions and 2.59% in pronouns. It is known, that patients with Broca aphasia use fewer prepositions and pronouns [1]. Thus, the results corresponds to the expected phenomenon.
We also made graphlet analysis of all texts [3], but this analysis did not provide any significant differences between webs of books RMP, PIF, SF and also between Dán's word webs. Number of n-nodes graphlets also depends on the size of the network, which is different for each text, and thus the individual results may be skewed.
Table 2 reflects results of the spoken texts analyses. Texts were obtained using the standardized test ASpoR = Analysis of Spontaneous Speech [1] in Slovak language, where participants were presented with pictures of known story in chronological order and their goal was to retell the story.

Table 2: Results of graph and linguistics analyses of some spoken texts, where PETOLG is person with aphasia. The values in bold in the table are differences between networks, which we will describe.

-	**PETOLG**	KD-25	JANTUR	SP-58
Number of nodes	767	850	784	688
Diameter	9	9	10	7
Number of loops	**45**	**2**	**3**	**1**
Number of sentences	**195**	**119**	**162**	**165**
Avg. length of sentence	10.70	17.21	12.17	11.47
Number of pronouns	212	176	282	283
Number of conjuctions	299	205	266	257
Number of prepositions	169	232	162	125
Size of text	2086	2048	1972	1893

From Table 1 and Table 2 we can observe, that the number of nodes of graphs from written texts are different and also the number of nodes of graphs from spoken texts are different. In spite of this, characteristics are similar between aphatics and non-aphatics text. On the other hand, diameter of networks do not match results of previous written texts analysis. We hypothesize

that this property is also influenced by individual communication skills, education, work etc. In number of prepositions and pronouns of spoken texts are lower differences then in the written texts.
High differences are in the number of loops. As these are spoken texts, the repetition of the words is included. One of the main symptoms of aphasia is the repetition of the same words in a sequence, which is also confirmed by our analysis.
As we mentioned above, patients with aphasia have tendency to use shorter sentences. In the results, we confirm this claim. The number of sentences is the highest for PETOLG although length of texts are similar. But in comparsion with SP-58 we can see that the number of sentences can be influenced by other factors too (communication skills, education, employment, etc...). We do not know anything personal about measured patients. Also, an interesting phenomenon is that the number of conjunctions is also highest in the text from PETOLG, even though he uses shorter sentences.

4. Conclusions

For both linguistic and graph analysis, we showed the most interesting results of our analysis. We make our analysis for both written and spoken texts. Unfortunately, for the crucial written text (SF) we do not have unedited version, therefore our results might be biased. The main differences in networks of written texts are: diameter, number of prepositions and number of pronouns. For the spoken texts, we found interesting differences, such as number of loops and number of sentences, related to the aphasia, but it would be necessary to analyze more extensive texts for more reliable results. Such texts are difficult to obtain for various reasons, ethical as well as practical. To continue the investigation of aphasia influence we suggest to analyze the development of the network from the scratch. It can reveal the way the text is produced using word networks, both in the authors' written form and in the spoken texts.

References

[1] Dr. Kevická from the Department of logopedy, Pedagogical faculty UK. *private communication*.

[2] Ferrer i Cancho, R., Sole, R. V. (2001). The small world of human language. *Proc. R. Soc. Lond. B 268*, 2261-2265.

[3] Pržulj, N. (2007). Biological Network Comparison Using Graphlet Degree Distribution. *Bioinformatics 23*, 177–183.

[4] Tippett, D. C., Niparko, J. K., Hillis, A. E. (2014). Aphasia: Current concepts in theory and praxis. *J Neurol Transl Neurosci.2 1*, 1042–1054.

Low-Energy Recognition and Counting Device for Cyclists and Pedestrians Based on Artificial Intelligence

[1]Daniel Gogola, [1,2]Hana Krakovská, [1]Andrej Krafčík, [1]Ivan Frollo, [1,3]Pavol Szomolányi

[1] Institute of Measurement Science, Slovak Academy of Sciences, Bratislava, Slovakia,
[2] Section for Science of Complex Systems, Medical University of Vienna, Vienna, Austria
[3] High Field MR Center, Medical University of Vienna, Vienna, Austria
Email: daniel.gogola@savba.sk

Abstract. *Nowadays, an ever greater accent is put on the use of alternative (eco-friendly) forms of transport. Alongside the requirements for environmentally friendly transport, there is also a rising need for the building of infrastructure such as pedestrian or cycling routes. For this purpose, it is necessary to have a study on the use of the infrastructure. The presented study deals with the design of a low-energy device, using artificial intelligence for the recognition and counting of cyclists and pedestrians.*

Keywords: Counter, Curve Recognition, Machine Learning, LiDAR, Artificial Intelligence

Introduction

There are six methods of tracking the use of traffic infrastructures. Each of them has its advantages and disadvantages, which need to be considered. These are, for example, cost, accuracy, the speed of implementation of any measuring equipment and also the time that the traffic monitoring will be carried out. One of the most common methods is manual counting. This is relatively inexpensive and suitable for low-traffic locations. It does not require an internet connection, but data processing is time-consuming. The following two methods require modification of the roadway: pressure sensors and inductive sensors. They are suitable for long-term traffic monitoring and possible automation of traffic lights. Another universal method using deep learning is the camera-based image acquisition method. It is suitable for places with heavy traffic or in cases where it is required to distinguish individual traffic participants (e.g., cars, cyclists, motorcyclists, pedestrians). The last group consists of radar sensors that can detect the size and speed of traffic participants based on reflected waves.
The TFmini Plus LiDAR sensor module was chosen for the sensing method proposed below. It parses on the Time of Flight principle. The module periodically emits a modulated wave of the near-infrared spectrum, which is then reflected after contact with an object. By measuring the bidirectional phase difference, the time of flight of the wave is obtained, from

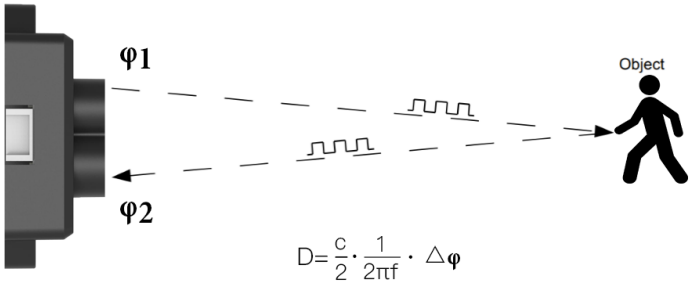

Fig. 1 Principle of operation [1].

which the relative distance between the module and the detection object is then calculated [1], as shown in Fig. 1.

Subject and Methods

Measured data should be pre-processed by normalization of the intensity of the measured signal to one and sampled to a time vector of defined length *m* (in our case *m* = 100 points) for each measured object. Such data are further processed by one of the two algorithms introduced in this section. Namely, **machine learning logistic regression** and **scaled absolute differences algorithm**.

Logistic Regression

Correctly sampled and normalized measured data were randomly divided into the train and test datasets in a ratio 80 : 20. Train dataset was defined as $D_{train} \equiv \{[X, y]\} = \{[\vec{x}_{[i]}, y_i]\}$, where $\vec{x}_{[i]} \in R^m$ and $y_i \in \{0,1\}$ is the *i*-th measured time vector and its label for $1 \leq i \leq n$ of n measurements, respectively. They create an input data matrix formed by *n* time vectors and vectors of labels shown in respective:

$$X = [\vec{x}_{[1]}, \vec{x}_{[2]}, \dots, \vec{x}_{[n]}]^T = \begin{bmatrix} x_{11} & x_{12} & \cdots & x_{1m} \\ x_{21} & x_{22} & \cdots & x_{2m} \\ \vdots & \vdots & \ddots & \vdots \\ x_{n1} & x_{n2} & \cdots & x_{nm} \end{bmatrix}, \qquad Y = \begin{bmatrix} y_1 \\ y_2 \\ \vdots \\ y_n \end{bmatrix}, \tag{1}$$

and enter the training part of the logistic regression algorithm [2]. The elements in Y take a binary form, indicating whether an observation is classified as a walker ($y_i = 0$) or cyclist ($y_i = 1$).

We used the algorithm as specified in [1]: Logistic regression describes the probability of occurrence of Y by comparing the input values X. The output value Y has the character of binominal distribution. It is needed to determine the probability of success $P(Y = 1|\mathbf{X})$ and defeat $P(Y = 0|\mathbf{X})$, to accomplish this, we start by defining the odds as:

$$\theta(\mathbf{X}) = \frac{P(Y=1|\mathbf{X})}{P(Y=0|\mathbf{X})} = \frac{P(Y=1|\mathbf{X})}{1-P(Y=1|\mathbf{X})} \tag{2}$$

Then the log-odds $\ln(\theta(\mathbf{X})) \in (-\infty, \infty)$ are set to have the form:

$$\ln[\theta(\mathbf{X})] = \ln\left[\frac{p(\beta_0, \vec{\beta}, \mathbf{X})}{1-p(\beta_0, \vec{\beta}, \mathbf{X})}\right] = \beta_0 + \mathbf{X}.\vec{\beta}, \tag{3}$$

where $\vec{\beta} = [\beta_1, \beta_2, \dots, \beta_m]^T \in R^m$, β_0 is in our case considered to be zero, therefore we further write $p(\beta_0, \vec{\beta}, \mathbf{X}) \equiv p(\vec{\beta}, \mathbf{X})$. From (3) we have $p(\vec{\beta}, \mathbf{X}) = exp(\mathbf{X}.\vec{\beta})/[1 - exp(\mathbf{X}.\vec{\beta})]$. The unknown parameter vector $\vec{\beta}$ can be found through maximum likelihood estimation by solving $max_{\vec{\beta}} L(\vec{\beta}, Y, \mathbf{X})$, where the likelihood function is of the form:

$$L(\vec{\beta}, Y, \mathbf{X}) = \prod_{i=1}^{n} p(\vec{\beta}, \vec{x}_{[i]})^{y_i} \left[1 - p(\vec{\beta}, \vec{x}_{[i]})\right]^{1-y_i}. \tag{4}$$

Finding a maximum of (4) is equivalent to maximizing log-likelihood $max_{\vec{\beta}} l(\vec{\beta}, Y, \mathbf{X})$, where

$$l(\vec{\beta}, Y, \mathbf{X}) = \sum_{i=1}^{n} \left\{ y_i (\mathbf{X}.\vec{\beta})_i - \ln\left[1 + exp(X.\vec{\beta})_i\right] \right\}. \tag{5}$$

As a method for estimating of $\vec{\beta}$ for which $l(\vec{\beta}, Y, \mathbf{X})$ is maximal we used the multivariable function derivative free simplex search method of Lagarias et al. [3] implemented in MATLAB as built-in *fminsearch* function, with the initial value of $\Delta \vec{\beta}_{[0]} = [1, \dots, 1]^T$.

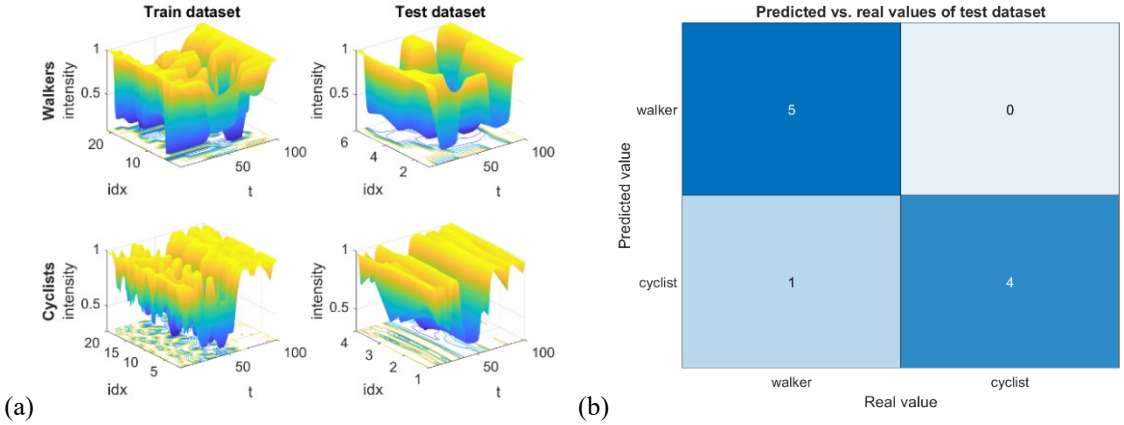

Fig. 2 Logistic regression classification. (a) Training and testing datasets visualization containing 51 measurements and two classes (walker and cyclist). (b) Heat map for results of testing dataset classification.

After the training part of the algorithm, the estimated vector $\vec{\beta}$ was used to the classification of test dataset $D_{test} \equiv \{[\mathbf{X}_{test}, Y_{test}]\}$ as a realization of prediction as $p(\vec{\beta}, \mathbf{X}_{test})$ and compared with real class Y_{test}.

Scaled Absolute Differences

To minimize the number of parameters and simplify the processing steps, we proposed an alternative approach with nonlinear data transformation. Similarly to the first procedure, we normalized the data and divided it into training and test dataset. Then we calculated the absolute differences for i-th measured time vector $1 \leq i \leq n$ of n measurements with length m and constructed a new variable

$$\Delta \vec{x}_{[i]} = [\Delta x_{i1}, \Delta x_{i2}, \dots, \Delta x_{i(m-1)}], \qquad \text{where } \Delta x_{ij} = |x_{i(j+1)} - x_{ij}|.$$

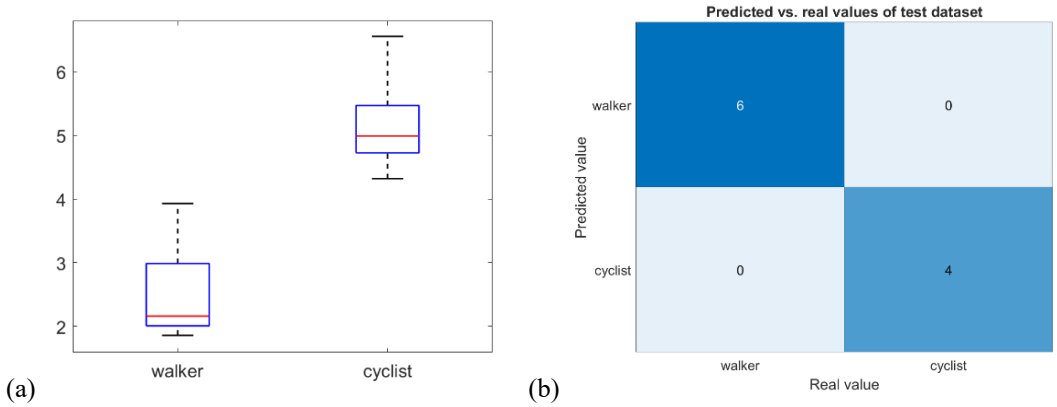

Fig. 3 Method with scaled absolute differences and threshold ~4.12. (a) Boxplots with calculated scaled absolute differences of the training dataset containing 41 measurements.(b) Heat map for results of testing dataset classification.

Next, we calculated the characteristic metric z_i for the i-th measured time vector $1 \leq i \leq n$, given as the scaled sum of the elements of the new variable $\Delta \vec{x}_{[i]}$:

$$z_i = \frac{1}{1 - M_i} \sum_{j=1}^{m-1} \Delta x_{ij}\,, \qquad \text{where } M_i = \min_{j \in \{1,2..,m\}} x_{ij}.$$

ISBN 978-80-972629-6-9

The transformed data set consisted of $D_{train} \equiv \{z_i, y_i\}$, where $z_i \in R$ and $y_i \in \{0,1\}$ are the i-th transformed vector and its label for $1 \leq i \leq n$ of n measurements, respectively. In Fig. 3 one can see the boxplots of scaled absolute differences z_i, for $1 \leq i \leq 41$ measurements from the training set for each of the two classes.
For the classification of the new sample from the test set, the absolute scaled differences of the sample is calculated and denoted z_{test}. Then the sample is classified according to the threshold ~4.12 that was chosen to maximize the margin between the groups and the threshold:

$$Y_{test} \begin{cases} walker\ z_{test} < 4.12 \\ cyclist \quad z_{test} > 4.12 \end{cases}.$$

Results and Discussion

The first proposed method based on logistic regression offered lower accuracy and required memory storage of 100 parameters. As the training set is smaller than the number of parameters, the parameter estimation is ill-posed, leaving room for further parameter restrictions. To use this classification method, one would need to perform a matrix multiplication with the measured vector and parameter $\vec{\beta}$ to classify new samples. This would require long processing times. Therefore, we implemented a different method that also offered higher accuracy. It was based on a non-linear metric of scaled absolute differences. In this method there is only one parameter needed that distinguishes the two classes. During the pre-processing we need to calculate the absolute differences, sum them and in the end scale the value with a found minimum value of the vector. Naturally, the two methods could be combined for better performance. The choice of the method would depend on the computational power of the hardware. Finally, we note that the current formulation limits the classification problem to two classes, excluding other pedestrian movements (e.g. people walking in pairs, walking their dog, or pushing prams). The methods would be more precise and robust if additional labeled training data were provided.

Conclusions

The study aimed to find a computationally nondemanding, but accurate algorithm for the analysis of vector data measured by a LiDAR sensor. From the analyzed methods, the Scaled absolute differences method appears to be the most suitable for low-energy systems with low computational power.

Acknowledgements

This work was supported by Slovak Scientific Grant Agency, project VEGA 2/0004/23, VEGA 2/0003/20 and within the projects of the Slovak Research and Development Agency Nr. APVV-21-0299 and APVV-19-0032.

References

[1] Benewake (Beijing) Co., Ltd. Product Manual of TFmini Plus. [Available online: 07.10.2022] http://en.benewake.com/product/detail/5c345cd0e5b3a844c472329b.html.

[2] T. Rymarczyk, E. Kozlowski, G. Klosowski, and K. Niderla. (2019). Logistic regression for machine learning in process tomography. *Sensors,* 19(15):3400.

[3] J.C. Lagarias, J.A. Reeds, M.H. Wright, and P.E. Wright. (1998). Convergence properties of the Melder-Mead simplex method in low dimensions. SIAM J. *Optim.*, 9(1):112-147.

A Note on Confidence Intervals for Kendall's Tau

František Rublík

Institute of Measurement Science, Slovak Academy of Sciences, Dubravska cesta 9, Bratislava, Slovakia
Email: umerrubl@savba.sk

Abstract. *Efficiency of several confidence intervals for the Kendall's tau is illustrated by sim-ulations. The simulations suggest that the interval of Samara and Randles yield acceptable coverage even for small sample sizes like $n = 15$, similar results yields the jackknife interval. A little weaker coverage yields a combined interval, defined in the text.*

Keywords: Kendall's Tau, Confidence Intervals, U-Statistics

1. Introduction

Throughout the paper we assume that $(X_1,Y_1),\dots,(X_n,Y_n)$ are independent copies of the 2-dimensional random vector (X,Y). Let $\tau = \tau(X,Y) = P((X_1 - X_2)(Y_1 - Y_2) > 0) - P((X_1 - X_2)(Y_1 - Y_2) < 0)$ denote the Kendall correlation coefficient. According to the classical result of Hoeffding, the sample Kendall correlation coefficient

$$\hat{\tau}_n = \frac{2}{n(n-1)} \sum_{i=1}^{n-1} \sum_{j=i+1}^{n} sign(X_i - X_j) sign(Y_i - Y_j)$$

is asymptotically normal estimate of τ in the sense that the convergence in distribution

$$\begin{gathered} \sqrt{n}(\hat{\tau}_n - \tau) \to N(0,\sigma^2), \\ \sigma^2 = 4\zeta_1, \quad \zeta_1 = E(\Psi_1(X,Y)^2) - \tau^2, \quad \Psi_1(x,y) = E(sign(x-X) sign(y-Y)) \end{gathered} \tag{1.1}$$

holds (here we use the standard notation $sign(a) = 1,0,-1$ if $a > 0, a = 0, a < 0$, respectively). This is used as a basis for interval estimate of τ. Let $\hat{\sigma}_n^2 = \hat{\sigma}_n^2((X_1,Y_1),\dots,(X_n,Y_n))$ be a consistent estimate of σ^2, and $\sigma^2 > 0$. If $z_{1-\alpha/2}$ denotes the $(1-\alpha/2)th$ quantile of $N(0,1)$, then

$$I_n(\hat{\tau}_n, \hat{\sigma}_n) = \langle Lo_n, Up_n \rangle,\ Lo_n = max(-1, \hat{\tau}_n - z_{1-\alpha/2}\sqrt{\frac{\hat{\sigma}_n^2}{n}}),\ Up_n = min(1, \hat{\tau}_n + z_{1-\alpha/2}\sqrt{\frac{\hat{\sigma}_n^2}{n}}) \tag{1.2}$$

is asymptotic confidence interval for τ, i.e., $P(\tau \in I_n(\hat{\tau}_n, \hat{\sigma}_n^2)) \to 1-\alpha$ as n tends to infinity. The topic of the paper is the simulation comparison of various confidence intervals for τ.

2. Subject and Methods

As has already been mentioned, a necessary condition for constructing an asymptotic confidence interval for τ is positivity of the variance of the limiting distribution (1.1). A simple sufficient condition for the positivity of σ is given in the following Lemma.

Lemma *Suppose that (X,Y) has a density $f(x,y)$ which is positive on $I = (a_1,b_1) \times (a_2,b_2)$, where $-\infty \le a_i < b_i \le +\infty$ for $i = 1,2$, and $\int_{a_1}^{b_1}\int_{a_2}^{b_2} f(x,y)dxdy = 1$. Then $\zeta_1 > 0$.*

In the next text we shall deal with continuous case, i.e., the case when (X,Y) has a density with respect to the Lebesgue measure. Hence with probability 1 the values $X_1,\dots,X_n$ are mutually different and also $Y_1,\dots,Y_n$ are mutually different with probability 1.

ISBN 978-80-972629-6-9

The classical approach for estimating the asymptotic variance is based on nonparametric approach. As τ_n is a U-statistic, its asymptotic variance can be estimated by the application of the general estimate of asymptotic variance proposed in [9], but as for not large n such an estimator does not yield good coverage of τ, it is not included into the simulations in this paper.

On p. 78 of the monograph [6] a consistent estimator of σ^2 is proposed, which in this continuous case (no ties) employs

$$\hat{\sigma}_{Nt,n} = \frac{\sqrt{N}}{\binom{N}{2}}\sigma^*_{Nt,n}, \quad \sigma^{*2}_{Nt,n} = 4\sum_{j=1}^{n} C_{o,j}^2 - 2\sum_{j=1}^{n} C_{o,j} - \frac{2(2n-3)}{n(n-1)}\Big(\sum_{j=1}^{n} C_{o,j}\Big)^2,$$

where $C_{o,j} = \#\{i; sign(X_i - X_j)sign(Y_i - Y_j) = 1\}$ is the number of pairs concordant with (X_j, Y_j).

As observed in [7], if $n = 8$ then $\sigma^{*2}_{Nt,n}$ may attain also negative values. As this is not the case with estimator defined in (2.3), in the following simulations we use

$$\tilde{\sigma}_{Nt,n} = \hat{\sigma}_{Nt,n} \;\; if \;\; \hat{\sigma}_{Nt,n} > 0, \;\; otherwise \;\; \tilde{\sigma}_{Nt,n} = \hat{\sigma}_{SaR,n}. \tag{2.1}$$

If $|(X_i - X_j)(Y_i - Y_j)| > 0$ for all $i \neq j$ (which for sampling from continuous distribution occurs with probability 1, in the case of ties an alternative formula for (2.3) is enclosed ibidem), define

$$C_i = \sum_{j=1}^{n} sign\Big((X_i - X_j)(Y_i - Y_j)\Big), \quad \overline{C} = \frac{1}{n}\sum_{j=1}^{n} C_j, \tag{2.2}$$

$$\hat{\sigma}_{SaR,n} = \sqrt{\frac{2}{(n-1)}\left(\frac{2(n-2)}{n(n-1)^2}\sum_{i=1}^{n}(C_i - \overline{C})^2 + 1 - \hat{\tau}_n^2\right)} \tag{2.3}$$

For this Samara-Randles statistic the equality $\hat{\sigma}_{SaR,n} = \sigma + o_P(1)$ holds and (2.3) can be used for construction of the confidence interval (1.2). The use of this interval is recommended also in [3].

The Kendall coefficient can be expressed as a U-statistic of order $m = 2$, i.e.,
$\hat{\tau}_n = U_n, \;\; U_n = \frac{1}{\binom{n}{m}}\sum_{\mathbf{r}\in C(m,n)} \Psi(\mathbf{X}_{r_1}, \ldots, \mathbf{X}_{r_m}), \; \Psi(\mathbf{X}, \mathbf{Y}) = sign(\mathbf{X}(1) - \mathbf{Y}(1))sign(\mathbf{X}(2) - \mathbf{Y}(2))$
where $C(m,n)$ denotes the system of all subsets of $\{1, \ldots, n\}$ consisting of m elements. For the estimation of the variance of this general form of U-statistics is on pp. 420–422 of [8] considered the plug-in estimate (which in the case of the order $m = 2$ has the form)

$$\begin{aligned} v_{ScB,n} &= 4\frac{n-2}{n-1}\tilde{\zeta}_1 + \frac{2}{n-1}\tilde{\zeta}_2, \quad \tilde{\zeta}_1 = \tilde{\zeta}_1^{(1)} - \tilde{\zeta}_1^{(2)} \\ \tilde{\zeta}_1^{(1)} &= \frac{1}{\binom{n}{3}}\sum_{\mathbf{r}\in C(3,n)} h_0^*(\mathbf{X}_{r_1}, \mathbf{X}_{r_2}, \mathbf{X}_{r_3}), \;\; \tilde{\zeta}_1^{(2)} = \frac{1}{\binom{n}{4}}\sum_{\mathbf{r}\in C(4,n)} h_c^*(\mathbf{X}_{r_1}, \mathbf{X}_{r_2}, \mathbf{X}_{r_3}, \mathbf{X}_{r_4}), \end{aligned}$$

where

$$\begin{aligned} h_0^*(\mathbf{X}_1, \mathbf{X}_2, \mathbf{X}_3) &= \frac{1}{3}(h_{12}h_{13} + h_{12}h_{23} + h_{13}h_{23}), \quad h_{rs} = \Psi(\mathbf{X}_r, \mathbf{X}_s), \\ h_c^*(\mathbf{X}_1, \mathbf{X}_2, \mathbf{X}_3, \mathbf{X}_4) &= \frac{1}{3}(h_{12}h_{34} + h_{13}h_{24} + h_{14}h_{23}), \\ \tilde{\zeta}_2 &= \frac{1}{\binom{n}{4}}\sum_{\mathbf{r}\in C(4,n)} k^*(\mathbf{X}_{r_1}, \mathbf{X}_{r_2}, \mathbf{X}_{r_3}, \mathbf{X}_{r_4}), \end{aligned}$$

$$k^*(\mathbf{X}_1, \mathbf{X}_2, \mathbf{X}_3, \mathbf{X}_4) =$$
$$= \tfrac{1}{6}\Big((\Psi(\mathbf{X}_1, \mathbf{X}_2) - \Psi(\mathbf{X}_3, \mathbf{X}_4))^2 + (\Psi(\mathbf{X}_1, \mathbf{X}_3) - \Psi(\mathbf{X}_2, \mathbf{X}_4))^2 + (\Psi(\mathbf{X}_1, \mathbf{X}_4) - \Psi(\mathbf{X}_2, \mathbf{X}_3))^2\Big)$$

ISBN 978-80-972629-6-9

and $C(m,n) = \left\{ \mathbf{r} = \{r_1, \ldots, r_m\}; \mathbf{r} \subset \{1, \ldots, n\}, \#\mathbf{r} = m \right\}$ denotes the collection all subsets of $\{1, \ldots, n\}$ consisting of m various elements. As this estimator sometimes yields negative values, in the next simulations we shall consider a modified Schucany-Bankson estimator

$$\sigma^2_{ScB,n} = v_{ScB,n} \;\; if \;\; v_{ScB,n} > 0, \;\; otherwise \;\; \sigma^2_{ScB,n} = \hat{\sigma}^2_{SaR,n}. \tag{2.4}$$

We remark that a user of MATLAB can obtain the set $C(m,n)$ by means of the command nchoosek(1:n,m).

It is proposed on p. 3 of [4] instead of an underlying estimator $\sigma^2_{J,n}$ to use $(1 - a/n)\sigma^2_{J,n}$ with $a \geq 0$. As simulations show that for sampling from normal distribution the estimator $\sigma^2_{ScB,n}$ yield for τ probability of coverage visible below the nominal level, we include into simulations of this paper its enlarged version

$$\sigma^2_{ScBm,n} = (1 + \frac{3}{n})\sigma^2_{ScB,n}, \tag{2.5}$$

where $a = -3$ is for our case chosen empirically. As $\sigma^2_{ScB,n}$ is often smaller than $\hat{\sigma}^2_{SaR,n}$, we shall consider also the estimator

$$\sigma^2_{comb,n} = (\sigma^2_{ScB,n} + \hat{\sigma}^2_{SaR,n})/2. \tag{2.6}$$

Another possibility is the use of the jackknife estimator

$$\begin{gathered} \sigma^2_{Jack,n} = (n-1)\sum_{i=1}^{n} (\tau_{n,i} - \overline{\overline{\tau}}_n)^2 \\ \tau_{n,i} = \frac{1}{(n-1)(n-2)} \sum_{j=1, j\neq i} \; \sum_{k=1, k\neq i} sign(X_j - X_k) sign(Y_j - Y_k), \quad \overline{\overline{\tau}}_n = \frac{1}{n}\sum_{j=1}^{n} \tau_{n,j}. \end{gathered} \tag{2.7}$$

Fligner and Rust proposed the confidence interval $I^{(FR)} = \langle \tau_n - k^*_{\alpha/2,n} \frac{\hat{\sigma}_{J,n}}{\sqrt{n}}, \tau_n + k^*_{\alpha/2,n} \frac{\hat{\sigma}_{J,n}}{\sqrt{n}} \rangle$, where $k^*_{\beta,n}$ are constants tabled on p. 1602 of their paper and (cf. (2.2))

$$\hat{\sigma}^2_{J,n} = \frac{4}{(n-1)(n-2)^2} \sum_{i=1}^{n} (C_i - \overline{C})^2. \tag{2.8}$$

3. Simulation Results

In the following tables the quantities $P^{(Noet)}$, $P^{(SaR)}$, $P^{(ScB)}$, $P^{(ScBm)}$, $P^{(comb)}$, $P^{(jack)}$ and $P^{(FlR)}$ denote simulation estimates of the probability of coverage of τ by the intervals based on the procedure of Noether, Samara-Randles, Schucany - Bankson, on the estimator (2.5), (2.6), on the jackknife estimator (2.7) and on the Fligner-Rust procedure using (2.8), respectively. $E^{(Noet)}$, $E^{(SaR)}$, $E^{(ScB)}$, $E^{(ScBm)}$, $E^{(comb)}$, $E^{(jack)}$ and $E^{(FlR)}$ denote simulation estimates of the length of the corresponding confidence intervals. The results are obtained for the asymptotic coverage $1 - \alpha = 0.95$ for $N = 5000$ trials in every case. We use the fact that for the 2-dimensional normal distribution with correlation coefficient ρ the equality $\tau = 2\frac{arcsin(\rho)}{\pi}$ holds. Further we consider Farlie–Gumbel–Morgenstern copula $C(u,v) = uv + \theta\, uv(1-u)(1-v)$ with $\theta = 1$. According to [1] for $\theta = 1$ its Kendall's tau $\tau = 2/9$. Random samples from this copula were generated by means of the algorithm described on p. 41 of [5].

ISBN 978-80-972629-6-9

normal distribution $n = 15$				
τ	0.2	0.3	0.5	0.7
$P^{(Noet)}$	0.8538	0.8548	0.8452	0.8396
$E^{(Noet)}$	0.6082	0.5757	0.4722	0.3297
$P^{(SaR)}$	0.9458	0.9464	0.9506	0.9592
$E^{(SaR)}$	0.7830	0.7507	0.6462	0.4875
$P^{(ScB)}$	0.8968	0.8962	0.8828	0.8718
$E^{(ScB)}$	0.7054	0.6675	0.5469	0.3800
$P^{(ScBm)}$	0.9178	0.9160	0.8996	0.8910
$E^{(ScBm)}$	0.7725	0.7310	0.5983	0.4135
$P^{(comb)}$	0.9260	0.9268	0.9236	0.9306
$E^{(comb)}$	0.7467	0.7120	0.6009	0.4406
$P^{(jack)}$	0.9400	0.9388	0.9372	0.9436
$E^{(jack)}$	0.7967	0.7602	0.6425	0.4702
$P^{(FlR)}$	0.9522	0.9510	0.9502	0.9536
$E^{(FlR)}$	0.8577	0.8183	0.6911	0.5026

FGM copula			
n	15	20	25
$P^{(Noet)}$	0.8502	0.8844	0.9032
$E^{(Noet)}$	0.5749	0.5067	0.4570
$P^{(SaR)}$	0.9462	0.9508	0.9524
$E^{(SaR)}$	0.7576	0.6272	0.5439
$P^{(ScB)}$	0.8908	0.9116	0.9240
$E^{(ScB)}$	0.6665	0.5646	0.4976
$P^{(ScBm)}$	0.9116	0.9290	0.9360
$E^{(ScBm)}$	0.7298	0.6055	0.5266
$P^{(comb)}$	0.9254	0.9356	0.9408
$E^{(comb)}$	0.7153	0.5973	0.5216
$P^{(jack)}$	0.9394	0.9462	0.9480
$E^{(jack)}$	0.7639	0.6263	0.5409
$P^{(FlR)}$	0.9504	0.9544	0.9536
$E^{(FlR)}$	0.8224	0.6582	0.5602

The results of these simulations (and also of simulations not included into the text for the space reasons) suggest that the best efficiency have the Samara-Randles and jackknife intervals. Both yield approximately equivalent result, Samara-Randles with somewhat better coverage and jackknife with somewhat shorter length. One could also consider the use of combined interval (2.6) to obtain better length, but they yield a little worse coverage. The Fligner-Rust interval yields good coverage but large length, the Noether interval requires larger sample sizes.

Acknowledgments

The research was supported by Grant VEGA 2-0096-21 and by grant SK-CZ-21-0109.

References

[1] Dengler, B., Schmock, U. (2010). On the Asymptotic Variance of the Estimator of Kendall's tau. Vienna University of Technology. (available on Internet)

[2] Fligner, M. A., Rust, S. W. (1983). On the independence problem and Kendall's tau. *Communications in Statistics - Theory and Methods,* 12, 1597 – 1607.

[3] Hollander, M., Wolfe, D.A., Chicken, E. (2014). *Nonparametric Statistical Methods. Third Edition.* John Wiley & Sons, New Jersey.

[4] Maesono, Y. (1998). Asymptotic mean square errors of variance estimators for U-statistics and their Edgeworth expansions. *Journal of Japan Statistical Society,* 28, 1–19.

[5] Nelsen, R. B. (2006). *An Introduction to Copulas. Second Edition.* Springer, New York.

[6] Noether, G. E. (1976). *Elements of Nonparametric Statistics.* John Wiley & Sons, New York.

[7] Samara, B., Randles, R. H. (1988) A test for correlation based on Kendall's tau. *Communications in Statistics - Theory and Methods,* 17, 3191-3205.

[8] Schucany, W. R., Bankson, D. M. (1989). Small sample variance estimators for U-statistics. *Australian Journal of Statistics,* 31, 417-426.

[9] Sen, P. K. (1960) On some convergence properties of U-statistics. *Calcutta Statist. Assoc. Bull.*, 10, 1-18.

Criteria of Goodness of Fit and Confidence Intervals for Polynomial Regression Models Through the Origin (i.e. Without the Intercept)

[1,2] Orest Kochan, [1]Ze Wang, [1]Yong Ouyang, [3]Valeriy Eromenko, [3]Andrii Aliluiko, [4]Krzysztof Przystupa

[1] School of Computer Science, Hubei University of Technology, Wuhan, China
[2] Lviv Polytechnic National University, Lviv, Ukraine
[3] West Ukrainian National University, Ternopil, Ukraine
[4] Department of Automation, Lublin University of Technology, Lublin Poland
Email: orest.v.kochan@lpnu.ua

Abstract. *There is often a need for fitting curves for conversion characteristics or error dependencies using polynomial regression models through the origin, i.e. without the intercept. Such regression models should have the criteria for evaluating their quality, i.e. the goodness of fit, for the automated evaluation of the parameters of measuring channels, because the conventional coefficient of determination does not work well in such models.*

Keywords: Polynomial Regression Model Through the Origin, Coefficient of Determination, Confidence Interval

1. Introduction

The development of the Internet of Things [1] increases the number of measurement channels (MC). Often there is a need for the transition from individual designing of MCs to their composition using conventional hardware and software modules [2, 3]. The modules for fitting conversion characteristics (CC) of components of MCs are often used [4]. The efficiency of the composition of MCs depends on these modules, so the criteria for evaluating their quality should be developed. One of the most common methods of CC identification is the method of least squares (LSM) to construct regressions [5, 6]. The polynomial regressions are often used because they require a minimum of computing resources [6]. The advantages of the LSM are the ability to evaluate the significance of the obtained models, and their individual coefficients, as well as they have the criteria to evaluate their quality. i.e. the goodness of fit [5, 7]. But if the CC of MC components passes through the origin of the Cartesian coordinate system, problems arise because the coefficient of determination for such polynomial regression models through the origin (i.e. without the intercept) inadequately estimates their goodness of fit [5, 8]. There are many such components in the MC [6] – generator sensors, amplifiers, analog-to-digital converters, and some software components. In addition, these are mathematical models of almost all error correction functions [6, 8]. In particular, the functions to correct errors due to temperature and time drift, are calculated as the difference between the instantaneous and initial values of the parameter, so they inevitably pass through the origin. The goal of this work is to develop the criteria to assess the goodness of fit for polynomial regression models through the origin.

2. Assessing the Goodness of Fit

The object of this study is a polynomial model [5, 7]

$$y = \alpha_1 t + \alpha_2 t^2 + \ldots + \alpha_m t^m + u, \tag{1}$$

where y u and are random variables, $\alpha_1, \alpha_2, \ldots, \alpha_m$ are unknown deterministic parameters, positive integer number m is to be selected for each particular sample. Let t_i $\overline{1,n}$ be observed values of the explanatory variable. Then model (1) will take the following form

$$Y_i = \alpha_1 t_i + \alpha_2 t_i^2 + \ldots + \alpha_m t_i^m + U_i,\ i = \overline{1,n}. \tag{2}$$

Let us write the system of n equations (2) in vector-matrix form:

$$\tilde{Y} = T\alpha + U, \tag{2*}$$

where $\tilde{Y} = \begin{pmatrix} Y_1 \\ Y_2 \\ \cdots \\ Y_n \end{pmatrix}$, $T = \begin{pmatrix} t_1 & t_1^2 & \cdots & t_1^m \\ t_2 & t_2^2 & \cdots & t_2^m \\ \cdots & \cdots & \cdots & \cdots \\ t_n & t_n^2 & \cdots & t_n^m \end{pmatrix}$, $\alpha = \begin{pmatrix} \alpha_1 \\ \alpha_2 \\ \cdots \\ \alpha_m \end{pmatrix}$, $U = \begin{pmatrix} U_1 \\ U_2 \\ \cdots \\ U_n \end{pmatrix}$ U'. Estimation of this model from the sample $\left\{ y_i, t_i, t_i^2, \ldots, t_i^m,\ i = \overline{1,n} \right\}$ of size *n* is a vector-matrix equation

$$Y = Ta + E, \tag{3}$$

where $Y = (y_1, y_2, \ldots, y_n)'$, $a = (a_1, a_2, \ldots, a_m)'$, $E = (e_1, e_2, \ldots, e_n)'$, a is the estimation of vector α, the apostrophe denotes the operation of matrix transposition. Let us assume that the following assumptions hold for model (2*) [5, 7]:

A.1. U is a random vector, T is a deterministic matrix;

A.2. $E(U) = O_n = (0,0,\ldots,0)'$;

A.3. $E(UU') = \sigma^2 I_n$, I_n is the identity matrix of order n, $\sigma > 0$ is the constant to be estimated;

A.4. U is a normally distributed random vector, i.e $U \sim N_n(0, \sigma I_n)$;

A.5. The rank of matrix *T* equals $m < n$.

Let us denote the deterministic component of the model (3) as $\hat{Y} = (\hat{y}_1, \hat{y}_2, \ldots, \hat{y}_n)$, that is

$$\hat{Y} = Ta \quad . \tag{4}$$

Then, the criterion for choosing the vector of estimations *a*n according to the least-squares method (LSM) is the minimization of the sum of squares of residuals: $Q(a) = \sum_{i=1}^{n} (y_i - \hat{y}_i)^2 = \sum_{i=1}^{n} e_i^2 = E'E = (Y - Ta)'(Y - TA) \to \min$. Taking into account the necessary condition for the extremum of the function of *m* variables, we get the system of normal equations in matrix form to determine vector *a*:

$$T'Ta = T'Y, \tag{5}$$

From which, taking into account A.5, we obtain the expression as follows:

$$a = (T'T)^{-1} T'Y. \tag{6}$$

The quality, i.e. the goodness of fit for a multiple regression model with intercept is characterized by the coefficient of determination R^2. It is based on the variance partitioning:

$$\sum_{i=1}^{n} (y_i - \overline{y})^2 = \sum_{i=1}^{n} (\hat{y}_i - \overline{y})^2 + \sum_{i=1}^{n} (y_i - \hat{y}_i)^2. \tag{7}$$

However, for the models without the intercept, this equality does not hold. Let us derive the analogue for equality (7). For this, we square and sum the left and right-hand sides of the

equality $y_i = (y_i - \hat{y}_i) + \hat{y}_i,\ \ i = \overline{1,n},: \ \sum_{i=1}^{n} y_i^2 = \sum_{i=1}^{n} (y_i - \hat{y}_i)^2 + 2\sum_{i=1}^{n} (y_i - \hat{y}_i)\hat{y}_i + \sum_{i=1}^{n} \hat{y}_i^2.$

The second term in the right-hand side equals zero, since according to (4) and (5)

$\sum_{i=1}^{n} (y_i - \hat{y}_i)\hat{y}_i = (Y - \hat{Y})'\hat{Y} = (Y - Ta)'Ta = Y'Ta - a'T'Ta = 0.$ We take into account that $Y'Ta$ is a scalar, therefore $Y'Ta = (Y'Ta)' = a'T'Y = a'T'Ta.$ So, $\sum_{i=1}^{n} y_i^2 = \sum_{i=1}^{n} (y_i - \hat{y}_i)^2 + \sum_{i=1}^{n} \hat{y}_i^2$ and by analogy with the general case, the coefficient of determination is determined from the following formulae

$$R_0^2 = \frac{\sum_{i=1}^{n} \hat{y}_i^2}{\sum_{i=1}^{n} y_i^2} = 1 - \frac{\sum_{i=1}^{n} e_i^2}{\sum_{i=1}^{n} y_i^2}. \quad (8)$$

The disadvantage of the coefficient of determination is that it, in general, increases with the rise of degree *m*, although this does not necessarily mean an improvement in the goodness of fit of the regression model. Therefore, it is reasonable to use the adjusted coefficient of determination, which is determined from the formula

$$\hat{R}_0^2 = 1 - \frac{n-1}{n-m}(1 - R^2) \quad (9)$$

The degree *m* of the polynomial in model (1), in general, is unknown, and such a contradiction should be considered when choosing it for a specific sample. It is reasonable to consider a wider class of functions, that is, polynomials of a higher degree since they better fit empirical data. However, it increases the number of unknown parameters, decreases the degrees of freedom and, as a result, increases the corresponding standard errors. Let us consider the issue of finding the degree *m* of polynomial (1) based on a specific sample. Let us assume that for the model

$$y^{(k)} = \alpha_1 t + \alpha_2 t^2 + \ldots + \alpha_k t^k + u \quad (10)$$

we will find LSM estimations $a_1, a_2, \ldots, a_k$ and it is found that all parameters $\alpha_1, \alpha_2, \ldots, \alpha_k$ are significant at the significance level α, that is, the following inequalities hold [5, 7]

$$\frac{|a_j|}{S_{a_j}} > t(1-\alpha; n-k),\ j = \overline{1,k}, \quad (11)$$

where the standard deviation (standard error) of the regression coefficient a_j is $S_{a_j} = \sqrt{S_e^2 \left[(T'T)^{-1}\right]_{jj}}$, $S_e^2 = \sum_{i=1}^{n} e_i^2/(n-k)$ is an unbiased estimate of the unknown parameter σ^2 or sample variance of residuals, $\left[(T'T)^{-1}\right]_{jj}$ is the *j*- th diagonal element of the matrix $(T'T)^{-1}$, $t(1-\alpha; n-k)$ is the value of the Student's *t*-distribution determined at the level of significance α for the degrees of freedom of $n-k$ [5, 7]. The next step is to refine model (10), that is, the study of the model

$$y^{(k+1)} = \sum_{i=1}^{k} \alpha_i t^i + \alpha_{k+1} t^{k+1} + u. \quad (12)$$

In this case, the coefficient of $\alpha_{k+1} t^{k+1}$ can be either accepted or rejected. The rejection of the coefficient can be considered as a consequence of the correctness of the null hypothesis $H_0: \alpha_{k+1} = 0$, that is, the insignificance of the estimate a_{k+1}. If the inequality

$$\frac{|a_{k+1}|}{S_{a_{k+1}}} > t(1-\alpha; n-k-1) \tag{13}$$

does not hold, then at the significance level of α $\alpha_{k+1} = 0$. If inequality (13) is fulfilled, then the model $y^{(k+2)} = \sum_{i=1}^{k+1} \alpha_i t^i + \alpha_{k+2} t^{k+2} + u$ should be examined in the same way. If two successive coefficients are rejected, i.e. $\alpha_{k+1} = \alpha_{k+2} = 0$, then it can be concluded that in the model (1) $m=k$. This approach studies model (1) for cases $m = 1, 2, \ldots, k$. Thus, an empirical regression equation is obtained for a certain sample $\hat{y} = \sum_{i=1}^{k} a_i t^i$, where the LSM estimates $a_i, i = \overline{1,k}$, are determined from (6). Then the point estimate for $t = t^*$

$$\hat{y}_0 = \hat{y}(t^*) = \sum_{i=1}^{k} a_i (t^*)^i, \tag{14}$$

and the $1-\alpha$ confidence interval for unknown $y_0^* = y(t^*)$:

$$\hat{y}_0 - t(1-\alpha; n-k) S_{\hat{y}_0} < y_0^* < \hat{y}_0 + t(1-\alpha; n-k) S_{\hat{y}_0}, \tag{15}$$

where $S_{\hat{y}_0} = \sqrt{S_e^2 \left[1 + T_0'(T'T)^{-1} T_0\right]}$; .

3. Conclusions

As shown in [5, 8], the coefficient of determination in polynomial regression models through the origin (i.e. without the intercept) incorrectly assesses the goodness of fit because the variance partitioning does not hold. Therefore, this paper developed other criteria for evaluating the goodness of fit for such models. The procedure for constructing a confidence interval is also developed.

References

[1] Xu, H., et al. (2020). A combination strategy of feature selection based on an integrated optimization algorithm and weighted k-nearest neighbor to improve the performance of network intrusion detection. *Electronics*, *9*(8), 1206.

[2] Hu, Z., et al (2021). Procedure for processing biometric parameters based on wavelet transformations. *International Journal of Modern Education and Computer Science*, *13*(2), 11-22.

[3] Kochan, R., Kochan, O., Chyrka, M., Vasylkiv, N. (2005). Precision data acquisition (DAQ) module with remote reprogramming. In *2005 IEEE IDAACS,* (pp. 279-282).

[4] Hu, Z., et al. (2020). Statistical Techniques for Detecting Cyberattacks on Computer Networks Based on an Analysis of Abnormal Traffic Behavior. *International Journal of Computer Network & Information Security*, *12*(6), 1-13.

[5] Mendenhall, W., Sincich, T., Boudreau, N. S. (2003). *A second course in statistics: regression analysis*. New York: Prentice Hall.

[6] Restivo, M. T., et al (2011). *Handbook of laboratory measurements and instrumentation*. International Frequency Sensor Association (IFSA).

[7] Kremer, N., Putko, B. (2022). Econometrics. Moscow: Litres.

[8] Yeromenko, V., Kochan, O. (2013). The conditional least squares method for thermocouples error modeling. In *2013 IEEE 7th IDAACS,* (Vol. 1, pp. 157-162).

A Difference Between an Optimal Parameter Set for a Statistical Inferring of Directionality of Coupling for Stochastic and Chaotic Deterministic Systems Based on Information Theory

Martina Chvosteková

Institute of Measurement Science, Slovak Academy of Sciences, Dúbravská cesta 9,
841 04 Bratislava, Slovakia
Email: martina.chvostekova@savba.sk

Abstract. *Conditional mutual information (CMI) is one of the most widely used tools to characterize causal influences in ensembles of complex systems from observed time series. This paper focuses on an optimal model-free method for detecting the directionality of coupling for stochastic processes and chaotic deterministic processes based on conditional mutual information. We consider a binning approach and the technique based on k nearest neighbours for estimating CMI. Two resampling procedures for generating the surrogate data are used to test the statistical significance of CMI. The numerical experiment is performed using a linear autoregressive model and the system of Hénon maps. For a correct statistical inferring of the directionality of coupling, it is recommended to use the binning approach for estimating CMI; however, a difference is observed between an optimal parameter set for the considered stochastic and the chaotic deterministic system. A small number of bins for the linear autoregressive model is recommended, while an upper limit of bins is found as optimal for the Hénon system.*

Keywords: Conditional Mutual Information, Causality, Surrogate Data

1. Introduction

Conditional mutual information (CMI) is a model-free approach to detect causal influences in ensembles of complex systems from observed time series. It is an information-theoretic measure, representing a generalization of the classical Granger causality. We select some of the usually used ways to estimate CMI and compare them according to the number of correct detection of coupling directionality. The numerical experiment is performed using a linear autoregressive model and the system of Hénon maps. We show the results of statistical analysis obtained by using surrogate data under consideration of weak coupling strengths and small numbers of observations.

2. Estimation and statistical testing of CMI

Consider random variables X, Y, and Z. The *conditional mutual information*, denoted $I(X;Y|Z)$, of variables X, Y given the variable Z is given as

$$I(X;Y|Z) = H(X,Z) + H(Y,Z) - H(Z) - H(X,Y,Z), \tag{1}$$

where $H(.)$ denotes the *Shannon entropy*, $H(.,.)$ and $H(.,.,.)$ denote the *joint Shannon entropies*, see e.g. [1]. It holds $I(X;Y|Z) \geq 0$ for discrete variables, and under certain regularity conditions, CMI is non-negative also for continuous random variables. The equality $I(X;Y|Z) = 0$ holds if and only if X and Y are independent conditionally on Z. Thanks to the non-negativity, CMI can be used for detecting causal influence.

Let $x(t)$, $y(t)$ represent the time series of two stationary processes X and Y, respectively. To use the CMI for detecting the direction of coupling between processes X and Y, we define

ISBN 978-80-972629-6-9

$X_n^- = [x(n-1), x(n-2), \ldots]$, and $Y_n^- = [y(n-1), y(n-2), \ldots]$. There is an information flow from X to Y, denoted $X \to Y$ if it holds

$$I(X_n^-; y(n)|Y_n^-) > 0. \tag{2}$$

The CMI quantifies the information provided by the past of process X about the future of Y that is not already provided by the past of process Y. The non-zero CMI can be interpreted as a presence of influence of process X on the future of process Y. Note that CMI in the form (2) is also referred to as transfer entropy (TE); see [2]. If $Z_1, \ldots, Z_m$ denote the other processes interacting with processes X and Y, then the pairwise CMI $X \to Y$ is calculated conditionally on the past of all processes of the system except the past of process X.

Nonparametric estimation of CMI

We consider the two mostly used estimators of CMI: binning estimator (BIN) and the estimator based on the k nearest neighbours technique (kNN). We compare two possible discretization schemes dividing the space into bins: equidistant binning (BIND) and equiquantal binning (BINQ). The sample space is divided into bins of equal size by equidistant binning regardless of the data distribution. By equiquantal binning, the sample space is uniformly divided into bins. Paluš [5] proposed that the number of bins should not exceed the $(n+1)$st root of the number of the sample length. The CMI is estimated by (1) based on the binning estimates of the entropies. The CMI estimator based on kNN is given as

$$I(X_n^-; y(n)|Y_n^-) = \psi(k) - \left\langle \psi(n_{xz}+1) + \psi(n_{yz}+1) - \psi(n_z+1) \right\rangle, \tag{3}$$

where ψ is the digamma function, n_A is the number of neighbours of the reference point in the space A with a distance smaller than the distance to the k-th neighbour of the given reference point in the joint space $(d_{X_n^-} + d_{Y_n^-} + d_{y(n)})$, n_{xz} denotes the space of dimension $(d_{X_n^-} + d_{Y_n^-})$, n_{yz} denotes the space of dimension $(d_{y(n)} + d_{Y_n^-})$, n_z denotes the space of dimension $d_{Y_n^-}$, and $\langle . \rangle$ denotes average over all points in the $(d_{X_n^-} + d_{Y_n^-} + d_{y(n)})$-dimensional space.

It is a crucial issue to approximate the infinite-dimensional variables (i.e., X_n^-, Y_n^-) representing the past processes before estimating CMI. This problem can be solved by the so-called uniform or non-uniform embedding; for more details, see, e.g. [4]. Here, we evaluate different statistical tests of CMI significance for the "best scenario", which means under the consideration of the known embedding dimension.

Statistical testing of CMI significance

The statistical significance of CMI estimates was tested by using surrogate data. We considered two resampling procedures for generating the data, which should preserve all the original time series properties except the one being tested. The time-shifted surrogates data are generated by cyclically time-shifting the components of the driving variable in the first shuffling scheme. Secondly, we used the nearest-neighbour local permutation test (P) proposed by Runge (2017) [3]. The local permutation test is based on the kNN estimator of CMI and the number of local permuted neighbours, denoted k_{perm}. The time-shifting method could be used to test a significance of a binning CMI estimator and the k-NN estimator of CMI. Runge's local permutation test is available only for the k-NN estimator of CMI.

3. Experiment

We investigated which combination of CMI estimators and shuffling methods is optimal in statistically detecting coupling directionality. The time series were generated from one stochastic

and one deterministic chaotic system. Particularly the linear autoregressive model

$$\begin{aligned} x_{1,t} &= 0.5x_{1,t-2} + \varepsilon_{1,t}, \quad \varepsilon_{1,t} \sim N(0,0.2) \\ x_{2,t} &= 0.5x_{2,t-2} + C_1 x_{1,t-1} + \varepsilon_{2,t}, \quad \varepsilon_{2,t} \sim N(0,0.2). \end{aligned} \tag{4}$$

and the system of Hénon maps was considered

$$\begin{aligned} x_{1,t} &= 1.4 - x_{1,t-1}^2 + 0.3x_{1,t-2} \\ x_{2,t} &= 1.4 - (C_2 x_{1,t-1} x_{2,t-1} + (1-C_2)x_{2,t-1}^2) + 0.3x_{2,t-2}. \end{aligned} \tag{5}$$

We set unidirectional causal connections for both systems from x_1 to x_2. The coupling strength was controlled by the parameters C_1 and C_2. To evaluate the performance of the causal detecting methods, we considered a very weak coupling and weak strength coupling for both systems. It was set to $C_1 = \{0.1, 0.25\}$ and $C_2 = \{0.06, 0.15\}$. We ran 100 simulations of a system for sample sizes $T = \{300, 3000\}$ obtained after discarding the first 10000 points.

The strength of the information flow $x_1 \to x_2$ was calculated by $I(x_{1,t-1}; x_{2,t}|x_{2,t-2})$, and the opposite information flow, i.e., $x_2 \to x_1$ was calculated by $I(x_{2,t-1}, x_{2,t-2}; x_{1,t}|x_{1,t-2})$ for the linear autoregressive model. The strength of the information flow $x_1 \to x_2$ was calculated by $I(x_{1,t-1}; x_{2,t}|x_{2,t-1}, x_{2,t-2})$, and the opposite information flow, i.e., $x_2 \to x_1$ was calculated by $I(x_{2,t-1}, x_{2,t-2}; x_{1,t}|x_{1,t-1}, x_{1,t-2})$ for the system of Hénon maps.

To assess the statistical performance of the two resampling methods, we tested the significance of the estimated CMI on 100 simulations from each system. For each simulation, we estimated CMI by equidistant binning approach and equiquantal binning approach with $bins = \{2, 3, \ldots, 12\}$, and by the k-NN approach with $k = \{2, 3, \ldots, 12\}$. The statistical significance of all estimated CMI was analysed by the time-shifted surrogates at the significance level of $\alpha = 0.05/2$, and the significance of the kNN estimates of CMI was also analysed by the local permutation test with $k_{perm} = 10$, and $\alpha = 0.05/2$. The surrogate sample size was set to 100. Note that an upper limit number of bins is 7 for a sample of length 300, and 14 for a sample of length 3000.

4. Results

Table 1 and Table 2 show the percentage of the correctly detected causal connection $x_1 \to x_2$ and simultaneously correctly detected absence of causal relationship $x_2 \to x_1$ from 100 realizations of the linear autoregressive model and Hénon maps, respectively. We observe a difference between obtained percentages by various combinations of the parameters $N, bins, k, C_1, C_2$, and CMI estimator for stochastic VAR and Hénon system. The best results are obtained by the equiquantal binning approach with a small number of bins for VAR in the case of $C_1 = 0.1$, while the best results are obtained by both binning approaches comparatively for limit values of bins for Hénon system in the case of $C_2 = 0.06$. Similar behaviour of the compared testing approaches is observed for considered stronger couplings for both systems. However, the qualitatively good results are obtained for all considered numbers of bins, kNN estimators tested by the time-shifted data for $k \geq 3$, and kNN estimators tested by the local permutation test for $k \geq 8$ in the case $N = 3000$, $C_1 = 0.25$. The excellent results are obtained by the local permutation test for $k \geq 4$ in the case $N = 3000$, $C_2 = 0.15$.

5. Discussion and Conclusions

It has been observed a difference between an optimal parameter set for statistical testing the significance of the causal connection for the stochastic VAR and the chaotic deterministic Hénon

N	bins/k	2	3	4	5	6	7	8	9	10	11	12
							$C_1 = 0.1$					
300	BINQ	10	9	10	7	4	5	5	2	6	4	1
	BIND	13	10	11	4	8	5	8	4	4	8	2
	kNN	2	4	2	4	3	5	4	6	9	6	6
	kNN P	17	0	0	0	0	0	0	1	0	0	0
3000	BINQ	90	89	87	57	41	29	26	12	20	7	13
	BIND	91	64	74	67	56	46	31	32	27	28	18
	kNN	8	5	5	4	9	7	9	11	11	14	13
	kNN P	0	0	0	0	0	0	0	0	0	0	0
							$C_1 = 0.25$					
300	BINQ	69	53	41	30	27	19	17	11	9	7	2
	BIND	71	54	49	40	34	14	12	14	8	12	7
	kNN	22	36	44	47	53	60	67	71	77	78	80
	kNN P	36	4	1	0	8	6	7	12	13	19	20
3000	BINQ	87	92	93	98	96	98	100	100	99	99	99
	BIND	83	95	99	97	100	98	100	100	99	100	100
	kNN	73	91	98	97	98	97	97	96	97	94	93
	kNN P	28	12	33	54	79	87	94	95	100	100	100

Table 1: The percentage of correctly detected coupling directionality for linear autoregressive model.

N	bins/k	2	3	4	5	6	7	8	9	10	11	12
							$C_2 = 0.06$					
300	BINQ	5	1	12	5	11	13	16	9	13	8	11
	BIND	1	9	6	9	10	9	15	16	16	9	14
	kNN	3	8	8	6	2	2	1	2	4	4	4
	kNN P	1	0	0	0	0	0	0	0	0	0	0
3000	BINQ	33	57	52	53	68	81	75	78	85	94	97
	BIND	11	15	56	73	61	76	82	84	89	89	95
	kNN	98	75	53	47	46	50	52	54	52	51	50
	kNN P	98	99	1	0	0	0	0	0	0	0	0
							$C_2 = 0.15$					
300	BINQ	15	54	56	68	81	67	67	58	57	43	36
	BIND	28	34	60	78	80	89	85	84	76	73	59
	kNN	85	82	77	71	71	71	63	63	61	63	63
	kNN P	61	52	8	0	0	0	0	0	0	0	0
3000	BINQ	0	0	0	0	0	5	11	44	66	98	100
	BIND	0	0	0	0	0	1	38	74	97	93	100
	kNN	20	1	0	0	0	0	0	0	0	0	0
	kNN P	20	27	100	100	100	100	100	100	100	100	100

Table 2: The percentage of correct detected coupling directionality for Hénon maps.

system. According to obtained results, it is recommended to use the binning approach with a small number of bins for the VAR, while it is recommended to use the binning approach with an upper limit value of bins for the Hénon system. The local permutation test for a larger number of observations and a stronger coupling between time series for both systems obtains excellent results. Whether the different tactics hold for the two analysed systems or the stochastic systems and the chaotic systems, in general, is the object of future research.

Acknowledgments

Supported by the Slovak Grant Agency for Science (VEGA 2/0023/22, VEGA 2/0096/21) and by the Slovak Research and Development Agency (SK-CZ-RD-21-0109).

References

[1] Vejmelka, M., Paluš, M. (2008). Inferring the directionality of coupling with conditional mutual information, *Phys. Rev. E*, 77, 026214.

[2] Schreiber, T. (2000). Measuring information transfer, *Phys. Rev. Lett.*, 85, 461–464

[3] Runge, J. (2018). Conditional independence testing based on a nearest-neighbor estimator of conditional mutual information, *Proceedings of the Twenty-First International Conference on Artificial Intelligence and Statistics*, PMLR 84, 938–947

[4] Montalto, A., Faes, L., Marinazzo, D. (2014). MuTE: A MATLAB Toolbox to compare established and novel estimators of the multivariate transfer entropy, *PLoS ONE*, 9, e109462.

[5] Paluš, M., Vejmelka, M. (2007). Directionality of coupling from bivariate time series: How to avoid false causalities and missed connections, *Phys. Rev. E*, 75, 056211.

Method Comparison for Numerical Inversion of Laplace Transform

Laura Hajzoková, Viktor Witkovský

Institute of Measurement Science, Slovak Academy of Sciences, Bratislava, Slovakia

Email: laura.hajzokova@savba.sk

Abstract. *Laplace transform has a wide spectrum of applications in various areas of mathematics and physics. It also finds use in statistics, where the evaluation of probability density function (PDF) or cumulative distribution function (CDF) of convolved probability distributions is required, as working with Laplace transform can be more efficient than working directly with PDF or CDF. The important factor is to have an effective algorithm for numerical inversion of the transform, so that the evaluation of PDF or CDF would be possible in reasonable time with sufficient accuracy. This article concerns the comparison of different methods for computation of the inverse transform and demonstration of their usage on particular probability distributions.*

Keywords: Laplace Transform, Numerical Inversion, Bromwich Integral, Talbot's Method

1. Introduction

The evaluation of PDF or CDF is required in various fields of statistics. As discussed in [1], the natural approach to this problem can be made through characteristic function which is defined as Fourier transform, of PDF. This leads to the idea to use the Laplace transform as an alternative tool. However, it is important to note that Laplace transform is defined on non-negative real numbers (Definition 1.1 [2]), hence this approach is not applicable to all distributions. On the other hand, from the relation between PDF and CDF $f(t) = F'(t)$ can be seen that the Laplace transform $\mathcal{L}(F(t))$ of CDF can be simply derived from the Laplace transform $\mathcal{L}(f(t))$ of PDF using equation

$$\mathcal{L}(f(t)) = s\mathcal{L}(F(t)). \tag{1}$$

Moreover, the convolution of densities $f_1(t), f_2(t)$ of two different probability distributions can be simply obtained from their Laplace transforms $\bar{f}_1(s), \bar{f}_2(s)$. Thus the Convolution theorem [2] gives the following expression

$$\mathcal{L}^{-1}\{\bar{f}_1(s)\bar{f}_2(s)\} = \int_0^t f_1(u)f_2(t-u)du. \tag{2}$$

However, this approach requires knowledge of the Laplace transform of essential probability distributions, which is not always easy to compute.

2. Method overview

Numerical methods - not only for finding the inversion of Laplace transform - are popular in recent research and various methods have already been developed. This paper focuses on three different methods that are compared: the method of Talbot [3] based on evaluating Bromwich integral, method based on Post-Widder inversion formula [4] and Hosono's method based on Euler approximation [5].

Talbot's method

As mentioned above, Talbot's method is based on evaluation of Bromwich integral (Theorem 2.2, [2]). The method uses the transformation of integration path $C : (c - i\infty, c + i\infty)$ from

ISBN 978-80-972629-6-9

Bromwich integral into $C: s = s(\theta),\ -\pi \leq \theta \leq \pi$, to handle the oscillations e^{st} as $\Im\mathfrak{m}(s) \to \pm\infty$. Following the contour transformation we obtain the inverse Laplace transform

$$f(t) = \frac{1}{2\pi i} \int_{-\pi}^{\pi} e^{s(\theta)t} \bar{f}(s(\theta)) s'(\theta) d\theta. \tag{3}$$

which can be approximated by some quadrature formula. We chose the midpoint rule due to the cotangent contour, since the cotangent function is undefined at the endpoints of the interval $[-\pi, \pi]$ for some values of parameter α (e.g. $\alpha = 1$ suggested in [3]). The number of nodes N should not be very low in order to achieve the required accuracy. However, with a high number of nodes, an increase in the oscillations is present, as the contours depend on N. Based on our numerical experiments and some suggestions from [7] we set $N = 32$. The three types of contours (Table 1) used in Talbot's algorithm are displayed in Fig. 1. The choice of parameters used in our implementation was analysed in [6], [7].

Parabola	$s(\theta) = \frac{N}{t}(\alpha - \beta\theta^2 + \gamma i\theta)$
Hyperbola	$s(\theta) = \frac{N}{t}\alpha(1 - \sin(\beta - \gamma i\theta))$
Talbot cotangent	$s(\theta) = \frac{N}{t}(-\sigma + \mu\ \theta\ \cot(\alpha\theta) + \nu\ i\ \theta)$

Table 1: Table of contours used in Talbot's method implementation.

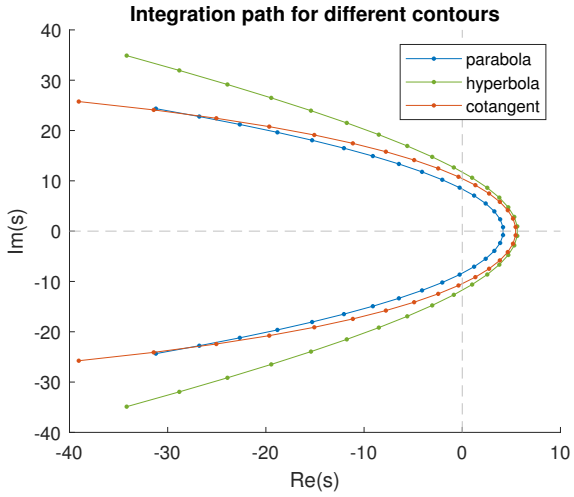

Fig. 1: Comparison of three types of integration paths mentioned above, displayed in complex plane for fixed value $t = 1$ and number of nodes $N = 32$.

Post-Widder

The second method is based on Post-Widder inversion formula [2] expressed as

$$f(t) = \lim_{n\to\infty} \frac{(-1)^n}{n!} \left(\frac{n}{t}\right)^{n+1} \bar{f}^{(n)}\left(\frac{n}{t}\right). \tag{4}$$

where $\bar{f}^{(n)}$ is the nth derivative of the Laplace transform $\bar{f}$. The version of the method implemented in our algorithm has been described by J. Abate and W. Whitt [4].

ISBN 978-80-972629-6-9

Hosono's method

The third compared method was suggested by Hosono [5], whereas in our algorithm the implementation from [8] was used. This method is based on approximation of the exponential factor e^{st} from Bromwich integral

$$e^{st} \doteq E(st,\alpha) = \frac{e^{\alpha}}{2\cosh(\alpha - st)} = \frac{e^{\alpha}}{e^{\alpha}e^{-st} + e^{-\alpha}e^{st}} = \frac{e^{st}}{1 + e^{-2\alpha}e^{2st}}, \tag{5}$$

where α is a parameter.

3. Results

The methods listed above were tested on multiple probability distributions and the numerical experiments were conducted on computer with AMD Ryzen 7 4700U CPU. These results are demonstrated on PDF of F-distribution, where Laplace transform is defined as

$$\mathcal{L}(f(t)) = \frac{\Gamma(\frac{d_1}{2})}{\beta(\frac{d_1}{2},\frac{d_2}{2})} U\Big(\frac{d_1}{2}, 1 - \frac{d_2}{2}, \frac{d_1}{d_2}s\Big). \tag{6}$$

In (6), $\Gamma(x)$ is the gamma function and $\beta(a,b)$ is the beta function defined as

$$\Gamma(x) = \int_0^{\infty} t^{x-1}e^{-t}dt, \qquad \mathfrak{Re}(x) > 0, \qquad\qquad \beta(a,b) = \frac{\Gamma(a)\Gamma(b)}{\Gamma(a+b)}.$$

$U(a,b,z)$ is a confluent hypergeometric function defined as

$$U(a,b,z) = \frac{1}{\Gamma(a)} \int_0^{\infty} e^{-zt}t^{a-1}(1+t)^{b-a-1}dt. \tag{7}$$

As we can see from the results in Table 2, we were able to achieve the best accuracy and also CPU time by using Talbot's method. The absolute error estimation was calculated as $E = \sum_{i=1}^{n} |\hat{f}(t_i) - f(t_i)|$, where $\hat{f}(t)$ is the approximation of $f(t)$ by the inverse transform of its LT and n is the number of values for which we want to evaluate the function $f(t)$. However, the Talbot's method still has several limitations, such as high computation demands as the contours depend on variable t. Based on our experiments, the scaling factor N/t in contours from Table 1 is not taken into consideration, as the absolute error would be of noticeably higher order. Also the evaluation of the confluent hypergeometric function is critical for time efficiency and

Method	Contour	CPU time	Abs. error
Talbot	Parabola	0.980380	2.1021×10^{-13}
	Hyperbola	0.890770	1.5304×10^{-12}
	Cotangent	0.896100	3.0689×10^{-12}
Post-Widder		5.879300	1.7237×10^{-7}
Hosono		1.062900	3.7401×10^{-5}

Table 2: Comparison of three methods demonstrated on PDF of F-distribution.

accuracy of the algorithm. Whereas, there is an effectively implemented symbolic toolbox in MATLAB, there is no effective implementation of numerical methods, as the evaluation of special functions is still a computational challenge. Some time can be saved by decreasing the number of nodes N in numerical integration, although the efficiency might still not be sufficient

for some more complicated Laplace transforms or convolutions. In Table 3 we compared the Talbot method for different distributions. The difference in CPU time is considerably higher for F-distribution than the others, since it is the only one that requires the evaluation of confluent hypergeometric function.

Method	Distribution	CPU time	Abs. error
Talbot	Chi-Squared	0.009922	1.8450×10^{-13}
	Exponential	0.001025	6.0011×10^{-12}
	Gamma	0.001108	4.4183×10^{-13}
	Fisher-Snedecor	0.959080	3.0689×10^{-12}

Table 3: Comparison of Talbot's method with cotangent contour for PDF of different probability distributions.

4. Conclusions

Talbot's algorithm turned out to have the best performance amongst all aforementioned methods in terms of absolute error and computation time. Although, there is still space for improvements, it shows to be a powerful tool for some other distributions, as shows Table 3. For some complicated Laplace transforms we might, however, run into obstacles. This could be a subject for further research and improvements. Furthermore, the additional objective is to extend the library of Laplace transforms of PDF and CDF of known probability distributions to have an alternative tool for computation of convolved probability distributions.

Acknowledgements

This work was supported by the Slovak Research and Development Agency, project SK-CZ-RD-21-0109, and by the project VEGA 2/0023/22.

References

[1] Witkovský V. (2016). Numerical inversion of a characteristic function: An alternative tool to form the probability distribution of output quantity in linear Measurement models, *ACTA IMEKO*, 5 (3)

[2] Cohen, A. M. (2007). *Numerical Methods for Laplace Transform Inversion*, Springer Science+Business Media

[3] Talbot, A. (1979). The Accurate Numerical Inversion of Laplace Transforms, *Ima Journal of Applied Mathematics*, 23, 97-120

[4] Abate J., Whitt, W. (1995). Numerical Inversion of Laplace Transforms of Probability Distributions, *ORSA Journal on Computing*, 7 (1), 36-43

[5] Hosono T. (1981). Numerical inversion of Laplace transform and some applications to wave optics, *Radio Science*, 16 (6), 1015-1019

[6] Dingfelder, B., Weideman, J.A.C. (2015). An improved Talbot method for numerical Laplace transform inversion, *Numerical Algorithms*, 68, 167-183

[7] Trefethen, L. N., Weideman, J. A. C., Schmelzer, T. (2006). Talbot quadratures and rational approximations, *BIT Numerical Mathematics*, 46, 653–670

[8] Valsa J., Brancik J. (1998). Approximate formulae for numerical inversion of Laplace transforms, *International Journal of Numerical Modelling-electronic Networks Devices and Fields*, 11, 153-166

Measurement in Biomedicine Posters II

ISBN 978-80-972629-6-9

Experimental Protocol for Biological Experiments on Petri Dishes

[1,2]Marek Bajtoš, [1]Ladislav Janoušek, [1]Roman Radil, [1]Lucia Čarnecká, [1]Kristína Paulecová

[1]Department of Electromagnetic and Biomedical Engineering, Faculty of Electrical Engineering and Information Technology, University of Zilina, Zilina, Slovakia

[2]Department of Electrical, Computer and Energy Engineering, University of Colorado Boulder, Boulder, Colorado, USA,

Email: ladislav.janousek@feit.uniza.sk

Abstract. *In this paper, the experimental protocol for the further exposition of low-frequency magnetic fields on biological cells is established. Experiments for one-week mass controlling of Petri dishes with YPD agar and Saccharomyces cerevisiae inoculum are performed. Firstly, four groups of samples are prepared to find out the proper volume of inoculum with the lowest standard deviation between the samples. Secondly, the dedicated volume of inoculum is used for another set of experiments for comparison with YPD agar plates without the yeast cells. The statistical evaluation of two groups of data is determined.*

Keywords: Mass Controlling, Saccharomyces Cerevisiae, Petri Dishes, Low-Frequency Magnetic Field

1. Introduction

Lack of understood mechanisms and difficulties in obtaining reproducible results cause issues in establishing the direct biological effects of long-term low-level exposures to low-frequency (LF) magnetic field (MF). The guidelines for exposure limits have been set based on relatively short-term exposures that show clear-cut damage. These limits have been set based on providing a significant safety factor over exposure levels known to cause damage, where the primary damaging mechanism is heating and an increase in temperature [1]. ICNIRP statement on LF knowledge gaps (1-100 kHz) from 2020 defined research areas to target, involved: pain perception, neurodegenerative disorders, childhood leukaemia, dosimetry, and modeling and interaction mechanisms with a focus on radical pair mechanism [2].

In this paper, preliminary experiments for LF MF exposition are presented. Experimental protocol and controlling the mass of Petri dishes with YPD agar and yeast cells are prepared. It takes place for subsequent exposition with an explanation of possible mechanisms of interaction. In Test 1, four different groups of samples are used to determine the initial volume of inoculum, where the lowest standard deviation was observed. In Test 2, the intended volume of inoculum is cultivated on 12 YPD agar plates, grown for seven days and compared to 10 agar plates without the inoculum. The two-sample t-test and the Kruskal-Wallis test are used for statistical evaluation.

Theoretical background

There are several different theories explaining how low frequency EMF could impact living organisms. The most probable and accepted by the scientific community are described.

Radical pair mechanism

Barnes and Greenebaum [3] outlined a model by which changes in radical concentrations may result from exposures to LF MF, noting that these changes can lead to biologically significant changes in metabolic rates and other processes. Transitions that alter the populations of the

ISBN 978-80-972629-6-9

combined electron and nuclear states, can take place at frequencies that correspond to the energy separation between the various states in the external magnetic fields, especially at low external field intensities.

The Feedback Effect
In biological organisms, several positive or negative feedback loops link output signals to their corresponding inputs. Barnes and Kandala [4] presented a simple model based on an electronic operational amplifier with a time delay τ in the feedback loop that shows that by changing the frequency, phase, or pulse repetition rate of an externally applied signal, we can change the sign of the feedback and thus switch the gain of the overall amplifier from amplification to attenuation.

Many biological time constants are involved in feedback loops that control processes like cell growth. Expected signals such as modulated sine waves or pulses at different repetition rates containing more than one frequency could modify more than one biological process. Overall, it is known that there are many feedback and repair processes in biological systems. With knowledge of time constants for various biological and medical responses, it may be able to signal the systems to increase or decrease such things as cell growth rates or immune responses.

Ion Cyclotron Resonance and Ion Parametric Resonance
These theories speculate on the method of interaction between ions and EMF. There are several papers dealing with the theory. Bajtos et al. [5] refer to a possible adjustment of IPR conditions to avoid diversity of results. As the Earth's magnetic field changes over time, it is more than acceptable to increase the static component of the magnetic field concerning exposition set-up.

2. Materials and Methods

The idea behind this experimental study is to establish a protocol for an exposition of cells cultured in Petri dishes.

Firstly, the control (non-exposition) experiments are performed. The main hypothesis of this research follows: 1. How the mass of the YPD agar changes over time? 2. How the mass of the YPD agar with cell culture changes over time? These questions are set because of the further investigation of how the mass of the agar with yeast cells changes over time in the incubator with temperature control while exposed to LF MF. This step-by-step strategy was chosen because of creating an experimental protocol and finding the proper concentrations of inoculum spread in Petri dishes. Because of growing the cells, we expect to grow the mass of our samples. It is suitable to examine these numbers because of determining the effect which is induced specifically by LF MF exposition in the future. Thus, it is appropriate to understand the growing behaviour with no exposition.

For the biological part, Saccharomyces cerevisiae cells, also known as wine or beer yeasts are used. Decimal dilution of cells with YPD solution in the ratio of 1:10 is prepared. Test 1 is performed to find out how the mass of biological culture cultured on YPD agar changes between the first and last day. Three different volumes of inoculum are used. For the first set of Petri dishes (1-5), the inoculum is not spread on YPD agar. For another set of Petri dishes (6-20), the inoculum was spread with a laboratory spoon.

After finding out the number of inoculum volumes for a set of Petri dishes with the lowest standard deviation, the exact volume of inoculum is used in Test 2 with more samples to reach more accurate statistical data. According to this, agar is prepared for Petri dishes in a volume of 10 ml. For Test 2, two sets of Petri dishes were prepared – the first one (1-10) is containing only the YPD agar and the second set (11-22) contained YPD agar with a spread inoculum of

ISBN 978-80-972629-6-9

100 µl. The mass of dishes for both sets is measured every day for 7 days, except the weekend, while for Test 1, measurement is performed only on the first and last day of the experiment.

The initial concentration of yeast cells for Test 1 is 213 444.44 cells/ml and 220 500 cells/ml for Test 2. Firstly, the YPD solution with yeast cells is placed in a shaker for 24 hours. The day after, agar is prepared in the Petri dishes where the inoculum is pipetted. Parafilm is used to prevent contamination. During cultivation, the yeasts have the same conditions: room temperature, nutrient medium, light, the amount of applied inoculum, and a growth time of 7 days. A scale with an accuracy of five decimal places is used to compare and evaluate the results correctly.

3. Results

Test 1

The assumption for this part is that the weight of the yeast in the Petri dishes would be higher after the weekly measurement, as the yeast was supposed to reproduce and grow for 7 days. In a blue set of experiments, the inoculum was put only with a pipette to YPD agar. In another set of experiments, the inoculum was spread with a spoon after putting with a pipette to YPD agar. In Fig. 1, the smallest differences in the mass are for samples of 100 µl of spread inoculum (SD 0.0029) and 300 µl of spread inoculum (SD 0.0048). The concentration with the lowest value of SD was used in the second set of experiments in Test 2.

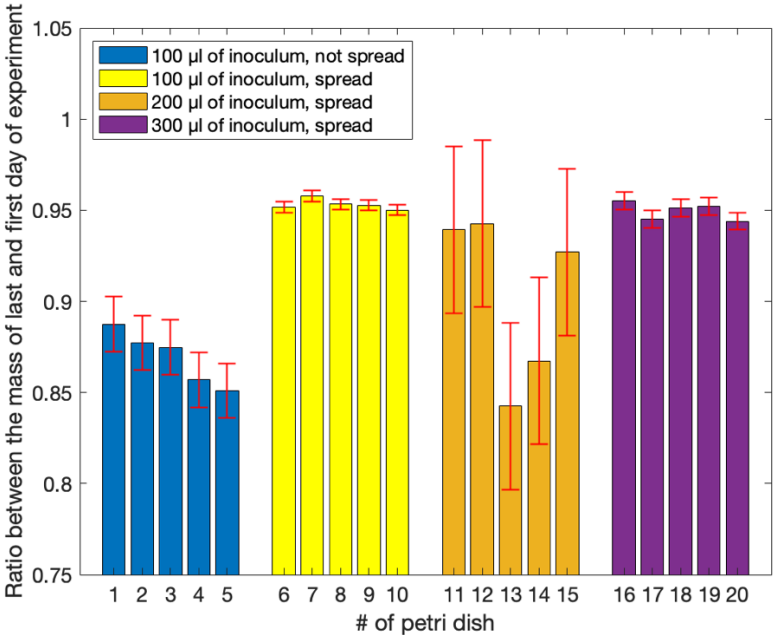

Fig. 1. Test 1 – The mass ratio of Petri dishes with *S. cerevisiae* after weekly measurement.

Test 2

In this part, Test 2 contains two sets of experiments. Firstly, the mass of 10 ml of YPD agar was controlled. Secondly, the same dilution (1:10) and volume (100 µl) for cultivation are used on another set of Petri dishes. The agar is weighed for 7 days. Fig. 2 contains the preliminary results. The p-value of the two-sample t-test is 0.484. The data sets from both experiments are from populations with equal means at the 5 % significance level. There is no significant data variation. For the Kruskal-Wallis test, the p-value is 0.5978. This accepts the null hypothesis, that data from both sets come from the same distribution at a 5 % significance level.

ISBN 978-80-972629-6-9

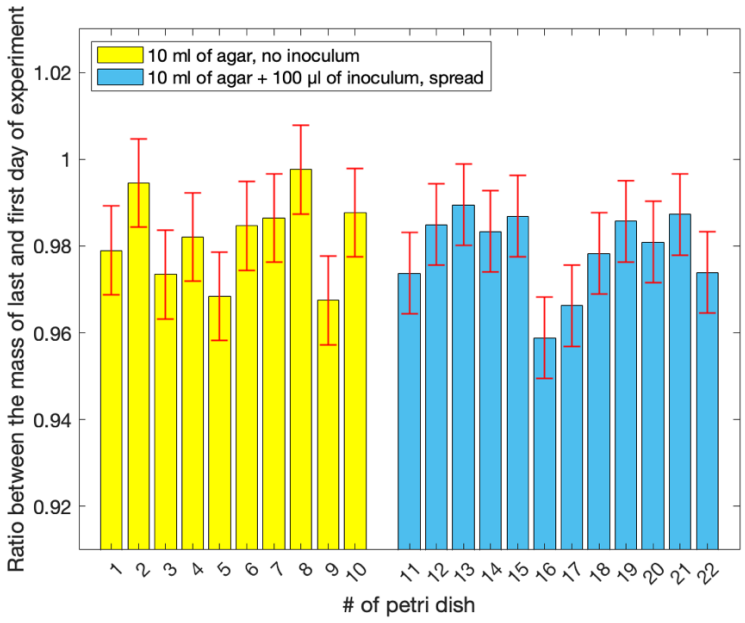

Fig. 2. Test 2 – The mass ratio of Petri dishes with *S. cerevisiae* after weekly measurement.

4. Discussion and Conclusion

Preliminary results presented herein have shown, that the weight of agar samples in Test 2 decreases as well as samples with the yeast inoculum. No statistically significant changes were observed. It is highly probable, that the mass of the nutrients in agar is transformed into the mass of cells. Otherwise, the parafilm is permeable for gases, the water vapor and carbon dioxide. It allows off-gassing without compromising the sample integrity. Thus, the initial volume of YPD agar and volume of yeast inoculum is determined. The next part of the research is to put YPD agar samples with yeast inoculum in the incubator with temperature control and exposition of LF MF for 7 days.

Acknowledgments

The Slovak Research funded this research under Contract No. APVV-19-0214.

References

[1] Barnes, F., Greenebaum, B. (2016). Some Effects of Weak Magnetic Fields on Biological Systems: RF fields can change radical concentrations and cancer cell growth rates. In: *IEEE Power Electronics Magazine*. 3(1), 60-68. ISSN 2329-9207.

[2] ICNIRP. (2020). Gaps in knowledge relevant to the "Guidelines for limiting exposure to time-varying electric and magnetic fields (1 Hz – 100 kHz)". In *HEALTH PHYS 118(5).* 533–542.

[3] Barnes, F., Greenebaum, B. (2015). The effects of weak magnetic fields on radical pairs. In: *Bioelectromagnetics.* Jan;36(1):45-54. ISSN 01978462.

[4] Barnes, F., Kandala, S. (2018). Effects of time delays on biological feedback systems and electromagnetic field exposures. In: *Bioelectromagnetics*. 39(3), 249-252. ISSN 0197-8462.

[5] M. Bajtos, R. Radil, L. Janoušek, K. Hargasova, S. Student and O. Kocikowska. (2022). Numerical adjustment of Ion Parametric Resonance conditions for biological experiments. In: *23rd International Conference on Computational Problems of Electrical Engineering (CPEE).* pp. 1-4.

The Benefits of Nuclear Cardiology Examinations Using Cardiologic SPECT Gamma Camera

[1]Martin Bereta, [1,2]Jozef Babečka, [2]Ján Straka, [2]Peter Valko, [1,2]Anton Lacko

[1]Faculty of Health, Catholic University in Ruzomberok, Ruzomberok, Slovakia
[2]Clinic of Nuclear Medicine, Central Military Hospital, Ruzomberok, Slovakia
Email: martin.bereta@ku.sk

Abstract. *This paper deals with the experience with the use of SPECT gamma camera Discovery CZT 530c at the Clinic of Nuclear Medicine, Central Military Hospital, Ruzomberok in recent years. The comparison with the previously used gamma camera is briefly stated, and the advantages arising from the physical and technical nature of the new camera are introduced. The results of examinations of a large sample of patients are presented, and the benefits of the new camera on behalf of the diagnostic results are described. The recommendations of the nuclear cardiology examinations for clinical practice are stated, since in Slovakia only a few departments realize this kind of nuclear medicine diagnostics.*

Keywords: Gamma Camera, Myocardial Perfusion, Scintigraphy, Coronary Angiography

1. Introduction

The basic imaging device in nuclear medicine is a gamma camera. There were various types of gamma cameras designed in the last decades. The widely used cameras are those using scintillation crystals and gamma cameras equipped with semiconductor detectors. The work on the construction of small cameras with semiconductor CdTe (Cadmium Telluride) detectors began in 1991. The first commercially available cameras with semiconductor detectors were special single-purpose cameras for nuclear cardiology. A breakthrough after 2016 was brought by a new commercially available double-head gamma camera for general SPECT/CT use (Discovery CZT fy GE). The abbreviation CZT refers to semiconductor composition (Cadmium-Zinc-Tellurium).

2. Materials and Methods

The cardio gamma camera Discovery CZT 530c (Fig. 1) has semiconductor detectors of ionizing radiation. In addition to the different physical and technical principles of gamma photons detection and conversion, there is a key difference regarding image reconstruction and processing. The design principle corresponds to the old multi-detector gamma cameras with scintillation detectors, which had high sensitivity and low dead time. The difference is that the spatial resolution of new semiconductor cameras (given by one pixel) is 2.5 mm, which is 5 – 10 times higher than that of multi-detector cameras and almost 2 times higher than scintillation cameras of classic design.

ISBN 978-80-972629-6-9

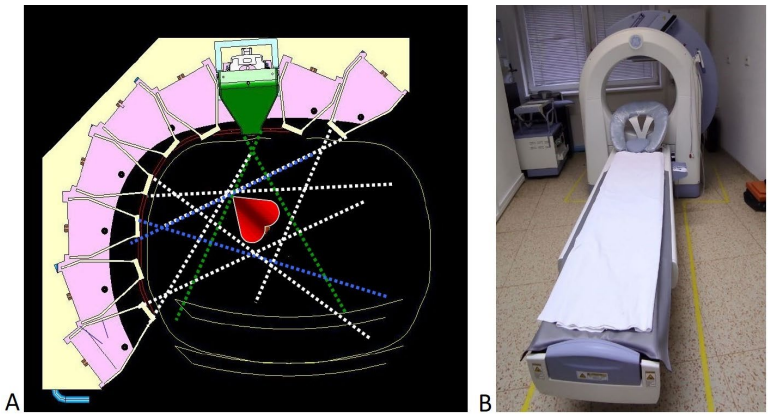

Fig. 1 Cardio gamma camera Discovery CZT 530c schematic (a) and photo (b)

3. Results

During the years 2003 - 2016, we performed myocardial perfusion scintigraphy on the Millenium gamma camera, VG Hawkay f. GE in about 18k patients. We analyzed a set of 4270 individuals examined for the years 2014-2016, who were examined by myocardial perfusion scintigraphy. In this set, there were 61% negative findings and 39% positive findings. In the group of positive findings, conservative treatment was recommended in 19%, Multi-slice CT (MSCT) coronary angiography in 7%, and selective coronary angiography in 13%. The sensitivity was around 93%, and the specificity was around 87% (Fig. 2a).

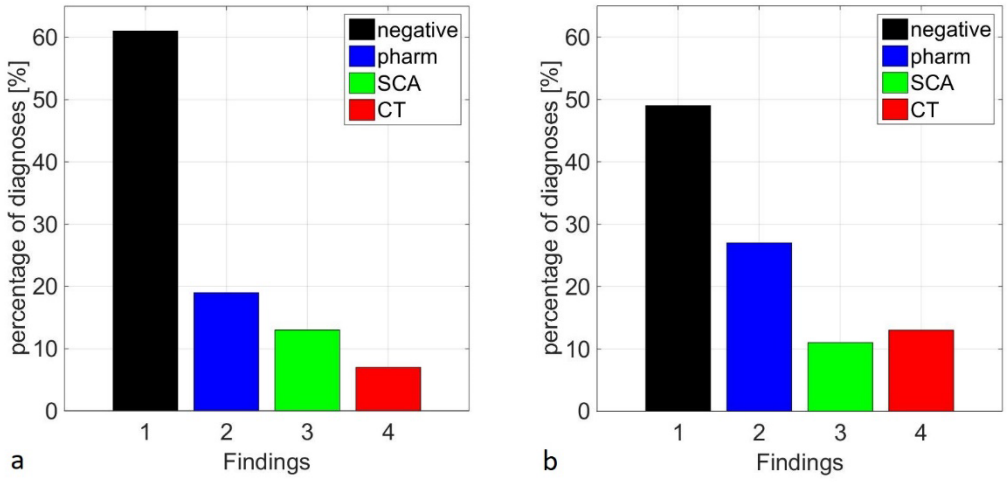

Fig. 2 (a) The results of the examination of 4270 individuals in the period 2014-2016 by the Millenium gamma camera, VG Hawkay f. GE. Negative – patients with no findings. Pharm – patients indicated for conservative treatment by pharmaceuticals. SCA – patients indicated for selective coronary angiography. CT – patients indicated for Multi-slice computer tomography. (b) The results of the examination of 2900 individuals in the period 2019-2021 by the gamma camera Discovery CZT 530c f

By using cardiology gamma camera Discovery CZT 530c f. GE over a period of years 2019-2021, we performed myocardial perfusion scintigraphy in 2900 individuals. In this group, we found a negative result in 49% of individuals and a positive result in 51% of individuals. From the set of positive findings indicative of coronary heart disease, we recommended

coronary angiography in 24% of examined patients, CT coronary angiography in 13%, and selective coronary angiography in 11% of individuals. For the remaining 27% of those examined, medical treatment was recommended (Fig. 2b). In the group of patients examined by coronary angiography, normal coronary angiographic findings were found in 2% of individuals.

4. Discussion and Conclusions

A scintigraphy examination records pathological differences at the molecular level, allowing the recording of time-dependent changes in the coronary microcirculation. In the case of negative coronary angiographic findings, a positive scintigraphy finding may detect changes at the level of small vessels, so-called *small vessels disease*. When a scintigraphy examination is indicated before coronary angiography, we can save the patient from this high-invasive examination. The cardio gamma camera Discovery NM CZT 530c f. GE enables shortening the examination, increasing the sensitivity and specificity of the examination, and reducing the dose of the radiopharmaceutical, thus reducing the radiation burden of patients by 50%. During the evaluation, it allows a better evaluation of the hemodynamic parameters. The result is more valid when compared with coronary angiography.

References

[1] Vitola, J. V. Nuclear Cardiology and Correlative Imaging: a teaching file. Springer-Verlag New York, LLC 2004. ISBN: 978-0-387-20707-0.

[2] Lee, B., Ficaro E.: Methods for the Estimation of Myocardial Blood Flow and Coronary Flow Reserve with 99mTc SPECT in Corridor 4DM. *Invia Medical Imaging Solutions*, 2016.

[3] Crea F., Lanza A.G., Camici P.G.: Coronary microvascular dysfunction: an update. *European Heart Journal*. 2014, 35(17): 1101-11.

[4] Udelson E.J., Dilsizian V., Bonow O.R.: Nuclear cardiology. In *Braunwalds heart disease. A textbook of Cardiovascular Medicine.* p. 293-339. Elsevier - Health Sciences Division, 2021. ISBN 0323722199.

[5] Wells R.G. et al. Dynamic SPECT measurement of absolute myocardial blood flow in a porcine model. *J. Nucl. Med.* 2014, 55(10): 1685-91.

[6] Ben-Haim S. et al. Quantification of Maocardial Perfusion Reserve Using Dynamic SPECT Imagung in Humans: A Feasibility Study. *J. Nucl. Med.* 2013, 54(6). 873-9.

Integrated Smart Patch for Heart Rate and Respiratory Rate Monitoring

[1]Daniel Gogola, [2]Nevena Ackovska, [1,3]Richard Bagín, [2]Bojana Koteska, [2]Ana Madevska Bogdanova, [2]Magdalena Kostoska, [1,3]Fedor Lehocki, [1]Milan Tysler

[1]Institute of Measurement Science, Slovak Academy of Sciences, Bratislava, Slovakia
[2]Faculty of Computer Science and Engineering, Skopje, North Macedonia
[3]Faculty of Electrical Engineering and Information Technology, STU in Bratislava, Slovakia
Email: Daniel.Gogola@savba.sk

Abstract. *A wearable smart patch was designed to monitor the vital parameters of mass casualties' victims after the first triage. The device captures ECG, PPG, and respiration signals and triggers an alarm if the heart rate (HR) or respiration rate (RR) exceeds the specified limits and indicates a threat to the victim's life. To obtain a robust and reliable solution, the same parameters are derived from two or three independent signals. In this study, ECG signals have been recorded from different positions on the chest, and the performance of several algorithms for HR and RR extraction was tested. The initial measurements show that HR estimation is more accurate and reliable than RR estimation. The best results, considering both, the HR and RR calculations, were achieved when Pan-Tompkins's algorithm was used, and ECG electrodes were placed vertically on the right anterior chest. Increasing the length of the evaluated ECG signal above 30 seconds did not significantly affect the HR and RR calculation, regardless of the algorithm used.*

Keywords: Wearable Sensors, Monitoring of Vital Parameters, Electrocardiogram, Heart Rate, Respiratory Rate

1. Introduction

In events with mass casualties, a multi-sensor patch-like device could be useful for monitoring Yellow-labelled victims after the first manual onsite triage process. Such a device should be capable of collecting and analyzing information on vital parameters such as respiration rate (RR), heart rate (HR), blood oxygen saturation level (SpO2), blood pressure (BP), and body temperature [1]. Electrocardiogram (ECG) and photoplethysmogram (PPG) are signals that can be recorded non-invasively and present different aspects of the cardiovascular system. Thus, using both signals also for BP classification seems like a viable strategy. PPG is already a commonly used technique to measure SpO2 [2]. Many research articles present SpO2 measurement models based on the PPG signal, including articles on the development of new pulse monitoring devices and BP predictions using machine learning models. The codependency between BP, ECG, and PPG has been explored in many studies [3], [4].

Quick evaluation of ECG and PPG signals during the triage process in cases of disasters with many injured subjects, is an essential measure for following the stability of the injured. The aim of our project is to utilize embedded ECG, PPG, and breathing sensors in the patch-like device to determine the vital parameters of the injured. The patch should start the alarm if the victim's HR or RR indicates that the triage label changes from Yellow to Red, indicating that the victim must be immediately transferred to the hospital.

2. Subject and Methods

For sensing the necessary biosignals representing individual vital functions such as respiration, heartbeat, and blood oxygenation, several sensors have been tested. During the testing, it was

confirmed that some vital parameters can also be obtained from sensors that were not originally designed to sense them. For example, a sensor for sensing respiration can also sense the heartbeat, or the ECG signal primarily used for the heartbeat can also be used for respiration sensing. The ability to obtain the same parameters from two or three independent sensors is advantageous for developing a robust (fault-tolerant) smart patch. However, it should be considered that the ability to extract desired parameters from several signals can be limited by the position of the sensors, which may depend on the type of injuries and available space on the chest for the patch placement.

Smart patch model

The heart of the proposed patch-like device is the MAX32630 microprocessor, a small-size Arm Cortex-M4 single-core microprocessor with ultra-low power consumption. It has sufficient computing power, big enough memory, and also contains a single 10-bit AD converter which makes it suitable for applications in portable and wearable medical devices [5]. For sensing ECG and PPG signals, the MAX86150 chip [6] was chosen. It requires a minimum of additional electrical components and communicates with the microprocessor via an I2C interface. A laser-induced graphene (LIG) sensor has been developed for sensing respiration [7].

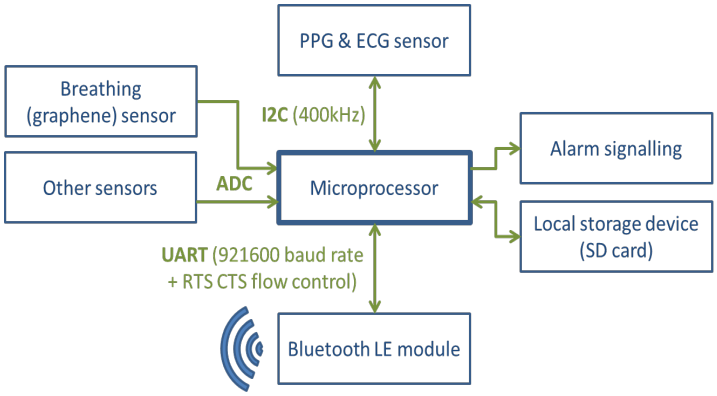

Fig. 1. Diagram of the smart patch concept.

In basic mode, the patch independently evaluates the vital parameters, and in case, that the HR or RR exceeds the specified limits and indicates a threat to the victim's life, it alerts the medical staff by light and sound signaling. In networked mode, the patch can send raw signals via a Bluetooth LE (Low Energy) module with long-range capabilities to a computer or tablet for more detailed monitoring and evaluation. The basic concept of the smart patch is shown in Fig.1.

Measurement protocol definition

Two disposable ECG electrodes with a distance of 120 mm and the PPG sensor between them were attached to the chest of lying healthy volunteers and connected by wires with a model of the smart patch electronics, as shown in Fig. 2. Recording of ECG and PPG signals was started by pressing a button on the patch electronics board, the signals were recorded on SD card in the patch. To obtain reference HR and RR values, HR and SPO2 were measured in parallel from a finger by a commercial oximeter and the number of respirations was counted by visually observing the subject. During the experiments, sensors were attached to the chest in five different position types: horizontally and vertically on the left anterior chest, horizontally and vertically on the right anterior chest, and horizontally on the upper middle part of the chest.

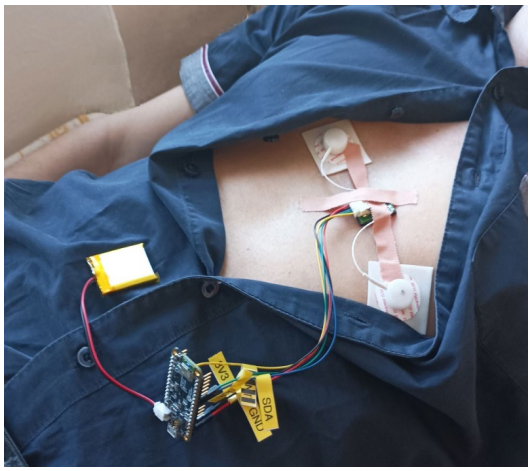

Fig. 2. Horizontal position of ECG and PPG sensors on the left anterior chest of a lying subject. The sensors are connected by wires with the model of the patch electronics.

No special preparation of the skin was performed, and the volunteers were only instructed to avoid larger and faster movements during the measurement.

In the first series of experiments, ten measurements were recorded, each with a duration of 30 seconds. Two measurements with different sensor locations were taken at each position type. The second series of experiments contained five measurements, each with a duration of 2 minutes. One measurement was taken at each position type.

The Pan-Tompkins algorithm and the Python heartPy toolkit were used to calculate HR and RR from recorded raw ECG signals. Additionally, bandpass ECG signal filtering was performed in cases where the results obtained from raw signals were too different from the reference values.

3. Results

The resulting HR and RR values from both series of experiments are presented in Table 1 and Table 2. The calculated HR and RR values can be compared with the reference values in the same row. The HR values are in good correspondence with the reference values, except the horizontal position on the right anterior chest, where both algorithms were not able to deliver correct results, and additional ECG signal filtering only slightly improved the bad results.

Extracted RR values were less precise, however, values obtained from positions on the right anterior chest can be considered acceptable. In one case (ID 9 in the first series), the RR value could not be evaluated by the heartPy toolkit.

Tab.1. Results from the first series of HR and RR [1/min] calculations from ECG segments 30 seconds long.

ID	Position of ECG electrodes on the chest	Reference measurements		Pan Tompkins HR / RR	heartPy raw signal HR / RR	heartPy filtered signal HR / RR
		HR range	RR (2x 30s)			
0	Horizontal – left anterior	77 – 80	16	76 / 14	76 / 13	75 / 14
1	Horizontal – left anterior	77 – 79	16	78 / 10	79 / 13	-
2	Vertical – left anterior	76 – 78	14	76 / 8	77 / 7	-
3	Vertical – left anterior	74 – 78	14	76 / 8	75 / 13	-
4	Horizontal – right anterior	74 – 78	16	**64** / 12	**188** / 16	**166** / 14
5	Horizontal – right anterior	74 – 78	16	**94** / 14	**185** / 12	**141** / 14
6	Vertical – right anterior	74 – 78	14	**74 / 12**	75 / 8	-
7	Vertical – right anterior	72 – 78	14	**72 / 12**	73 / 12.5	-
8	Horizontal – upper middle	74 – 78	16	74 / 8	78 / 10	-
9	Horizontal – upper middle	72 – 78	12	74 / 10	73 / **0**	-

The HR and RR values from the second series in Table 2 follow the same patterns as the 30-second measurements and apparently, the prolongation of evaluated signal segments to 2 minutes did not lead to substantial improvement of the extracted HR and RR values, regardless of the used algorithm.

Tab. 2. Results from the second series of HR and RR [1/min] calculations from ECG segments 2 minutes long.

ID	Position of ECG electrodes on the chest	Reference measurements		Pan Tompkins HR / RR	heartPy raw signal HR / RR	heartPy filtered signal HR / RR
		HR range	RR			
0	Horizontal – left anterior	65 – 72	15	67 / 11	67 / 8	67.5 / 16
1	Vertical – left anterior	65 – 72	14	69 / 11	68 / 10	-
2	Horizontal – right anterior	65 – 76	13	**85** / 14	**211** / 16	**124** / 14
3	Vertical – right anterior	63 – 76	14	**67 / 12.5**	67 / 12	-
4	Horizontal – upper middle	62 – 71	15	**83 / 20**	**157** / 14	**139** / 16

The best combination of HR and RR results was achieved with the sensors placed in a vertical position on the right anterior chest. When comparing results from both algorithms, Pan-Tompkins's algorithm delivered slightly better results than heartPy toolkit.

ISBN 978-80-972629-6-9

4. Discussion and Conclusions

The developed smart patch is built around a low-power microprocessor suitable for wearable medical devices. The current patch design includes sensors for ECG and PPG integrated on a single chip and a resistive LIG breathing sensor. Outputs of the sensors can depend on the placement of the patch on the chest. Initial experiments have already shown that qualitatively the most problematic are PPG signals sensed from the chest. Evaluation of SpO2 from such signals will require the development of a sophisticated postprocessing algorithm. In some patch positions, breathing can also be taken from ECG and PPG signals and heartbeats can be taken from the LIG sensor. A combination of these outputs can increase the robustness and reliability of the patch that might be placed in different positions on the chest, due to possible injuries.

In this study, only the possibility of extracting HR and RR from the ECG signal was investigated. HR calculation was more accurate than RR calculation, except when the electrodes were placed horizontally on the right anterior chest, where the HR values were calculated with large errors. On the other hand, this was the best position of electrodes to calculate the RR. Lower precision of RR is not unexpected as only "breathing artefacts" in ECG signal are evaluated.

From the above results, it can be concluded that the best results, considering both, the HR and RR calculations, were achieved when ECG electrodes were placed vertically on the right anterior chest. On the left anterior chest, horizontal positions yielded better results than vertical ones. The length of the signal did not substantially affect the correctness of HR and RR calculations. It can be perceived that 30 seconds long ECG segment can be satisfactory for HR and RR calculations. Additional filtering of the signals improved the results, but not to a satisfactory extent which is probably due to the inappropriate placement of the electrodes.

Acknowledgements

This work was supported by NATO Science for Peace Multi-Year Project G5825, Smart Patch for Life Support Systems (SP4LIFE).

References

[1] Lehocki, F., Bogdanova, A.M., Tysler, M., Ondrusova, B., Simjanoska, M., Koteska, B., Kostoska, M., Majak, M., Macura, M. (2021) Smart patch for victims management in emergency telemedicine. In *2021 13th International Conference on Measurement*, IEEE, 146–149.

[2] Haque CA, Hossain S, Kwon TH, Kim KD. (2021) Comparison of Different Methods to Estimate Blood Oxygen Saturation using PPG. In *2021 International Conference on Information and Communication Technology Convergence (ICTC)*. IEEE, 792-794.

[3] Y.-H. Li, L. N. Harfiya, K. Purwandari, and Y.-D. Lin. (2020) Real-time cuffless continuous blood pressure estimation using deep learning model. *Sensors*, 20 (19). https://www.mdpi.com/1424-8220/20/19/5606.

[4] Y.-C. Hsu, Y.-H. Li, C.-C. Chang, and L. N. Harfiya, (2020) Generalized deep neural network model for cuffless blood pressure estimation with photoplethysmogram signal only, *Sensors*, 20 (19). https://www.mdpi.com/1424- 8220/20/19/5668.

[5] MAX3260. Ultra-Low Power, High-Performance Cortex-M4F Microcontroller for Wearables. *Maxim Integrated Products*. https:\\www.farnell.com/datasheets/2108640.pdf

[6] MAX86150. Integrated Photoplethysmogram and Electrocardiogram Bio-Sensor Module For Mobile Health. *Maxim Integrated Products*. https://www.analog.com/media/en/technical-documentation/data-sheets/MAX86150.pdf.

[7] Vicentic, T., Rafajilovic, M.R., Ilic, S.D., Koteska, B., Bogdanova, A.M., Pašti, I.A., Lehocki, F. and Spasenovic, M. (2022). Laser-Induced Graphene for Heartbeat Monitoring with HeartPy Analysis. Sensors, 22, 6326. https://doi.org/10.3390/s22176326.

Triple PPG Sensor for Measurement of Heart Pulse Transmission Parameters in Weak Magnetic Field Environment

Jiří Přibil, Anna Přibilová, Ivan Frollo

Institute of Measurement Science, SAS, Bratislava, Slovak Republic.
Email: Jiri.Pribil@savba.sk

Abstract. *The paper describes the design, realization, and testing of a prototype of a wearable device based on the photoplethysmography (PPG) principle consisting of three optical sensors working on transmittance/reflectance principle with wireless connection for real-time data transfer to the control device. The measurement in normal laboratory conditions confirms that PPG signals sensed in parallel can have adequate quality for use in the arterial blood pressure estimation based on heart rate and heart pulse transmission parameters. Experiments in a weak magnetic field environment with an inherent radiofrequency and electromagnetic disturbance verify functionality of the developed PPG sensor.*

Keywords: Blood Pressure Estimation, Photoplethysmography, Pulse Transmission Time

1. Introduction

Persons examined in a weak-field magnetic resonance imager (MRI) are exposed to noise and vibration causing them stress that manifests mainly in heart rate (HR) and arterial blood pressure (ABP) changes [1]. In praxis HR changes are often detected from the photoplethysmography (PPG) signal and systolic/diastolic (SBP/DBP) blood pressure values are measured by a blood pressure monitor (BPM) [2]. Such a measurement arrangement is less comfortable for tested persons, and it also brings some problems with the practical realization of experiments. ABP values can also be estimated directly from PPG wave features by the linear regression method. The estimation error of this cuffless method achieves about 5-10 % [3]. To improve the ABP determination precision, the method based on the pulse transit time (PTT) is often applied. The PTT represents the time difference between the electrocardiogram (ECG) and PPG peaks measured in parallel by sensors located at a known distance *D*x [4]. This approach is more accurate than the PPG alone, and the ABP estimation error decreases to 1.5-5 %. PTT values can also be determined from two or three PPG waves picked up by sensors placed on a wrist and fingers [5]. Next parameters – pulse wave velocity (PWV) and relative PTT (rPPT) – describe the current state of a cardiovascular system of a tested person and can be used for the detection and evaluation of the stress induced by scanning inside the MRI device. While the ECG signals cannot be measured in the scanning area of the running MRI device due to strong radiofrequency (RF) disturbance together with the stepwise changed magnetic field by a gradient system, the signals from the optical PPG sensor can be successfully measured if PPG sensor parts are non-ferromagnetic and fully shielded [6].

The motivation of this work was to test the applicability of a multi-channel PPG signal – sensed inside the running MRI device based on a low magnetic field – for the determination of PTT and other pulse wave parameters. We designed, realized, and tested a special prototype of a wearable device consisting of three optical sensors working on transmittance/reflectance principles with a wireless Bluetooth (BT) connection for real-time data transfer to the recording device. The functionality of the developed PPG sensor was tested in normal laboratory conditions using two PPG signals sensed from one hand at the same time as BP and HR values were measured by a BPM device with its pressure cuff on the opposite arm. The determined time distance parameters were subsequently statistically analyzed to find relations with

ISBN 978-80-972629-6-9

SBP/DBP and HR parameters. Finally, the tested subject lay inside the MRI device and PPG samples from three optical sensors parallel were transmitted wirelessly through the shielding metal cage to the control device for further processing and analysis.

2. Subject and Methods

The developed prototype of a wearable multiple PPG sensor consists of the following parts: (1) optical sensors for PPG signal pickup, (2) analogue interface for raw PPG signal pre-processing and filtering, (3) micro-controller with a multi-channel A/D converter and an USB interface, (4) BT communication module, (5) power supply using rechargeable batteries or power banks. In general, the optical PPG sensor can use a transmission (TRX) or reflection (RFX) principle. In the case of TRX PPG probe a light source (LS), and a photodetector (PD) are placed on opposite sides of the sensed tissue, and it may have a form of a finger ring or clip. In the RFX sensor, the PD and LS elements are placed on the same side of the skin surface on fingers or a wrist fixed by an elastic/textile ribbon.

While the PTT was originally defined as the time difference between ECG and PPG peaks, it can also be determined from PPG signals of optical sensors worn on the wrist and fingers [5]. For real-time PTT determination, the algorithm must be relatively simple but stable, and sufficiently accurate. We use a technique similar to one-channel PPG signal acquisition [6]. For each wave (PPG_A, PPG_B, etc.) the signal level threshold L_{THR} is determined to clip them and obtain sequences c_{PPG} of segments of ones T_1 and zeros T_0 corresponding to the input signal above/below L_{THR}. The PPG cycle period T_{CP} is equal to T_1+T_0 and the heart rate $HR = 60\times f_s/T_{CP}$ [min^{-1}] for T_{CP} in samples. The PPG wave typically contains systolic and diastolic peaks. Systolic peaks position P_{SYS} can be localized in the middle of every T_1 interval (see Fig. 1). The PTT values are calculated from differences between P_{SYS} positions in samples and f_s in kHz as $PTT = \Delta P_{SYS}/f_s$ [ms]. The pulse wave velocity represents the relationship between PTT and the measuring distance $PWV = Dx/PTT$ [m/s]. The relative PTT parameter calculated as a percentual ratio $rPPT = (PTT/T_{PC}) \times 100$ [%] is invariant on the current HR value. Using a linear model, the ABP values can be determined as $ABP = \alpha \times PTT + \beta \times HR + \gamma$ [mmHg], where α, β, and γ are subject-specific constants obtained by regression analysis [5].

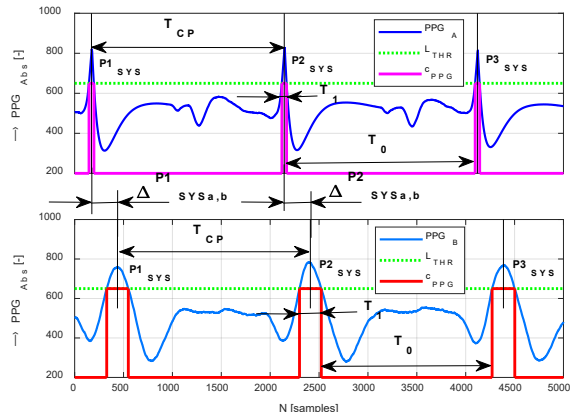

Fig. 1. Example of PTT determination: parts of waves $PPG_{A,B}$, sequences $c_{PPGa,b}$, systolic pulses $P1,2_{SYS}$, and $\Delta P_{SYSa,b}$; $f_s = 2$ kHz.

3. Experiments and Results

The current realization of the wearable triple PPG sensor (PPG-3P) represents a relatively simple and low-cost solution. It consists of: Arduino Nano v. 3.3 board based on the processor ATmega328P with $f_{CLK} = 16$ MHz and eight 10-bit A/D converters; BT module of the BT4.0 BLE standard working at 2.4 GHz; Easy Pulse-mikro module including a TRX PPG optical pulse sensor and two RFX sensors: Pulse Sensor Amped and Crowtail-Pulse Sensor. All

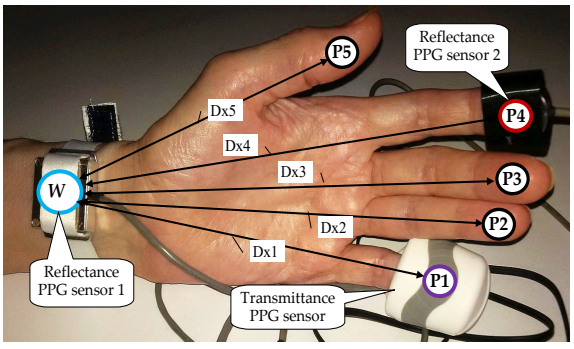

Fig. 2. Principal arrangement of parallel measurement by the multiple PPG sensor.

parts are powered via an USB port by a 5 V power bank. The control application running on an external device manages real-time data transfer from the PPG sensor and stores sensed PPG signals for further off-line analysis.

After testing of functionality of the PPG-3P sensor including the BT data transmission, two types of measurements were performed: (1) parallel sensing of two PPG waves in normal laboratory conditions, (2) parallel recording of three PPG signals in the MRI tomograph environment. In the case of parallel two-channel PPG signals recording, optical PPG sensors were located as follows: the first RFX sensor (*W*) was placed on the wrist artery and the second RFX sensor was worn successively on each of the fingers of the left/right hand (*P*1, *P*5) to obtain different distances *D*x – as demonstrates the arrangement photo in Fig. 2. Simultaneously, the ABP and HR control measurement on the opposite hand was realized by the BPM device (Microlife BP A150-30 AFIB). Seven male (M1-7) and three female (F1-3) non-smoker volunteers (aged from 22 to 60 years) took part in this part of the measurements. In this way, we obtained a small database of (5 + 5) × 10 = 100 records of two parallel PPG signals with duration of 64 s (f_s = 1 kHz). The correlation of PPG waves sensed in parallel and differences in determined PTT and PWV values were subsequently evaluated – see partial results in Table 1 (for the dominant right hand of M1 male), and graphs of PTT, PWV, and HR values for M1 and F1 tested persons in Fig. 3. Each of PPG signal recording procedures was preceded by measurements of *D*x distances for all five fingers – see a box-plot of basic statistical parameters for all participants in Fig. 4a. Summary mean PTT-HR_{PPG}, PWV-SBP, and PWV-DBP mutual positions grouped for L/R hand are present in graphs of Fig. 4b-d.

Table 1. Partial PTT, PWV, and rPTT values determined from $PPG_{A,B}$ waves sensed in distances *D*x; right hand of M1, f_s = 1 kHz.

PPG_A-PPG_B	*D*x [mm]	PTT[A)] [ms]	PWV [m/s]	rPTT [%]	By BPM [mmHg/min]
W-*P*1	155	23.4 (11)	6.76	2.46	121/67 62
W-*P*2	175	28.0 (8)	6.61	2.94	120/68 64
W-*P*3	200	24.9 (10)	7.98	2.66	124/67 67
W-*P*4	185	20.2 (8)	8.14	2.15	119/69 64
W-*P*5	130	18.7 (6)	6.40	2.09	125/71 67

A) Mean values together with std (in parentheses).

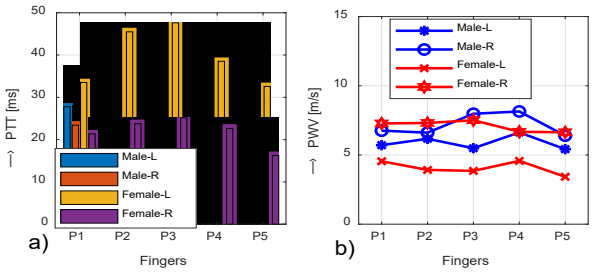

Fig. 3. Comparison for M1 and F1 persons per a finger: a) PTT values, b) PWV values for L/R hand separately.

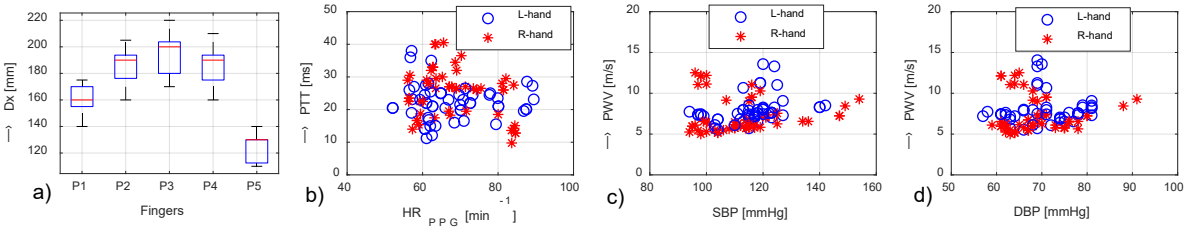

Fig. 4. Summary results for all tested persons: a) box-plot of distances *D*x per a finger, b) mean PTT-HR_{PPG}, c) PWV-SBP, d) PWV-DBP mutual positions grouped by L/R hands.

For parallel triple PPG wave sensing, the first optical RFX sensor was again placed on a wrist, the TRX one on a pinkie (*P*1), and the second RFX on a forefinger (*P*4) according to the measure arrangement in Fig. 2. The tested person was lying in the scanning area of the open-air MRI device E-SCAN Opera. The 64-s PPG signals were recorded in two states: (i) "Silent" – no scan sequence, (ii) "Running" – the high-resolution scan sequence[1] is executed. Four males (M1, 3, 4, 6) participated in these measurements. In this phase of experiments, we tested the

[1] High-resolution SE-HF sequence with setting of: TE=26 ms, TR=500 ms, sagittal orientation, slice thickness = 4.5 mm.

ISBN 978-80-972629-6-9

practical usability of RXF/TXF types of an optical PPG sensor and differences (if any) in determined heart pulse transmission parameters between silent and running sensing states. A summary comparison of mean PWV, rPTT, and HRa,b,c values from triple PPG signals sensed inside the MRI device is shown in Fig. 5.

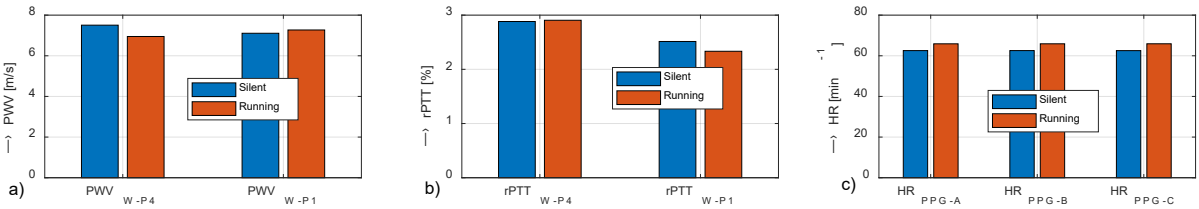

Fig. 5. Summary results of measurements inside the MRI device: a) mean PWV values, b) mean rPTT values, c) mean HRa,b,c values for silent/running state of the MRI; PPG signals sensed at a wrist (PPG_A), a finger P4 (PPG_B), and a finger P1 (PPG_C) of the left hand, f_s = 1 kHz.

4. Discussion and Conclusion

The first-step measurements verified the functionality of the developed triple PPG sensor. Obtained results confirm the usability of parameters determined from sensed PPG waves for stress detection and evaluation which was our main research aim. However, more measurements must be performed to obtain a larger database of PPG signals before its practical usage for the estimation of ABP values. The higher f_s =1 kHz must be used to obtain the PPG wave with adequate quality for correct PTT determination while f_s =125 Hz is sufficient for normal PPG sensing. Partial results of the measurements in the normal laboratory conditions introduced in Table 1 demonstrate that the PWV parameter stays approximately constant for similar values of HR and BP. Comparison in Fig. 3 shows that there are visible differences between results for the left/right hands of M1 and F1 persons. Summary graphical results for all tested persons in Fig. 4 show that the obtained PTT and PWV results depend on an actual physiological/psychical state manifested in BP and HR values. Graphs in Fig. 5 show slight differences between mean PWV, rPTT, and HR values for MRI silent/running states. However, the data obtained from 4 persons are not sufficient to generalize the results.

Acknowledgements

This work was funded by the projects VEGA 2/0004/23, and APVV-19-0531.

References

[1] Steckner, M.C. (2020). A review of MRI acoustic noise and its potential impact on patient and worker health. *eMagRes*, 9 (1), 21-38.

[2] Celka, P. et al. (2020). Influence of mental stress on the pulse wave features of photoplethysmograms. *Healthc Technol Lett, 7*, 7–12.

[3] Liu, M., Lai-Man, P., Fu, H. (2017). Cuffless blood pressure estimation based on photoplethysmography signal and its second derivative. *Int J Comput Theory Eng*, *9*, 202.

[4] Zhang, M., Wei, P.F, Li, Y. (2008). A LabVIEW based measure system for pulse wave transit time. In *International Conference on Information Technology and Applications in Biomedicine*, ITAB 2008.

[5] Manlises, C.O. et al. (2016). Monitoring of blood pressure using photoplethysmographic (PPG) sensor with aromatherapy diffusion. In *6th IEEE International Conference on Control System, Computing and Engineering*, 476-480.

[6] Přibil, J., Přibilová, A., Frollo, I. (2022). Comparison of Three Prototypes of PPG Sensors for Continual Real-Time Measurement in Weak Magnetic Field. *Sensors*, 22 (10), 3769.

Laboratory System of Electrical Impedance Tomography

Jan Mikulka, David Zimniok, Jan Dušek
Brno University of Technology, Brno, Czech Republic
Email: mikulka@vut.cz

Abstract. *This scientific paper deals with the development of an analogue-digital card for electrical impedance tomography. The aim of the paper is to address the problems of measuring impedance, frequency and excitation current levels, and measured voltage, which are crucial for the efficient reconstruction of inhomogeneity distributions using electrical impedance tomography. The paper presents the design of an active probe system to suppress interference and increase sensitivity in impedance measurements. This design is based on the use of signal amplifiers and the switching of reference measurement electrodes. Experimental results show the high accuracy and sensitivity of the newly developed system. These results suggest that the new system can be used to improve systems in various disciplines of non-destructive diagnostics.*

Keywords: Electrical Impedance Tomography, EIT, Active Probe, EIDORS, Electrical Impedance

1. Introduction

There are currently various non-invasive techniques available for measuring objects with unknown internal structures. These techniques include X-ray, computed tomography, magnetic resonance imaging, ultrasound, positron emission tomography, and single-photon emission tomography. However, these techniques share common drawbacks such as high cost, limited mobility, and the requirement for trained professionals to operate them. In contrast, electro-impedance tomography (EIT), although less well-known among the general public, offers a relatively affordable and portable solution for such measurements. This technique involves measuring voltage between 16 electrodes, after which the computer calculates conductivity matrices between the electrodes and generates a two-dimensional image. However, this method is not suitable for all types of objects since one electrode is always powered by current, which typically ranges from a few microamperes to 10 mA. Thus, electro-impedance tomography is best suited for inanimate objects with small voltage or current sensitivity. The method does not require the use of radioactive or magnetic material but instead requires a current source and a measuring card. The data obtained from this technique must include the real and imaginary impedance components, which can be expressed mathematically using eq. 1:

$$\mathbf{Z} = R + jX\,, \tag{1}$$

where $\mathbf{Z}$ represents the complex impedance, R represents the electrical resistance, and X represents the reactance.

The process of acquiring data for the reconstruction of electro-impedance tomography images is based on the measurement of voltage and signal phase shift between the input current and electrodes of the tomograph. Over the years, various stimulation patterns have been developed to enable the application of alternating current to specific electrodes of the system while facilitating the measurement process with suitable electrode combinations. Among these stimulation patterns, the most commonly used include Adjacent, Opposite, and Skip-X driving, as shown in Fig. 1 [1].

ISBN 978-80-972629-6-9

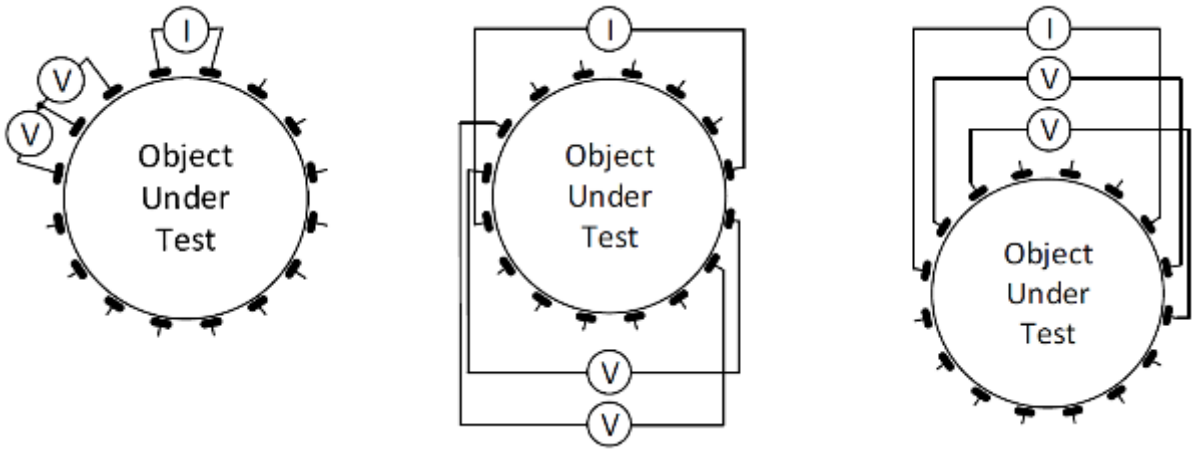

Fig. 1. Stimulation patterns in electrical impedance tomography (from left to right): adjacent, opposite, skip-5

2. Subject and Methods

Active Probe Design

The active probe serves the purpose of converting the signal into a current loop, thereby eliminating unwanted interferences and maintaining high input impedance [2]. π resistor attenuators are used at the inputs to provide high impedance, while an attenuator is employed to protect against voltages higher than the supply voltage. The attenuator automatically connects to the signal trace in case the input voltage exceeds the voltage set by the divider, and the signal attenuation is conveyed to the measuring card through a single wire. This is done to ensure that the voltage is measured at both electrodes by attenuating the signal at both points or compensating for it in the microprocessor. In case only one electrode signal is attenuated, it may result in evaluation errors. Thus, if one signal is attenuated, the measuring card will attenuate the other signal. The active probe, as shown in Fig. 2b, is connected to the measuring card through a flat cable comprising ethernet connectors, without twisted pairs. Fig. 2a shows a simplified block diagram of the active probe. The measurement probes need to have the ability to turn their power on and off or ground themselves automatically for accurate readings. This is made possible by two relays that are controlled by signals from the measuring unit. Although unipolar transistors were initially considered for switching, simulations showed that their transient parasitic capacitance could interfere with the power signal quality. When the control signal is negative, the probe should connect to ground at the measurement point. When the signal is positive, the probe supplies current to the phantom. If the control signal oscillates around zero, both relays remain disconnected.

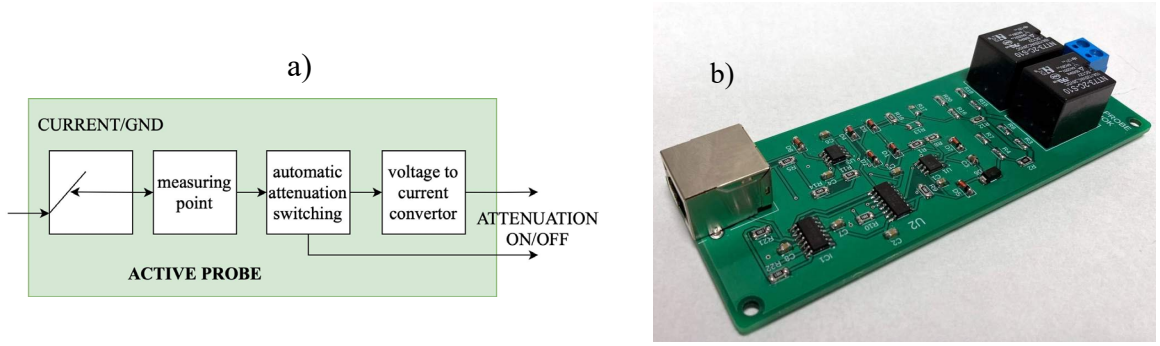

Fig. 2. Active probe: a) simplified block diagram, b) completed probe

Multiplexor

The scalability of this idea is its primary advantage. The measuring card is made up of two types of printed circuit boards. The first is the microprocessor board, which contains two amplifiers with programmable gain and optocouplers for galvanic isolation between the computer and the measuring component. This board also provides power to all other boards and ensures communication with the computer. Communication is provided through a customised Matlab library, directly connected to EIDORS library, or a simple terminal. The firmware defines commands for measuring between two electrodes, measuring the whole level, multi-level measurements, and calibration function.

The second board represents the measuring card, with its assembly dependent on whether it is the first board (master) or an extension board (slave). In the master mode, the board evaluates the signal processing performed on the active probes, while also ensuring switching the control signal to the probes and between measuring probes. In the slave mode, the board is only responsible for the switching, while the master evaluates the signal. The board is addressable, allowing up to 256 electrodes to be connected by addressing. This can be used to measure more than one phantom or more planes. Fig. 3 shows a block diagram for collecting voltage from a single probe, using multiplexors to control the signal, electrode addressing, and attenuation signalisation. Multiplexors are crucial as the current loop must be loaded with the appropriate resistance, necessitating the recalculation of the load resistance to the corresponding load after selecting the multiplexor. The remaining elements of the measurement chain, such as programmable amplifiers, microprocessors, or optocouplers, are not strictly defined and can be selected variably.

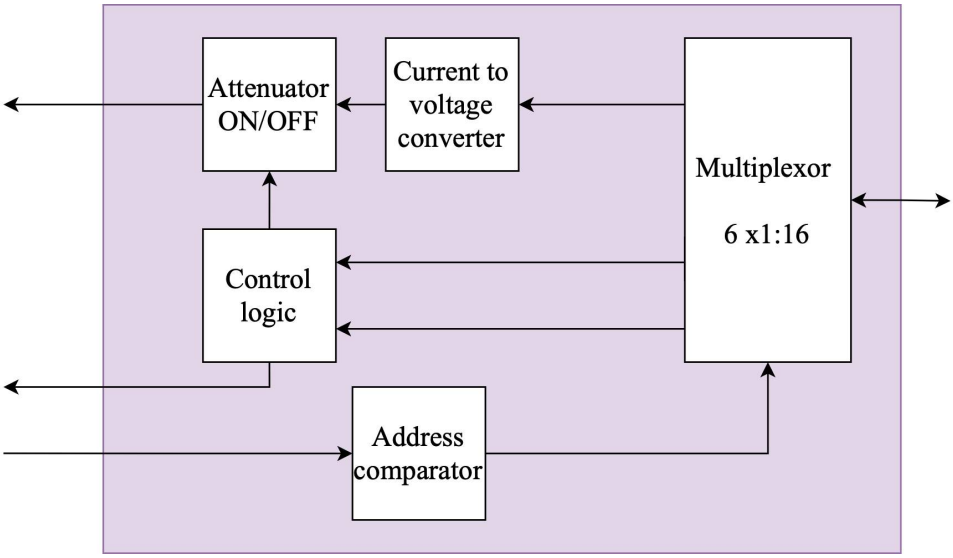

Fig. 3. Multiplexor simplified block diagram

3. Discussion

The accuracy of the measurement is primarily determined by the electronic components utilized. The operational amplifiers restrict the bandwidth of the system since there are no other frequency-dependent elements included in the analog signal processing. The sampling frequency for the two synchronous captured channels is 677.4 kHz for the prototype using the STM32F407VG. As per the Nyquist theorem, the maximum signal speed is approximately 338 kHz. For frequency measurement, it is advisable to have at least ten samples per period to get better results, which limits the bandwidth to 67.74 kHz. However, this can be enhanced by

increasing the sampling frequency. The bandwidth was improved to a minimum of 135.48 kHz (five samples per period).

To adjust the measuring voltage and current level, the calibration function can be utilized. It should measure voltage and current on a known resistive load. The algorithm is designed to measure the voltage on a resistor that is connected to two probes and supplied with a known current. Afterwards, the microprocessor corrects all measured values with an absolute error calculated from the difference between the uncalibrated and precise measurements using a voltmeter and an ammeter. This process can only be conducted between two probes, and the measurement offset should be identical for all probes if the same components are used.

Moreover, calibration also corrects the phase measurement. Typically, the phase cannot be zero for signals on a resistive load due to the length of the measurement chain (approximately two amplifiers for the current and at least four amplifiers for the voltage). During calibration mode, the firmware quantifies the phase shift of the two signals on a resistive load and then adds this constant to all the results.

The paper describes the design of a custom multiplexer unit including active probes that provide both power and measured signals to reconstruct the specific electrical conductivity distribution. In contrast to the systems presented at the same time, the proposed system allows a large range of scalability from measurements on small samples (laboratory use) to large objects (water dams).

Acknowledgements

The preparation of this paper was assisted by project No. FEKT-S-23-8425 of the BUT internal grant office.

References

[1] Avis, N.J., Barber, D.C. Image reconstruction using non-adjacent drive configurations (electric impedance tomography). *Physiol. Meas.* 1994, 15, A153–A160.

[2] Dušek, J.; Mikulka, J. Measurement-Based Domain Parameter Optimization in Electrical Impedance Tomography Imaging. *Sensors*, 2021, roč. 21, č. 7, s. 1-20. ISSN: 1424-8220.

Connectivity and Causality in EEG or other Biological Signals

ISBN 978-80-972629-6-9

EEG Connectivity in Treatment of Major Depressive Disorder: Tackling the Conductivity Effects

[1]Milan Paluš, [1]Aditi Kathpalia, [2]Martin Brunovský

[1]Department of Complex Systems, Institute of Computer Science of the Czech Academy of Sciences, Prague, Czech Republic,
[2]Clinical Research Programme, National Institute of Mental Health, Klecany, Czech Republic
Email: mp@cs.cas.cz

Abstract. *Brain connectivity, extracted from EEG is considered for quantitative characterization of changes in brain function due to a mental disease and its treatment. Weighted imaginary coherence is chosen as a connectivity measure reflecting true brain interactions without distortions due to scalp conductivity and a common reference electrode. This measure is used in analyses of EEG data from patients suffering from major depressive disorder and its potential in prediction of efficacy of antidepressant treatment is demonstrated.*

Keywords: Brain Connectivity, EEG, Imaginary Coherence, Major Depressive Disorder, Antidepressant Treatment

1. Introduction

Description and quantification of brain connectivity (i.e., communication between neuronal assemblies) is not only important for understanding the brain function and consciousness, but also for diagnosis and treatment of neuropsychiatric diseases [1].

Electroencephalogram (EEG) is probably the most spread and the lowest cost technology able to record electrical brain activity in millisecond resolution. Traditionally, coordination of brain areas, adjacent to different electrodes, is inferred from EEG recordings by means of coherence analysis [2]. Since we will consider scalp EEG with a common reference electrode, we will inevitably face the problems of scalp conductivity and a common component in EEG recordings from any scalp location. As we will see, these phenomena induce a false connectivity, i.e. statistically significant coherence in any pair of channels and in all spectral bands. If a connectivity measure is dominated by technical artifacts rather than reflecting true interactions between different brain areas, we cannot expect useful descriptions of brain states in health or pathology. In order to remove the effects of conductivity and the common reference electrode we will consider imaginary coherence, as well as its weighted version. The latter will be applied in analysis of EEG data of patients suffering with the Major Depressive Disorder in order to assess the ability of this measure to predict the efficacy of antidepressant treatment.

2. Methods

Coherence is a spectrally-resolved measure of dependence or connectivity and is traditionally defined using the Fourier transform [2]. Here we redefine the coherence and its versions using the complex continuous wavelet transform (CCWT) thus making the results of coherence analysis directly comparable with time-domain measures of connectivity based on the ideas of phase synchronization and causality defined in the phase dynamics approach which are studied in other branches of this project. Here, however, we focus on the coherence analysis.

A measured (EEG) signal is recorded as a time series $X(t)$. Considering a set of wavelet central frequencies f_k and a mother wavelet function $\psi(t)$ (basis functions), a complex contin-

ISBN 978-80-972629-6-9

uous wavelet transform converts the time series $X(t)$ into a set of complex wavelet coefficients $W(t, f_k)$:

$$W(t,f) = \int_{-\infty}^{\infty} \psi(t')X(t-t')dt'. \tag{1}$$

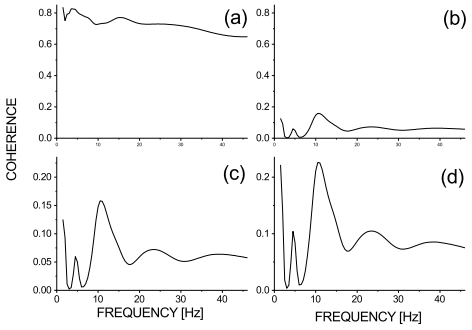

Fig. 1: Connectivity between EEG channels O_1 and O_2: (a) wavelet coherence, (b) imaginary wavelet coherence, common scale with (a); (c) imaginary wavelet coherence, common scale with (d); and (d) weighted imaginary wavelet coherence.

Wavelet coherence measures

Having the sets of the complex wavelet coefficients $W_X(t,f)$ and $W_Y(t,f)$ for the time series $X(t)$ and $Y(t)$, respectively, we define the time-averaged complex-valued quantity

$$W_{X,Y}(f) = \frac{1}{N}\sum_{t=1}^{N} W_X(t,f)W_Y^*(t,f), \tag{2}$$

where the star * stands for the complex conjugate. We consider that the time series $X(t)$ and $Y(t)$ were obtained by discrete-time sampling for time instances $t = 1,\ldots,N$. $W_{X,X}(f)$ will be marked as $W_X(f)$, $W_{Y,Y}(f)$ as $W_Y(f)$. The complex wavelet coherence is

$$\Gamma_{X,Y}^W(f) = \frac{W_{X,Y}(f)}{\sqrt{\|W_X(f)\|\|W_Y(f)\|}}, \tag{3}$$

where $\|W\|$ is the norm, or the magnitude, given as $\sqrt{WW^*}$. We will use the term wavelet coherence for the magnitude of the complex wavelet coherence:

$$\gamma_{X,Y}^W(f) = \|\Gamma_{X,Y}^W(f)\|. \tag{4}$$

As an example we present the wavelet coherence (WC) between EEG channels O_1 and O_2 in Fig. 1a. For the whole spectral range WC gives high, statistically significant values (statistical tests not presented). This result would mean that the two selected channels are connected within the whole investigated spectrum. This is not realistic and this false connectivity is the consequence of the conductivity and the common reference electrode inducing a common component to all channels.

In order to measure true brain interactions not affected by the conductivity effects, Nolte et al. [3] have proposed to use the imaginary coherence, which we define in the wavelet domain as

$$\gamma_{X,Y}^I(f) = |\,\mathbb{I}\mathrm{m}\{\Gamma_{X,Y}^W(f)\}|, \tag{5}$$

where $|.|$ marks the absolute value.

Pascual-Marqui et al. [4] have proposed a weighted form of the imaginary coherence which they call lagged coherence, or lagged phase synchronization, redefined here in the wavelet domain (weighted imaginary wavelet coherence or WIWC) as

$$\gamma_{X,Y}^P(f) = \frac{|\,\mathbb{I}\mathrm{m}\{\Gamma_{X,Y}^W(f)\}|}{\sqrt{1-\mathbb{R}\mathrm{e}\{\Gamma_{X,Y}^W(f)\}^2}}. \tag{6}$$

Taking only the imaginary part of coherence all effects of immediate dependence from common components are removed and only time-delayed physiological interactions in standard EEG bands are detected (Fig. 1). The true connectivity is relatively amplified using WIWC, therefore we use this measure in our EEG study.

ISBN 978-80-972629-6-9

3. Data

EEG data used in this study was obtained from the database of the National Institute of Mental Health, Czech Republic. Details of the sample and participant recruitment criteria are available in [5] and references therein. For this study, EEG recordings from 176 patients with MDD were taken. These patients were in the age range of 18 to 65 years. Four weeks of antidepressent treatment was administered to the patients based on the decision of the psychiatrist. Two EEG recordings (approximately 10 minutes long), one before starting medication (referred to as Visit 1) and the other, one week after starting medication (referred to as Visit 2) were obtained from each patient. MADRS score, a questionnaire-based score assessment criteria, was used by the psychiatrists to assess the state of the depressive syndrome in patients before starting treatment and at the end of the treatment. The patients which thus responded/ did not respond to treatment were decided on the basis of this MADRS score. Out of the considered 176 patients, 86 were found to be respondents and the rest 92 were non-respondents.

19 standard electrode positions: Fp1, Fp2, F3, F4, C3, C4, P3, P4, O1, O2, F7, F8, T3, T4, T5, T6, Fz, Cz, Pz were analyzed. The recordings were preprocessed using the EEGLab toolbox [6]. The sampling rate for some recordings was 250 Hz while for the others was 1000 Hz. The latter were subsampled to 250 Hz by taking every fourth sample. First and the last 30s of the data were removed, the EEG was set to average reference and consequently band pass filtered from 1-40 Hz. In order to remove artifacts, individual 2s segments of data were assessed and those segments which contain high-power artifacts in 20% or more of the considered channels were eliminated from the dataset.

4. Results

Using 19 channel EEG recordings for each patient, WIWCs were computed between all 171 distinct pairs of channels. As only every 2s of EEG signal recordings were expected to be continuous after preprocessing, $\|W_X(f)\|$, $\|W_Y(f)\|$ and $W_{X,Y}(f)$, were computed from 2s or equivalently 500 time point windows and then summed up over consecutive 8 windows to yield coherences and consequently WIWCs over 4000 time point or 16s length segments. FFT-based surrogate data were used to assess the significance of WIWCs at each scale in each segment.

Further, the significant WIWCs computed for 78 different frequencies (in the range of 1-40 Hz) were summed up to give the WIWCs associated with 6 meaningful EEG bands. These were δ [1.5 - 3.5 Hz], θ [4 - 7.5 Hz], α [8 - 12Hz], β_1 [12.5 - 17.5 Hz], β_2 [18 - 25.5 Hz] and γ [26 - 40 Hz]. WIWCs from 16s length segments associated with the 6 frequency bands were further used to construct functional brain networks.

Cross-hemispheric (CH) connectivity was estimated for WIWCs computed for all the frequency bands. To compute **weighted CH connectivity** for a particular band, the significant WIWCs estimated for all connections between the left and the right hemisphere were averaged for all the 16s segments available in the patient's recording. In order to compute average **binary CH connectivity** across segments for a particular band, the number of non-zero significant WIWCs identified for connections between the left and the right hemisphere were averaged over all the segments available for that patient.

In order to check if there was a statistically significant change in CH connectivity before and after one week of medication, the quantity CH_{Vis2} (CH connectivity at Visit 2) and CH_{Vis1} (CH connectivity at Visit 1) were compared for the respondent and the non-respondent patients separately. A significant decrease in CH_{Vis2} as compared to CH_{Vis1} (both weighted and binary) was found using the non-parametric Wilcoxon test at a significance level of 0.05 for the respondents in the β_1 band. No such significant change was found for the non-respondents. For all the other frequency bands, no significant changes in CH connectivity were identified for either the

ISBN 978-80-972629-6-9

respondents or the non-respondents. Further, the quantity $CH_{Vis2} - CH_{Vis1}$ in the β_1 band was compared for the respondents and the non-respondents. This quantity was found to be statistically different between the two groups using the Wilcoxon test at a significance level of 0.05 for both weighted and binary CH connectivity cases. Further, for the binary case, this change was also significant for the Wilcoxon test with Bonferroni correction using a factor of 6 (for the 6 frequency bands considered).

5. Discussion and Conclusions

We have demonstrated that the weighted imaginary coherence reflects only a connectivity in physiologically relevant spectral bands and therefore can reflect changes in brain activity due to a mental illness and/or changes due to a successful treatment of a particular mental disorder. Building on this hypothesis we have applied the weighted imaginary coherence to EEG data from a database of EEG signals recorded from a group of patients suffering with the Major Depressive Disorder before and one week after treatment by an antidepressant drug. We have observed a statistically significant decrease of cross-hemispheric connectivity after one week of the antidepressant treatment in the group of responders, i.e., patients whose clinical state improved after one month of the antidepressant treatment, while no connectivity change was observed in the patients not responding to the antidepressant treatment. Thus the properly quantified brain connectivity can potentially be used for predicting the efficacy of antidepressant treatment.

Acknowledgements

This study is supported by the Czech Science Foundation, Project No. GF21-14727K and by the Czech Academy of Sciences, Praemium Academiae awarded to M. Paluš.

References

[1] Bardin, J. (2012). Making connections. *Nature* 483(7390), 394.

[2] Nunez, P. L., Srinivasan, R., Westdorp, A. F., Wijesinghe, R. S., Tucker, D. M., Silberstein, R. B., Cadusch, P. J. (1997). EEG coherency I: statistics, reference electrode, volume conduction, Laplacians, cortical imaging, and interpretation at multiple scales. *Electroencephalogr Clin Neurophysiol* 103(5), 499–515.

[3] Nolte, G., Bai, O., Wheaton, L., Mari, Z., Vorbach, S., Hallett, M. (2004). Identifying true brain interaction from EEG data using the imaginary part of coherency. *Clinical Neurophysiology* 115(10), 2292–2307.

[4] Pascual-Marqui, R. D., Lehmann, D., Koukkou, M., Kochi, K., Anderer, P., Saletu, B., Tanaka, H., Hirata, K., John, E. R., Prichep, L., et al. (2011). Assessing interactions in the brain with exact low-resolution electromagnetic tomography. *Philos. Trans. R. Soc. A* 369(1952), 3768–3784.

[5] Bučková, B., Brunovský, M., Bareš, M., Hlinka, J. (2020). Predicting sex from EEG: validity and generalizability of deep-learning-based interpretable classifier. *Frontiers in Neuroscience* 14, 589303.

[6] Delorme, A., Makeig, S. (2004). EEGLAB: an open source toolbox for analysis of single-trial EEG dynamics including independent component analysis. *J. Neurosci. Meth.* 134(1), 9–21.

Pattern Discovery in an EEG Database of Depression Patients: Preliminary Results

[1,2] Kateřina Hlaváčková-Schindler, [1]Christina Pacher,[1] Claudia Plant,[1]Mykola Lazarenko, [2] Milan Paluš, [2]Jaroslav Hlinka, [2]Aditi Kathpalia, [3]Martin Brunovský

[1]Data Mining and Machine Learning Research Group, Faculty of Computer Science, University of Vienna, Vienna, Austria
[2]Department of Complex Systems, Institute of Computer Science, Czech Academy of Sciences, Prague, Czechia
[3]Clinical Research Programme, National Institute of Mental Health, Klecany, Czechia
Email: katerina.schindlerova@univie.ac.at

Abstract. *The ability to predict response to medication treatment of depressed patients, either early in the course of therapy or before treatment even begins can avoid trials of ineffective therapy and save patients from prolonged intervals of suffering. Symptom alleviation requires 4-6 weeks after starting current antidepressive medication. Based on the data basis of the patients and their EEG before and on the 7th day of treatment we apply data mining, causal discovery and machine learning approaches to discover interactive patterns between patient's brain regions to separate the treatment responders from non-responders. In this paper we report the preliminary results of our international project "Learning Synchronization Patterns in Multivariate Neural Signals for Prediction of Response to Antidepressants" ongoing at the University of Vienna, the Czech Academy of Sciences and the National Institute of Mental Health in the Czech Republic.*

Keywords: Major Depressive Disorder, Interactive Clustering, Granger Causality, Classification Methods

1. Introduction

Major depressive disorder (MDD) or clinical depression is a mental disorder characterized by low self-esteem, persistent sadness, and loss of pleasure in activities that are normally enjoyable. Modern antidepressant drugs have a response rate only up to 65% whereas the response requires usually 4-6 weeks to decide whether to continue with the treatment strategy or to change. The diagnosis of the disease is based on the person's experience, behavior, and mental status examination such as Montgomery-Åsberg Depression Rating Scale (MADRS). Medication treatment seems to be effective but mostly in patients with moderate to severe depression [3]. In comparison to epilepsy, in which seizure focus and/or events are represented by typical high-amplitude rhythmic epileptiform patterns in the EEG signal in corresponding brain areas, the EEG signal for MDD do not exhibit these explicit patterns. Having this in mind, we postulate that patients who have not responded to antidepressant treatment, may exhibit information patterns not within EEG trajectories but in the way how the brain regions temporarily interact with each other. To find these patterns and their differences for medication responders and non-responders, we explore the EEG databasis of MDD patients by methods of signal processing, interactive clustering, causal inference and machine learning.

2. Description of the Data Basis

The EEG data base used consisted of 176 patients, out of which 128 were females and 48 were males. These EEG recordings were acquired as a part of the study described in [2]. Every patient

ISBN 978-80-972629-6-9

was recorded before the start of anti-depression treatment and on the 7th day after the start of the treatment which lasted for around 4 weeks. Patients were recorded for 10 minutes, laying on a bed with elevated upper body at 30-45 degrees in a room with dimmed light with closed eyes (alerted when drowsiness appeared in EEG). Recordings from 19 standard electrode positions, namely, Fp1, Fp2, F3, F4, C3, C4, P3, P4, O1, O2, F7, F8, T3, T4, T5, T6, Fz, Cz, and Pz, were used for analysis. The initial and the last 30 seconds of recordings were removed for each subject. For the task of interactive clustering, a subset of 134 patients were used and their EEG recordings pre-processed as described in [2]. For the task of classification of causal graphs, data from all the patients were used and pre-processed using the EEGLab toolbox [8] as follows. Since some patients' recordings were sampled at 1000 Hz and others at 250 Hz frequency, the recordings at 1000 Hz were subsampled to 250 Hz by taking every fourth sample. Further, the EEG was set to average reference and consequently band pass filtered from 1-40 Hz. In order to remove segments of data with artifacts, individual 2s segments of data were assessed and those segments which contain high-power artifacts in 20% or more of the considered channels were eliminated from the dataset.

In both data sets, each patient is assigned a label either 0 (non-responder) or 1 (responder) which was determined by psychiatric experts using MADRS score after the 4th week visit. In every experiment, we use the patients' EEGs from the 7th day of therapy or this EEG combined with the EEG before the therapy (day 0), ordered timely after each other.

3. Interactive Clustering

One way of finding patterns among the brain regions of patients is applying clustering on patients algorithm called interaction K-means (IKM) [6]. IKM models each subject as a multivariate time series, where the single dimensions represent the EEG signal at different electrode. In contrast to common clustering approaches, the cluster notion of IKM is based on the interactions between the univariate time series within a data object (patient). The objective is to assign objects exhibiting a similar intrinsic interaction pattern to a common cluster. A cluster is defined by a set of mathematical models describing the cluster-specific interaction patterns. To be able to separate patients into two clusters (responders and non-responders) by IKM, we performed exploratory analysis of the influence of preprocessing on the cluster purity (CP) of IKM on the EEG data set. To improve clustering accuracy of the algorithm on the given data we used sinusiodal, discrete wavelet transformation, z-normalization, exponential smoothing, Hilbert transform and Box-Cox transform, various distance metrics as well various subsets of electrodes (all 19 electrodes or electrodes in different hemispheres). The best clustering result with highest clustering purity $CP = 60.5\%$, was for the Box-Cox and z-score transformation (non-specific frequency band) in Euclidean distance for electrodes Cz, Fp1, F3, F7, C3, T3, P3, T5, O1.

Figure 1 illustrates the identification of electrodes P3 and T5 (the outgoing electrode of the arrows, in color green) as the most discriminative among the clusters. In the cluster of non-responders (left two), P3 and T5 were strongly related to the Fp1 and F3 electrodes, respectively. In the cluster of responders, P3 had strong relationships to the F3, Fp1, F7, and Cz electrodes, while T5 was strongly related to the O1 electrode. Based on the identified electrodes and their relationships within and between clusters, one may make some observations about the underlying neurological differences between responders and non-responders. We can hypothesize that the observed differences in electrode relationships between responders and non-responders may be related to underlying differences in neural connectivity or functional networks. Furthermore, the identified electrodes and their relationships may have clinical implications for predicting treatment response in depressed patients.

ISBN 978-80-972629-6-9

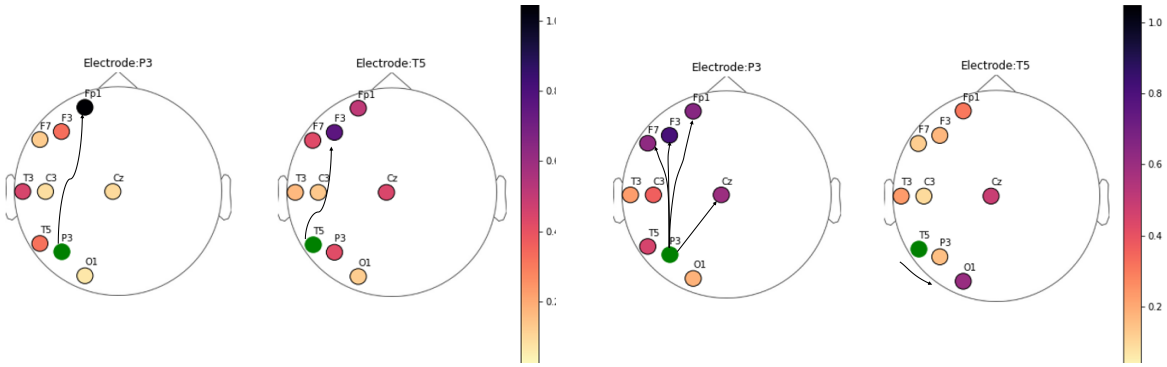

Fig. 1: Results of IKM with $CP = 60.5$. Left two heads are for the non-responders, right two ones for responders. Interactions w.r.t. electrodes P3 and T5 are visualized.

4. Granger Causal Graphs as Discriminative Patterns

Granger causality between two variables [4] as a temporal and computational concept of causality was extended to the case of $p \geq 2$ variables in terms of vector auto-regressive models with the lasso variable selection method [1] and is in literature called a graphical Granger model (GGM). To overcome the rate of false negatives of lasso, [5] used the so-called statistical minimum description length (MDL) principle to discover the Granger causal graphs with a high $F1$ precision.

A GGM among p Gaussian variables can be represented by a binary adjacency matrix A of size $p \times p$ where $A_{ij} = 1$ means that time series x_j is causal to x_i and $A_{ij} = 0$ that x_j is non-causal to x_i. Each row of A is computed by the criterion derived from stochastic MDL, more details can be found in [5].

5. Classification of Causal Graphs

Motivated by [2] that EEG structure of male and female patients may differ, we split the data set of 134 patients into male (31) and female (103) subjects. Classifiers were trained and evaluated separately for those two groups. Due to small sample of men we used 5-fold cross validation. The used classifier were: Support vector classifier with linear, RBF and polynomial kernels, k-nearest neighbor classifier, decision tree classifier, random forest classifier and naive Bayes classifier. We explored a number of different experiment settings: Hemisphere: left hemisphere (8 electrodes), left hemisphere with center electrodes (11 electrodes), or whole brain (19 electrodes); Frequency band: alpha band, theta band or the unfiltered data, i.e. in total nine different input data settings. Additionally, we applied a Box-Cox transformation to the input data before computing the causal graphs, in order to improve the normality of the data, required by GGM. On the training set consisting of only women, the best classification result was with a mean $F1 = 0.72$. On the training set consisting of only men, the best classification result on this data set was a mean $F1 = 0.86$.

6. Discussion and Future Work

Concerning the results achieved by the IKM clustering method, future studies could answer whether measuring activity in the discovered specific electrode locations could be used as a biomarker for predicting treatment response in depressed patients. Concerning the classification by the GGM causal graphs, the results still need to be validated on completely unseen data, using the test set that was previously set aside for this purpose. In addition to it, we will proceed in applying other data mining and machine learning methods on the data set. Concerning the applied classifiers to the GGM representation of patients we can conclude that there is a

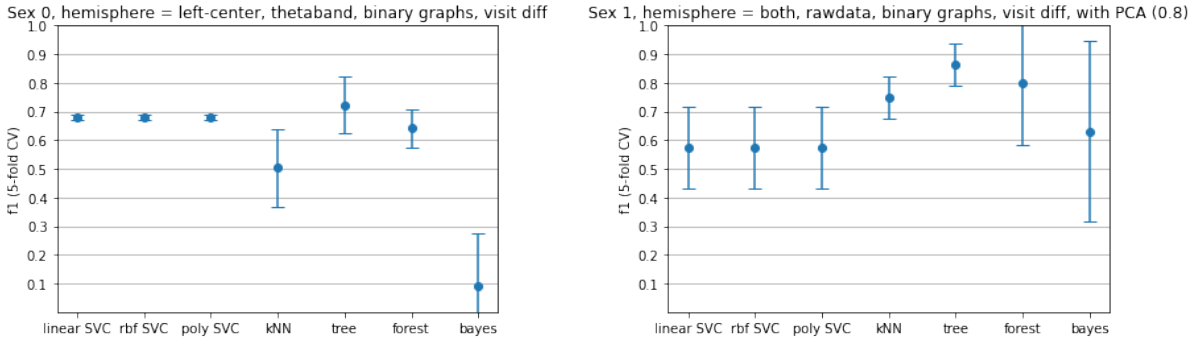

Fig. 2: Left: $F1$ for the left hemisphere of females with center electrodes on the theta band, using the difference between the GGM graphs as input. The best result is for the decision tree (DT) classifier. Right: $F1$ for the full brain of males on unfiltered data. PCA was applied to the input data, keeping enough components to explain 80% of the variance. The best result is for DT.

significant difference in precision among them and that for both separated sets (male, female), see Figure 2. Our results contradict to the opposite observations in the recent paper on a similar topic [7]. However, the size of the investigated data sets (different number of patients, a different duration of EEG monitoring and different feature extraction methods/representations) may play an important role in these contradictory observations.

Acknowledgements

This work was supported by the Czech Science Foundation GACR (Project No. GF21-14727K) and by the Austrian Science Foundation FWF (Project No. I5113).

References

[1] Arnold, A., Liu, Y., Abe, N. (2007). Temporal causal modeling with graphical Granger methods. In *Proceedings of the 13th ACM SIGKDD International Conference on Knowledge Discovery and Data Mining* (pp. 66–75).

[2] Bučková, B., Brunovský, M., Bareš, M., Hlinka, J. (2020). Predicting sex from EEG: validity and generalizability of deep-learning-based interpretable classifier. *Frontiers in Neuroscience*, 14, 589303.

[3] Fournier, J.C., DeRubeis, R.J., Hollon, S.D., Dimidjian, S., Amsterdam, J.D., Shelton, R.C., Fawcett, J. (2010). Antidepressant drug effects and depression severity: a patient-level meta-analysis. *Jama*, 303(1), 47–53.

[4] Granger, C.W.J. (1969). Investigating causal relations by econometric models and cross-spectral methods. *Econometrica: Journal of the Econometric Society*, 424–438.

[5] Hlaváčková-Schindler, K., Plant, C. (2020). Graphical Granger causality by information-theoretic criteria. In *Proceedings of ECAI 2020* (pp. 1459–1466), IOS Press.

[6] Plant, C., Zherdin, A., Sorg, C., Meyer-Baese, A., Wohlschläger, A.M. (2013). Mining interaction patterns among brain regions by clustering. *IEEE Transactions on Knowledge and Data Engineering*, 26(9), 2237-2249.

[7] Čukić, M., Stokić, M., Simić, S., Pokrajac, D. (2020). The successful discrimination of depression from EEG could be attributed to proper feature extraction and not to a particular classification method. *Cognitive Neurodynamics*, 14, 443-455.

[8] Delorme, A. and Makeig, S. (2004). EEGLAB: an open source toolbox for analysis of single-trial EEG dynamics including independent component analysis. *Journal of Neuroscience Methods*, 134 (1), 9–21.

Phase-based Causality Analysis of EEG in Treatment of Major Depressive Disorder

[1]Madhurima Bhattacharjee, [1]Aditi Kathpalia, [2]Martin Brunovský, [1]Milan Paluš

[1]Department of Complex Systems, Institute of Computer Science of the Czech Academy of Sciences, Prague, Czech Republic,
[2]Clinical Research Programme, National Institute of Mental Health, Klecany, Czech Republic
Email: bhattacharjee@cs.cas.cz

Abstract. *This study analyzes causal connections between cross-hemispheric brain regions in individuals diagnosed with major depressive disorder (MDD) through Electroencephalography (EEG) data. A phase-based causality analysis technique is first validated on coupled Rössler systems and then employed on EEG recordings from MDD patients. Our results provide significant insights regarding causal influences in cross-hemispheric brain connectivity of MDD patients who exhibit an early response to medication after commencing treatment.*

Keywords: Brain Connectivity, Phase-Based Causality, Eeg, Major Depressive Disorder, Mutual Information

1. Introduction

Major depressive disorder (MDD) is a prevalent psychiatric condition affecting millions worldwide that can also serve as an underlying factor for various physiological illnesses. Finding effective and non-invasive ways to diagnose and treat MDD is crucial and a significant challenge for clinical neuroscience. One such diagnostic non-invasive neuroimaging technique is EEG which measures the brain's electrical activity with a reasonably high temporal resolution in the millisecond range compared to other brain imaging techniques. Causality analysis of multi-channel EEG signals can potentially guide the development of more effective treatment strategies. It can reveal the direction and strength of causal influences between EEG channel locations, which can help elucidate the underlying mechanisms of the brain. In this study, we conduct a bivariate causality analysis on various channel pairs of EEG signals that were recorded from patients with MDD before and after one week of medication. Having knowledge of the directional connectivity alteration in the brain can prove to be highly beneficial at the initial stage of treatment approaches for identifying characteristics that can anticipate the clinical outcome of treatment after 4-6 weeks. We employ an information-theoretic method called the partial mutual information from mixed embedding (PMIME) [1], which utilizes phase variables of oscillatory signals. This model-independent measure is widely applicable for detecting causal relationships in multivariate systems like multi-channel EEG signals. We use phases in PMIME algorithm to study causality between cross-hemispheric brain regions and the changes in cross-hemispheric connectivity after the start of anti-depression treatment. Our methodology and results are discussed in the following sections.

2. PMIME Methodology

PMIME [1] is an iterative method that uses forward selection to estimate inherent lag dependence in coupled multivariate non-linear dynamical systems. It generates mixed embedding vectors from multiple observed time series of connected subsystems to reveal causal relationships. The method employs conditional mutual information (CMI) $I(X;Y|Z)$ as a selection criterion and uses a statistical test as a stopping criterion. CMI measures the average shared information

ISBN 978-80-972629-6-9

between random variables X and Y, conditioned by variable Z. Consider a coupled dynamical system consisting of K subsystems. The time series data for these K variables are denoted by $x_{i,t}$ where $t = 1,\ldots,N$, $i = 1,\ldots,K$. PMIME aims to predict the future of a target variable x_i by finding a mixed embedding vector $\mathbf{w}_i = [w_{(1)}, w_{(2)} \ldots]$ with an undetermined dimension that maximizes the mutual information (MI) term $I(x_{i,t+1}; \mathbf{w}_i)$. The elements of $\mathbf{w}_i$ belongs to the superset $\mathbf{W} = \bigcup_{i=1}^{K} \mathbf{X}_i = \{w_j\}$, $j = 1,\ldots,K \cdot L_{max}$. L_{max} is the maximum lag which can be chosen to be appropriately large. The set $\mathbf{X}_i$ contains the lagged version of each variable i.e. $\mathbf{X}_i = \{x_{i,t}, x_{i,t-1}, \ldots, x_{i,t-L_{\max}+1}\}$, $i = 1,\ldots,K$. If any element of $\mathbf{X}_j$ is contained in $\mathbf{w}_i$ then we can say x_j causes x_i. The causality measure is given by the following normalized CMI term, bounded between 0 and 1:

$$R(j \to i) = \frac{I\left(x_{i,t+1}; \mathbf{w}_{i,j} \mid \mathbf{w}_{i,rest}\right)}{I\left(x_{i,t+1}; \mathbf{w}_i\right)}. \tag{1}$$

In Eq. 1, $\mathbf{w}_i$ is split into elements that belong to $\mathbf{X}_j$ and all other elements, i.e. $\mathbf{w}_i = \left[\mathbf{w}_{i,j}, \mathbf{w}_{i,rest}\right]$ and, $R(j \to i)$ corresponds to the proportion of information in x_i that can be explained by the past values of x_j. PMIME essentially tries to detect which of the present and past values (lags) of x_i , $i = 1 \ldots K$, i.e., $x_{i,t}, x_{i,t-1} \ldots x_{i,t-Lmax+1}$ can be used to optimally predict the future values $x_{i,t+T}$, where T can be any value of $T = 1, 2, \ldots T_{max}$. Similarly, when applied on phases, the algorithm tries to detect which of the present and past lags of ϕ_i, i.e., $\phi_{i,t}, \phi_{i,t-1}, \ldots, \phi_{i,t-Lmax+1}$ can be used to predict the values of $\Delta_T \phi_{i,t+T} = \phi_{i,t+T} - \phi_{i,t}$. The modified CMI using the phase variables $\phi_1(t), \phi_2(t)$ of a bivariate system exhibiting oscillatory behaviour is given by:

$$I(\phi_1(t+T) - \phi_1(t); \phi_2(t) \mid \phi_1(t)) = I(\Delta_T \phi_1(t); \phi_2(t) \mid \phi_1(t)) \tag{2}$$

Equation 1 is modified accordingly using the phase variables. The phase time series $\phi_1(t)$ and $\phi_2(t)$ are extracted from the original time series $x_{1,t}$ and $x_{2,t}$ respectively using the commonly used Hilbert transform method. In this case, the embedding vector $\mathbf{w}_i$ is created for the response variable, phase increment $\Delta_T \phi_{i,t+T} = \phi_{i,t+T} - \phi_{i,T}$ instead of the instantaneous phase $\phi_{i,t+T}$, where T is the time step value by which the phase is incremented. The objective was to create a model that relates frequency to phase since the instantaneous frequency is the first-order time derivative of the instantaneous phase $\omega_t = \frac{d\phi_t}{dt}$.

3. Results and Discussion

We apply PMIME on phases extracted from time series data of two unidirectionally coupled Rössler systems. The parameters of the coupled system are chosen such that system 1 is driving system 2. The exact form of the equations and the parameters chosen to generate the time series data for the above system is mentioned in section (3) of [2]. Top panel of Fig. 1(a) shows the result of PMIME when applied on 4064 time points for each coupling value, results are averaged over 32 such segments. However, for comparison with EEG data which is continuous for every 500 time points, PMIME is also tested on shorter segments of 500 time points of the Rössler data, results averaged over 8 segments, shown in the bottom panel in Fig. 1(a). For both Rössler and EEG data, the parameters L_{max} and k required for creating the embedding vector were chosen as 20 and 5, respectively, where k is the number of neighbours for estimating CMI with k-nearest neighbours approach. Fig. 1(a) illustrates that PMIME accurately predicts the direction of causality in the simulated system for both choices of the longer and shorter segments of data as the coupling parameter α increases. R_{12} i.e $R(1 \to 2)$ increases until the onset of synchronization at approximately $\alpha = 0.08$. After the synchronization sets in for higher coupling values, R_{12} drops and R_{21} increases. It is known that in the synchronized state, the

ISBN 978-80-972629-6-9

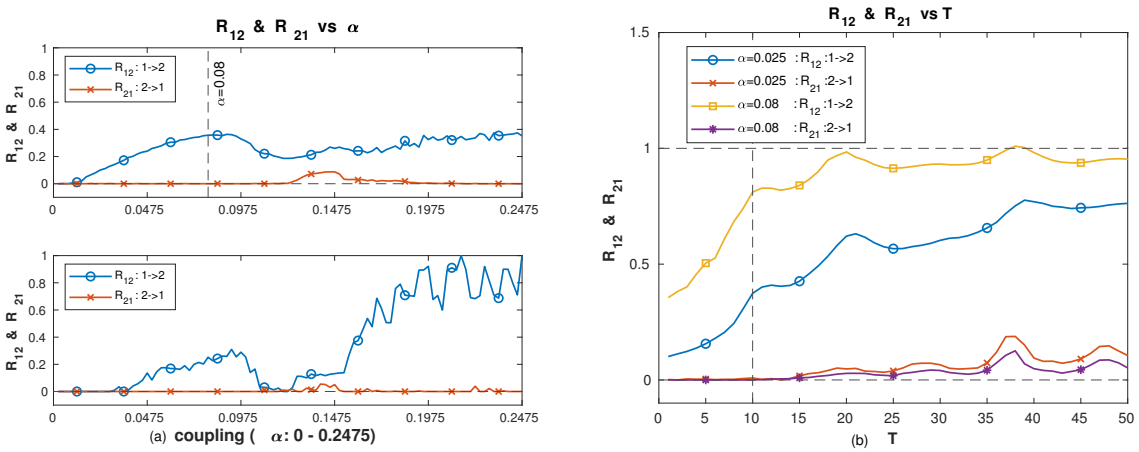

Fig. 1: (a) Variation of R_{12} (blue, round markers) and R_{21} (red, cross markers) with coupling strength, α for $T_{max} = 1$. Top and bottom panels depict the results for PMIME applied on 4064 and 500 time points, respectively. (b) Variation of R_{12} and R_{21} with T for two different coupling strengths.

detection of causality is unreliable or even impossible. Fig. 1(b) depicts the dependency of R_{12} and R_{21} on T. It is desirable to choose a T value within one cycle of the CMI measure (cycle length is 20 here). The maxima in the direction of coupling for this cycle length occurs at $T = 10$, and hence it is chosen as the T value for further causality analysis of this system.

We now focus on the coherence study of the EEG data. We analyzed EEG data recorded from patients suffering from MDD. The details of the data are available in [3]. Our study is a part of the project discussed in [3]. In [3], the authors studied brain connectivity changes in patients in response to anti-depression treatment and found that cross-hemispheric (CH) connectivity is a valuable biomarker to assess response to medication early on in the course of treatment. Specifically, the respondents showed a significant decrease in CH connectivity one week after starting medication (Visit 2) compared to before (Visit 1). No such significant decrease was observed in the non-respondents. CH connectivity estimation was done using weighted imaginary wavelet coherences (WIWC) between all CH channel pairs. This change was observed only in the β_1 (12.5 Hz-17.5 Hz) frequency band and in no other band. As PMIME estimation is computationally intensive, we shortlisted a set of four respondent subjects and eight channel pairs from [3], which showed the highest decrease in binary CH connectivity using WIWCs. We identified the following eight channel pairs: $(P4,T5)$, $(P3,T6)$, $(O2,T5)$, $(O1,T6)$, $(F3,T6)$, $(Fp2,T5)$, $(F7,T6)$, $(F8,T5)$ and use them for PMIME analysis for the four patients. The results for the selected patients and channel pairs using WIWC are shown in Fig. 2(a). The WIWC represented for each channel pair and patient is estimated using 16s segments and then averaged over all available segments (approximately 30) in the patient's recording.

As coherence is non-directional, we are interested in determining the direction of causality between the selected channel pairs. All causality calculations are done on 2s data containing 500 time points as only 2s segments of data could be considered continuous after preprocessing of the EEG data. Since the T5 and T6 channels are consistently found to contribute to the observed coherence change among the patients, we investigate the causal influence of other brain regions on T5 and T6. Specifically, we aim to study the change in causal influence from the brain's parietal, occipital, and frontal regions to the temporal region in Visit 2 compared to Visit 1. Causality analysis can help us to give a clear insight into the direction of this decrease in Visit 2 compared to Visit 1. For our analysis, we chose $T_{max} = 5$ to characterize our results for all patients and channel pairs because the CMI value at $T_{max} = 5$ lay near the maxima within one cycle of the CMI calculated upto $T_{max} = 34$. This choice was made in a similar way as

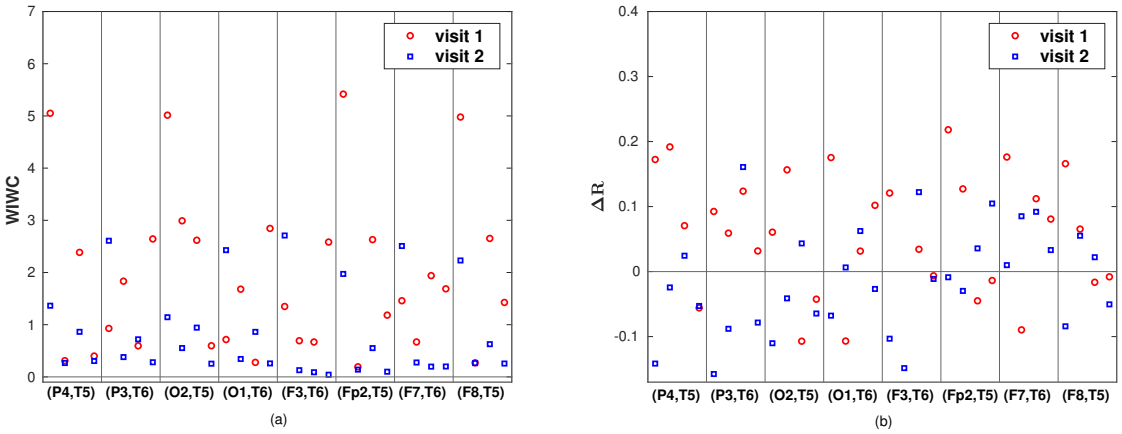

Fig. 2: (a) WIWC and (b) ΔR ($T_{max} = 5$) for both the visits of four subjects and eight channel pairs. Vertical lines separate the channel pairs, with each block displaying the results of all four patients in the same order in all the blocks.

discussed previously for the Rössler case (Fig. 1(b)). In Fig. 2(b), we plot the relative difference $\Delta R = \frac{R_{12}-R_{21}}{R_{12}+R_{21}}$ for the considered patients and channel pairs. Due to the computational intensity of causality calculations, ΔR for all patients and channel pairs are estimated by averaging the ΔRs calculated from only eight consecutive 2s segments, which result in a total time length of 16s from the available data. This figure confirms a decrease in CH connectivity in Visit 2 compared to Visit 1. It is also evident from the figure that for the first patient and channel pair $(P4, T5)$, $P4$ has a more causal influence on $T5$ than $T5$ on $P4$ in visit 1. However, the dominant direction of causality is reversed in visit 2. Results for all the other patients and channel pairs can be interpreted similarly. Both WIWC and CMI results shown in Fig. 2 for all four patients and channel pairs put together are found to be statistically significantly different for visits 1 and 2 using the Wilcoxon test (at 5% significance level) as the p-values estimated were 2.8118×10^{-4} and 5.8×10^{-3} respectively.

Multivariate causality estimation using PMIME instead of bivariate causality between channel pairs and use of longer time segments may help to provide better insights into the changes in brain connectivity in depression and its treatment. This will be explored as part of future work.

Acknowledgements

This study was supported by the Czech Science Foundation (Project No. GF21-14727K). We would like to thank Dr. Ioannis Vlachos for providing the PMIME code in MATLAB and for engaging in valuable discussions.

References

[1] Vlachos, I., Kugiumtzis, D., Paluš, M. (2022). Phase-based causality analysis with partial mutual information from mixed embedding. *Chaos: An Interdisciplinary Journal of Nonlinear Science* 32(5), 053111.

[2] Ghosh, A., Bhattacharjee, M., Kathpalia, A., Brunovský, M., Paluš, M. (2023). Phase dynamics and directed EEG connectivity in treatment of major depressive disorder. *Submitted to Conference Measurement 2023*.

[3] Paluš, M., Kathpalia, A., Brunovský, M. (2023). EEG connectivity in treatment of major depressive disorder: Tackling the conductivity effects. *Submitted to Conference Measurement 2023*.

Phase Dynamics and Directed EEG Connectivity in Treatment of Major Depressive Disorder

[1]Anupam Ghosh, [1]Madhurima Bhattacharjee, [1]Aditi Kathpalia, [2]Martin Brunovský, [1]Milan Paluš

[1]Department of Complex Systems, Institute of Computer Science of the Czech Academy of Sciences, Prague, Czech Republic,
[2]Clinical Research Programme, National Institute of Mental Health, Klecany, Czech Republic
Email: ghosh@cs.cas.cz

Abstract. *In this paper, we infer the direction of information transfer between interacting subsystems using a cross-dependence index derived from the phase dynamics of coupled subsystems. First, we apply this method to unidirectionally coupled Rössler oscillators. This index always has a higher value along the direction of coupling than that opposite to the coupling. Finally, we employ this method in analysis of EEG signals. The aim of this analysis is to identify the direction of information transfer in the brain in patients suffering from depression and quantify its changes during the treatment process.*

Keywords: Coupled Oscillatory Systems, Coupling Direction, EEG, Major Depressive Disorder

1. Introduction

In recent years, nonlinear dynamics has become a valuable approach in the study of brain and its various disorders. This paper focuses on studying one such brain disorder known as major depressive disorder (MDD) using tools from nonlinear dynamics. MDD is a mental illness that lasts at least two weeks and is characterized by persistent melancholy, low self-esteem, and a lack of interest in or enjoyment from formerly pleasurable activities. The World Health Organization ranked MDD, one of the most prevalent psychiatric conditions in the world, as the third leading global cause of disease burden in 2008. As per [1], only 65% of individuals who receive modern antidepressant medication exhibit a positive response, and it typically takes $4-6$ weeks to determine whether a modification or extension of treatment is necessary. Medication treatment has demonstrated success predominantly in individuals with moderate to severe depression. The current study aims to investigate the direction of information transfer in the brain of patients diagnosed with MDD and changes in this information flow after one week of the treatment to find features that predict the clinical effect after $4-6$ weeks of the treatment.
In our analysis, we are interested to study the dependence between phases of time series recorded from different regions of brain. Determining the influence of one oscillator's phase on the dynamics of another oscillator's phase is straightforward when the mathematical form of interacting oscillators is available. However, such a relationship is challenging to identify when working with time series data, for which the underlying equations are unknown. We use the directionality index proposed in [2] to detect driver-driven relationships for given time series data. First, this technique is validated on unidirectionally coupled Rössler [3] oscillators, and then used to analyze EEG signals recorded from MDD patients to identify the direction of information transfer in the brain. Before the detailed analysis, we elaborately discuss this technique in Sec. 2.

2. Methodology

The method proposed in [2] is used to identify the coupling direction in coupled oscillator models. This technique can be applied to chaotic and noise-perturbed systems. We use $\phi_{1,2}(t_k)$

ISBN 978-80-972629-6-9

to represent the phases $\phi_1(t_k)$ and $\phi_2(t_k)$ of two interacting oscillators 1 and 2 respectively. Here, $t_k = k \cdot \Delta t$ and $k = 0, 1, 2, \cdots$. We unwrap $\phi_{1,2}(t_k)$ such that their values do not restrict within the interval $[0, 2\pi)$. Now, we introduce the parameters $\Delta_{1,2}(k)$ that measure the increment in phases as follows:

$$\Delta_{1,2}(k) = \phi_{1,2}(t_k + \tau_0) - \phi_{1,2}(t_k), \tag{1}$$

where τ_0, an integer with $\tau_0 \geq 1$, is the time lag. Note that $\Delta_{1,2}(k)$ may be higher than 2π as we have unwrapped the phases $\phi_{1,2}(t_k)$. In other words, we can consider that $\Delta_{1,2}(k)$ are generated from unknown two-dimensional noisy systems as follows:

$$\Delta_{1,2}(k) = \omega_{1,2}\tau_0 + \mathscr{F}_{1,2}\left(\phi_{2,1}(t_k), \phi_{1,2}(t_k)\right) + \eta_{1,2}(t_k), \tag{2}$$

where $\omega_{1,2}$ are the natural frequencies, and $\eta_{1,2}(t_k)$ are the noise terms. The functions $\mathscr{F}_{1,2}$ represent the deterministic parts. They can be estimated by fitting $\Delta_{1,2}(k)$ as a function of phases $\phi_1(t_k)$ and $\phi_2(t_k)$ because such a fitting can help to remove the noise parts. In our analysis, we adopt finite two-dimensional Fourier series $F_{1,2} = \sum_{m,l} A_{m,l} e^{(im\phi_1 + il\phi_2)}$ to approximate $\mathscr{F}_{1,2}$ as any function of phases should be 2π-periodic.
We introduce the indices $c_{1,2}$ to measure cross-dependence between $\phi_1(t_k)$ and $\phi_2(t_k)$ as follows:

$$c_{1,2}^2 = \int_0^{2\pi} \int_0^{2\pi} \left(\frac{\partial F_{1,2}}{\partial \phi_{2,1}}\right)^2 d\phi_1 d\phi_2. \tag{3}$$

As per Eq. 3, the index c_1 quantifies the impact of ϕ_2 on ϕ_1, while c_2 measures the effect of ϕ_1 on ϕ_2. We use these indices $c_{1,2}$ to study the phase dynamics of interacting dynamical systems.

3. Results and Discussions

The equations of unidirectionally coupled Rössler oscillators [3] are given by:

$$\frac{dx_1}{dt} = -\omega_1 y_1 - z_1, \tag{4a}$$
$$\frac{dy_1}{dt} = \omega_1 x_1 + a y_1, \tag{4b}$$
$$\frac{dz_1}{dt} = b + z_1(x_1 - c), \tag{4c}$$
$$\frac{dx_2}{dt} = -\omega_2 y_2 - z_2 + \alpha(x_1 - x_2), \tag{5a}$$
$$\frac{dy_2}{dt} = \omega_2 x_2 + a y_2, \tag{5b}$$
$$\frac{dz_2}{dt} = b + z_2(x_2 - c), \tag{5c}$$

where $a = 0.15$, $b = 0.2$, $c = 10$, and $\omega_{1,2} = (1 \pm 0.015)$. The parameter α in Eq. 5a measures the coupling strength between the driving (x_1, y_1, z_1) and driven (x_2, y_2, z_2) oscillators. Equations 4 and 5 are integrated with a time step of 0.314 and 130048 data points are generated for analysis. MATLAB (Version R2022a) has been used for all analysis in this work.
The phases $\phi_{1,2}(t_k)$ of the driving and driven oscillators, Eqs. 4 and 5, have been calculated using the standard Hilbert transform of the first coordinates of the two systems (i.e., using variables x_1 and x_2), respectively. After introducing a delay τ in either variable, we have calculated cross-dependent indices $c_{1,2}$ between the phases $\phi_1(t_k)$ and $\phi_2(t_k + \tau)$ (Figs. 1a–1c) and between $\phi_1(t_k + \tau)$ and $\phi_2(t_k)$ (Figs. 1d–1f) as a function of τ at different values of the coupling strength α. The black plots in Figs. 1a–1c correspond to c_1, which returns the effect of $\phi_2(t_k + \tau)$ on $\phi_1(t_k)$ and the cyan plots correspond to c_2, which measures the influence of $\phi_1(t_k)$ on $\phi_2(t_k + \tau)$. Similarly, the black plots in Figs. 1d–1f correspond to c_1, which returns the effect of $\phi_2(t_k)$ on $\phi_1(t_k + \tau)$ and the cyan plots correspond to c_2, which measures the influence of $\phi_1(t_k + \tau)$ on $\phi_2(t_k)$. In Figs. 1g and 1h, we plot the variations of $c_{1,2}$ with α, at a fixed value of τ. It is apparent that, in all the subplots in Fig. 1, c_2 exceeds c_1. Thus, we can conclude that the cross-dependent index always has a higher value along the direction of coupling.

ISBN 978-80-972629-6-9

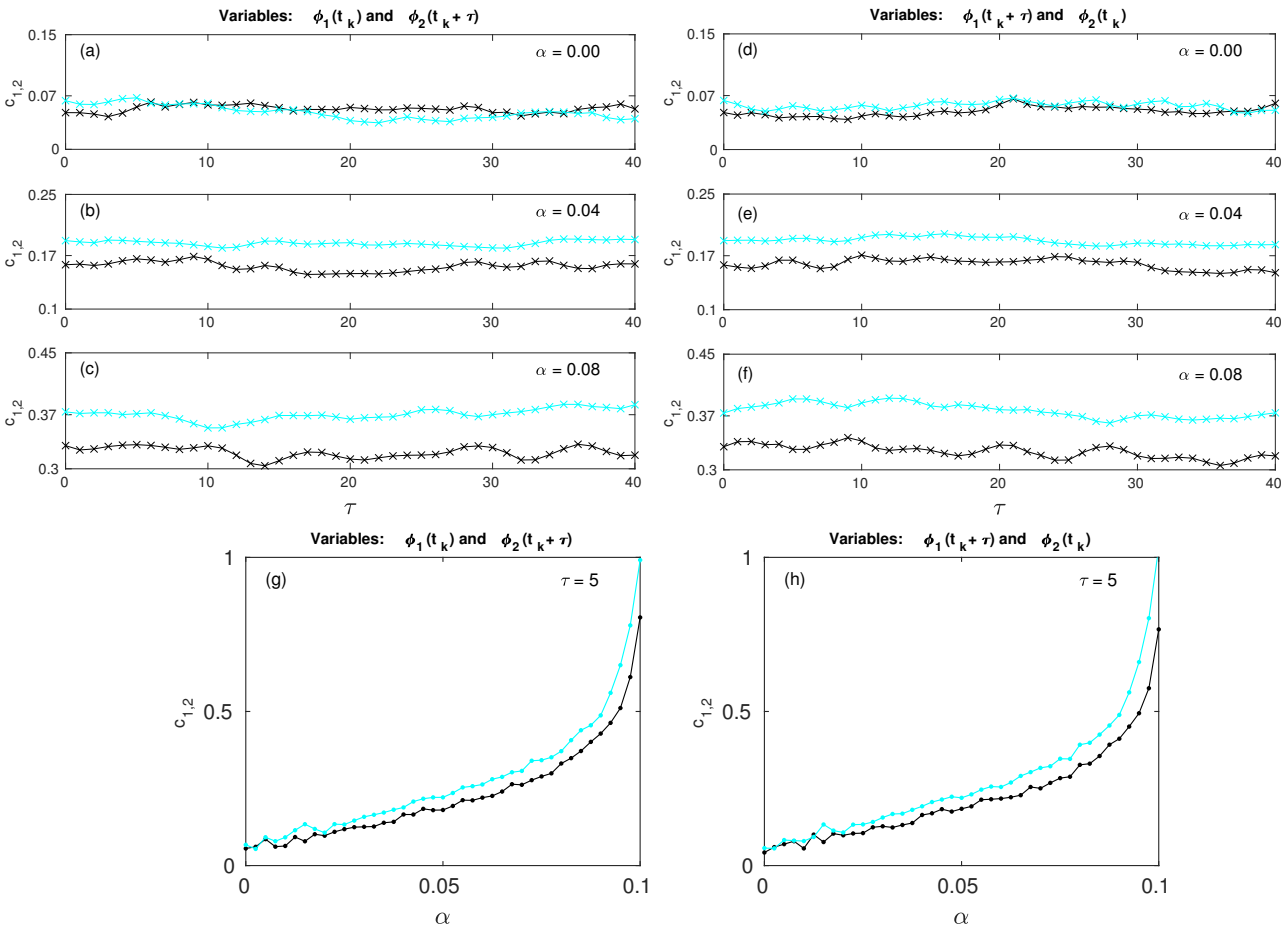

Fig. 1: Indices $c_{1,2}$ are calculated as a function of time delay τ (subplots a–f) and coupling strength α (subplots g and h) for coupled Rössler oscillators with $\omega_{1,2} = (1 \pm 0.015)$. In all plots, cyan color corresponds to c_2 (along the direction of coupling, i.e. from system 1 to 2) and black color represents c_1 (opposite to the direction of coupling, i.e. from system 2 to 1). Also, following Bhattacharjee et al. [4], we have adopted $\tau_0 = 5$ to construct $\Delta_{1,2}(k)$ in all cases.

Our focus now turns to utilize the method described above to examine the direction of influence between various brain regions using EEG signals. We have EEG recordings for a total of 176 patients, 128 of them are females and 48 are males. The EEG for all patients was recorded before the beginning of the treatment (visit 1) and again after seven days of starting antidepressant treatment (visit 2). The entire course of treatment lasted for around four weeks. Total 19 electrode positions have been taken into consideration which are Fp1, Fp2, F3, F4, C3, C4, P3, P4, O1, O2, F7, F8, T3, T4, T5, T6, Fz, Cz, and Pz. Further details about data acquisition and preprocessing are available in [5]. However, for our analysis, we have selected eight channel pairs: (P4,T5), (P3,T6), (O2,T5), (O1,T6), (F3,T6), (Fp2,T5), (F7,T6), and (F8,T5) and four patients who responded to the medication depending on the coherence study as discussed in [4]. It was found that there was a reduction in coherence between these cross-hemispheric channel pairs in visit 2 compared to visit 1 for these respondent patients. To employ this finding as a biomarker for early response to anti-depression treatment and get an understanding of the physiological changes leading to reduction in coherences between brain regions, directional connectivity analysis can be helpful.

In order to study the directional connectivity between considered EEG channel pairs, we introduce a quantity called the directionality index, defined as follows:

$$d = \frac{c_2 - c_1}{c_1 + c_2}. \tag{6}$$

The index c_2 returns the influence of $\phi_1(t_k)$ on $\phi_2(t_k+\tau)$, whereas c_1 measures the dependence of $\phi_2(t_k)$ on $\phi_1(t_k+\tau)$.

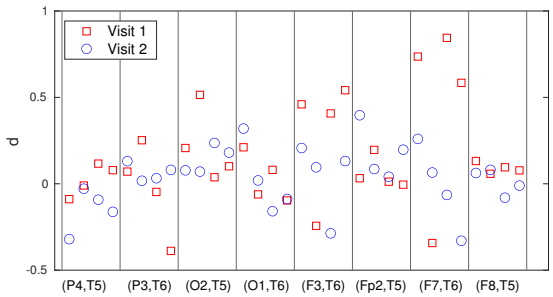

Fig. 2: The directionality index d is plotted for both visits of the four patients and eight channel pairs. The channel pairs are separated by vertical lines, and each block presents the results of all four patients in the same order across all the blocks.

We calculate d for visits 1 and 2 separately with $\tau = \tau_0 = 5$ and study a change in its value to get an insight into directional connectivity changes happening in the brain soon after the start of the treatment. The directionality index has been calculated by averaging eight consecutive 2s (500 time points) data segments, resulting in a total time 16s of the processed EEG signal. This is because only every 2s segments of data could be considered continuous after preprocessing the EEG data.

Based on Fig. 2, we can visualize that d is predominantly higher for the selected patients and channel pairs in visit 1 than in visit 2. For visit 1, the direction of influence in the channel pair (F7,T6) is more from F7 to T6 compared to the opposite direction. Conversely, for visit 2, the direction of influence is more from T6 to F7. Similar interpretations can be made for all the other channel pairs and patients' results. This observation is in agreement with the causality analysis presented in [4], however unlike the coherences in [5] and the phase causalities in [4], in our result this difference is not statistically significant.

To improve the results obtained in this study and make conclusive inference about the direction of information transfer in the brain and its changes using our technique, it is required to analyze EEG data from patients over longer time segments and to use multivariate analysis techniques. Furthermore, analysis of data from more patients in the available MDD database can help to make our study more comprehensive and will be done as a future work.

Acknowledgements

The authors thank Prof. M. G. Rosenblum for providing the MATLAB code to calculate the directionality index. This study was supported by the Czech Science Foundation (Project No. GF21-14727K).

References

[1] Fournier, J. C., DeRubeis, R. J., Hollon, S. D., Dimidjian, S., Amsterdam, J. D., Shelton, R. C., Fawcett, J. (2010). Antidepressant drug effects and depression severity: a patient-level meta-analysis. *JAMA* 303, 47.

[2] Rosenblum, M. G., Pikovsky, A. S. (2001). Detecting direction of coupling in interacting oscillators. *Phys. Rev. E* 64, 045202.

[3] Rössler, O. E. (1976). An equation for continuous chaos. *Phys. Lett. A* 57, 397.

[4] Bhattacharjee, M., Kathpalia, A., Brunovský, M., Paluš, M. (2023). Phase-based causality analysis of EEG in treatment of major depressive disorder. In: *2023 14th International Conference on Measurement*.

[5] Paluš, M., Kathpalia, A., Brunovský, M. (2023). EEG connectivity in treatment of major depressive disorder: Tackling the conductivity effects. In: *2023 14th International Conference on Measurement*.

Do Scalp EEG Measurements Allow Causal Inference?

Anna Krakovská, Zuzana Rošťáková, Martina Chvosteková, Jana Maslíková

Institute of Measurement Science, Slovak Academy of Sciences, Bratislava, Slovakia,
Email: krakovska@savba.sk

Abstract. *Rapidly developing methods of causal inference are being extensively applied to analyze electroencephalographic (EEG) measurements. However, there is considerable uncertainty surrounding the interpretation of the results. Is what the methods reflect from brain activity truly causality? In this study, we first simulate a ground-truth causal process in the cortex. Next, we project the cortex activity onto the surface of the head with a forward model, thereby obtaining data closely mimicking real noninvasive EEG signals. We argue and demonstrate that if the correct interpretation of the EEG measurement from any single electrode is a linear combination of all source cortical signals, a standard causal inference may fail on fundamental levels.*

Keywords: Simulated EEG, Causality, Effective Connectivity, Granger Test, Cross-Predictions

1. Introduction

The idea of causality in the brain usually means assuming that neuronal populations in different brain regions can causally influence each other in a large-scale network. Since causes must precede effects in time, causal relations can be inferred through time series analysis. However, the signals from which we try to reconstruct causal connections are mostly measured on the surface of the head, while the real effects take place in the depth of the cortex. If the analyzed time series are noninvasive EEG recordings, they reflect the time-varying voltage fluctuations spread from brain tissue to electrodes placed on scalp. Multiple sources of deeper brain activity contribute, albeit with different weights, to the measurement at each electrode. In this study, we point out that this can present a serious obstacle to causal analysis.

To do so, we first simulated a simple ground-truth latent causal structure inside the cortex, which we then projected onto the surface of the head model [1]. In this way, we obtained signals closely mimicking real EEG measurements from scalp electrodes. Then we subjected the data to causal analysis. Methods for discovering the causal link $X \rightarrow Y$ between two processes are often similar in that they ask whether there is information in the past of X that helps predict the evolution of Y. When reaching for a particular method, it is important not to ignore the type of data that a method was intended for, and not to use the method blindly elsewhere. Here we considered three representatives of causal approaches, namely the well-known Granger test [2], cross-predictions (CP) [3] and the use of the correlation dimension [4]. The results revealed the difficulties of all three strategies with the detection of causality from simulated scalp EEG.

2. Subject and Methods

Simulated EEG data

In order to simulate the real EEG data properties as closely as possible, we used a realistic head model and projections of the cortical activity following the work of Cohen et al. [1]. The model comprises 2004 dipoles distributed throughout the gray matter cortex. In our very simple simulation, two dipoles (positions visible in the left part of Fig. 1) were selected in the cortex to represent sources of oscillatory rhythms, resembling the visual α rhythm of around 9 Hz, with a sampling rate of 600 Hz. The driving source x in frontal region was causally affecting the driven source y in an occipital region. Two variants of simulated oscillations were created.

ISBN 978-80-972629-6-9

1. In the first variant, the exact causal relation was ensured by generating $x = x_1$ and $y = y_1$ within the deterministic model of coupled chaotic Rössler oscillators [3, 5]. The equations for system X driving Y with the coupling strength $C = 0.05$ were as follows

$$\begin{array}{rclcrcl} \dot{x}_1 &=& -1.015x_2 - x_3 & & \dot{y}_1 &=& -0.985y_2 - y_3 + C(x_1 - y_1) \\ \dot{x}_2 &=& 1.015x_1 + 0.15x_2 & \rightarrow & \dot{y}_2 &=& 0.985y_1 + 0.15y_2 \\ \dot{x}_3 &=& 0.2 + x_3(x_1 - 10) & & \dot{y}_3 &=& 0.2 + y_3(y_1 - 10) \end{array} \quad (1)$$

2. In the second variant of the data, x and y came from the bivariate autoregresive (AR) model of order two

$$x(t) = 2r_x \cos(f_x \Delta t 2\pi 0.08)x(t-1) - r_x^2 x(t-2) + \sqrt{0.2}\varepsilon^x(t)$$
$$y(t) = 2r_y \cos(f_y \Delta t 2\pi 0.08)y(t-1) - r_y^2 y(t-2) + 0.1^2 x(t-1) + \sqrt{0.2}\varepsilon^y(t),$$

where $r_x = r_y = 0.97$, $f_x = f_y = 10\ Hz$, $\Delta t = 1/128\ Hz^{-1}$, and $\varepsilon^x, \varepsilon^y$ are independent, normally distributed with zero mean and a unit variance.

Finally, a forward model from the Brainstorm toolbox in Matlab [6] was used to map the source signals of 2004 dipoles to scalp electrodes. This gave us 64 simulated EEG measurements arranged according to the international 10–20 system.

Causal methods

1. For data with oscillations simulated by deterministic, chaotic Rössler systems, we first used an approach based on the idea that the driven system also includes the driver's complexity, and thus complexity measures should be able to make causal connections apparent. The procedure, specifically using the correlation dimension (D_2), has been reported in [4]. For this type of data, we also used the CP method which calculated cross- and self-predictions of time series and then compared the prediction errors statistically to detect the type of causal relationship [3].
2. In the second variant of artificial EEG signals, where the processes were linearly interconnected and the oscillatory parts were generated as stochastic AR processes, we used the Granger test [2] designed specifically for AR modelable data.

3. Results and Discussion

Results for EEG simulations with Rössler oscillations

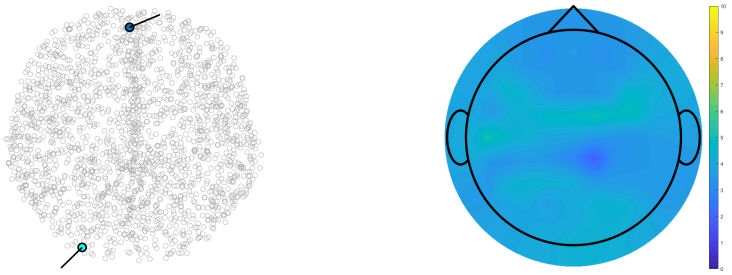

Fig. 1: Positions of the two activated dipoles (left) and D_2 estimates for projections at electrodes (right). The dipole signal simulations come from coupled Rössler systems. No background noise.

Left part of Fig. 1 shows positions of two dipoles activated using variables x_1, y_1 of coupled Rössler systems. For the driver in the frontal region the complexity estimate $D_2 \approx 2$, while for the driven dipole in the occipital region, which also contains information about the driving dynamics, $D_2 \approx 3.6$. The remaining dipoles are inactive ($D_2 = 0$). The right part of Fig. 1 shows D_2 estimates for signals from 64 surface electrodes. Since, as a result of the mapping, there is a weighted linear mixture of the signals from all active dipoles in each electrode, D_2 estimates are quite close to 3.6 everywhere. It is important to note this observation, however trivial, because it has the consequence of leaving the latent causal structure undetectable. Unsurprisingly, the D_2-based method [4] saw bidirectional links between any pair of electrodes. In practice, however,

we do not always get the expected bidirectional detections. Causal methods have their limits and fail due to sensitivity to various aspects in data. But knowing the weaknesses could be useful this time. In contrast to D_2, for example, the CP method [3] is relatively insensitive to components that had a minor impact on the simulated EEG (i.e., cortical sources that are far away from a given electrode). Consequently, statistical (Wilcoxon) testing of the prediction errors in Fig. 2, calculated for 1000 point segments, shows that x from frontal AFz electrode is better predicted from y in occipital PO3 than vice versa, consistent with the cortical ground truth of $x \rightarrow y$.

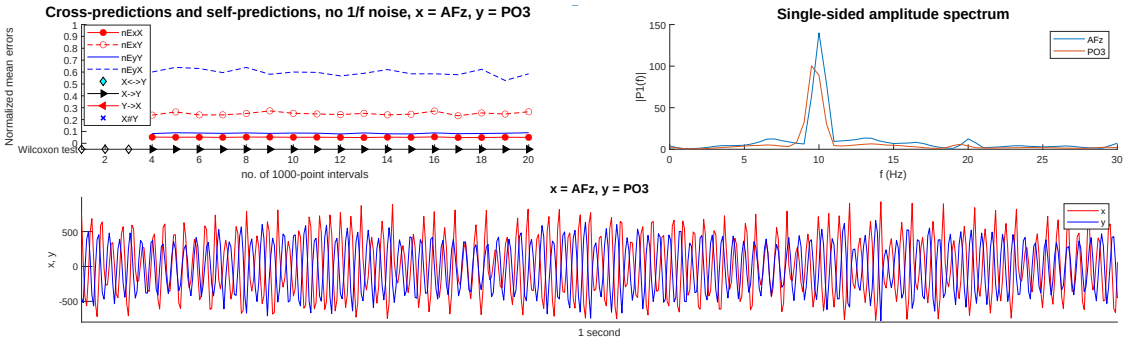

Fig. 2: Cross-predictions and self-predictions of noise-free simulations x and y from the frontal (AFz) and occipital (PO3) electrode correctly reveal the causal link $x \rightarrow y$. No background noise is considered.

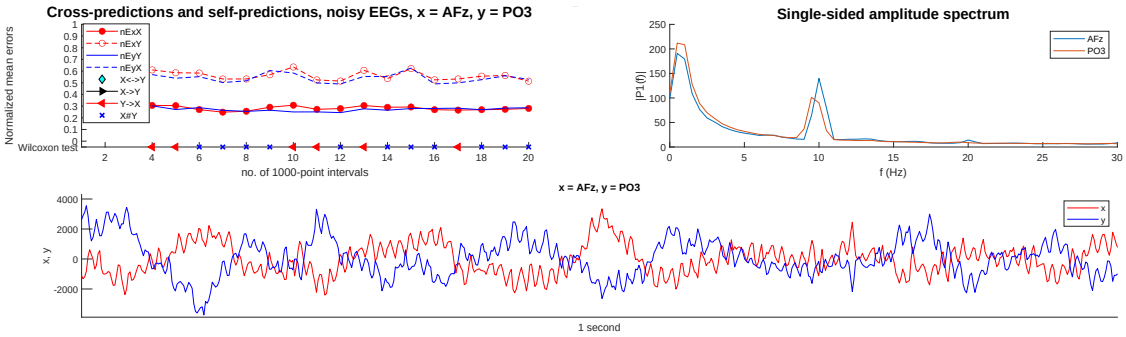

Fig. 3: Cross-predictions and self-predictions of the noisy EEG signals x and y from the frontal (AFz) and occipital (PO3) electrode fail to reveal the causal link x→y if 1/f background activity is considered.

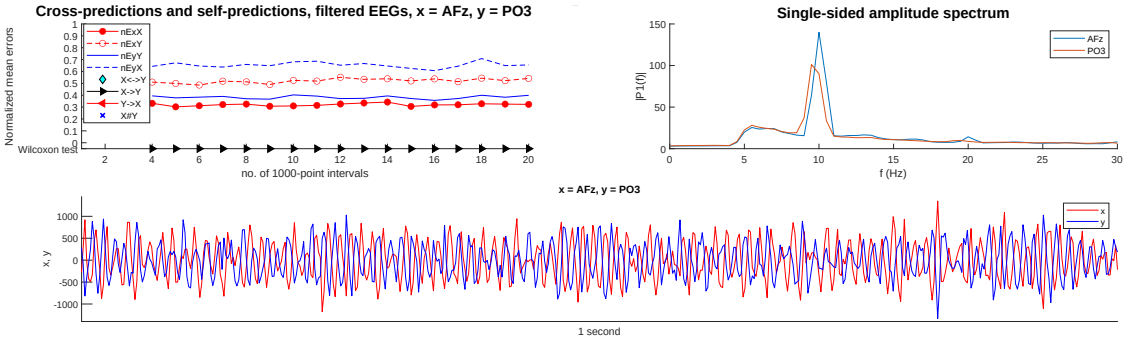

Fig. 4: Cross-predictions and self-predictions of the high-pass filtered EEG simulations x and y from the previous figure. Statistical testing of the errors clearly reveals the ground-truth causality $x \rightarrow y$.

However, once we added fractional Brownian motion with a Hurst exponent of 0.6 to the clean data to mimic the well-known 1/f property of the background EEG [7], x was no longer predictable from y (see Fig. 3). The 1/f noise components, projected from dipoles into each electrode, represented a significant portion of the signal power, obscuring useful information from which causality was to be detected. With the idea that the reduction of frequencies of the background EEG might help, we used high-pass filter with a cutoff frequency of 5 Hz. The filter

allowed the information in the scale around the key oscillatory component (9-10 Hz) to prevail and lead to the detection of $x \to y$ again, as shown in Fig. 4. Such results, however, should not be expected as a general rule. Multiple cortical sources, smaller distance between driver and the driven source, or causal dynamics pronaunced at lower frequencies, might complicate the analysis by this type of methods much further.

Results for EEG simulations with AR oscillations

Interestingly, for data with stochastic AR oscillations, even with the 1/f background component, Granger analysis exposed the two regions near sources of cortical activity involved in causality. Regardless of the truth, however, they were mostly labeled as drivers of other areas. This is because information from activated cortical sources was projected with high weight into them. The same information appeared in other electrodes, but with little impact, so the two with a larger amplitude were helpful with predictions and therefore identified as drivers. Obviously, with this and any Granger-like methods again, additional cortical sources and their linear mixture in the electrodes would further complicate the results.

4. Conclusions

If there is causality in the cortex and any scalp EEG recording can be explained as a weighted combination of all cortical sources - but only under these assumptions - we argue that:

- We cannot expect to identify brain regions with lower-dimensional dynamics (estimated, for example, by D_2) as potential causal drivers, since the same information (leading to the same complexity) is combined in each electrode.
- The applicability of Granger-like methods is also very limited.
- Partial success in inferring latent causality can be demonstrated with a cross-mapping method when the analysis is restricted to signals of maximal strength and if the scales relevant to causality are distinct from 1/f noise.

The investigation of possible causality in EEG seems to require further research and fundamental modifications of the existing methodology.

Acknowledgements

Supported by the Slovak Grant Agency for Science (VEGA 2/0023/22) and by the Slovak Research and Development Agency (APVV-21-0216). Thanks also go to Roman Rosipal for ideas and critical comments.

References

[1] Cohen, M. X. (2017). Comparison of linear spatial filters for identifying oscillatory activity in multichannel data. *Journal of neuroscience methods*, 278, 1 – 12.

[2] Granger, C. W. (1969). Investigating causal relations by econometric models and cross-spectral methods. *Econometrica: Journal of the econometric society*, 37(3), 424 – 438.

[3] Krakovská, A., Jakubík, J. (2020). Implementation of two causal methods based on predictions in reconstructed state spaces. *Physical review E*, 102 (2), 022203.

[4] Krakovská, A. (2019). Correlation dimension detects causal links in coupled dynamical systems. *Entropy*, 21 (9), 818.

[5] Paluš, M., Vejmelka, M. (2007). Directionality of coupling from bivariate time series: How to avoid false causalities and missed connections. *Physical review E*, 75 (5), 056211.

[6] Tadel, F. et al. (2011). Brainstorm: a user-friendly application for MEG/EEG analysis. *Computational intelligence and neuroscience*, 1–13.

[7] He, B. J. (2014). Scale-free brain activity: past, present, and future. *Trends in cognitive sciences*, 18 (9), 480–487.

Inadequacy of the Liang Information Flow for Causal Analysis

Martina Chvosteková

Institute of Measurement Science, Slovak Academy of Sciences, Dúbravská cesta 9,
841 04 Bratislava, Slovakia
Email: martina.chvostekova@savba.sk

Abstract. *The Liang information flow is a measure of causality between components of d-dimensional observed time series X. The power of the approach was recently presented on an example of a realization of two unidirectly coupled chaotic Rössler systems. Different from Liang's publication, where a causal inference involved only the magnitude of the information flow estimates, here, statistical significance is tested, and the properties of the estimators are analysed. It is demonstrated that the approach is not efficient for application in non-linear deterministic systems in general. Instead of correctly detecting a unidirectional connection, the bidirectional connection was statistically detected between analysed variables.*

Keywords: Information Flow, Causality, Statistical Inference

1. Introduction

Causal analysis has been applied in a variety of disciplines. Information flow proposed by Liang [1], thanks to its simple formula involving easily computed sample covariances, has become a widely used tool for causal analysis, especially in climate science, see, e.g. [2]. The same formula is used for both deterministic and stochastic systems, and it can be tested for statistical significance. Although the formula for the information flow was derived under consideration of a linear model with an additive Gaussian noise for a dynamical system, promising numerical results have also been published for an example of non-linear Rössler oscillators system, see [3]. However, the results for the system of chaotic oscillators missed a statistical inference. In this short study, we repeated the experiment and analysed the statistical performance of the information flow-based causal inference.

2. Information Flow Between Time Series

In a d-dimensional dynamical system $X = (X_1, \ldots, X_d)$, the information flow from a component X_k to another component X_l is written as $T_{k\to l}$.

Definition: *X_k is causal to X_l if and only if $T_{k\to l} \neq 0$.*

Theorem: *Given d-dimensional $X = (X_1, X_2, \ldots, X_d)$, under the assumption of a linear model with additive noise and X obeys a Gaussian distribution (i.e., $X \sim N(\mu, \Sigma)$), the maximum-likelihood estimator of the information flow X_k to X_l between components k and l of X is given as*

$$\hat{T}_{k\to l} = \frac{1}{detC} \sum_{m=1}^{d} \Delta_{km} C_{m,dl} \frac{C_{lk}}{C_{ll}}, \tag{1}$$

where

$$C_{i,dj} = \overline{(X_i - \bar{X}_i)(\dot{X}_j - \overline{\dot{X}_j})}, \quad \dot{X}_{i,n} = \frac{X_{i,n+\tau} - X_{i,n}}{\tau \Delta t}, \tag{2}$$

$C = (C_{ij})$ is the sample covariance matrix, Δ_{ij} are the cofactors of matrix C, $\bar{X}_i$ is the mean of component X_i, $\overline{\dot{X}_i}$ is the mean of derived series $\dot{X}_i$, Δt is the time step size, $C_{j,di}$ is the sample covariance between X_j and $\dot{X}_i$, μ is a mean vector, and Σ is a diagonal covariance matrix.

ISBN 978-80-972629-6-9

In the case of deterministic chaos and dense sampling, it is recommended to choose $\tau = 2$; otherwise, $\tau = 1$ can be used [3].

The estimator (1) is an unbiased estimator of $T_{k\to l}$, approximately normally distributed with variance $(C_{lk}/C_{ll})^2\hat{\sigma}^2_{a_{lk}}$ for a large N. The estimator $\hat{\sigma}_{a_{lk}}$ is determined from the inverse, denoted $\mathscr{I}$, of the covariance matrix of $\hat{\theta} = (f_l, a_{ll}, a_{l2}, \ldots, a_{ld}, b_l)$, within which is $\hat{\sigma}_{a_{lk}}$, see [3]. The symmetric matrix $\mathscr{I}$ derived under the instructions from [3] is given as

$$\mathscr{I} = \begin{pmatrix} N\Delta t/b_l^2 & \Delta t/b_l^2\sum X_{1,n} & \Delta t/b_l^2\sum X_{2,n} & \ldots & \Delta t/b_l^2\sum X_{d,n} & 2\Delta t/b_l^3\sum R_{l,n} \\ & \Delta t/b_l^2\sum X_{1,n}^2 & \Delta t/b_l^2\sum X_{2,n}X_{1,n} & \ldots & \Delta t/b_l^2\sum X_{2,n}X_{d,n} & 2\Delta t/b_l^3\sum R_{l,n}X_{1,n} \\ & & \vdots & \vdots & \vdots & \vdots \\ & & & & \Delta t/b_l^2\sum X_{d,n}^2 & 2\Delta t/b_l^3\sum R_{l,n}X_{d,n} \\ & & & & & 3\Delta t/b_l^4\sum R_{l,n}^2, \end{pmatrix} \tag{3}$$

where

$$R_{i,n} = \dot{X}_{i,n} - (f_i + \sum_{i=1}^{d} a_{ij}X_{j,n}), \quad i = 1,2,\ldots,d. \tag{4}$$

3. Application to Deterministic Dynamical System

We consider the system of two unidirectionally coupled Rössler systems

$$\begin{aligned} \dot{x}_1 &= -\omega_1 x_2 - x_3 & \dot{y}_1 &= -\omega_2 y_2 - y_3 + C(x_1 - y_1) \\ \dot{x}_2 &= \omega_1 x_1 + 0.15x_2 & \dot{y}_2 &= \omega_2 y_1 + 0.15y_2 \\ \dot{x}_3 &= 0.2 + x_3(x_1 - 10) & \dot{y}_3 &= 0.2 + y_3(y_1 - 10), \end{aligned}$$

with $\omega_1 = 1.015$, and $\omega_2 = 0.985$. Clearly, the system X is unidirectionally coupled with system Y through the first component, i.e., from X to Y (i.e., $X \to Y$). A similar system was investigated by Liang [3], but also considering a third Rössler system Z coupled with system X through the first component from X to Z. Here, we are interested in a statistical inference according to the information flow between $\{x_1(n)\}$ and $\{y_1(n)\}$ under consideration of $d = 6$, and, different to [3], also for $d = 2$. The information flow between x_1 and y_1 for $d = 2$ is analysed without taking into account the rest four time series (i.e., x_2, x_3, y_2, y_3). This resembles a typical real-world situation where only one observable is measured for each system. The time series corresponding to the above differential equations were obtained by numerical integration using the adaptive Runge-Kutta method in Matlab. Note that only one realisation of the considered Rössler systems undertaking an integration step size $\Delta t = 0.001$, $\tau = 2$, $N = 40000$ and the random numbers for initialisation were analysed in [3]. Here, we considered the same step size and initialised with $[0,0,0.4,0,0,0.4]$, and the state was integrated forward for $N = 40000 \cdot 100 + 100000$ steps, where 100000 initial steps were discarded. The statistical significance of the causal connection between x_1 and y_1 was tested for 100 realisations of the Rössler systems, each of length 40000. The coupling parameter C has been taken $C = \{0, 0.1, 0.2, \ldots, 0.24, 0.25\}$. Note that the information flow is easy to compute by any standard numerical software since only the computation of sample covariances is required. Here, we used a MatLab obtainable at dx.doi.org/10.6084/m9.figshare.14985381.

4. Results

Fig. 1 shows the average information flows $\overline{\hat{T}}_{x_1\to y_1}$, $\overline{\hat{T}}_{y_1\to x_1}$, and the 95%-confidence intervals.

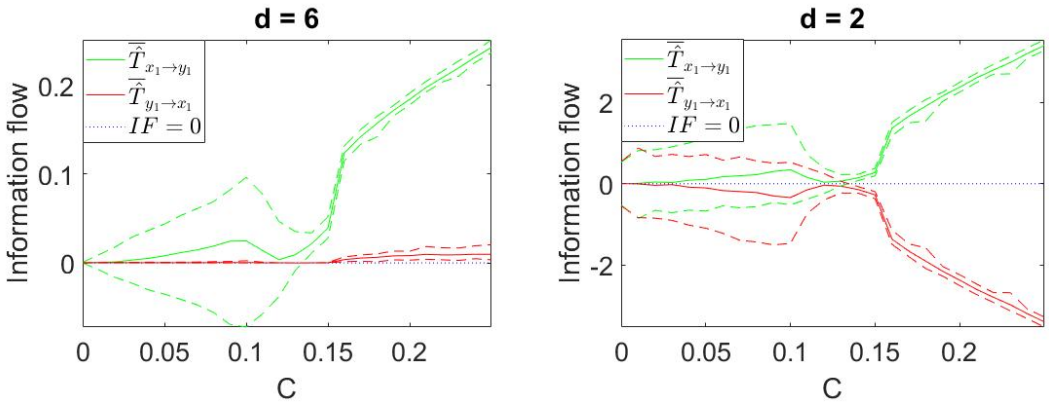

Fig. 1: The average estimated information flows between x_1 and y_1 (solid lines) with the 95%-confidence intervals (dashed lines) against the coupling strength $C = \{0, 0.1, \ldots, 0.25\}$ calculated under taking $d = 6$ (on the left side) and $d = 2$ (on the right side) for Rössler systems generated with step size $\Delta t = 0.001$.

The limits of the depicted confidence intervals were determined as $0.05/2$-quantile and $(1 - 0.05/2)$-quantile from the 100 estimates of (1). It must be emphasized that the confidence intervals are not constructed for statistical testing the significance of an information flow. They indicate a variance of the estimates for each considered coupling parameter. The construction of the confidence intervals used for testing is described in the text below.

Look at the first results for the case $d = 6$. Since $\overline{\hat{T}}_{x_1 \to y_1} > 0$ and $\overline{\hat{T}}_{y_1 \to x_1} = 0$ for $C \leq 0.15$, the one-way causality $x_1 \to y_1$ is correctly detected according to the depicted estimates. After C exceeds 0.15, the systems begin to synchronize, the average $\overline{\hat{T}}_{y_1 \to x_1}$ is not zero, but it is remarkably less than $\overline{\hat{T}}_{x_1 \to y_1}$. Remind that this observation was presented as a correct detection of $x_1 \to y_1$ even after synchronisation and attestation of qualitatively good performance of the information flow-based inference. On the other hand, we obtained different conclusions by testing the statistical significance of $\hat{T}_{x_1 \to y_1}$ and $\hat{T}_{y_1 \to x_1}$ for 100 realisations of the dynamical system. The statistical significance of an estimated information flow was concluded at significance level $\alpha = 0.05$ if a confidence interval $\hat{T} \pm u(1 - \alpha/2) var^{1/2}(\hat{T})$ did not contain zero, where $u(1 - \alpha/2)$ denotes the $(1 - \alpha)$-quantile of the standard normal distribution. Since the estimated values $var(\hat{T})$ by (3) were small ($< 10^{-7}$), almost all non-zeros estimates of both information flows were statistically significant. The bidirectional connection between x_1 and y_1, i.e., $x_1 \leftrightarrow y_1$, was detected in more than 90 per cent for each $C > 0$, except the case $C = 0.13$, where $x_1 \leftrightarrow y_1$ was detected in more than 60 per cent of cases.

It was stated that a nonzero $T_{X_k \to X_l}$ means that X_k is causal to X_l: a positive value means that X_k makes X_l more uncertain, while a negative value indicates that X_l tends to stabilize X_k, see [3]. But, as it can be seen in Fig. 1, the sign of $\hat{T}_{x_1 \to y_1}$ differs for $C < 0.15$, even though they were calculated for the same dynamical system.

Both $\overline{\hat{T}}_{x_1 \to y_1}$, $\overline{\hat{T}}_{y_1 \to x_1}$ seen non-zeros and they are axially symmetrical around the x-axis in case $d = 2$. The statistical testing also detected the bidirectional connection in more than 99 per cent of the cases (the estimates $var(\hat{T})$ were smaller than 10^{-3}). In contrast to the case $d = 6$, the signs of both estimates $\hat{T}_{x_1 \to y_1}$, $\hat{T}_{y_1 \to x_1}$ vary for $C < 0.15$.

5. Discussion and Conclusions

The observed information flow estimates were affected by the number of available variables influencing system dynamics d. While the correct connection was detected at least before synchronisation of the systems in case $d = 6$, the incorrectly bidirectional connection was visually

detected for all considered couplings in case $d = 2$. Instead of correctly detecting a unidirectional connection, the bidirectional connection was statistically detected between analysed variables for both values of d.

Note that the formula (1) was derived under the consideration of a linear model with additive noise, where it was assumed that X has a d-dimensional Gaussian distribution, i.e., $X \sim N_d(\mu, \Sigma)$, with a diagonal covariance matrix Σ, see [3]. Then, an application of the information flow formula to deterministic systems is excluded due to the assumptions. Note that the classical Granger causality test associated with similar assumptions of linearity and normality also typically detects bidirectional connection when applied to nonlinear time series such as the used observables of the coupled Rössler systems, see [4].

Originally, the information flow was discovered for a bivariate deterministic system with fully known dynamics. The derived information flow satisfies the *principle of nil causality* saying that *an event is not causal to another if the evolution of the latter is independent of the former*, see, e.g. [1]. The formalism was applied to the Hénon map

$$x_1(t) = 1 + x_2(t-1) - 1.4x_1^2(t-1) \quad x_2(t) = 0.3x_1(t-1), \tag{5}$$

where both information flows were analytically determined, and it holds $T_{x_1 \to x_2}, T_{x_2 \to x_1} \neq 0$, see [1]. Hence the bidirectional connection between x_1 and x_2 is detected for the Hénon map (5). However, one should expect by following the principle of nil causality that since $x_1(t)$ can be rewritten to the form $x_1(t) = 1 + 0.3x_1(t-2) - 1.4x_1^2(t-1)$, i.e., the evolution of x_1 is independent of x_2, the unidirected connection $x_1 \to x_2$ should be detected. Therefore, it is questionable if the information flow in its original form follows the principle of nil causality and does not reflect a functional (correlative - not causal) connection between the components.

Acknowledgments

Supported by the Slovak Grant Agency for Science (VEGA 2/0023/22, VEGA 2/0096/21) and by the Slovak Research and Development Agency (APVV-21-0216).

References

[1] Liang, X.S. (2016). Information flow and causality as rigorous notions ab initio. *Phys. Rev. E*, 94, 052201.

[2] Cheng, C.-H., Redfern, S. (2022). Empirical assessment of normalized information flow for quantifying causal contributions. *Geosci. Model Dev. Discuss*. [preprint], https://doi.org/10.5194/gmd-2022-106.

[3] Liang, X.S. (2021). Normalized multivariate time series causality analysis and causal graph reconstruction. *Entropy*, 23, 679.

[4] Krakovská, A., Jakubík, J., Chvosteková, M., Coufal, D., Jajcay, N., Paluš, M. (2018) Comparison of six methods for the detection of causality in a bivariate time series, *Phys. Rev. E*, 97, 042207.

The Effectiveness of Three Neural Spike Validation Methods in Setting Appropriate Spike Boundaries

Zuzana Rošťáková, Roman Rosipal

Institute of Measurement Science, Slovak Academy of Sciences, Dubravská cesta9, Bratislava, Slovakia

Email: zuzana.rostakova@savba.sk

Abstract. *Thresholding methods usually detect neural spikes or bursts of electrical pulses in a cortical electrophysiological signal. Due to the possibility of multiple threshold crossings representing the same spike, it is essential to set spike temporal boundaries to prevent double detection appropriately. We consider three spike validation methods and compare their performance on a set of simulated electrophysiological data mimicking the spiking activity of a neuron with different amounts of background noise. Since the results of one method rapidly deteriorated with decreasing signal-to-noise ratio, we formulate a modification leading to the algorithm's performance improvement.*

Keywords: Spike Validation, Neural Action Potential, Threshold Crossing

1. Introduction

Neural spikes are short bursts of electrical pulses, or action potentials, through which neural cells communicate with each other (Fig. 1, right). They are usually recorded as the voltage changes by the thin glass or metal electrodes (pipettes) in the vicinity of a target neuron [1]. Among other approaches, neural spikes are detected by comparing the signal or its appropriate transformation with a fixed or adaptive (time-varying) threshold. Points with their amplitude over the positive threshold or under the negative threshold are denoted as spike candidates.

If one point crosses a threshold and is part of a spike, the neighbouring samples will also cross the threshold [2]. Many threshold crossings in a short period can therefore be viewed as the same event. Consequently, it is essential to determine spikes' start and end points correctly to avoid double detection. Performing this validation step may significantly reduce the number of false alarms, that is, spikes that are incorrectly detected [3].

This study aims to compare the performance of three spike validation methods in terms of their ability to detect the actual neural spike positions while minimising false alarms. However, in real-world data, the exact spike timing is unknown. Therefore, we used simulated data with known spike positions and different levels of background noise closely mirroring the properties of the real-world neural electrophysiological signal.

2. Data

Inspired by the work of Smith and Mtetwa [4], we simulated a five-second spiking activity of a neuron with the Poisson distribution of firing times and the sampling rate of 100 kHz. The spike shapes followed the realistic Naundorf model [5] with a spike duration of 4.44 ms and positive polarity. The number of spikes within this five-second long period varied between 316 and 334. The refractory period (Fig. 1, left) – a short interval after a spike during which a neuron is not able to fire – was set to a larger value (10 ms) to avoid too close or partially overlapped spikes.

The background noise included i) spike trains of seven neurons correlated with the spike train of the target neuron, and ii) the activity of other 100 neurons firing independently from the target neuron. The background noise amplitude was divided by 10 to avoid overlaying the target spikes. Finally, the signal was distorted by different amounts of Gaussian noise, resulting in six

ISBN 978-80-972629-6-9

levels of signal-to-noise ratio $SNR \in \{50, 35, 25, 10, 0, -5\}$ dB. For each SNR, we considered a set of 10 electrophysiological signals (Fig. 1, right).

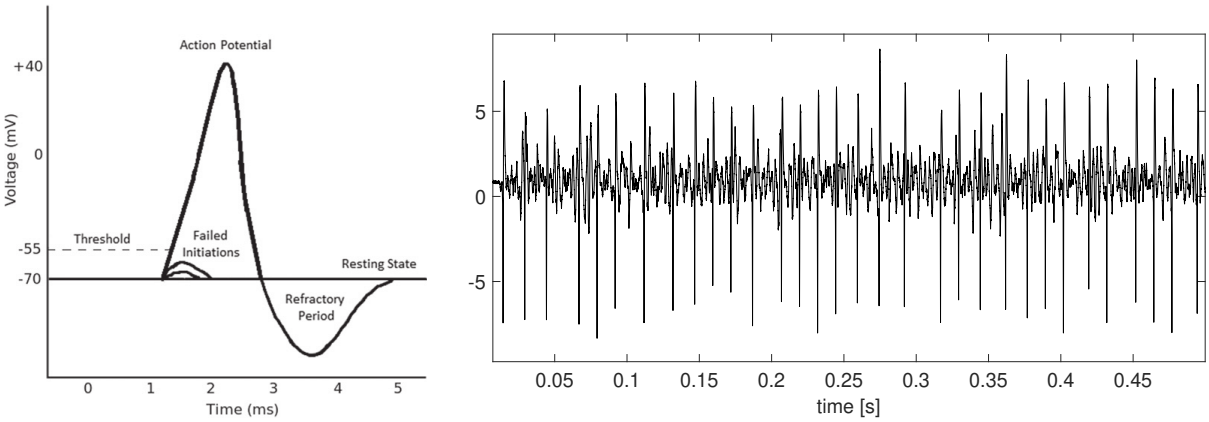

Fig. 1: *Left:* Schema of a neuron spike. Original image from [6]. *Right:* An example of a simulated electrophysiological signal with neural spikes and signal-to-noise ratio SNR = 35 dB.

3. Methods

In the first step, an adaptive threshold was set by the *AdaBandFlt* method [1], and an indicator vector for successful threshold crossings was computed for each simulated signal.

In the method of Wagenaar [3, 1], a candidate threshold crossing x represents a spike's centre only if it forms the highest peak of either polarity over the ± 1 ms time interval. Moreover, its amplitude should be at least two times higher than the amplitude of the second-highest peak with the same polarity on this interval (Condition 2). Finally, the distance between two consecutive spike centres should be at least θ_{refrac}, where θ_{refrac} represents the refractory period.

Toosi's method [2] sets the spike's center as the local minimum point to the right of the first threshold crossing if it does not occur within the previous spike's refractory period. Consequently, the spikes are aligned to their global minimum.

Nenadic [7] used a different approach. Time points where 0 changes to 1 or vice versa in the indicator vector represent starting and ending points of spikes. Then, the spike's centre candidate is computed as the mean between the corresponding starting and ending points. Consecutive candidate centre points x_i and x_{i+1} are analysed sequentially. If x_{i+1} and x_i are close to each other ($x_{i+1} - x_i \leq \theta_{merge}$), these two points represent the same spike with a high probability, and a new candidate centre point is computed $\left\lceil \frac{x_i + x_{i+1}}{2} \right\rceil$. If $x_{i+1} - x_i > \theta_{merge}$, but x_{i+1} lies within the refractory period of the i^{th} spike $\left(x_{i+1} - x_i < \theta_{refrac}\right)$, the candidate point x_{i+1} is discarded. Otherwise, x_i and x_{i+1} represent the centre of the i^{th} and $(i+1)^{th}$ spike, respectively.

After neural spike validation, we set the spike boundaries as $x \pm 2,22$ ms, where x represents the selected centre of a spike. Then, we computed the number of

i) correctly identified spikes (true positives, TP),
ii) undetected actual spikes (false negatives, FN),
iii) incorrectly detected spikes (false positives, FP), and
iv) the mean distance between detected and actual spikes starting points (mD)

for each method.

A spike was considered to be correctly identified if it overlapped at least 80% with one of the actual spikes. Then, the positive prediction rate (PPR), and sensitivity or recall (R) were evaluated by the following formulas

$$PPR = \frac{TP}{\#\text{ detected spikes}} = \frac{TP}{TP + FP} \qquad R = \frac{TP}{\#\text{ actual spikes}} = \frac{TP}{TP + FN}.$$

ISBN 978-80-972629-6-9

4. Results

All three methods successfully detected all generated spikes when data includes a small amount of Gaussian noise ($SNR = 50$ dB, Fig. 2).

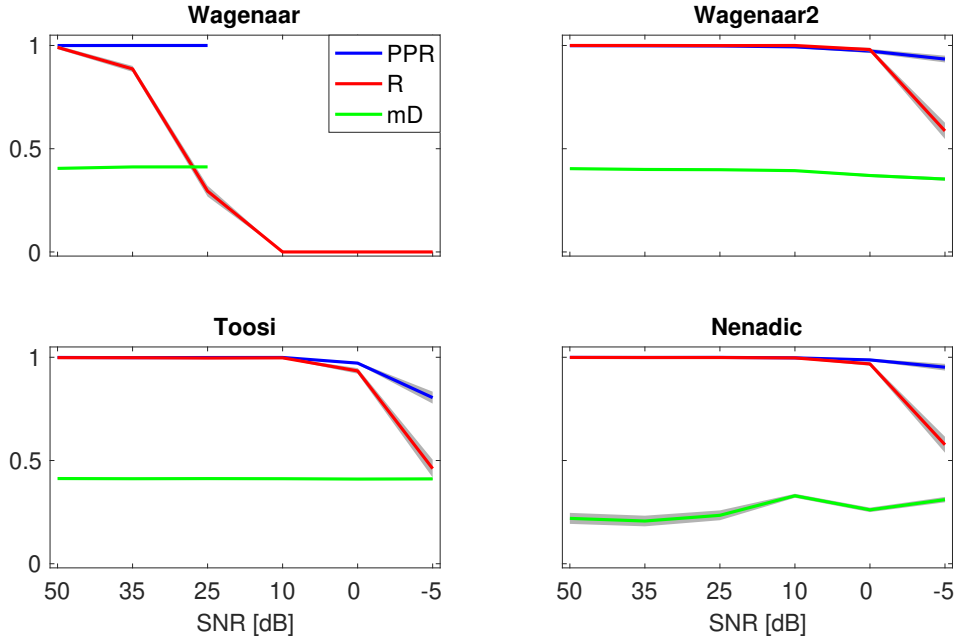

Fig. 2: The mean (solid line) $\pm$ standard deviation (shaded area) of positive prediction rate (*PPR*), recall (*R*) and the mean difference (*mD*) in starting points between actual spikes and spikes detected by the two versions of Wagenaar's method, Toosi's and Nenadic's approach.

The performance of Wagenaar's method deteriorated for $SNR \in \{25\text{ dB}, 35\text{ dB}\}$. Moreover, the algorithm was not able to detect any spike for $SNR \leq 10$ dB resulting in $R = 0$ and missing values of *PPR* and *mD* (Fig.2, top left). After a deeper inspection of Wagenaar's algorithm, we observed that the method's failure was caused by Condition 2, which was never met for data with a higher amount of noise. After removing Condition 2 from the algorithm (Wagenaar2), the method's performance improved. As depicted in Fig. 2 (top right), *PPR* and *R* for Wagenaaar2's and Nenadic's methods reached approximately the same values.

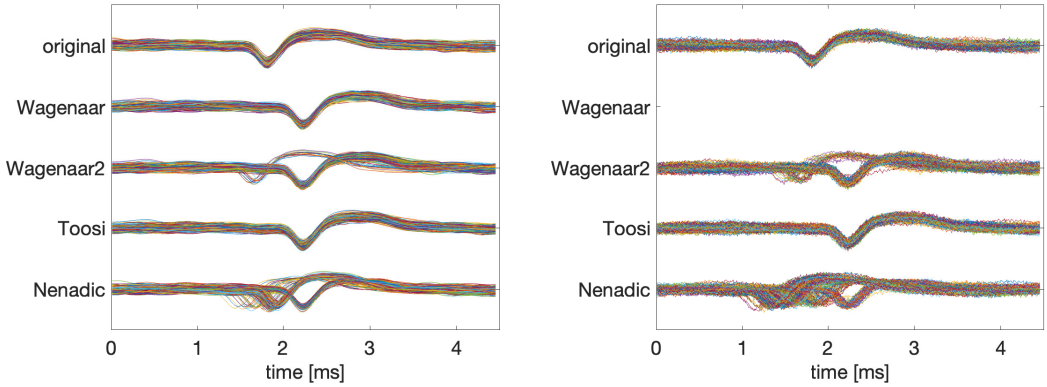

Fig. 3: Original simulated spikes with $SNR = 35$ dB (left) and $SNR = 10$ dB (right) and corresponding spikes detected by the two versions of Wagenaar's method, Toosi's and Nenadic's approach.

Methods of Toosi and Nenadic were able to detect almost all generated spikes, and their performance deteriorated only for $SNR \leq 0$ dB (Fig. 2, bottom). Nevertheless, this was expected because data with such a low *SNR* includes approximately the same amount of the target signal and noise.

ISBN 978-80-972629-6-9

Nenadic's algorithm achieved the lowest average temporal distance between the starting points of generated spikes and those correctly detected ($0.2 - 0.3$ ms, Fig. 2, bottom right), but at the cost of misaligned spikes characteristics (local minima and maxima, Fig. 3). On the other hand, constant $mD \approx 0.41$ ms was observed for all levels of *SNR* in Toosi's approach due to spike alignment to their global minima. Although Wagenaar's approach does not align the spikes a priori, its *mD* values were similar to Toosi's results, and the detected spikes were also aligned to the local minimum. However, as depicted in Fig. 3, the spikes alignment disappears after removing Condition 2 (Wagenaar2) for $SNR \leq 35$ dB.

5. Discussion and Conclusions

In this article, we compared the ability of three spike validation methods to identify spikes in simulated neural electrophysiological data. Wagenaar's method was unable to detect spikes when more noise was present because any candidate spike satisfied the condition of having the global peak amplitude at least twice as high as the second-highest peak of the same polarity. After removing this condition from the algorithm, the method's performance increased and was comparable to Toosi's and Nenadic's methods.

Nenadic's method sets the starting points of detected spikes closest to the generated spikes but at the cost of spikes misalignment. Spike validation is usually followed by spike clustering in order to detect dominant spike patterns. When using Nenadic's approach, we recommend aligning spikes before clustering because misalignment may result in many spurious or outlier clusters. On the other hand, this alignment step is not necessary when considering Toosi's algorithm. It's only required to realize that Toosi's spikes start a bit earlier than the actual spikes. Therefore we can conclude that Toosi's and Nenadic's methods can be used for spike validation.

Nevertheless, in this study we examined a specific case with spikes following the same amplitude and having a relatively long refractory period. Therefore, further analysis of simulated data with spikes following varying amplitudes or shorter refractory periods is needed.

Acknowledgements

This research was supported by the grant APVV-21-0105 and by the VEGA grant 2/0057/22.

References

[1] Biffi, E., Ghezzi, D., Pedrocchi, A., Ferrigno, G. (2010). Development and validation of a spike detection and classification algorithm aimed at implementation on hardware devices. *Computational Intelligence and Neuroscience* 2010(659050).

[2] Toosi, R., Akhaee, M., Dehaqani, M.-R. (2021). An automatic spike sorting algorithm based on adaptive spike detection and a mixture of skew-t distributions. *Scientific Reports* 11(13925).

[3] Wagenaar, D., DeMarse, T., Potter, S. (2005). MeaBench: a toolset for multi-electrode data acquisition and on-line analysis. In: *2nd International IEEE EMBS Conference on Neural Engineering, 2005.* pp. 518–521.

[4] Smith, L. S., Mtetwa, N. (2007). A tool for synthesizing spike trains with realistic interference. *Journal of Neuroscience Methods* 159(1), 170–180.

[5] Naundorf, B., Wolf, F., Volgushev, M. (2006). Unique features of action potential initiation in cortical neurons. *Nature* 440, 1060–1063.

[6] Ajayan, A., James, A. (2021). Edge to quantum: Hybrid quantum-spiking neural network image classifier. *Neuromorphic Computing and Engineering* 1(024001).

[7] Nenadic, Z., Burdick, J. (2005). Spike detection using the continuous wavelet transform. *IEEE Transactions on Biomedical Engineering* 52(1), 74–87.

Measurement in Biomedicine

ISBN 978-80-972629-6-9

Simulation of Body Surface Potentials During Ventricular Pacing

Elena Cocherová, Milan Tyšler

Institute of Measurement Science, SAS, Bratislava, Slovakia
Email: elena.cocherova@savba.sk

Abstract. *The goal of the study was to simulate body surface potentials (BSP) during ventricular pacing using a realistic homogeneous model of cardiac ventricles and the patient torso. Simulated BSP were compared with BSP measured in a real patient during pacing of the right ventricle. Ventricular activation in the model was started in the known position of the implanted stimulation electrode in the right ventricle near the apex as well as in several other sites near this position. The propagated electrical activation in the ventricular model was modeled using bidomain reaction-diffusion (RD) equations with the ionic transmembrane current density defined by the modified FitzHugh-Nagumo (FHN) equations. The torso was treated as a passive volume conductor region. The whole model was numerically solved in the Comsol Multiphysics environment. The measured BSP were compared with simulated BSP calculated for several positions of the stimulated region. The polarity and shape of selected simulated and measured ECG leads were in the best accordance when the stimulated region was close to the real position of the stimulating electrode. In this case, also the overall distribution of simulated and measured BSP was similar. In the initial phase of ventricular activation, the simulated BSP were strongly dependent on the position of the stimulated region.*

Keywords: Bidomain Reaction-Diffusion Model of Ventricular Activation, Ventricular Pacing, Realistic Heart and Torso Model, Simulation of Body Surface Potentials

1. Introduction

In healthy heart ventricles, the electrical activation starts from the atrioventricular node and propagates through the fast conduction system to the working ventricular myocardium [1]. Since the velocity of activation propagation in the conduction system is several times higher than that in the working ventricular myocardium, activation occurs rapidly during the first about 20 milliseconds at several regions of the ventricular myocardium and spreads along the endocardium and toward the epicardium. The electrical activity of the heart is manifested on the patient torso as body surface potentials (BSP). During ventricular stimulation, the electrical activation begins at only one site in the myocardium, near the tip of the stimulating electrode, and spreads mainly through the working myocardium. The activation sequence is changed, and the time needed to activate both ventricles is markedly prolonged. This is reflected in changed BSP dynamics and the QRS complex in the ECG signal is prolonged over 120 ms.

In this study, we simulated the ventricular activation and corresponding BSP during ventricular pacing at a single site in the right ventricle. The model of ventricular activation was based on bidomain reaction-diffusion (RD) equations and BSP were computed in homogeneous patient-specific heart and torso model. Several positions of the simulated pacing site were tested in order to obtain the BSP distribution and ECG signals as close as possible to the measured ones.

2. Subject and Methods

The ECG signals from limb leads and BSP maps were recorded in a patient (P034) with implanted pacemaker [2]. The torso geometry, position of the stimulating electrode and positions of 128 measuring ECG electrodes on the chest were obtained from a CT scan of the torso taken immediately after the BSP measurement with ECG electrodes attached. The model

ISBN 978-80-972629-6-9

of the patient specific torso and heart ventricles was constructed using the Tomocon and the Comsol Multiphysics software.

The Bidomain RD Model

The electrical activation of the cardiac tissue can be described by the bidomain RD model [3] by two partial differential equations:

$$\frac{\partial V_e}{\partial t} - \frac{\partial V_i}{\partial t} + \nabla \cdot \left(-D_e \nabla V_e\right) = i_{ion} - i_s, \tag{1}$$

$$\frac{\partial V_i}{\partial t} - \frac{\partial V_e}{\partial t} + \nabla \cdot \left(-D_i \nabla V_i\right) = -i_{ion} + i_s, \tag{2}$$

where V_e is the extracellular potential, V_i is the intracellular potential, D_e and D_i is the extracellular and intracellular tissue diffusivity, i_{ion} is the local ionic transmembrane current density, and i_s is the stimulation current density. Current densities were normalized to the membrane capacitance with units A/F. The tissue diffusivity D (in this model $D = D_e = D_i$):

$$D = \sigma / \left(\beta C_m\right), \tag{3}$$

is dependent on the tissue conductivity σ, on the membrane surface-to-volume ratio β, and on the membrane capacitance per unit area C_m. The ionic transmembrane current density i_{ion} and the membrane potential ($V_m = V_i - V_e$) were modeled using the modified FitzHugh-Nagumo (FHN) equations [4], [5]). Initial value of the intracellular potential was set to -0.085 V and the other variables were set to 0. Fluxes through all external boundaries of the torso were set to zero and the potential on the internal torso boundary with the ventricles was set to V_e.

Model of the Torso and Ventricles Geometry

The geometry of the torso and ventricles (Fig. 1) was obtained from the patient CT scan. The size of the ventricular model was approximately 130 mm in base-to-apex direction (height), 140 mm in the left-to-right and 100 mm in the anterior-to-posterior direction. The thickness of the ventricular wall was 5–9 mm in the right ventricle and 8–11 mm in the left ventricle.

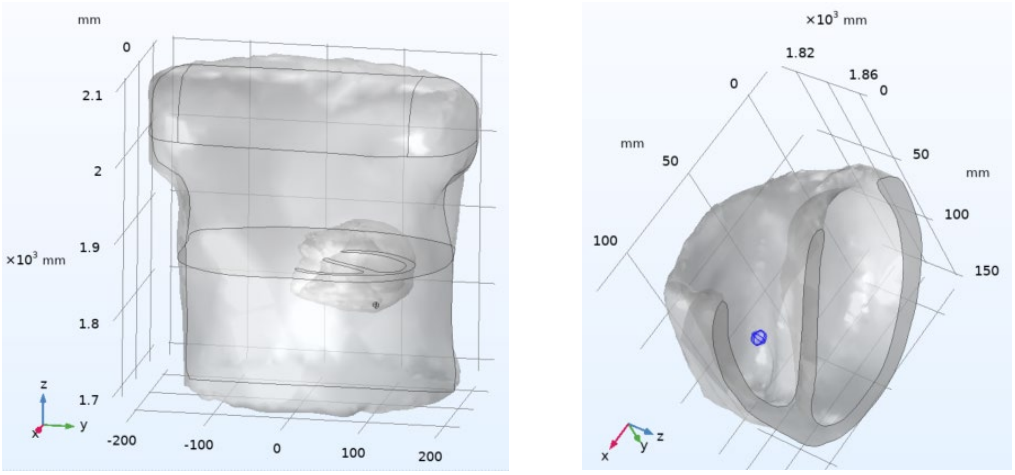

Fig. 1. The fontal view on the torso model (left) and the heart model (right). The stimulated region situated in the right ventricle is highlighted in blue.

Model Tissue Parameters

For homogeneous model of the ventricles, value of the tissue diffusivity in the myocardium was set to $D = 0.0008$ m^2/s (relating to tissue conductivity $\sigma = 0.8$ S/m). Values of the modified FHN model parameters were the same as in [5]. For these parameters, the activation propagation velocity of a planar wave front was about 0.7 m/s. Torso conductivity was set to $\sigma = 0.02$ S/m.

Cardiostimulation Parameters

The stimulated ventricular region spanned mostly between the known position of the tip of the stimulating electrode and the endocardium. In the model, the stimulated region was spherical with a radius of 4 mm. The center of the stimulated region was situated in the position of the electrode tip as well as in several other positions, with up to 25 mm around the known electrode tip position. The "smoothed rectangular" pulse with a duration of 10 ms and an amplitude of 40 A/F was used for stimulation.

3. Results

The ventricular activation and BSP were simulated for more than twenty positions of the stimulated region around the position of the stimulating electrode tip. Spatial distribution of the simulated membrane potential V_m and BSP in time instant $t = 21$ ms for the case when the best agreement between measured and simulated BSP was obtained are shown in Fig. 2. Corresponding measured BSP map and positions of 128 measuring ECG electrodes are shown in Fig. 3, and measured and simulated time courses of ECG potentials in limb leads I, II and III are shown in Fig. 4.

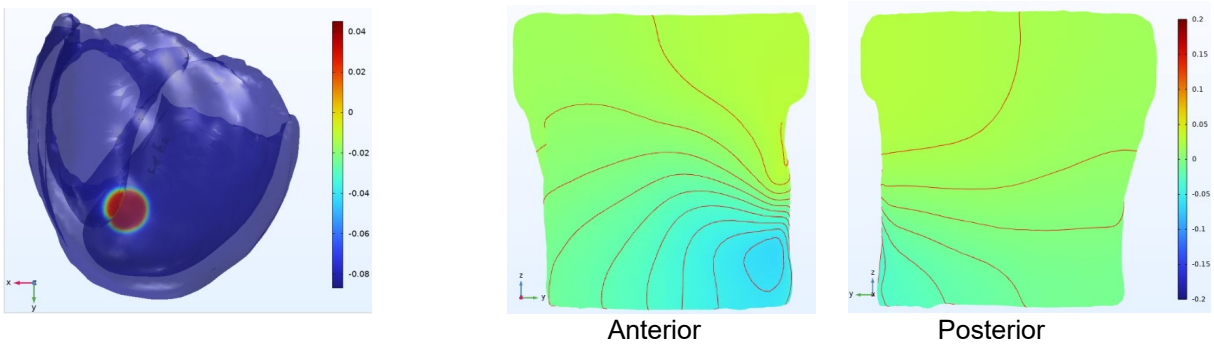

Fig. 2. Spatial distribution of the membrane potential V_m [V] and simulated BSP [mV] in time $t = 21$ ms for the case when the best agreement between measured and simulated BSP was obtained.

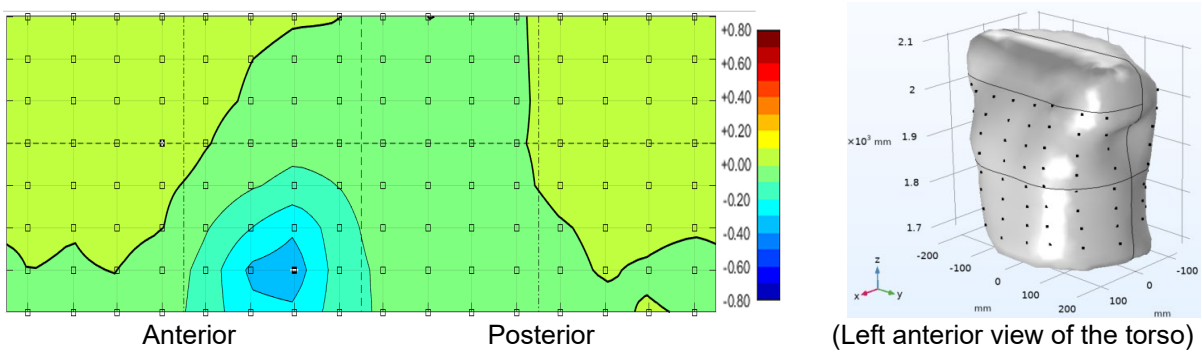

Fig. 3. Measured BSP map [mV] in time $t = 21$ ms (left). Positions of measuring ECG electrodes (right).

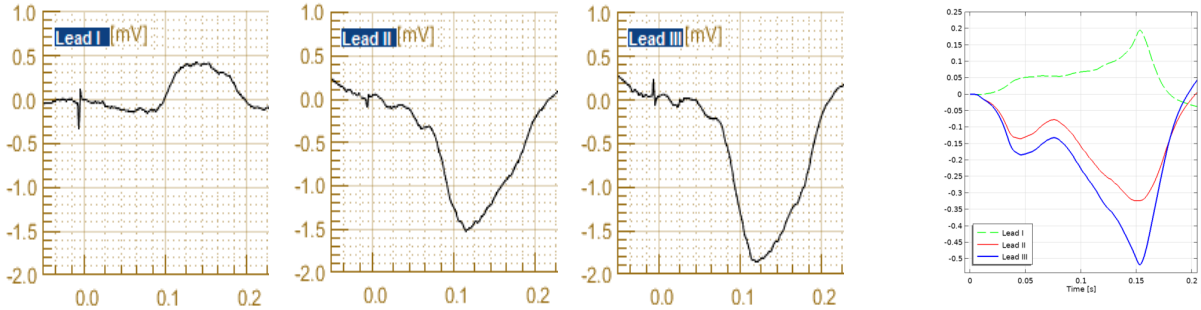

Fig. 4. Measured (left) and simulated (right) potentials in limb leads I, II and III during QRS complex in ECG.

ISBN 978-80-972629-6-9

The best accordance between the measured and simulated data was obtained for the stimulated region situated about 10 mm posteriorly from the electrode tip position. For other positions of the stimulated region, the simulated ECG potentials in limb leads changed their shape, namely in the initial phase of the ventricular activation, and in a few cases also the polarity of limb lead I was reversed. The whole BSP distribution was also changed accordingly.

4. Discussion and Conclusions

Obtained BSP distribution from the simulated ventricular pacing was similar to the measured one, however, there were differences in the position of the positive maxima, and the best agreement between the measured and simulated data was obtained when the stimulated ventricular region was about 10 mm posteriorly from the real position of the stimulating electrode. When looking on the QRS complexes in simulated limb leads ECG, the polarity of leads II and III was correctly negative in all tested positions of the stimulated region, except during the initial 25 ms, where in many cases small positive potentials could be seen. In lead I, there was a difference in polarity between measured and simulated QRS complexes during the initial activation and small negative deflection that was seen in measured ECG was not observed in any simulation. The positive measured amplitudes during the late activation were present in simulated ECG only when the stimulated region was shifted posteriorly from the real position of the stimulating electrode.

Differences between the measured and simulated BSP could be caused namely by the inaccurate model geometry of the right ventricle, by not taking into account myocardium anisotropy and torso heterogeneity, by not considering an anterior myocardial infarction region present in patient P034, and by neglecting the role of the conduction system in the ventricular model.

From these results it can be concluded that the simulation of the ventricular pacing can produce BSP close to reality, but the results are very sensitive to inaccuracies in the model geometry and simulated properties of the myocardial tissue.

Acknowledgements

The work was supported by research grant APVV-19-0531 from the Slovak Research and Development Agency and grant VEGA 2/0109/22 from the VEGA grant agency.

References

[1] Malmivuo, J., Plonsey, R. (1995). *Bioelectromagnetism: Principles and Application of Bioelectric and Biomagnetic Fields*. Oxford University Press.

[2] Švehlíková, J., Zelinka, J., Haška, M., Tyšler, M. (2019). Simulation of measured body surface potential map during early right ventricular pacing. In *12th International Conference on Measurement.* IMS SAS, 34-37.

[3] Potse, M., Dube, B., Richer, J., Vinet, A., Gulrajani, R. M.(2006). A comparison of monodomain and bidomain reaction-diffusion models for action potential propagation in the human heart. *IEEE Transactions on Biomedical Engineering,* 53 (12), 2425-2435.

[4] Sovilj, S., Magjarevic, R.. Lovell, N. H., Dokos, S. (2013). A simplified 3D model of whole heart electrical activity and 12-lead ECG generation. *Computational and Mathematical Methods in Medicine,* doi.org/10.1155/2013/134208.

[5] Cocherová, E. (2015). Analysis of the activation propagation velocity in the slab model of the cardiac tissue. In *10th International Conference on Measurement.* IMS SAS, 105-108.

Assessment of Yeast Cells Electroporation by Autoluminescence and Impedance Measurements

[1]Martin Bereta, [2]Michal Teplan, [3]Djamel Eddine Chafai, [4]Tomáš Zakar, [2]Hoang Vu Viet, [4]Michal Cifra

[1]Faculty of Health, Catholic University in Ruzomberok, Slovakia
[2]Institute of Measurement Science, Slovak Academy of Sciences, Bratislava, Slovakia
[3]WPI Nano Life Science Institute, Kanazawa University, Kakuma-machi, Kanazawa 920-1192, Japan
[4]Institute of Photonics and Electronics of the Czech Academy of Sciences, Prague, Czechia
Email: martin.bereta@ku.sk

Abstract. *The application of pulsed electric field (PEF) is nowadays becoming a very promising tool for application in medicine or the food industry. However, the mechanisms of PEF interaction with living matter are still not fully elucidated. The aim of the presented work is to assess the electroporation phenomena in yeast cells using autoluminescence and impedance measurements. The yeast cell culture (Saccharomyces cerevisiae) is exposed to 8 pulses of 100 µs width. The corresponding electric field strength magnitude range is 2-7 kV.cm^{-1}. The frequency of the pulsing is 2 Hz, and autoluminescence is monitored during exposure. The results indicate detectable differences in autoluminescence dynamics when PEF is applied. Due to its non-invasive and label-free application, the autoluminescence could be used as a beneficial tool for monitoring PEF biological effects.*

Keywords: Yeast Cells, Autoluminescence, Pulsed Electric Field, Electroporation

1. Introduction

The mechanisms of pulsed electric field (PEF) interaction with biological matter are not fully established, but PEF treatments are nowadays becoming widely used in biomedicine and the food industry [1]. The research challenges for PEF biological effects are still present, with potential novel applications in diagnostics, therapy as well as in industry. Because this research field still has many open questions not possible to be answered with current tools, it is essential to find novel methods for the assessment of various facets of biological effects. Here we suggest using autoluminescence as an externally detectable manifestation of the oxidative metabolic activity of living cells [2]. The aim of this work is to show the use of autoluminescence and impedance measurements to detect the PEF effects on yeasts *Saccharomyces cerevisiae*.

2. Materials and Methods

Yeast culture and cell suspension preparation

The yeast culture *Saccharomyces cerevisiae* (genetic background BY4741, MATa) used in the experiments is stored on agar plates (1% (w/v) yeast extract, 2% (w/v) peptone, 2% (w/v) agar, 2% (w/v) D-glucose in purified water) in a refrigerator at 4 °C. Yeasts are inoculated from agar plate into glass Erlenmeyer flask (250 mL) with 100 mL of YPD medium (1% (w/v) yeast extract, 2% (w/v) peptone, 2% (w/v) D-glucose in purified water) and cultivated for 24 hours at 30 °C on an orbital shaker (Biocer) at 180 rpm.

ISBN 978-80-972629-6-9

Electroporation- autoluminescence sensing setup

PEF treatment of the samples was executed in a special chamber designed and manufactured in the Institute of Photonics and Electronics of the Czech Academy of Sciences, Prague, Czechia. The chamber consists of a dielectric (transparent polymethylmethacrylate, PLEXIGLAS GS, Zenit) housing equipped with an anode (bottom electrode) and a cathode (top electrode) positioned in a parallel-plate arrangement. The central part of the cathode was perforated by hexagonally arranged holes with a diameter of 1.0 mm and spacing of 1.5 mm between the centres of the holes, creating 50% voids. The cathode-anode gap was 2.00 mm for the steel and glassy carbon anode, respectively. For PEF generation we use the high-power pulse generator (ELECTROcell B15, Leroy-Biotech) to expose the samples to 8 pulses with a duration (pulse width) of 100 μs. The corresponding voltage-to-gap ratio (electric field strength magnitude) was 2, 3, 4, 5, 6, and 7 $kV.cm^{-1}$. The frequency of the pulsing is 2 Hz. The yeast cell culture is PEF-treated in low conductive buffer (LCB) and autoluminescence during PEF application is measured. autoluminescence measurement for each set of parameters is performed in triplicate. The photomultiplier (PMT) module H7360-01, selected type, (Hamamatsu Photonics K.K.) with spectral sensitivity in the range 300-650 nm is used to detect autoluminescence. The typical dark count (noise) of PMT module H7360-01 is about 20 counts per second (cps). Measurement of the sample takes place in a light-tight chamber (standard black box, Institute of Photonics and Electronics, CZ) specially designed for the purpose of autoluminescence measurements. The PMT module is mounted on the top of the chamber viewing the sample inside the chamber.

Impedance measurements

The impedance of the sample before and immediately after pulsing was measured in the range of 30 Hz to 300 kHz (BK891, BK PRECISION). The impedance measurement was done on the same chamber, which was used for pulses delivery. We also recorded the amplitude of current pulses delivered to the samples by the PEF generator.

Data analysis

Autoluminescence raw data were preprocessed and smoothed using Matlab, version R2021b (MathWorks, Inc.). For the statistical analysis, an unpaired two-sample t-test was performed for the datasets when the normal distribution of data was not refused and paired Wilcoxon signed-rank test was performed for the cases when the normal distribution of data was refused.

3. **Results and Discussion**

The effects of 6 different settings of PEF amplitudes were investigated. Here we show the results of autoluminescence from the yeast cell sample treated with 8 pulses of 100 μs duration. In Fig. 1A one can see representative autoluminescence intensity evolution during the delivery of 8 pulses, with corresponding E-field intensity 6 $kV.cm^{-1}$. It can be seen that the autoluminescence intensity level from a buffer (LCB) throughout the pulses delivery is significantly lower than the level of autoluminescence intensity from the cell solution (Fig. 1A).

ISBN 978-80-972629-6-9

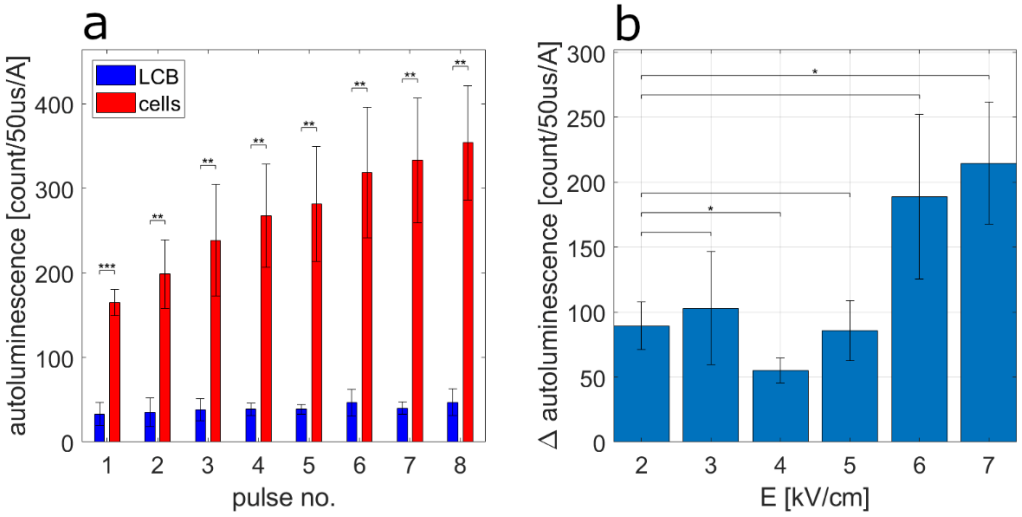

Fig. 1. Autoluminescence: (a) Gradually elevated autoluminescence response to the train of 8 PEF pulses with 6 kV.cm^{-1}. (b) Autoluminescence response of cells - differences between the last and the first PEF pulse.

In order to analyze the PEF effects on cells we calculated the difference in autoluminescence intensity during the 8th and 1st pulse (Fig. 1B). The results indicate an increasing difference between the final and initial autoluminescence intensity from cells with the increasing E-field intensity. There seems to be a threshold between 5 and 6kV/cm from where autoluminescence production is enhanced. For interpretation of these preliminary results, we hypothesize that the rate of the cell wall and cell membrane permeabilization is raised after each pulse delivered to the solution, as was shown in several studies [3, 4]. Then the parts of the intracellular content could be released from the cell [5], and, extracellular medium, *e.g.* ions from the solution, could be transported in the reverse direction - into the cell [4]. The answer to the question, of why the autoluminescence is increased during this transport, is not straightforward. We know that the autoluminescence intensity can be modulated by the presence of reactive oxygen species (ROS) [6], which are formed in the cell solution under both normal and excessive oxidative processes, but also as a product of cell apoptosis [7]. Therefore, we suppose the PEF could initiate oxidative reactions in solution or even induce apoptotic processes, which are accompanied by enhanced ROS production and the following increase of autoluminescence intensity.

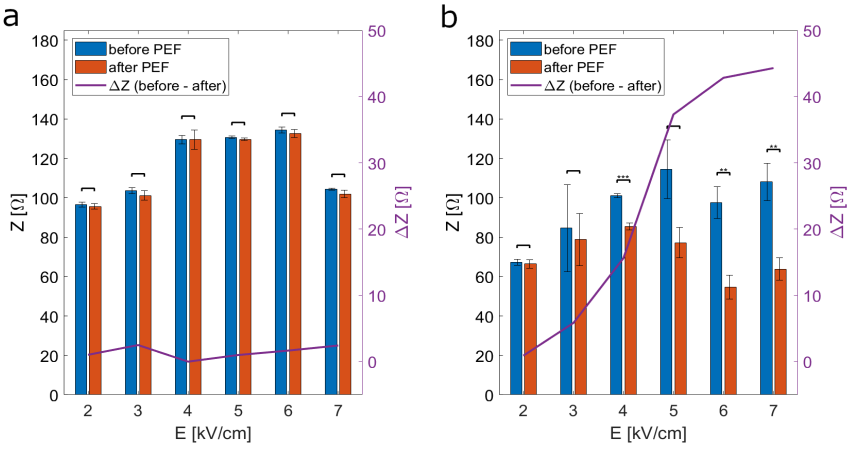

Fig. 2. Impedance characteristics at 50 kHz before and after application of PEF: (a) LCB medium, (b) cells in LCB medium.

ISBN 978-80-972629-6-9

We can look at these processes also from the perspective of dielectric parameters. The permeabilization of the cell wall and cell membrane by applied PEF (electroporation), and following ions leakage from intracellular space to medium, leads to the increase of medium conductivity. This assumption is supported by the results of impedance measurements used in the electroporation assessment of cells in the literature [9], which we performed before and immediately after each single experiment. It can be seen that the impedance of samples is not significantly changed in the case of LCB medium without cells (Fig. 2A), whereas a significant decrease of impedance after pulsing to cell samples at higher values of intensity is observed (Fig. 2B). The lower impedance and corresponding higher conductivity of the samples allows a flow of higher current, which stimulates reaction pathways leading to higher ROS production and autoluminescence enhancement.

4. Conclusions

We present the use of autoluminescence for label-free investigation of PEF biological effects. The results indicate the dose-dependent response of autoluminescence - with an increasing number of pulses delivered to the cell solution, the autoluminescence intensity is gradually enhanced. We suggest that this could be the result of progressive permeabilization of the cell wall, followed by the release of intracellular content and enhanced transport of extracellular ions into the cells. These processes might be accompanied by oxidative reactions or cell apoptosis when ROS production is enhanced, and therefore the increase of autoluminescence is observed. We also observed a significant decrease in the impedance of samples after pulsing to cell samples at higher values of intensity, which also indicate the progressive ions leakage into the medium, due to cell wall permeabilization.

Acknowledgements

We acknowledge VEGA Grant Agency, grant no. 2/0124/22 for funding. The authors also participate in the COST Action CA17115.

References

1. L. Rems, D. Miklavčič, “Tutorial: Electroporation of cells in complex materials and tissue,” *J. of Applied Physics*, 119, 2016.

2. M. Cifra, P. Pospíšil, “Ultra-weak photon emission from biological samples: definition, mechanisms, properties, detection and applications,” *J. of Photochemistry and Photobiology B: Biology*, 139, pp. 2-10, 2014.

3. A. Stirke et al., “Permeabilization of yeast Saccharomyces cerevisiae cell walls using nanosecond high power electrical pulses,” *Applied Physics Letters,* 105, 2014.

4. A. Stirke et al., “The link between yeast cell wall porosity and plasma membrane permeability after PEF treatment,” *Scientific Reports,* 9, 2019.

5. Martínez, J. M. et al., “Factors influencing autolysis of Saccharomyces cerevisiae cells induced by pulsed electric fields,” *Food Microbiology,* 73, pp.67-72, 2018.

6. P. Pospíšil et al., “Role of reactive oxygen species in ultra-weak photon emission in biological systems.” *J. of Photochemistry and Photobiology B: Biology.* 139, pp. 11–23, 2014.

7. G. G. Perrone et al., “Reactive oxygen species and yeast apoptosis,” *Biochimica et Biophysica Acta (BBA) - Molecular Cell Research,* 1783, pp. 1354–1368, 2008.

8. Bereta, M., et al., “Biological autoluminescence as a non-invasive monitoring tool for pulsed electric field effects on yeast cells.” *2020 XXXIIIrd GASS of the International Union of Radio Science,* pp. 1-3. IEEE, 2020.

9. Chafai, DE, et al., “Assessment of the electrochemical effects of pulsed electric fields in a biological cell suspension” *Bioelectrochemistry*, *106*, 249–257, 2015.

Development of an experimental platform for the measurement of biological response of low-frequency magnetic fields

Hoang Vu Viet, Michal Teplan

Institute of Measurement Science, Slovak Academy of Sciences Bratislava, Slovakia
Email: hoang.vuviet@savba.sk

Abstract. *This contribution presents the development of an innovative experimental platform to investigate the effect of low-frequency magnetic fields on biological structures. Impedance spectroscopy is a key method for concentration estimation in the field of cell culture growth rate. The research is focused on the development of a methodology based on impedance measurement used for the characterization of living cells and the dynamics of cell growth which could be the basis for novel diagnostic and therapeutic methods for the treatment of civilization diseases.*

Keywords: Impedance Spectroscopy, Magnetic Field, Biological Response.

1. Introduction

Living cells contain free and bound electric charges in the form of ions and polar molecules, thus they are sensitive to magnetic fields (MF) and currents [1]. Several studies indicated the potential connection between low-frequency (LF) MF exposure and cancer [2], or cardiovascular diseases [3]. On the other hand, there are reports on the potential beneficial application of LF MF for treating arrhythmia [4]. Numerous works focusing on experiments with living cells showed the impact of LF MF on the proliferation processes of cells or cell viability. Other studies found alteration of cell proliferation gene expression or reactive oxygen species production.

Physical mechanisms of biological LF MF interaction, such as ion cyclotron resonance [5], ion parametric resonance [6], or radical pair mechanism were proposed [7]. Their experimental verification is still largely absent, due to the fact, that most experimental studies focus only on a small set of frequencies. Meanwhile, most studies investigated the effects of fields with a frequency of 50/60 Hz, we've taken quite a different perspective. Our proposal is unique, as we are proposing to cover a wider frequency range (Hz - kHz). The effects of these fields have not been studied systematically from the point of view of varying frequencies.

2. Subject and Methods

One way to determine the impact of LF MF on living cells is to compare the concentration of cell samples after cultivation. Cell counting represents one of the basic methods for almost all microbiological research applications, however, there are many pitfalls in the process of cell counting. In order to address these issues, there have been advances in cell counting over the last decades, enabling the process to become highly automated. Concentration estimation based on electrical impedance spectroscopy is one of the essential methods. Because cells in the medium can be modeled as an equivalent circuit consisting of capacitors and resistors, their growth can be expressed by the changes in electrical impedance. Estimated cell concentration can be acquired by applying a proper estimation approach to the obtained impedance spectra. One of the approaches for estimation of the cell concentration N_c was proposed by K. Asami & T. Yonezawa. This approach is based on the analysis of the dielectric dispersion. This dielectric technique has been proven to be useful for monitoring cell concentration [8] through the following formula:

$$N_c = \frac{\varepsilon_0}{3\pi r^4 C_m} \cdot \frac{\Delta\varepsilon(t,f)}{F(t,f)} \quad (1)$$

where N_c is the cell concentration (the number of cells per unit volume), C_m is the membrane capacitance, which is regarded as a constant (about 1 μF/cm^2), r is the radius of the cell shell-sphere (about $2 \cdot 10^{-6}$ m), ε_0 is the permittivity of vacuum (0.08854 pF/cm), $\Delta\varepsilon$ shows the change in permittivity of the sample at two different times $\Delta\varepsilon = \varepsilon_2(t_2,f) - \varepsilon_1(t_1,f)$, $F(t,f) = 1/(1 + (f/f_c(t))^2)$, f is the applied frequency, and f_c is the central frequency.

The realization of the experimental platform is shown in Fig. 1. The platform consists of five main parts: pair of cultivation chambers, an optical microscope, a system for MF generation, an impedance spectroscopy analyzer, and central control and data acquisition unit. Yeast *Saccharomyces cerevisiae* is used as a biological model. The cells are cultivated in yeast extract peptone dextrose (YPD) medium. Starting cell concentration is approximately 2.5x10^5 cells/ml.

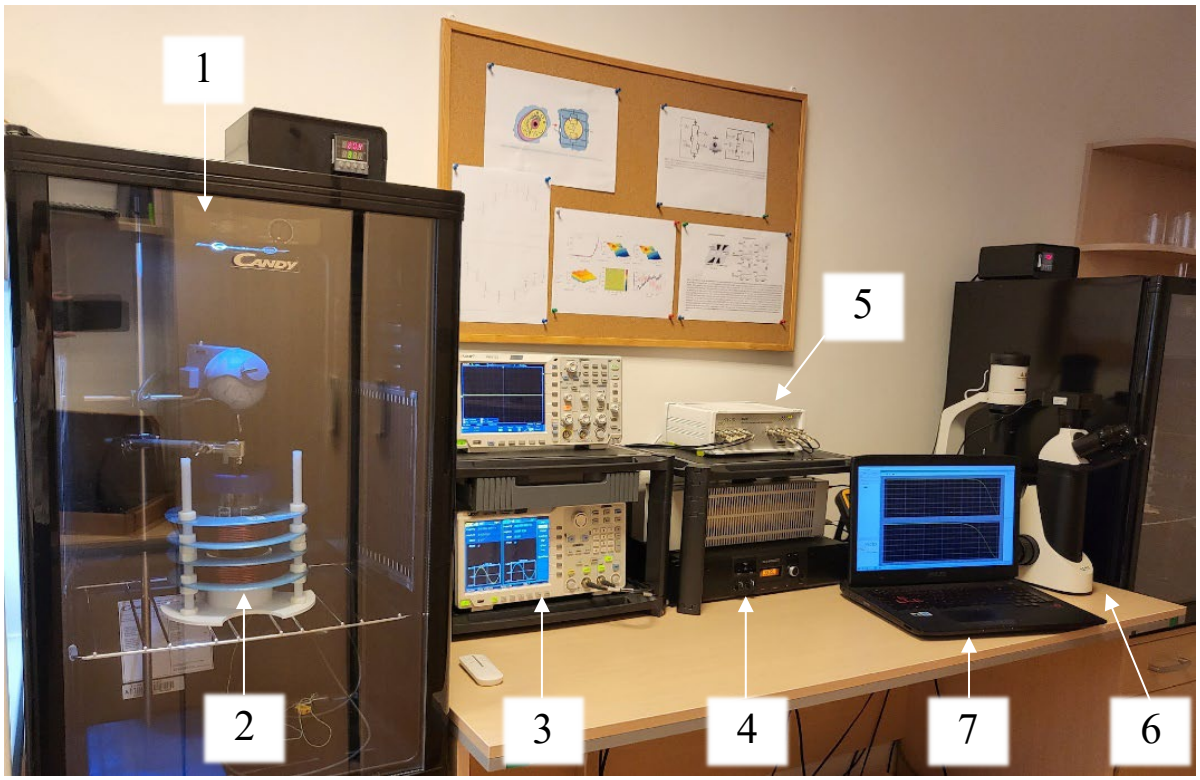

Fig. 1. Composition of the experimental platform: Pair of cultivation chambers with proportional–integral–derivative (PID) temperature regulators (1), Helmholtz coils (2), signal generator (3), power amplifier (4), impedance spectroscopy analyzer (5), inverted light microscope (6), and central computer (7).

3. Results

The impedance spectra measurement is performed using the continual impedance measurement mode of the impedance spectroscopy analyzer consisting of the whole spectrum measurements (10 Hz - 10 MHz) with 350 logarithmically distributed frequency points and 60 s duration. The cell samples with different cell concentrations (calculated from microscopic images of the Bürker counting chamber) displayed different impedance spectra, as depicted in (Fig. 2).

ISBN 978-80-972629-6-9

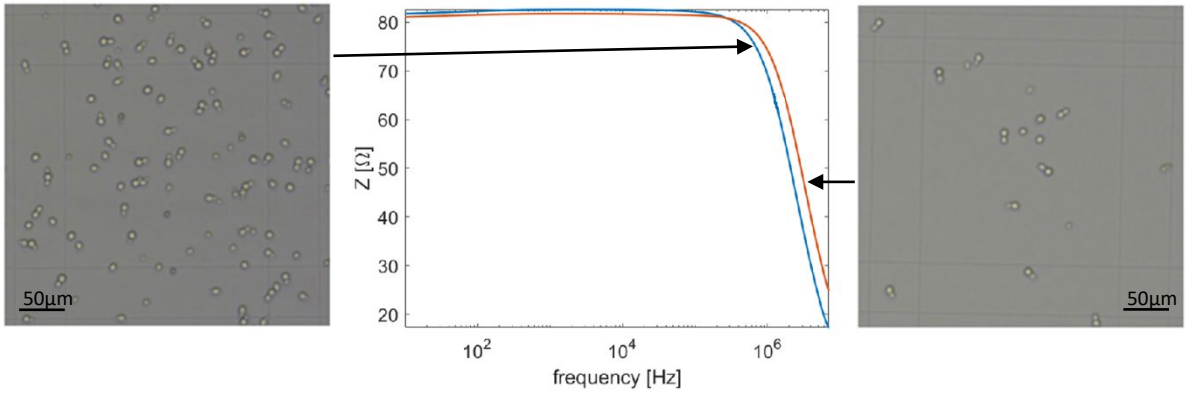

Fig. 2. Samples of impedance spectra for 2 different concentrations of yeast cells.

Following the experiment adjustments of the "test vs control" mode was performed, during which the cell sample in one cultivation chamber was set to be exposed to the MF while in the other chamber, MF was not applied. The outcome of one "test vs control" experiment is shown in Fig. 3 where MF with the magnetic induction of 3 mT at the frequency of 800 Hz was applied in chamber 1 while chamber 2 was without the application of MF.

The result displays the estimated cell concentrations of the measurement were calculated by applying the cell concentration estimation approach from obtained impedance spectra. The selected frequency for the calculation of Eq. (1) was 3.2 MHz. The calculated concentrations of both samples have an upward trend, where a period from minute 400 to approximate minute 650 indicates the exponential growth phase in both samples. Due to the fact that the two cultivation chambers are not ideally identical, there is an offset in the measured spectra, resulting also in the obtained concentrations. The curves in Fig. 3 are thus calibrated by the 2-point calibration method, where the starting and ending points are set according to the real concentrations obtained by the hemocytometer method.

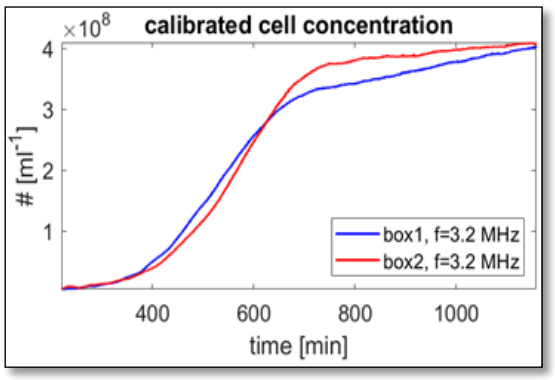

Fig. 3. Calculated concentration estimation using the approach proposed by Asami and Yonezawa.

The resulting multiplication rate reflects how many times the cell population increased from the starting concentration of cells in the two samples (primary y-axis) is shown in Fig. 4. From minute 600, there is a visible sign of inhibition of the cell sample in chamber 1 which was exposed to MF. The ratio between the two samples (secondary y-axis) reached 0.89 at its minimum, meaning the concentration of the sample which was exposed to MF is about 11% lower than the one that was placed in the chamber with the active MF. It is to be noted that in the beginning, the ratio between the two multiplication rates has a high level of noise mainly due to the stabilization of cell concentration during the lag phase and the stabilization of temperature inside the cultivation chambers.

ISBN 978-80-972629-6-9

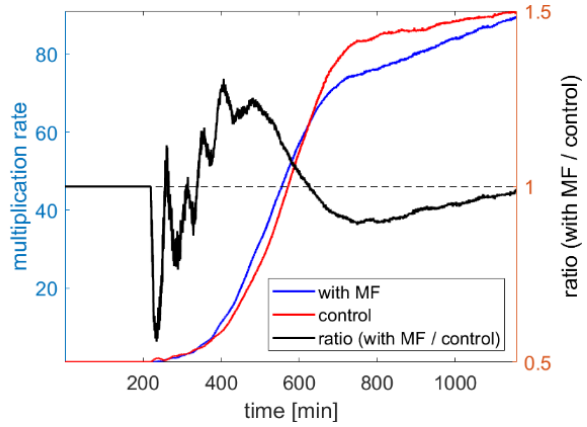

Fig. 4. Multiplication rate (primary y-axis) for exposed (blue) and control (red) samples. The ratio of control to exposed concentrations (secondary y-axis). MF parameters were 3 mT at 800 Hz.

4. Discussion and Conclusion

Obtained preliminary results display the promising outcome of our study, showing LF MF with specific parameters can distort the yeast cell growth curve. Such a type of distortion can generally be interpreted as inhibition or stimulation which is visible after the end of the exponential growth phase. In particular, this can indicate changes in cell viability or vitality. However, more experiments must be performed in order to collect enough data for proper analysis and conclusions to broaden knowledge about the impact of external low-frequency electromagnetic fields on the functioning of selected biological objects that could be the basis for novel diagnostic and therapeutic methods for the treatment of civilization diseases.

Acknowledgments

The research was supported by the research grant 2/0124/22 from the VEGA Grant Agency. Authors also participate in COST Action CA17115.

References

[1] Cifra M., Fields J. Z., Farhadi A. (2011) Electromagnetic cellular interactions, *Prog Biophys Mol Biol.* 105(3), 223-46.

[2] Turner M. C. et al. (2014) Occupational Exposure to Extremely Low-Frequency Magnetic Fields and Brain Tumor Risks in the INTEROCC Study, Cancer Epidemiology, *Biomarkers and Prevention* 23 (9), 1863-1872

[3] Savitz D. A. et al. (1999) Magnetic Field Exposure and Cardiovascular Disease Mortality among Electric Utility Workers, *American Journal of Epidemiology* 149 (2), 135-142

[4] Wang S. et al. (2016) Noninvasive low-frequency electromagnetic stimulation of the left stellate ganglion reduces myocardial infarction-induced ventricular arrhythmia, *Scientific Reports* 6, 30783

[5] Liboff A. R. (1985) Geomagnetic cyclotron resonance in living cells, *Journal of Biological Physics* 13, 99-102

[6] Belova N. A. and Panchyeluga V. A. (2010) Lednev's model: Theory and experiment, *Biophysics* 55, 661-674

[7] Barnes F. S. and Greenebaum B. (2015) The effects of weak magnetic fields on radical pairs, *BioElectroMagnetics* 36 (1), 45-54

[8] Asami K. and Yonezawa T. (1995) Dielectric analysis of yeast cell growth, *Biochimica et Biophysica Acta* 1245, 99-105

On the Way to Detection and Classification of Biogenic Iron in Tissues of Laboratory Animals with the Help of SQUID Magnetometry.

[1]Martin Škrátek, [1]Ján Maňka, [1]Alexander Cigáň, [2]Iveta Bernátová

[1]Institute of Measurement Science, Slovak Academy of Sciences, Bratislava, Slovakia,
[2]Institute of Normal and Pathological Physiology, Centre of Experimental Medicine, Slovak Academy of Sciences, Bratislava, Slovakia
Email: martin.skratek@savba.sk

Abstract. *Tissues of the left heart ventricle (LHV), liver and aorta of normotensive WKY rats were studied using SQUID magnetometry. Presented is the sample mounting and stabilization procedure, which allows the creation of geometrical and time-stable samples. Described SQUID magnetometry method enables the detection of different types of biogenic iron. In all tissues, a paramagnetic iron, most likely haemoglobin was detected. In samples of the liver was additionally detected also iron in the form of mineralised nanoparticles with a blocking temperature of 11 K, which is indicative of ferritin-like iron.*

Keywords: SQUID Magnetometry, Biogenic Iron, WKY Rats

1. Introduction

Iron is an essential element included in many metabolic processes. However, the amount of iron in the body must be balanced, because its excess or deficiency can lead to serious health problems. Due to its toxicity, iron is found in the body embedded in ferritin, haemoglobin or transferrin proteins. Determination of the amount of iron in tissues can be done using colorimetric, spectrophotometric, and histochemical methods or by atomic absorption spectrometry [1]. It is known, that deoxyhaemoglobin, methaemoglobin and myoglobin exhibit paramagnetism, which originates on the single ion magnetism of Fe^{2+} or Fe^{3+} incorporated in their molecules. On the other hand, ferritin, the iron storage protein, contains Fe atoms mineralised in the form of oxyhydroxide nanoparticles, whose behaviour is superparamagnetic [2]. In light of this knowledge, SQUID magnetometry offers the possibility of detection and quantification of different iron forms with high sensitivity. Measurement of biogenic iron using SQUID magnetometric technique was successfully performed in tissues of mice [2,3] and rat blood [4]. In this work the possibility of detection and qualification of biogenic iron by the SQUID magnetometry in the left heart ventricle (LHV), liver and aorta of Wistar Kyoto (WKY) rats is presented.

2. Subject and Methods

Animals

In this study, we used normotensive WKY male rats at the age of 14–16 weeks. Rats were born in the certified animal facility of the Institute of Normal and Pathological Physiology, Centre of Experimental Medicine, Slovak Academy of Sciences, in order to maintain a standardized environmental background for all animals. Rats were fed with pelleted chow Altromin 1314 (Altromin Spezialfutter, Lage, Germany) until their ninth week of age and afterwards with Altromin 1324. The iron content in both chows was 192.51 mg/kg. The pellet food and water were available ad libitum. Rats were housed under standard conditions at 22–24 °C, humidity 45–65%, and with a 12 h light/dark cycle. Rats were killed by decapitation after brief exposure to CO2 (until the loss of consciousness). Tissues (liver, LHV and aorta) were dissected using

ceramic scissors and forceps, cleaned of connective tissues, and immediately frozen in liquid nitrogen. All samples were kept at - 80 °C until magnetometric measurements were performed. All of the procedures used were approved by the State Veterinary and Food Administration of the Slovak Republic in accordance with the European Union Directive 2010/63/EU.

Sample preparation

Special attention was devoted to the preparation of samples for magnetisation measurements. The most common arrangement for measurements of biological samples is a plastic or gelatine capsule fixed into the drinking straw with a cotton stopper. However, this arrangement brings several problems. There is always a need to subtract the signal generated by the capsule and the cotton. To have a sufficiently strong signal from the sample compared to the signal of the capsule, it is necessary for the sample to be more voluminous. Also, if the signal value from the sample is close to that of the capsule, but in the opposite direction, it often leads to instability of the measured signal. Considering all these restrictions and that the tissues of laboratory animals are small in size and limited in amount because many other analyses are made during the experiments, the method of mounting and stabilising the samples was improved. Defrosted tissue (LHV and liver) was cut with a cylindrical-shaped instrument (diameter of 5.5 mm) and was mounted on 18 cm long copper wire (0.2 mm diameter). The aorta was mounted by a wire embedded via the lumen of the artery. Then the sample was vacuum dried for 1 h. During drying, the sample shrinks and sticks to the wire (see Fig. 1a). After this the dry weight of the sample was measured (see Tab. 1). The Cu wire itself is diamagnetic and long enough to have a negligible output signal to the sample's magnetic moment.

SQUID magnetometry

Magnetic properties of such prepared dry tissues were measured by the Quantum Design MPMS XL-7T AC SQUID magnetometer. The temperature dependence $M(T)$ of the magnetic moment was measured in the zero-field cooling (ZFC) and field cooling (FC) mode by applied field of 4000 A/m. The DC magnetisation $M(H)$ was measured at 2 and 300 K up to 7 T field. The data were normalized to the dry weight of the samples. Measured data of LHV, liver and aorta (5 samples each) were averaged and plotted on a graph.

3. Results

Figure 1b represents parts of the $M(H)$ curves measured at 300 K. From the curves is clear, that all of the samples have a linear dependence of magnetisation at the applied field and a negative magnetic susceptibility. Aorta has slightly bigger negative magnetic susceptibility, compared to LHV and liver. This is probably due to the higher content of paramagnetic components in LHV and liver tissues. Figure 1c shows M(H) curves measured at 2 K, whose diamagnetic component was subtracted. All of the samples showed ferromagnetic-like behaviour, with visible curvature, but only liver samples showed clear hysteresis (see inset in Fig. 1c). The main parameters read from the measured $M(H)$ dependences – the saturation magnetisation (M_S) and coercivity (H_C) are presented in Table 1. Figure 1d presents measured $M(T)$ dependences. Samples of the aorta showed diamagnetism (negative value of magnetisation) in the whole temperature range. There is a visible increase in magnetisation under 20 K (paramagnetic tail), indicating the presence of paramagnetic substances. The curve measured for LHV also showed diamagnetism; under 20 K there is again but sharper paramagnetic tail indicating the presence of more paramagnetic substances compared to aorta samples. Liver samples showed diamagnetism, but under 20 K there is a visible bifurcation between ZFC and FC curve which suggests ferromagnetism. Again, the paramagnetic tail is visible. More interesting is the visible peak on the ZFC curve with a clearly visible maximum (see inset in Fig. 1d), indicating that superparamagnetic nanoparticles are present, with a blocking temperature at 11 K.

ISBN 978-80-972629-6-9

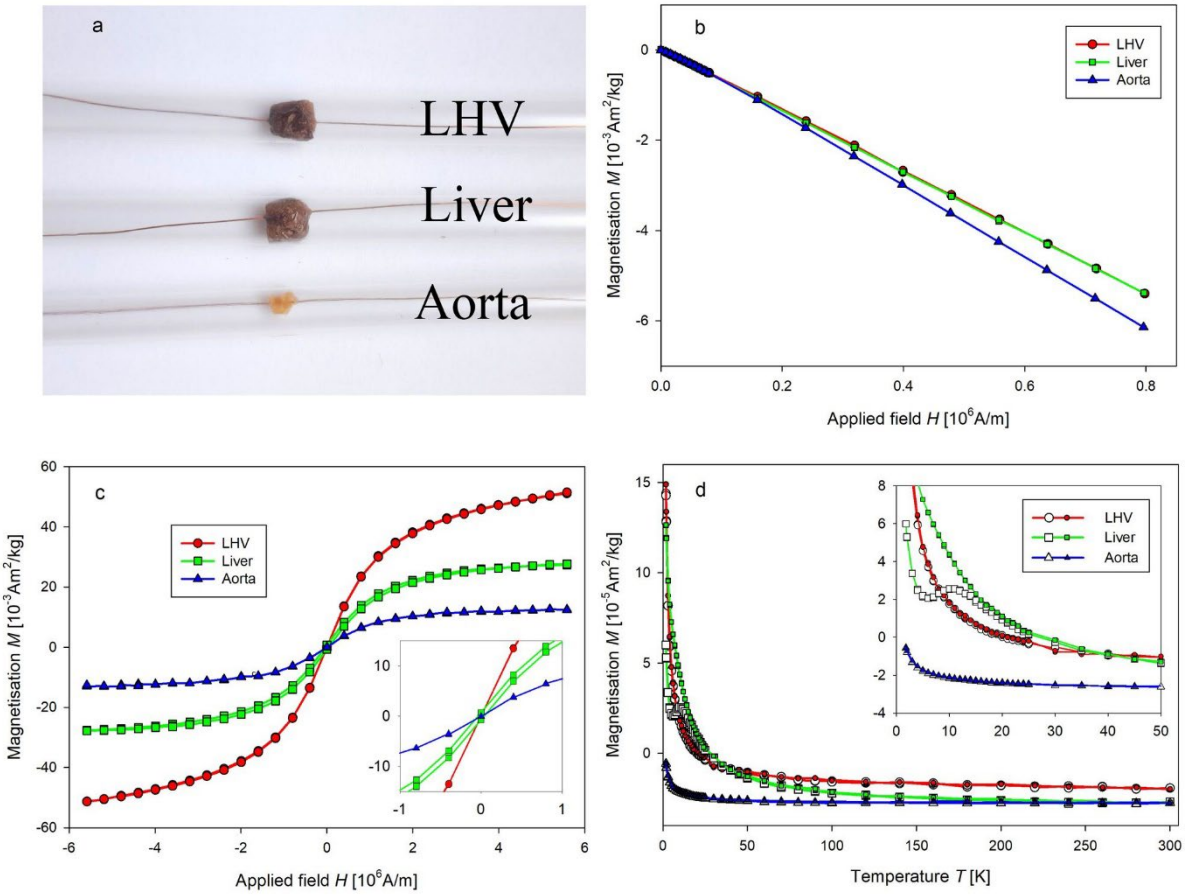

Fig. 1. a) Example of prepared samples attached to a wire and placed in a measuring straw; b) parts of $M(H)$ curves measured at 300 K for the LHV, liver and aorta samples; c) $M(H)$ curves measured at 2 K, inset shows the enlarged part in the centre of the curves; d) ZFC (open symbols) and FC (full symbols) parts of $M(T)$ curves, inset shows the enlarged part in the low-temperature region. Each curve represents an average of 5 samples measured.

Table 1. Saturation magnetisation MS and coercivity HC measured at 2 K and dry weight for samples of LHV, liver and aorta. Results are presented as mean ± SEM.

Sample	M_S [10^{-3}Am^2/kg]	H_C [10^3A/m]	Sample dry weight [mg]
LHV	51.0 ± 2.8	1.3 ± 0.3	19.2 ± 1.3
Liver	27.3 ± 0.9	38.2 ± 0.3	15.9 ± 0.9
Aorta	12.7 ± 0.6	N.A.	3.9± 0.5

4. Discussion

The proposed solution for preparing samples for SQUID magnetometry is functional and simple. It enables the preparation of samples in large series. The samples have the required geometry and fixed position, which enables repeatability of use. And since the samples are dried, they are not perishable and can be stored for a long time at laboratory temperature. However, the aorta samples, which were approximately 1 cm long before preparation, are close to the limit of sensitivity of the used magnetometer. It was not possible to read the values of H_C from the hysteresis loops measured at 2 K. $M(H)$ curves of all tissues measured at 300 K have only limited applicability in the detection of biogenic iron, as diamagnetism is more pronounced

at this temperature. But this type of measurement allows rapid screening of samples and was successfully used in the quantification of iron oxide nanoparticles in rat tissues [5]. Measured $M(H)$ curves at 2 K bring more light to the iron qualification. Much higher H_C in the case of liver tissue indicates the presence of another type of biogenic iron. M_S can be used as a measure of the relative concentration of iron between the same type of tissue [4], but probably cannot be used to compare the contents between two different types of tissues since they contain different magnetic forms of iron. Measurement of $M(T)$ dependences showed in all tissues the presence of paramagnetic iron-containing species, very likely in the form of haemoglobin [2]. But in the liver tissues, a very significant contribution arises from superparamagnetic iron behaviour with a blocking temperature of 11 K, which is indicative of ferritin-like iron. This type of measurement is likely to be most helpful in determining the type of biogenic iron and together with the measurement of hysteresis curves could be used also for the quantification of its various forms.

5. Conclusions

In this paper, the method of detection and classification of biogenic iron in tissues of normotensive WKY male rats is presented. Simple sample mounting and stabilization procedure allows the creation of geometrical and time-stable samples. The use of SQUID magnetometry procedure enables the detection of different types of biogenic iron and in the future, it could also provide data on the content of its different forms in the examined tissues.

Acknowledgements

The financial support of this work by the projects VEGA 2/0157/21 and VEGA 2/0141/21 is gratefully acknowledged.

References

[1] Miranda, J.L.A., Mesquita, R.B.R., Leite, A., Silva, A.M.N., Rangel, M., Rangel, A.O.S.S. (2023). Non-transferrin-bound iron determination in blood serum using microsequential injection solid phase spectrometry–proof of concept. *Talanta*, 257, 124345.

[2] Gutiérrez, L., Spasić, M.V., Muckenthaler, M.U., Lázaro, F.J. (2012). Quantitative magnetic analysis reveals ferritin-like iron as the most predominant iron-containing species in the murine Hfe-haemochromatosis. *Biochimica et Biophysica Acta (BBA) - Molecular Basis of Disease*, 1822(7), 1147-1153.

[3] Hautot, D.; Pankhurst, Q.A.; Dobson, J. (2005). Superconducting quantum interference device measurements of dilute magnetic materials in biological samples. *Rev. Sci. Instrum*., 76, 045101.

[4] Kluknavsky, M., Balis, P., Škrátek, M., Maňka, J., Bernátová, I. (2020). (–)-Epicatechin Reduces the Blood Pressure of Young Borderline Hypertensive Rats During the Post-Treatment Period. *Antioxidants*, 9, 96.

[5] Škrátek, M., Dvurečenskij, A., Kluknavský, M., Barta, A., Bališ, P., Mičurová, A., Cigáň, A., Eckstein-Andicsová, A., Maňka, J., Bernátová, I. (2020). Sensitive SQUID Bio-Magnetometry for Determination and Differentiation of Biogenic Iron and Iron Oxide Nanoparticles in the Biological Samples. *Nanomaterials*, *10*, 1993.

Theoretical Problems of Measurement

ISBN 978-80-972629-6-9

Peculiarities of Measurement Uncertainty Evaluation At Calibrating a Ring Gauge

[1]Igor Zakharov, [1]Olesia Botsiura, [2]Dimitar Diakov, [3]Dariusz Świsulski

[1]Kharkov National University of Radio Electronics, Kharkov, Ukraine
[2] Technical University of Sofia, Sofia, Bulgaria
[3] Gdansk University of Technology, Gdansk, Poland
Email: newzip@ukr.net

Abstract. *Example S13 from EA-4/02 M:2013 "Calibration of a ring gauge with a nominal diameter of 90 mm" is analyzed. The report uses the kurtosis method and the law of propagation of expanded uncertainty developed by the authors to the expanded uncertainty evaluation. It is shown that the introduction of a coaxiality correction for the ring gauge and the measuring axis of the comparator leads to the need to estimate its standard measurement uncertainty using the second-order terms of the Taylor series and taking into account the kurtosis of input quantities using the method of partial increments. A good agreement between the results obtained by applying the described procedure and the results obtained by the Monte Carlo method is shown.*

Keywords: Measurement Uncertainty, Kurtosis Method, Calibration, Ring Gauge

1. Introduction

Standard ISO 17025-2017 [1] (sec. 7.8.6) provides for the possibility of introducing into the calibration certificate of a measuring instrument (MI) the decision whether a calibrated MI is in compliance with metrological requirements. This decision must be made taking into account the expanded measurement uncertainty [2]. Therefore, the level of risk (for example, a false positive or false negative decision) related to an applied compliance decision rule will depend on the precision of the expanded uncertainty evaluation [1], 7.8.6.1. A reliable estimate of the expanded uncertainty cannot be obtained without taking into account the laws of distribution of input quantities [3], which is usually done by the Monte Carlo method (MCM) [4]. To solve this problem, the authors proposed the kurtosis method (KM) and expanded uncertainty propagation law (EUPL) [5]. Their application makes it possible to automate the uncertainty calculation, while the estimates of the expanded uncertainty will be close to the estimates obtained by the MCM. Supplement 2 of document EA-4/02 M:2013 [6] considers examples for situations where the measurement uncertainty budget is dominated by one or two abnormal contributions, which makes it impossible to use the coverage factor k=2 when expanded uncertainty evaluation. For examples S9-S12, the application of the kurtosis method was considered by the authors in [3, 7]. Below we will consider the use of the proposed methods for measurement uncertainty evaluation at calibration of a ring gauge (example S13 from Supplement 2 [6]).

2. Subject and Methods

The diameter d_X of the ring to be calibrated at the reference temperature is obtained from the relationship S13.1 [6]:

$$d_X = d_S + \Delta l + \delta l_i + \delta l_T + \delta l_P + \delta l_E + \delta l_A ,$$

where d_X is diameter of the reference setting ring at the reference temperature, Δl is observed difference in displacement of the measuring spindle when the contact tips touch the inner surface of the rings at two diametrically apart points; δl_i is correction for the errors of indication of the comparator; δl_T is correction due to the temperature effects of the ring to be calibrated, the reference setting ring and the comparator line scale; δl_P is correction due to coaxial misalignment of the probes with respect to the

ISBN 978-80-972629-6-9

measuring line; δl_E is correction due to the difference in elastic deformations of the ring to be calibrated and the reference setting ring, δl_A is correction due to the difference of the Abbe errors of the comparator when the diameters of the ring to be calibrated and the reference setting ring are measured.

Since the quantity Δl is measured by carrying out n repeated measurements, taking into account the recommendations of [8], this expression should be rewritten as:

$$d_X = d_S + (\Delta l + \varepsilon_{\Delta l}) + \delta l_i + \delta l_T + \delta l_P + \delta l_E + \delta l_A, \tag{1}$$

where $\varepsilon_{\Delta l}$ is correction for a random error, the value of which $\hat{\varepsilon}_{\Delta l} = 0$ and the standard uncertainty is determined by the formula [5]:

$$u(\varepsilon_{\Delta l}) = \sqrt{\frac{1}{n(n-1)} \sum_{q=1}^{n} (\Delta l_q - \overline{\Delta l})^2} \sqrt{\frac{n-1}{n-3}}, \tag{2}$$

and $\overline{\Delta l}$ is estimated as the arithmetic mean of repeated measurements:

$$\overline{\Delta l} = \frac{1}{n} \sum_{q=1}^{n} \Delta l_q \,. \tag{3}$$

To improve the accuracy of the calculations, the standard uncertainties of the input quantities were refined based on the data given in example S13 [6]. For the results of five-time measurements of Δl given in S13.9 [6], $\overline{\Delta l}$ =49.999536 mm and $u(\varepsilon_{\Delta l})$ =0.2073 μm. With this quantity Δl, we attribute the standard uncertainty $u(\Delta l)$ =0.2898 μm, associated with the zero setting of the comparator readings, which was determined a priori. Standard uncertainties $u(\delta l_i)$ $u(\delta l_E)$, and $u(\delta l_A)$ calculated with accurate to fourth significant digit. Therefore, $u(d_x)$ will be equal to 0.4048 μm (Table 1) and not 0.433 as in S13.10 [6].

Table 1. Refined Measurement Uncertainty Budget S13.10 [6]

X_i	x_i	$u(x_i)$	PDF	c_i	$u_i(y)$
d_S	40.000 7 mm	0.10 μm	normal	1.0	0.10 μm
Δl	49.999 536 mm	0.2898 μm	normal	1.0	0.2898 μm
δl_i	0.0 mm	0.2165 μm	rectangular	1.0	0.2165 μm
δl_T	0.0 mm	0.15 μm	normal	1.0	0.15 μm
δl_P	0.000 004 mm	0.0065 μm	rectangular	1.0	0.0065 μm
δl_E	0.0 mm	0.01732 μm	rectangular	1.0	0.01732 μm
δl_A	0.0 mm	0.01154 μm	rectangular	1.0	0.01154 μm
Y	y	$u(y)$	p	k	U
d_X	90.000 24 mm	0.4048 μm	0.9545	2	0.8095 μm

Thus, the expanded uncertainty for the confidence level p = 0.9545 is 2·0.4048=0.81 μm. For p = 0.95, it will be, respectively, 1.96·0.4048=0.79 μm.

Uncertainty budgets constructed in accordance with the EUPL for the confidence level p=0.9545 are presented in Table 2 and 3. Expanded uncertainty in Table 2 was calculated by the kurtosis method [5] according to the formula

$$U_B = k \cdot u_B(d_X), \tag{4}$$

in which the coverage factor depending on the level of confidence p was calculated as:

$$k_B = \begin{cases} 0{,}1085\eta_B^3 + 0{,}1\eta_B + 1{,}96, & \text{for } p = 0{,}95; \\ 0{,}12\eta_B^3 + 0{,}1\eta_B + 2, & \text{for } p = 0{,}9545, \end{cases} \tag{5}$$

ISBN 978-80-972629-6-9

where η_B is the kurtosis of the measurand, calculated according to the data in Table 2.

Table 2. Measurement Uncertainty Budget for Type B Components

X_i	x_i	$u(x_i)$	$\eta(x_i)$	c_i	$u_i(y)$
d_S	40.000 7 mm	0.10 µm	0	1.0	0.10 µm
Δl	49.999 536 mm	0.25 µm	0	1.0	0.25 µm
δl_i	0.0 mm	0.2165 µm	-1.2	1.0	0.2165 µm
δl_T	0.0 mm	0.15 µm	0	1.0	0.15 µm
δl_P	0.000 004 mm	0.0065 µm	-1.2	1.0	0.0065 µm
δl_E	0.0 mm	0.01732 µm	-1.2	1.0	0.01732 µm
δl_A	0.0 mm	0.01154 µm	-1.2	1.0	0.01154 µm
Y	y	$u_B(y)$	$\eta(y)$	k	U_B
d_X	90.000 24 mm	0.3773 µm	-0.105	1.989	0.7506 µm

Table 3. Measurement Uncertainty Budget for Random Errors

X_i	x_i	$u(x_i)$	ν_i	c_i	$u_i(y)$
$\varepsilon_{\Delta l}$	0	0.2073 µm	4	1	0.2073 µm
Y	$\hat{\varepsilon}$	$u_A(\hat{\varepsilon})$	p	$t_{p;(n-1)}$	U_A
ε	0	0.2073 µm	0.9545	2.869	0.4206 µm

Expanded uncertainty U_A in Table 3, was calculated by EUPL [5] using the formula:

$$U_A = t_{p;(n-1)} \cdot c \cdot u(\varepsilon_{\Delta l}) \sqrt{(n-3)/(n-1)}\,, \tag{6}$$

where $t_{p;(n-1)}$ is the Student's coefficient for the probability p and the number of degrees of freedom $\nu = n-1$. The total expanded measurement uncertainty will be calculated using the formula [5]:

$$U(d_x) = \sqrt{U_B^2 + U_A^2}\ . \tag{7}$$

From the data given in tables 2, 3 them, in accordance with the EUPL, we have a standard uncertainty of 0.43 µm and an expanded uncertainty of 0.86 µm for p=0.9545 and 0.84 µm for p=0.95.

An estimate of the measurement uncertainty by the Monte Carlo method is obtained using the program [9]. The combined standard and expanded measurement uncertainties for p=0.95 are 0.43 µm and 0.8365 µm, respectively. Comparison of the results obtained by various methods is given in table. 4

Table 4. Calculation results obtained by different methods

Method	y	$u(y)$	U	k
EA-4/02	90.00024	0.4048	0.7933	1.96
EUPL	90.00024	0.4305	0.8406	1.953
MMC	90.00026	0.43	0.837	1.947

When calibrating a ring gauge with a length comparator, a specific error occurs due to misalignment between the ring gauge and the measuring axis of the comparator (Fig. 1). The chord length d_1 observed during the measurement is related to the diameter of the ring d by the following relation:

$$\frac{d}{2} = \sqrt{\left(\frac{d_1}{2}\right)^2 + \delta_c^2} = \frac{d_1}{2}\sqrt{1 + \frac{4\delta_c^2}{(d_1)^2}} \approx \frac{d_1}{2} + \frac{\delta_c^2}{D}\,, \tag{8}$$

ISBN 978-80-972629-6-9

where D is the nominal value of the ring diameter.

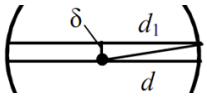

Fig.1. Misalignment of the ring gauge and the measuring axis of the comparator

Using the method of partial increments, we get:

$$\Delta d = \hat{d} - \hat{d}_1 = 2\{[\hat{\delta} + u(\hat{\delta})]^2 + [\hat{\delta} - u(\hat{\delta})]\}^2 / 2D = 2[\hat{\delta} + u(\hat{\delta})]^2 / D, \quad (9)$$

those the estimate d for $\hat{\delta}_c = 0$ will be equal to:

$$\Delta d = 2u^2(\hat{\delta}) / D. \quad (10)$$

Expression for unbiased estimate of the measurand derived from recommendations [6]:

$$u(\Delta d) = 2u^2(\delta)\sqrt{\eta(\delta) + 2} / D = \Delta d \sqrt{\eta(\delta) + 2}. \quad (11)$$

For the given in [6] values: $D_X =$ 90 mm, $\delta = \pm 20\ \mu m$, and the uniform PDF of δ, we have $u(\delta) = 11.5\ \mu m$, $\eta(\delta) = -1.2$, and we obtain $\Delta d = 0.003\,\mu m$ and $u(\Delta d) = 0.0027\,\mu m$.

3. Results

Measurement uncertainty evaluation at calibrating of ring gauge with an Abbe comparator is considered based on the approaches outlined in the COOMET R/GM/35:2022 recommendation: the kurtosis method, the law of propagation of expanded uncertainty, the method of partial increments, the method of finding the bias of the estimate of the standard uncertainty of the measurand for a nonlinear model with taking into account the kurtosis of input quantities. The measurement uncertainty estimate obtained using the MCM differs by 1% from the estimate by the proposed methods and by 6% from the estimate obtained by the [6].

References

[1] ISO/IEC 17025:2017 General requirements for the competence of testing and calibration laboratories.

[2] OIML G 19:2017 The role of measurement uncertainty in conformity assessment decisions in legal metrology.

[3] Botsiura O.A., Zakharov I.P. (2020). Increasing the Reliability of Evaluation of Expanded Uncertainty in Calibration of Measuring Instruments // Measurement Techniques, Volume: 63, Issue: 6, pp. 414-420.

[4] JCGM GUM-7 Guide to the expression of uncertainty in measurement – Part 7: Propagation of distributions using a Monte Carlo method.

[5] COOMET R/GM/35:2022 Expression of the expanded measurement uncertainty (method of kurtosis).

[6] EA-4/02 M: 2013. Evaluation of the Uncertainty of Measurement in Calibration.

[7] Zakharov I., Serhiienko M., Chunikhina T. (2020). Measurement uncertainty evaluation by kurtosis method at calibration of a household water meter // Metrology and Metrology Assurance (MMA-2020): Proceedings of 2020 XXX International Scientific Symposium, Sozopol, Bulgaria, 7-11 Sept. 2020, pp. 83-86.

[8] JCGM GUM-6:2020 Guide to the expression of uncertainty in measurement – Part 6: Developing and using measurement models.

[9] https://uncertainty.nist.gov/

ISBN 978-80-972629-6-9

OEFPIL: New Method and Software Tool for Fitting Nonlinear Functions to Correlated Data With Errors in Variables

[1]Radek Šlesinger, [1]Anna Charvátová Campbell,
[2]Zdeňka Geršlová, [2]Vojtěch Šindlář, [2,3]Gejza Wimmer

[1]Czech Metrology Institute, Brno, Czech Republic,
[2]Masaryk University, Brno, Czech Republic,
[3]Mathematical Institute of Slovak Academy of Sciences, Bratislava, Slovakia,
Email: rslesinger@cmi.cz

Abstract. *We present a new method, called OEFPIL, as well as its software implementation for nonlinear function fitting to data with errors in variables where correlation, both within variables and among variables, might be present. In principle, OEFPIL can be employed for fitting both explicit and implicit functions of any number of variables. Importantly, apart from the parameter estimates, OEFPIL also yields their covariance matrix, required for further analyses. Multiple comparisons with existing methods on various types of problems, some of which are presented in this paper, have shown excellent agreement between OEFPIL and other methods.*

Keywords: Function Fitting, Nonlinear Regression, Errors in Variables, Correlated Data

1. Introduction

Evaluation of measurement of mechanical properties of materials using the instrumented indentation technique [1] heavily depends on fitting some data by a non-straight curve.

First, it is fitting the load- (F) and depth- (h) sensor data by a nonlinear function. A typical case is the method due to Oliver and Pharr [2], allowing to determine material hardness and elastic modulus based on the parameters α, h_p, and m of the relation $F(h) = \alpha(h - h_\mathrm{p})^m$. For the finest measurement range with maximum loads and depths not exceeding units of millinewtons and hundreds of nanometers, sensor noise can be noticeable for both load and depth data. Common nonlinear least squares regression tools, as provided e.g. by Levenberg-Marquardt or Gauss-Newton method, need not be adequate for such data with errors in both variables. If calibration of the sensors is available, data may be equipped with additional covariance information.

Second, parameters of the so-called indenter contact area function have to be determined in order to evaluate the area of contact between the indenter and the sample. When properly evaluated, such data exhibit correlation among all y-values as well as correlations for individual (x_i, y_i) pairs.

The authors were thus searching for a method able to handle all the aspects given above.

2. Subject and Methods

A new method named *OEFPIL* (Optimum Estimate of Function Parameters by Iterated Linearization) has been proposed to suit the problems presented above as a further development of the approach presented in [3]. It is based on iterative restating of the nonlinear regression problem as a linear model with nonlinear constraints on parameters and variables, linearizing the constraints by their Taylor expansion around the current estimate, and applying the linear model theory presented in [4] to improve the estimate of the parameters in each iteration.

The user (programmer of the application calling the library) provides a procedure that computes function values (both explicit or implicit functions can be treated) as well as values of

ISBN 978-80-972629-6-9

first-order derivatives along all variables and parameters, the initial parameter estimates, and the actual data together with their covariance matrix. On successful convergence, OEFPIL yields the estimates of function parameters and their covariance matrix. The weighted sum of squared residuals

$$S = \begin{pmatrix} \mathbf{x} - \mathbf{x}^* \\ \mathbf{y} - \mathbf{y}^* \end{pmatrix}^\top \Sigma^{-1} \begin{pmatrix} \mathbf{x} - \mathbf{x}^* \\ \mathbf{y} - \mathbf{y}^* \end{pmatrix}$$

can also be calculated, although this quantity is not subject to minimization in OEFPIL.

As we focus on efficient implementation of the algorithm, there are multiple modes for representing the covariance matrix to facilitate efficient storage and matrix operations (tiles for covariance in a pair of variables; covariance matrices on diagonal). This allows for a significant speedup when the covariance of data is not assumed to be completely general.

3. Results

The first implementation of OEFPIL has been written for the R statistical software, and made available later as a freely available package [5]. Based on the implementation in R, a standalone library written in C programming language has been created [6], where current development takes place. This library should eventually allow easy integration into third-party software tools, and is also accompanied with an executable tool for demonstration and testing.

We have compared the performance of OEFPIL to other methods or software tools based on reference data and results presented by the respective authors. The comparisons, some of which we present here, have shown very good agreement between OEFPIL and the other methods.

Pearson's data with York's weights

This data set is a classical example of a weighted straight-line fit by $f(x) = ax + b$ to a collection of points, with all x- and y-values having a prescribed weight, with no additional correlation. This problem has been solved in a number of papers (see e.g. [7], [8]). For OEFPIL, the weights have been converted to variances using the common weighing scheme $\sigma^2(x_i) = \frac{1}{w(x_i)}$. Comparison with some of the solutions available is provided in Table 1.

Table 1: Pearson's data with York's weights: straight-line fit, x- and y-values weighted.

	Exact solution	Lybanon [7]	Puchalski [8]	OEFPIL
a	-0.480 533 407	-0.480 533 415	-0.480 533 37	-0.480 533 407
b	5.479 910 22	5.479 910 25	5.479 910 07	5.479 910 22
$u(a)$			0.057 617 55	0.057 985 01
$u(b)$			0.291 935 82	0.294 970 74
ρ_{ab}			-0.962 304 11	-0.963 088 14
S	1.866 353 194 1	1.866 353 194 1		1.866 353 194 1

Surface brightness and Sérsic index of galaxies

An example of a straight-line $(f(x) = ax + b)$ fit to data from astronomy observations, with correlations for (x_i, y_i) present, was studied in [9]. Table 2 shows a slight difference between OEFPIL and the method presented, but the estimated parameters still match within uncertainties.

ISBN 978-80-972629-6-9

Table 2: Surface brightness and Sérsic index of galaxies: straight-line fit, correlation between x_i and y_i.

	Amen [9]	OEFPIL
a	1.174 2	1.176 2
b	-21.911 1	-21.955 3
$u(a)$	0.000 8	0.016 6
$u(b)$	0.144 4	0.368 2
σ_{ab}	3.337 E-04	-6.065 E-03

Flow meter calibration

A WTLS (weighted total least squares) algorithm implemented in CCC (Calibration Curve computing) software version 2.0 was demonstrated in [10] on data from a flow meter calibration. The function to be fitted is $f(x) = ax^{-1} + bx^{-0.5} + c + dx^{0.5} + ex$ (nonlinear in x, linear in parameters), and the covariance matrix for x-values is nondiagonal, consisting of two full blocks originating from the use of two test benches. Table 3 provides the comparison.

Table 3: Flow meter calibration: function linear in parameters, nontrivial covariance for x.

	CCC 2.0	OEFPIL		CCC 2.0	OEFPIL
a	-14.474 789 9	-14.474 854 7	$u(a)$	1.758 48 E+00	1.758 61 E+00
b	-9.589 981 1	-9.589 982 5	$u(b)$	1.238 77 E+00	1.238 74 E+00
c	4.795 202 7	4.795 205 7	$u(c)$	2.385 13 E-01	2.385 03 E-01
d	-0.192 837 0	-0.192 837 2	$u(d)$	1.106 82 E-02	1.106 79 E-02
e	0.001 526 9	0.001 526 9	$u(e)$	1.340 76 E-04	1.340 74 E-04
S	5.305 675 2	5.305 721 6			

Pseudo-Cassinian curve

A method and an associated software tool COLSGN presented in [11] allow fitting of both implicit and explicit nonlinear functions to data where correlation between x_i and y_i can be present. As one of examples, nonlinear implicit fit of a pseudo-Cassinian curve, given by equation

$$F(x,y) = \left[(x-x_1)^2 + (y-y_1)^2\right] \cdot \left[(x-x_2)^2 + (y-y_2)^2 \cdot b\right] - a = 0$$

to a collection of points in plane was demonstrated. The x_i-y_i correlation in this example comes from converting polar coordinates with uncertainties to Cartesian system. Comparison between COLSGN and OEFPIL is shown in Table 4.

Table 4: Pseudo-Cassinian curve: implicit nonlinear function, correlation between x_i and y_i.

	COLSGN	OEFPIL		COLSGN	OEFPIL
x_1	-3.246 408 5	-3.246 408 6	$u(x_1)$	0. 4386	0.7624
y_1	7.606 215 9	7.606 215 9	$u(y_1)$	0.1616	0.5560
x_2	5.097 509 9	5.097 509 9	$u(x_2)$	0.1929	0.3934
y_2	3.855 190 1	3.855 190 1	$u(y_2)$	0.2832	0.5256
a	437.692 47	437.692 48	$u(a)$	48.76	168.9
b	0.376 844 61	0.376 844 61	$u(b)$	0.1324	0.1644
S	3.469 719 340 38	3.469 719 340 38			

ISBN 978-80-972629-6-9

4. Discussion

OEFPIL has been demonstrating almost perfect match in function parameter estimation when compared to other methods. The estimates of parameter covariance/correlation can differ in some comparisons, which can be attributed to different approaches to their estimation.

However, the full potential of OEFPIL has not been validated yet due to absence of reference data and solutions, namely for nonlinear problems with correlated data.

Work is still ongoing on making the computer implementation efficient and well-performing from the numerical point of view, as well as on designing a convenient function interface to allow other developers to integrate OEFPIL in their software easily.

Acknowledgements

Project TJ02000203 "Advanced mathematical and statistical methods in evaluating instrumented indentation measurements" was solved with financial support from the Technology Agency of the Czech Republic within the Zéta 2 programme. Project "Efficient computation methods for nanoscale material characterization" has been supported by the Ministry of Education, Youth and Sports of the Czech Republic within the INTER-EXCELLENCE II programme.

References

[1] Fischer-Cripps, A. (2011). *Nanoindentation*, Mechanical Engineering Series. New York: Springer-Verlag.

[2] Oliver, W. C., Pharr, G. M. (1992). An improved technique for determining hardness and elastic-modulus using load and displacement sensing indentation experiments. *J Mater Res* 7, 1564–1583.

[3] Köning, R., Wimmer, G., Witkovský, V. (2014). Ellipse fitting by nonlinear constraints to demodulate quadrature homodyne interferometer signals and to determine the statistical uncertainty of the interferometric phase. *Meas Sci Technol* 25(11).

[4] Kubáček, L. (1988). *Foundations of Estimation Theory*, Vol. 9 of *Fundamental Studies in Engineering*. North Holland: Elsevier.

[5] Geršlová, Z., Šindlář, V., Zámečník, S. (2021). OEFPIL R package. Available at https://github.com/OEFPIL/OEFPIL/.

[6] Wimmer, G., Geršlová, Z., Šindlář, V., Šlesinger, R. (2021). OEFPIL C library. Available at https://gitlab.com/cmi6014/oefpil/.

[7] Lybanon, M. (1984). A better least-squares method when both variables have uncertainties. *American Journal of Physics* 52, 22–26.

[8] Puchalski, J. G. (2021). A new algorithm for generalization of least square method for straight line regression in cartesian system for fully correlated both coordinates. *International Journal of Automation, Artificial Intelligence and Machine Learning* 2, 20–54.

[9] Amen, S. K. (2012). Linear estimation for data with error ellipses. Master's thesis, University of Texas at Austin.

[10] Lecuna, M., Pennecchi, F., Malengo, A., Spazzini, P. G. (2020). Calibration curve computing (CCC) software v2.0: a new release of the INRIM regression tool. *Meas Sci Technol* 31.

[11] Celmiņš, A. (1973). Least-squares adjustment with finite residuals for non-linear constraints and partially correlated data. Technical report, USA Ballistic Research Laboratories.

Measurement of Physical Quantities I

ISBN 978-80-972629-6-9

Measurement of Frequency Dependence of Self-Inductance of Power Capacitors

Zdeněk Roubal, Tomáš Kříž, Tibor Bachorec

Department of Theoretical and Experimental Electrical Engineering, FEEC, BUT, Technická 3082/12, 616 00 Brno; Czech Republic,

Email: roubalz@vutbr.cz

Abstract. *Power polypropylene capacitors are an essential element of power converters and power quality conditioning equipment. Another major area of application is high power switching power supplies for powering drives. Real capacitors are not only representative of electrical capacitance, their parasitic parameters, especially the equivalent series inductance (ESL), can significantly affect the operation of switching power supplies. Conductive couplings are another important source of this inductance. Usually, a substitution scheme corresponding to a series resonant circuit is given for the capacitor, but by the measurements given in the paper, we can clearly see that ESL is frequency dependent, as is equivalent series resistance (ESR).*

Keywords: Power Capacitors, Polypropylene Capacitors, Self-Inductance, Equivalent Series Resistance, Replacement Capacitor Model

1. Introduction

There are several methods to measure the self-inductance of a capacitor [1], [2]. From the point of view of the accuracy of measuring very small capacitor self-inductance in the order of tens of nH, the method of measuring the frequency dependence of the capacitor impedance was chosen. The capacitor is excited by a signal of one frequency during the measurement, which gives unambiguously interpretable results applicable also for possible simulations and calculations in the case of frequency-dependent self-inductance of the capacitor.

For the measured capacitor we consider the model with lumped parameters in Fig. 1. At a low frequency of 50 Hz the capacitor is measured for its loss factor tg δ, here the parallel combination of capacitance *C* and conductance *G* is crucially applied in the model. The impedance of the self-inductance *L* and the series resistance *R* are negligible with respect to them.

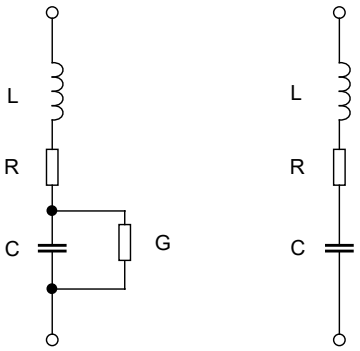

Fig. 1. The capacitor model with lumped parameters (left) and its simplification for the working range of measured high frequencies (right).

ISBN 978-80-972629-6-9

At higher frequencies, the capacitance impedance C decreases and the capacitor's self-inductance L and series resistance R become the decisive components of the total impedance of the capacitor. The conductance G is short-circuited by the capacitance of the capacitor, so it can be neglected at higher frequencies.

2. Design of the Measuring Configuration

The modulus of the measured capacitor impedance for the measured frequencies (10 kHz to 1 MHz) is in the range 1 mΩ to 10 Ω, so it is necessary to use a four-wire connection of the measured capacitor so that the impedance of the supply wires and connection contacts is not applied. For this reason, fixtures for the specific capacitor type have been developed in the form of a printed circuit board. Each designed circuit board has contact plates for voltage and current contacts placed according to the specific drawing of the power polypropylene capacitor. Since the capacitor types to be measured are connected to the circuit either via a nut or a screw, and this connection element would contribute its impedance to the measured impedance of the capacitor, advantage was taken of the fact that in most types the screw plate contact is accessible (Figure 2). The current terminal is on the top of the plate and a mounting nut or bolt is screwed onto it with a defined torque specified by the manufacturer for each type manufactured. A torque wrench was used for repeatability of measurements. The voltage clamp is then on the other side of the plate and is pressure connected to the contact of the screw plate. (Figure 3.). The design on the PCB is shown in Figure 4.

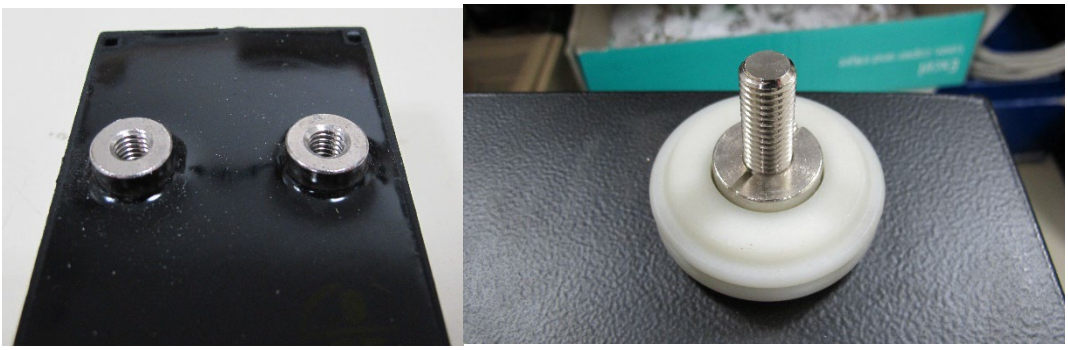

Fig. 2. Contacts of screw terminals.

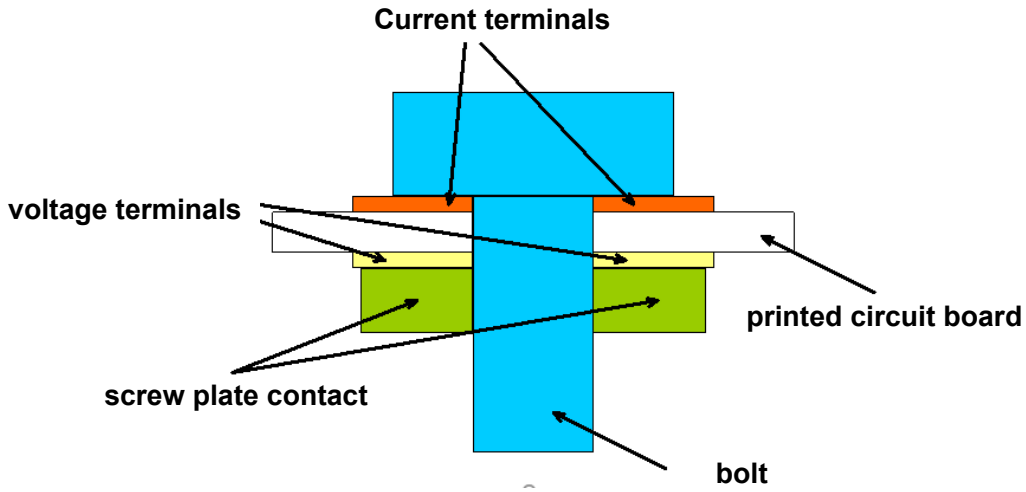

Fig. 3. Arrangement of current and voltage terminals on measuring fixtures for suppressing the impedance of the screw connection

ISBN 978-80-972629-6-9

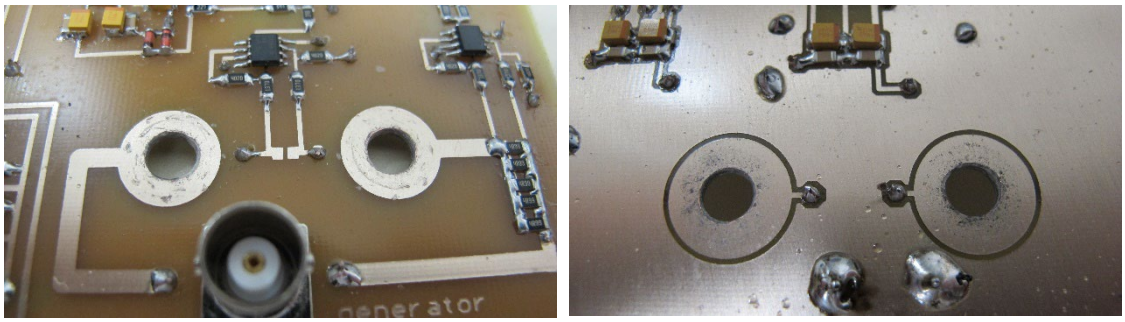

Fig. 4. Current clamps on the top of the PCB (left) and voltage clamps on the bottom of the PCB (right)

The overall proposed measurement arrangement is shown in Fig. 5.The generator is a source of harmonic signal with sufficient maximum excitation level U_{out}=20 V Up-p. Since it has an output resistance of 50 Ω, the measured circuit is essentially powered from a current source. From its output, the capacitor to be measured is excited in series with a 0.998 Ω shunt to measure the current. The voltage on the measured capacitor and shunt is amplified by identical differential amplifiers with gain A=2.921. Their frequency characteristics are very similar due to the identical circuit and the used OA OPA842, which is advantageous in the calculation of impedance, where the same deviations in both channels are shorted. The difference in the modulus and phase characteristics of the two channels is mainly due to the subsequent amplifier in the voltage channel with gain A=10, which is used to increase the level of the measured voltage, since the oscilloscope used does not have the necessary sensitivity. A logarithmic converter is added at the output of the voltage channel for possible more accurate measurements at low levels of the measured voltage. Its DC output voltage is proportional to the logarithm of the AC input voltage.

Precision low-noise resistors with a tolerance of 0.1% are used in the differential amplifiers to suppress consonant noise. The required type of differential amplifier with sufficient frequency bandwidth is not available, so the option of using a conventional low noise and fast OZ type OPA842 along with high precision resistors was chosen.

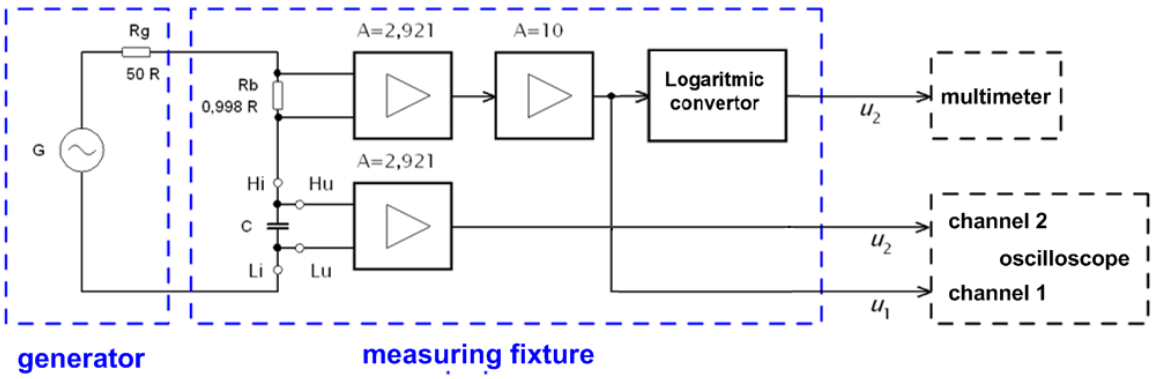

Fig. 5. Block diagram of the measuring setup

3. Results

For the PVAJP 341-1.1/800 capacitor, the frequency dependence of its self-inductance and series resistance was measured from 10 kHz to 1 MHz.

ISBN 978-80-972629-6-9

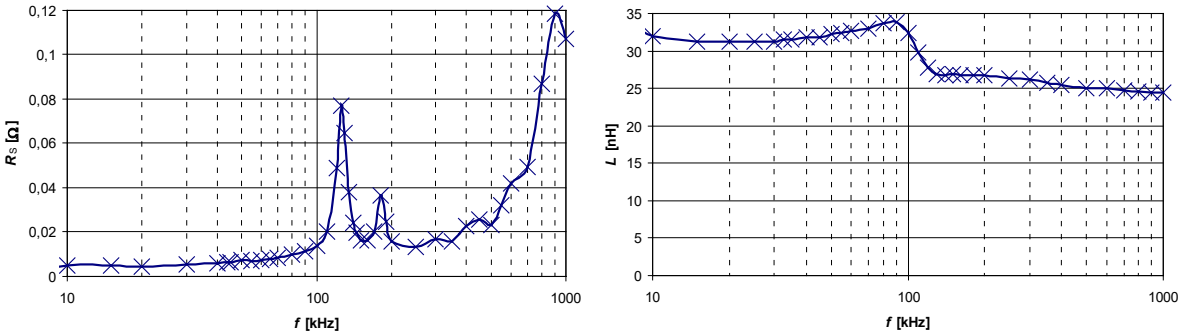

Fig. 6. Frequency characteristic of ESR (left) and ESL (right) of PVAJP 341-1,1/800 capacitor

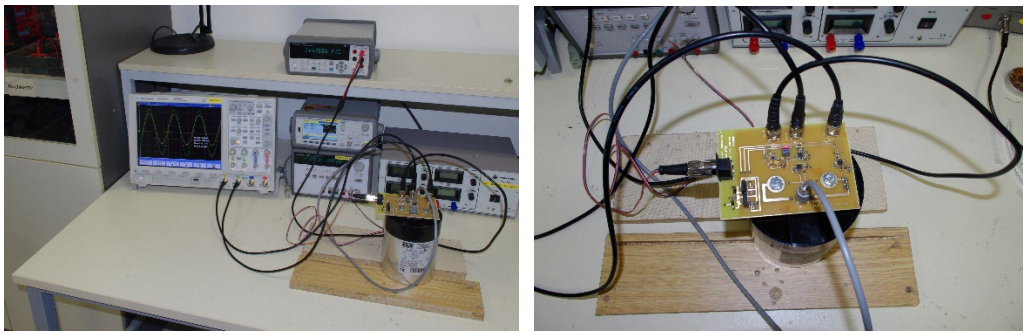

Fig. 7. Measurement of PVAJP 341-1,1/800 capacitor on the left and measuring fixture on the right

4. Conclusions

The proposed excitation signal connection and evaluation methodology gives high repeatability and the possibility of detecting unwanted resonances caused by the manufacturing design of the capacitors under test. The calibration was performed with a 50 mΩ SMD resistor and its self-inductance was measured along package 0805 2 nH. SMD inductances were also used and a flat frequency response was confirmed up to 10 MHz. The decrease in the self-inductance of the capacitor and the increase in the equivalent series resistance is due to the effect of eddy currents and has been described by the authors in [3]. Further research will aim to explain why the change from static to dynamic self-inductance is steeper than according to the ANSYS simulation.

Acknowledgements

The research was funded via a BD 2023-2025, FEKT-S-23-8425.

References

[1] Brubaker, M. A., Hosking, T. A., & Sawyer, E. D. (2012). Characterization of equivalent series inductance for dc link capacitors and bus structures. Proceedings of PCIM, Nuremberg, Germany. 1–6.

[2] Sawyer, E. D. (2010). Low Inductance-Low Temp Rise DC Bus Capacitor Properties Enabling the Optimization of High Power Inverters. Proceedings of PCIM 2010. 1–21.

[3] Kříž, T, Roubal, Z., T. Bachorec, & Prokopec, M. (2015). Numerická simulace a experimentální ověření parazitní indukčnosti výkonových kondenzátorů. In Sborník XXXIV. celostátní konference o elektrických pohonech. 1–6.

[4] Gescheidtová, E., Rez, J., & Steinbauer, M. (2002). Měření v elektrotechnice. Vysoké učení technické v Brně, Fakulta elektrotechniky a komunikačních technologií.

Measuring the Radiation Pattern of Large FM Antenna System

Michal Dzuris, Rene Hartansky, Jakub Krchnak

Slovak University of Technology, Faculty of Electrical Engineering and Information Technology, Institute of Electrical Engineering, Ilkovicova 3, 812 19 Bratislava, Slovakia, Email: michal.dzuris@stuba.sk

Abstract. *The article presents a radiation pattern measurement performed on a real antenna system delivering over 100 kW of effective radiated power (ERP) in the FM frequency band. The measurement of the received signal was performed by a custom measurement device, „Pixla 1“ with the use of a quadcopter DJI Matrice 300. This measurement resulted in the normalized radiation pattern characteristics of a given antenna system. Radiation pattern measurement was performed at various radii and at various heights with respect to the geometrical center of the antenna system.*

Keywords: Radiation Pattern, Quadcopter, Large Antenna System, FM

1. Introduction

Large antenna systems are used for the terrestrial broadcasting of analog or digital signals. In order to transmit the signal as efficiently as possible, antenna systems are mounted on tall objects and on high ground (the top of the hill) to increase the coverage area. When verifying the functionality or replacing the antennas of such antenna system, it is necessary to measure its properties, such as the radiation pattern. This measurement is challenging [1], because the measuring device must be elevated to the height of the antenna system and it must be selectively sensitive to the measured frequency band and resistant to the high-frequency radiation of other systems installed nearby. This is usually accomplished by an aerial helicopter measurement with a trained crew and the measurement equipment onboard. This type of helicopter measurement is expensive and time consuming. Radiation pattern measurements with a quadcopter and a specialized measurement device is not only cheaper, but also much faster. While the measurement of the radiation pattern using a helicopter has well developed measurement methodologies and procedures, due to the relatively recent introduction of capable quadcopters, the methodology for the measurement of the radiation pattern using a quadcopter is yet to be developed. The differences between helicopter and quadcopter measurements are not only in the radii in which the vehicle can measure around the antenna system, but they also have different attributes, such as maximum payload, geometry, flight distance, maneuverability, and many more. Measuring the 3D radiation pattern of such antenna system would be very complicated, therefore in general only horizontal and vertical cuts of the radiation pattern are measured. Due to the lack of methodology in radiation pattern measurement with a quadcopter, it is necessary to set the correct measurement height and distance from the antenna system itself. The goal of this paper is to present radiation pattern measurement with various measurement setups to find a suitable solution for quadcopter radiation pattern measurement.

2. Subject and Methods

The antenna system is mounted on a monotube (see Fig.1a) with eight anchor points distributed on two floors (under and above the antenna system) and in four azimuths. There is also a lower tower on site, in close proximity to the monotube, with antennas for other purposes. As a result, flight paths that would have resulted in a collision with this tower had to be omitted.

ISBN 978-80-972629-6-9

Horizontal radiation pattern measurement

Previous attempts to measure the radiation pattern of similar antenna systems failed due to the insufficient electromagnetic immunity of the measurement device [1]. With a new EMI-hardened measurement device („Pixla 1“) mounted under the quadcopter (see Fig.1b), we have managed to measure the signal strength at multiple points ($\sim$ 450 points).

(a) (b)

Fig. 1: (**a**) Measurement site - view of the monotube and a quadcopter with „Pixla 1“ in the background, (**b**) quadcopter with „Pixla 1“.

The measurement is performed at a constant radius R from the antenna system, while the receiving monopole antenna is always parallel to the tangent of a circular flight pattern. After the measurement, synchronization of the measured data to the position of the quadcopter as well as data analysis are essential to knowing not only the radiation pattern itself but also the rotation of the pattern with respect to the monotube. Acquired data is then filtered out, and a moving average is used to minimize the dispersion of measured data. The radiation pattern is then normalized. Two sets[1] of radiation pattern measurements are performed in order to confirm whether the measurement has already been conducted in the far-field region of the antenna system. If two normalized radiation patterns measured at different distances from the antenna system are very similar or even identical to each other, then we can state that they are the far-field radiation patterns of a given antenna system.

The first measurement of the horizontal radiation pattern shown in Fig.2a and in Fig.2b was performed at the height of the geometrical center of the antenna system with a constant flight radius of 50 meters and 150 meters, respectively. In Fig.2b data between 335° and 0° is inconsistent, which was caused by an error in the flight path. This error was revealed only after the on-site measurement. The three different color traces represent the three different measured frequencies[2]. It is clear, that Fig.2a and Fig.2b are very similar and thus the distances were set correctly. To prove that the measurement of the horizontal radiation pattern this close to the antenna system had to be done at the height of the center of the antenna system, measurements above and below[3] the antenna system were conducted as well.

In Fig.3a we can see that a low altitude flight near the monotube certainly can not represent a far-field radiation pattern of such antenna system. In Fig.3b it is clear that a far-field radiation pattern is forming, but there is still enough interference to cause an incorrect interpretation of the

[1]Each set representing one radiation pattern measurement at unique distance from the antenna system.

[2]Frequencies, that are transmitted by the antenna system.

[3]Data collection between 330 ° and 0 ° with a flight radius of 50 meters and height 30 below the antenna system center (see Fig.3a) was not possible, due to the collision of the flight path and the second antenna tower seen in Fig.1a.

ISBN 978-80-972629-6-9

radiation pattern. Horizontal radiation pattern measurements taken above the antenna system in Fig.4a and in Fig.4b are also deformed. This deformation is not caused by ground interference, but is due to the vertical radiation pattern itself. The radiation pattern is not uniform above the antenna system, which is not surprising because that is not the desired direction to transmit the FM signal.

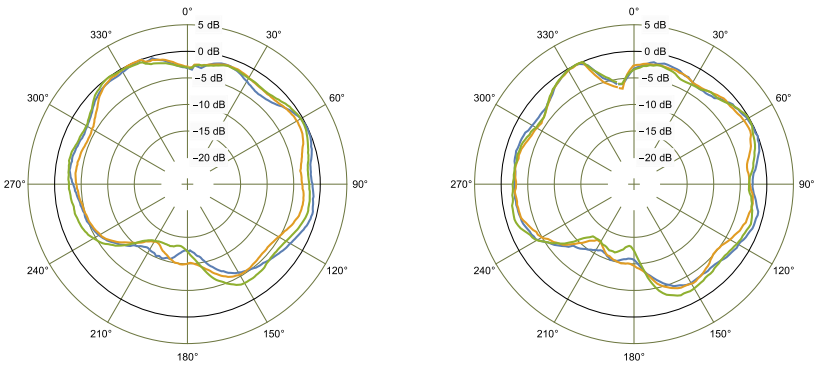

(a) (b)

Fig. 2: (**a**) Measurement of the radiation pattern (R = 50 m, center of the antenna system), (**b**) (R = 150 m, center of the antenna system).

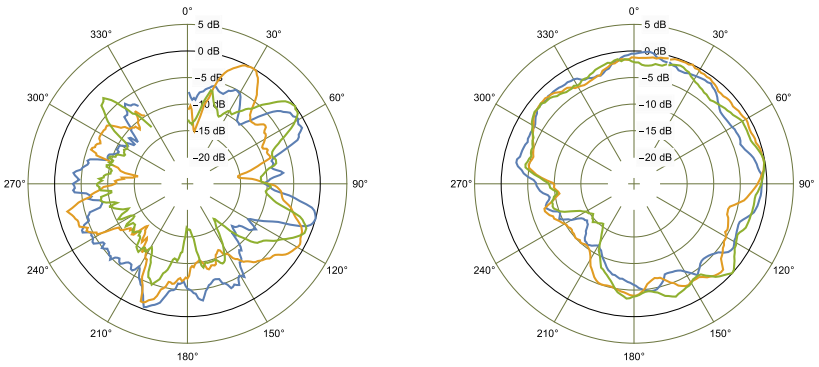

(a) (b)

Fig. 3: (**a**) Measurement of the radiation pattern (R = 50 m, 30 m under the center of the antenna system), (**b**) (R = 150 m, 30 m under the center of the antenna system).

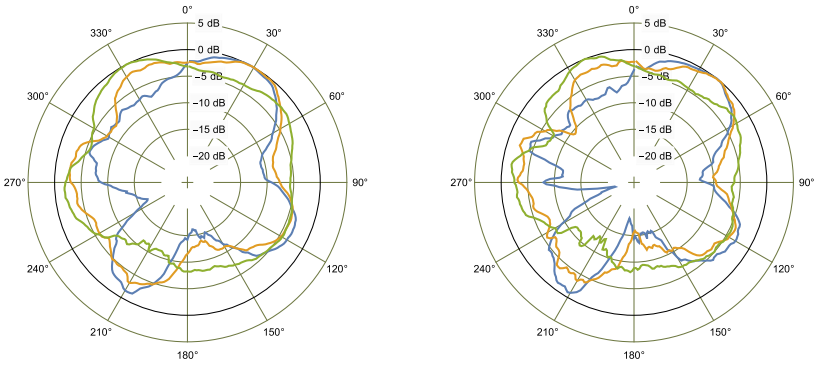

(a) (b)

Fig. 4: (**a**) Measurement of the radiation pattern (R = 50 m, 30 m above the center of the antenna system), (**b**) (R = 150 m, 30 m above the center of the antenna system).

Vertical radiation pattern measurement

As said in the introduction, horizontal, as well as vertical radiation pattern measurements are performed, in order to inspect the antenna system. For vertical measurements, the measurement

ISBN 978-80-972629-6-9

device was lowered 40 m under the antenna system center and then, at constant speed, it was elevated 60 m above the antenna system center. Three vertical measurements were acquired in the same azimuth but at different distances from the monotubes. The result of vertical flights can be seen in Fig.5a - Fig.5c [4].

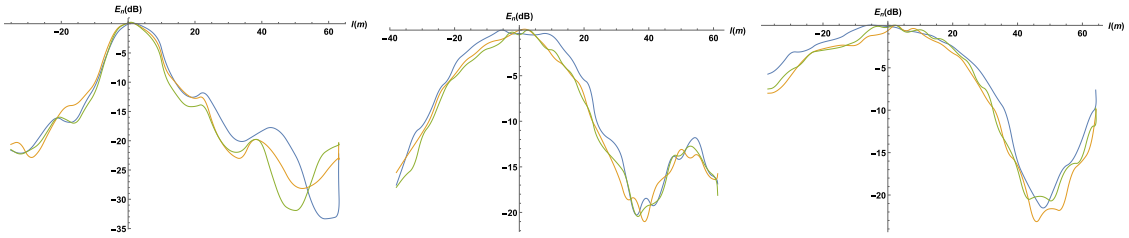

(a) (b) (c)

Fig. 5: Measurement of the vertical radiation characteristic (constant azimuth) from 40 m under the center of the antenna system to 60 m above the center of the antenna system : (**a**) R = 50 m, (**b**) R = 150 m, (**c**) R = 200 m.

These graphs show the expansion of the main lobe depending on the measured distance and also give a hint at the vertical side lobe, while the main lobe maximum is in the center of the antenna system.

3. Conclusions

Measurement of the horizontal and vertical radiation pattern of a large antenna system using a quadcopter with the prototype device „Pixla 1“ proved to be possible to some extent. As seen in Fig.2a to Fig.4b, measurement setup, choice of flight radius, and correct flight height are essential to acquiring relevant data for processing. When all these parameters were chosen correctly, we can state that the radiation pattern measurement was successful, while the time and resources used for the measurement were greatly reduced in comparison to the traditional methods of radiation pattern measurement with a helicopter. This allows for faster and easier measurement in a matter of minutes, instead of hours or days.

Acknowledgements

This work was supported by the national scientific grant agency VEGA under the project No.: 2/0155/19 "Processing sensoric data via Artificial Intelligence methods", projects APVV 14-0076 "MEMS structures based on load cell", APVV 20-0042 "Microelectromechanical sensors with radio frequency data transmission",project VEGA 1/0045/21 "Electromagnetic compatibility of wireless IoT devices", and project MSYST “Device for large antenna system measurement”.

References

[1] Dzuris, M., Grilli, N., Szolik, I., Hallon, J. (2021). Radiation pattern antenna system measurement. *In Measurement 2021 : 13th International conference on measurement. Smolenice, Slovakia, May 17-19, 2021.*

[2] Dzuris, M., Hartansky, R. (2022). Sensor of electromagnetic field for large antenna systems measurement. *Master thesis*

[4] Height of the measurement "*l*" in the graph is relative to the center of the antenna system - that is, the center of the antenna system is relatively at 0 m.

Calculation of Induced Currents in Antenna System Anchoring Cables by Equivalent Source Substitution

[1]Jakub Krchnak, [1]Rene Hartansky, [1]Michal Dzuris, [2]Michal Stibrany

[1]FEI STU, Ilkovicova 3, 812 19 Bratislava, Slovakia
[2]MWTC, s. r. o., S. Straku 46, 914 01 Trencianska Tepla, Slovakia
Email: jakub.krchnak@stuba.sk

Abstract. *The antenna systems for terrestrial broadcasting of FM radio signal are mounted on tall monotubes, which are held in place by anchoring steel cables. Due to harsh conditions and material ageing, these anchoring cables have to be subdued to regular maintanance and periodic replacements. The process of replacing the anchoring cables is difficult, lengthy and results in signal outages as currents induced in the anchoring cables, caused by strong electromagnetic field, could pose a danger to maintenance crew, therefore the antenna system cannot be radiating. The main goal of this study is to explore possible induced current calculation methods in anchoring cables as the basis for measurement in the field. Based on the calculated data it may later be possible to determine when is it necessary for the antenna system to be shut down completely and when lowering the radiated power results in the induced currents of harmless values.*

Keywords: Large Antenna System Radiation, Far Field, Near Field, FEKO, Numerical Solution

1. Introduction

Large antenna systems (AS) for terrestrial broadcasting in VHF and UHF ranges are comprised of multiple complex antennas. To achieve desirable coverage and transmit as much power as possible, these antennas are mounted on tall towers or monotube structures. In most cases these structures are placed on hilltops which often exposes such structures to harsh meteorological conditions especially during winter. The monotube structures are held in place by number of anchoring steel cables. In the case of very tall monotubes the number of anchoring cables can be up to 24 cables divided into three sets of 8. The environmental stress as well as the material aging takes a heavy toll on the steel cables and therefore they have to be subjected to periodic maintenance and replacements if necessary. The replacement is performed by technicians on the ground. With the help of auxiliary cable and a hoist they lower down the old cable and pull the new one up. Once the cable is at a desirable height the crew is elevated to the cable and attach the new cable in its place. Full replacement of 24 cables can take up to 50 days of work in favourable weather conditions which means many long signal outages during this period. This study aims to explore a suitable calculation method for currents induced in individual cables while the information given by calculations can later be tested in the field by various measurements. Based on calculations and measurements it can then be decided if individual antenna systems have to be shut down completely and when it is possible to lower their output power to, for example, 10 % of their maximum output power. The AS would radiate only when the crew is on the ground. In the past we have explored a possibility to calculate radiating parameters of large AS in computational software Altair FEKO by using equivalent point sources of antenna far-field radiation [1]. Later we have shown the possibility to simulate near-field radiation as well as far-field radiation by using equivalent Hertzian dipole structures in the place of full antenna models [2]. In this paper we will utilize both these approaches in order to calculate induced currents in individual cables. Based on the comparison of methods, more suitable one will be chosen for further research.

ISBN 978-80-972629-6-9

2. Subject and Methods

The computational software FEKO has the ability to assign the far-field generated by the antenna to an infinitesimal point source. This equivalent source has the same far-field properties, as numerically simulated antenna itself. Creating the AS using such equivalent source significantly reduces the time required for computations and calculation and can accurately simulate the behaviour of AS in far-field region. However far-field equivalent sources may prove to be unreliable when used to calculate the behaviour of EM field radiated by the antenna (antenna system) in near-field regions. To calculate near-fields, we can use the antenna substitution by equivalent Hertzian dipole structures. In this case FEKO simulates the electromagnetic field of the antenna in certain distance by replacing the antenna with an array of Hertzian dipoles. Using this method slightly raises the calculation time and computational power required compared to point source substitution, but allows for approximation of near-field as well as far-field. The numerical model of AS created by using equivalent point sources can be seen in Fig. 1a, while AS comprised of equivalent dipole structures is shown in Fig. 1b. The spatial layout is similar for both cases as well as are the input parameters of individual elements.

(a) (b)

Fig. 1: Antenna system comprised of far-field point sources (**a**) Antenna system comprised of Hertzian dipole structures (**b**).

In figures Fig. 2a and Fig. 2b we can see the far-field radiation patterns of AS in Fig. 1. The radiation patterns are similar, verifying the statement that far-field radiation of AS can be achieved by using either equivalent point source substitution, or dipole structure substitution. Figures Fig. 3a and Fig. 3b show radiation of the AS in near-field environment, specifically the Fig. 3a shows the electric component of electromagnetic field distribution at the distance $3.5m$ and vertical angle $\Theta = 90\,\text{deg}$. The blue curve represents the radiation from AS comprised of far-field point sources and the red curve represents the AS comprised of Hertzian dipole structures. The Fig. 3b displays the radiation at the distance $4.5m$. These figures demonstrate the behaviour of EM field in near-field region according to [3] - [5] and show that while equivalent point sources are able to simulate far-field properties of EM field, equivalent dipole structures can be used to simulate EM fields even in near-field region, as well as far-field region.

Currents induced in anchoring cables

Both created AS numerical models will be used respectively to calculate the currents in the anchoring cables. Mutual layout of the AS and a few anchoring cables is shown in Fig. 4a and 4b. The anchoring cables are modeled with resistive lossy material. For purposes of this study, the main topic of focus will be the currents in the auxiliary cable since the auxiliary cable is frequently used during the replacement process and runs closest to the AS. Fig. 5 displays the

ISBN 978-80-972629-6-9

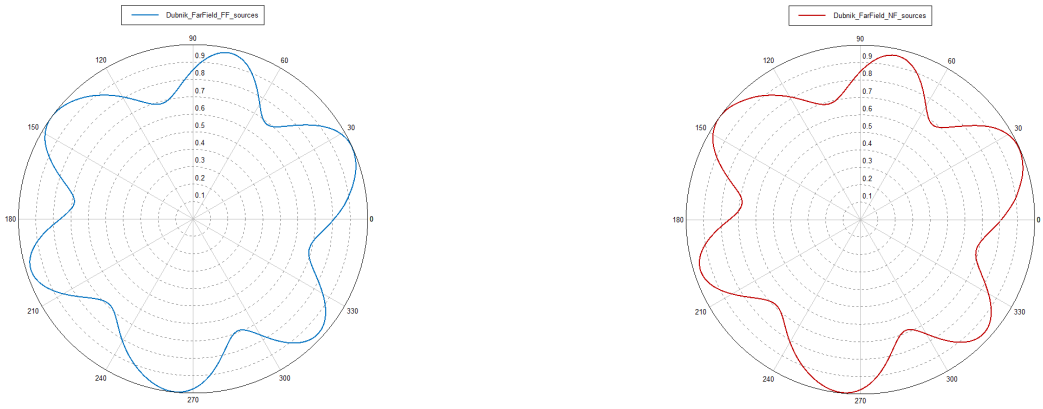

(a) (b)

Fig. 2: Radiation pattern of AS in Fig. 1a in Far-field (**a**) Radiation pattern of AS in Fig. 1b in Far-field (**b**).

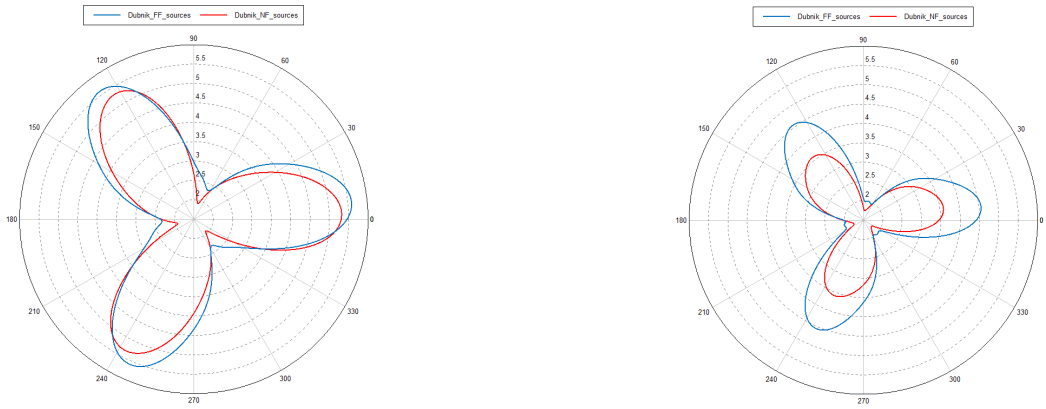

(a) (b)

Fig. 3: Radiation of the antenna system at a distance of 3.5 m (**a**) Radiation of the antenna system at a distance of 4.5 m (**b**).

currents induced in the auxiliary cable calculated for the layouts in Fig. 4. As expected the current induced by EM field of AS created using Hertzian dipole structures dissipates faster with the distance, due to intensity of individual EM field components decreasing with higher order polynoms in near-field region. This phenomenon cannot be recreated with the use of point sources that utilize only first order polynomials even for near-field regions.

(a) (b)

Fig. 4: Model layout for current calculation with the AS comprised of point sources (Fig. 1a) (**a**) Model layout for current calculation with the AS comprised of Hertzian dipole structures (Fig. 1b) (**b**).

ISBN 978-80-972629-6-9

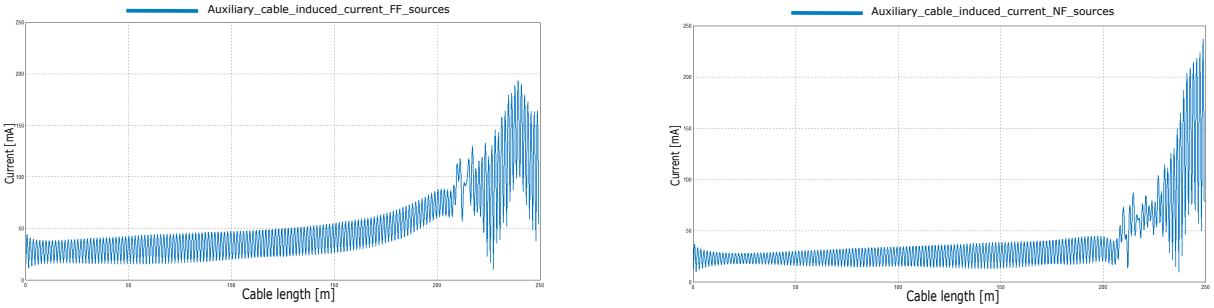

(a) (b)

Fig. 5: RF current induced in auxiliary cable for model in Fig. 4a (**a**) RF current induced in auxiliary cable for model in Fig. 4b (**b**).

3. Conclusions

In this study we have explored two different methods of determining the currents induced in the anchoring cables of large antenna systems. The method of equivalent point source of far-field substitution was explored as well as equivalent Hertzian dipole structure substitution. It was shown for equivalent point sources to exhibit inaccurate properties in near-field regions while results in far-field region apear to accurately simulate real AS radiation. It was also shown that using equivalent Hertzian dipole structures better simulates EM fields in near-field regions while it can still be used for far-field calculations as well. Both methods of AS substitution were used for induced current calculations in auxiliary cable where the difference in near-field behaviour proved to be noticeable. Based on the results, the method of equivalent dipole structures substitution will be used for further research. The applicability of these calculations is yet to be tested by measurements in field.

Acknowledgements

This work was supported by the national scientific grant agency VEGA under the project No.: 2/0155/19 "Processing sensoric data via Artificial Intelligence methods", projects APVV 14-0076 "MEMS structures based on load cell", APVV 20-0042 "Microelectromechanical sensors with radio frequency data transmission", project VEGA 1/0045/21 "Electromagnetic compatibility of wireless IoT devices" and project MSYST "Device for large antenna system measurement"

References

[1] Krchnak, J., Hartansky, R., Grilli, N. (2021). UHF DTV antenna system diagnostics by radiation pattern measuring. In *Measurement 2021:* 13^{th} *International Conference on Measurement*. Slovak Academy of Sciences, 232–235.

[2] Krchnak, J., Hartansky, R., Dzuris, M., Stibrany, M. (2022). Detection of faulty antenna in antenna system using equivalent hertzian dipole structures. In *Halgoš, J. Electromechanical systems application in industry 2022*, 47–50.

[3] Balanis, C. A. (1989). *Advanced Engineering Electromagnetics*. John Wiley & Sons Inc..

[4] Balanis, C. A. (2015). *Antenna Theory, Analysis and design* 4^{th} *ed.*. John Wiley & Sons Inc..

[5] Hartansky, R., Hallon, J. (2016). *Senzory pre meranie elektromagnetického poľa*. ÚE FEI STU.

An Improved Circular Array of Sensors for Wideband Current Measurement in Rectangular Busbar

[1]Noby George, [2]Pavel Ripka

[1]Faculty of Electrical Engineering, Czech Technical University, Prague, Czech Republic
[2]Faculty of Electrical Engineering, Czech Technical University, Prague, Czech Republic
Email: noby.george@fel.cvut.cz

Abstract. *An improved circular array of magnetic field sensors for the wideband current measurement in rectangular busbar conductors is presented in this paper. The yokeless current transducers that do not require a magnetic core are widely used for the measurement of current in rectangular busbars, but their performance is affected by the eddy current effect, especially in the wide frequency range. The existing frequency compensation techniques for yokeless transducers require position optimization algorithms and digital filters. For the first time, we propose that adjusting the angle between the sensors in the array in a circular array-based yokeless transducer reduces its frequency dependency. The Finite Element Method (FEM) based simulation studies showed that the frequency dependency is reduced from 8.5 % (conventional) to 0.66 % at 1 kHz using the proposed method.*

Keywords: Current Measurement, Magnetic Field Sensors, Yokeless Current Transducer.

1. Introduction

The yokeless current transducers are simple, lightweight, and not affected by the saturation-related issues of the yoke. The performance of a yokeless current transducer for a rectangular busbar is affected by the eddy current effect. The eddy current effect in a wide frequency range can be compensated by changing the shape of the busbar (in the sensing region) [1]- [2], using position optimization algorithms [3], and with the help of digital filters [4]. These methods are complex and introduce phase errors in the measurement.

The circular array-based yokeless current transducer is used for the measurement of rectangular busbar [5]. The performance of a circular array-based transducer for a wide frequency current measurement is not studied in the literature, in detail. We propose a method to reduce the frequency dependency of circular array-based sensors by adjusting the angle between the sensor in the array. The detail about the proposed method is presented in the next section of the paper.

2. Improved Circular Array of Sensors

A conventional circular array-based transducer with 8 sensors in the array is shown in Fig.1a. The angle (θ) between the sensors in the array is 45^0. The average of the sensor output voltages or magnitude of the flux density at the sensor points in the array is proportional to the current in the busbar [5]. A Finite Element Method (FEM) based analysis showed that the magnitude of the flux density at the sensor points S_1, S_2, S_4, S_5, S_6, and S_8 decrease with an increase in the frequency of the current in the busbar. Also, the magnitude of the flux density at the sensor points S_3, and S_7 increases with an increase in the frequency of the current in the busbar. The increase in flux density values at S_3, and S_7 are high compared to a decrease in other sensor points. This is prone to introduce errors in the measurement and FEM analysis

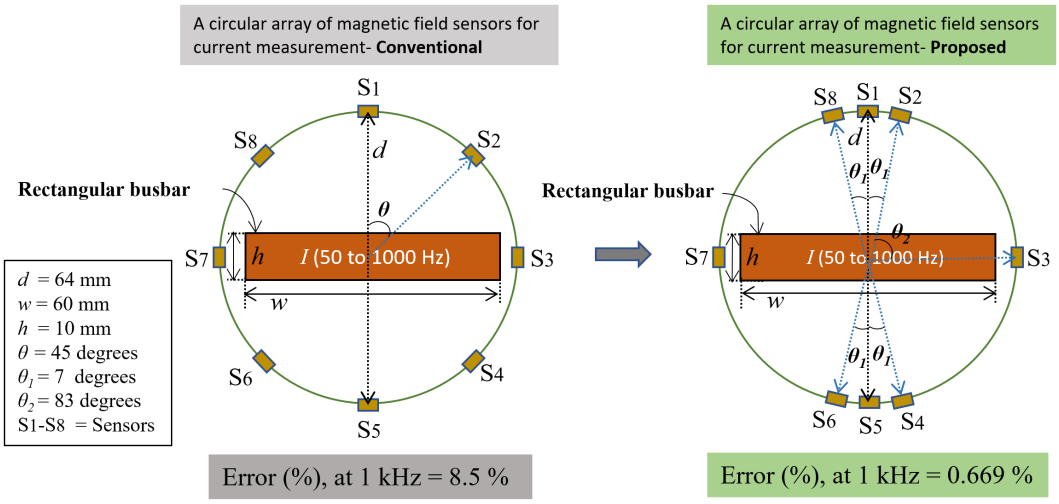

Fig. 1. The conventional (a) and proposed (b) yokeless current transducer with 8 sensors in the array.

showed an 8.5 % error at 1 kHz. We propose that this error can be compensated by equalizing the magnitude of both increase (at S_3, and S_7) and decrease (at S_1, S_2, S_4, S_5, S_6, and S_8) in flux density values with frequency. It can be achieved by bringing the sensors S_2, and S_8 close to S_1 because the decrease in magnitude of flux density is more at the locations closer to S_1 (similarly S_5). The angle between sensor S_1 and S_2 (also S_8) reduced from 45^0 to 7^0 as shown in Fig.1b. The complete structure of the proposed circular array is shown in Fig.1b.

The frequency characteristics of each sensor point in the array of the proposed scheme are shown in Fig.2 with the help of the 3D- FEM model of the busbar. The frequency characteristics of the conventional and proposed method are shown in Fig.3. It is visible from Fig.3. that the frequency dependency of the proposed circular array is much less compared to the conventional one. The same will be verified experimentally in the future by keeping the Hall-Effect-based sensor elements at the sensor points (as in Fig.1b) and computing the average of the output voltage of the sensors.

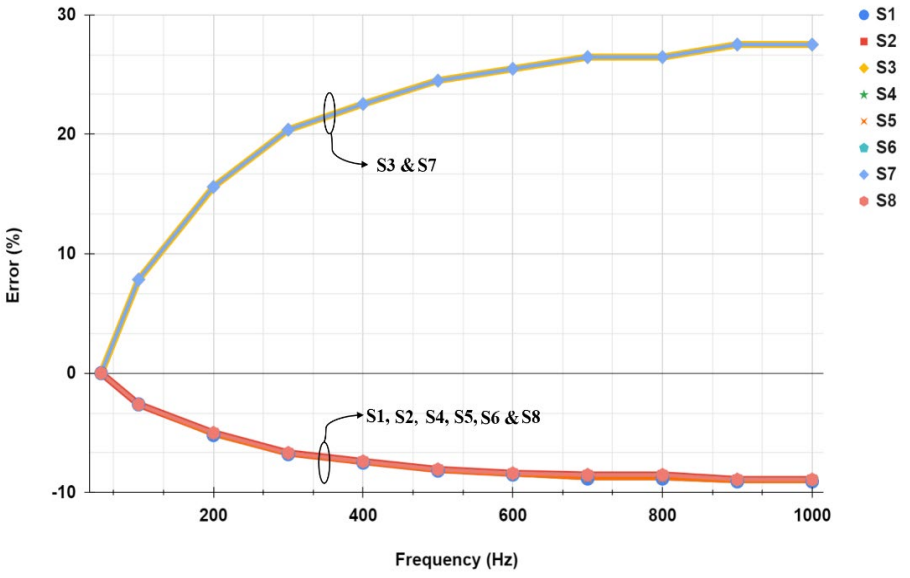

Fig. 2. The frequency characteristics of the individual sensor points in the array of the proposed transducer.

ISBN 978-80-972629-6-9

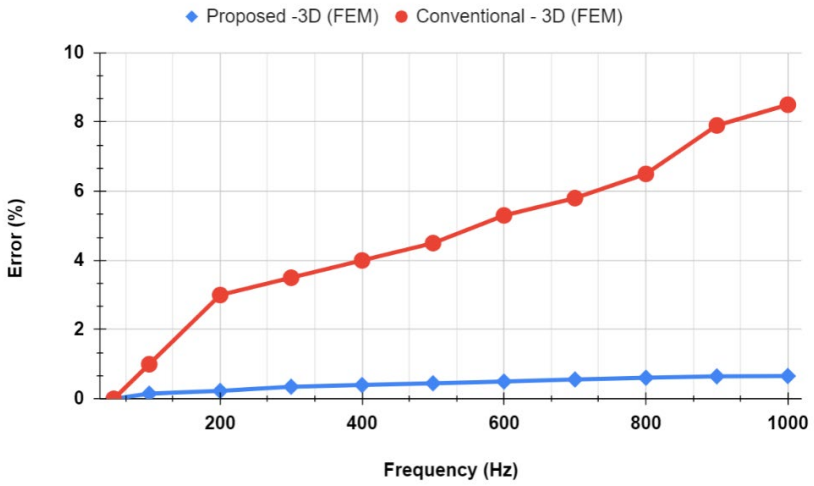

Fig. 3. The frequency characteristics of the conventional and proposed yokeless current transducer.

3. Conclusions

An improved circular array-based yokeless current transducer for wideband current measurement in rectangular busbar is presented in this paper. The frequency dependency of the yokeless transducer is improved by adjusting the angle between the sensors in the array. The 3D- FEM results showed that the frequency dependency can be minimized from 8.5% to 0.66 % at 1 kHz using the proposed transducer.

References

[1] P. Ripka, M. Přibil, V. Petrucha, V. Grim and K. Draxler (2016). A Fluxgate Current Sensor With an Amphitheater Busbar. In *IEEE Transactions on Magnetics*. IEEE,1-4.

[2] P. Ripka, V. Grim and V. Petrucha (2017). A Busbar Current Sensor With Frequency Compensation. In *IEEE Transactions on Magnetics*. IEEE, 1-5.

[3] X. P. Xu, S. Wang, T. Z. Liu, M. Zhu and J. G. Wang (2021). TMR Busbar Current Sensor With Good Frequency Characteristics. In *IEEE Transactions on Instrumentation and Measurement*. IEEE, 1-9.

[4] W. Li, G. Zhang, H. Zhong and Y. Geng (2021). A Wideband Current Transducer Based on an Array of Magnetic Field Sensors for Rectangular Busbar Current Measurement. In *IEEE Transactions on Instrumentation and Measurement*. IEEE, 1-11.

[5] L. Di Rienzo, R. Bazzocchi and A. Manara (2001). Circular arrays of magnetic sensors for current measurement. In *IEEE Transactions on Instrumentation and Measurement*. IEEE, 1093-1096.

ISBN 978-80-972629-6-9

Measurement of Physical Quantities Posters III

ISBN 978-80-972629-6-9

Analysis of the Mechanical Condition of the Dry Transformer by Contact Frequency Measurement Method

Miroslav Gutten, Daniel Korenciak, Martin Karman, Peter Brncal
Faculty of Electrical Engineering and Information Technology,
University of Zilina, Zilina, Slovakia
Email: miroslav.gutten@feit.uniza.sk

Abstract. *The article describes the contact analysis of 800 kVA dry power transformer using a frequency analyzer with automatic sweeping for low-middle frequency areas. In the case of dry transformers, the most common error in changing the acoustic emission can also be the incorrect connection of the screws on the fixing structure or when connecting the windings. As a complementary method, a set of different contact measurements can be used, thanks to which it is possible to detect a fault more accurately in the insulation or structural system of transformers. The most suitable additional methods include the SFRA (Sweep Frequency Response Analysis) method using the Megger FRAX instrument. The mentioned method measures the frequency dependence of the transformer conductivity from 20 Hz to 2 MHz in no-load and short-circuit conditions. With the help of these measurements, it is possible to detect a fault in the iron core, in individual windings, branches or connections. The problem of insufficient or incorrect clamp-screw connection was identified by the frequency method SFRA.*

Keywords: Transformer, Frequency Method, Incorrect Connection

1. Introduction

Transformers are among the most important electrical devices in the transmission and distribution system; therefore, it is necessary to prevent serious breakdowns in these insulating, structural and mechanical parts. It is necessary to regularly carry out diagnostic measurements and testing during measurement as well as outside of operation, which can identify possible aging of the material and thus prevent extensive damage to the machine [1], [2].

Offline contact diagnostic methods can be added to the non-contact methods mentioned, thanks to which it is possible to identify a possible error on the structural, mechanical, or insulating part of the power transformers as reliably as possible. For the diagnosis of the structural system of transformers, the most reliable analysis is the SFRA (Sweep Frequency Response Analysis) method, and for the analysis of the epoxy insulation system of high-voltage machines, the analysis of partial discharges is the most advantageous [3].

To analyze the mechanical condition or possible damage to the transformer (core, winding, taps, fixing screws), the off-line contact method Sweep Frequency Response Analysis (SFRA) is often used, which can be used as a complementary method after the non-contact analysis of power transformers by acoustic or thermal emission analysis.

This method is used especially when the analysis of acoustic emission, an increased amplitude of harmonic acoustic components in the frequency range up to 1 kHz is also found, and in the analysis of thermal emission, an increased rate of warming of the damaged site is shown compared to other parts of the transformer [4].

The equivalent transformer RLC circuit used for SFRA broadband frequency analysis includes electrical and magnetic bonds between the individual transformer elements. Such an RLC circuit has unique frequency characteristics for a specific geometry [5], [6].

ISBN 978-80-972629-6-9

The connection of the SFRA analyzer to the measured transformer is shown in Fig. 1. The indicated internal connection of the SFRA analyzer is for the apparatus Megger FRAX.

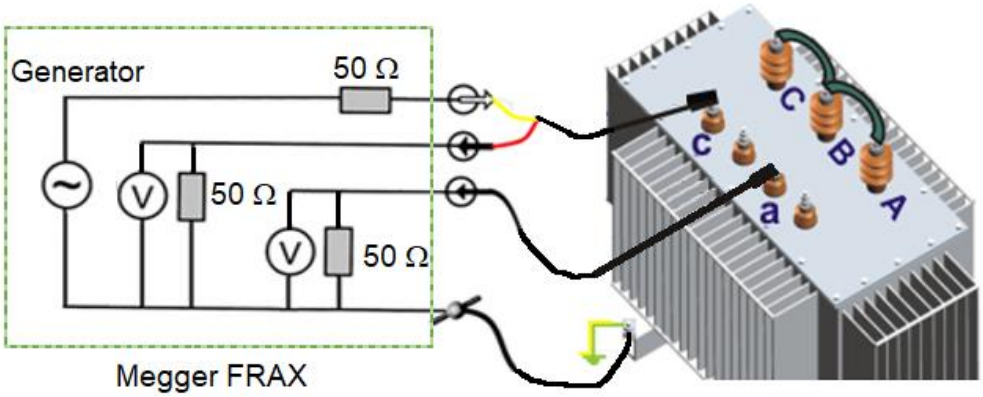

Fig. 1. The connection of the SFRA analyzer (Megger FRAX apparatus) to the measured transformer

2. Experimental Measurement

The frequency contact measurement was carried out on a 1 MVA dry transformer, which was found to be noisier than on a parallel transformer of the same power.

For the analysis of the correct connections and the tightening of the screws on the dry transformers, it is possible to use the contact off-line method Sweep Frequency Response Analysis (SFRA) using the Megger FRAX apparatus.

In the analysis of acoustic emission, an increased rate of harmonic acoustic components in the frequency range up to 1 kHz is also found, and in the analysis of thermal emission, an increased rate of warming of the damaged site is shown compared to other parts of the transformer.

The equivalent transformer impedance RLC circuit used for SFRA broadband frequency analysis includes electrical and magnetic bonds between the individual transformer elements. Such an RLC circuit has unique frequency characteristics for a specific geometry.

The faulty identified dry transformer was out of operation and disconnected from the electrical network and subsequently measured with the appropriate measuring equipment for SFRA analysis.

Fig. 2 shows the frequency analysis of the transformer impedance attenuation before fixing the winding screw (line red) and after fixing the winding screw (blue line). The problem of insufficient or incorrect clamp-screw connection was shown in the source range of frequency above 200 kHz to 2 MHz.

In the area of the highest frequencies above 2 MHz for larger machines, the response is less repeatable and is affected by the measuring set-up, especially the grounding, which depends on the length of the bushing.

If the clamp on the ferromagnetic core were enabled (analysis up to 10 kHz frequency), it would not be possible to detect such a defect using the SFRA method. In this way, the defect can be detected by measurement only for monitoring at higher frequencies, where the importance of the transition resistance increases.

ISBN 978-80-972629-6-9

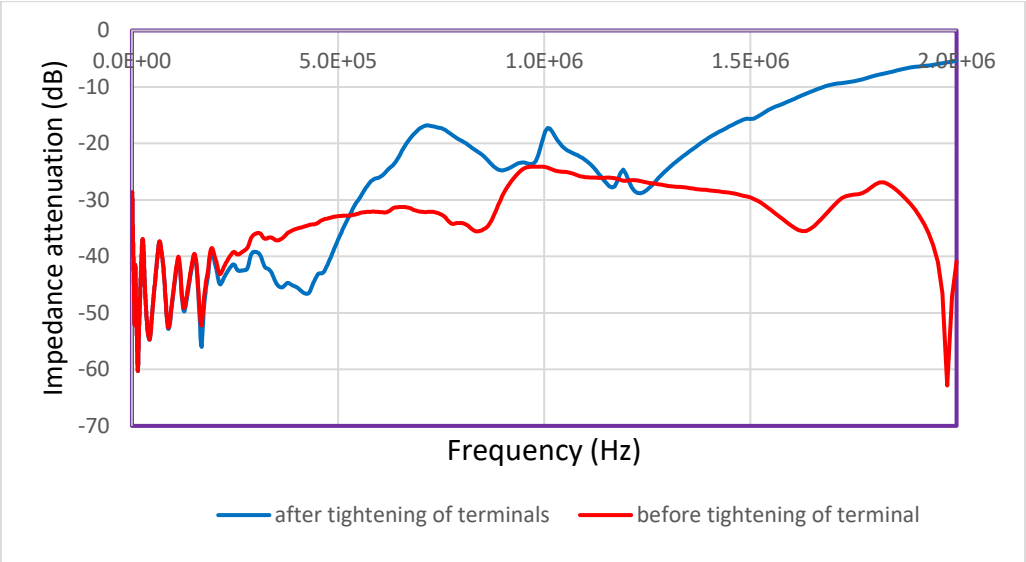

Fig. 2. Measurement on dry transformer for analysis of impedance attenuation depending on the frequency before tightening the winding terminals (red line) and after tightening the terminals (blue line).

If it is an insufficient connection of the terminals, it is possible to measure from Fig. 2 to add an analysis of the purely resistive component in the frequency band when measuring shortly before tightening the winding terminals (red curve) and after tightening the terminals (blue curve) according to Fig. 3, where a substantial difference between the red and blue curves can be observed due to the increased transition resistance at the relaxed coil terminal, which results in the phase shift approaching zero in the frequency range above 1 MHz (red line above 1,0E+06).

After tightening the clamp on the winding of the dry transformer, resistance effect minima were recorded at several frequency points (Fig. 3 - increase in phase shift). Thanks to the observed increased transition resistance at higher frequencies (above 500 kHz) due to the skin effect, it is possible to find a loose terminal in a simple way.

Such a measurement is suitable e.g. when comparing curves on individual phases of a three-phase transformer.

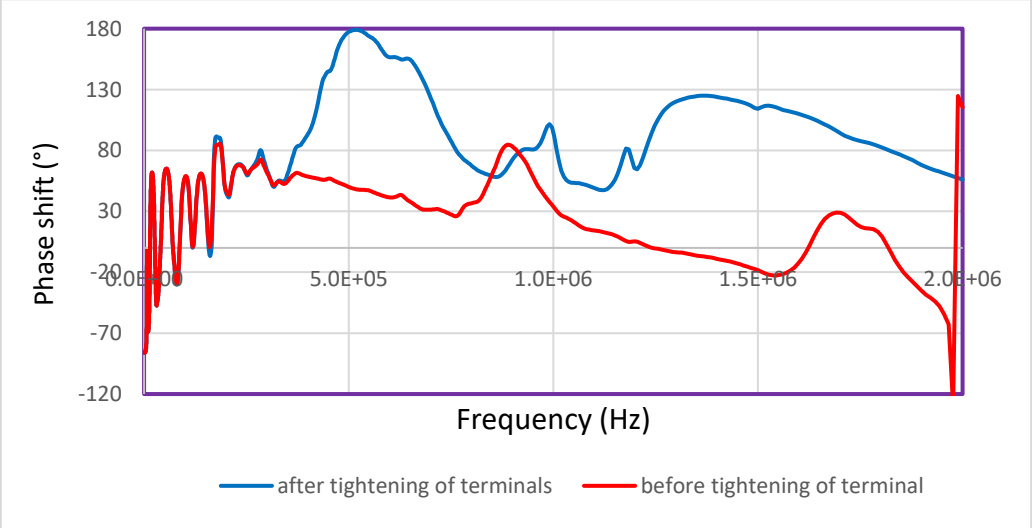

Fig. 3. Measurement on the dry transformer for analysis of phase shift depending on the frequency before tightening the winding terminals (red line) and after tightening the terminals (blue line).

ISBN 978-80-972629-6-9

3. Conclusions

The use of the mentioned diagnostic method is significant from the point of view of detection of aging and their effects on the analysis of the mechanical and structural parts of power dry transformers during operation. The mentioned methods, if used correctly, can be resistant to interference and their implementation is simple directly at the place of installation of the transformer. Using a contact method using add a non-contact measurement is a good starting position for the analysis of the transformer, thanks to which it is possible to propose a deeper analysis of the condition equipment.

In the long run, the progressive contact frequency method SFRA is the most useful, as it provides enough information about the structural condition of the transformer (ferromagnetic core, winding, taps, connections). Data measured from the manufacturer or before commissioning are considered references and can be used for comparison with data during the operation of a specific transformer. However, the disadvantage of the contact method remains in the shutdown of the power transformer from the network, therefore, to ensure the supply of electricity, a second parallel machine must be used to power the operation during the tested measurement.

If the clamp on the ferromagnetic core were enabled (analysis up to 10 kHz frequency), it would not be possible to detect such a defect using the SFRA method. In this way, the defect can be detected by measurement only for monitoring at higher frequencies, where the importance of the transition resistance increases.

Method SFRA contributes to a better understanding of the structural state of the power transformer and the exclusion of the incorrect diagnosis of a possible fault.

Acknowledgements

This work was supported by the Slovak Research and Development Agency under the contract No. APVV-21-0449 and No. APVV-21-0078.

References

[1] Brandt, M. (2016). Identification failure of 3 MVA furnace transformer. *Conference DEMISEE 2016*, Papradno, Slovakia 6–10.

[2] Usha, K., Usa, S. (2015). Inter Disc Fault Location in Transformer Windings Using SFRA. *IEEE Transaction on Dielectrics and Electrical Insulation* 22 (6), 3567-3573.

[3] Yoon, Y., Son, Y, Cho, J., Jang, S., Kim, Y.G, Choi, S. (2021). High-Frequency Modeling of a Three-Winding Power Transformer Using Sweep Frequency Response Analysis. *Energies***,** 14 (13), 4009.

[4] Lewandowski, K., Moranda, H. (2018). Detection of windings short-circuits in a power transformer using the SFRA method. *Przeglad Elektrotechniczny*, 94 (10), 118-121.

[5] Rajamani, R, Rajappa, M., Madanmohan, B. (2017). Sweep frequency response analysis based diagnosis of shorts within transformer windings. *IET Generation Transmission & Distribution*, 11 (17), 4274-4281.

[6] Ludwikowski, K., Siodla, K., Ziomek, W. (2012). Investigation of Transformer Model Winding Deformation Using Sweep Frequency Response Analysis. *IEEE Transactions on Dielectrics and Electrical Insulation,* 19 (6), 1957-1961

Development of the Illumination System of Recombination Sensor for Compound Concentration Measurements

[1,2]O. Kochan, [1]X. Ning, [1]J. Su, [3]B. Sus, [3]O. Kozynets, [3]S. Lytvynenko, [2]A. Ivanyshyn,

[1]School of Computer Science, Hubei University of Technology, Wuhan, China
[2]Lviv Polytechnic National University, Lviv, Ukraine
[3]Kyiv Institute of High Technologies, Taras Shevchenko National University of Kyiv, Kyiv, Ukraine
Email: orest.v.kochan@lpnu.ua

Abstract. *The technical implementation of the illumination device for the semiconductor sensor structures with the recombination principle of operation is suggested. The change in the state of charge is recorded from measurements of the photocurrent in various points on the illuminated surface with light from the region of strong optical absorption in silicon. The developed recombination sensors use new physical principles of transformation of external influence into a useful signal. It is shown that the portable versions of devices using the proposed sensors can be easily integrated into various automated systems for monitoring the condition of the human body or the external environment.*

Key words: Recombination Sensor, Lighting Unit, Analytes, Photo Feedback, LED, Surface Recombination

1. Introduction

Measurements [1] are very important part of the concept of Internet of Things [2]. Measuring the composition or concentration of a specific component in a mixture of substances is very important for industry. As a tool for such research, it is reasonable to use sensor systems that allow either qualitative or quantitative analysis in an almost real-time mode [1-5]. The development of modern sensor systems is related to the search for new effective sensor elements with high sensitivity, selectivity and the possibility of integration. It becomes possible to supplement the information received by other sensors and increase sensitivity and selectivity if a separate sensor implements a new physical principle of transforming external influence into a useful signal. Therefore, the study of recombination structures based on the photoelectric principle of signal conversion is relevant. Such structures allow a relatively simple technical execution and implement a conversion principle different from the currently well-studied potentiometric sensors with light addressing (LAPS) [5]. The operation of recombination sensor structures based on the effect of a controlled and reproducible change in the recombination characteristics of the interface of the semiconductor surface as a result of adsorption. The directly measured parameter is the photocurrent of the deep silicon barrier structure under illumination from the strong optical absorption region. Sensors of this type combine high sensitivity to analytes containing molecules with an intrinsic or induced dipole moment. For the effective application of the sensor, the photocurrent must depend significantly on changes in the surface recombination rate. This condition is valid when the regions of light absorption and space charge are spatially separated. The sensor differs from the similar ones because the analytical signal is the photoelectric current generated by light from the region of strong absorption in silicon. The value of the absorption is determined by the physical and chemical state of the interface. According to the principle of operation, the sensor allows forming an artificial distribution of properties on the surface and light addressing. It is compatible with the concept of the electronic nose devices. Structurally, the

ISBN 978-80-972629-6-9

recombination sensor consists of an illumination unit that provides sequential irradiation of specified points on the surface of the semiconductor barrier structure and units that provide measurement of the corresponding photocurrents, their amplification and visualization. In the stationary versions of the unit, illumination is provided by a helium-neon laser with a positioning system based on acousto-optic crystals. In this work, an effective compact version of the illumination unit based on the laser for recombination sensor structures is proposed. It meets the conditions of compactness and expressivity of analyte research. Portable versions can be integrated into various automated systems for monitoring the state of the human body (through the study of enzymatic reactions) [6] or to monitor the external environment [7-10].

2. Results and Discussion

Physical basis of recombination sensor operation and technical requirements for illumination unit parameters

Let us first formulate the basic physical principles of the recombination sensor. To study the peculiarities of adsorption processes, a "deep" silicon barrier structure is used (see Fig. 1.). Silicon substrates with the specific resistance of 30-50 Ω, n-type and orientation (100) are used to create sensor structures. In order to determine and compare photocurrent distributions (matrices - 512 × 512 pixels, 324 × 324 or 128 × 128), the surface of the sensor is scanned by laser irradiation with the wavelength of $\lambda = 532$ nm ($\alpha(\lambda) \sim 10^5$ cm^{-1}). In the works [4, 7] it is shown that the photocurrent significantly depends on changes in the surface recombination rate, when the regions of light absorption and space charge are spatially separated. On the other hand, the thickness of the base region must be close to the diffusion length or exceed it. Based on these considerations, we chose the thickness of the plate to be equal to 200 μm $<<1/a\ (l) \sim 0.07$ μm. The physical mechanism of the surface recombination rate change can be explained within the frame of the Stevenson- Keyes theory [9], taking into account the changes in the surface bending of the zones, the capture cross sections, and the energy position of the recombination levels during adsorption. When the band bending in the surface region changes and close concentrations of carriers occur near the surface, the photocurrent drops significantly (maximum recombination rate). When there is a shortage of carriers of a certain sign - the photocurrent increases and reaches saturation (the minimum recombination). This principle is the basis of operation of the sensory structure of the specified type (Fig.1). It is important to note that by creating films of different materials (e.g. Si_3N_4, SiO_2 etc.) on the silicon surface, it is possible to obtain interfaces with different recombination parameters [4]. In this case, changes in the photocurrent during adsorption depend on the technology and parameters of the modification. Light addressing in laboratory setup is implemented by the acousto-optic crystals system. The illumination units for portable versions of such structures were developed.

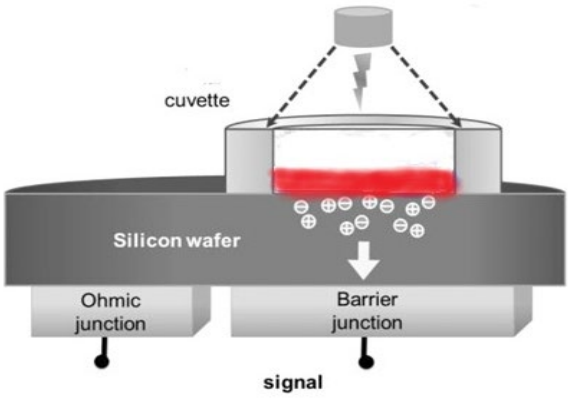

Fig.1 Simplified representation of the sensor structure

Illumination unit based on semiconductor LEDs

The microcontroller controls the strings (LED anodes) using BC547 transistors (T1 to T9) which are connected to the port pins. The collectors of the transistors are connected to the

output of the digital-to-analog converter through the transistor Q2, which makes it possible to change the brightness within wide limits. Brightness can be changed programmatically or using potentiometer R5. To limit the current, resistors with the resistance of 220 Ω (from R1 to R9) are connected to the collectors of these transistors. The tenth pin of the microcontroller is connected to the clock (CLK) pin of the modulator as a timing input. The columns of LEDs are controlled by BC547 transistors (T10-T18), which are connected to the cathodes of the LED matrix. The outputs of the microcontroller are connected to the bases of transistors T10-T18 through resistors R10-R18. The circuitry of the illumination unit is presented in Fig. 2.

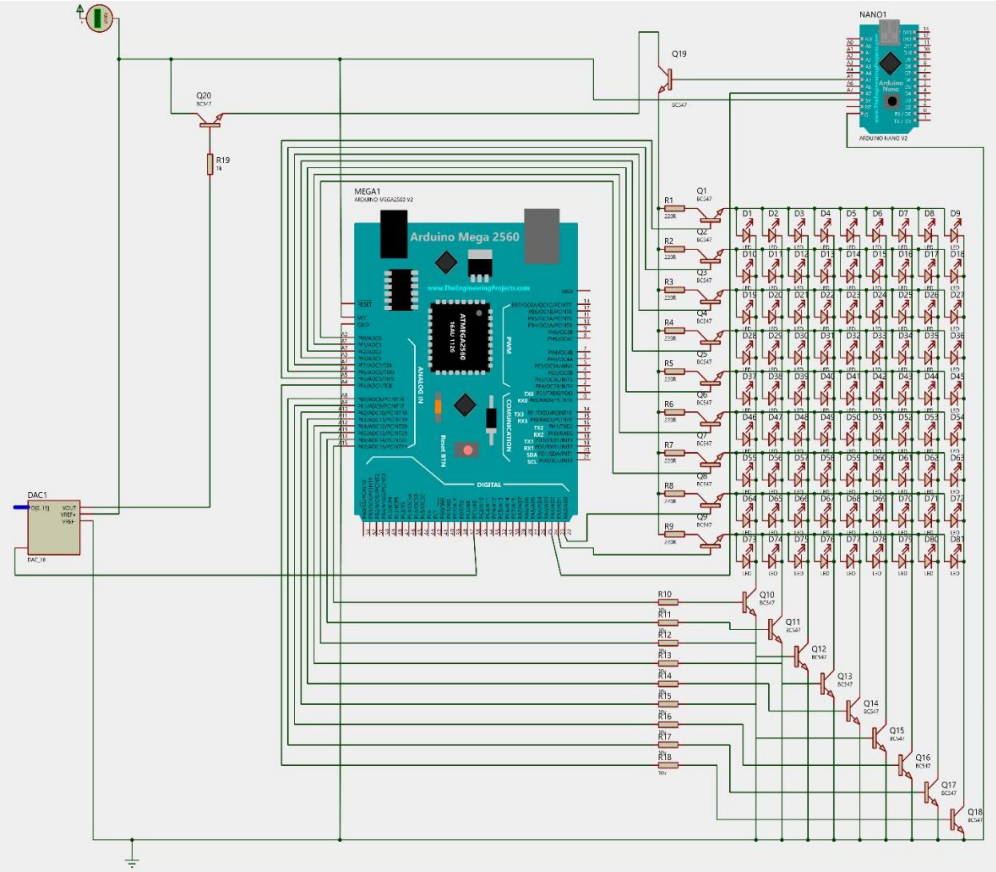

Fig. 2 Circuitry of the illumination unit

Fig.3 illustrate the operation of the recombination sensor with the developed LED illumination unit and a standard photo signal receiver Unipan-232. Brighter areas correspond to a larger photocurrent that is measured at fixed points on the surface (*x,y*). In our case, the number of surface points at which scanning takes place. The scanning of the surface corresponds to the number of diodes in the matrix (81 LEDs). Picture a) corresponds to the distribution of photocurrent, with a polar analyte (e.g. water, isopropyl alcohol) and picture b) - when surface contact with air. This test case shows the suitability of the illumination unit and the surface point polling algorithm for the miniaturized systems with the recombination principle of conversion. Note that the proposed unit allows researchers to control the illumination intensity and the modulation frequency of individual LEDs in the unit and to apply various algorithms for scanning the sensor surface. In principle, this option can increase the flexibility of using the sensor structure for various practical tasks. Physically, detection is possible due to changes in the surface bending of the bands due to the contact of the silicon surface with the polar molecules of the analyte and the influence on the recombination parameters at the interface. On the other hand, the quality of the illumination

ISBN 978-80-972629-6-9

and the scanning modes of the sensor surface allow photocurrent measurements to be performed with the accuracy sufficient to distinguish the test analytes.

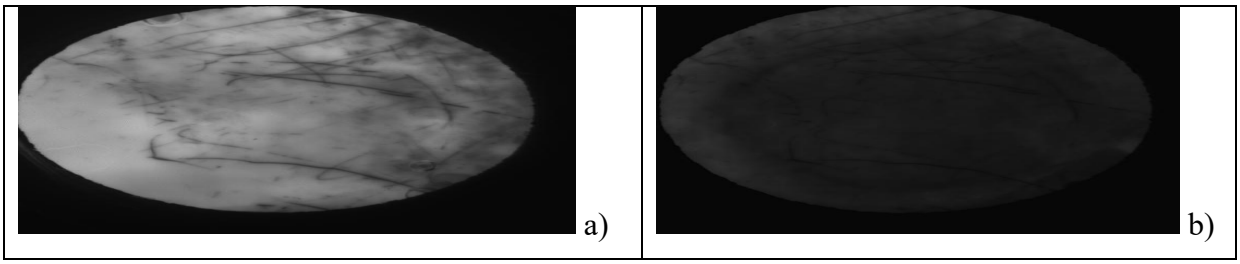

Fig. 3 Results of photocurrent measurements in the conditions of surveying the sensor surface of the LED hygrometer for contact of the surface with polar molecules (a) and air (b).

3. Conclusions

A design of the LED controlled system for measuring the surface distribution of photoresponse in sensor systems based on the recombination conversion principle has been developed. This system can accurately measure photoresponses across the surface of a sensor, making it useful for a range of application. The discussed illumination unit can be easily integrated into portable devices for monitoring the condition of the human body or external environmental sensors. The implementation of a portable controlled illumination unit system for detection of polar analytes has been demonstrated. This system is capable of accurately detecting polar analytes using controlled illumination, making it a powerful tool for applications such as environmental monitoring or medical diagnostics.

References

[1] Jun, S., et al. (2016). Development and investigation of the method for compensating thermoelectric inhomogeneity error. *International Journal of Thermophysics*, *37*(1), 1-14.

[2] Hu, Z., et al (2017). Determination of structural parameters of multilayer perceptron designed to estimate parameters of technical systems. *International Journal of Intelligent Systems and Applications*, *9*(10), 57-62.

[3] R. Kochan et al. Approaches of voltage divider development for metrology verification of ADC. In proc. Of the *2013 IEEE 7th International Conference IDAACS-2013*, Berlin, Germany, 2013, vol. 1, pp. 70–75.

[4] Kozinetz A., Litvinenko S., Skryshevsky V. (2017) Physical Properties of Silicon Sensor Structures with Photoelectric Transformation on the Basis of “Deep” p–n-Junction. *Ukrainian Journal of Physics*.. 62(4), 318–325.

[5] Wagner T., Schöning M. J. Chapter 5 Light-addressable potentiometric sensors (LAPS): recent trends and applications. *Electrochemical Sensor Analysis*. 2007. P. 87–128.

[6] Ghafar-Zadeh E. CMOS capacitive sensors for lab-on-chip applications: A multidisciplinary approach. Dordrecht: Springer, 2010. 146 p.

[7] Litvinenko S., Kozinetz A., Skryshevsky V. Concept of photovoltaic transducer on a base of modified p–n junction solar cell. *Sensors and Actuators A: Physical*. 2015. 224, 30–35.

[8] Kozinetz A., et al. The first application of sensory structures based on photoelectric transducer for study of the enzymatic reactions, Studia Biologica. 2022. 16(4), 3-18.

[9] Stevenson D. T., Keyes R. J. Measurement of Carrier Lifetimes in Germanium and Silicon. *Journal of Applied Physics*. 1955. Vol. 26, no. 2. P. 190–195.

[10] Manilov A., et al. Effect of nano-carbon dispersions on signal in silicon-based sensor structure with photoelectrical transducer principle. *Current Applied Physics*. 2019, 19(3), 308–313.

Measurement of Effect of Ultrasonic Mixing on the Properties of Polyurethane Potting Compounds Doped With ZnO Nanoparticles

[1]Štefan Hardoň, [1]Jozef Kúdelčík, [2]Anton Baran, [1]Peter Hockicko

[1]Department of Physics, University of Žilina, Žilina, Slovakia,
[2]Department of Physics, Technical University of Košice, Park Komenského 2, Košice, Slovakia
Email: stefan.hardon@uniza.sk

Abstract. *The main goal of an experimental measurement was to determine how ZnO nanoparticles added to polyurethane affected the composite's properties. According to the results of the experiment, the samples to which the ultrasonic needle was applied had visibly different dielectric properties. The frequency dependence of relative permittivity and dissipation factor was investigated in this study. A decrease of real permittivity and a shift of local relaxation peaks of dissipation factor with addition of ZnO was observed due to a lower mobility of polymer chains connected to nanoparticles. Polyurethane's glass transition temperature has shifted because of nanoparticle addition, according to DMA measurements.*

Keywords: Ultrasound Needle, Dielectric Spectroscopy Measurement, DMA Measurement

1. Introduction

The research into nanocomposites based on polymers has attracted the interest of many industries. Various thermoset polymers (epoxy resins, polyesterimide, polyurethanes) are used in mechanical, electrical, and construction applications. Power energy, electronic information, rail transit, and aerospace are some of the industries that are taking advantage of nanocomposite dielectric materials as novel materials [1 - 3]. Electrical equipment's operational reliability is directly related to its insulation, because these systems are constantly under thermal, mechanical, and electrical stress [4, 5]. Polymer materials, including their dielectric properties, are continuously being developed and improved, which plays a significant role in electrical insulation. The nanoparticles alter the physical and chemical properties of a matrix. Several basic phenomena characterize the various effect of nanoparticles, such as small size, a large active surface, quantum size effects, type, etc. Many materials scientists design new nanostructures, but they are still difficult to realize the potential of nanocomposites because conventional powder mixing techniques and suspension-based techniques do not provide accurate structural formation and a sufficiently homogeneous dispersion of nanoparticles in the matrix [6 - 9].

Various nano-fillers dispersed in polymer matrixes have been studied in numerous studies [10 - 13]. By comparison with pure polymers, these materials exhibit improved electrical, thermal, optical, and physic-chemical properties. It is important to note that nanocomposite systems have a specific surface area and this is one of their unique properties. There is a problem with control of uniformly dispersion of nanoparticle - when nanoparticles are mechanically mixed with each other, they agglomerate, producing larger structures or an inhomogeneous mixture that affects the expected result. Dispersion of nanoparticles realized only by mechanical mixing is not sufficient, because they have a strong tendency to agglomerate. Many nanoparticles used in the production of nanocomposite dielectric materials have high cohesive forces between them. To assess the feasibility of the mixing process for highly cohesive nanoparticles, the value of these forces arising during mixing must be determined in advance [10 - 13]. In other words, as particle size decreases, the interaction zone increases. As a result, the final material properties are

improved by improved bonding with the matrix material. As the nanoparticles are blended into the matrix, problems begin to arise. An important factor influencing the properties is the correct distribution of the nanoparticles. There is a possibility that agglomerates may influence space charge phenomena in addition to reducing overall dielectric properties. In this study, one of the main goals was to investigate the effects of nanoparticles on the properties of nanocomposite materials. Additionally, it was to see if ultrasonic additions to the preparation process affected the distribution of nanoparticles in the matrix and their dielectric properties [14 - 16].

2. Methods of Preparation Samples

The final nanocomposites prepared and investigated in this study were consisted of 3 materials. Matrix was two-component polyurethane (VUKOL N22, produced by VUKI a.s. Slovakia) cured with hardener VUKIT M in ratio 100:47. Based on our previous experiments [14, 16], the ZnO nanoparticles have been selected as a filler to enhance dielectric properties. The investigated nanocomposites were prepared in laboratory conditions and fabricated by the direct dispersion method with / without the influence of ultrasound needle (20 kHz).

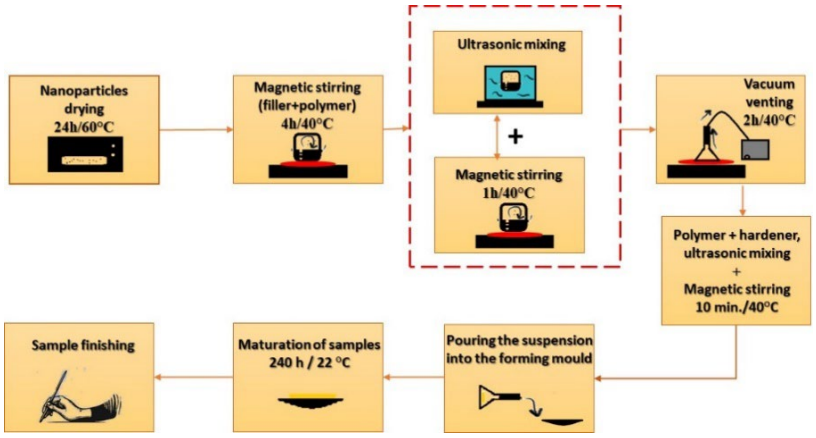

Fig. 1. Process of the preparation of investigated nanocomposites

To remove surface moisture from the nanoparticles before they were mixed mechanically with VUKOL N22, they were dried in a laboratory vacuum hot air dryer for 24 hours. VUKOL N22 was heated to 40 °C to improve viscosity during mechanical mixing. In a vacuuming process for 2 h (10 mbar), the polymer matrix base and ZnO nanoparticles were mixed mechanically for 4 h at 40 °C using a magnetic stirrer (400 rpm). An ultrasonic needle and a magnetic stirrer (400 rpm) were used simultaneously to control and uniformly disperse the suspension for only one type of investigated samples. During the vacuuming process, all air bubbles in the suspension are removed. Following the preparation of the sample mixture, the hardener was added to the prepared mixture as the last step in the preparation process.

3. Frequency Dielectric Spectroscopy

The comparison of the real part of the complex relative permittivity (ε_r) of the pure VUKOL N22 and its mixtures with 1.0 wt. % ZnO in wide frequency range for two temperatures are shown in Fig. 2a. ZnO nanoparticles were dispersed also by the ultrasound needle (4h+U). At both temperatures we can see that ZnO nanoparticles influence on the development of measured parameters. There is a decrease of the relative permittivity due to influence of nanoparticles at temperature 60 °C. At both temperatures we can see that the dispersion of ZnO nanoparticles by ultrasound have influence on the development of measured parameters. We can see a next

ISBN 978-80-972629-6-9

decrease of the relative permitivity value due to ultrasound. The main drop is observable for frequencies below 10 Hz and for 100 ˚C. When nanoparticles were dispersed only magnetic stirring, we cannot ensure their high-quality dispersion in polymers, and large clumps or clusters may form. Charges are captured on these clusters caused a significant increase in ε_r at low frequencies. This shift is due to also a change of mobility of polymer chains bonded on nanoparticles [14, 16].

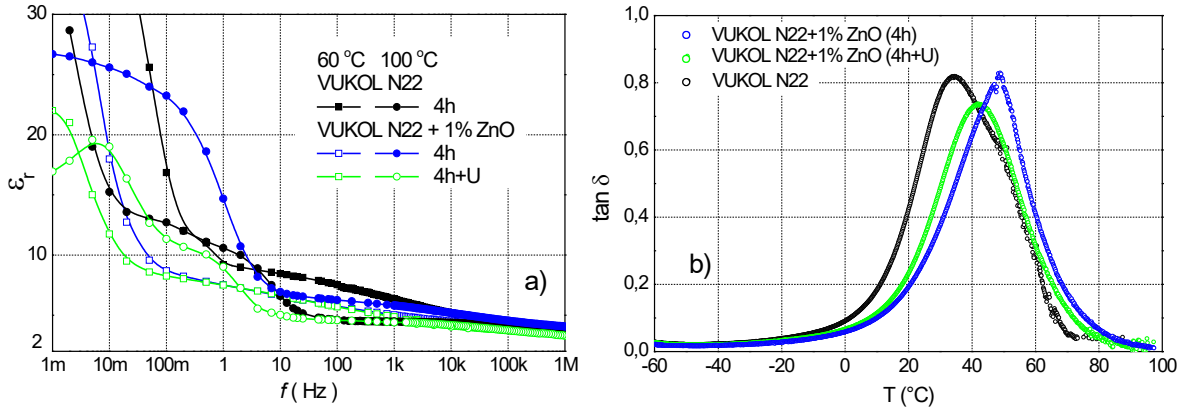

Fig. 2. a) The frequency dependence of real part of the complex permittivity for VUKOL N22 and the influence of ultrasound for VUKOL N22 with 1wt. % ZnO. b) Temperature dependence of damping factor *tan δ* for pure N22 and its nanocomposites containing of 1% ZnO nanoparticles.

4. DMTA Measurements

Dynamic mechanical thermal analysis was carried out on DMA Q800 (TA Instruments, New Castle, DE, USA) analyzer in dual cantilever operational mode. The samples were quickly cooled to - 60 ˚C, equilibrated at that temperature for 3 min, and then heated to 100 ˚C at the frequency of 1 Hz with a constant heating rate of 3 ˚C/min under nitrogen atmosphere.

Dynamic mechanical thermal analysis provides information concerning the degree of molecular motion and glass transition temperature of polymer. In Fig. 4 is depicted the damping factor *tan δ* as a function of temperature for VUKOL N22 and its nanocomposites. The glass transition temperature (*Tg*) is associated with its peak in temperature dependence. It is clearly visible, that addition of 1% .wt. of ZnO nanoparticles shift the *Tg* of VUKOL N22 to higher temperatures for composite prepared without or using ultrasound. Lower polymer chains mobility in both composites in comparison to VUKOL N22 can be deduced from the increase of *Tg*.

5. Conclusion

This experiment was primarily focused on confirming the positive effects of ultrasonic needle application on samples of a modern type of polyurethane with ZnO nanoparticles. DMA measurement and the frequency dielectric spectroscopy (dissipation factor, relative permittivity) presented indicate that the ultrasonic needle breaks down nanoparticle agglomerates. This has a visible influence on the dielectric properties of the polyurethane. Additionally, it reduces air bubbles during curing, which also affects all dielectric parameters. In addition to reducing sample preparation time, we can also reduce the mechanical mixing of nanoparticles and polyurethane by applying ultrasonics.

Acknowledgements

This work was supported by the Grant System of University of Zilina No. 1/2022 (17292) and the Slovak Research and Development Agency under the contract No. APVV-21-0078 and

APVV-21-0449 and under the project of Operational Programme Integrated Infrastructure: Independent research and development of technological kits based on wearable electronics products, as tools for raising hygienic standards in a society exposed to the virus causing the COVID-19 disease, ITMS2014+ code 313011ASK8. The project is co-funding by European Regional Development Fund.

References

[1] Utara, S., et al. (2023). Enhanced dielectric constant and mechanical investigation of epoxidized natural rubber with TM-doped CeO2 nanocomposites. Journal of Alloys and Compounds, 939, 168601.

[2] Kim, S., Lee, Y., Park, J., So, Y, H.T. et al. (2023). Green and Facile Synthesis of Hybrid Composites with Ultralow Dielectric Properties from Water-Soluble Polyimide and Dual-Porous Silica Nanoparticles. ACS Applied Materials and Interfaces, 15 (3), 4408 - 4418.

[3] Yu, G., Cheng, Y., Duan, Z. (2022). Research Progress of Polymers/Inorganic Nanocomposite Electrical Insulating Materials. Molecules, 27 (22), 2022.

[4] Rajňák, M. et al. (2022). Effect of ferrofluid magnetization on transformer temperature rise. Journal of Physics D: Applied Physics, 55 (34), 345002.

[5] Cimbala, R. et al. (2022). Dielectric response of a hybrid nanofluid containing fullerene C60 and iron oxide nanoparticles. Journal of Molecular Liquids, 359, 345002.

[6] Gutten, M., et al. (2016). Measurement of short-circuit effects on transformer winding with SFRA method and impact test. Metrology and Measuring Systems. 23, 521–529.

[7] Hornak, J. (2021). Synthesis, properties and selected technical applications of magnesium oxide nanoparticles: A review. International Journal of Molecular Sciences, 22(23), 12752.

[8] Mentlík, V., Michal, O. (2018). Influence of SiO2 nanoparticles and nanofibrous filler on the dielectric properties of epoxy-based composites. Materials Letters, 223, 41 - 44.

[9] Yu, Y., et al. (2022). Dielectric properties and dielectric relaxation process of polymethylphenylsiloxane/silicon dioxide nanocomposites. Journal of Applied Polymer Science, 139 (31), e52716.

[10] Muto, H., et al. (2022). Controlled formation of carbon nanotubes incorporated ceramic composite granules by electrostatic integrated nano-assembly. Nanoscale, 14, 9669–9674.

[11] Pradhan, S., et al. (2016). Effect of sonication on particle dispersion, administered dose and metal release of non-functionalized, non-inert metal nanoparticles. Journal of Nanoparticle Research, 18, 285.

[12] Michal, O., Mentlík, V., Hornak, J. (2021). Impact of Ultrasonic Mixing on the Electrical Properties of PEI/SiO2 Nanocomposites. AIP Conference Proceedings International Conference on Applied Physics of Condensed Matter, APCOM 2021, 2411, 050005.

[13] Wei, D., Dave, R., Pfeffer, R. (2002). Mixing and characterization of nanosized powders: An assessment of different techniques. Journal of Nanoparticle Research, 4, 21–41.

[14] Hardoň, Š., et al. (2022). Influence of Nanoparticles on the Dielectric Response of a Single Component Resin Based on Polyesterimide. Polymers, 14, 2202.

[15] Parvathi, K., et al. (2023). Tailoring the structural, electrical and thermal properties of zinc oxide reinforced chlorinated natural rubber/poly (indole) blend nanocomposites for flexible electrochemical devices. Journal of Polymer Research, 30 (2), 55.

[16] Kúdelčík, J., et al. (2021). Dielectric Responses of Polyurethane / Zinc Oxide Blends for Dry-Type Cast Cold-Curing Resin Transformers. Polymers, 13, 375.

Variability of Electromagnetic Field Homogeneity During Immunity Test According to EN 61000-4-3

Martin Gabrišák, Jozef Hallon, Mikuláš Bittera, Karol Kováč

Slovak University of Technology in Bratislava, Faculty of Electrical Engineering and Information Technology, Institute of Electrical Engineering, Slovak Republic
Email: xgabrisak@stuba.sk

Abstract. *In this article, an alternative way of calibrating the field strength of an electromagnetic field for electromagnetic compatibility (EMC) testing is proposed. The reason of this method is to improve the uniformity of field in the area, where the equipment under test (EUT) and its cabling are located, and to improve the worst-case conditions and quantified overtesting margins. Three different frequency dependent uniform field area (UFA) configurations are presented in this article. The main purpose is to use special configurations of calibration points, so the testing field strength will be only minimally above the prescribed field strength levels.*

Keywords: Radiated Immunity Test, Isotropic Field Probe, Uniform Field Area, Field Strength

1. Introduction

Radiated, radio-frequency, electromagnetic (EM) field immunity testing is applicable to the immunity requirements of electrical equipment to radiated electromagnetic energy [1]. Test levels and the required test procedures are in detail described in standard EN 61000-4-3:2020. It determines also the configuration of the EUT during testing and standard operating mode of the EUT. This standard establishes a common reference for evaluating the immunity of the EUT when subjected to radiated field.

The standard UFA, where the calibration ensures a homogeneity of field strength in the area, is very large (1.5 x 1.5 m), because of different sizes of EUTs. Different aspects of used test places and transmitting antennas are reasons why the allowed difference between the nominal field strength and the actual field strength is in a range from 0 to +6 dB above nominal value of the generated EM field [2], [3]. This means that the actual field strength may be two times higher than the nominal field strength. Due to non-linear processes occurring in tested semiconductor systems, this unwanted increase of field strength can lead to a non-objective increase of stringency of the test [4].

For small EUTs, the standard allows to reduce the area of the UFA. However, this reduction may result in the change of the homogeneity of the modified UFA. For this reason, we decided to calibrate the electric field strength in the area where a small EUT and its cabling are usually located when applying precalibrated values of the field obtained for different UFA sizes and subsequently evaluate the impact of different UFA sizes on the test reproducibility.

2. Calibration Method

The main purpose of the EM field calibration is to ensure that the field strength of an EM field in the UFA has both the required field strength and homogeneity. Homogeneity means minimal variation of field strength values in 16 measured points in the UFA. The prescribed calibration set-up is shown in Fig. 1, left. At the prospective of an EUT, a broadband isotropic electromagnetic field probe, which measures the electric field, is located. Because of

ISBN 978-80-972629-6-9

frequency dependent properties of both the anechoic chamber and the field generating chain, the field is calibrated for the complete defined frequency range for both antenna polarizations.

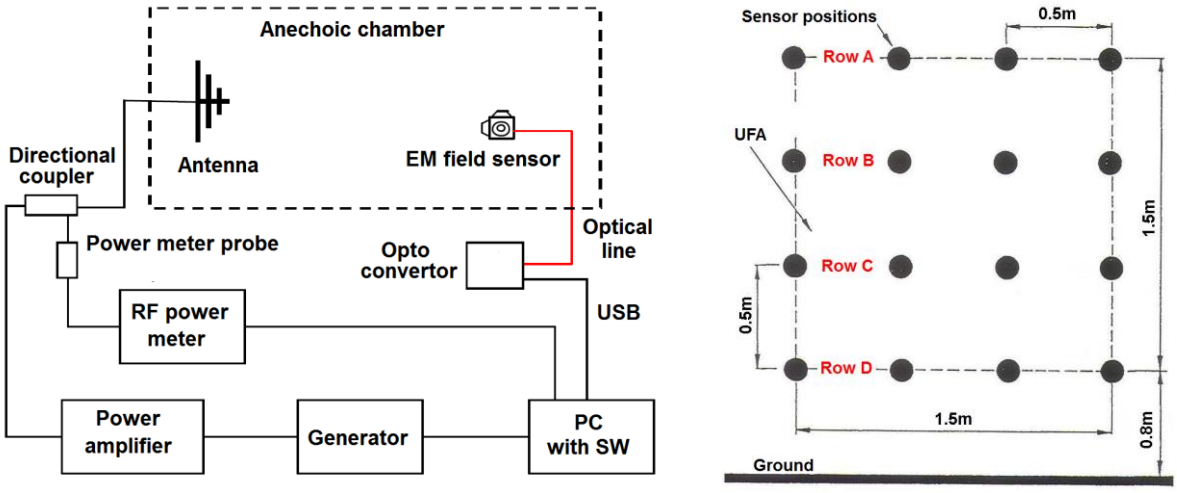

Fig. 1. Calibration system (left); Geometric arrangement of measurement points in UFA (right).

The field strength shall be measured in 16 points of the UFA. The geometrical arrangement of the points (Fig. 1, right) is prescribed by the standard. The UFA can be reduced to a smaller area, but it must cover the front surface of the EUT and the associated cabling. EUTs cabling should have a length of 1 m and should be placed parallel to the front edge of the table, hence perpendicularly to the direction of the field propagation. The set-up of the EUT is shown in Fig. 2. From this figure it is evident that the EUT and its cabling covers up only the lower section of the UFA. Such small EUTs occur quite frequently in practice, so it is reasonable to discuss these UFA modifications. The partial square UFAs (0.5 × 0.5 m, 1 × 1 m, …) proposed by the standard do not fully suits demands on small EUTs, because they consider only on the dimensions of EUTs thus disregarding the external cabling. This is why we propose a rectangular UFA with one or maximum two lower rows of calibration points.

3. Measurement

To evaluate the impact of UFA size on the homogeneity of EM field, we choose 3 configurations. First, we performed a full calibration for a complete 16 point of 1.5 × 1.5 m UFA, then for a UFA with only 8 points of the two lower rows (C and D), and finally for a UFA with only the 4 points of the lowest row (D). When using the reduced UFAs, the forward power fed to the transmitting antenna for testing purposes was obtained as the maximum of the forward power values obtained for each of all measurement points within the given reduced EFA, with homogeneity of the field still complying with the standard. The calibration ran in a anechoic chamber (4.5 × 4.5 m × 8.5 m) with hybrid absorbers (a combination of ferrite tiles and pyramidal foam absorbers).

A frequency range from 80 to 500 MHz was applied, because experience indicates that most EUT malfunctions caused by coupling to the external cabling occurs in this frequency range. For calibration and testing, a logarithmic-periodical antenna for a frequency range from 80 to 1300 MHz was used. The antenna was at a height of 1.75 m above the ground plane and the distance between the antenna tip and the UFA was 3 m. Both antenna polarizations were applied during calibration and testing. Applying the constant field method described in the standard, a fully automated control system measured the forward power fed to antenna necessary to yield a nominal EM field of a 10 V/m level, which was measured by the isotropic electric field probe. The adjusting of the field strength level had a precision of ±0.5 dB.

ISBN 978-80-972629-6-9

Subsequently, applying the evaluation procedure prescribed by the standard, the automated control system calculated the field generating power for each frequency using the acquired field generating forward power values from the points of the given UFA. In this way, we obtained for each individual UFA configuration the calibration data files (for the given test set comprising signal generator – amplifier - antenna) for both antenna polarizations.

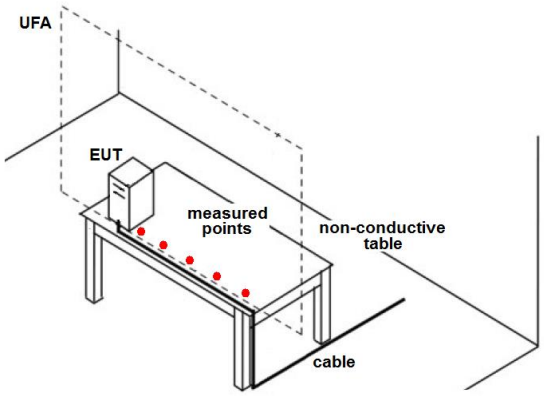

Fig. 1. Setup of a small tabletop EUT with external cabling and choice of

To evaluate the homogeneity of EM field, we focused on the EM field at the prospective of an EUT and its cabling. This is outlined by five red points in Fig. 2. These points were evenly spaced along a length of 1m. The EM field was then generated with the calibration files for different UFA configurations to obtain nominal field strength of 10 V/m. This means, that the EM field should have been in a range from 10 to 20 V/m. Using the field probe, the electric field strength was measured at each of the five points in the UFA. After measurement, for each test frequency and each polarization separately, an arithmetic mean and a standard deviation of the values measured at those 5 points was calculated as the representative value of the EM field strength at the given frequency and polarization. This evaluation was carried out for each chosen UFA.

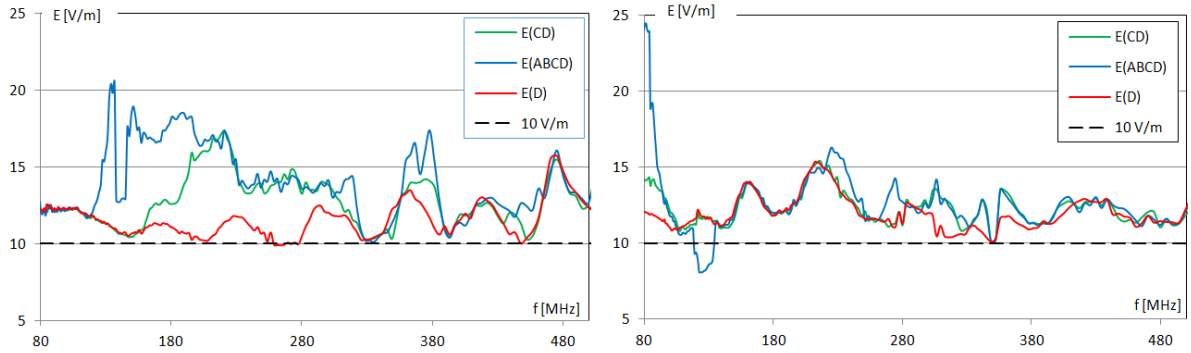

Fig. 2. Frequency dependences of mean EM field strength at measurement points for different UFA configurations (horizontal polarization – left, vertical polarization – right).

4. Results

In Fig.3 and 4, the arithmetic mean and the standard deviation of the measured EM field strength for each frequency and for each UFA configuration is presented. It can be seen that for the horizontal polarization the homogeneity of field was worse when the larger UFA was used during calibration. With increase in the area of the UFA, there is an increase in both average and the peak the field strength in the analysed frequency range. It is evident that the field strength values did not exceed allowed homogeneity range 0 to 6 dB given by the standard, but the test is more stringent. The deviations of measured field strengths are smaller at vertical polarization. For the maximal UFA area, two phenomena appear: an extreme field strength increase (up to 25 V/m) for the lower frequencies and a decrease of field strength under the nominal level in the frequency range from 120 to 134 MHz. Numerical values of maximal deviations are summarized in Table 1. On the other hand, the spread of field homogeneity expressed by standard deviation is almost with same values for all the all the chosen UFA.

ISBN 978-80-972629-6-9

Polarization	Parameter	UFA (D)	UFA (CD)	UFA (ABCD)
Horizontal	Average value above required level of 10 [V/m]	1.5	2.7	4.2
	Maximal value above required level of 10 [V/m]	5.7	7.3	10.5
Vertical	Average value above required level of 10 [V/m]	2.0	2.4	2.8
	Maximal value above required level of 10 [V/m]	5.3	5.4	14.4

Table 1. Average and maximal value above nominal level EM field for different UFA configurations.

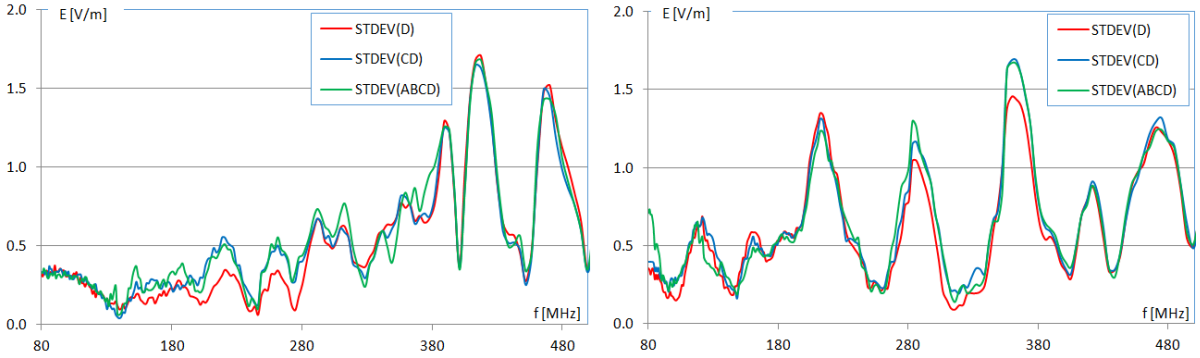

Fig. 3. Frequency dependences of EM field stranght standard deviation at measurement points for different UFA configurations (horizontal polarization – left, vertical polarization – right).

5. Conclusions

In the paper the alternative calibration procedure for EM field strength of immunity testing is proposed. The presented results of the visibly show that the homogeneity of the field in the UFA and the reproducibility of the EMC test is improved when the UFA used during calibration is chosen taking into account the physical properties of each individual EUT.

Acknowledgements

Work was supported by the Slovak Grant Agencies of Ministry of Education, Science, Research and Sport of the Slovak Republic VEGA 1/0045/21 and Slovak Research and Development Agency APVV, No. APVV-15-0062. This publication was created on the basis of the major project "*Advancing University Capacity and Competence in Research, Development and Innovation*"(ITMS project code: 313021X329) supported by Operational Program Integrated Infrastructure and funded by the European Regional Development Fund.

References

[1] Montrose, M.I., Nakauchi, E.M. (2004). *Testing for EMC Compliance: Approaches and Techniques*. Wiley-IEEE Press.

[2] Smith, J. (2019). Antenna selection for IEC 61000-4-3. *In Compliance Magazine, Electornic Design, Testing and Standards*, March, 2019, from the internet: https://incompliancemag.com/article/antenna-selection-for-iec-61000-4-3/.

[3] Liang, T., Xie, Y.Z. (2020). Optimizing Antenna Orientation and Positioning in a Radiated Susceptibility Test for Matched Transmission Line System. In: 6th Global Electromagnetic Compatibility Conference (GEMCCON), XI'AN, China, 2020, p. 1-6.

[4] Liang, T., Spadacini, G., Grassi, F., & Pignari, S. A. (2017). Crosstalk-based radiated susceptibility test enforcing worst-case conditions and quantified overtesting margin. In IEEE 5th International Symposium on EMC (EMC-Beijing), p. 1-7.

Analytical Model of Measurement Deviation of Platinum Resistance Temperature Detectors

[1]Jan Mikulka, [2]Vladislav Šmarda

[1]Brno University of Technology, Brno, Czech Republic,
[2]ENBRA, a. s., Brno, Czech Republic
Email: mikulka@vut.cz

Abstract. *In this article we focus on the issue of temperature measurement using platinum sensors and their deviations. We describe the analytical solution of measurement deviations with one sensor or a pair of two sensors. We also compare the actual deviations with the limit deviations given by the applicable standards. Our results show that the measurement deviations by platinum sensors are relatively small and the accuracy of the deviation regression and its numerical modeling is a critical problem to solve. The paper presents mathematical models to verify the accuracy of single sensors and their pairs using optimization techniques. This paper provides useful information for all those involved in temperature measurement in industry, science and technology.*

Keywords: PT Sensors, Interpolation, Regression, Accuracy Verification

1. Introduction

In recent decades, platinum sensors have become a very important tool in many industries such as chemical, food, pharmaceutical and energy. These sensors are used to measure temperature in a wide range of applications due to their high accuracy and stability. However, to ensure the reliability of the measurement, it is important to verify the accuracy of these sensors. This article deals with the verification of the accuracy of platinum sensors according to EN 1434 [1] and EN 60751 [2]. These standards describe how to calibrate and verify the accuracy of platinum sensors. The first standard [1] deals with the calibration of sensors for temperature measurement in heating and cooling systems, while the second standard [2] focuses on platinum sensors for industrial applications. In this study, the current state of knowledge used in the ENBRA, a. s. testing facility is used to verify the accuracy of industrial platinum sensors. These results suggest that the accuracy of platinum sensors can vary depending on their properties and the conditions under which they are used. The current solution consists of numerically solving and searching the definitional domains of the functions of the temperature dependence of the measurement deviation or temperature differences. The aim of this study is therefore to verify the accuracy of platinum sensors according to [1] and [2] and to compare the results with the current verification methodology. The results of this study could provide important information for industrial applications of platinum sensors and help to improve and accelerate their verification accuracy and reliability.

2. Subject and Methods

The following paragraphs describe the input data for the verification of platinum sensors according to current standards. The current methodology for verifying the accuracy of sensors and sensor pairs is then described, followed by a proposed analytical solution to the problem in order to speed up the process and reduce its computational complexity.

Experiment Setup

ISBN 978-80-972629-6-9

In practice, there are 2 separate experiments:

- The first is to measure the actual deviation of the platinum sensor over its entire working range of measured temperatures. The deviation dependence function is compared with the maximum allowable deviation function given by the standard. In the last stage of the experiment, the temperature of the maximum deviation detected is evaluated and recorded in a test report.
- The second experiment is to measure the actual deviation of a pair of platinum sensors over its entire working range of temperatures and temperature differences. The deviation dependence function is compared with the deviation allowance function given by the standard. In the last stage of the experiment, the temperature and temperature difference of the maximum deviation detected is evaluated and recorded in a test report.

There are two test reports of the tests carried out. In the case of the first protocol, a total of 14 sensors were available, 7 on the inlet side of the apparatus with the measuring medium (higher temperature) and 7 on the outlet side of the apparatus with the measuring medium (lower temperature). The second protocol contains a total of 12 sensors, which together form 6 complementary pairs. In all cases, the sensors are of the Pt500 type, the operating range is defined by a temperature range of 0 – 180 °C and a temperature difference range of 3 – 180 °C. A Pt100 standard is used to accurately measure the bath temperature. All sensors are three-wire connected with 5 m lead length and 530 mΩ resistance. This is the most common type of resistive temperature sensor wiring. Thanks to the third wire it is possible to measure the resistance of the line.

Current Methodology and Motivation

The principle of verification of the transfer characteristic according to the standard is shown in the block diagram, see Fig. 1.

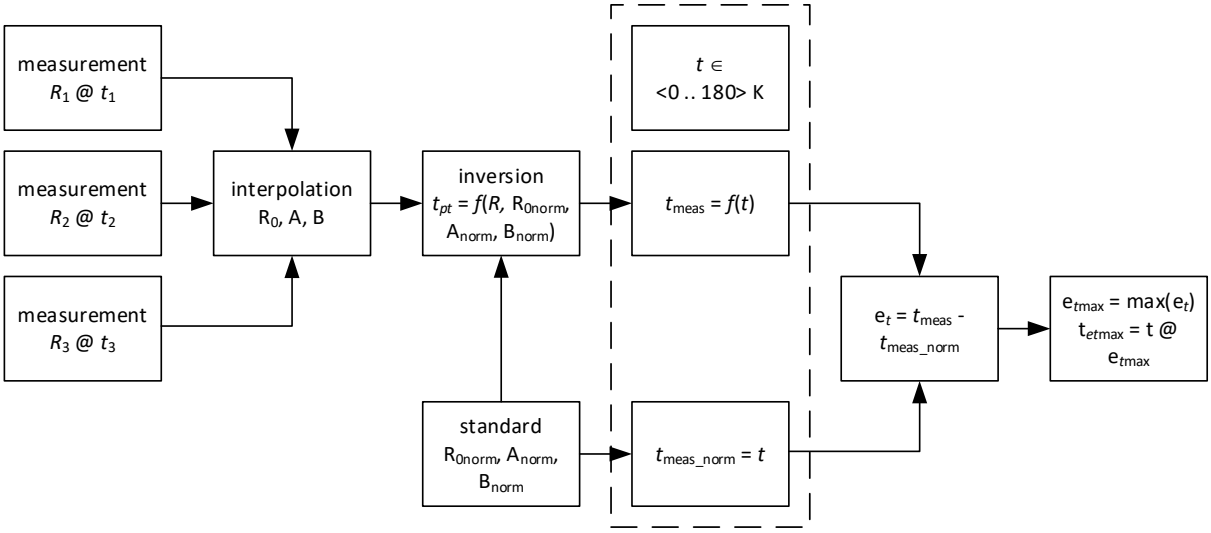

Fig. 1. The principle of verification of the temperature-resistance characteristic of an individual sensor

In the first step, the sensor to be verified is placed in an oil/water bath at temperature t_1 and the value of its resistance R_1 is measured with a precision laboratory multimeter Keithley 2010. The process is repeated for the next two temperatures t_2 and t_3 and the corresponding values of resistances R_2 and R_3 are determined. From the three characteristic function values, a substitute polynomial transfer function $R = f(t)$ can be obtained. Then, using the normalized constants of platinum resistive sensor given by international standards [2], the inverse function $t_{pt} = f(R, R_{0norm}, A_{norm}, B_{norm})$ for the sensor under verification is determined. The temperature t_{norm}

determined by the normalized standard is identical to the temperature of the test bath. The difference of the function e_t (absolute deviation of the temperature measurement) is then analysed to find the extreme (absolute maximum value), which is compared with the limit deviation defined by the standard, which is ±2 °C [2]. The sensor passes if the maximum deviation found in the working range is less than the limit deviation. The protocol result is the maximum absolute deviation and the corresponding temperature at which the detected extreme occurs. The numerical solution to the problem described in Fig. 1 consists of searching the feature vector e_t and finding the maximum value. The time and computational complexity of the task is closely related to the resolution of the implementation. If the defining domain of the function e_t is defined on the interval <0..180> °C with a step of 0.1 °C, the following operations have to be performed for 1,800 values: a) difference $e_t(i) = t_{meas}(i) - t$, b) finding the maximum value of e_t. When verifying a set of 14 sensors, on which the current test bench is implemented, the named operations are performed on a total of 14·1800 = 25,200 values of the double data type. If we consider an 8 byte data type, this is a total of 14,400 bytes (t_{meas}), 14,400 bytes (t), and 14,400 bytes (e_t) of data for a single sensor, for a total of 3×14,400×14 = 590.6 kB of data over which the mentioned operations are performed.

Two selected resistance temperature sensors (with or without built-in transmitter) have similar metrological properties and form an uninterchangeable pair. The maximum allowable error of the temperature sensors in verification is then [2]

$$E_{td} = \pm\left(0,5 + 3\frac{\Delta\theta_{min}}{\Delta\theta}\right), \tag{1}$$

where E_{td} is the limit error of the sensor pair, $\Delta\theta_{min}$ is the smallest considered temperature difference between the input and output sensor, in our case 3 °C and $\Delta\theta$ is a function of the temperature difference between the input and output sensor.

The numerical solution to the two sensors verification problem consists of searching the matrix of functional values of E_t and comparing these values with the functional values according to the relation (1). The time and computational complexity are closely related to the resolution of the implementation. If the defining domain of the function E_t is defined on the intervals $t \in$ <0..180> °C and $\Delta t \in$ <3..180> °C with a step of 0.1 °C, the following operations must be performed for 1,800×1,770 values: a) difference $\Delta t_{meas} = t_{in} - t_{out}$, b) difference $E_{tmax} = E_t - E_{td}$, c) finding the maximum value of E_{tmax}. When verifying a set of 7 pairs of sensors, on which the current test bench is implemented, the named operations are performed on a total of 7×1,800×1,770 = 22,302,000 values of the double data type. If we consider the 8 byte type, there are a total of 14,400 bytes (t_{in}), 14,400 bytes (t_{out}), 25,488,000 bytes (E_t), 25,488,000 bytes (E_{td}), 25,488,000 bytes (E_{tmax}) of data for one pair of sensors, a total of (2×14,400 + 3×25,488,000) × 7 = 510.6 MB of data over which the operations are performed.

Proposed Methodology

The derived functional dependencies $t_{pt} = f(R, R_{0norm}, A_{norm}, B_{norm})$, deviation e_t cannot be reported here due to their complexity and the limited scope of the paper. The objective of the analytical solution is to find the first and second derivatives e_t' and e_t'', respectively. In the case of a sensor pair, the functional dependencies $t_{ptin} = f(R_{in}, R_{0norm}, A_{norm}, B_{norm})$, $t_{ptout} = f(R_{out}, R_{0norm}, A_{norm}, B_{norm})$ must be expressed analytically. Subsequently, the relative deviation of the measured temperature as a function of the measured input temperature t_{ptin} and the measured temperature difference Δt_{meas} is expressed symbolically:

$$E_{T\max} = \frac{\Delta t_{meas} - \Delta t}{\Delta t} \cdot 100, \text{ where } \Delta t_{meas} = t_{ptin} - t_{ptout} \tag{2}$$

ISBN 978-80-972629-6-9

3. Results

Fig. 2 shows the functional dependence of the relative deviation of the temperature difference measurement of the selected sensor pair. This function is obtained by numerical synthesis for the input temperature and temperature difference vector (input-output). The verification of the limiting deviation of the sensor pair then consists in finding the maximum of the difference between the function and the limiting deviation given by the standard (1). In order to perform this analysis analytically, it is necessary to perform a suitable approximation of the function.

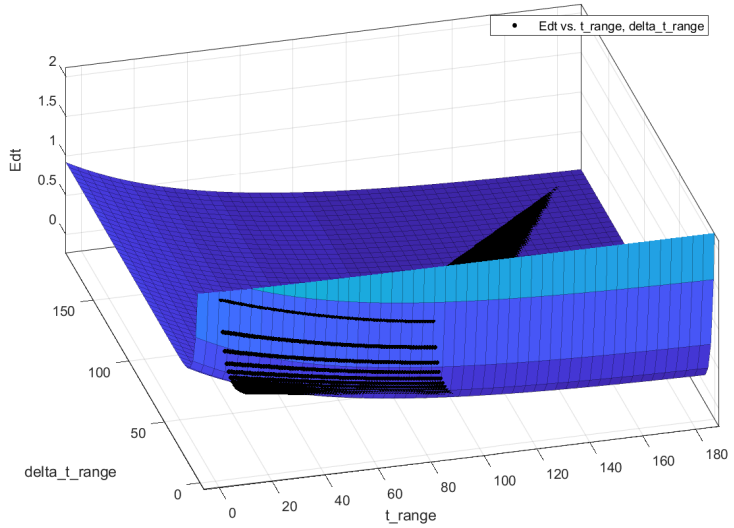

Fig. 2. Aapproximation function of the relative deviation of the verified sensor pair

By successive analysis of the data, a function was found which is very close to the function in Fig. 2, but unfortunately the approximation error exceeds the standard deviation for the sensor pair to be verified. The approximation function found is of the form:

$$E_{T\,\max_{aprox}} = k + a^{b\cdot\left(t_{ptin}+c\right)} + d^{e\cdot\left(\Delta t_{měř}+f\right)}, \tag{3}$$

where a, b, c, d, e, f, and k are the coefficients of the approximation function, t_{ptin} is the input temperature measured by the platinum sensor of the verified pair, and $\Delta t_{měř}$ is the measured temperature difference by the verified pair.

4. Discussion

Two experiments were presented to verify the platinum sensors for the case of a single sensor and pairs of sensors. For the verification of the sensor pair, the approximating function was proposed to analytically determine the maximum error of temperature drop measurements. The function needs to be verified and refined by analysing a larger number of sensor pairs.

Acknowledgements

The preparation of this paper was assisted by the project No. FEKT-S-23-8425 of the BUT internal grant office.

References

[1] ČSN EN 1434. Thermal Energy Meters. Czech Standardization Agency, 2019.

[2] ČSN EN 60751. Industrial platinum resistance thermometers and platinum temperature sensors. Czech Standardization Agency, 2014.

Monitoring of Printing Quality In Additive Manufacturing

Rebeka Tauberova, Peter Lazorik, Julia Nazarejova, Lucia Knapcikova

Faculty of Manufacturing Technologies with seat in Prešov, Department of Industrial Engineering and Informatics, Technical University of Košice, Slovakia

Email: rebeka.tauberova@tuke.sk

Abstract. *The term of quality is subjective designation of several factors that affect the level of quality in general. Advantage of quality is the ability to measure it. The possibility to create a connection between the Additive Manufacturing and quality provide us overall improving the efficiency of the printing process. Input analyzed data of first layer height were obtained using laser profiler for non-contact measurement. Measured printed samples were produced from PLA (Polylactic Acid) by Fused Deposition Modeling method. Measuring device chosen by us, namely Laser Profiler, has met our requirements for detecting first layer height. The presented paper is focusing on the impact of changing parameters and how they affect the resulting quality of printed samples in Additive Manufacturing.*

Keywords: Additive Manufacturing, Quality, Laser Profiler, Fused Deposition Modeling

1. Introduction

In general, the concept of Additive Manufacturing offers provides countless definitions. While each of the definitions offers different view of the significant specifics and benefits of the selected technology. The field of Additive Manufacturing represents the area with great potential in the future. Additive Manufacturing combines several fields of science at the same time, for instance, automotive industry, medicine, aerospace, engineering, and mass customization. The wide applicability of Additive Manufacturing testifies to it´s important position in modern industry. Directly proportional to the growing possibility of wide applications, the demands on quality are also increasing. In general, the concept of quality is disputable because everyone perceives and evaluates quality differently. It is well known that the level of quality in every area is constantly rising. Technology of Additive Manufacturing enables to create arbitrary physical objects from 3D models layering and application of material. But due to the usability of parts produced by said method (printed samples), the highest possible level of quality must be achieved at the end of the whole printing process. Quality in Additive Manufacturing refers to the accuracy, precision and reliability of the final printed object. Achieving quality in the printed samples requires attention to several key factors, including printer calibration, material selection, design and software, print settings and post processing. This paper discusses the impact of the selected parameters, namely, printing speed, layer thickness, and layer heights. Purpose of this paper is to analyze modification of printed samples in relation to the given parameters from the quality viewpoint. Types of defects, which are result of changing printing speed and layer thickness can be delamination, incomplete fusion, or porosity.

2. Subject and Methods

In the present, there are several methods of 3D printing, which are using different techniques and materials to create desired printed sample. For our needs the material extrusion method namely, Fused Deposition Modeling technology (FDM), was chosen. This technology is most often used. In this method, thermoplastic materials are melted and extruded through a nozzle

ISBN 978-80-972629-6-9

layer by layer to build the specific 3D object from 3D model. Advantage of this technology is relatively low price and it´s simple operation. In effort to achieve the desired fiber connection effect, it is necessary to control the printing parameters. Monitored parameters in this paper will be printing speed and layer heights and it´s impact on quality of printed samples.

Following Fig.1 shows specifics 3D printer FLSUN QQ-S, on which the samples were printed and Keyence Laser Profilometer LJ-X8020, on which the quality of samples will be analyze. Printed samples were created from PLA (Polylactic Acid) filament.

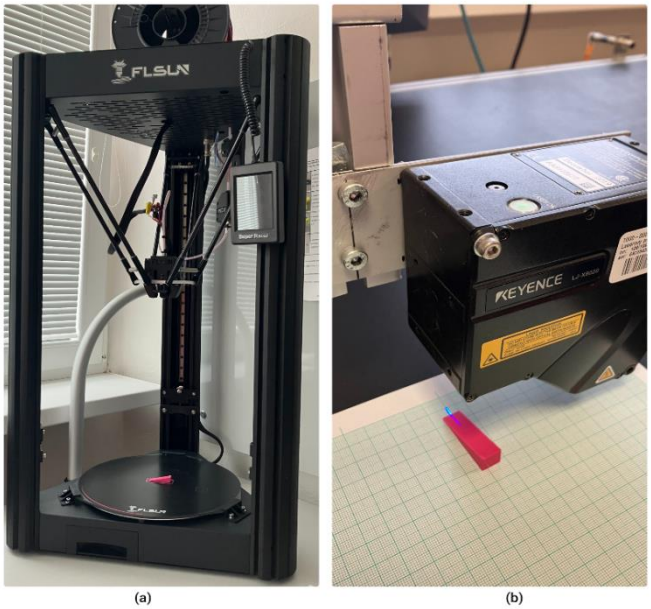

Fig. 1 (a) 3D printer FLSUN QQ-S, (b) LJ-X8020 laser profiler with sample

The aim of presented paper is to identify first layer height for determining the scale height of irregularities on freshly printed samples from PLA using laser profilometry for non-contact measurement. Investigation of defects occurring in the first layer of printed samples helps to prevent preserve the overall quality of whole printed products, and helps to eliminate waste of materials, which is necessary for printing process.

Following table represent primary parameters of 3D printer, laser profiler, and printing parameters.

Table 1. Parameters of 3D printer, Laser Profiler, Printing parameters

Printer Parameters	Measuring Device	Name	Value/ Units
Printing tech - FDM	Reference Distance		20 mm
Filament size – 1.75 mm	Light Source	Blue Semiconductor	
Filament type - PLA	Laser wavelength		405 nm
Bed temperature – 60 °C	Measurement range (X axis)	Width closer side	7mm
Printing temperature – 210 °C		Reference distance	7.5 mm
Nozzle diameter – 0.4 mm		Far side	8 mm

ISBN 978-80-972629-6-9

3. Results

For our needs were printed two samples with same printing speed and different layer heights. Sample n. 1 was printed on speed 50 mm/s and layer heights was 0.1 mm. Sample n.2 was printed on speed 50 mm/s also and layer heights changed from 0.1 mm to 0.25 mm. With the help of utilization of non-contact measurement is possible to study, how printing speed and layer heights affects quality of printed samples. Following Fig. 2 represents result of non-contact measurement using laser profiler. Part (a) is representing printed sample with layer height 0.1 mm. It is possible to see the first layer of sample and 3D model of whole sample. Part (b) is representing printed sample with layer height 0.25 mm. And also is possible to see the first layer of sample and 3D model of whole sample. The first layer is often problematic, and from this reason we decided to measure, whether the first layer height of sample corresponds to initial settings and to 3D model.

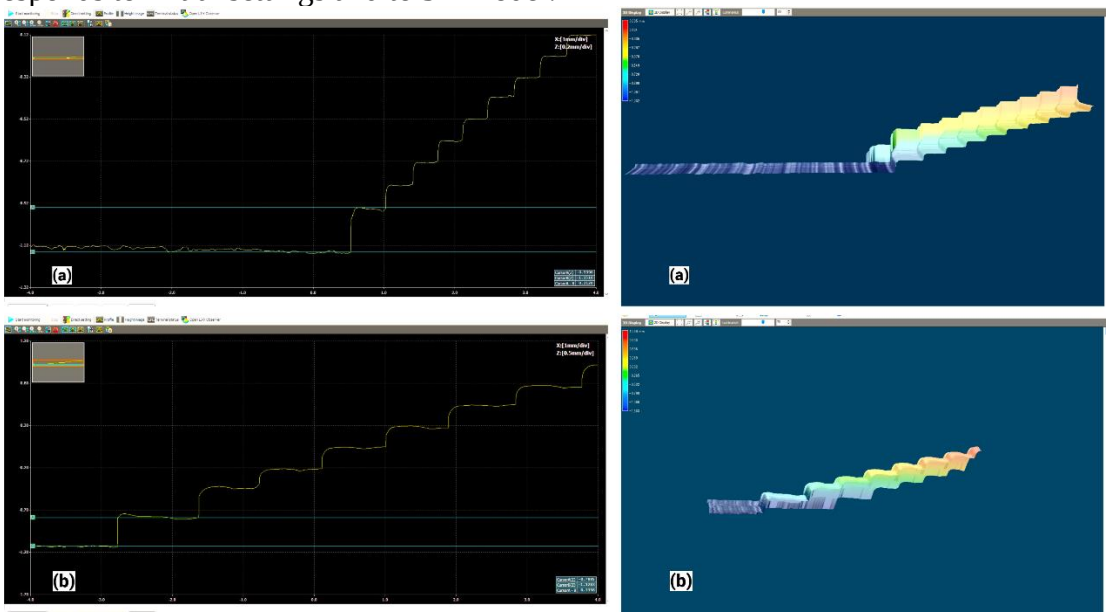

Fig. 2 Sample (a) layer height 0.1 mm, Sample (B) layer height 0.25 mm

According to measurements it is possible to admit, that first layer height does not correspond to initial settings. But this effect is normally observed during the printing process. First layer height is often two time bigger than normal. Primary the first layer heigh depends on calibration of specific printer and initial setting in the software. Specific measurement was obtained from the software LJ-X Keyence Navigator, which is cooperating with the laser profiler. LJ-X Keyence Navigator is used for measuring the object. To obtaining the 3D model it is necessary to use LJ-X Keyence Observer.

Table 2. Parameters of printed samples

Parameter	Sample n.1	Sample n.2
Layer Height	0.1 mm	0.25 mm
Angle Height	15°	15°
Printing speed	50 mm/s	50 mm/s
Cursor A (Z)	-0.9396 mm	-0.7885 mm
Cursor B (Z)	-1.1516 mm	-1.1283 mm
Cursor A-B	-0.2120 mm	-0.3398 mm

ISBN 978-80-972629-6-9

By performing the non-contact measurement using a laser profiler, it was possible to measure the first layer height. According to the obtain results it can be concluded, that in the case of first printed sample with layer height 0.1 mm, the real measured heigh of the specific sample was two time bigger. In the case of second printed sample the layer height was approximately also two time bigger than it supposed to be.

4. Conclusions

The aim of the presented paper is to monitor and control the quality of samples produced by the additive manufacturing and using the Fused Deposition Modeling technology. Print quality evaluation has been carried out through non-contact measurement method. Utilization of laser profiler was used to measure the first layer height of printed samples. According to the results, which were obtained from the software LJ-X Keyence Navigator, it is possible to admit, that first layer height does not always correspond to the settings in the software in which the 3D model of the printed samples was designed. Future direction of presented work will be investigation of surface properties in order to ensure the quality of printed products.

Acknowledgements

This work was supported by the project VEGA 1/0268/22, granted by the Ministry of Education, Science, Research and Sport of the Slovak Republic.

References

[1] Husár, J., Knapčíková, L., & Kaščak, J. (2022, June). Optimization of the Production Process and Defect Identification in the Production of Face Shields Using Fused Deposition Modeling Technology. In *6th EAI International Conference on Management of Manufacturing Systems* (pp. 141-153). Cham: Springer International Publishing.

[2] Lishchenko, N., Lazorik, P., Demčák, J., Pitel', J., & Židek, K. (2022, May). Quality control monitoring in 3D printing. In *Advances in Design, Simulation and Manufacturing V: Proceedings of the 5th International Conference on Design, Simulation, Manufacturing: The Innovation Exchange, DSMIE-2022, June 7–10, 2022, Poznan, Poland–Volume 1: Manufacturing and Materials Engineering* (pp. 31-40). Cham: Springer International Publishing.

[3] Lishchenko, N., Piteľ, J., & Larshin, V. (2022). Online Monitoring of Surface Quality for Diagnostic Features in 3D Printing. *Machines*, *10*(7), 541.

[4] Keyence.(2023). LJ-X 8020. https://www.keyence.eu/cscz/products/measure/laser-2d/lj-x8000/models/lj-x8020/

[5] Ansari, A. A., & Kamil, M. (2021). Effect of print speed and extrusion temperature on properties of 3D printed PLA using fused deposition modeling process. *Materials Today: Proceedings*, *45*, 5462-5468.

[6] Kristiawan, R. B., Imaduddin, F., Ariawan, D., & Arifin, Z. (2021). A review on the fused deposition modeling (FDM) 3D printing: Filament processing, materials, and printing parameters. *Open Engineering*, *11*(1), 639-649.

[7] Mohamed, O. A., Masood, S. H., & Bhowmik, J. L. (2015). Optimization of fused deposition modeling process parameters: a review of current research and future prospects. *Advances in manufacturing*, *3*, 42-53.

[8] Singh, S., Ramakrishna, S., & Singh, R. (2017). Material issues in additive manufacturing: A review. *Journal of Manufacturing Processes*, *25*, 185-200.

Using LabVIEW to Record and Measure the RMS Voltage Of a Distorted Waveform

Przemysław Otomański, Zbigniew Krawiecki
Poznan University of Technology, Institute of Electrical Engineering and Electronics,
Piotrowo street 3A, 60-965 Poznań, Poland

Email: przemyslaw.otomanski@put.poznan.pl

Abstract. *This paper presents a measuring stand designed to record and measure distorted signals. The study used selected measuring instruments and a PC with an application written in the LabVIEW environment. The developed programme algorithm includes SCPI commands for instrument configuration, signal generation and remote measurements. Communication with the instruments was realised via USB and LAN. The performed computer measuring stand makes it possible to record the waveform and its generation and to compare the results of measuring the RMS value of the distorted voltage with different instruments.*

Keywords: LabVIEW, Virtual Instrument, RMS Value, Acquisition Module

1. Introduction

The developed measurement stand enables the registration of the distorted signal, the measurement of its parameters including the processing and visualisation of the measurement results. The stand was built as a virtual measuring instrument using physical devices and software written in the LabVIEW environment. The software includes drivers for measuring instruments and allows control of the signal source, which is a two-channel digital generator. The applied generator enables the generation of standard sine, rectangle and triangle waveforms, as well as user-defined waveforms. The THD value for a sinusoidal waveform is less than 0.075%. For an arbitrary signal, the resolution of the D/A converter in the generator is 14 bits. The waveform is reproduced at 200 MSa/s. This provides the functionality for the generation of deformed waveforms, which are determined by the operator. The waveforms of this shape can reflect the actual signals present in electrical grids. The following instruments were used in the developed application: a digital oscilloscope, a DAQ measurement module and digital multimeters with different transducers. The use of the LabVIEW environment in the measurement of many quantities is the subject of a number of publications, e.g. [1, 2].

2. Subject and Methods

The measurement stand presented in the article consists of the following components: desktop instruments with USB and LAN communication bus, manual instruments without communication bus and NI USB-6211 measurement data acquisition module. The measurement application based on the NI USB 6211 module was carried out in the LabVIEW environment [3]. The virtual instrument, presented in this article, enables signal generation, recording, measurement, presentation of results and their comparison. It is also possible to relate the measurement result to a calculated value based on the definition of the measurand. This functionality is achieved by recording the actual signal and processing the samples in the program. SCPI programming commands were used in the program algorithm for configuration and remote measurements. The module uses a 16-bit converter for acquisition, with a sampling rate of 250 kSa/s for a single channel. For the USB-6211 module, on the ±5V

ISBN 978-80-972629-6-9

range, the manufacturer reports a random noise value with a standard deviation of 118 μV_{RMS}. The realised measurement stand is shown in Figure 1. The control software was made in NI's LabVIEW environment. The operating algorithm is based on a so-called state machine, which consists of a While loop, a Case structure and Shift register elements. The state automaton controls a multi-layer Case structure with the code implemented in a selected layer of this structure.

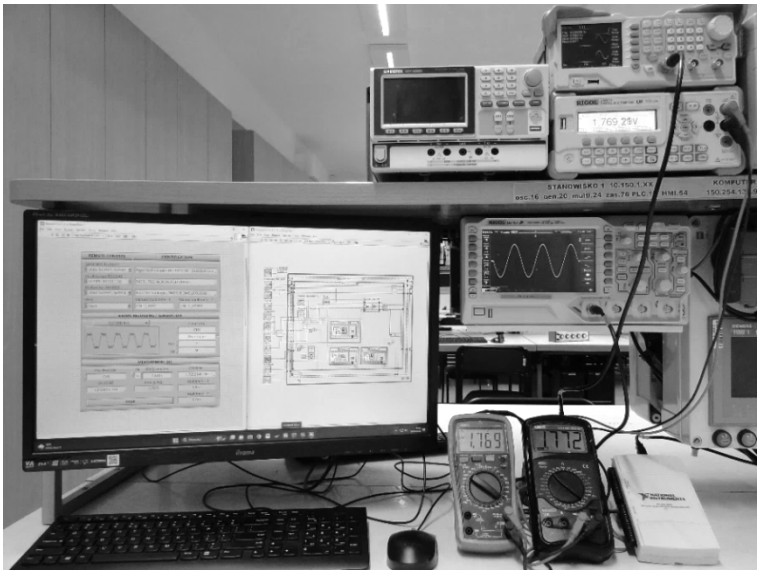

Fig. 1. View of the laboratory stand for recording, signal generation and measurement of the rms value of the distorted voltage.

An example of an excerpt of graphical code from the control programme is shown in Figure 2.

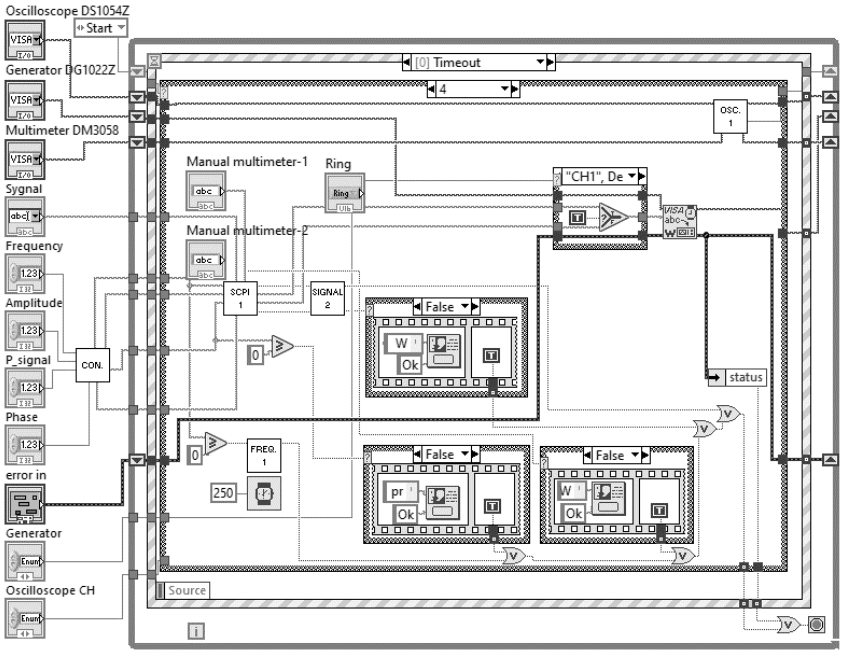

Fig. 2. Excerpt from the graphic code the measurement stand control programme.

The first state is the START state and this is the initialisation of the instruments. This step aims to establish a connection with the devices. After identification, the next stage of the state machine is the signal registration mode or the generation of a test waveform. Recording can

be performed using an oscilloscope then, using SCPI commands, the waveform is downloaded from the instrument to the computer and saved to a file. In signal generation mode, on the other hand, the following settings are required: waveform, voltage value, frequency, channel number. Figure 3 shows the programme dashboard with example settings.

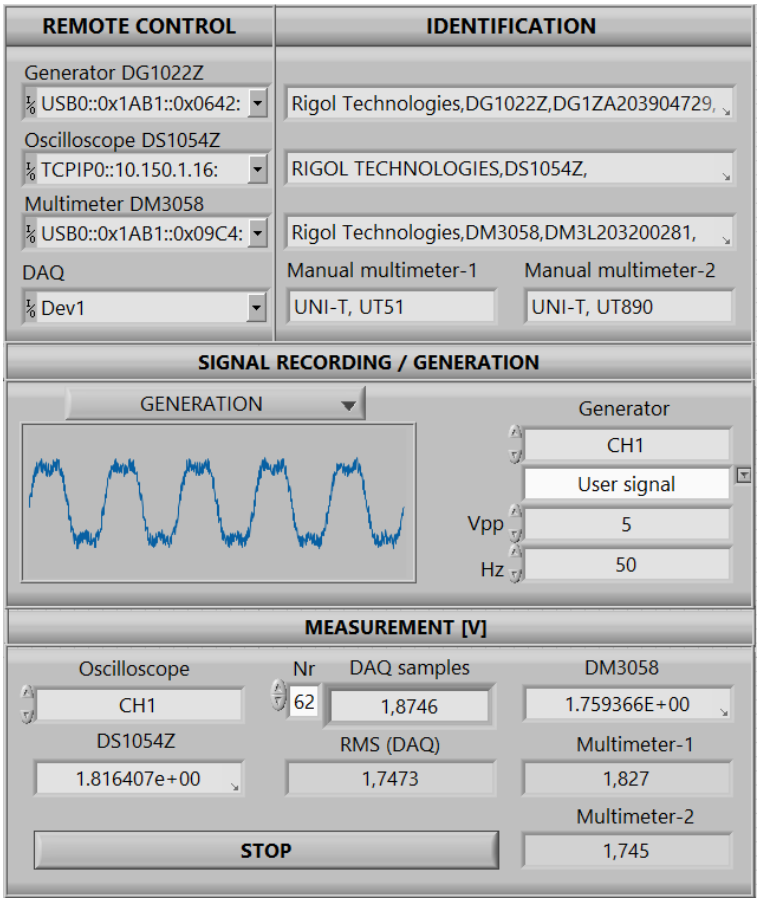

Fig. 3. Control panel of the measurement stand software

The top panel of the programme, shown in Figure 3, shows the measurement instruments used. The middle section (signal recording/generation) shows the generated signal together with the parameters that were entered in the generator. The lower section (Measurement) shows the recorded measurement results.

Measurement results from remotely controlled instruments are acquired using SCPI commands. The format of the result is represented by the form SX.XXXXXXESXX, where: (S stands for sign, X for number, E- for exponent).

The final step is to take remote measurements and enter into the programme the results indicated by manual multimeters that do not have interfaces. In addition, the state machine contains another structure whose function is to control so-called programme events. This is the structure of Event. A programme stop by the operator has been assigned to it. At any point in time chosen by the user, it is possible to interrupt the operation and stop the programme.

3. Results

Table 1 presents examples of measurement results obtained for selected waveforms: sinusoidal, rectangular and triangular. For the above waveforms, the peak-to-peak voltage

value was 3 V_{pp}. In the case of the arbitrary waveform, the signal was composed of a 50 Hz sinusoidal waveform with a fundamental component of 3 V_{pp} peak-to-peak voltage, a third harmonic of 20% of the fundamental component voltage and white noise of 0.4 V_{pp} peak-to-peak voltage. The relative error values given in Table 2 were determined with reference to the DM3058 reference multimeter.

Table 1. Summary of measurement results, for the tested measuring instruments, for selected test signals.

Signal	DM3058 [V]	USB-6211 [V]	DS1054 [V]	UT890 [V]	UT51 [V]
sinus	1.061095	1.062428	1.069715	1.061	1.063
rectangular	1.501671	1.502820	1.500237	1.498	1.654
triangle	0.866549	0.867842	0.874511	0.866	0.837
arbitrary	1.086264	1.096523	1.110788	1.080	1.130

Table 2. Summary of relative errors of tested measuring instruments

Signal	USB-6211 Error [%]	DS1054 Error [%]	UT890 Error [%]	UT51 Error [%]
sinus	0.13	0.82	- 0.01	0.18
rectangular	0.08	- 0.10	- 0.25	10.15
triangle	0.15	0.92	- 0.07	- 3.41
arbitrary	1.00	2.26	- 0.58	4.03

4. Conclusions

The paper presents the development and implementation of a measurement stand for recording and measuring signals of arbitrary shapes. A programme developed in the LabVIEW environment was used to control the operation of the measuring instruments. The programme's algorithm enables the generation of deformed waveforms, which are specified by the user. Such waveforms can reflect real signals in electrical circuits. Communication with the instruments was via USB and LAN buses. The instruments used in the work included various types of analogue-to-digital converters including TrueRMS - DM3058 and UT890, double integral with rectifier UT51. The error values shown in Table 2 indicate that the measurement with a double-integrating converter meter with a rectifier has a significant error. For other measuring instruments, the highest error value is for the arbitrary signal.

References

[1] Otomański P., Krawiecki Z., Odon A. (2010). The application of the LabVIEW environment to evaluate the accuracy of alternating voltage measurements, *Journal of Physics*: Conference Series, 2010, vol. 238, 6pp.

[2] Živanović D., Simić M., Kokolanski Z., Denić D., Dimcev V. (2018). Generation of Long-time Complex Signals for Testing the Instruments for Detection of Voltage Quality Disturbances, *Measurement Science Review*, 2018, 18(2), pp. 41 – 51.

[3] Sokoloff, L. (2004). *Applications in LabVIEW*. Pearson Prentice Hall: Upper Sadle River, NJ, USA.

Optical Fibre Components Calibration Setup with Thermal Compensation Based on FBG Sensors

Gabriel Hencze, Branislav Korenko, Jozefa Červeňová, Jozef Jasenek

Institute of Electrical Engineering, FEI STU, Bratislava, Slovakia,
Email: xhencze@stuba.sk

Abstract. *In this work, we describe the design, implementation and testing of a unique automated measurement system that enables the measurement and characterization of parameters of passive fiber optical elements. The system also allows the calibration of both passive and active optical elements in environments with different temperatures using a thermal chamber. It is especially important if the elements are used outdoors in extreme temperature conditions. We use an optical spectrum analyzer and a tunable laser in the range of 1520 - 1600 nm. Temperature is measured by FBG sensors. This is an uncommon solution too. The insertion losses of optical hubs are measured at different temperatures.*

Keywords: Insertion Loss Measurement, Fiber Bragg Grating, Fiber Optic Couplers

1. Introduction

For optical components such as isolators, circulators, and splitters, the first parameter in the datasheet is attenuation. Attenuation is one of the most important parameters of passive optical components. In general, attenuation is defined as the ratio of the output signal level to the input signal level, expressed in decibels (dB) according to the relationship 1: [2]

$$A_{dB} = 10\,log\,\frac{P_{out}}{P_{in}} \tag{1}$$

The system we designed allows measuring the attenuation of any optical component, but in this paper, we will deal with the measurement of optical hubs. An optical splitter is one of the most important components in an optical network. It is often used to split and join optical signals together. A hub is created by the connection of two parallel optical fibers. When the cores of both fibers are close enough to each other, their fields begin to overlap, and optical power is transferred between these two fibers. The principle of measuring the attenuation of the hub is shown in Figure 1.

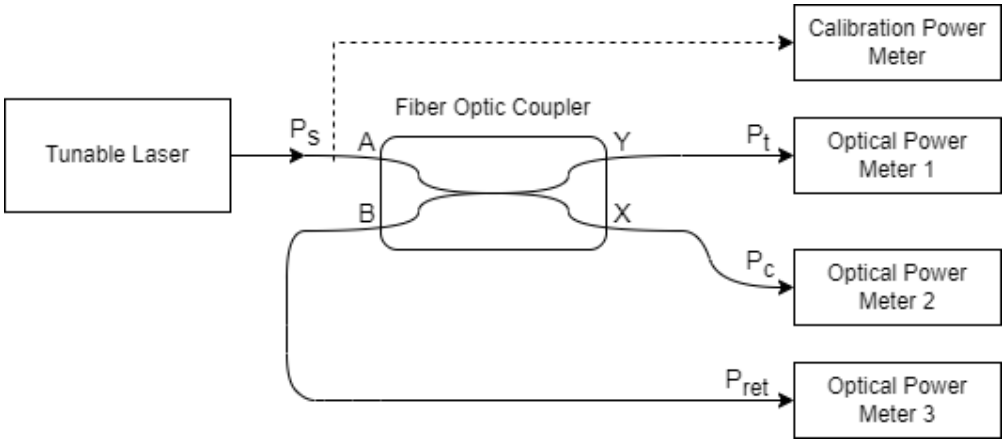

Fig. 1. Insertion losses measurement as a function of wavelength.

For the measurement, a tunable laser and 4 optical power meters are used. They can be used for measurement of the input, transmitted and reflected power. Attenuation, isolation, directivity, coupling or other parameters characterizing the element can be easily calculated from the measured optical powers. [2]

Insertion loss $T_{t,c}$ is the ratio of the input power P_s to the output power P_{tc}, of the given port:

$$T_{t,c} = 10 \log \frac{P_s}{P_{t,c}} \tag{2}$$

Coupling C is given by the ratio of the input power P_s to coupled power P_c:

$$C = 10 \log \frac{P_s}{P_c} \tag{3}$$

2. Basic Instrumentation for Optical Measurement

Figure 2 shows the block diagram of the measuring system. The system is used to measure the attenuation of passive optical elements, as well as to measure temperature using FBG sensors and to calibrate passive components at different temperatures using a thermal chamber.

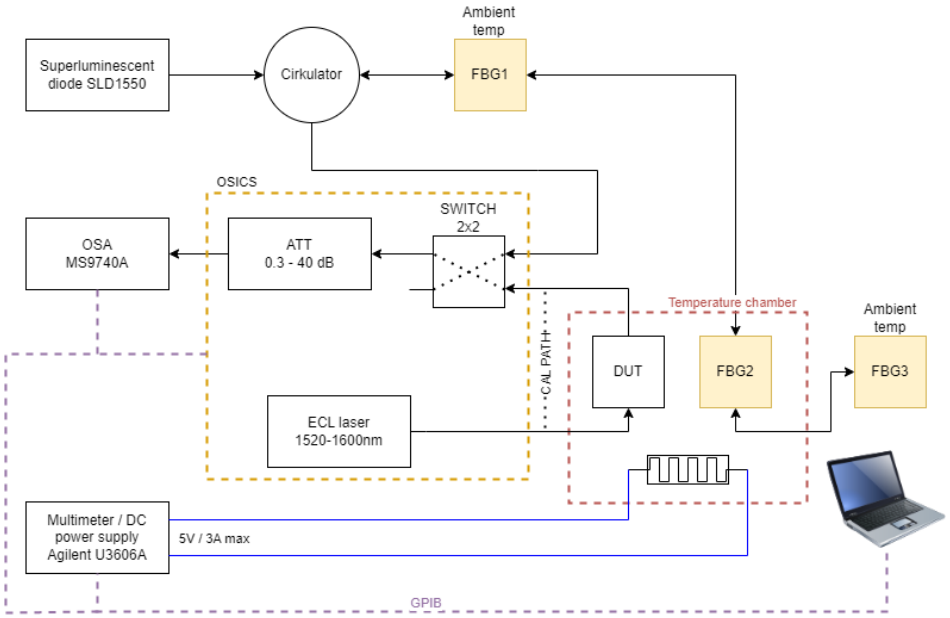

Fig. 2. Block diagram of the system

The main part of the system is the optical spectrum analyzer MS9740A Anritsu (OSA), and the 8-channel OSICS modular system, YENISTA. The OSICS system includes a tunable laser in the range of 1520-1600 nm, an optical attenuator and an optical switch. These devices are connected to the control computer via the GPIB bus. It supports reading the optical spectrum, configuring the spectrum analyzer, setting the wavelength and power of the laser, controlling the attenuator and the switch. Control takes place using standard SCPI commands. FBG sensors connected in series are used for temperature measurement, while the individual sensors are tuned to different wavelengths. A broadband light source and a circulator are needed for temperature measurement. The broadband light source is an SLD diode working at a wavelength of 1550±30 nm, it is used to drive the FBG sensors. The reflected optical signal is separated from the sensors by a circulator. The first sensor and the third sensor measure the ambient temperature, and the second sensor measures the temperature of the thermal chamber.

ISBN 978-80-972629-6-9

The advantage of using FBG together with an OSA is that the analyzer will very accurately measure the shift of the reflected wavelength of the signal caused by temperature change.

The thermal chamber was made by our research team. The thermal chamber consists of a glass tube with a diameter of 3 cm and a length of 10 cm, in which is a spiral heating element. For safety reasons, the chamber is surrounded by heat-resistant material.

The response of the optical sensors goes through the circulator, switch and attenuator to the spectrum analyzer. The temperature determination is based on the wavelength of the measured signal using the function centroid [1]. The data processing is performed by the control software. A tunable laser whose wavelength can be controlled by software is required to measure the attenuation. Before measurement, system calibration is necessary. Attenuation measurement is possible only after calibration is completed. To measure the attenuation, we connect the laser in series to the measured optical element.

During the attenuation measurement in the same range, as the calibration was performed, we measured the power levels and corrected these measured data with the calibration constants. This gives the attenuation of the passive optical element at different wavelengths.

Using a thermal chamber, the system also enables the measurement of attenuation at different temperatures. The thermal chamber contains a heating element that is powered by the U3606 source. The U3606 source can also be controlled via the GPIB interface, so it is possible to set the voltage and thus the temperature by software. We monitor the temperature of the chamber with an FBG sensor and start the measurement only after the temperature in the chamber has stabilized. The thermal chamber works in the range of 20-90°C, and stabilization of temperature after setting takes approximately 30 to 40 minutes.

The thermal chamber does not contain cooling, therefore it only works from room temperature.

3. Results

As a part of the experiment, we measured the attenuation of two different splitters from different manufacturers depending on the temperature in the range of 20-90 °C. In the first case, we measured an asymmetric splitter in the range of 1540-1560 nm with the step of 0.1 nm. We measured the attenuation between the input and the direct port (A>Y), and then between the input and the bound port (A>X). In the second case, we measured a symmetrical splitter with a division ratio of 1:1, in the range of 1520-1600 nm, with a step of 0.5 nm. We measured the attenuation between the input and the direct port (A>Y) and then between the input and the bound port (A>X).

4. Conclusions

We have assembled a unique automated measurement system for the measurement and characterization of parameters fiber optical elements. The system allows the calibration of both passive and active optical elements in environments with different temperatures using a thermal chamber. The system used nontrivial FBG-based fiber sensors as feedback for temperature measurement. Our results show that a temperature change can affect the attenuation of the hub. In the case of the first, asymmetric hub, we observed that as the temperature increases, its attenuation decreases, and higher output power appears at the output**s**. Periodic change in attenuation with a period of ~ 3nm is caused by interference, as multiple reflections occur on unconnected connectors. A commercial splitter has this phenomenon.

The second splitter worked much more stably, where the effect of temperature on attenuation was negligible. We focused on the fact that changes in temperature cause change

ISBN 978-80-972629-6-9

affects the index of refraction of the fibers [3], and due to the thermal expansion of the sheath, the distance between two fibers can also change, which affects the coupling coefficient value and thus the attenuation.

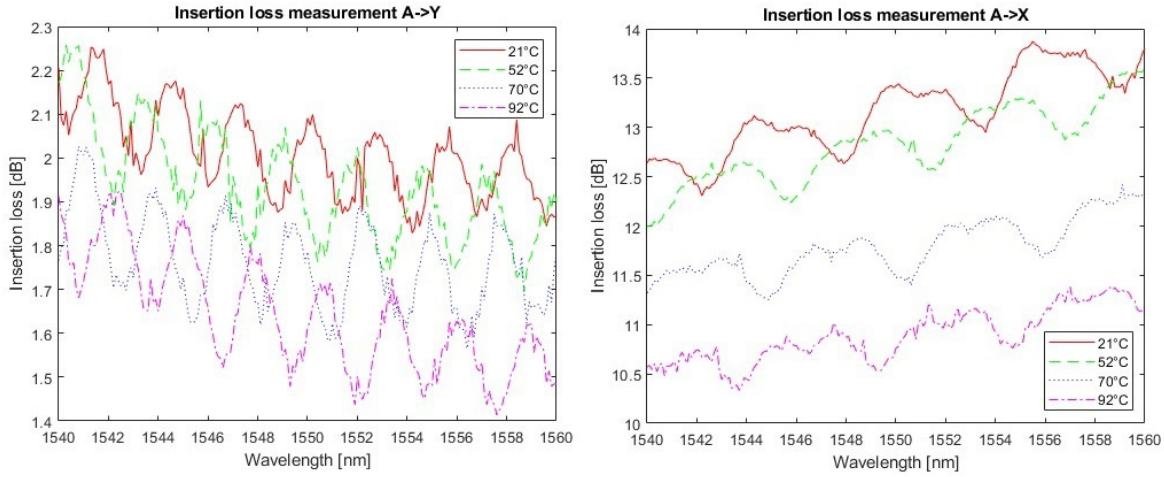

Fig. 3. Inserted losses of the asymmetric hub as a function of temperature

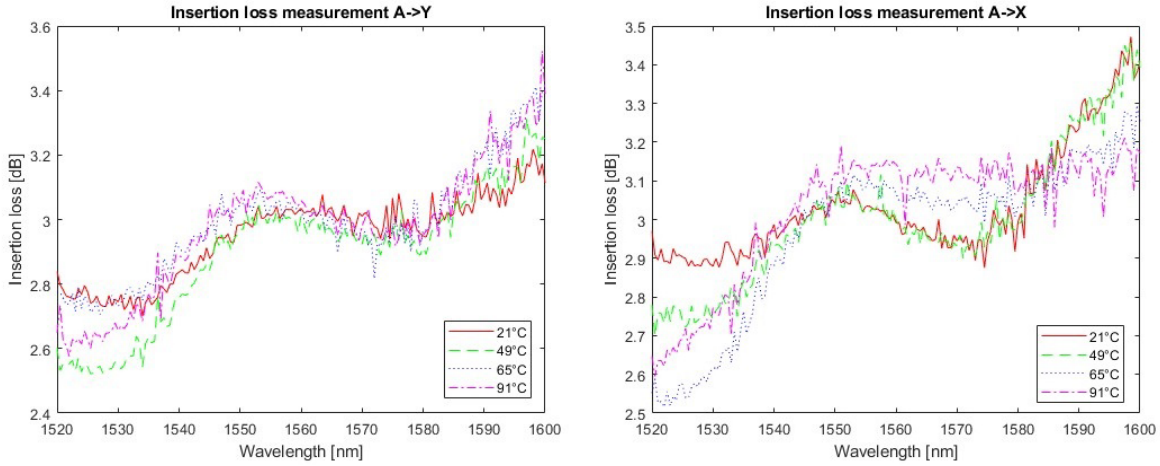

Fig. 4. Inserted losses of the symmetric hub as a function of temperature

Acknowledgement

This work was supported in part by the Scientific Grant Agency (VEGA) of the Slovak Republic under Project 1/0135/20 and in part by the Slovak Research and Development Agency under Contract APVV-16-0059.

References

[1] Korenko, B., Jasenek, J., Červeňová, J. (2015). *Data Processing Techniques for Fiber Bragg Grating (FBG) Reflectivity Characteristics Measurements.* MEASUREMENT 2015, Proceedings of the 10th International Conference, Smolenice, Slovakia

[2] Hui, R., O'Sullivan, M. (2009). *Fiber Optic Measurement Techniques*. Elsevier Academic Press: Burlington. ISBN: 978-0-12-373865-3

[3] Tan, C.Z., Arndt, J. (1999). *Temperature dependence of refractive index of glassy SiO_2 in the infrared wavelength range*. Journal of Physics and Chemistry of Solids 61 (2000) 1315–132

Faulty Antenna Detection in Large Antenna Systems by Measuring the Phase of Reflected Wave

[1]Michal Stibrany, [2]Rene Hartansky, [2]Jakub Krchnak, [2]Michal Dzuris

[1]MWTC, s.r.o., S. Straku 46/25, 914 01 Trencianska Tepla, Slovakia
[2] Slovak University of Technology, Faculty of Electrical Engineering and Information Technology, Institute of Electrical Engineering, Ilkovicova 3, 812 19 Bratislava, Slovakia
Email: mwtc@mwtc.tech

Abstract. *The paper deals with a detection of a faulty antenna in large antenna system. The method consists of phase shift measurement, of both incident and reflected waves. For this purpose, the design and construction of a directional coupler with a 20 dB coupling factor for 1 kW of average power in the FM band is described in this study.*

Keywords: Antenna System Diagnostics, Phase Measurement, Directional Coupler, Stripline

1. Introduction

Terrestrial broadcasting is one of the most common ways of transmitting radio and television signals. The backbone of terrestrial broadcasting is a network of high-power broadcasting stations with the antennas mounted on monotubes, often situated on hilltops. Typically, the broadcasted signal is not radiated by a single antenna but rather is split among multiple antenna sections. As a result, the desired radiation pattern is achieved [1]. Various reasons can cause the degradation of broadcasted signal and thus a reduction in the quality of reception. Some of the possible causes may be various malfunctions that can occur on the antenna or coaxial feed line, as they are exposed to outside weather conditions. We consider an antenna to be without defects if VSWR (voltage standing wave ratio) does not exceed the value stated by the manufacturer. If a fault occurs, VSWR starts to rise. Among the common antenna faults belongs a short or open circuit on the connector, presence of moisture in the connector due to gasket aging, or in general the end of the antenna system lifespan. During winter, antenna can be covered with a thick layer of ice.

While dealing with the diagnostics of a faulty antenna in the antenna system, several options are available, for instance, VSWR measurement at the transmitter output, reflection coefficients measurement of each separate antenna, and radiation pattern measurement. Each of the methods has its advantages and disadvantages, such as time and financial demands, accuracy, and more accurate faulty antenna identification. However, the most impactful feature of a diagnostic method is the need for a broadcasting interruption during diagnostics. An example of another diagnostic method is in [2], where authors propose a comparison between the measured radiation pattern with a simulated model. A faulty antenna can then be assumed to be in the direction with the most significant deviations.

2. Subject and Methods

The method described in this paper assumes that each antenna in the antenna system has a different feeding line length. It implies that in case of RF power reflection from the faulty antenna, the power will return to the transmitter with a different phase shift depending on the antenna, or the distance that the reflected wave must travel. A simplified layout of the transmitter site can be seen in Fig. 1. A directional coupler is inserted at the output of the transmitter, where

ISBN 978-80-972629-6-9

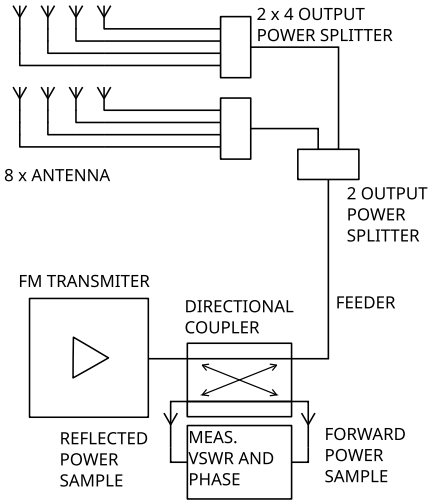

Fig. 1: Simplified diagram of an FM transmitter site.

a small sample of forward and reflected power can be measured. From the coupler, RF power is distributed via a feeder, usually, tens to a few hundred meters long coaxial cable, depending on the location of the antennas on the monotube, where the power is divided by multiple splitters in a cascade. The phase will be measured, after the voltage standing wave ratio (VSWR) increase is detected. As described in [3], for phase delay of reflected wave at the feeder input φ with respect to forward wave applies

$$\varphi = \Phi - 2\beta l, \tag{1}$$

where

Φ phase of reflected power (argument of reflection coefficient at the end of the line)

$\beta = \frac{2\pi}{\lambda}$ wave constant (known from transmission line properties)

l length between the feed line input and the faulty antenna.

As other quantities are known or measured, length l can be calculated.

Now, we will investigate two fatal faults of the antenna, i.e., a short circuit and an open circuit. In the case of the short circuit, reflected wave has an inverted phase $\Phi = 180^\circ$ with respect to incident wave, in the other case, reflected wave is in phase, $\Phi = 0^\circ$. However, less serious antenna faults may cause different Φ, thus further research and measurements are needed. Due to various possible Φ as well as phase measurement uncertainty, the precise position of the antenna may not be exactly determined, but still, the number of possibly faulty antennas will be narrowed. We decided to experimentally verify the proposed method using an FM transmitter TEM A07A1100S with a nominal output power of 1 kW and 3 antennas (2 x Kathrein 752038, 1 x Yagi).

Directional coupler design

Dual directional couplers with the needed parameters are usually custom built. Therefore, we have designed a coupler with 20 dB coupling factors in both directions and isolation of > 45 dB using stripline topology with an air dielectric. The design was made in AWR Design Environment software with courtesy of CERN. For practical reasons, it would be useful to choose the forward coupling factor of 30–40 dB, so that there is an appropriate level of power (less than

+30 dBm) on the coupled port, suitable for further signal conditioning. However, during the development, it turned out that an asymmetrical coupler with coupling factors of 40 dB and 20 dB, has insufficient directivity, mostly because the propagation uniformity of even- and odd-mode waves is disrupted [4]. Therefore, we decided to use a symmetrical directional coupler. Figure 2 shows the resulting characteristics for designed dimensions reached by simulations.

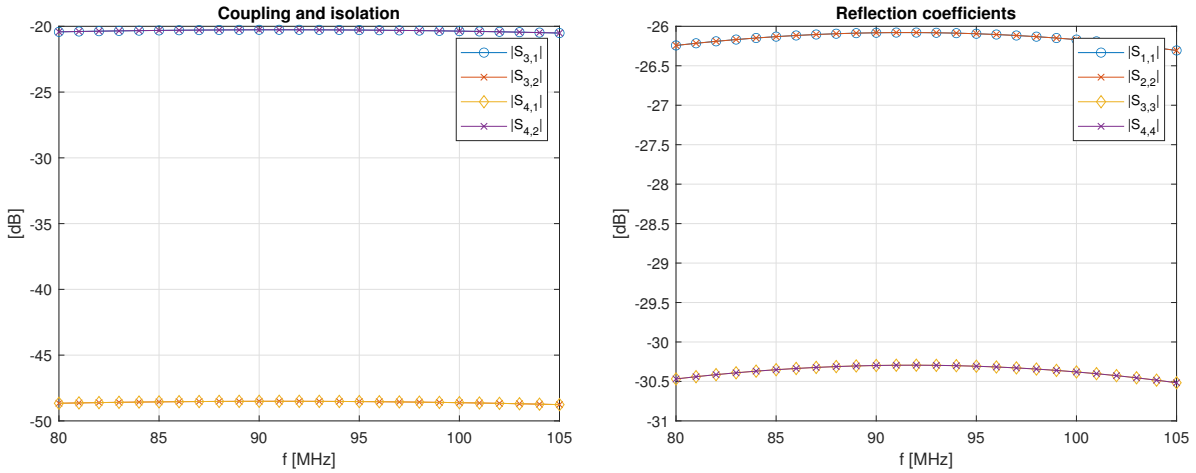

(a) Coupling factors $S_{3,1}$ and $S_{4,2}$, isolation $S_{4,1}$ and $S_{3,2}$.

(b) Reflection coefficients – port 1 input, port 2 – output, port 3 – coupled with the forward wave, port 4 – coupled with the reflected wave.

Fig. 2: Characteristics of a module of S-parameters of the simulated coupler.

Directional coupler construction

Fig. 3: Picture of the manufactured directional coupler.

The manufactured directional coupler has input and output power connected using a 7/8" connector, the remaining ports (coupled and terminated) are connected by N connectors. The overall dimensions of the coupler are 91 x 14.4 cm. The insertion of Teflon dielectric used as line supports influences the reflection coefficients, as it represents an inhomogeneity on the line, but by measuring the S-parameters, we have verified that this effect can be neglected. Measurement of the S-parameters was performed on 4-port Network Analyzer Agilent E7050B, S-parameters measurements can be seen in Fig. 4. The measured insertion loss is 0.18 dB, which causes about 40 W of incident power loss at full transmitter output power.

With the mentioned transmitter running at full power of 1 kW, we are able to measure reflected power starting at 2.3 W with an uncertainty of 5% due to non-ideal isolation of ports, causing also phase uncertainty. With an increase of reflected power, the uncertainty decreases. The maximum reflected power is determined by the transmitter lockout itself to 100 W [5]. Based on the above, the VSWR range in which we are able to measure the phase of reflected wave is from 1.1 to 1.9.

ISBN 978-80-972629-6-9

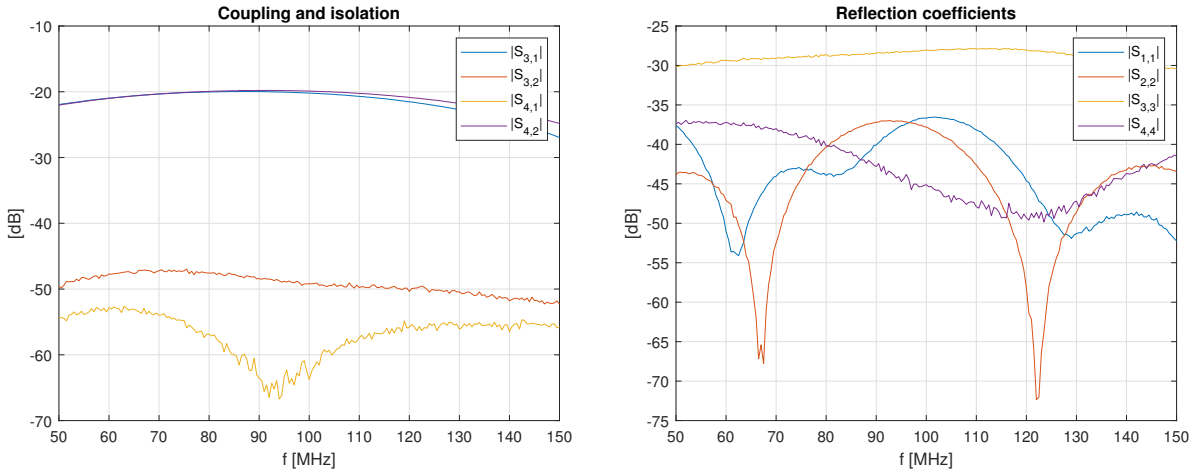

(a) Coupling factors $S_{3,1}$ and $S_{4,2}$, isolation $S_{4,1}$ and $S_{3,2}$.

(b) Reflection coefficients: port 1 – input, port 2 – output, port 3 – coupled to port 1, port 4 – coupled to port 2.

Fig. 4: Measured characteristics of a module of S-parameters of the manufactured directional coupler.

3. Results

The result of this work is the theoretical analysis of the method, using which, we should be able to detect faults in antenna systems during nominal operation. The proposed method should detect faults immediately, without the presence of an operator.

We designed and manufactured the directional coupler (Fig. 3) needed for the proposed method verification. The measured S-parameters shown in Fig. 4 satisfy the required coupling and directivity. The subject of further research will be the phase measurement with directional coupler, harmonic driving and changing load impedance, analysis of the typical antenna faults and reflection coefficient investigation as well as signal conditioning circuits design.

Acknowledgements

This publication was supported by the national scientific grant agency VEGA under the project No.: 1/0045/21 "Electromagnetic compatibility of wireless IoT devices" and project APVV 20-0042 "Microelectromechanical sensors with radio frequency data transmission".

References

[1] Vavra, S., Turan, J. (1989). *Anteny a Sirenie Elektromagnetickych Vln*. Alfa.

[2] Krchnak, J., Hartansky, R., Dzuris, M., Stibrany, M. (2022). Detection of faulty antenna in antenna system using equivalent hertzian dipole structures. In: *Electro-Mechanical Systems Application in Industry 2022*. pp. 47–50.

[3] Hajach, P. (2008). *Mikrovlnna Technika*. STU, Bratislava, 1st edition.

[4] Howe, H. (1974). *Stripline Circuit Design*. Artech House, Inc.

[5] Technical, maintenance and installation manual 1000 W FM transmitter A07A1110S. TEM S.r.l.

Power Loss Measurement for Small Closed Material Samples

Lukáš Zdražil, Zdeněk Roubal

Department of Theoretical and Experimental Electrical Engineering, FEEC, BUT, Brno; Czech Republic,
Email: Lukas.Zdrazil1@vutbr.cz

Abstract. *When measuring the specific losses on small ferrite cores, high demands are placed on the wattmeter used. Commonly available wattmeter types suitable for 50 Hz frequency do not achieve sufficient sensitivity for ferrite materials for switching power supplies, and the measurement uncertainties are too high. For the current channel, it is necessary to achieve very small phase errors and high sensitivity. These demanding requirements are necessary for measurements at low magnetic induction saturation B_{max}. The proposed sensitive wattmeter achieves higher gain accuracy for both channels than the oscilloscope solution, while maintaining a high bandwidth of approximately 50 kHz with a measurement uncertainty below 2%. The ability to quickly measure the dependence of specific losses on excitation reduces the error caused by self-heating.*

Keywords: Soft Ferrites, Wattmeter, Specific Losses in Ferromagnetics, Magnetic Measurements

1. Introduction

Magnetically soft ferrites for switching power supplies represent a large segment of the magnetic materials market today. As innovations require increasing the efficiency of switching power supplies, there is pressure to develop new ferrite materials with lower specific losses [1], [2]. These depend on the inductance B used as well as the temperature and shape of the excitation signal [1]. In the following, we assume the provision of a harmonic waveform of the magnetic induction B by a suitably chosen excitation amplifier and temperature stabilization of the sample, ideally in an oil bath. If these conditions are not met, they can introduce considerable uncertainty into the result obtained.

Great demands are also placed on the sensitivity of the wattmeter. The wattmeter should be able to measure losses on both large and very small samples. On small samples, small losses are measured. The minimum value that the wattmeter should be able to measure is 10^{-7} W/kg, and the maximum value is 10^{1} W/kg. Sensitivity will be provided by a cascade of operational amplifiers with adjustable gain. The operational amplifiers must have a small offset voltage and a very small phase change in the operating band so that the accuracy of the wattmeter is not compromised. It is also important to use an accurate analog multiplier to achieve high measurement accuracy.

The magnetic induction at which the measurement will be made should be in the range of 1 mT to 0.7 T. The magnetic induction waveform will be harmonic only. A large bandwidth is also required, nominally from 10 Hz to 50 kHz. Within this bandwidth, the wattmeter should measure with an accuracy of ±2 % [3].

2. Important parameters of the wattmeter in terms of its accuracy

In [1], type B uncertainties in ferrite specific loss measurements using a shunt and a digital oscilloscope were analyzed. A deeper analysis in that paper shows that while for the

ISBN 978-80-972629-6-9

uncertainties in the determination of the amplitude of the corresponding voltage and current measurements by the sample, together with the uncertainty in the determination of the shunt value, their contribution depends on the cosine function, for the uncertainty in the phase shift between voltage and current $\phi_{U\text{-}I}$ depends on the sine function. This leads to the important conclusion that for a typical value of the phase shift between voltage and current on a measured ferrite sample in the range of 80-90°, the contribution of the uncertainty of the phase shift between voltage and current is decisive. The smaller the core loss, the more the phase shift between voltage and current will be close to 90°. This will lead to a larger error in determining the total losses in the core. Thus, the greatest care should be taken to ensure that the phase shift of the designed amplifier elements in the measurement chain is negligible.

3. The block structure of the designed wattmeter

The output of the wattmeter will express the area of the dynamic hysteresis loop [4], [5]. The proposed wattmeter consists of a current and voltage channel. In our case, the current channel will receive the instantaneous value of the current flowing through the primary winding of the sample, and the voltage channel will receive the instantaneous value of the voltage across the secondary winding of the sample. The schematic of the proposed wattmeter is shown in Fig. 1. A frequency-compensated resistive divider will be placed at the input of the voltage channel, and a current-to-voltage converter with an operational amplifier will be placed at the input of the current channel.

The cascades of operational amplifiers with adjustable gain will be placed downstream of the resistive divider and current-to-voltage converter. The cascades will be independently adjustable. Both cascades will consist of six operational amplifiers. The amplifier cascades, the resistive divider, and the current-to-voltage converter will be designed so that the output voltage is the same for all input ranges. Both channels will then input to a precision analog multiplier. The instantaneous value of the voltage output from the multiplier will be equal to the instantaneous value of the sample loss. In addition, a voltage rectifier will be connected downstream of the amplifier cascade of the voltage channel, and its output will be a DC voltage value proportional to the amplitude of the magnetic induction of the sample. The necessary low passes will have a switchable time constant [3].

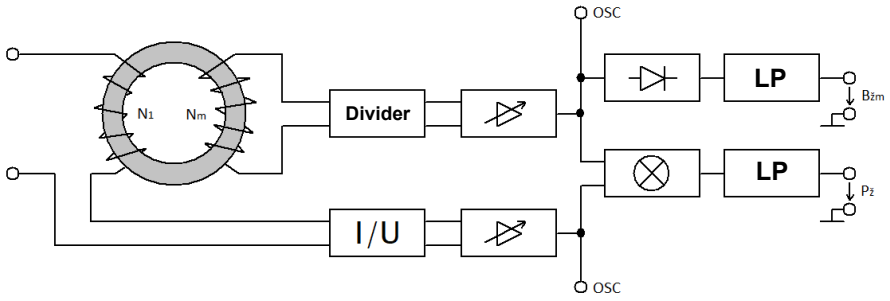

Fig. 1. Block diagram of the designed wattmeter.

4. Suitable choice of analogue multiplier

From a search of available analogue multipliers, the two best ones were selected, namely AD534 and AD734. By measuring their static conversion characteristics and frequency characteristics, it turned out that the more modern AD734 analogue multiplier actually achieves better performance even at lower frequencies. Its frequency characteristic does not have a resonant overshoot. Its measured parameters are shown in Figure 2. The optimum input voltage

of the analog multiplier for best accuracy is set between 3-9 V for both channels.

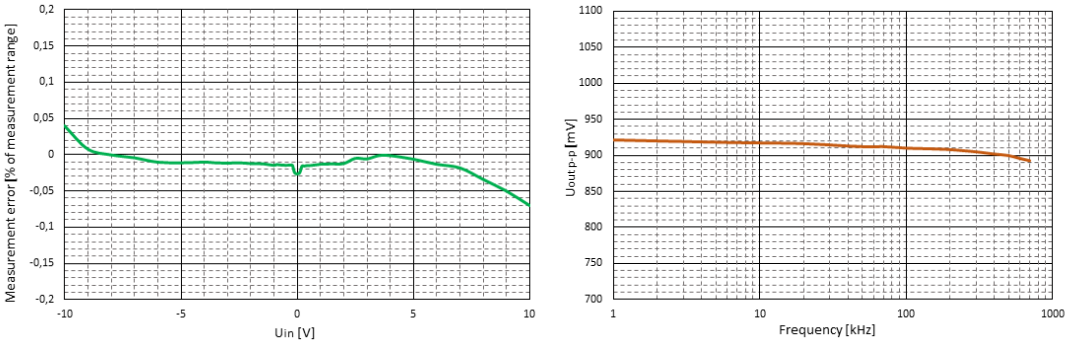

Fig. 2. Measured parameters of the AD734 analogue multiplier. Relative error of the conversion characteristic on the left and frequency characteristic on the right

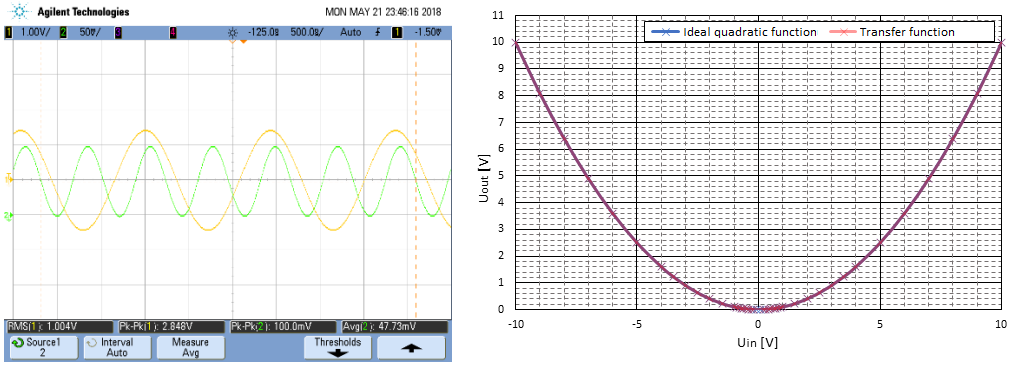

Fig. 3. The yellow curve shows the voltage waveform at the input, and the green curve shows the voltage waveform at the output of the analog multiplier. On the right is transfer characteristic AD734

For lower input voltages, the bandwidth drops significantly.

5. Designed voltage and current channel ranges, achieved parameters

To achieve optimum accuracy of the analog multiplier, a step of 10 dB ranges in series 1-3 was chosen. The input connector was chosen to be BNC so that a common voltage probe could be used.

Table 1. Wattmeter voltage and current channel ranges and gain.

Voltage channel			Current channel		
Input range	**Voltage divider**	**Amplifier gain**	**Input range**	**Rezistors in I/U convertor**	**Amplifier gain**
10 mV	None	900	1 µA	10K	900
30 mV	None	300	3 µA	10K	300
100 mV	None	90	10 µA	1K	900
300 mV	None	30	30 µA	1K	300
1 V	1:10	90	100 µA	100R	900
3 V	1:10	30	300 µA	100R	300
10 V	1:100	90	1 mA	10R	900
30 V	1:100	30	3 mA	10R	300
			10 mA	1R	900
			30 mA	1R	300
			100 mA	0.1R	900
			300 mA	0.1R	300

OPA842 was selected as the appropriate OZ for the individual blocks. Their disadvantage is a higher input quiescent current and output ripple of only +-5V. Therefore, OPA656 was selected as the input amplifier, but it showed undesirable oscillation. It was replaced by the OPA211 with very good input noise performance. The THS4631 then achieves the necessary spread

ISBN 978-80-972629-6-9

before the analogue multiplier. The I/U converter significantly degrades the phase characteristic of the current channel. Therefore, the feedback resistance was chosen as low as possible with subsequent amplification using OPA842 inverting amplifiers.

The measurements were performed using a BODE 100 analyzer. The outputs for the voltage channel are shown in Table 2.

Table 2. Measured results for the voltage channel of the wattmeter.

Frequency	Phase change for gain 900		Phase change for gain 300		Phase change for gain 90		Phase change for gain 30	
	Simulation	Measurement	Simulation	Measurement	Simulation	Measurement	Simulation	Measurement
10 kHz	-0,05°	-0,16°	-0,05°	-0,12°	-0,04°	-0,11°	-0,04°	-0,08°
30 kHz	-0,16°	-0,52°	-0,15°	-0,29°	-0,14°	-0,19°	-0,12°	-0,13°
50 kHz	-0,27°	-1,11°	-0,25°	-0,76°	-0,23°	-0,35°	-0,21°	-0,28°

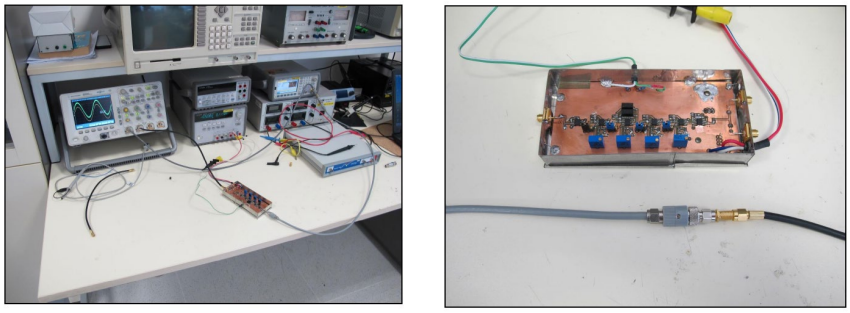

Fig. 4. Output voltage measurement of the current channel (left) and the proposed module (right).

6. Conclusions

The proposed wattmeter was analyzed mainly in terms of minimum phase error. Due to the possibility of fast measurement (time constant output 30 ms) with an external DC voltmeter, it is possible to detect the dependence of the measured losses on the magnetic induction B with the limitation of self-heating of the measured sample. This offers the possibility of increasing the repeatability of measurements for samples where an oil bath cannot be used for temperature stabilization.

Acknowledgements

The research was funded via a BD 2023-2025, FEKT-S-23-8425.

References

[1] Roubal, Z. (2015). Core Loss Measurement at High Frequencies. Przegląd Elektrotechniczny, 91(4), 51-52.

[2] Roubal, Z., Marcon, P., Cap, M. (2012). Analysis of magnetic properties measurement in closed samples. In: 2012 *ELEKTRO*. IEEE, 460-464.

[3] Zdražil, T. (2018). *Přesný wattmetr pro měření měrných ztrát feritových jader*. Bachelor Thesis.

[4] Roubal, Z., Smejkal, V. (2013). Determination of parameters in the Jiles–Atherton model for measured hysteresis loops. In 9th International Conference Measurement.

[5] Eichler, J., Novák, M., & Košek, M. (2017, May). Improvements of Preisach model for soft magnetic materials, experiments on filtering of input excitation signal. In 2017 11th International Conference on Measurement, 107-110. IEEE.

Advances in EMP Objectification Through Mathematical Modelling Using Innovative Technologies

Ľuboš Skurčák, Ľuboš Pavlov, Peter Bojda, Ján Gbelec

VUJE, a. s., Trnava, Slovakia,
Email: lubos.skurcak@vuje.sk

Abstract. *Decree of the Ministry of Health of the Slovak Republic No. 534/2007 Coll. lists the requirements for the protection of the health of inhabitants in the environment in connection with exposure to electromagnetic fields (EMF) on the human body. According to this decree, scientifically based standards, procedures, and recommendations must be used to assess, measure or calculate exposure to electromagnetic fields. It is important that the application of the chosen procedure to objectify the electromagnetic field exposure is not simply a matter of determining "a few precise values" at randomly determined locations, since the aim of any measurement or calculation must be to objectively assess the overall situation with regard to the protection of the health of persons in relation to exposure to electromagnetic fields. Within the Slovak Republic, the objectification of EMF exposure is most often carried out by means of measurements. However, this procedure has its specific limits of use, which are often overlooked in practice. However, they have the potential to influence the outcome of the assessment. In contrast, the objectification of EMF exposure by calculation, in combination with the innovative means of remote sensing with Light Detection And Ranging (LiDAR) technology, brings several advantages.*

Keywords: Low-frequency Electromagnetic Field, Electric Field Strength, Magnetic Induction, LiDAR

1. Introduction

In the field of low-frequency EMFs of the 50 Hz network frequency, the currently valid Decree of the Ministry of Health of the Slovak Republic No. 534/2007 Coll. establishes action levels of electric field strength (E) and magnetic induction (B) in order to ensure the protection of the health of the population in relation to their exposure to electromagnetic fields. In accordance with this legal standard, scientifically based standards, procedures and recommendations are used to assess, measure or calculate exposure to electromagnetic fields [1].

The aim of the present paper is to highlight the advantages in the objectification of EMF by mathematical modelling using innovative technologies.

One of them, for example, is LiDAR technology, which is the method for determining ranges by targeting an object with a laser and measuring the time for the reflected light to return to the receiver. The output of a system working with this technology is a georeferenced point cloud providing multiple applications. In the case of objectifying the magnitude of the exposure to the electromagnetic field, the point cloud allows the creation of very accurate models of the facilities and spaces under consideration. The paper presents the authors' real experience of using the LiDAR system outputs to model the distribution of non-ionizing low-frequency electric and magnetic fields in the vicinity of outdoor power lines [2] and in the vicinity of power substations [3], which they have acquired during research projects and EMF measurements within the framework of an accredited testing laboratory of electromagnetic fields.

Our experience, presented in the past [4], shows that direct EMF measurements allow to assess compliance with the action values defined in [1] only for specific operating conditions

ISBN 978-80-972629-6-9

of existing power installations. However, mathematical modelling is a means to objectify EMF exposure levels at any operating conditions, including the maximum ones [5]. This knowledge and experience are also used in the current research project supported by the Research and Development Agency under Contract No. APVV-19-0214. One of the solved subtasks of this project is the objectification of the electromagnetic field levels of the 50 Hz network frequency in selected densely populated areas, in the vicinity of distribution transformer stations and power lines. The creation of mathematical models based on remote sensing data of the Earth's surface using LiDAR technology will allow to achieve more accurate results of EMF exposure calculation in the vicinity of power installations or to verify the effectiveness of the measures taken to reduce it.

2. Use of LiDAR technology in the creation of mathematical models

Mathematical modelling is an interactive process that is based on knowledge of the terrain profile, shapes and structural sections, function and materials of all facilities, including their spatial location. It is LiDAR technology that is the appropriate tool for obtaining most of the above information. The data acquired through LiDAR technology is represented as a point cloud in 3D space with a very precise position, which after processing, can be categorized into different classes, creating 3D models of the objects being imaged or georeferenced output in the form of a digital model of the surface or terrain.

VUJE, a. s. uses a system that provides a maximum measurement range of up to 1350 m, an effective measurement rate of up to 750 000 measurements/sec. and an operational flight height of up to 530 m in the implementation of aerial diagnostics of overhead power lines. The minimum point density for a single aerial laser scan declared by the manufacturer according to the equipment specification for a scanning speed of 820 kHz and a flight speed of 30 kn (approx. 55 km/h), shall reach a density of at least 100 points per m^2 at a distance of 100 m, always higher for shorter distances. The laser scanning technology used, according to the manufacturer's data, allows an unlimited number of reflections of a single beam to be captured.

The acquired data were used in the creation of a digital terrain model (DTM) and a digital surface model (DSM). The DTM model representing the earth's surface model can be used as a part of mathematical models to calculate EMFs. The point cloud in 3D space allows to obtain the most accurate geometric layout of the modelled transformation station. In the case of overhead power lines, it is possible to obtain the necessary information about the geometric (spatial) arrangement and layout of the conductors on the power line mast as well as the deflection at any point of the investigated power line span.

3. Verification of measured and calculated values

Verification of the calculated values with the measured ones was carried out using the correlation index IK (1), i.e. by generalizing the correlation coefficient, which characterizes the strength (quality) of the general dependence of two variables (in our case, measured and calculated). The correlation index, in the case of similar curves, takes values from the interval <0-1>. The closer the correlation index is to 1, the more appropriate the dependence between the variables *X*, *Y*. Using the distribution (according to Cohen) of the calculated correlation indices, it was possible to evaluate the dependence of the calculated and measured values as follows:

- <0.0-0.1> represents a trivial dependence (the curves being compared are different),
- (0.1-0.3> a small dependence,
- (0.3-0.5> medium dependence,
- (0.5-0.7> large dependence,
- (0.7-0.9> very large dependence,

ISBN 978-80-972629-6-9

- (0.9–1.0> almost perfect dependence.

$$IK = \sqrt{\frac{\sum_{i=1}^{n}(x_{inam}-\bar{x}_{nam})^2-\sum_{i=1}^{n}(x_{inam}-x_{ivyp})^2}{\sum_{i=1}^{n}(x_{inam}-\bar{x}_{nam})^2}}, \quad (1)$$

where: X_{nam} – measured value,

$\bar{X}_{nam}$ – average measured value,

X_{vyp} – calculated value.

Verification of the method was carried out by comparing the measured and calculated values of electric field strength and magnetic induction with a frequency of 50 Hz in the vicinity of five different types of 22/04 kV concrete block transformer substations. An example of the result of the magnetic induction distribution B (μT) around HKP (GRAPER) type transformer stations is shown in the figure below (Fig. 2). An example of the result of the magnetic induction distribution B (μT) around HKP (GRAPER) type transformer stations is shown in the figure below (Fig. 1). The overall results of the comparison are presented in table 1, which shows the results of the correlation index for the electric field strength (IKE) and magnetic induction (IKB).

The results of the IKE comparison show a very large dependence between the measured and calculated values in the four cases considered. In one case, a nearly perfect dependence was calculated. In the case of the IKB comparison, almost perfect dependence is obtained in two cases and in the other cases, it was a very large dependence. Based on the results obtained, it can be concluded that the objectification of the electric field strength and magnetic induction levels by means of the developed mathematical models provides a comparable qualitative level compared to the measurements of an accredited testing laboratory. However, the application level, especially when using LiDAR technology, is considerably higher and allows a large number of real situations to be investigated.

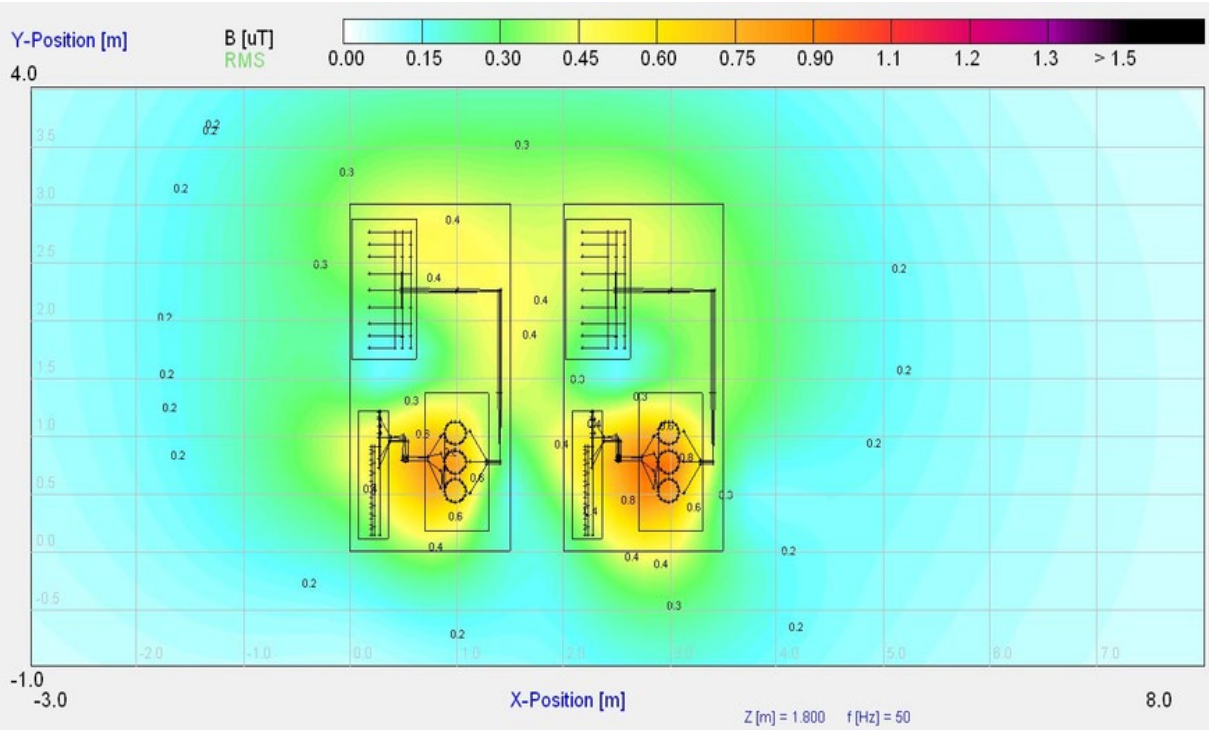

Fig. 1. Distribution of magnetic induction B (μT) in the vicinity of transformer stations of HKP type (GRAPER)

Table 1. Calculated correlation index values for *E* and *B* around different types of 22/0.4 kV substations

No.	Type of transformer station	*IKE*	*IKB*
1.	EH8C	0.835	0.857
2.	EH6	0.931	0.843
3.	EH8D.1	0.830	0.922
4.	HKP (GRAPER)	0.830	0.931

4. Conclusions

The results presented in the present paper show the benefits of using innovative and modern technical means, in this case, a system using LiDAR technology in the field of creating mathematical models for the needs of determining the level of EMF exposure in the vicinity of electricity transmission and distribution facilities. In this way, it is possible to make an informed objectification of the exposure of persons to electromagnetic fields at any operating conditions, including the maximum ones. In the event of exceedances of the applicable action values, measures to reduce the magnitude of EMF can be proposed, and their effectiveness verified based on the results of mathematical modelling. In the vicinity of overhead power lines, the EMF exposure level can be reduced by measures such as site landscaping, design or construction modification of the source, or shielding, e.g. using tall vegetation, and its beneficial effect on the EMF exposure level can be declared by several verified mathematical models [2,3,4,5]. Such possibilities are severely limited when determining EMF exposure levels by measurement.

In practice, LiDAR system outputs such as digital terrain model (DTM) or digital surface model (DSM), in combination with point cloud in 3D space with very precise position, can be used for the needs of objectification of other environmental factors, e.g. simulations of noise load generated by operating overhead lines, etc.

Acknowledgements

This work was supported by the Research and Development Agency under Contract No. APVV-19-0214.

References

[1] Vyhláška Ministerstva zdravotníctva SR č.534 zo 16. augusta 2007 o podrobnostiach o požiadavkách na zdroje elektromagnetického žiarenia a na limity expozície obyvateľov elektromagnetickému žiareniu v životnom prostredí.

[2] PAVLOV, Ľ., SKURČÁK, Ľ., BOJDA, P., GBELEC, J.: *Výpočet intenzity elektrického poľa a magnetickej indukcie v úsekoch medzi stožiarmi p.b.č. 4 - 5 a p.b.č. 7 - 8 na 400 kV vedení V045*, technická správa VUJE 2022, Ev č: 1230/11/2022

[3] SKURČÁK, Ľ., PAVLOV. Ľ., BOJDA, P.: *Inovatívne trendy v objektivizácii elektromagnetických polí,* Fyzikálne Faktory Prostredia, ročník XII, číslo 2-2022; s. 72-75.

[4] SKURČÁK, Ľ., BOJDA, P., CHOVANEC, J.; *Výhody matematického modelovania elektromagnetických polí v procese posudzovania vplyvov na životné prostredie líniových energetických stavieb*, 8.ročník HKP, Poráč, 2017.

[5] LAGO, J. SAVČÁK, M. SKURČÁK, L. BOJDA P.: *Transmission Capacity Increasing of Overhead Heavy-Current Lines with the Respect of the Environmental Limits of Population Protection against the Effect of Electromagnetic Field*, Ref. B2-107, CIGRÉ, Paris 2008.

Non-Contact Measurement Dry Transformers Using an Acoustic Camera with a Modular System

Daniel Korenciak, Miroslav Gutten, Martin Karman, Peter Brncal

Faculty of Electrical Engineering and Information Technology,
University of Zilina, Zilina, Slovakia
Email: daniel.korenciak@feit.uniza.sk

Abstract. *The article describes the non-contact measurement of 1 MVA dry power transformers with epoxy resin insulation using an acoustic camera with a modular system. In this way, it is possible to analyze the frequency spectrum with the possibility of 3D monitoring of the transformer with the identification of the place with the greatest noise. The acoustic emission of two distribution dry transformers with the same type and power is compared, and then the condition of the structural parts of the "noisier" transformer is evaluated. Noise measurement in dB alone is sometimes not enough to detect a fault. It is necessary to perform an acoustic emission analysis through noise visualization and frequency analysis of the individual components of the transformer noise at idle and under load.*

Keywords: Acoustic Camera, Acoustic Emission, Dry Transformers

1. Introduction

The principle of acoustic field analysis is the formation of feedback within the frequency spectrum from the noise source. The acoustic emission analysis method for transformer diagnostics may have some advantages in comparing electrical as well as optical and chemical methods [1], [2].

A dish carrying several microphones can be the best alternative for the analysis of the acoustic spatial spectrum with the possibility of visualizing the measured electrical equipment, thanks to which it is possible to determine the source of the largest or most intense noise [3], [4].

Using the acoustic camera with a modular system, it is possible to identify the maximum point of noise and acoustic emission with the possibility of tracking the frequency spectrum and tracking the measured object in a 3D sound field. Thanks to the displayed 3D acoustic field of the sound camera, it is possible to spatially identify a potential fault on the measured device during its operation. The advantage of these systems is that thanks to the displayed frequency spectrum, there is no need to use an external frequency filter, which some measuring devices use for noise measurement.

In diagnostics, the acoustic camera can be applied wherever an incipient transformer failure can cause a change in vibrations and thus a change in the amplitudes of the frequency spectrum of the acoustic emission for the measured object [5].

The application of non-contact analysis using acoustic emission for the diagnosis of distribution transformers has significant advantages over off-line contact methods [6], [7]:

- it is possible to identify the area of the source of the increased noise intensity, and thus a possible defect in the equipment,
- when using a modular camera system, it is possible to direct the microphone plate to the place of increased acoustic emission or noise,
- the possibility of using the analysis of a wide range of the frequency spectrum.

ISBN 978-80-972629-6-9

2. Experimental measurement

Experimental diagnostics with measurement of acoustic emission (AE) was carried out at power transformers 22000/400 V, 1 MVA with insulation epoxy resin at standard power supply operation. One of the T-01 transformers was noisier to the human ear than the T-02 transformer. The analyzed machines were in normal insulating and mechanical condition.

The diagnostic dry-type transformers are placed in the closed cells of the distribution transformer, where the distribution of electricity is ensured for the work organization dealing with lighting technology. Next to the transformer cells, the offices are separated by only one wall. The T-01 transformer was noisier than the T-02 transformer in the office, which made the working atmosphere in the office unpleasant. The noise of the T-02 transformer in the other office was hardly heard at all.

For the analysis of the acoustic emission of both distribution of dry transformers T-01 and T-02, a Nor848A camera with a modular system was used, where it was installed at the same distance for the nearest safety location 1.8 meters from the measured object and turned at the same angle. Since the standard recommends measuring the noise of the transformer at a distance of 1 m, it was necessary to set the acoustic emission measurement on the camera to the required value.

Fig. 1 and 2 are pictures of the analysis AE of the "noisy" transformer T-01 in the no-load of and state at 10%-load in normal operation. The acoustic camera was focused on measuring the whole surface of the tested transformer in the same place, and both pictures (Fig. 1 and 2) demonstrate the locations of points with the maximum noise.

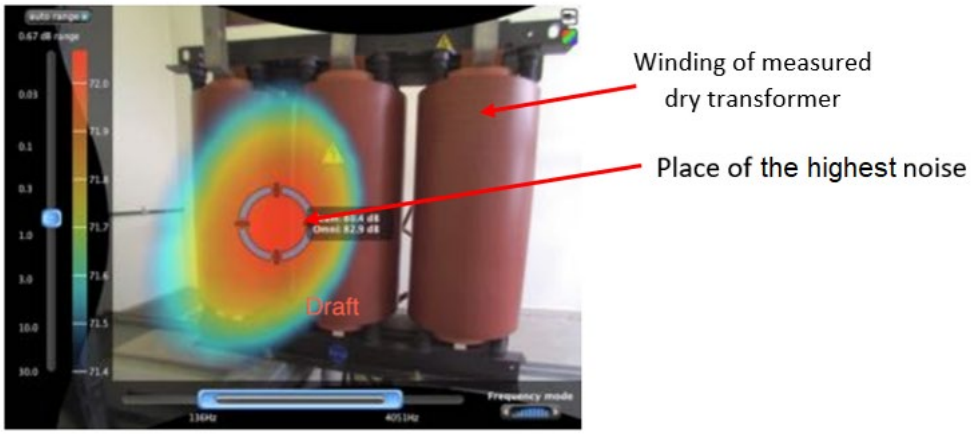

Fig. 1. Picture of the found spatial noise maximum on the transformer T-01 in the no-load state

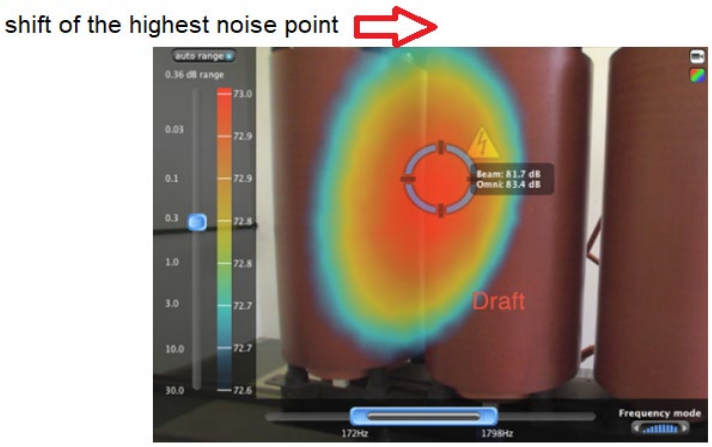

Fig. 2. Picture of the found spatial noise maximum on the transformer T-01 in the 10 % load

Fig. 1 and 2 show a significant shift in the increased activity of the acoustic spectrum towards the winding of the middle phase. By increasing the load, the influence of the Lorentz force begins to activate in the windings.

The graph in Fig. 3 shows the acoustic signal's spectrum at a given point of the field AE of the dry transformer T-02 at 10-% load. The picture shows a lower acoustic emission than the tonally "noisier" transformer T-01. The graphic representation of the frequency spectrum of the loaded dry transformer T-02 is shown in Fig. 2. In the graph, there are comparatively smaller acoustic signals in the frequency spectrum than in the case of the dry transformer T-01 at the same load.

Fig. 4 shows a percentage comparison of tonal frequency increase for the transformer with T-01 no load and 10 % load to transformer T-02. The highest percentage increase at transformer T-01 to quieter T-02 is above 30 % at frequencies 400, 500, 600, and 1000 Hz. At 800 Hz frequency, there is a higher value at transformer T-01 no-load to load following magneto-acoustic emission.

In dry transformers, the most common fault in changing the acoustic emission can also be an incorrect connection of the screws on the fastening structure or when connecting the windings. As a complementary method, a set of different contact measurements can be used, because of which it is possible to detect a fault more accurately in the insulation or structural system of transformers.

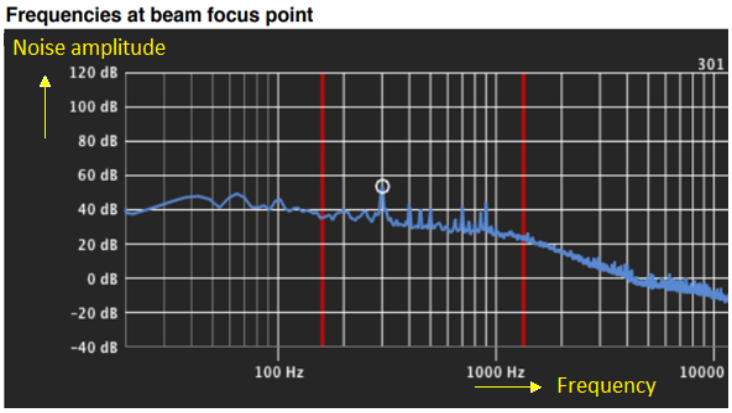

Fig. 3. Acoustic emission of transformer T-02 in the 10 % load

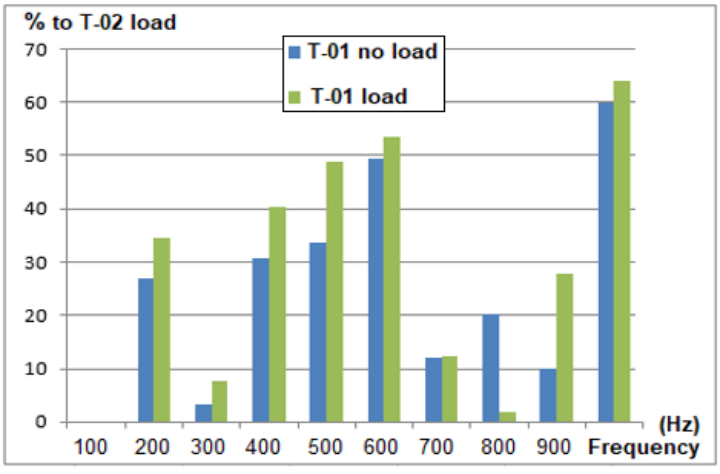

Fig. 4. Percentage comparison of tonal frequency increase for transformer T-01 no load and 10% load to transformer T-02.

ISBN 978-80-972629-6-9

3. Conclusions

During the analysis of the acoustic emission, an increased rate of harmonic acoustic components was found in the frequency range up to 1 kHz. Therefore it is appropriate for the analysis of the correct connections and the tightening of the screws on the dry transformers by using the contact off-line method, for example, Sweep Frequency Response Analysis (SFRA).

The use of the mentioned diagnostic method is significant from the point of view of ageing detection and its effects on the analysis of the mechanical and structural parts of the power dry transformers during operation. The mentioned methods, if used correctly, can be resistant to interference and their implementation is simple directly at the place of installation of the transformer.

Using a non-contact method using acoustic emission measurement is a good starting position for the analysis of the transformer, thanks to which it is possible to propose another, but contact, off-line diagnostic method. The advantage of the microphone acoustic systems is that thanks to the displayed frequency spectrum, there is no need to use an external frequency filter, which some measuring devices use for noise measurement.

The method of acoustic emission contributes to a better understanding of the structural state of the power dry transformer and the exclusion of the incorrect diagnosis of a possible fault.

Acknowledgements

This work was supported by the Slovak Research and Development Agency under contract No. APVV-21-0449 and No. APVV-21-0078.

References

[1] Kanakambaran, S, Sarathi, R., Srinivasan, B. (2018). Robust Classification of Partial Discharges in Transformer Insulation Based on Acoustic Emissions Detected Using Fiber Bragg Gratings. *IEEE Sensors Journal*, 18 (24), 10018-10027.

[2] Kudelcik, J., Hardon, S., Trnka, P., Michal, O., Hornak, J. (2021). Dielectric Responses of Polyurethane/Zinc Oxide Blends for Dry-Type Cast Cold-Curing Resin Transformers. *Polymers* 2021, 13, 375.

[3] Rathod, V.B., Kumbhar, G.B., , Bhalja, B.R. (2022). Partial Discharge Detection and Localization in Power Transformers based on Acoustic Emission: Theory, Methods, and Recent Trends. In: *IETE Technical Review*, 39 (3), 540-552.

[4] Hornak, J., Cernohous, J., Prosr, P., Rous, P., Trnka, P., Baran, A., Hardon, S. (2023). Comprehensive Study of Polyurethane Potting Compounds Doped with Magnesium Oxide Nanoparticles. *Polymers* 2023, 15 (6).

[5] Olszewska, A., Witos, F. (2016). Identification of Acoustic Emission Signals Originating from the Core Magnetization of Power Oil Transformer. *Archives of Acoustics*, 41 (4), 799-812.

[6] Bartoletti, C., Desiderio, M., Di Carlo, D., Fazio, G., Muzi, F., Sacerdoti, G., Salvatori, F. (2004). Vibro-acoustic techniques to diagnose power transformers, *IEEE Transactions on Power Delivery*, 19 (1), 221-229.

[7] Jin, M., Pan, J. (2016). Vibration transmission from internal structures to the tank of an oil-filled power transformer. *Applied Acoustics*, 113, 1-6.

Measurement of Noise Instability of Dry Transformer in a Test Room

Daniel Korenciak, Miroslav Gutten, Martin Karman, Peter Brncal

Faculty of Electrical Engineering and Information Technology,
University of Zilina, Zilina, Slovakia
Email: daniel.korenciak@feit.uniza.sk

Abstract. *The article is focused on the method of measuring the instability of noise of a dry transformer in a test laboratory. The experimental measurement was carried out for the method of obtaining reference values of the acoustic emission size and its stability of a good dry transformer 22000/6000 V in the laboratory and their possible comparison with the real values of the transformer during its operation. The measurement was performed using a noise measuring device with a three-octave spectral filter in the frequency range from 100 Hz to 10 kHz for a period of 20 s. The mentioned measurements can form reference values for the analysis of the state of dry transformers with the same type and performance after their operation or repair sent for inspection to test laboratories.*

Keywords: Dry Transformer, Noise Instability, Frequency, Test Room

1. Introduction

Currently, it is necessary to use non-contact measurements, with the help of which, on the basis of acoustic emissions (AE), a possible malfunction of the technical equipment could be detected. Such systems can be part of the diagnostics and analysis of energy systems, especially in transmission and distribution systems of high and very high voltage [1].

Acoustic and noise measurement is one of the important methods for non-contact diagnostics of dry transformers during their operation.

Important sources of noise and acoustic emission in transformers include vibrations in the winding and in the ferromagnetic core. Increased vibrations occur in the transformer mainly due to loose clamps on the plates of the ferromagnetic core and loose contacts on the windings and coils. Basic operational sources of acoustic emission include phenomena in the ferromagnetic core, such as the Barkhausen effect (magnetoacoustic emission) and magnetostriction [2], [3].

During the operation of the transformer, vibrations in the winding and ferromagnetic core create acoustic emissions in a very audible low-frequency range. This acoustic emission can acquire a fundamental tonal sound with the frequency of electrical energy. The fundamental frequency of electromagnetic forces and mechanical vibrations is usually twice as high as the flowing electric current (e.g. 100 Hz in European power systems), which creates a spectrum of higher harmonics due to acoustic emission. In addition, noise generated by magnetoacoustic emission causes random high-frequency fluctuations in the sensed signal [4], [5].

It is also necessary to analyze the instability of the acoustic emissions of power transformers through regular measurements in order to detect a possible malfunction or deterioration of the service life of the given equipment [6].

2. Experimental measurement

The CESVA SC250 measuring device was used for noise measurement using acoustic emission analysis, i.e. a class 1 sound meter expandable to an octave band and a three-octave spectrum

ISBN 978-80-972629-6-9

analyzer in the frequency range from 6.3 to 20000 Hz, which measures all parameters simultaneously with all frequency and time parameters in different time bases. The SC250 device saves the registers in CSV format, so they can be exported to the application in MS Excel and simultaneously measures all functions of the sound level meter, spectrum analyzer in 1 octave bands (from 8 Hz to 16 kHz) and 1/3 octave bands (from 6.3 Hz to 20 kHz) for an integration time of 1 second.

An overview situation diagram of noise measurement on a tested dry transformer 22000/6000 V using the CESVA SC250 device is shown in Fig. 1.

To simulate a possible change in the magnitude and instability of the noise on the dry transformer, we varied the torque of the clamps on the ferromagnetic core, which can significantly affect the measured acoustic emission parameters. We tightened the clamps using a digital torque wrench to a value of 5 – 30 – 40 Nm. We placed the CESVA measuring device in front of the selected phase C of the transformer successively from the front and from the side at a distance of 1 m and for a period of 20 s.

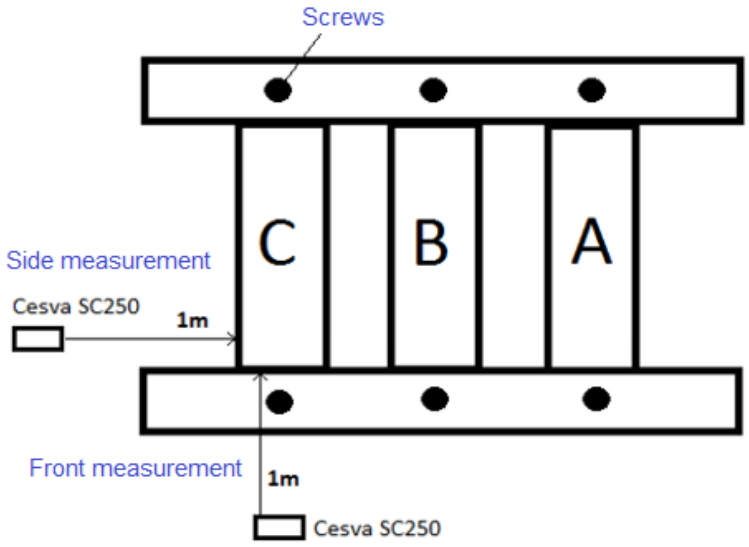

Fig. 1. Overview situation diagram of noise measurement on the measured dry transformer 250 kVA, 22000/6000 V using the CESVA SC250 device

The graph shown in Fig. 2 represents the amount of noise instability measured from the front from the side of phase C of the measured dry transformer (according to Fig. 1) depending on the frequency in the range of 100 Hz - 10 kHz. The analysis of noise instability was performed within the measurement for 20 s, where 20 changing values of the transformer noise in dB were measured.

In the MS Excel program, we used the AVEDEV function, which calculates the average of absolute deviations of data points from their average. The AVEDEV function is a statistical function and is actually a measure of variability, and thus instability, in a data set and calculates the average of the absolute values of the deviations from the mean value.

We measured the values using the CESVA measuring device, placed in front of phase C and the transformer.

The measured values show that the largest increase in instability was from a frequency of 1.6 kHz and higher, while the highest level of instability for all frequencies was when the screws were tightened to a torque of 30 Nm. Conversely, the lowest level of instability was only 5 Nm when the screws were tightened. With the increase in frequency from 1.6 kHz to 10 kHz, the instability for individual moments changed only slightly.

ISBN 978-80-972629-6-9

The most stable noise values were recorded at the frequency of 100, 250 and 315 Hz, which results from the design and parameters of the magnetic circuit of the dry transformer.

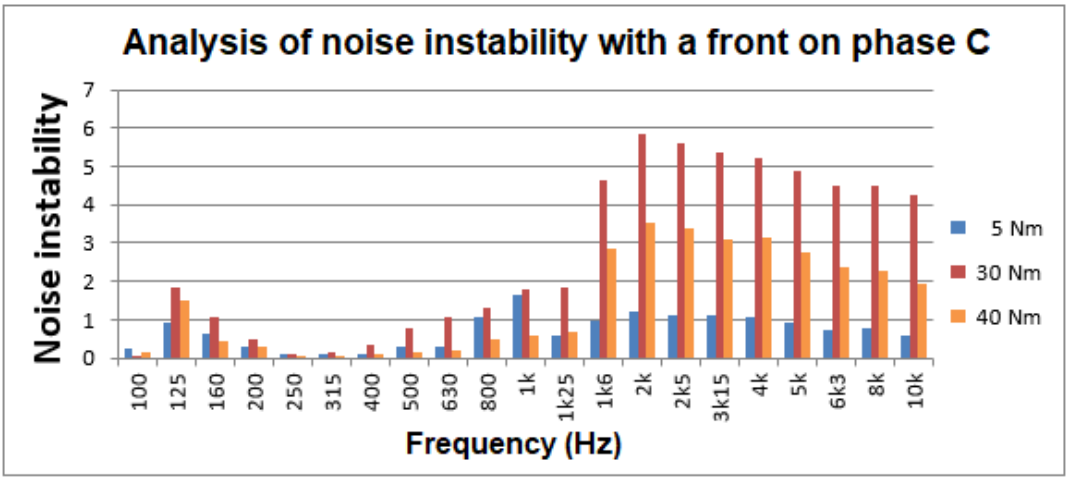

Fig. 2. Graph of the magnitude of noise instability measured from the front from the phase C side of the measured transformer as a function of frequency in the range 100 Hz - 10 kHz

The graph shown in Fig. 3 represents the magnitude of noise instability measured from the side of phase C of the measured dry transformer (according to Fig. 1) depending on the frequency in the range of 100 Hz - 10 kHz. The noise instability analysis was performed in the same way as in case 1, i.e. within the measurement for 20 s, where 20 changing transformer noise values in dB were measured.

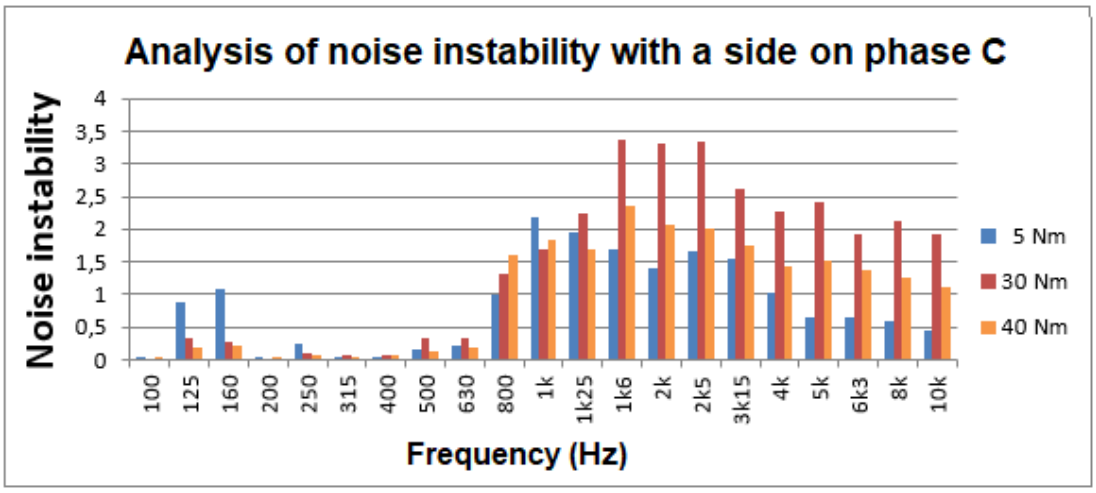

Fig. 3. Graph of the magnitude of noise instability measured from the side of phase C of the measured transformer as a function of frequency in the range 100 Hz - 10 kHz

When measuring from the side, there is an increase in stability from a frequency of 800 Hz. At a bolt tightening torque of 30 Nm, the increased measured instability magnitude was almost identical for frequencies from 1.6 kHz to 2.5 kHz. At a torque of 5 Nm, there was a significant fluctuation in stability at frequencies of 125 Hz and 160 Hz. The measured values show that the greatest increase in instability was recorded from the side of the transformer again from the frequency of 1.6 kHz above, similar to the front, while the highest level of instability for all frequencies was when the screws were tightened to a torque of 30 Nm.

The most stable noise values were recorded again at the frequency of 100, 250 and 315 Hz and also at the frequency of 400 Hz.

ISBN 978-80-972629-6-9

3. Conclusions

Overall, compared to measuring the transformer from the front, the noise instability recorded in this case was much lower (almost up to 100 % at some frequencies), which may be influenced by the noise measurement from the side of phase C of the dry transformer, where further propagation of sound from other phases can be masked and another part of the magnetic circuit of the power transformer.

The highest level of instability for all frequencies was when the screws were tightened to a torque of 30 Nm. On the contrary, the lowest level of instability was only at 5 Nm when tightening the screws.

The most stable noise values of the dry transformer were recorded around the tonal frequency, especially at values of 100, 250, and 315 Hz. The highest values of acoustic emission and noise of the measured dry transformer were found at these frequencies using with measuring apparatus CESVA SC250.

Using the same procedure as above, it is also possible to evaluate the median or mean value of the noise in 1 s intervals from the measured 20 data, depending on the frequencies in the range of 100 Hz - 10 kHz.

The mentioned measurements can form reference values for the analysis of the condition of dry transformers after their operation or repair sent for inspection to testing laboratories.

Acknowledgements

This work was supported by the Slovak Research and Development Agency under contract No. APVV-21-0449 and No. APVV-21-0078.

References

[1] Kudelcik, J., Hardon, S., Trnka, P., Michal, O., Hornak, J. (2021). Dielectric Responses of Polyurethane/Zinc Oxide Blends for Dry-Type Cast Cold-Curing Resin Transformers. *Polymers* 2021, 13, 375.

[2] Hornak, J., Cernohous, J., Prosr, P., Rous, P., Trnka, P., Baran, A., Hardon, S. (2023). Comprehensive Study of Polyurethane Potting Compounds Doped with Magnesium Oxide Nanoparticles. *Polymers* 2023, 15 (6).

[3] Olszewska, A., Witos, F. (2016). Identification of Acoustic Emission Signals Originating from the Core Magnetization of Power Oil Transformer. *Archives of Acoustics*, 41 (4), 799-812.

[4] Bartoletti, C., Desiderio, M., Di Carlo, D., Fazio, G., Muzi, F., Sacerdoti, G., Salvatori, F. (2004). Vibro-acoustic techniques to diagnose power transformers, *IEEE Transactions on Power Delivery*, 19 (1), 221-229.

[5] Jin, M., Pan, J. (2016). Vibration transmission from internal structures to the tank of an oil-filled power transformer. *Applied Acoustics*, 113, 1-6.

[6] Kunicki, M., Cichon, A., Borucki, S. (2016). Study on Descriptors of Acoustic Emission Signals Generated by Partial Discharges under Laboratory Conditions and in On-Site Electrical Power Transformer. *Archives of Acoustics* 41 (2), 265-276

Employing LabVIEW Web Service in Design of Application Twins with Remote Access

Miroslav Kamenský, Karol Hilko, Mikuláš Bittera, Eva Králiková

Slovak University of Technology in Bratislava, Faculty of Electrical Engineering and Information Technology, Institute of Electrical Engineering, Bratislava, Slovakia, Email: miroslav.kamensky@stuba.sk

Abstract. *While the design of basic local PC control for a workplace in LabVIEW is usually manageable for a non-programmer, creating remote access can require considerable effort. Therefore, a design based on application pairs could be preferred where the remote access part is prepared by a more experienced designer. Such a system is presented in the paper with a focus on publishing part of application twins. An important task is to implement a web interface accessible from any browser, even on mobile devices. The cooperation of HTML, JavaScript and LabVIEW Web service for achieving the task will be explained.*

Keywords: Remote Access, LabVIEW, HTML, JavaScript

1. Introduction

Remote access applications have encountered major growth over recent years. Fortunately, technology [1] already existed before the outbreak of the corona pandemic, and in times of necessity, it was available. The situation at our Institute of Electrical Engineering FEI STU was corresponding. We had been developing our special system of remote workplaces used as supporting teaching tool. The circumstances encourage our team to achieve further progress.

Subjects taught at our Measurement department of the institute are mainly oriented toward electrical measurement, where LabVIEW software represents state of the art. We can also claim that experiences with LabVIEW from the subject Distributed Measurement Systems can be used for the design of workplaces for other subjects like Measurement technology and vice versa. The web Publishing Tool of LabVIEW with Remote Panel technology behind enables quick and easy distribution of an application via the Internet. Its main drawback is the necessity of LabVIEW Runtime Engine installation on the client side, which, for example, makes it impossible to establish the connection from a smartphone. Therefore, we focused on finding a suitable strategy for combining the concept used in [2] with Web Services and HTML 5.0 (HyperText Markup Language), also supported by recent LabVIEW editions. Our design is based on pair of cooperating applications. One was developed using Web Services and JavaScript to enable remote access to a general workplace accessible from any browser without the need of special plugins, which is the main topic of the paper. The second application in the pair was controlling a real workplace.

2. Subject and Methods

LabVIEW (from Laboratory Virtual Instrument Engineering Workbench) is a development environment for the graphical programming language G from NI (National Instruments). Gradually it became rich on advanced libraries, and today it is a widely used environment for measurement applications [3]. Support for Web services was introduced in LabVIEW 8.6. In this paper, we will rather reference LabVIEW 2014 or later. A Web service can be understood as a set of protocols and standards that allow data to be exchanged between different applications via computer networks such as the Internet. Its runtime engine is loaded and run by LabVIEW's built-in Web Server. The Web Server is a gateway to a modern virtual lab [4],

and we can benefit from its existence under the LabVIEW package, especially when creating a modular system enabling the mixing of programming languages.

A typical project of Web service consists of *.vi files of G code implementing main programming tasks and then HTML and JavaScript part forming project front-end for displaying an application user interface (UI) on Internet browser clients. HTML and JavaScript are well-known technologies for Web design, and nothing special in terms of syntaxes is behind the LabVIEW Web service. In HTML code, visual elements are defined. JavaScript part uses DOM (Document Object Model) for accessing HTML elements and is suitable for adding interactivity to a website. It includes a fast and feature-rich jQuery library supporting AJAX (Asynchronous JavaScript and XML-eXtensible Markup Language).

3. Implementation

Our system with Web service consists of application twins similar to our previous system employing Remote Panels [2]. Newly designed parts can coexist with older application modules in the same environment as depicted in Fig.1. Control of the target workplace is realized by the project called *Do_Project*, where the local functionality is implemented. It makes intervention with real circuits, collects and processes measured data, takes snapshots by webcam etc. The purpose of *Go_Project* is data distribution to a remote user; therefore, Web service is employed here. It passes requests to a target application, receives replies, and sends them back to the client browser within the Web service response. Data exchange between *Go_Project* and *Do_Project* is accomplished via DataSocket variables.

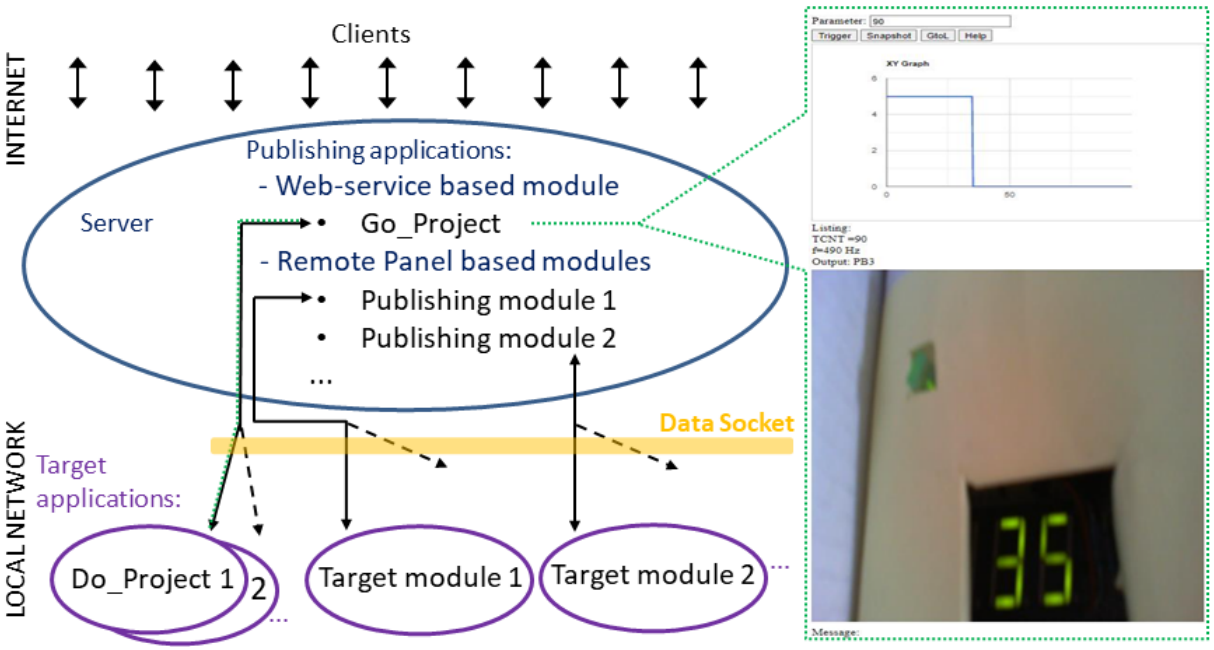

Fig. 1. Structure of designed remote access system and UI appearance for application of LED lighting control. Dashed black lines represent alternative connections. Dotted green lines highlight the tested application where the PWM duty cycle was set by the user to 90/255=35%.

On the *Go_Project* side the communication with a target application is realized using two .vi files, which can be invoked via their URL (Uniform Resource Locator): *GoRequest.vi* and *readPicture.vi*. The task is covered mainly by *GoRequest.vi* (Fig.2), which sends a command to *Do_Project* and retrieves a cluster of numerical data and strings to be published. Interaction of *GoRequest.vi* with HTML frond-end is provided by Web service processing blocks: *LabVIEW Web Service Request* receives the request itself, *Read Form Data* separates *GCommand*, and *parameter* as strings, *Set HTTP Response MIME Type* sets *text/JSON*

(JavaScript Object Notation) format of response suitable for the application [4]; *Write Response* sends cluster of data back to the client. If the reply indicates that a picture was provided on *the Do_Project* side, then it should be read via *readPicture.vi*, where the response type is *image/png* (Portable Network Graphic) instead of JSON.

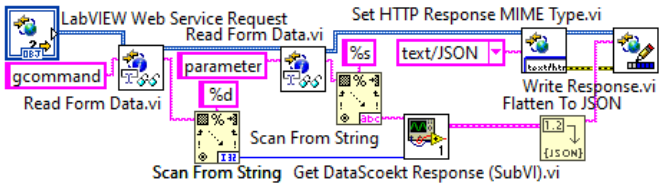

Fig. 2. Simplified block diagram of *GoRequest.vi*.

```
jQuery(document).ready(pageReady);
google.charts.setOnLoadCallback(initItems);
...
function pageReady() {
  jQuery( "#butt1" ).click(butt1ButtonClick);
  ...                              // similar for buttons 2..5,
}                                  // static button names can be also initiated or unused buttons hided

function initItems() {             // chart initialization, the table is used to draw to the chart
  var dataTable = new google.visualization.DataTable();
  ...
  var chart = new google.visualization.LineChart(document.getElementById('number_format_chart'));
  chart.draw(dataTable, options);
}

function butt1ButtonClick() { // callback on button 1 click
  getRequest(97);
} ...                              // similar implementations for buttons 2..5

function getRequest(GCommand) {
  URL = document.URL;      // preparing URL for jQuery
  URL = URL.replace("home.html", "") + "GoRequest";
  URL=URL+"?gcommand="+GCommand+"&parameter="+document.getElementById("parameter").value;
  jQuery.ajax({ url: URL,      // sending AJAX request
                dataType: 'json',
                success: processRequest, ... })...
}

function processRequest(data) { // processing jQuery.ajax response, data argument contains values
  if (data.DCommand & 0x2) { // data.DCommand is received command
                                   // data.Graph contains X and Y values for drawing a Graph
    for (var i = 0; i < data.Graph[0].X.length; i++) {
      dataTable.addRow([data.Graph[0].X[i], data.Graph[0].Y[i]]);
    }
    ...
  }
  …                                // checks of other bits of data.DCommand follow
  if (data.DCommand & 0x8) nextPicture(); // 3th bit indicates that picture is ready to be read
}

function nextPicture() {
  ...                              // reading and displaying picture, d.getTime() assures picture update
  $("#image_tab").attr("src", "readPicture?" + d.getTime());
}
```

Fig. 3. The skeleton of JavaScript code of *home.js*.

The appearance of UI is defined in HTML and in complementary JavaScript file. Elements of UI (Fig. 1 right) are created in *home.html* and aligned in a table of 6 rows. The first row is only the input string (the identifier is *a parameter*). In the second row series of buttons is placed. Rows 3-6 contain items where results will be shown: graph, listing, picture, and message. Besides those, also button names are included in Web service replies. Buttons give the user possibility of interaction. After pushing one of them, a request including a parameter from the 1st row of the HTML table is sent to the Web Server.The interactivity of the webpage is managed by a JavaScript code inside *home.js*. The main skeleton of the program is displayed in Fig.3, with color-coded names of implemented functions. Function references are in italic, bold are their headers and in black bold italics are references to .vi files achievable within Web service. Two functions (blue) are related to the loading of the overall page: *initItems()* and *pageReady()*. Function *initItems()* – linked to the event via *google.charts.setOnLoadCallback(initItems)* – is called after the google chart package was loaded. Its purpose is to initiate selected Google Visualization API (Application Programming Interface) components. Two such classes are utilized: *DataTable* and *LineChart*. Function *pageReady()* – linked to the event by code *jQuery(document).ready(pageReady);* – is executed when the document is fully loaded. The button press callback function is defined inside *pageReady()* by a method *jQuery("#buttX").click(buttXButtonClick)* where *X* represents the button number. If a user clicks a button and the callback function *buttXButtonClick()* (green) is invoked, a function *getRequest(GCommand)* (violet) is executed. The parameter *GCommand* means really command number to be send with Web service request and it is added to the URL of the *GoRequest.vi* file, which will be called by *jQuery.ajax()* method. Reply obtained via LabVIEW Web service mechanism is processed by function *processRequest(data)* (red), which updates the graph, listing and message parts of the page. Item *data.DCommand* of the reply describes the data content. If it indicates that a picture should be included in the response it is obtained separately via a call to a dedicated function *nextPicture()* (Orange).

4. Results and discussion

Our application was tested in the subject Microprocessor technology 1 focused on 8-bit microcontrollers. To support teaching Timer/Counter modes, we set up a testing workplace where the intensity of LED lighting was controlled from a microcontroller. Firmware with *Do_Project* enabled changes in the PWM duty cycle from PC. Once Arduino receives a byte via serial interface, it is used as a new duty cycle value meaning the level of incrementing Timer Counter register (TCNT) at which the generated output changes from logic high to logic low. At the overflow, the output is set back; hence finally generated signal is controlled PWM. Target *Do_Project* collects data on new PWM settings, its graphical sketch and LED picture captured by webcam together with the segmented display showing duty cycle in percentage. *Go_Project* provides the remote connection. In Fig.1, right, the remote UI is depicted just after the change of duty cycle to 90. To explore student opinions, we establish a survey under Ms Teams with several questions. The feedback can be evaluated positively: 7 votes from 7 participants liked the usage of remote access workplace by the lecturer, and 6 of them appreciated their own remote connection. For 6 of 8 students, more functionalities would make the tool more attractive. Of course, we plan to cover more complex applications in the future.

5. Conclusions

A new web publishing project has been designed cooperating with an application twin controlling a real workplace. It includes LabVIEW Web service with two .vi files of graphical programming code, JavaScript and HTML file and provides remote access to target application from any web browser. It was tested in the workplace with PWM-controlled LED lighting monitored by a webcam. It simplifies the design of new teaching aids accessible remotely and improves the flexibility of their utilization. A survey realized on a rather small number of students suggested a good perspective of the system after future expansion in terms of functionalities of controlled workplaces.

Acknowledgements

This work was supported by grants of the Slovak Scientific Grant Agency No. VEGA 1/0135/20, No. VEGA 1/0045/21 and by the Slovak Research and Development Agency, grant APVV-20-0042.

References

[1] García-Guzmán, J., Villa-López, F.H., Vélez -Enríquez, J.A., García-Mathey, L.A., Ramírez - Ramírez, A. (2017). Remote Laboratories for Teaching and Training in Engineering. *Design, Control and Applications of Mechatronic Systems in Engineering*, May 2017, doi: 10.5772/67459.

[2] Kamenský, M., Králiková, E., Červeňová, J. (2018). Employing remote access teaching system for diode measurement. In *10th Annual International Scientific Conference Theoretical and Practical Aspects of Distance Learning (DLCC 2018)*. Katowice: Studio NOA for University of Silesia, 465-476.

[3] Otomański, P., Pawlowski, E., Szlachta, A. (2021). The Evaluation of Expanded Uncertainty of DC Voltages in the Presence of Electromagnetic Interferences using the LabVIEW Environment. *Measurement Science Review*, 21(5), 136-141.

[4] Guo, L., Abdul, N.M.M., Vengalil, M., Wang, W., Santuzz, A.A. (2022). Engaging Renewable Energy Education Using a Web-Based Interactive Microgrid Virtual Laboratory. *IEEE Access 2022*, 10, 60972–60984.

The Creep Behaviour of a 2 kN·m Torque Transducer Tested at GUM and PTB

[1]Janusz Fidelus, [1]Jacek Puchalski, [1]Anna Trych-Wildner, [2]Paula Weidinger

[1]Główny Urząd Miar (GUM), Warszawa, Poland
[2]Physikalisch-Technische Bundesanstalt (PTB), Braunschweig, Germany
Email: janusz.fidelus@gum.gov.pl

Abstract. *This article outlines the metrological characterisation of a 2 kN·m torque transducer conducted at the Central Office of Measures (GUM) and Physikalisch-Technische Bundesanstalt (PTB). The linear regression equations for this torque transducer were determined using the weighted least squares method. In all calculations, the Monte Carlo method was used to estimate the expanded uncertainties, which were found to be lower than those calculated using the law of propagation of uncertainty. Additionally, a creep study was conducted at eight measurement points ranging from 200 N·m to 2000 N·m.*

Keywords: Creep, Torque Transducer, Uncertainty, Calibration, Wind Energy

1. Introduction

Wind energy has increased in popularity as a clean and sustainable source of electricity in recent years [1, 2, 3]. It is even more pronounced with the retreat from fossil fuels that is being amplified by ecological policies and strategies [4, 5]. As new policies encourage the diversification of energy sources, this requires the development of new technologies and the intensification of research to improve existing ones.

Torque transducers play an important role in the wind turbine sector as they provide information about turbine behaviour generated by the rotor blades as they turn. This information can be used to optimise the wind turbine performance by adjusting its operation based on changing wind conditions.

Creep behaviour refers to the gradual change in a material's deformation over time when subjected to a constant load. For torque transducers, creep can affect their accuracy and performance. To assess the suitability of a torque transducer for dynamic or high-precision tasks, as in the wind energy sector, its creep behaviour must be known. For this reason, DIN 51309 [6] stipulates that during the calibration of torque transducers, corresponding creep measurements must be carried out [7, 8].

This article details the comparative studies of creep behaviour in torque transducers performed by GUM and PTB in their own laboratories.

2. Subject and Methods

The Hottinger Baldwin Messtechnik GmbH (HBM) special torque transducer (type MPZ1512005b, serial number #210940007) with a lifting capacity of 2000 N·m and a sensitivity of 1.0 mV/V, designed to measure clockwise and anti-clockwise torque, was calibrated on the reference Torque Standard Machine up to 5 kN·m at GUM (TSM-GUM) with an expanded relative measurement uncertainty of 0.04 % ($k = 2$). It was also calibrated on the reference Torque Standard Machines at PTB (TSM-PTB) up to 1 kN·m and 20 kN·m, with $U_1 = 0.003$ % ($k = 2$) and $U_2 = 0.007$ % ($k = 2$), respectively. The deformation of the torque transducer was measured electrically in mV/V units using the MGCplus/ML38B/DMP41 measuring amplifier (with a 0.5 Hz Bessel digital filter), characterised by the best accuracy

class and a resolution of 1 ppm in the measuring range ± 2.5 mV/V. The tests were conducted at ambient temperatures.

The calibration was performed at 8 measurement points: ±200 N·m, ±400 N·m, ±600 N·m, ±800 N·m, ±1000 N·m, ±1200 N·m, ±1600 N·m and ±2000 N·m, following the procedure "Calibration of torque measuring devices and torque transducers" which was based on the standard DIN 51390:2022. Creep tests were carried out for the 2 kN·m torque transducer in clockwise and anti-clockwise directions, following the ISO 376:2011 standard [9].

Calibration of the torque transducers to the electric signal

The linear regression method was used to determine the linear dependence of the electric signal *y (dependent variable)* as a function of the torque *x (independent variable)* based on *n* measurement points. The weighted least squares method (WLS) was used to minimise the sum of squares of errors normalised to the variances along the OY axis. The uncertainties of the *x*-coordinate are negligible, and there are also no correlations in any pairs of measured coordinates. The measurements were carried out at points with coordinates x_i and y_i where $i = 1, \ldots, n$ and the standard uncertainties relate only to the torque measurement, and $u(y_i) = y_i \cdot \delta(y_i)/100$ where the relative standard uncertainties of the torque are denoted by $\delta(y_i)$.

For a linear regression defined by the uncertainty equation, the standard uncertainty for a regression line along the OY axis is given by equation (1) :

$$u_y^2 = x^2 u_a^2 + 2|x| u_a u_b \rho_{ab} + u_b^2 \tag{1}$$

according to the Law of Propagation of Uncertainty (LPU) as the sum of distributions in generally correlated variables: ax with a standard uncertainty $|x| u_a$ and the distribution of variable *b* with a standard uncertainty u_b, where ρ_{ab} is the correlation coefficient between these random variables. The expanded uncertainty for a linear regression is increased by the coverage factor, which is determined by the inverse distribution function from the Student's t-distribution with *n*-2 degrees of freedom for the coverage factor with coverage probability 0.95 (α = 0.05), is $U_y = t_{n-2,1-\alpha/2} u_y$. The uncertainty range of the regression line is described by $ax + b \pm U_y$.

In the Monte Carlo Method (MCM), random variables corresponding to the *x*-coordinates of measurement points are generated as random samples (10^7 samples were drawn) from Gaussian distributions $N(\mu, \sigma^2)$ with expected values $\mu = y_i$ and variances $\sigma^2 = u^2(y_i)$ where $i = 1,\ldots,n$.

The values of the coverage area are intervals for a 0.95 probability of the selected *x* and are determined as the sum of the distributions *ax* + *b*, using formulas defining the slope *a* and intercept *b* parameters described above.

3. Results and Discussion

The calibration of the 2 kN·m torque transducer on the TSM-GUM in the measuring range from 200 N·m to 2000 N·m in clockwise and anti-clockwise direction confirmed its class 0.2 both for creep and for hysteresis [10]. The TSM-PTB calibration covered two ranges: up to 1 kN·m and up to 2 kN·m. The results from the 2 kN·m calibration on the TSM-PTB are described in two calibration certificates [11, 12].

The linear regression equation for a 2 kN·m torque transducer tested on the TSM-GUM and TSM-PTB using WLS is shown in Table 1.

Table 1. Equations of the linear regression determined by WLS for the 2 kN·m torque transducer tested on TSM-GUM and TSM-PTB

Calibration site	Linear regression equation determined by WLS					
	Clockwise direction			Anti-clockwise direction		
TSM-GUM	$y = 0.000533598\ x + 0.061$			$y=0.00053398\ x - 0.0000407$		
	u_a=8.06E-08	u_b=3.98E-05	ρ_{ab}=- 0.776	u_a=9.62E-08	u_b=4.63E-05	ρ_{ab}= -0.785
TSM-PTB	$y = 0.00053398\ x - 0.00001141$			$y=0.00053399\ x + 0.00001144$		
	u_a=1.06E-08	u_b=5.63E-06	ρ_{ab}=- 0.863	u_a=1.19E-08	u_b=5.92E-06	ρ_{ab}= -0.841

Fig. 1 illustrates the relative uncertainties of LPU and MCM methods across the entire calibration range.

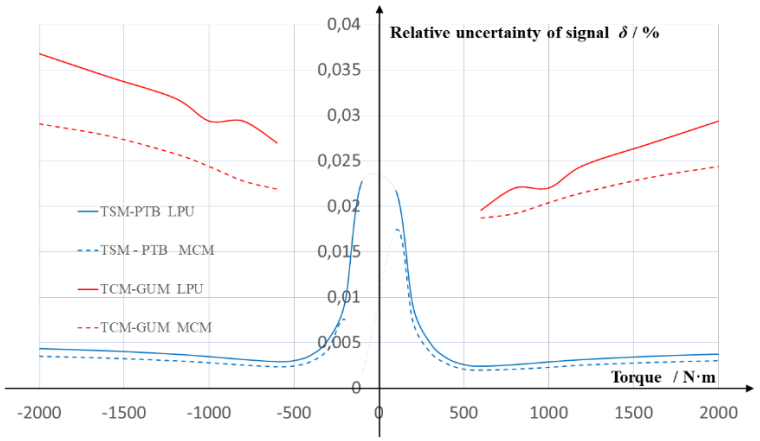

Fig. 1. Comparison of the relative uncertainties determined via LPU and MCM for the calibration on TSM-PTB and TSM-GUM in the range from -2000 N·m to -500 N·m and from 500 N·m to 2000 N·m

The relative uncertainties for the transducer signal in the measuring ranges above 500 N·m were found to be less than 0.005 %, for both clockwise and anti-clockwise measurements at TSM-PTB, while at TSM-GUM, the relative uncertainties for the same range were from about 0.02 % to 0.04 % for anti-clockwise torque and nearly 0.02 % to 0.03 % for clockwise torque. However, the relative expanded uncertainty values determined for decreasing torque values measured below 500 N·m in both directions increased significantly, and therefore, they are not included in Fig. 1. This is because the relative expanded uncertainty for torque values closer to zero decreases. In all cases, the estimation of the expanded uncertainties obtained from MCM is at a lower level compared to the values calculated from the LPU.

A creep study was carried out for 8 measurement points from 200 N·m to 2000 N·m. The creep of the 2 kN·m torque transducer for measurements after applying the maximum reference torque of 2 kN·m and for measurements after removing this reference torque is shown in Fig. 2. The mV/V reading was measured after 5 s and then every 2 s for the first 30 s after the desired torque was applied or released. After applying the maximum reference torque of 2 kN·m, a plateau can be observed (Fig. 2, upper inset). On the other hand, removing the maximum reference torque (after applying M_{max} for 35 s) showed an increase in creep in the first few seconds (Fig. 2, lower inset).

4. Conclusions

The linear regression equations determined by WLS for the 2 kN·m torque transducer, tested on TSM-GUM and TSM-PTB, have yielded expanded uncertainties, with those obtained from the more accurate MCM estimated at a lower level than those from the LPU. Additionally, a creep study was conducted for 8 measurement points from 200 N·m to 2000 N·m. The results indicate that the creep was minimal after the maximum reference torque of 2 kN·m was applied.

ISBN 978-80-972629-6-9

However, upon removing the maximum reference torque, an increase in creep can be observed in the first few seconds.

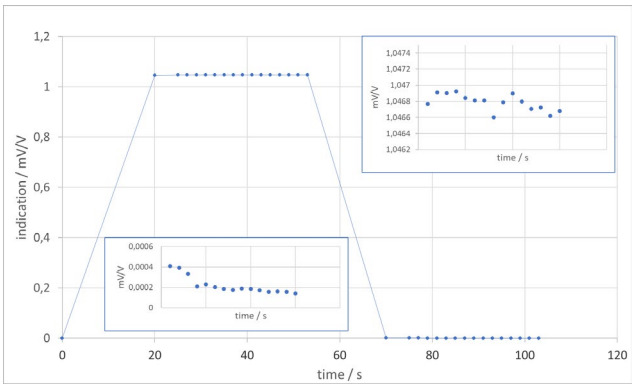

Fig. 2. Graph of 2 kN·m torque transducer indication given in electrical units (mV/V) versus time (s) for measurements performed after applying the maximum reference torque (at 2 kN·m, ~ 1.04 mV/V) and for measurements conducted after removing the maximum reference torque. The insets represent the creep in the first 30 s of the measurement after the load application. For clarity, there are no error bars.

Acknowledgements

The following research has been conducted with financing from the project 19ENG08 – WindEFCY, which has received funding from the EMPIR programme co-financed by the Participating States and from the European Union's Horizon 2020 research and innovation programme.

References

[1] Kaygusuz, K. (2009). Wind power for a clean and sustainable energy future. *Energy Sources, Part B*, *4*(1), 122-133.

[2] Tavner, P. (2008). Wind power as a clean-energy contributor. *Energy Policy*, *36*(12), 4397.

[3] Hannan, M. A., et. al. (2023). Wind Energy Conversions, Controls, and Applications: A Review for Sustainable Technologies and Directions. *Sustainability*, *15*(5), 3986.

[4] Gnatowska, R., & Moryń-Kucharczyk, E. (2019). Current status of wind energy policy in Poland. *Renewable Energy*, *135*, 232-237.

[5] Directive 2009/28/EC on the promotion of the use of energy from renewable sources and amending and subsequently repealing Directives 2001/77/EC and 2003/30/EC.

[6] DIN 51309:2022. Werkstoffprüfmaschinen - Kalibrierung von Drehmomentmessgeräten für statische Drehmomente

[7] Brüge, A. (2010). Creep measurements in reference torque calibration machines. In *Proc. of 21st IMEKO TC3 Int. Conf., Pattaya, Thailand*.

[8] Weidinger, P., et. al. (2018, August). Investigations towards extrapolation approaches for torque transducer characteristics. In *Journal of Physics: Conference Series* (Vol. 1065, No. 4, p. 042057). IOP Publishing.

[9] ISO 376:2011 Metallic materials — Calibration of force-proving instruments used for the verification of uniaxial testing machines.

[10] Fidelus J.D., Cybul K., „Realizacja projektu EMPIR JRC 18SIB08 'Comprehensive traceability for force metrology services' w Głównym Urzędzie Miar", rozdział w monografii naukowej Politechniki Śląskiej, MKM 2020.

[11] Calibration Certificate up to 1 kN·m issued by PTB.

[12] Calibration Certificate up to 2 kN·m issued by PTB.

Processing of Nanocrystalline Wire for a Fluxgate Sensor Application

Diana Hrakova, Pavel Ripka

Faculty of Electrical Engineering, Czech Technical University in Prague, Prague, Czech Republic
Email: hrakodia@fel.cvut.cz

Abstract. *This work is dedicated to the study of fluxgate sensors based on the $Fe_{73.5}Cu_1Nb_3Si_{13.5}B_9$ nanocrystalline wire as a core and comparing them to the performance of amorphous wire with chemical composition $(Co_{94}Fe_6)_{75}Si_{15}B_{10}$ [1]. We demonstrate that proper processing of nanocrystalline alloys can bring sensors with properties comparable to the traditionally used amorphous alloys, but with better stability at elevated temperatures.*

Keywords: Fluxgate, Sensitivity, Noise, Nanocrystalline, Annealing

1. Introduction

One of the ways to decrease the magnetic noise is to change the material of the magnetic core. Fluxgate cores from permalloy and amorphous wires were widely used, but we are not aware of any paper on the application of nanocrystalline wires for fluxgate. FINEMET stands for "Finely Dispersed Magnetic" material, it is known for its excellent soft magnetic properties. It's a specialized type of amorphous magnetic material that offers improved magnetic performance compared to traditional crystalline materials. In this paper, we are focusing on the study of the annealing process on the properties of FINEMET wires and its impact on the characteristics of the material for the fluxgate sensor's application. We concentrate on parallel-type fluxgate.

2. Subject and Methods

For all experiments described in this paper, we have been using amorphous master alloy wires with a nominal composition of $Fe_{73.5}Cu_1Nb_3Si_{13.5}B_9$ manufactured by the Institute of Technical Physics, Iasi, Romania. The wire diameter is 0.12 mm. During the annealing process, we could control such parameters as the gas environment, annealing time, annealing current, and applied tension to control the crystals' growing process. [2] The flash annealing is performed by passing the current through the wire in the Ar atmosphere, which prevents oxidation. Using the annealed wires, we built the Förster-type fluxgate sensors. The same sensors were used for studies of amorphous wire as a core. [1] For the measurement of the sensor noise, we have used 6-layer permalloy shielding.

3. Results

To reach different temperatures for controlled crystallization, it is necessary to apply different currents for different values of applied stress. High tension prevents the fast growth of crystals. However, when the temperature reaches a higher value, the crystal growth is uncontrollable, and the impact of tension is negligible. In general, the annealing temperature for Finemet is typically in the range of 400 to 500 degrees Celsius. Summarizing the conducted experiments, the optimum annealing conditions for $Fe_{73.5}Cu_1Nb_3Si_{13.5}B_9$ nanocrystalline wires with 0.12 mm diameter are the following: annealing time should be in the range of 15-60 s; annealing current should be in the range of 490-505 mA; applied stress for the wire 0.12 mm in diameter should be in the range of 8-12 MPa. The measured parameters of the Förster type sensor with the core wires annealed under different tensile stress are shown in Fig.1. Fig.2 represents how the tensile

ISBN 978-80-972629-6-9

stress could impact the crystals grown and hence coercivity. The comparison of fluxgate sensor performance with the amorphous and nanocrystalline core is depicted in Fig.3.

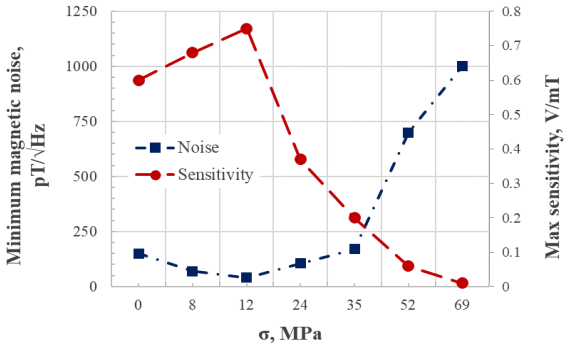

Fig. 1. The change in the measured magnetic noise and max sensitivity with the applied tension stress, 8kHz, 497mA of annealing current, the duration of the annealing is 15s

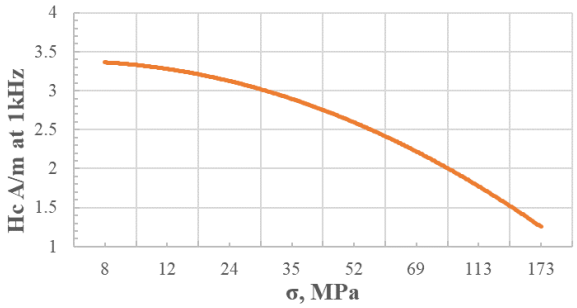

Fig. 2. The change of the coercivity with the change of applied tension stress, 1kHz, 497mA of annealing current, the duration of the annealing is 15s

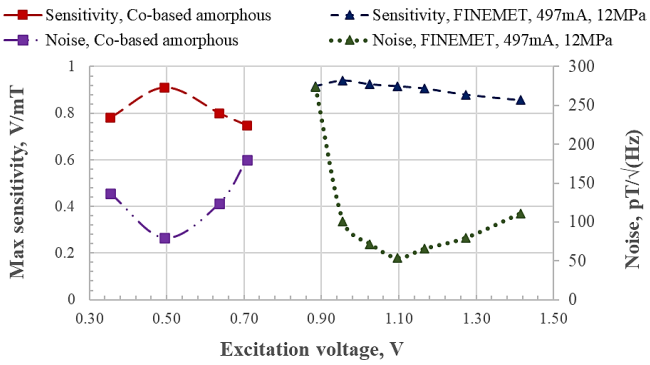

Fig. 3. Sensitivity and noise of the Forster-type fluxgate as a function of the excitation voltage with different core materials, fexc = 8kHz

4. Conclusions

FINEMET wires annealed under tensional stress show better results as a magnetic core for a fluxgate sensor than Co-based amorphous ones, but the main advantage of using nanocrystalline alloy as a fluxgate core is its better stability under elevated temperatures. We observed the change of coercivity with tension. With plastic deformation, it is possible to form such a finely dispersed structure, which cannot be obtained by conventional heating.

Acknowledgements

This study was supported by the Student Grant of CTU within the Soft magnetic particles project (SGS21/163/OHK3/3T/13).

References

[1] D. Hrakova, P. Ripka, M. Butta, Sensitivity and noise of parallel fluxgate sensor with amorphous wire cores, Journal of Magnetism and Magnetic Materials, Volume 563, 2022, 169981, ISSN 0304-8853, https://doi.org/10.1016/j.jmmm.2022.169981.

[2] Giselher Herzer, Modern soft magnets: Amorphous and nanocrystalline materials, Acta Materialia, Volume 61, Issue 3, 2013, Pages 718-734, ISSN 1359-6454, https://doi.org/10.1016/j.actamat.2012.10.040.

Modular Instrumentation for Phasor Measurement Unit (PMU) Testing

Jure Konjevod, Marko Jurčević

Faculty of Electrical Engineering and Computing, University of Zagreb, Zagreb, Croatia
Email: jure.konjevod@fer.hr

Abstract. *A phasor measurement unit (PMU) installed in a power system is a device which usually serves for its protection, monitoring and control. Accordingly, such devices are required to satisfy special qualifications on synchronization, calibration and testing before the installation in power system. In this paper, a testing system based on a modular and versatile electronic instrumentation as well as a time and frequency synchronization platform is presented. Relevant measurements have been conducted with a developed testing system taken as a reference, and total vector error (TVE) is calculated for a commercial calibrator. Obtained results of calculated TVEs for the tested PMU at 50 Hz are well below the maximum limit of 1 % stipulated by the relevant standard.*

Keywords: Phasor measurement unit, Synchrophasor, Modular PXI Instrumentation, Modular Timing Platform, PTP synchronization

1. Introduction

Phasor measurement unit (PMU) is a device able to sample analog voltage and current signals in synchronization with a GPS-clock in order to compute so-called synchro phasors (time-stamped phasor values). Its hardware integration in the smart power grids constantly increases, especially in the U.S. [1,2]. As it provides monitoring of different events in the power grid with much greater resolution than traditional SCADA (Supervisory control and data acquisition) system, then such support provides better integration of renewable energy sources into the grid [3]. PMU device can be implemented as a standalone device, or it can be integrated with some other functions, e.g. protection relay's function. The active standard which is relevant for the definition of PMU's accuracy is 60255-118-1-2018 - IEEE/IEC International Standard [4]. Respectively, the maximum synchronization error is prescribed to be 1 μs, i.e. it means a maximum phase error of 0.018° for a 50 Hz system. The same IEEE Standard defines two classes of PMUs, i.e. P and M PMU classes. P class implies protection applications and M class is mostly used when measurement accuracy has priority over its speed. Regarding mentioned, there are already different commercial PMU devices available on the market, and as such it is required to test them properly and according to the mentioned Standard [5].

2. Synchrophasors and related measurement errors

Generally, UTC time, ac voltage and ac current are common PMU input quantities. Synchrophasor (PMU output) is a term that describes a phasor which has been referenced to an absolute point in time (time tag). Other PMU outputs are frequency and *ROCOF* (rate of change of frequency) estimations. The modelled voltage or current signal in the ac power grid can be described with the following equation:

ISBN 978-80-972629-6-9

$$x(t) = X_m\,(t) \cdot cos\,[\theta(t)] + D(t), \tag{1}$$

where

t time in seconds,

X_m peak magnitude of the sinusoidal ac signal,

θ angular position of the sinusoidal ac signal in radians,

D disturbance signal that contains additive contributions to the signal.

The synchrophasor phase angle $\Phi(t)$ is defined as the phase difference between the angular position $\theta(t)$ and phase due to the nominal frequency f_0 [4]:

$$\Phi(t) = \theta(t) - 2\pi f_0 t, \tag{2}$$

The signal frequency ω is defined by:

$$\omega = 2\pi f_0 t, \tag{3}$$

Taking into account equations (1) and (2), the phasor representation of the sinusoidal signal is given by:

$$X = \frac{X_m}{\sqrt{2}} \cdot e^{j\Phi} = \frac{X_m}{\sqrt{2}}(cos\Phi + jsin\Phi), \tag{4}$$

where

$\frac{X_m}{\sqrt{2}}$ rms value of the sinusoid.

To calculate phasor from input sinusoidal signal, it is needed to use data samples taken from the waveform and apply the algorithm to determine the fundamental frequency component in which its peak value is then converted to rms value by dividing by √2, which actually represents the magnitude of the phasor. Some of the algorithms for data processing are e.g. Kalman Filter, weighted least squares, artificial neural networks, and the most commonly used is the discrete Fourier transform (DFT) algorithm.

The total vector error (*TVE*) is a measure of the difference between the synchrophasor estimates from a PMU and the reference value determined by evaluating the formulas describing the measurand. *TVE* combines together magnitude and angle error into a single quantity. *TVE* can be determined by the following expression [4]:

$$TVE = \sqrt{2(1 + ME)(1 - \cos(PE)) + ME^2}, \tag{5}$$

where

ME magnitude error (in p.u.),

PE phase error (in deg or rad).

One type of measurement equipment which is proposed for the PMU testing system is PXI (PCI eXtensions for Instrumentation), i.e. hardware architecture based on NI PXI 1062Q chassis [6]. PXI systems are already widely used in metrology institutes system and, as such characterized in many relevant publications [7-8].

The proposed PXI measurement setup is based on the mentioned PXI 1062Q chassis which hosts a data acquisition module and timing module for synchronization. NI PXI 4461 digitizer is the module relevant for sampling of input signals with a high resolution of 24 bits and with a maximum full-scale range of ± 42.4 V_{pk} [9]. NI 6683 is the relevant module utilized for synchronization purposes [10]. Besides, signals are synchronized to the referent timing signal, i.e. to the GPS reference provided by Meinberg M3000 over Ethernet using IEEE 1588 [11]. The commercial PMU device from [5] has been tested with the proposed referent testing measurement setup. The measurement setup used to test PMUs is represented in Fig.1.

Fig.1. Measurement setup

3. Results

The measurement results are derived with the measurement setup described in the previous chapter. The voltage input signal with a nominal frequency of 50 Hz has been measured. All obtained samples are processed with the DFT algorithm to obtain relevant parameters (rms magnitude and phase angle). The set of ten calculated *TVE*s for three voltage input channels of the tested PMU, i.e. for V_a, V_b, and V_c is presented in Table 1.

Table 1. *TVE* (%) results obtained with DFT algorithm at 50 Hz

TVE_{Va}	TVE_{Vb}	TVE_{Vc}
0.52	0.51	0.55
0.62	0.61	0.60
0.63	0.54	0.57
0.60	0.52	0.55
0.57	0.49	0.58
0.58	0.55	0.59
0.60	0.58	0.57
0.59	0.57	0.50
0.54	0.57	0.59
0.61	0.55	0.61

ISBN 978-80-972629-6-9

4. Discussion and Conclusions

As can be seen from the results, calculated *TVE*s for the tested PMU at 50 Hz shown in Table 1. are well below the maximum limit of 1 % stipulated by the relevant standard mentioned earlier in the paper. The architecture of the testing system based on metrology-grade modular equipment for PMU devices is proposed. The proposed testing system based on modular metrology-grade equipment is suitable for PMU testing. As smart power grids are already largely based on renewable energy sources, PMUs integration in the grid ensure more reliable power, which means that advanced monitoring represents greater reliability. Accordingly, future work will take into consideration the frequency oscillations around 50 Hz and data processing with other algorithms to further validate the proposed system.

Acknowledgements

This paper is fully supported by Croatian Science Foundation under the project Metrology infrastructure for support of the intelligent power grid IP-2019-04-7354. Any opinions, findings, conclusions or recommendations expressed in this material are those of the author(s) and do not necessarily reflect the views of the Croatian Science Foundation.

References

[1] A. G. Phadke and J. S. Thorp, "HISTORY AND APPLICATIONS OF PHASOR MEASUREMENTS," 2006 IEEE PES Power Systems Conference and Exposition, 2006, pp. 331-335, doi: 10.1109/PSCE.2006.296328.

[2] A. P. Meliopoulos et al. Synchrophasor Measurement Accuracy Characterization, North American SynchroPhasor Initiative (NASPI) Performance & Standards Task Team, November 30, 2007.

[3], M. Agustoni and G. Frigo, "Characterization of DAC Phase Offset in IEC 61850-9-2 Calibration Systems," in IEEE Transactions on Instrumentation and Measurement, vol. 70, pp. 1-10, 2021, Art no. 6503710, doi: 10.1109/TIM.2021.3084294.

[4] IEEE/IEC International Standard - Measuring relays and protection equipment - Part 118-1: Synchrophasor for power systems - Measurements, in IEC/IEEE 60255-118-1:2018 , vol., no., pp.1-78, 19 Dec. 2018, doi: 10.1109/IEEESTD.2018.8577045.

[5] SEL-735 Power Quality and Revenue Meter Instruction Manual, [Online]. Available: https://selinc.com/products/735/docs/

[6] NI PXIe-1062Q User Manual, national Instruments, [Online]. Available: https://www.ni.com/pdf/manuals/371843d.pdf

[7] Jure Konjevod, Roman Malarić, Petar Mostarac and Marko Jurčević, "The AC Amplitude and Channel Characterization of High-resolution Digitizers", Measurement, Volume 195, 2022, 111144, https://doi.org/10.1016/j.measurement.2022.111144

[8] R. Rybski, J. Kaczmarek and M. Kozioł, "A PXI-Based Calibration System for Low-Value AC Resistors," in IEEE Transactions on Instrumentation and Measurement, vol. 67, no. 4, pp. 905-911, April 2018, doi: 10.1109/TIM.2018.2791298.

[9] NI 4461/4462 Specifications, [Online]. Available: https://www.ni.com/docs/en-US/bundle/ni-4461-4462-specs/resource/373770k.pdf

[10] NI PXI-6683 and NI PXI-6683H Timing and Synchronization Modules for PXI, National Instruments, [Online].Available: https://www.ni.com/pdf/manuals/373656b.pdf

[11] Configuration and Management Manual, Meinberg Funkuhren GmbH & Co. KG, [Online].Available: https://www.meinbergglobal.com/download/docs/manuals/english/ltos_7-04.pdf

Simulating Error Due to Inhomogeneity of Type K Thermocouples

[1]Xu Ping, [1]An Li, [1]Hu Jiwei, [2]Orest Kochan, [3]Krzysztof Przystupa, [3]Jacek Majewski

[1]Wuhan Fiberhome Technical ServicesCo., Ltd, Wuhan, China
[2]Hubei University of Technology, Wuhan 430068, China
[3]Lublin University of Technology, Lublin, Poland

Email: orest.v.kochan@lpnu.ua

Abstract. *The base metal thermocouples are the most popular temperature sensors. However, their inhomogeneity is main source of their error. The modelling of error due to inhomogeneity error for the conventional thermocouple and the thermocouple with a controlled temperature field (TCTF) is carried out in this paper. It was found that the TCTF reduces the contribution of inhomogeneity to the measurement error in 60 times to less than 0.2°C.*

Keywords: Thermocouple, Inhomogeneity, Thermocouple with Controlled Temperature Field.

1. Introduction

Degradation of TC legs leads to the appearance of two closely related errors [1, 2]: (i) error due to drift (EDD) of the TC conversion characteristics (CC) - gradual change of the developed thermal electromotive force (emf) with time in a constant temperature field along the TC legs; (ii) error due to acquired thermoelectric inhomogeneity (ATI) of TC legs - changes in the developed emf when the temperature field along the TC legs changes. The cause of both errors is the degree of degradation of the TC legs. During the long-term operation of the TC, there is a dependence of the developed emf on the temperature distribution along its legs. For the most common type K TC error due to ATI can reach 10 ºC or even more [1, 3]. To cope with this error the method of forced stabilization of the temperature field along the legs of the main TC (MTC), which measures the temperature of the object, was proposed in [4]. This new TC-based sensor is called the thermocouple with a controlled temperature field (TCTF). This method is the most effective [2]. In TCTF, changes of the external temperature field have no effect on the MTC, so error due to ATI of the MTC cannot manifest itself. The aim of the article is to model error due to ATI for both the conventional TC and the TCTF.

2. The technique of modelling error due to inhomogeneity

The theoretical basis of the estimation error due to ATI are conclusions made in [2] - errors due to ATI and EDD of TC CC are the manifestations of one phenomenon - the degradation of TC legs. Thus, the experimental determination of EDD under the influence of operating temperature and time can be used to estimate error due to ATI. The complete results of such studies for the type K TC are presented in [3]. For TC that are operated in stationary thermal objects, the change in the CC of each TC section ΔE, caused by degradation, depends on three variables – temperature of its stable operation t_e, time of operation τ_e and its instantaneous temperature t_d (at which the section appears after the change in the temperature field), that is $\Delta E = f(t_e, \tau_e, t_d)$. In general, such a function is difficult to fit due to an insufficient amount of experimental data in [3]. Therefore, it is proposed to estimate the error for a certain instant of operation. It is reasonable to use a function of two variables like $\Delta E = k \cdot f(t_e) \cdot \varphi(t_d)$, in which functions $f(t_e)$, $\varphi(t_d)$ are polynomials without intercepts, that is, they are equal to zero for

$t_e = 0$ or $t_d = 0$ respectively. In this case, the data from [3] are sufficient for fitting function for the type K TC drift. First, we approximate the drift of the TC CC for the temperature of the measuring junction of 800 °C. Drift of chromel ΔE_A^{1000} and alumel ΔE_A^{1000} legs for 1000 hours of operation, according to [3], can be described by these functions [1, 2]

$$\Delta E_X^{1000} = 0{,}035\sqrt{t_e}(-4{,}6\cdot 10^{-7} t_d^3 + 0{,}275\cdot 10^{-3} t_d^2 + 0{,}213\cdot t_d)\mu V \,, \tag{1}$$

$$\Delta E_A^{1000} = 0{,}035\sqrt{t_e}(-4\cdot 10^{-9} t_d^4 + 0{,}71\cdot 10^{-5} t_d^3 - 0{,}38\cdot 10^{-2} t_d^2 + 0{,}715\cdot t_d)\mu V \,. \tag{2}$$

To estimate error due to ATI, we split both TC legs, similarly to [1], into 24 identical sections (Fig. 1), and accept the following assumptions:

1. The reference junctions' temperature is 0˚ C. At 0˚ C, sections from 1 to 8 are operated.

2. The measuring junction is in 800 ˚C. At 800 ˚C sections from 17 to 24 are operated.

3. The temperature field changes uniformly from 0˚ C to 800˚ C. In the temperature gradient zone, there are sections from 9 to 16. The temperature difference between the beginning and the end of the i-th section $\Delta t = t_i - t_{i-1} = 100\ °C$. For the details, see Fig. 1.

4. The TC sections are homogeneous along their length (no ATI within each section).

5. As the operating temperature t_e of a TC section is taken the average value of the operating temperatures the section's ends before the change of the temperature field.

6. The instantaneous temperature t_d of a TC section is the average of the temperatures of the section's ends after the change of the temperature field. Error due to ATI is equal to the change in the emf developed by the TC, for instance, when the temperature field changes from ABCD to AB1C1D. According to [2], the reason for the change in emf is scattering of deviations of the real TC CC from the nominal one for different instantaneous temperatures t_d.

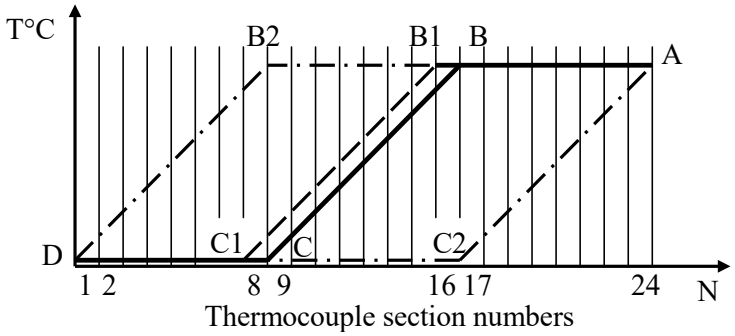

Fig. 1. Splitting the legs of an inhomogeneous TC into sections

We calculate the deviation of the CC of chromel and alumel legs from the nominal one in field ABCD (operating and instantaneous temperatures of sections are equal, i.e. $t_{di} = t_{ei}$):

$$\Delta E = \sum_{i=1}^{24} \Delta E_i = \sum_{i=1}^{24} \Delta e_i(t_{ei}, t_{di}) \cdot \Delta t_i \,, \tag{3}$$

where ΔE_i is deviation of emf of the i-th section of the corresponding TC leg from the nominal one; t_{ei}, t_{di} are operation and instantaneous temperatures for the i-th section of a TC leg, respectively; $\Delta e_i(t_{ei}, t_{di})$ is deviation of specific emf of the i-th section of a TC leg; Δt_i is the temperature difference across each section of a TC leg. We assume $\Delta t_i = 100°C$ in the gradient

zone. The drift of the specific emf $\Delta e_i(t_{ei}, t_{di})$ of the TC section can be determined from (1), (2) as their partial derivatives with respect to t_d. For chromel and alumel legs, we get:

$$\Delta e_X^{1000} = 0{,}035\sqrt{t_e}\,(-13{,}8\cdot 10^{-7}\cdot t_d^2 + 0{,}55\cdot 10^{-3}\cdot t_d + 0{,}213)\mu V/°C, \quad (4)$$

$$\Delta e_A^{1000} = 0{,}035\sqrt{t_e}\,(-16\cdot 10^{-9}\cdot t_d^3 + 2{,}73\cdot 10^{-5}\cdot t_d^2 - 0{,}76\cdot 10^{-2}\cdot t_d + 0{,}715)\mu V/°C\ . \quad (5)$$

Then we calculate the deviations ΔE_X and ΔE_A from the nominal one when field changes from ABCD to AB1C1D, (i.e. $t_{di} \neq t_{ei}$ for sections 8…16, while the temperatures of all other sections remain constant). We calculate ΔE_X and ΔE_A from (3), by substituting the corresponding value t_{di} in (4) and (5). The difference of ΔE_X and ΔE_A obtained before and after the change of the temperature field, is equal to error due to ATI. We repeat these calculations for each field toward AB2D and AC2D, by shifting the gradient zone one section each time. For field AB2D, sections 1...8, which generate emf in this case, are operated at 0˚ C, that is, according to [1, 2], they do not undergo degradation, so we get the initial TC CC. For field AC2D, sections 17...24, which generate TC emf, are operated at 800 ˚C. According to [1, 2], the TC error in field AC2D will be maximum. Thus, the difference of ΔE_X and ΔE_A in the fields AB2D and AC2D corresponds to the maximum EDD of TC CC. Also, this difference corresponds to the maximum error due to ATI. Thus, the conclusion made in [1, 2] about the equality of the maximum values of EDD of TC CC and error due to ATI is confirmed. However, the values of the drift for chromel ΔE_X and alumel ΔE_A legs are not congruent to the experimental studies [3], which are the base for (2) and (3). This is because conventional studies of EDD are carried out in a stable the temperature field, that is, in field ABCD (see Fig. 1). Then the total change in the emf is formed both by sections 15, 16, which degraded maximally (the higher temperature the higher rate of degradation [1, 3]), and by sections 8, 9, which degrade weakly [1, 2]. Therefore, experimental data are significantly lower than the maximum values. To adjust EDD and error due to ATI, we use the similarity of the dependence of the drift curves of TC versus operating time for different temperatures [3]. So we introduce the proportionality coefficients Kp, equal to the ratio of the calculated maximum error due to ATI ΔE_{NEOD} to the experimentally determined in [3] EDD ΔE_{DR}^{MAX} for a certain operating time

$$K_P = \Delta E_{NEOD} \big/ \Delta E_{DR}^{MAX} \quad . \quad (6)$$

The values got from (4), and (5) should be divided by the corresponding K_P to adjust them to the experimental studies [3]. This allows estimating error due to ATI of the conventional type K TC. It should be adapted for the TCTF. Its temperature control subsystems placed along the MTC legs, counteract the change the temperature field along these legs regardless of the changes in the external temperature field. So, when calculating the deviations of chromel ΔE_X and alumel ΔE_A legs from the nominal CC after the change of the temperature field, the condition $t_{di} \approx t_{ei}$ holds. But the difference $\Delta t_i = t_{di} - t_{ei}$ is not zero, which causes a residual error due to ATI. This temperature difference is estimated in [5], from the studies of the influence of the external temperature field on the internal one and the error of controlling the temperature field. The influence of external temperature field on the internal one Δt_P for the TCTF is determined by multiplying the change in external temperature Δt_Z by the penetration coefficient K_{REAL}. The TCTF is $K_{REAL} \leq 0{,}04$ [5]. The random error of control of temperature field Δt_K is 1.3 ˚C [5]. Then, the section's instantaneous temperature t_{di} is

$$t_{di} = t_{ei} \pm 2\Delta t_K \pm \Delta t_P \quad . \tag{7}$$

when calculating, for example, for even sections $t_{di} = t_{ei} + 2\Delta t_K + \Delta t_P$ should be substituted in formulae (4) and (5), and for odd ones – $t_{di} = t_{ei} - 2\Delta t_K - \Delta t_P$. So, the maximum error due to ATI of the TCPTF will be determined.

3. The Results of the Study of Error due to Inhomogeneity

Results of modelling of error due to ATI when the external temperature field changes, for both the conventional TC and the TCTF are given in Fig. 2. The proportionality coefficients *Kp* determined from (6) are equal to 2.11 and 1.39 for chromel and alumel respectively. From fig. 2a the maximum change in emf reaches 430 μV, or 10.75 ˚C for type K TC and 7 μV or 0.18 ˚C for the TCTF. So the TCTF mitigates error due to ATI in about 60 times.

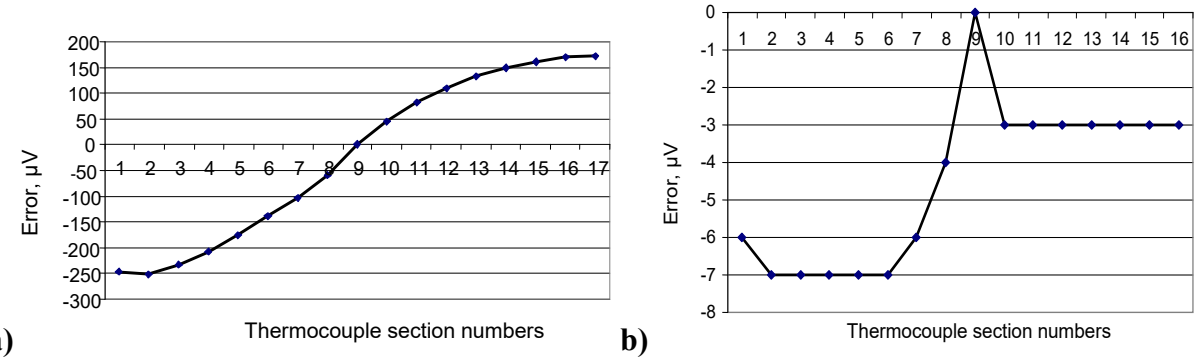

Fig. 2. Error due to acquired inhomogeneity of the conventional type K TC for 1000 hours of operation at the temperature of 800 ˚C (a) and for the TCTF with the MTC based on type K TC (b)

4. Conclusions

The following conclusions can be drawn: (i) error due to ATI for the conventional type K TC can exceed 10 °C and for the TCTF 0.2°C; (ii) the maximum sensitivity of both conventional TC and TCTF to temperature changes is for small changes of it, which makes ATI even more dangerous; (iii) the TCTF reduces error due ATI in about 60 times. This allows using all known drift correction methods considered in [2], which can be used in data acquisition devices.

References

[1] Jun, S., Kochan, O. (2015). The mechanism of the occurrence of acquired thermoelectric inhomogeneity of thermocouples and its effect on the result of temperature measurement. *Measurement Techniques*, 57 (10), 1160-1166.

[2] Jun, S., Kochan, O. V., Jotsov, V. S. (2015). Methods of reducing the effect of the acquired thermoelectric inhomogeneity of thermocouples on temperature measurement error. *Measurement Techniques*, 58 (3), 327-331.

[3] Rogelberg N., et al. The stability of the chromel-alumel thermocouples' thermoelectric power at temperatures up to 800 C during up to 10000 hours. Investigation of alloys for thermocouples: In Proceedings of "Giprotsvetmetobrabotka" No. XXIX. Moscow: Metallurgy, 33-41. (1969).

[4] Jun, S., et al. (2016). Development and investigation of the method for compensating thermoelectric inhomogeneity error. *International Journal of Thermophysics*, 37 (1), 10.

[5] Wang, J., et al. (2019). Information-measuring System to Study the Thermocouple with Controlled Temperature Field. *Measurement Science Review,* 19 (4), 161-169.

Ad-hoc Correction of Error due to Input Resistance of DAQ Units

[1]Xu Aibo, [2]Li Haitao, [1]Zhao MingMing, [1]Hu Jiwei, [2]Orest Kochan, [3]Krzysztof Przystupa

[1]Wuhan Fiberhome Technical ServicesCo., Ltd, Wuhan, China
[2]School of Computer Science, Hubei University of Technology, Wuhan, China
[3]Department of Automation, Lublin University of Technology, Lublin Poland
Email: orest.v.kochan@lpnu.ua

Abstract. *To measure the bipolar voltage at a unipolar power supply (from the USB port), many data acquisition units have a complex input circuit containing a voltage divider and a bias voltage source. An ad-hoc correction technique of error due to input resistance of data acquisition (DAQ) units without reference and high-precision equipment is proposed. The technique does not require complex hardware and software. The results of modelling show that with a confidence probability of 0.9973, the deviations of electromotive force and resistance do not exceed 0.9% and 5.6%, respectively*

Keywords: Error, Error Correction, Input Resistance, Data Acquisition Units

1. Introduction

Ad-hoc measurements are quite frequent in praxis. One of the main requirements for ad-hoc measurements is the use of existing or easily accessible equipment to solve unexpected problems. This often requires unconventional approaches and the development of new measurement methods. Conventional data acquisition (DAQ) units usually measure DC voltage [1-3]. Their advantages are the ability to transfer data to a computer for further storage and processing as well as accompanying software. All this enables the use of DAQ units as peripheral devices in multichannel measuring and control systems. However, the cheap units (e.g. NI USB 6009 [3] produced by National Instruments), have a complex input circuit containing a bias voltage source and a voltage divider to measure bipolar voltage (±10V) using the USB port as a unipolar power supply. Thus, the development ad-hoc technique for correcting error due to input resistance is a relevant task. A usual way to increase the input resistance of DAQ units is using the operational amplifier [4]. However, problems with power supply appear. So the solutions based on aggregate and combined measurement methods [4] are more appropriate for Ad-hoc measurements [2]. So, between the output of a signal source and the input of a DAQ unit, a circuit (mostly resistor based) is wired, and the voltages across resistors are measured, and a system of equations is constructed and solved to compute the input resistance. The goal of this work is to develop the technique for ad-hoc correcting error due to the input resistance of DAQ units, which requires minimal and widely accessible equipment and a simple algorithm for measurement data processing.

2. The Proposed Method for Reducing Error due to Input Resistance of DAQ Units

A typical input circuit of a simple DAQ unit powered by the USB port is given in Fig. 1 [3]. It consists of a source of the bias voltage Ev, resistors Rv1 ... Rv3 and the source of measured voltage Ux. The latter consists of an equivalent source of the electromotive force Ex and internal resistance Rw. It should be noted that the values of Ev and the resistances of Rv1 ... Rv3 are often missed in datasheets, whereas the actual values may have considerable deviations from the nominal ones. Therefore, it is necessary to determine the individual parameters of the input

circuit of the DAQ unit before applying the correction technique. We simplify the circuit given in Fig. 1 by replacing the bias voltage source Ev and resistors Rv2 and Rv3 with the Thevenin equivalent circuit, see Fig. 2. Ev, Rv2 and Rv3 are replaced with Eve, Rv1e and Rv2e.

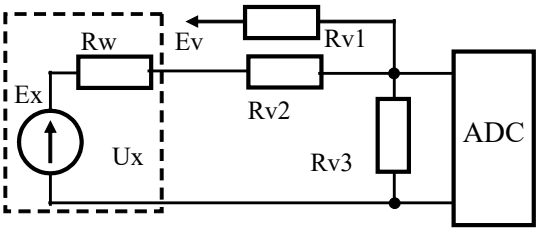

Fig. 1. The input of the DAQ unit powered using the USB port.

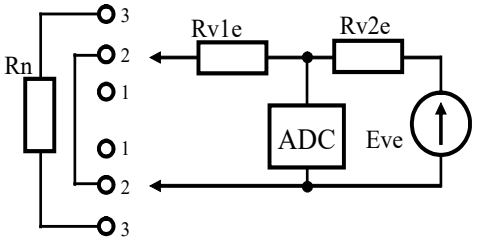

Fig. 2. The circuit for determining the input parameters of the DAQ unit.

To determine Eve, Rv1e i Rv2e it is enough to use one resistor Rn, whose resistance is measured with adequate accuracy. The determination consists of the following operations:

1. Measuring bias voltage Eve. To do this, open DAQ input terminals (open circuit mode, position 1 of the switch in Fig. 2) and measure U1, which is equal to Eve.

2. Measuring voltage U2 when the DAQ input is short-circuited (position 2 of the switch).

3. Measuring voltage U3 when resistor Rn is wired to the input (position 3 of the switch).

Then we construct a system of two equations to determine the unknown Rv2e and Rv3e

$$\begin{cases} U2 = U1 - U1 \cdot Rv1e/(Rv1e + Rv2e) \\ U3 = U1 - U1 \cdot (Rv1e + Rn)/(Rv1e + Rv2e + Rn) \end{cases} \tag{1}$$

Resistances Rv1e and Rv2e are the solution of (1)

$$Rv1e = Rn\frac{U1 \cdot U2 - U2 \cdot U3}{U1 \cdot U3 - U1 \cdot U2} \tag{2}$$

$$Rv2e = Rv1e\frac{U1 - U2}{U2} \tag{3}$$

3. Correcting Error due to Input Resistance of DAQ Units

The proposed technique of error correction consists of two measurements (see Fig. 3). The first measurement is carried out with the switch K closed and voltage U4 is measured. The second measurement is carried out with the switch K open and voltage U5 is measured.

$$\begin{cases} U4 = U1 - \dfrac{(Ex - U1) \cdot Rv2e}{Rv1e + Rv2e + Rwx} \\ U5 = U1 - \dfrac{(Ex - U1) \cdot Rv2e}{Rv1e + Rv2e + Rwx + Rn} \end{cases} \tag{4}$$

These measurement results allow constructing a system of two equations with two unknowns such as electromotive force (emf) Ex of the signal source and its internal resistance Rwx

ISBN 978-80-972629-6-9

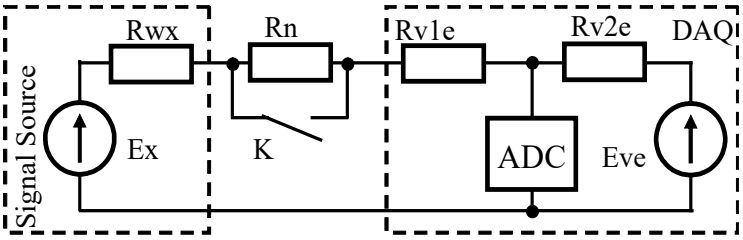

Fig. 3. The proposed technique for correcting error due to input resistance of DAQ unit.

The solution of (4) is internal resistance Rwx of the signal source and its emf, respectively. Formulae (5) and (6) can be used in software for processing the measurement results.

$$Rwx = (U4 - U1)\cdot(Rv1e + Rv2e) - (U5 - U1)\cdot(Rv1e + Rv2e + Rn)/(U5 - U4) \quad (5)$$

$$E_X = [(U4 - U1)\cdot(Rv1e + Rv2e + Rwx) + U1\cdot Rv2e]/(Rv2e) \quad (6)$$

The disadvantage of the technique is the need to switch the circuit with switch K and thus lower speed of DAQ because of two measurements and the delay due to transient processes after switching the circuit. However, when Rwx remains constant (there are no non-linear components), these two measurements can be carried out before an experiment to avoid delay. For computing Ex according to (6), the already computed value of Rwx can be used. There is no need for the constant operation of switch K. It can be replaced by a piece of wire, which is unsoldered while measuring voltage U5. However, to study its capabilities, it is necessary to investigate the influence of errors of Rn and U1 ... U5 on the calculations of Ex and Rwx.

4. Results and Discussion

It is necessary to study the influence of errors of Rn and U1 ... U3 on the calculations of Rv1e, Rv2e, and Eve. Analytic estimation is difficult, so we use modelling. The values of Eve, Rv1e and Rv2e are calculated for ideal values of Rn and U1 ... U3, then are calculated for maximum errors of Rn and U1 ... U3. The deviations of Eve, Rv1e and Rv2e are used for evaluating the errors of Ex and Rwx. We substitute in (5) and (6). Eve, Rv1e, Rv2e as well as U4 and U5 computed without and with errors. All values of errors, such as 0% and 1% were sequentially put to (5) and (6). The results of the studies are given in Table 1. The study was carried out for the 14-bit DAQ unit of NI USB6009 [3]. The column headers show parameters, whose error effect is studied, and the row headers show the maximum errors of Ex and Rwx. In most cases, these errors are acceptable. However, they are caused by separate errors of Rn and U1 … U5.

Table 1. The study results of the influence errors of the input parameters of the DAQ unit on the measurements of the parameters of the signal source

	Rn	U1	U2	U3	U4	U5
Ex	0,01%	0,2%	0,13%	0,36%	0,03%	0,046%
Rwx	0,03%	0,9%	1,4%	2%	0,4%	0,41%

The influence of 110 random combinations of errors of Rn and U1 ... U5 on calculations of Ex and Rwx was studied. The errors were uniformly distributed within the range of ±0.1%. The resulting Ex and Rwx errors are given in Fig. 4 and Fig. 5. The figures show the combinations of errors of Rn, U1…U5 lead to much larger errors of Ex and Rwx than those given in Table 1. Thus, we use statistical methods to evaluate the influence of Rn and U1 … U5 on Ex and Rwx. The standard deviation of Ex according to Fig. 4, does not exceed 0.029 V. The maximum deviation of Ex according to the 3σ-rule (confidence probability of 0.9973) does not exceed 0.9%, which is acceptable for many cases of ad-hoc measurements. The standard deviation of Rwx, according to Fig. 5, does not exceed 0.37 kΩ. The maximum deviation of Rwx according

to the 3σ-rule (confidence probability of 0.9973) does not exceed 5.6%. This is quite a large error. It is because there is a significant number of voltage differences in (5). So the obtained values are relatively little while their errors are summed up. Therefore, the relative influence of these deviations rises. However, for most ad-hoc measurements, the value of Rwx is an auxiliary result, often redundant. Thus, the obtained value of 5.6% is acceptable in most cases.

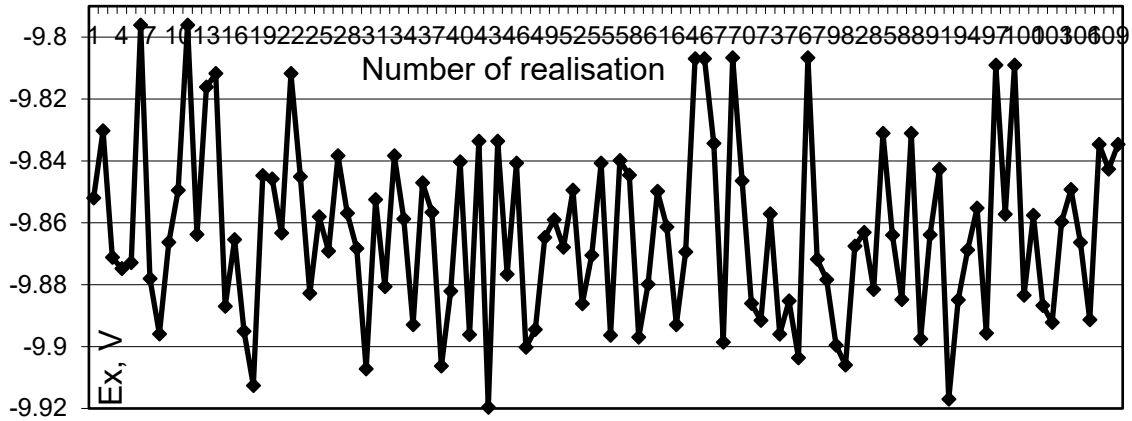

Fig. 4. Net errors of Ex under the combined influence of random errors of Rn, U1…U5

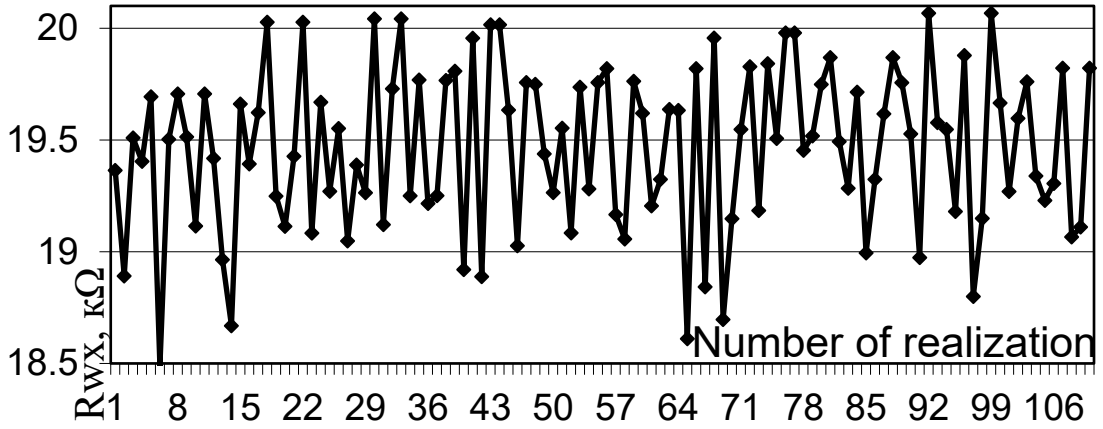

Fig. 5. Net errors of Rwx under the combined influence of random errors of Rn, U1…U5

5. Conclusions

The technique of ad-hoc correction of error due to the input resistance of DAQ units shows its efficiency. It requires minimum hardware and does not require complex measurement data processing, i.e., it does not require significant improvement of the used software. However, the techniques enable the use of widely distributed DAQ units, which have low input resistance.

References

[1] Webster, J. G. (1998). *The measurement, instrumentation and sensors handbook*. CRC.

[2] Kochan, R., Kochan, O., Chyrka, M., Vasylkiv, N. (2005). Precision data acquisition (DAQ) module with remote reprogramming. In 2005 IEEE Intelligent Data Acquisition and Advanced Computing Systems: Technology and Applications (pp. 279-282).

[3] USB-6009 Specifications. https://cutt.ly/g5R62BU

[4] Tumanski, S. (2006). *Principles of electrical measurement*. CRC press.

Measurement of Physical Quantities II

ISBN 978-80-972629-6-9

Comparison of Characteristics for Two Selected Inductors for Levitation Melting

Błażej Nycz, Roman Przyłucki, Łukasz Maliński

Silesian University of Technology, Gliwice, Poland
Email: blazej.nycz@polsl.pl

Abstract. *Electromagnetic Levitation Melting (EML) is one of the melting metals methods. It is based on the use of an inductor that generates an alternating electromagnetic field. In this study, the effect of changing the geometric parameters of the inductors on the electrical parameters of the system, the melting time of the batch, and the lifting force of the batch was investigated. The measurements were carried out in relation to two inductors for EML, the first being the base and the second one being the result of optimization aimed at finding the best geometrical parameter for the presented class of inductors. On this basis, we recommend the use of an optimized inductor.*

Keywords: Electromagnetic Levitation Melting, Metal Melting, Position Measurements

1. Introduction

Electromagnetic Levitation Melting (EML) is one method of melting metals. The inductor, which is a coil made of a highly conductive metal, is connected to an alternating current source. Currents generally have a relatively high current and frequency [6]. To prevent excessive heating of the inductor, the wire from which it is wound may be shaped like a tube through which coolant flows. As a result of the current skin effect, the flow is not obstructed. As a result of AC current flow, an alternating electromagnetic field is created, which induces eddy currents in the batch, resulting in its heating and, thus, melting [2]. A Lorentz force is also induced in the batch, which can be sufficient to oppose the force of gravity, resulting in the levitation of the batch [1].

The main disadvantage of the EML method is the low efficiency of the process; for this reason, its application is in specialized fields [5]. In industrial settings, it is used for processes that require high purity of alloys and alloys that need to be thoroughly mixed , especially for refractory alloys. The second field is materials research, in which EML is widely used. Due to the fact that the batch levitates during the process, it is possible to freely record the phase transformation process on it with simultaneous control over the dynamics of the process [3]. Furthermore, thermophysical properties such as emissivity, thermal expansion, mass density, thermal diffusivity, electrical resistivity, thermal conductivity, surface tension, and viscosity can be measured.

2. Subject and Methods

Preliminary results

The results presented here are a continuation of a series of studies carried out by researchers. The first stage was the preparation of a computational model of the finite element method whose reliability was confirmed against measurements made in the laboratory. On this basis, the effect of changes in the electrical and geometric parameters of the inductor on the efficiency of the process and the lifting force was studied [4]. The next step was the preparation of an optimization algorithm and its coupling with the computational model. Once the suboptimal

variant was selected, it was designed and made, and the measurements were executed against the initial and optimized inductor, as presented in the following chapter.

Comparative measurements

The measurements were made against two inductors for Electromagnetic Levitation Melting, the first of which is the base and the second of which is the result of a search for the best geometrical parameters for the class of inductors presented. Both inductors are made of copper tubes with an inner radius of 4 mm and an outer radius of 6 mm. During the experiment, water flows inside the tube actively cooling it. The inductor is connected to a current source that generates an alternating current, the parameters of which depend on the connected inductor and the setup of the resonant circuit. An aluminum ball (batch) with a diameter of 6 mm is inserted inside. Aluminum was chosen because of its relatively low melting point and light weight, which is a common practice among researchers. The differences between the two inductors are shown in Figure 1.

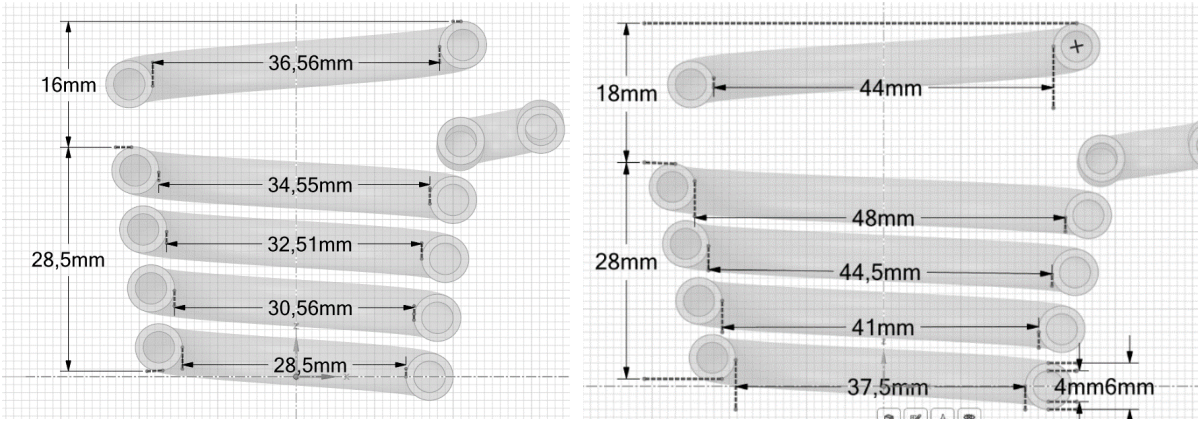

Figure 1. Geometrical parameters marked on the cross-section of the tested inductors. On the left is the base inductor and on the right is the optimized inductor.

The measuring station (Fig. 2) consists of a set of sensors that are sufficient to measure the characteristics of interest. Around the wire of the inductor was placed a Roggowski coil, which in turn through the transducer is connected to an oscilloscope and allows reading the parameters of the current that flows through the circuit. The second channel of the oscilloscope is connected through the measuring probes to the beginnings of the inductor, which allows one to measure

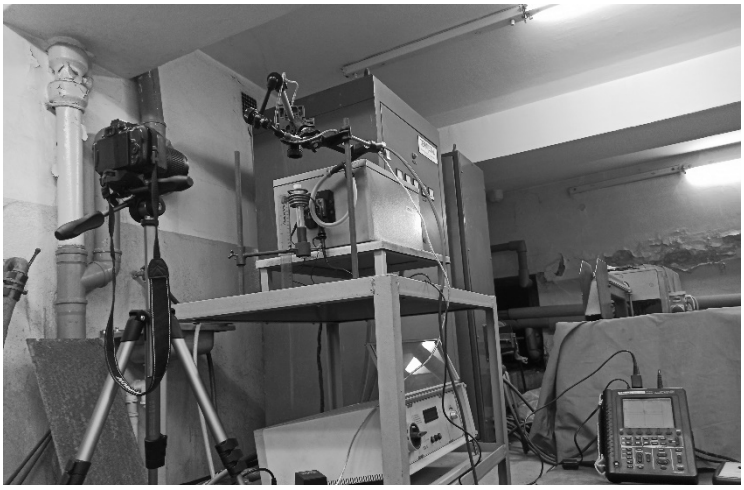

Figure 2. Measurement station

the voltage on the inductor. Inside the inductor, there is a tube made of transparent glass so that

the behavior of the batch can be observed. A thermal imaging camera was placed above the inductor to determine the temperature and melting moment of the batch. The whole experiment is recorded by a video camera that allows one to determine the batch position and the beginning of batch melting. If the video recording is juxtaposed with the readings from the thermal camera, the melting time can be determined with relative accuracy. Below the inductor, there is a bowl with water in which the batches are cooled after the process. The position of the batch is determined by the number of pixels between the bottom of the inductor and the batch. The distance that represents 1 pixel is verified by the ruler in the batch plane.

3. Results

The following are the results of the measurements carried out at the test station presented in the section 'Subjects and Methods'. Table 1 shows the values of the current parameters for both inductors. Values during operation under load and at idle do not show differences greater than the accuracy of the measurement.

Table 1. Current parameters of both inductors tested.

Electric parameter	Base inductor	Optimized inductor
Current (RMS)	364 A	359 A
Voltage (RMS)	203 V	358 V
Frequency	277 777 Hz	246 154 Hz
Phase shift	87.56	88.62
Effective power	3145.816 W	3095.223 W

Figure 3 shows the measurements of the batch levitation height for both inductors. Black indicates measurements made for the base inductor, and gray color indicates measurements for the optimized inductor. The dashed lines indicate the average value for the categories of measurements in the corresponding color.

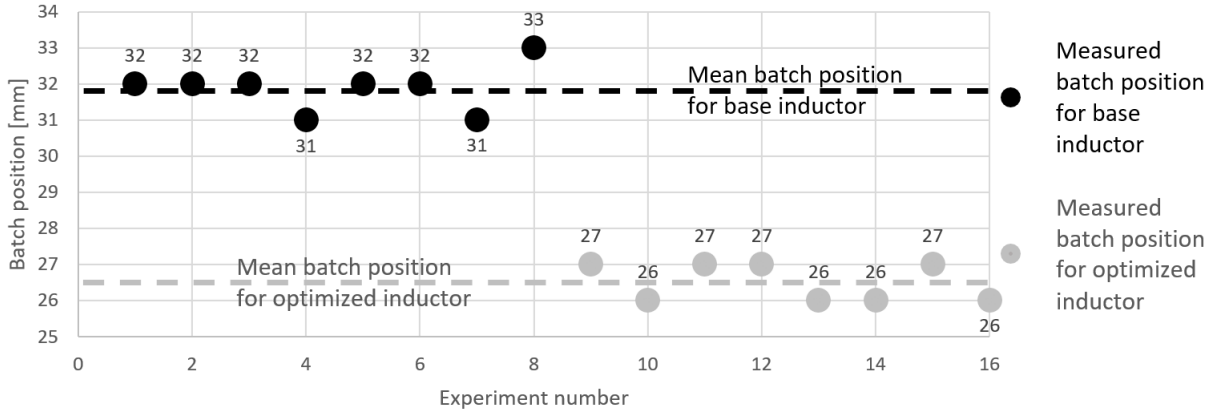

Figure 3. Position of batch levitation during melting.

Figure 4 shows the results of the measurements of the time it took for the batch to melt from the time it was inducted until the temperature of 660ºC was recorded by the thermal imaging camera. Black indicates the measurements carried out for the base inductor, and gray indicates the measurements for the optimized inductor. The dashed lines indicate the average value for the categories of measurements in the corresponding color.

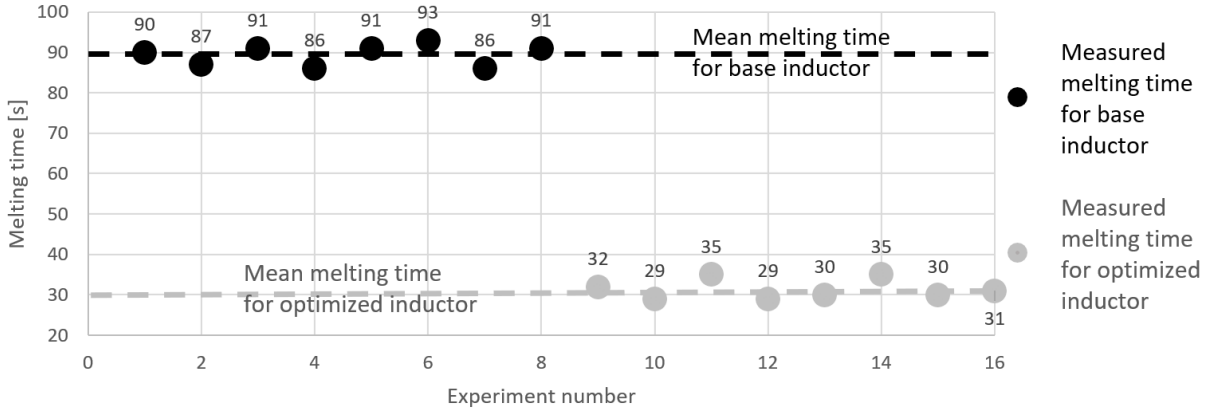

Figure 4. Melting time of the batch during the process.

4. Discussion

From the measurements presented, it can be seen that the current characteristics with the same power source for the optimized inductor differ significantly from those of the basic inductor. The current intensity is lower for the optimized inductor by 5 A. On the other hand, it is higher for the optimized inductor by 155 V. The difference in frequency is 31 623 Hz and is lower for the optimized inductor. The difference measured in the current parameters is a clue for future consideration in computational models. In this matter, it would be helpful to create more inductors with different geometries to prepare an appropriate mathematical model.

Observations of the batch behavior, including its position and heating time, provide information on the process properties. For the base inductor, the average position during levitation is higher than in the optimized inductor. Furthermore, the average melting time for the optimized inductor is lower. On this basis, we recommend the use of the optimized inductor for industrial purposes.

Acknowledgements

The publication is funded by Silesian University of Technology from 11/040/BK_23/0029

References

[1] Bojarevics, V.; Hyers, R.W. Levitated liquid dynamics in reduced gravity and gravity-compensating magnetic fields. JOM 2012, 64, 1089–1096.

[2] Buliński, P.; Smolka, J.; Golak, S.; Przyłucki, R.; Palacz, M.; Siwiec, G.; Melka, B.; Blacha, L. Numerical modelling of multiphase flow and heat transfer within an induction skull melting furnace. International Journal of Heat and Mass Transfer 2018, 126, 980–992.

[3] Feng, L.; Shi, W.Y. The influence of eddy effect of coils on flow and temperature fields of molten droplet in electromagnetic levitation device. Metallurgical and Materials Transactions B 2015, 46, 1895–190

[4] Nycz, B.; Malinski, L.; Przylucki, R. Influence of Selected Model Parameters on the Electromagnetic Levitation Melting Efficiency. Applied Sciences 2021, 11, 3827.

[5] Przylucki, R.; Golak, S. The Stress Effects Occurring During Induction Heating of Titanium. In Proceedings of the Solid State Phenomena. Trans Tech Publ, 2014, Vol. 211, pp. 149–154.

[6] Witteveen, J.; van Gastel, R.; van Houselt, A.; Zandvliet, H. 3D modeling of electromagnetic levitation coils. Current Applied Physics 2021, 32, 45–49.

The Influence of Various Dopants on Magnetic Properties of Gehlenite Glasses

[1]Melinda Majerová, [1]Martin Škrátek, [2]Anna Prnová, [3]Jozef Kraxner, [1]Andrej Dvurečenskij, [1]Ján Maňka, [2, 3]Dušan Galusek

[1]Institute of Measurement Science, Slovak Academy of Sciences, Bratislava, Slovakia
[2]Vitrum Laugaricio – Joint Glass Center of the IIC SAS, TnU AD and FChPT STU, Trenčín, Slovakia
[3]Centre for Functional and Surface Functionalized Glass, Alexander Dubček University of Trenčín, Trenčín Slovakia
Email: Melinda.majerova@savba.sk

Abstract. *The Bi and Ni-doped gehlenite glasses were prepared by flame synthesis. The concentration of Bi and Ni was 0.0, 0.5 and 3.0 mol. %. Scanning electron microscopy (SEM) confirmed that spherical particles which did not contain any formations indicating the presence of crystalline phases were prepared by the flame synthesis. The amorphous nature of the prepared systems was also confirmed by the results of X-ray diffraction analysis. Both the Ni and Bi-doped gehlenite glass microspheres exhibited complex magnetic properties.*

Keywords: Gehlenite Glasses, Bi-doped Glasses, Ni-doped Glasses, Magnetic Properties

1. Introduction

Gehlenite ($2CaO.Al_2O_3.SiO_2$) is a very interesting and recently intensively studied material, mainly due to its excellent resistance to abrasion, chemical stability, industrial availability, and economical feasibility [1]. Gehlenite glasses as well as crystalline gehlenite have been intensively studied not only because of the cheap and easily available raw materials for their preparation, but also because of their ability to absorb a high amount of optically active dopants into the glass matrix [2]. The magnetic properties of aluminate and generally of oxide glasses have been little investigated. Some studies were focused on the influence of transition metals on the magnetic properties of oxide glasses [3, 4] while others reported on the influence of rare-earth ions addition on the magnetic properties of glasses [5, 6]. As for aluminate glasses, aluminosilicate glasses doped with various metals have been studied to the greatest extent [7, 8]. Currently, there is a certain trend in which the information on the structure of glasses is sought to be supplemented or better explained using SQUID magnetic measurements [9]. The aim of this work is to study the influence of two different dopants on the magnetic properties of gehlenite glasses.

2. Subject and Methods

Two series of gehlenite glasses were prepared in order to monitor the influence of different dopants on the magnetic properties of the prepared glasses. The first series of samples was doped with Bi and the second with Ni. Gehlenite glasses doped with different amount (0.0, 0.5 and 3.0 mol.%) of Bi and Ni were prepared by flame synthesis from precursors powders prepared by solid-state reaction. The nominal composition of prepared systems is summarized in Table 1. High-purity chemicals (Al_2O_3, SiO_2, Bi_2O_3, NiO and $CaCO_3$) were used as raw materials. The morphology of the prepared systems was studied by scanning electron microscopy (JEOL JSM-7600 F/EDS/WDS/EBSD). The amorphous nature of prepared glasses

ISBN 978-80-972629-6-9

was verified by XRD analysis using a Panalytical Empyrean diffractometer (CuKα radiation, at ambient temperature in the 2θ range 10-80°). The diameter distribution of glass microspheres was determined by Mastersizer 2000 instrument (Malvern Instruments). The magnetization of prepared systems was determined by Quantum Design MPMS XL-7AC SQUID magnetometer at 300K and 2K.

Table 1. The nominal composition of prepared powder precursors, XRD quality of prepared glasses after flame synthesis, median ($d_{(50)}$) of prepared glass microspheres

Sample	Composition [mol.%]					XRD quality	$d_{(50)}$ [μm]
	CaO	Al_2O_3	SiO_2	Bi_2O_3	NiO		
GBi0.0	50.00	25.00	25.00	0.0	0.0	amorphous	10
GBi0.5	49.87	24.94	24.94	0.25	0.0	amorphous	11
GBi3.0	49.24	24.63	24.63	1.5	0.0	amorphous	18
GNi0.5	49.76	24.87	24.87	0.0	0.5	amorphous	21
GNi3.0	48.50	24.25	24.25	0.0	3.0	amorphous	14

3. Results

SEM examination confirmed spherical morphology of prepared glass particles. The surface of the microspheres as well as the polished cross-sections of microspheres did not contain any signs indicating the presence of crystalline phases (Fig. 1.). The amorphous nature of the prepared microspheres was also confirmed by XRD analysis. The particle size distribution in individual samples was determined in order to rule out the effect of particle size on their magnetic properties. Microspheres have a monomodal particle size distribution with the median (d_{50}) ranging in the interval 11 – 21 μm (Table 1.).

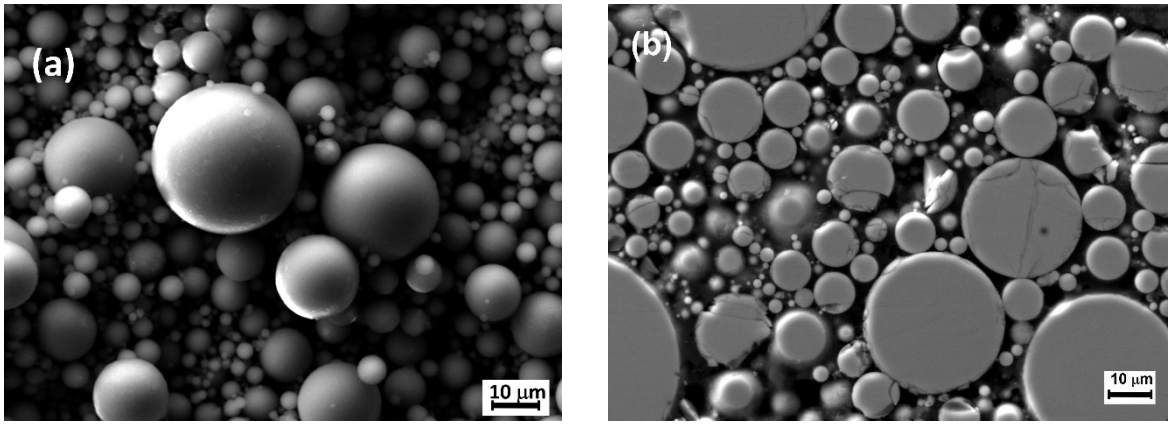

Fig. 1. (a) SEM images of GBi0.5 sample, (b) SEM images of the polished cross section of GNi0.5 sample

Fig. 2. shows the influence of the applied magnetic field on the magnetization of gehlenite glass microspheres doped with Bi (a) and Ni (b) measured at 300K at the magnetic field of up to 10 kOe. The comparison of *M(H)* dependences showed that in the case of microspheres without dopants as well as in the case of Bi-doped samples, the diamagnetic component of magnetization prevailed (Fig. 2a). In case of microspheres with the highest amount of Bi (GBi3.0) a weak ferromagnetic behavior (with narrow hysteresis) was observed in a low field range (inset of Fig. 2a). The *M(H)* dependences of the Ni-doped samples revealed a significant

ISBN 978-80-972629-6-9

influence of the presence of Ni on the magnetic properties of the glass matrix (Fig. 2b). Instead of diamagnetism, ferromagnetic behavior prevailed in these samples.

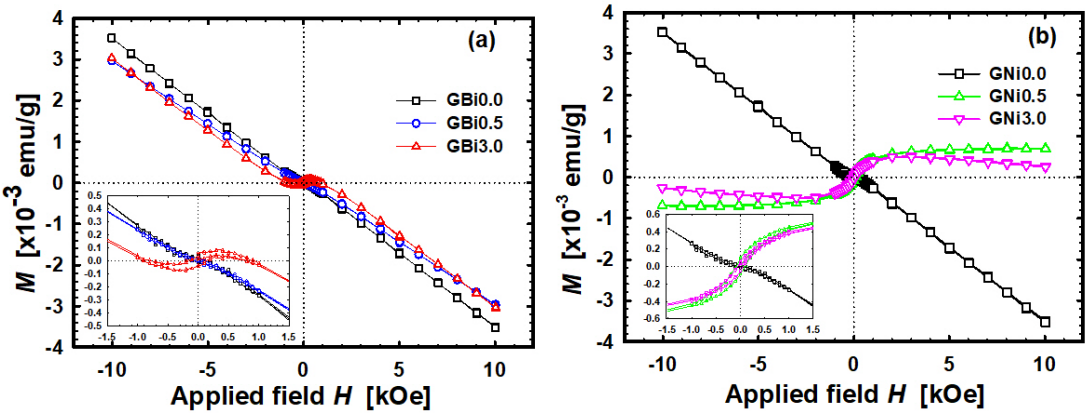

Fig. 2. *M* vs *H* dependences of Bi (a) and Ni (b) doped gehlenite glass microspheres measured at 300 K. The insets show an enlarged view at near zero magnetic field.

To make other components of magnetization visible, their magnetic properties at various temperatures were determined. While diamagnetism is temperature-independent, other components of magnetization have an inverse temperature dependence [10, 11]. The *M(H)* dependences measured at 2K showed that, for both dopants, the paramagnetic component of magnetization predominates (Fig. 3.). In case of Ni-doped samples, there was a significant increase in magnetization over the Bi-doped samples. Based on the literature, we assume that diamagnetism originates from the glass matrix [8]. Paramagnetism and ferromagnetism can be attributed to the presence of Ni^{2+} ions. The Ni^{2+} ions in the glass structure can be tetragonally or octahedrally coordinated. Bismuth can be present in the form of of Bi^{2+} and Bi^{+} ions since Bi can be incorporated into the gehlenite structure in different oxidation states [3, 12 - 14].

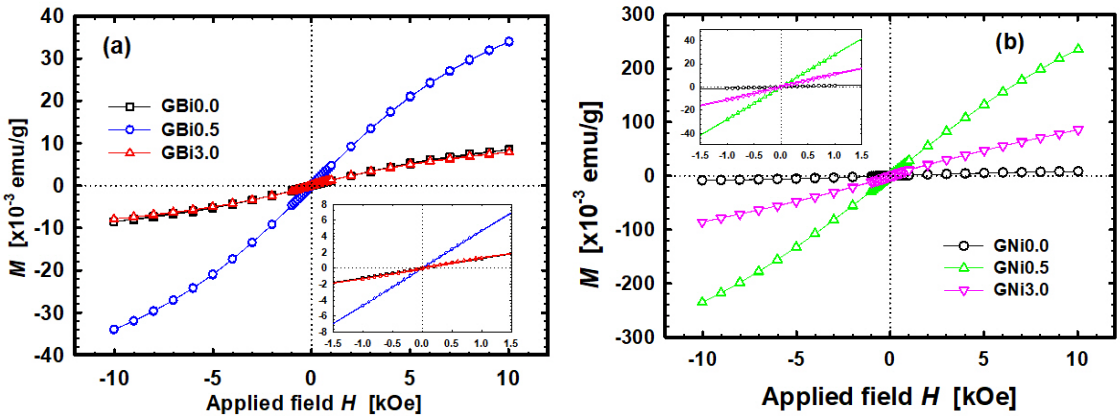

Fig. 3. *M* vs *H* dependences of Bi (a) and Ni (b) doped gehlenite glass microspheres measured at 2 K. The insets show an enlarged view at a near zero magnetic field.

4. Conclusions

The influence of the addition of Bi and Ni dopants on the magnetic properties of gehlenite glasses was examined. The glasses were prepared by flame synthesis in the form of glass microspheres. The prepared microspheres were XRD amorphous, with a relatively narrow diameter distribution, with the medians ranging for different compositions from 11 to 21 µm. The addition of Ni significantly influenced the magnetic properties of the glass matrix at 300

K. While diamagnetism prevailed in glass microspheres without dopants as well as in the Bi-doped samples, ferromagnetic behaviour prevailed in the Ni-doped samples at 300K. At 2 K, the paramagnetic component of magnetization was predominant.

Acknowledgements

The financial support of this work by the projects VEGA 2/0028/21 and VEGA 2/0141/21 is gratefully acknowledged. The idea of studying the transition metal doped compounds with melilite structure was based on discussions with Prof. Lothar Wondraczek from the Otto-Schott Institute, Friedrich Schiller University of Jena, Germany.

References

[1] Merkit, Z.Y., Toplan, H.Ö., Toplan, N. (2018). The crystallization kinetics of CaO-Al_2O_3-SiO_2 (CAS) glass-ceramics system produced from pumice and marble dust. *Journal of Thermal Analysis and Calorimetry*, 134(1), 807-811.

[2] Shih, S.J., Lin, Y.Ch., Lin, S.H., Veteška, P., Galusek, D., Tuan, W.H. (2016). Preparations and characterization of Eu-doped gehlenite glassy particles using spray pyrolysis. *Ceramics International*, 42(9), 11324-11329.

[3] Ardelean, I., Ilonca, Gh., Simon, V., Jurcut, T., Filip, S., Hagau, T. (1997). Magnetic properties of nickel-strontium-borate oxide glasses, *Journal of materials science letters*, 16, 200-201.

[4] Mekki, A., Khattak, G.D., Holland, D., Chinkhota, M., Wenger, L.E. (2003) Structure and magnetic properties of vanadium-sodium silicate glasses. *Journal of Non-Crystalline Solids*, 318(1-2), 193-201.

[5] Dupas, C., Renard, J.P., Fonteneau, G., Lucas, J. (1982) Magnetic susceptibility of fluoride glasses with 3d and 4f elements. *Journal of Magnetism and Magnetic Materials*, 27, 152-158.

[6] Akamatsu, H., Kawabata, J., Fujita, K., Murai, S., Tanaka, K. (2011) Magnetic properties of oxide glasses containing iron and rare-earth ions. *Physical Review B*, 84, 144408-144418.

[7] Meert, T.A., Wenger, L.E. (1981) Frequency dependent susceptibility of cobalt aluminosilicate glasses. *Journal of Magnetism and Magnetic Materials*, 23, 165-172.

[8] Ozabaci, M., Aksan, M.A., Kirat, G., Kizilaslan, O., Yakinci, M.E. (2016) Preparation and characterization of CaO-Al_2O_3-SiO_2 (CAS) glass-ceramics. *Journal of Non-Crystalline Solids*, 454, 8-12.

[9] Bonfanti, S., Jug, G. (2015) On the Paramagnetic Impurity Concentration of Silicate Glasses from Low-Temperature Physics. *Journal of Low Temperature Physics*, 180, 214-237.

[10] Matyáš, M. (1972) Magnetic properties of semiconductive glasses. *Journal of Non-Crystalline Solids*, 8-10, 592-597.

[11] Legendre, B., Sghaier, M. (2011) Curie temperature of nickel. *Journal of Thermal Analysis and Calorimetry*, 105, 141-143.

[12] Ali, M., Akram, M., Zafar Iqbal S.M., Ashfaq, M. (2020) Synthesis, thermal, electrical and magnetic properties of $Bi_{0.6-x}Mn_{0.5}Ni_{0.5}Fe_2O_4$ ferrite. *Digest Journal of Nanomaterials and Biostructures*, 15, 491-500.

[13] Majerová, M., Klement, R., Prnová, A., Kraxner, J., Bruneel, E., Galusek, D. (2018) Crystallization and VIS-NIR luminescence of Bi-doped gehlenite glass. *Royal Society Open Science*, 5:181667.

[14] Guan, H., Zhang, X., Xie, Y. (2014) Soft-Chemical Synthetic Nonstoichiometric $Bi_2O_{2.33}$ Nanoflower: A New Room- Temperature Ferromagnetic Semiconductor. *The Journal of Physical Chemistry*, 27170-27174.

Simultaneous Measurement of the Lifting Force, Joule Heating and Axial/Radial Components of EM Field Inside an Electromagnetic Levitation Coil

[1]Viesturs Silamiķelis, [1]Aigars Apsītis, [1,2]Jānis Sniķeris*, [1]Austris Pumpurs, [3]Samuel Biggs

[1]Institute of Atomic Physics and Spectroscopy, University of Latvia, Riga, Latvia
[2]G. Libert's Center of Innovative Microscopy, Daugavpils University, Daugavpils, Latvia
[3]Brigham Youth University, Provo, Utah
Email: janis.snikeris@lu.lv

Abstract. *Electromagnetic levitation (EML) is a prospective method for the growth of high-purity crystals. There are separate measurements of axial EM field along the z-axis, lifting force, and total emitted heat for EML coils, but these values have not yet been measured simultaneously. Additionally, distribution of the heat emission should be considered in EML coil design. It was recently shown that 3D models of EML coils produce significantly different results in comparison to 2D approximations. Experimental measurements are needed to verify and improve theoretical models. In this paper, we present a method for simultaneously measuring lifting force, distribution of Joule heating along the z-axis for a conductive sample inside an EML coil, as well as axial and radial components of the EM field around the sample. This paper includes measurement results for a cylindrical Al sample inside an EML coil with 3 turns and 1 counterturn, but the method should be applicable to different types of samples and EML coil geometries.*

Keywords: EM Levitation Coils, Lifting Force, Heating Distribution, EM Field Measurement

1. Introduction

Growing high-quality crystals is important for a variety of scientific and technological fields. Electromagnetic levitation (EML) enables growth of crystals without a crucible, which is the main source of contamination in conventional crystal growth methods. EML relies on the Lorentz force between the coil and the conductive sample to counterbalance the force of gravity. A high-frequency alternating current, that is passed through the coil, generates an electromagnetic (EM) field, which induces eddy currents in the conductive sample. The eddy currents generate an opposing EM field from the sample. Many EML coils use a "counterturn" setup, where the bottom part of the coil generates the lifting force, and the top part of the coil is wound in the opposite direction to provide stabilization for the sample [1]. Since eddy currents cause Joule heating in the sample, EML melting can often be performed without additional heat sources. However, the coupling between the lifting force and the heating makes it difficult to work with some materials due to their physical properties because the sample material should be at or below the melting point in order to crystallize, while satisfying the conditions for levitation.

The EM field generated by different configurations of coils is commonly estimated through 2D models in combination with empirical data [2]. Husley [3] studied the efficiency of heating alongside EM field in EML coils. Fromm and Jehn [4] developed a model for calculating lifting force and power absorption for EML coils. Adapting the design of EML coils for specific applications is not a trivial task, but methods are being developed to make the process easier and faster[5]. Recently, 3D models of EML coils have been developed and quantitative

differences were shown, compared to simpler 2D models [6].
To our knowledge, current models of EML coils do not consider the distribution of the heating of the sample in detail and simply assume that the coil is hottest at the point where the intensity of the EM field is highest, and experimental measurements have only determined the maximum temperature for levitating samples [3]. Since conductive samples interact with the EM field from the EML coil, calculation of the distribution of the Joule heating and EM field becomes a non-trivial task. We believe that information about this distribution, in conjunction with the EM field as well as lifting force of EML coils, is extremely important for the design of EML coils and for the development of new techniques for using EML for crystal growth. Therefore, we set up a study for simultaneously measuring the acting force, EM field, and Joule heating along the *z*-axis of an EML coil. The coil was made after the design by Priede [1], with 3 turns and 1 counter-turn. It should be noted that the physical properties (electrical conductivity, density, etc.) of materials change upon heating and melting. A molten sample would damage the measuring instrument, so we operated in low-power mode in this study to avoid excessive heating of the sample.

2. Subject and Methods

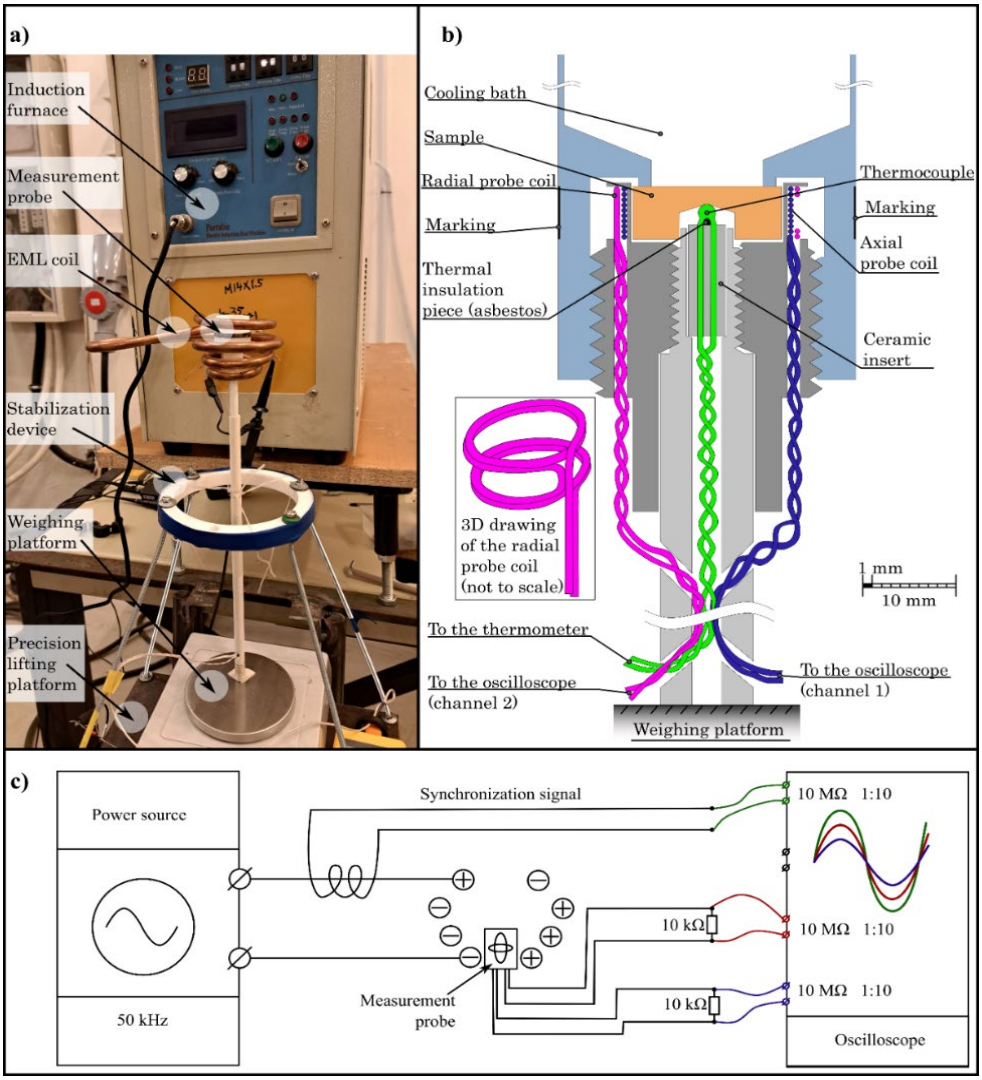

Fig. 1. a) An image of the experimental setup; b) Schematic of the measurement probe; c) Electrical diagram of the experimental setup.

The setup of the experiment is shown in Figure 1a. and its electrical diagram is shown in Figure

1c. A high-frequency induction furnace (MXBAOHENG LH-25A) was used to power an EML coil made of copper tubing (8 mm diameter) with water cooling. Additional insulation was added to the primary circuit of the induction furnace in order to prevent electric discharges during operation in low-load mode. The body of measurement probe was made from heat-resistant plastic (Teflon) and was located beneath the coil. It was moved into the coil by a mechanical precision lifting platform. A stabilization device was used to ensure frictionless weight measurement while keeping the measurement probe in a vertical position. A measurement scale beneath the lifting platform was used to determine the position of the sample and the turns of the coil. Figure 1b shows a schematic of the measurement probe. The sample was an Al cylinder with a height of 6.00 +/-0.02 mm and a diameter of 16.00 +/-0.02 mm with an opening 6.05 +/- 0.05 mm wide and up to 4.0 +/-0.1 mm deep for the thermocouple. The probe coils were positioned to be at the same height as the sample. The axial probe coil was located 0.5 mm from the surface (diameter 17 mm) of the sample and had 9 turns. The radial probe coil was located 1.5 mm from the surface (diameter 19 mm) of the sample, the distance between the top and bottom sets of windings was 5 mm, and each winding had 2 turns. Both sets were wound in opposite directions (see inclusion in Figure 1b). The probe coils were made from copper wire with Teflon insulation. The total diameter of the wire was 0.74 mm. For each measurement, the EML coil was powered for four seconds. At the third second were recorded the measurements of weight (measured by a Kern 440-33 precision balance) and the EM field (measured by a Siglent SDS1104X-E oscilloscope). The oscilloscope also measured the RMS voltage in the EML coil, and the phase inversion was determined from the oscillograms. The temperature increase was determined as the difference between the initial temperature and the maximum temperature the sample reached after the power was turned off. The sample was allowed to cool to a temperature below 25°C after each measurement. Liquid nitrogen was poured into the cooling bath to accelerate the cooling process. Measurements were done with a z distance step of 2 mm, starting from underneath the EML coil and lifting the measurement probe through it. Every 5 steps, the measurements were repeated 5 times in order to estimate the measurement errors, which were calculated within 95% confidence intervals. The position $z = 0$ was set to be in the centre of the first (bottom) turn of the coil.

The measurement results for Al sample and a control measurement without a sample, are illustrated in Figure 2. The force acting on the sample F was calculated as $F = (m_1 - m_0) \times g$, where $g = 9.81$ m/s^2 is the gravitation acceleration, m_0 is the weight reading (in grams) before powering the EML coil and m_1 is the weight reading after powering it for 3 seconds. The change of the temperature of the sample is denoted by ΔT. U_a and U_r represent the RMS voltage induced in the axial and radial probe coils, which we assume to be proportional to the intensity of the EM field strength in their respective directions. RMS voltage on the EML coil was observed concurrently with U_a and U_r measurements (synchronization signal in Figure 1c.). Negative values of U_a and U_r represent phase inversion relative to voltage on the EML coil. While displaying all the measurements in a single graph, all curves were scaled so that their maximum value was equal to 1 for the sake of clarity. The max values of U_a and U_r during the control measurement were 25.41 V and 1.11 V, respectively, while with the Al sample, they were reduced to 14.09 V and 1.01 V. The max values of F and ΔT for Al sample were 31.98 mN and 32.3 K. The horizontal grey lines in Figure 2 represent the average positions where the centre of the sample and the turns of the EML coil intersect. The amount of absorbed radial field is relatively small. Similarities between the curves of radial field U_r and weight change F have been noted.

ISBN 978-80-972629-6-9

3. Results

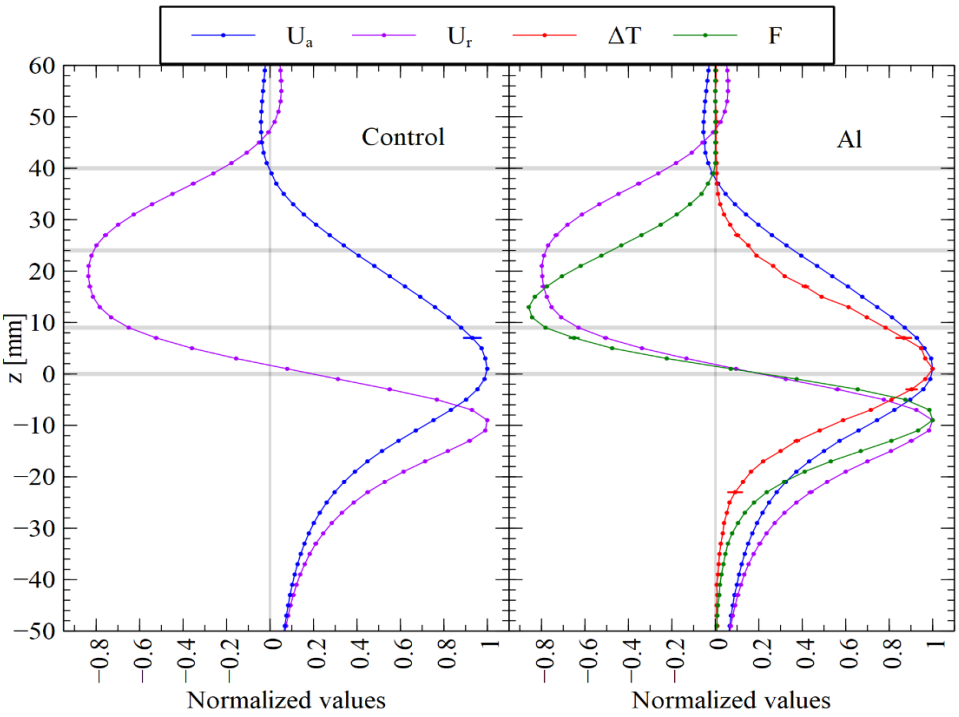

Fig. 2. The values of temperature increase ΔT, acting force F and induced EMF in indicator-contours (U_a and U_r for axial and radial, respectively) depending on the sample material and position in the coil.

4. Discussion

We successfully performed a concurrent measurement of axial and radial components of EM field, Joule heating, and force acting on a metallic sample inside EML coil with a high degree of accuracy. By subtracting EM field values measured with a sample from EM field values in control measurement, we can calculate EM field which is "absorbed" in the sample. The curve of the square of the absorbed axial field in Al sample coincides with the curve of the temperature increase ΔT in Al sample. By multiplying values of the absorbed axial field in Al sample by the radial field observed around Al sample, we obtained a curve which closely matches the acting force F. It is our hope that this method of measurement will help to verify and advance theoretical models and simulations of processes in EML coils.

Acknowledgements

This research was financed by the Institute of Atomic Physics and Spectroscopy of the University of Latvia project "Development of next-generation technology for ultra purity crystal growth based on MHD semi levitation" (Levitation, project No. 1.1.1.1/20/A/070) budget.

References

[1] Priede, J., Baptiste, L.C.B., Gleijm, G., van Westrum, J.A.F.M.S. (2005). Apparatus And Method For Levitation Of An Amount Of Conductive Material. *United States of America Patent,* 20080190908.

[2] Okress, E.C., Wroughton, D.M., Comentez, G., Brace, P.H., Kelly, J.C.R. (1952). Electromagnetic Levitation of Solid and Molten Metals. *Journal of Applied Physics,* 23, 545.

[3] Husley, W.J. (1963). The design and performance of levitation melting coils. *Union Carbide Nuclear Co. Y-12 Plant.* Oak Ridge, Tennessee.

[4] Fromm, E., Jehn, H. (1965). Electromagnetic forces and power absorption in levitation melting. *British Journal of Applied Physics*, 16, 653.

[5] Royer, Z.L., Tackes, C., LeSar, R., Napolitano, R.E. (2013). Coil optimization for electromagnetic levitation using a genetic like algorithm. *Journal of Applied Physics*, 113, 214901.

[6] Witteveen, J.P., van Gastel, R., van Houstel, A., Zandvliet, H.J.W. (2021) 3D modeling of electromagnetic levitation coils. *Current Applied Physics*, 32, 45-49.

UV Spectral Characterization and Quantitative Study of Ethanol in Ethanol/Water Solutions Using Spectrophotometry for Standardization Applications

[1]Abdullah S. AlOsaimi, [1]Fahd A. AlKharraa and [1,2,*]Khaled M. Ahmed

[1] National Measurement and Calibration Center, Saudi Standards, Metrology and Quality Org. (SASO-NMCC), Riyadh, Saudi Arabia,
[2]National Institute for Standards (NIS), Giza, Egypt
Email: k.abdelftah@saso.gov.sa / khaled55eg@gmail.com

Abstract. *Ethanol/Water aqueous solution as a reference material (RM) is of great importance for many applications and disciplines, e.g. food industry. The present work describes the spectroscopic quantitative study of solutions of ethanol in water in five different concentrations. Concentration range from 600 ppm to 8000 ppm has been studied and shown excellent fulfilment of Beer's Lambert Law. The concentration measurement method comprises the use of a simple gravimetric preparation method of standard solutions, as well as using a high-accuracy spectrometric system. Using the high-performance spectrophotometer, the results show good repeatability, reproducibility, and relatively low associated uncertainty in concentration measurements, which can be considered a great advantage toward producing new reference material of Ethanol/Water solutions with different concentrations following the main guidelines of the relevant standards to produce a certified reference material (CRM) as per international standards such as ISO/IEC 17034, and ISO Guides 30, 31, 33, and 35.*

Keywords: Reference Material (RM), Ethanol Aqueous Solutions, Concentration, Spectra, Spectrophotometry

1. Introduction

The production of ethanol from sugars is linked to the industries of some food and beverages, and even the production of biofuels, which has become of global importance as a new type of fuel that may contribute to solving the global energy gap and provide a new source of clean energy that is suitable for modern sustainable societies, which gives special importance and great advantage to ethanol and stimulates National Metrology Institutes (NMIs) to produce ethanol/water reference materials. In the medical field, ethanol has long been utilized as a potent disinfectant. It is also employed in the food and pharmaceutical industries as an extraction solvent or carrier. For its functional characteristics, it is also included naturally or artificially in food and beverage items. Ethanol can be created within the food itself, such as in fermented meals and beverages and in bread products made through yeast fermentation, giving the products both a flavour and a preservation effect. It is frequently used as a flavouring agent in dishes, especially when it is packaged as a liqueur [1-4].

In addition, Ethanol/Water solutions reference material is the main reference for calibration of an important type of device called "Breath Alcohol Analyzer", which is a device used by traffic authorities to check the breath of drivers on the roads to ensure that they do not use alcohol while driving, which affects their breathing, which might cause traffic accidents [5-7].

The role of the National Measurement and Calibration Center (NMCC) is important in developing new methods that support such measurements with high accuracy and relatively low associated uncertainty so that the new reference material meets the main requirements of the standardization purposes for which it is produced [2, 8-10].

In this work, we studied the main spectral characteristics of Ethanol/Water solutions using spectrophotometry, then conducting new spectrophotometric methods to quantitatively evaluate the concentration of the samples using highly-accurate detector modules with high-grade optics that provide excellent sensitivity in the UV range with resolution up to 0.05 nm with better signal-to-noise

ISBN 978-80-972629-6-9

ratios (SNR) with the possibility to use optical attenuators for highly absorbing samples. The high-performance spectrophotometer (Perkin Elmer, Lambda 1050) has many characteristics that make it possible to find out some characteristic peaks of ethanol with optimal reproducibility and a high level of accuracy in the quantitative analysis. The method of preparation and instrument used in this work are given below in the next sections.

2. Materials and Methods

Ethanol (99.96% reagent grade) was obtained from VWR BDH CHEMICALS. The water used for solution preparation was HPLC grade. The gravimetric method is used for solution preparation, as it is a primary method [3]. In 0.1 L silica (boron silicate) glass bottles, the components ethanol and water are separately weighed and combined. The hydro-alcoholic solution container is manually shaken after mixing. All weighing is done with a calibrated balance that has been given stated uncertainty values. This balance is suitable for the concentration values required for the forthcoming CRM solutions. Refer to the preparation table 1.

The ethanol concentration is calculated using Eq. 1, with a cause-and-effect (fish-bone) diagram for uncertainty estimation in the preparation procedure, shown in Fig. 4:

$$[Ethanol] = \frac{mEthanol}{(mEthanol + mWater)} * p * e \qquad (1)$$

Where mEthanol is the mass of ethanol, mWater is the mass of water, p is ethanol purity, and e is the evaporation factor of ethanol.

Several mixtures of ethanol in distilled water were prepared with different concentrations ranging from 600 ppm to 8000 ppm. The gravimetric method is advised as the one to use in the preparation of solutions and in the general handling of samples because the uncertainty associated with the volumetric method is larger than that associated with the gravimetric. For the preparation of the solutions, ethanol and water were both weighed using a balance with a 0,00001 g resolution (METTLER TOLEDO, model: XPE205). The balance has been calibrated at the mass laboratory of the National Measurement and Calibration Center (NMCC), assuring the traceability of the measurements to the International System of Units (SI). For the preparation process of the standard solutions, refer to Table 1.

Table 1. Preparation scheme of the standard solutions

Stock solution	
Prepare Stock solution (20,000ppm) from Ethanol	
Purity(%)	100
Ethanol (mg)	2,000
Water (mg)	98,500
Total (mg)	100,000
Conc. (mg/kg)	20,000

Prepare four points from (20,000ppm)				
Level (mg/kg)	C1	C2	C3	C4
Ethanol (20,000 mg/kg)	4,000.00	15,000.00	25,000.00	40,000.00
Water (mg)	96,000.00	85,000.00	75,000.00	60,000.00
Total (mg)	100,000	100,000	100,000	100,000
Conc. (mg/kg)	800	3,000	5,000	8,000

While the widely used analytical method for the determination of ethanol concentration is Gas Chromatography with Flame Ionization Detector (GC-FID) [1-2], in this study, we used a spectrophotometric analytical technique to spectrally investigate the solutions and quantitatively measure the solutions' concentrations using the optimal calibration curves and the proper baseline corrections and stability via well-prepared algorithms and automation software.

The used instrument is a high-performance reference spectrophotometer. We must compare the spectrophotometer's stray light specs to the necessary sample absorbance levels in order to perform fine absorbance scanning, with careful consideration at peak positions. Moreover, we should allow the highest energy throughput in order to get the highest performance. Reference beam attenuation can be used to increase the precision and signal-to-noise ratio of spectra collected at high absorbance. The photomultiplier voltage for UV measurements adjusted extremely high when measuring high absorbance samples in order to distinguish between the extremely low light levels on the sample beam (i.e. 0.0001%T) and the energy (i.e., 100%T) on the reference beam. The photomultiplier voltage is

ISBN 978-80-972629-6-9

reduced, and the spectral signal-to-noise ratio is raised by more evenly distributing the energy between the sample and reference beams to distinguish the absorbance peak effectively.

3. Results and Discussion

The spectral measurement data were collected with scanning mode in the range from 180 nm to 300 nm using a Deuterium lamp as a light source, and Photomultiplier Tube (PMT) as a detector with 2 nm bandwidth (FWHM). Real-Time scans are used to investigate the stability of the absorption profile. Some representative scans with real-time patterns are shown in Fig. 1 left. The calibration curve drawn is shown in Fig. 1 right, along with the correlation parameters.

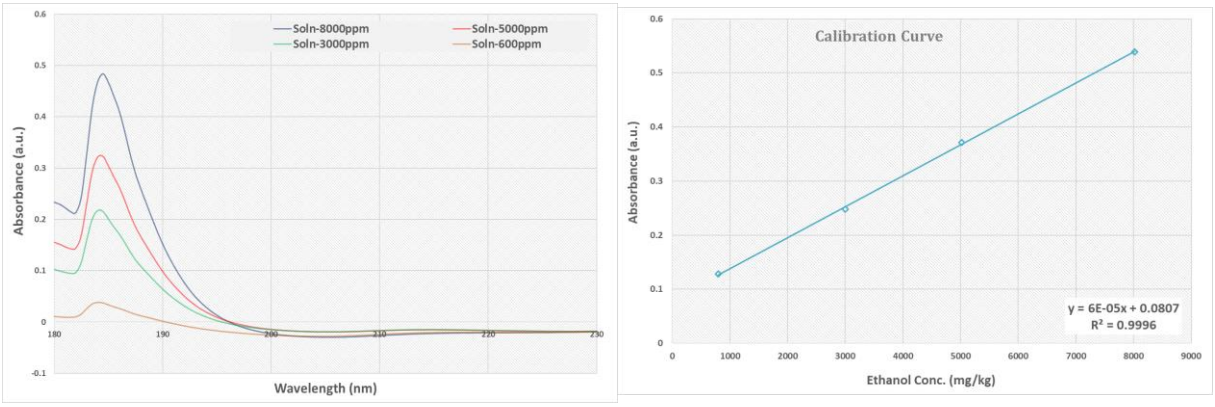

Figure 1. Left: Spectral scans of solutions with different concentrations. Right: Calibration curve drawn from absorbance values at peaks as concluded from the scans.

4. Uncertainty Analysis (preliminary)

The uncertainty estimation of the measurement of ethanol concentration was carried out using the bottom-up approach based on EURACHEM/CITAC Guide CG4. The measurand is the ethanol concentration, and the mathematical model of the preparation of Ethanol/Water solutions has been shown in Eq. 1. The explicit sources of uncertainty that can be identified are: the preparation of stock solution (Purity, Mass, Volume). Other implicit sources of uncertainty are the effect of the calibration curve, evaporation and that of the instrument calibration (spectrophotometer). The fish-bone diagram in Fig.2 summarizes the uncertainty components and sources for simplicity.

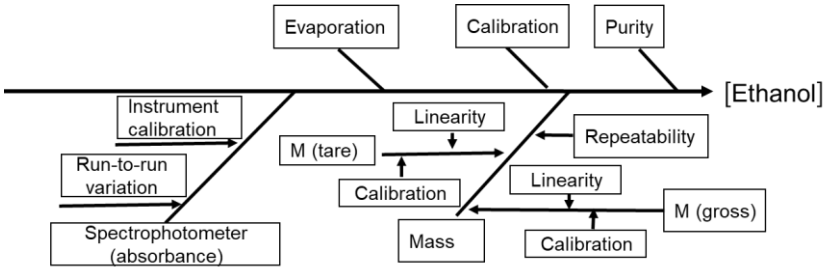

Figure 2. Fish-bone (cause-and-effect) diagram showing uncertainty sources in ethanol concentration measurements

The uncertainty analysis and evaluation of different uncertainty sources are currently under investigation to conclude the full uncertainty budget of the measurement of the concentration of ethanol in water solutions. Some of the uncertainty equations for estimating uncertainty components, to draw the overall uncertainty budget are shown below, Eq. 2 to 5. The first one (Eq. 2) presents the uncertainty in stock solution preparation.

$$u(C_{\text{stock solution}}) = \sqrt{(u_{purity})^2 + (u_{mEthanol})^2 + (u_{mWater})^2 + 2(u_{tare})^2} \qquad (2)$$

Uncertainty in the calibration curve is shown in the below equations (3 through 5):

$$u(C_0) = \frac{S}{B_1}\sqrt{\frac{1}{p} + \frac{1}{n} + \frac{(C_0 - C_{Average})^2}{S_{xx}}} \qquad (3),$$

$$S_{xx} = \sum_{j=1}^{n} (C_j - C_{average})^2 \quad (4),$$

$$S = \frac{\sum_{j=1}^{n} \left[A_j - (B_0 + B_1.C_j)\right]^2}{n-2} \quad (5).$$

Where, C_0: determined concentration in the measured solution, $C_{Average}$: the mean value of different calibration solutions, S: the residual standard deviation, B_1: the slope, p: the number of measurements to determine C_0, n is the number of measurements for calibration, C_i: calculated concentration of calibration solution by using the calibration curve and response of instruments against the calibration solution, j: index for a number of calibration standards, and j: index for the number of measurements to acquire the calibration curve. The uncertainty evaluation and uncertainty budget is under investigation and would be shown elsewhere. It is beyond the main scope of this paper.

5. Conclusions and Ongoing Work

Throughout the concentration range of 600 ppm to 8000 pm, the spectroscopic apparatus employed in this research study has successfully detected ethanol in the ethanol-water mixture. Nonetheless, the concentration ranges between 600 ppm and 8000 ppm have demonstrated greater than 99% fulfilment when validated to Beer's Lambert Law. The results obtained by using the high-performance spectrophotometer demonstrate good repeatability, reproducibility, and relatively low associated uncertainty in concentration measurements, which can be considered a great advantage toward producing new reference material of Ethanol/Water solutions with various concentrations in accordance with the primary directives of the pertinent standards to produce a certified reference material (CRM) from aqueous ethanol solutions. The used instrument showed relatively low run-to-run variation as well as low uncertainty in absorbance measurements. Traceability to SI units was maintained, where all the measurements during preparation had been done using high-accuracy calibrated balance, and all absorbance measurements had been done against the regular spectral transmittance/absorbance national scale of Saudi Arabia. The detailed investigation of the associated uncertainty is on-going, and it is a current task of moving further with this work.

Acknowledgement

The authors thank SASO Research and Studies Center (RSC) for supporting this work.

References

[1] Sneha A. Parke, Gordon G. Birch (1999). Solution properties of ethanol in water, Food Chemistry 67, 241-246.

[2] Vanderlea de Souza et al. (2006). Development of a Certified Reference Material: Ethanol in Water – a Practical Case, Brazilian Archives of Biology and Technology, Vol.49, Special: pp. 107-114.

[3] Milton, M. J. T. and Quinn, T. J. (2001). Primary methods for the measurement of amount of substance, Metrologia, 289-296.

[4] Ingram, L. O. (1990). Ethanol tolerance in bacteria. Critical Reviews in Biotechnology, 9(4), 305-319.

[5] Martelo-Vidal M J, Vazquez M. (2014). Evaluation of ultraviolet, visible, and near infrared spectroscopy for the analysis of wine compounds. Czech Journal of Food Science, 32(1):37-47.

[6] Di Egidio V, Sinelli N, Giovanelli G, Moles A, Casiraghi E. (2010). NIR and MIR spectroscopy as rapid methods to monitor red wine fermentation. European Food Research and Technology, 230(6):947-955.

[7] Nose A, Hojo M. (2006). Hydrogen bonding of water-ethanol in alcoholic beverages. Journal of Bioscience and Bioengineering, 102(4):269-280.

[8] Cozzolino D, Cynkar W U, Dambergs R G, Janik L, Gishen M. (2007). Near infrared spectroscopy in the Australian grape and wine industry. Cooperative Research Centre for Viticulture-Technology Application Note.

[9] Sanda F M, Victor M E, Monica T A, Alina C. (2012). Spectrophotometric measurements techniques for fermentation process, http://imtuoradea.ro/bioethanol/UV.VIS.theory.pdf.

[10] Saad H, Othman S, Ali M T, Abd-Rahman M K. (2014). Optical sensing of low ethanol concentration via absorption rate in visible wavelength. In IEEE 5th International Conference on Photonics, pp. 38-40.

Low Field MRI vs. High Field MRI Future Perspectives

ISBN 978-80-972629-6-9

Noninvasive Characterization of Tissue Microvessel Architecture in MRI

[1]Jiří Kratochvíla, [2]Marek Jüttner, [1]Radovan Jiřík, [1]Zenon Starčuk

[1]Institute of Scientific Instruments of the Czech Academy of Sciences, Brno, CZ,
[2]Gymnázium Brno, Křenová, Brno, CZ
Email: kratochvila@isibrno.cz

Abstract. *Noninvasive determination of microvessel architecture is important in oncology, but has never been shown. Here, new parameters describing the microvessel architecture based on perfusion MRI are introduced and a flow phantom is created to evaluate them. Two different MRI perfusion methods were used for describing the microvessel architecture, and the result parameters were evaluated on phantom data and illustrated on in vivo preclinical data.*

Keywords: IVIM-MRI, DCE-MRI, Tissue Architecture, Phantom Imaging, In Vivo Imaging

1. Introduction

The possibility to noninvasively distinguish tissues with a chaotic orientation of microvessels from those with microvessels with a prevailing orientation has a big potential for the assessment of the treatment effect during morphological vascular normalization of tumor microvasculature. This process of rebuilding the microvascular structure is captured by structure-related biomarkers earlier and more specifically than by the standard perfusion parameters (describing, e.g. the blood flow and volumes within the tumor regions). Two MRI methods, IVIM and DCE-MRI, have the potential to show the microvessel architecture.

IVIM-MRI [1] has been used in preclinical and clinical research in oncology, cardiology and of stroke. It is based on common diffusion-weighted imaging methods (DWI). DWI provides in vivo images of biological tissues showing the diffusion process of water molecules. Fitting an exponential model to DWI data provides quantification of the rate of diffusion of water molecules in the measured direction. With diffusion gradient pulses applied in more directions, the information about the directivity of the diffusion can be exploited for tracking white-matter tracts in the brain and the spine. IVIM can be understood as an extension of DWI, capturing not only diffusion, but also blood-flow related motion of water molecules by an additional parameter, the flowing-blood fraction (f). In almost all published literature, IVIM MRI has been implemented with the assumption of isotropic blood motion [1]. As in DWI, diffusion gradient pulses can be generated in different directions and used to estimate the directional patterns of the parameter f. To the authors' knowledge, only in [2,3] was the anisotropy of IVIM investigated on simulated on in vivo healthy human data.

A method with a similar potential to characterize the architecture of microvessels is DCE-MRI [4]. This perfusion imaging technique is based on the acquisition of a time series of MR images, describing the distribution of an intravenously administered contrast agent. This image sequence is then converted to a contrast-agent-concentration sequence and analyzed by fitting the tracer distribution by a pharmacokinetic model yielding several perfusion parameters (blood flow/volume, the volume of EES, mean transit time, etc.). DCE-MRI has been used in clinical and preclinical (oncology, cardiology) research. However, the potential of the DCE-MRI pharmacokinetic models to describe the architecture of microvessels has never been shown.

In this paper, new perfusion biomarkers describing the architecture of microvessels in tissues and their evaluation using a created flow phantom based on a dialysis filter is described. The evaluation on phantom data is done for IVIM and DCE-MRI and the determination of microvessels is illustrated on in vivo preclinical data.

ISBN 978-80-972629-6-9

2. Subject and Methods

The created flow phantom is shown in Fig. 1. Table 1 characterizes the phantom.

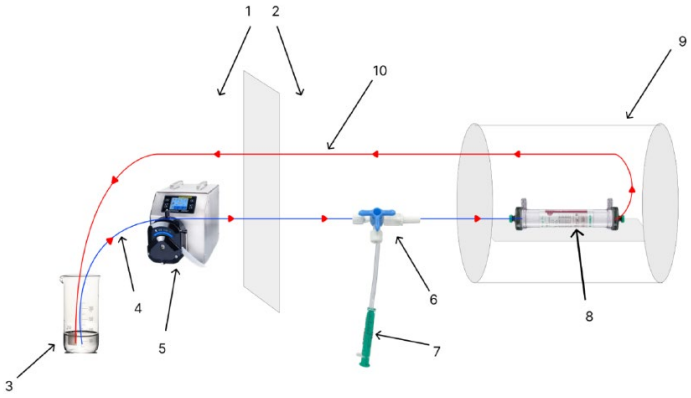

Fig. 1. Perfusion phantom, 1 – control room, 2 - magnet room, 3 – water reservoir, 4 – connecting tube to the magnet, 5 – peristaltic pump, 6 – contrast agent valve, 7 – contrast agent, 8 – dialysis filter, 9 – magnet, 10 – connecting tube from the magnet. The arrows show the direction of water flow.

The MRI data were acquired in a 9,4 T magnet (Bruker, Germany) with different flow rates inside the phantom (0, 5.67 and 8.5 mL/min) for IVIM. For DCE, the flow rate of 5.67 mL/min and contrast agent Multihance (0.075 mL, with 3 mL of water) were used. The flow rate was converted to flow speed inside the dialysis filter (using values in Table 1). The obtained values of 0, 0.015, 0.03 and 0.045 cm/s cover the values for humans and rats in microvessels [5,6]. IVIM data were acquired with a diffusion-weighted EPI sequence with TR/TE 2500/70 ms, 1 segment, 24 axial slices, 1.5 mm slice width, 128×128 pixels, FOV 6×6 cm, 4-25 b-values with values from 0 up to 800 s/mm2 and 6 or 30 diffusion directions (at least one direction same as the tube orientation). For DCE, a FLASH acquisition sequence was used with TR/TE 10.396/1.334 ms, sampling period 1.33 s, FA 25°, 3 coronal slices, each 1.5 mm thick, 128×128 pixels, FOV 6×6 cm, 1000 repetitions and 6 pre-contrast datasets (different TR). The measured data were then fitted in ROIs (Fig. 2, mean values within the ROIs) by IVIM (mono-exponential for pure diffusion, bi-exponential for perfusion effect) and DCE (AATH [7]) pharmacokinetic model. The resulting estimates of tissue perfusion parameters were obtained and analyzed.

Table 1. Characterization of dialysis filter (B-Braun DiaCap Pro 16-L) used as the phantom

Parameter	Value	[unit]
Number of fibers inside	10000	[-]
Inner diameter of one fiber	200	[um]
Inner diameter of filter	4	[cm]
Flowed area in axial slice of filter	3.14	[cm^2]
Whole area in axial slice of filter	12.57	[cm^2]
Volume inside fibers in whole filter	100	[mL]
Filter weight	150	[g]
Weight of fully watered filter	450	[g]

ISBN 978-80-972629-6-9

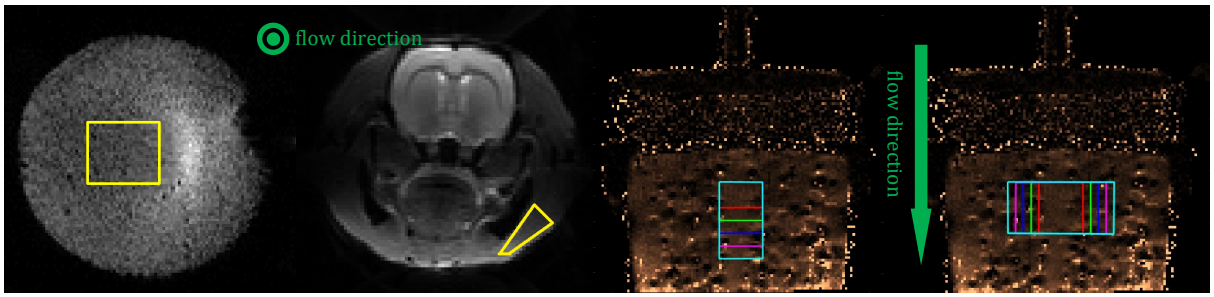

Fig. 2. Measured data and ROIs. Left - IVIM B0 image of a dialysis filter and a rat (ROI masseter muscle), right - dialysis filter measured by DCE (after conversion to contrast-agent concentration) with color-coded increasing ROI sizes along and perpendicular to tubes.

3. Results

Fig. 3 shows the effect of increasing flow speed in the filter on the measured diffusion-weighted signal. The decrease of the signal intensity is detected only for diffusion directions parallel (cyan and purple lines) to the tube orientation. The pure diffusion anisotropy of tubes is seen in the cyan and purple curves in the case of no flow, where these two curves are the lowest ones.

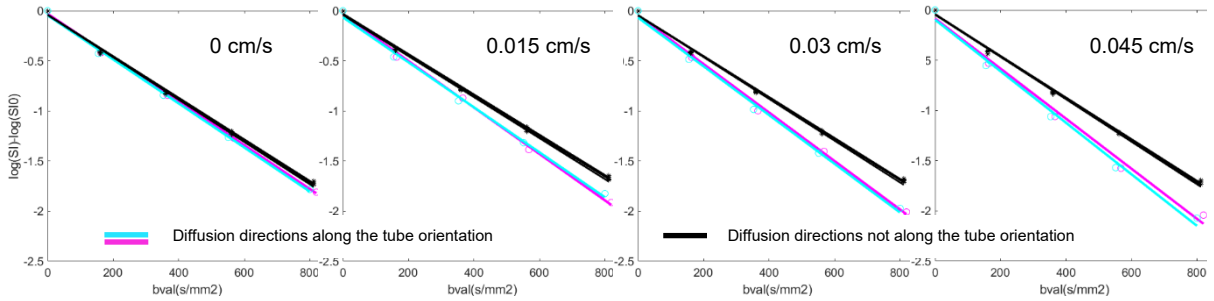

Fig. 3. The effect of increasing flow speed in dialysis filter. Cyan and magenta lines denote the direction along the tubes, and black lines denote directions perpendicular and rotated (45°) to the tubes in the dialysis filter.

The curves in Fig. 4 show the approximation of measured data by the IVIM model for flow speed 0.03 cm/s on phantom data and for rat in vivo data from masseter muscle (where the orientation of micro-vessels is the same as in the phantom tubes [5]). The red (bi-exponential) and blue (mono-exponential) curves show the diffusion gradient direction coinciding with the orientation of tubes/microvessels (the b-value threshold to separate the perfusion and the diffusion effects is approx. 200 s/mm^2 [1]). The green and black curves approximate the measured data for other directions. The flow fraction f, defined as the relative difference (in %) between the signal intensity for zero b-value in the biexponential case (perfusion effect included), and the mono-exponential case (pure diffusion), is 22% and 11% along the tubes and microvessels. The images in Fig. 4 show the prevailing perfusion direction (highest value of f) of the three perpendicular directions. Results reflect the tube/microvessel architecture.

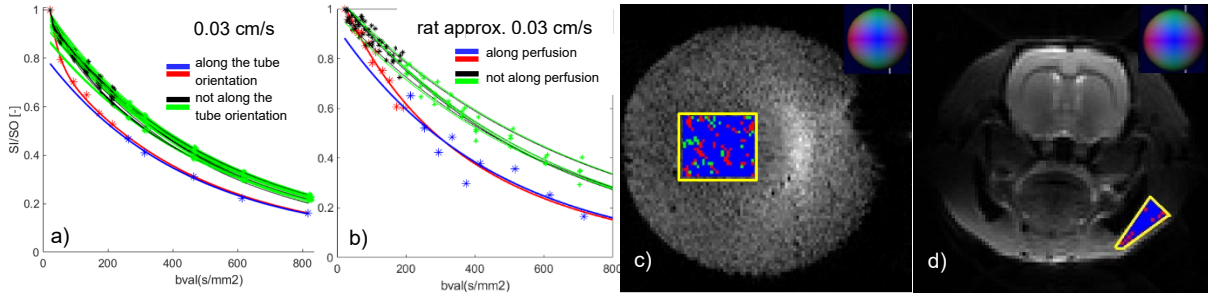

Fig. 4. Approximation of measured datasets with IVIM model (a,b) and voxel-wise perfusion-directional maps (c,d) for phantom (a,c) and in vivo rat data (b,d).

ISBN 978-80-972629-6-9

Fig. 5 shows results for DCE measurements for a flow speed of 0.03 cm/s. Here, the mean transit time was estimated for all ROIs in Fig. 2. The comparison of the measured values with the theoretical values obtained by using Table 1 shows an acceptable match. If the length of ROIs in the same direction as the orientation of microtubes is increased, the mean transit time increases, but it stays the same in the event of increasing the ROI in a direction perpendicular to the tubes.

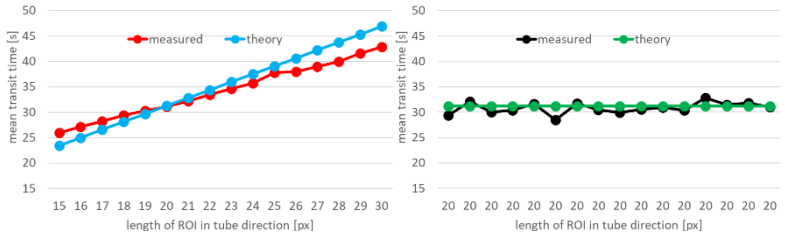

Fig. 5. Results for DCE measurement. The mean transit time evolution for increasing ROIs defined along (left) and perpendicular (right) to the orientation of tubes in the dialysis filter.

4. Discussion and conclusions

The noninvasive determination of microvessel architecture was evaluated for two acquisition methods, DCE and IVIM MRI, using a flow phantom. This flow phantom was created to approximate real flow speeds and tissue structures in rats and humans, and its benefit lies in the expansion of the possibilities to evaluate methods describing the microvessel architecture by clearly defined phantom measurements (in literature, only synthetic and in vivo human data were used). Moreover, the directionality of microvessels was shown in vivo in a healthy rat.

For future work, we will adopt the tensor model [1] for a more accurate data analysis and determination of microvessel directionality. This will allow us to track the microvessel architecture throughout whole tissues using methods similar to those applied in DWI. This will allow us to characterize, besides the architecture of tissues, also the architecture of microvessels in these tissues, from which mainly oncology (but also other applications benefiting from microvascular-architecture-related biomarkers) may benefit.

Acknowledgements

All MR experiments were carried out by the JmK and by the ISI-MR facility of the Czech-BioImaging infrastructure, supported by grants LM2018129 and LM2023050 of the MEYS CR.

References

[1] Bihan, D.L. et al. (2019). Intravoxel Incoherent Motion (IVIM) MRI: Principles and Applications. Singapore: *Pan Stanford Publishing*, 534 pages. ISBN 978-981-4800-19-8.

[2] Notohamiprodjo, M. et al. (2015). Combined Intravoxel Incoherent Motion and DTI of Renal Diffusion and Flow Anisotropy. *Magn. Reson. Med.*, 73(4), 1526-1532.

[3] Mozumder, M. et al. (2018). Simultaneous Magnetic Resonance Diffusion and Pseudo-Diffusion Tensor Imaging. *Magn. Reson. Med.*, 79(4), 2367-2378.

[4] Jackson, A., et al. (2005). Dynamic Contrast-Enhanced Magnetic Resonance Imaging in Oncology. Berlin: *Springer*, 312 pages.

[5] Dylevský I. (2009). Funkční anatomie. Praha: *Grada*, 544 p. ISBN 978-80-247-3240-4.

[6] Henrich, H.N. et al. (1978). A Gracilis Muscle Preparation for Quantitative Microcisrculatory Studies in the Rat. *Microvascular research*, 15(3), 349-356.

[7] St Lawrence, K.S., et al. (1998). An Adiabatic Approximation to the Tissue Homogeneity Model for Water Exchange in the Brain. *J. Cereb. Blood Flow Metab.*, 18(12), 1365-1377.

Repeatability of 7T Human Cardiac 3D ^{31}P-MRSI Using Concentric Ring k-Space Trajectories

[1,2]Ladislav Valkovič, [2]Ferenc E. Mózes, [1]Ivan Frollo, [3]William T. Clarke, [2]Damian J. Tyler, [1]Pavol Szomolányi

[1]Department of Imaging Methods, Institute of Measurement Science, Slovak Academy of Sciences, Bratislava, Slovakia
[2]Oxford Centre for Clinical MR Research (OCMR), RDM Cardiovascular Medicine, University of Oxford, Oxford, UK
[3]Wellcome Centre for Integrative Neuroimaging, Nuffield Department of Clinical Neurosciences, University of Oxford, Oxford, UK
Email: ladislav.valkovic@savba.sk

Abstract. *Cardiac phosphorus magnetic resonance spectroscopy (^{31}P-MRS) provides insight into metabolism of the failing heart. The commonly employed 3D-MRS imaging (MRSI) acquisitions are rather slow, even at 7T. Fast readout trajectories, such as concentric ring trajectories (CRT) have been recently suggested to substitute the slow Cartesian sampling of typical chemical shift imaging (CSI), however, their repeatability is yet unknown. We have tested the intra-session and inter-session repeatability of the suggested rapid acquisition (2.5 min) and the time equivalent (6.5 min) high resolution CRT sequences in three healthy volunteers and compared them to the standard 6.5 min CSI scan. The intra-session repeatability was performed as a scan-rescan with the subject in the scanner and the inter-session repeatability was checked by repeating the whole scan three days later. Our preliminary data suggest comparable intra-session repeatability, but somewhat lower inter-session repeatability for mid septal voxels using 2.5 min CRT in comparison to 6.5 min CSI. Similar trends were observed for higher resolution CRT. This work starts to establish the feasibility of using fast or high-resolution cardiac ^{31}P scanning at 7T using CRT.*

Keywords: MRSI, 7T, Cardiac Metabolism, Concentric Ring, Repeatability

1. Introduction

Phosphorus magnetic resonance spectroscopy (^{31}P-MRS) can probe the energy metabolism of the human heart in vivo by measuring the phosphocreatine to adenosine triphosphate concentration ratio (PCr/ATP), an indicator of heart failure [1], or the potentially more sensitive chemical kinetics of the oxidative phosphorylation system. In both cases fast scanning is desirable, to either fit ^{31}P-MRS into a clinical protocol, or to mitigate the multiple acquisitions required for the latter metrics.

Employing fast MRSI readout trajectories, it could be possible to leverage the full 2.8 times increase in SNR [2] to achieve close to the theoretical 7.8-times (2.82) speed increase when moving from 3 to 7 T. This is not possible using the most common approach, point-by-point Cartesian sampling (CSI). A new method employing a fast MRSI readout trajectory, concentric ring trajectory (CRT), has recently been described [3]. CRT can measure PCr/ATP maps as CSI sampling in a fraction of the time (with matched resolution) or with a higher spatial resolution (in a matched time).

While the repeatability of cardiac 3D ^{31}P-MRSI sequences using Cartesian sampling at 7T is known [4], the repeatability of the CRT sequences is yet to be determined. Hence, the aim of this study was to evaluate the intra- and inter-session repeatability of different CRT protocols.

ISBN 978-80-972629-6-9

2. Subject and Methods

Four sequences were evaluated: Cartesian acquisition-weighted MRSI, termed CSI henceforth, (matrix size 10x10x10, 4 averages at k=0, 6:31 mins) and the CRT sequence with a matched matrix size employing 12 (2:31 mins) and 10 rings (1:37 mins), and with a matrix size of 12x12x12 and 19 rings (6:55 mins, labelled as high-res CRT [HRCRT]). These four sequences were run twice in a session and on two different days, 72 hours apart, to evaluate intra- and inter-session repeatability (Fig. 1).

Three healthy participants (1 female, 67 kg, 30 years) were scanned supine in a Siemens Magnetom 7T scanner (Siemens, Erlangen) equipped with a square surface transmit and 16 channel receive array coil (Rapid Biomedical) positioned over the heart [4]. CSI was run with 240x240x200 mm3 field of view, 1 s TR, 8 kHz bandwidth, and 2048 time-samples. CRT had matched field of view and TR, but 2778 Hz bandwidth with 720 time-samples.

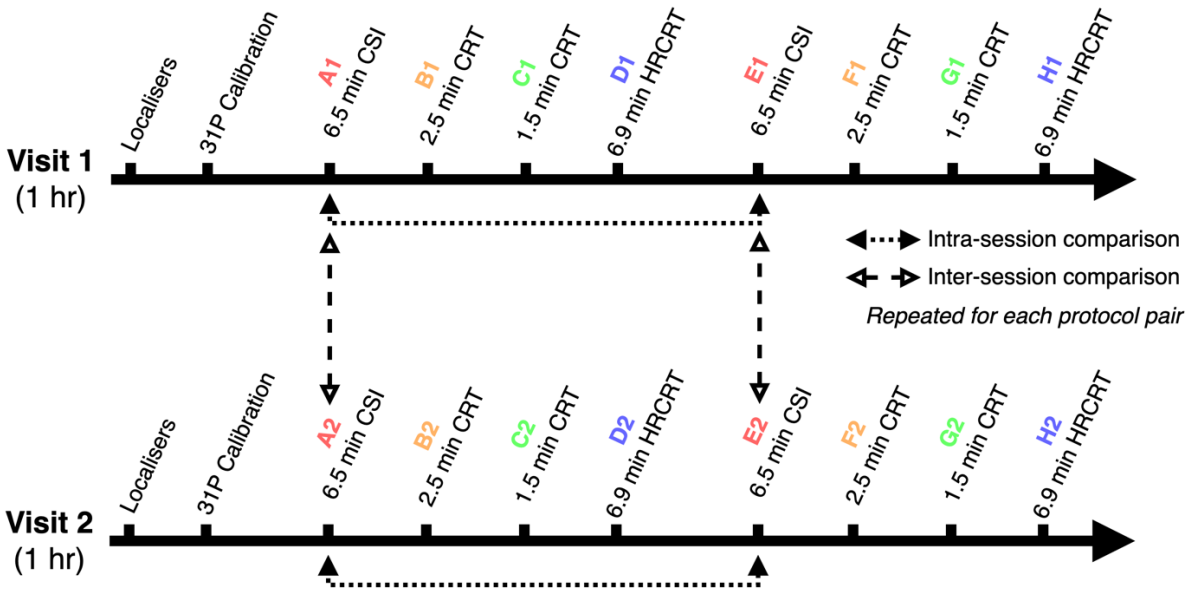

Fig. 1. Scan protocol: schematic timeline of within- and between-scan repeatability acquisitions. Comparisons are made between repeats (intra-session) of sequence type and between matched sequences between sessions (inter-session).

CSI data were reconstructed online and CRT data offline using the non-uniform Fast Fourier Transform (NUFFT) toolbox with min-max Kaiser-Bessel kernel interpolation and twofold oversampling [5] in MATLAB (MathWorks, Natick, USA). No density compensation was required. CSI/MRSI data fitting was performed using the OXSA toolbox [6]. Sequences were compared using phosphocreatine (PCr) over adenosine tri-phosphate (ATP) ratios, using the γ-ATP peak and were corrected for partial saturation and blood contamination, as previously described [2], in mid-septal voxels from apical, mid, and basal slices.

The intra-session variability was assessed through the mean and difference between PCr/ATP ratios from equivalent datasets within the same session, e.g., by comparison of datasets A1 with E1 and A2 with E2 of each volunteer for the CSI acquisitions. And the inter-session variability was assessed through the mean and difference between PCr/ATP ratios from equivalent datasets in both protocols for each subject (see Fig. 1 for a detailed description).

The coefficient of repeatability (CoR) was calculated from SD of the signed differences in PCr/ATP between two scans for each subject according to $CoR = SD_{intrasubject} \times \sqrt{2} \times 1.96$. A lower CoR reflects higher repeatability.

ISBN 978-80-972629-6-9

3. Results

Fig. 2 depicts the typical position of the analysed voxels as well as representative spectra from the mid septal voxel of one subject demonstrating good agreement between the acquired data for all sequences. There were no significant differences (paired t-test) in the calculated cardiac PCr/ATP between repeated measurements for all voxels, sequences, and repetitions.

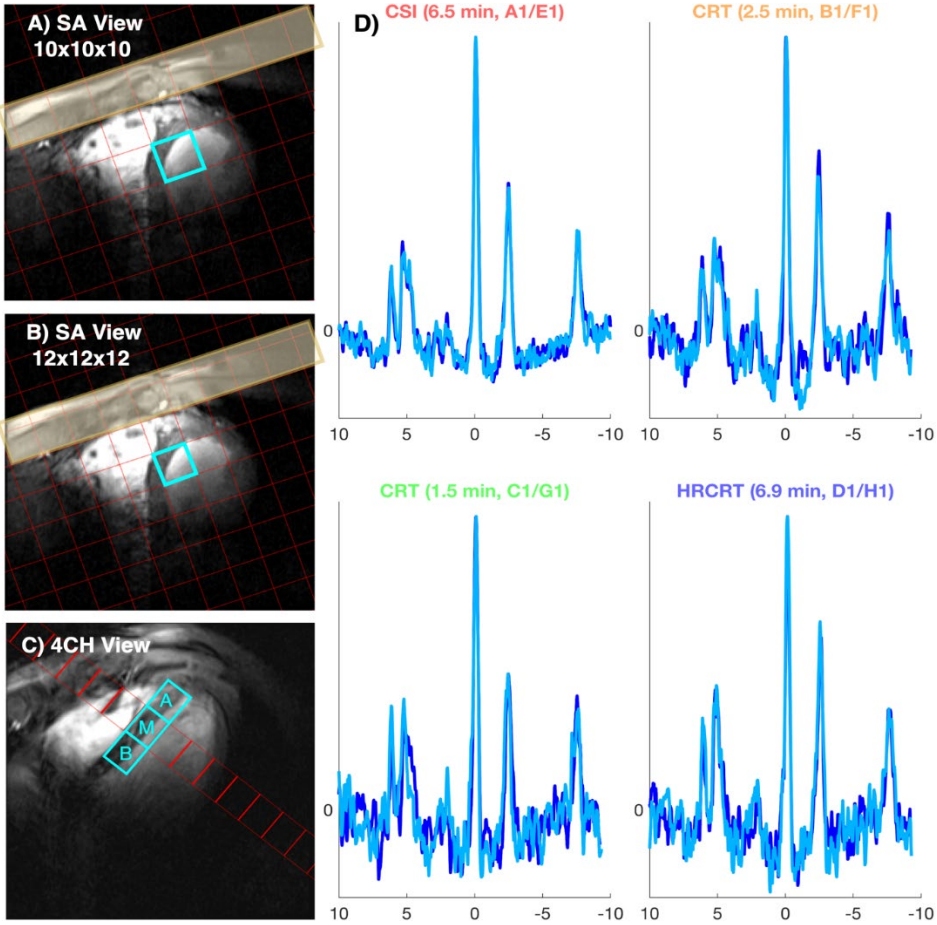

Fig. 2. Signal localisation and example spectra. A & B show the lower resolution (10x10x10) and high-resolution (12x12x12) MRSI grid for overlaid on short axis localisers. Saturation bands (yellow) suppress skeletal muscle signal. Voxels for analysis were selected from the mid intraventricular septum in an apical, mid, and basal slice of the heart (C). D Example spectra from mid-septal voxels of a single subject. The spectra shown are the repeated measurements within a single session.

The calculated CoRs for apical, mid and basal voxels of the septum are given Table 1.

Table 1. Coefficients of Repeatability for each sequence, voxel position and intra- and inter-session comparison

CoR		CSI (6.5min)	CRT (2.5min)	CRT (1.5min)	HRCRT (6.9min)
Apical	intra	1.04	2.05	1.09	Bold
	inter	0.99	2.65	3.16	0.80
Mid	intra	0.40	1.37	5.91	2.09
	inter	1.17	2.52	6.08	2.80
Basal	intra	1.23	9.05	41.69	12.40
	inter	1.01	5.64	40.91	11.40

ISBN 978-80-972629-6-9

4. Discussion

We have investigated intra- and inter- session repeatability of the rapid CRT readout for 3D ^{31}P-MRSI of the heart at 7T. High repeatability was observed for the long CSI scan with CoR for mid septal voxel 0.40 for intra-session and 1.17 for inter-session comparison. While our subject numbers are currently low, this falls into the same range as previously reported repeatability of 8x16x8 CSI matrix by Ellis et al. [4] with CoR of 0.95 and 1.06 for intra- and inter-session comparisons, respectively. To achieve the increase in speed, the CRT protocols sacrifice some signal-to-noise (SNR), which leads to higher CoR, i.e., 1.37 for the intra-session and 2.52 for the inter-session comparison of mid septal voxel of the 2.5 minute CRT sequence. The high CoR values for basal voxels reflect the very low SNR suggesting that with the current setup these voxels are effectively not usable. This could be potentially mitigated in the future by the use of a whole-body transmit coil [7].

5. Conclusions

Our preliminary results suggest comparable intra-session repeatability, but somewhat lower inter-session repeatability, of highly accelerated 3D-MRSI acquisition using CRT trajectory, providing either improved speed (2.5 minutes in comparison to 6.5 minutes CSI) and increased spatial resolution (6.66 mL in comparison to 11.5 mL nominal resolution).

Acknowledgements

LV is supported by a Sir Henry Dale Fellowship of the Wellcome Trust [221805/Z/20/Z]. LV, IF and PS would like to acknowledge the support of the Slovak Grant Agencies VEGA [2/0004/23] and APVV [19-0032]. WTC acknowledges grant funding from the Wellcome Trust [225924/Z/22/Z] and [224430/Z/21/Z]. The Wellcome Centre for Integrative Neuroimaging is supported by core funding from the Wellcome Trust [203139/Z/16/Z and 203139/A/16/Z]. DJT is a Senior Basic Science Research Fellow of the BHF [(FS/19/18/34252].

References

[1] Neubauer S. (2007). The Failing Heart — An Engine Out of Fuel. *New England Journal of Medicine*, 356 (11), 1140–1151

[2] Rodgers CT, Clarke WT, Snyder C, Vaughan JT, Neubauer S, Robson MD. (2014). Human cardiac ^{31}P magnetic resonance spectroscopy at 7 tesla. *Magnetic Resonance in Medicine,* 72 (2), 304–315

[3] Clarke WT, Hingerl L, Strasser B, Bogner W, Valkovič L, Rodgers CT. (2023). Three-dimensional, 2.5-minute, 7T phosphorus magnetic resonance spectroscopic imaging of the human heart using concentric rings. *NMR in Biomedicine,* 36 (1), e4813

[4] Ellis J, Valkovič L, Purvis LAB, Clarke WT, Rodgers CT. (2019). Reproducibility of human cardiac phosphorus MRS (^{31}P-MRS) at 7 T. *NMR in Biomedicine,* 32 (6), e4095

[5] Fessler JA, Sutton BP. (2003). Nonuniform fast Fourier transforms using min-max interpolation. *IEEE Transactions on Signal Processing,* 51 (2), 560–574

[6] Purvis LAB, Clarke WT, Biasiolli L, Valkovič L, Robson MD, Rodgers CT. (2017). OXSA: An open-source magnetic resonance spectroscopy analysis toolbox in MATLAB. *PLoS ONE*, 12 (9), e0185356

[7] Valkovič L, Dragonu I, Almujayyaz S, Batzakis A, Young LAJ, Purvis LAB, Clarke WT, Wichmann T, Lanz T, Neubauer S, Robson MD, Klomp DWJ, Rodgers CT. (2017). Using a whole-body ^{31}P birdcage transmit coil and 16-element receive array for human cardiac metabolic imaging at 7T. *PLoS ONE*, 12 (10), e0187153

Eddy Currents Compensation in MRI

[1]Daniel Gogola, [1]Andrej Krafčík, [1]Ivan Frollo, [1,2]Pavol Szomolányi

[1]Institute of Measurement Science, Slovak Academy of Sciences, Bratislava, Slovakia,
[2]High Field MR Center, Medical University of Vienna, Vienna, Austria
Email: daniel.gogola@savba.sk

Abstract. *MRI manufacturers invest huge effort into the suppression of eddy currents or at least eliminate their effects. Suppression of eddy currents can be realized by active or passive shielding of gradients coils. Several eddy currents compensation methods have been developed over time. These methods do not suppress eddy currents itself, but only compensate their manifestations. In this study, we showed one of the methods for eddy current compensation together with preliminary results.*

Keywords: MRI, Eddy Currents, Gradients, Calibration

1. Introduction

The presence of eddy currents in MRI is a natural phenomenon, occurring due to the action of gradient coils. These eddy currents are induced in the surrounding conductive parts of the MRI scanner. Their magnitude and the associated degree of influence on the measured images depend, among other things, on the diameters ratio of the main magnet bore and the gradient insert [1]. Induction of the eddy currents can be reduced to a large extent by active and passive shielding of the gradient coils. Both of the above mentioned approaches require additional space and thus reduce the imaging space. On the other hand, if we know the response of the system to the magnetic field change induced by switching on-off gradients, we can largely compensate for this response by proper modelling of the gradient pulses. It should be noted that the change in the shape of the gradient pulses due to eddy currents [1], [2], [3] leads to various artifacts [4] and changes in the phase and intensity [5], [6] of the signal in the imaged volume. Another way to reduce eddy currents is to design the measurement sequence using crusher gradient pulses, which should be used whenever gradient switching occurs, if the sequence design allows it. The effect of eddy currents can also be compensated by various postprocessing methods. Even though these are relatively inexpensive solutions, they are computationally intensive and require extra time. All of the methods mentioned above have their undeniable importance for suppressing the eddy current effect on the measurement, although none of them is 100% effective [7]. In practice, it turns out that it is preferable to reduce the occurrence of eddy currents rather than to compensate them [8], e.g. by opposing currents in the shielding coils of gradients.

2. Subject and Methods

The exposition of electrically conducting materials to the time dependent magnetic fields causes the induction of eddy currents in it. These eddy currents in MRI device take place primarily during the switch on/off of the gradient, which should have a ramp shape. In this case, eddy currents time dependence can be fitted by the summation of *n* exponentially decaying functions in time $\left(A_i exp(-t/\tau_i)\right)$ with A_i and τ_i for $i = 1, \dots, n$ as their characteristic amplitudes and times constants.

In general, separation of each exponentially decaying time dependent function can be realized by simple gradient ring down (GRD) experiment (Fig. 1) when a specific NMR

measurement sequence is executed. In this experiment, the gradient is switched-on and next switched-off. After that, the FID signal is measured.

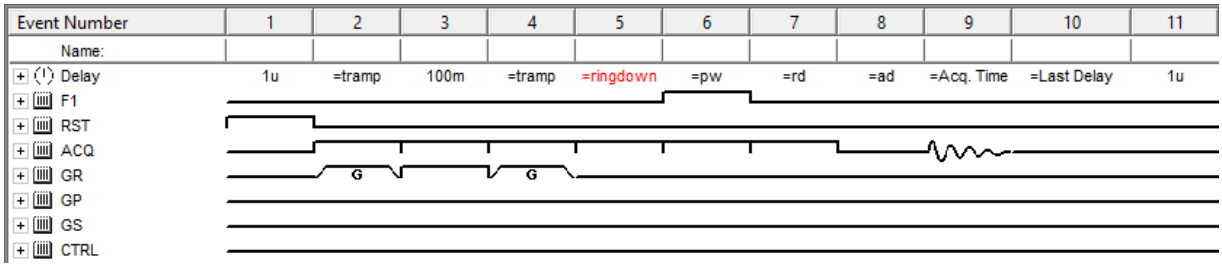

Fig. 1. Diagram of gradient ring down sequence. tramp – is a time of rising edges of tested gradient, pw – is a time of applying of the excitation pulse, Acq.Time – is a time of signal acquisition.

However, there is a question, what variable could be a measure of the induced eddy currents effect, from which we calculate amplitude and time constants. The answer is as simple as: to Calculate the fast Fourier transform (FFT) of the FID signal, evaluate its absolute value, and find the maximal peak and its width w_j for each used delay d_j. By increasing of eddy currents effect (by decreasing of used delay d_j) obtained peak is lowering instead of its width, which is rising. Therefore, peak width w_j should be a measure of the eddy currents effect. As per the convention, we used as width w_j the peak width in the half of peak height for each delay d_j.

Then, the least-square minimization fitting function of the form

$$f_{LS}(d) = K + \sum_{i=1}^{n}\left[A_i exp\left(-\frac{d+sto}{\tau_i}\right)\right], \tag{1}$$

where $d\epsilon[d_1, d_m]$, and d_1 and d_m are the shortest and the longest delay values, fits dependence of peak width w on used delay d: $f_{LS}(d) \equiv w(d)$. The two parameters K and sto, defined as $K \equiv \min_{j=1,\dots,m}(w_j)$ [Hz] and sto ≡ hard-pulse-width + rd + ad [s], are the minimal peak width and sample-time-offset values, respectively, where rd and ad are the delay time constants between the end of the excitation pulse and the start of the acquisition.

It should be emphasized, that obtained A_i values are raw amplitudes for the currently set relative gradient strength in the gradient ring down experiment (in our case $Gr = Gr_{GRD} \equiv 20$) and should be therefore scaled. For this purpose, we make gradient strength (GS) experiment: For the spherical phantom in the NMR device with observing frequency in resonance and correct value of pulse-width for 90° pulse, in the first, we ensured that signal is in resonance for zero relative gradient strength ($Gr = 0$). Then, we set $Gr = Gr_{GS} \equiv 2$ and measure the FID signal. Next, process FID with FFT, and from its absolute value, determine the width of its peak (w_{GS}) in half of the peak height. Finally, scaled amplitude constants were evaluated from the expression

$$\widehat{A_i} = 100\frac{A_i}{w_{GS}}\frac{Gr_{GS}}{Gr_{GRD}} \quad [\%], \qquad \text{for } i = 1, \dots, n. \tag{2}$$

For the real system in general, the $\vec{B}(t)$ should be changed to general input signal $X(t)$, and also, DC offset should be added:

$$\tilde{X}(t) = DC + \hat{A}_0 X(t) + \left[\sum_{i=1}^{n}\hat{A}_i exp\left(-\frac{t}{\tau_i}\right)\right] * \Delta X(t), \tag{3}$$

Where the second term on the right-hand-side (RHS) is the input signal multiplied by the scaled $\hat{A}_0$term, i.e. scaled K according (2), and $\Delta X(t)$ is the instantaneous input signal step in time t. The obtained expression represents full gradient pre-emphasis modulation in the direction defined in the gradient ring-down experiment.

ISBN 978-80-972629-6-9

3. Results

The calibration itself consisted of two parts. Initially, we measured the strength of the gradients for all three XYZ gradient directions. The measurement was performed on a spherical phantom of 22 cm diameter, with a simple measurement sequence. In the measurement sequence, a radio-frequency hard pulse is applied after setting the measured gradient to 5% of its maximum power. After applying the Fourier transform to the measured 1D data, the power of the measured gradient was calculated from the spectral width, according to formula (4).

$$G_{5\%} = \frac{2\pi * Peak_{width}}{\gamma * Phantom_{diameter}} \tag{4}$$

Where $Peak_{width}$ – is the width of the measured spectrum in [MHz], γ – is an H_1 gyromagnetic ratio in $[\frac{rad}{s.T}]$, $Phantom_{diameter}$ – is the diameter of the used phantom in [m].

In the second step, the calibration measurement itself was performed, using the measurement sequence described in Fig.1. Afterwards, from the measured data for each gradient direction, the response waveforms of the system to the onset of the gradients were obtained. The results are shown in Fig.2, where measured (d_j, w_j) points for uncompensated and compensated cases together with least-square minimization fit [with fitting function (1)] for uncompensated data are visible. Gradient pre-emphasis compensation reduced the effect of induced eddy current on peaks width w_j for the shortest delays of more than a half and also significantly for the rest of the delays. The same effect was present for each direction of the gradient pre-emphasis experiment.

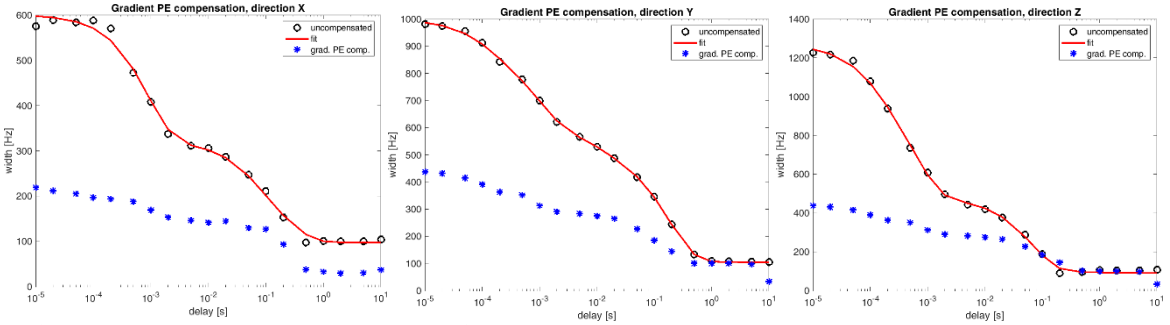

Fig. 2. (Color online.) Measured eddy currents effect gradient pre-emphasis compensation in gradient ring down experiment: the ◦ uncompensated data, (red line) fitting function, the ∗gradient pre-emphasis compensated data.

4. Discussion and Conclusions

This study describes methods of reduction and compensation of eddy currents produced by gradient coils. Subsequently, one method for compensation of eddy currents was described, which compensates the effect of eddy currents by appropriate modelling of the shape of the gradient pulses. Preliminary results were shown.

Acknowledgements

This work was supported by Slovak Scientific Grant Agency, project VEGA 2/0004/23 and within the projects of the Slovak Research and Development Agency Nr. APVV-21-0299 and APVV-19-0032.

References

[1] F.David Doty. *MRI Gradient Coil Optimization*. Doty Scientific, Inc. 700 Clemson Road, Columbia. SC 29229, USA

[2] Ahn, C.B., Cho, Z.H. *Analytic Solution of Eddy Currents and its Temporal Compensation in Nuclear Magnetic Resonance Imaging*, Department of Radiological Sciences, University of California, Irvine, CA 92717

[3] Ahn, C.B., Cho, Z.H. Analysis of the Eddy-Current Induced Artifacts and the Temporal Compensation in Nuclear Magnetic Resonance Imaging (1991) IEEE Transactions on Medical Imaging, 10 (1), pp. 47-52.

[4] Wang Y., Wang Q., Guo L., Chen Z., Niu C., Liu F. An actively shielded gradient coil design for use in planar MRI systems with limited space (2018) Review of Scientific Instruments, 89 (9), art. no. 095110, DOI: 10.1063/1.5043331

[5] Tao S., Weavers P.T., Trzasko J.D., Shu Y., Huston J., III, Lee S.-K., Frigo L.M., Bernstein M.A. *Gradient pre-emphasis to counteract first-order concomitant fields on asymmetric MRI gradient systems* (2017) Magnetic Resonance in Medicine, 77 (6), pp. 2250 – 2262

[6] Weavers P.T., Tao S., Trzasko J.D., Frigo L.M., Shu Y., Frick M.A., Lee S.-K., Foo T.K.-F., Bernstein M.A. *B0 concomitant field compensation for MRI systems employing asymmetric transverse gradient coils* (2018) Magnetic Resonance in Medicine, 79 (3), pp. 1538 – 1544

[7] Ma, C., Jiang, X. H. *A new eddy-current compensation method in MRI* (2007) PIERS Online, 6 (3), pp. 874 – 878

[8] Boesch, Ch., Gruetter, R., Martin, E. Temporal and spatial analysis of fields generated by eddy currents in superconducting magnets: Optimization of corrections and quantitative characterization of magnet/gradient systems (1991) Magnetic Resonance in Medicine, 20 (2), pp. 268-284.

Low Field MRI vs. High Field MRI Future Perspectives - Posters IV

ISBN 978-80-972629-6-9

In vivo Volumetric, DTI and ^{1}H MRS Rat Brain Analysis for Monitoring Early Neurodegeneration and Efficacy of the Used Therapy

[1,2]Tvrdík Tomáš, [1,2]Melicherčík Ľubomír, [1]Bačiak Ladislav, [1]Maková Marianna, [4]Szabó Jakub, [3]Janáčová Veronika, [3]Just Ivica, [1]Kašparová Svatava

[1]Central Laboratories, Faculty of Chemical and Food Technology, Slovak University of Technology in Bratislava, Bratislava, Slovakia
[2]Department of Radiology, Faculty of Medicine of Comenius University in Bratislava, Slovak Medical University and University hospital Bratislava, Bratislava, Slovakia
[3]High-Field MR Centre, Department of Biomedical Imaging and Image-guided Therapy, Medical University of Vienna, Vienna, Austria
[4]Institute of Molecular Biomedicine, Faculty of Medicine of Comenius University in Bratislava, Bratislava, Slovakia
Email: sk.tomas.tvrdik@gmail.com

Abstract. *The aim of our study was to develop a multimodal experimental protocol for in vivo imaging and metabolic parameters (MRI, DTI and ^{1}H MRS) in an animal model of neurodegeneration. This experiment should generate several "bio-markers" of structure and metabolism in the brain to monitor pathological as well as therapeutic changes in our simulated brain degeneration.*

Keywords: Animals, Multimodal imaging, In-vivo, DTI, MRS

1. Introduction

The goal of our study was to advance the technical possibilities in the preclinical research of neurodegeneration investigated in animal models. We designed and optimised an *in vivo* multimodal experiment in which it would be possible to measure and compare several MRI, DTI/tractographic and MRS parameters of small animal brains with the complete acquisition in one measurement session. These data could then be noninvasively and repeatedly compared for each animal throughout the experiment. For the pilot study, we chose the non-genetical model of neurodegeneration using the metabolic effects of D-galactose overdose in Wistar rats. We compared the hippocampal regions as well as selected white matter structures in the brain to find out which of the measured parameters would have the best validity for detecting the early stages of neurodegeneration, and at the same time, would reflect the disease-modifying effects of neuroprotective therapy with Huperzine A.

Preclinical animal research showed that chronic administration of high doses of D-galactose is a widely used model for ageing and neurodegeneration in small rodents based on an alternative biochemical pathway producing galactitol and galactonate [1,2]. Among the mechanisms of D-galactose overdose are oxidative stress, pro-inflammatory state and energetic metabolism changes in the hippocampus [3,4]. The D-galactose model simulating the ageing of brain structures has not yet been investigated from the view of diffusion and tractographic imaging; therefore, we included this relatively demanding MR method in our multimodal experiment. We wanted to find out whether the pre-inflammatory conditions in the brain will be reflected in the measured parameters.

ISBN 978-80-972629-6-9

2. Subject and Methods

We used a model of age-related dementia by daily D-galactose administration for experimental group *two* (n=8); treatment of Huperzine A as a neuroprotective agent applied with D-galactose (group *three*, n=8) and control group *one* administered with saline (n=6). During the 2 months course of the experiment, all animals received daily treatment with subcutaneously administered drugs dosed by weight. Two consecutive *in vivo* MRI/MRS measurements of each of the animals were performed on days 1-9 (baseline), and during days 55-58 after the treatment commenced. The animals were anaesthetised with isoflurane in the air before and during the scanning. The study was approved by the State Veterinary and Food Administration of the Slovak Republic (Ro-990/16-221).

In vivo MRI and ^{1}H MRS

In vivo MRI and ^{1}H MRS measurements were performed on a 4.7T horizontal magnet with a bore diameter of 12.5 cm and with a 400 mT/m gradient insert interfaced to a DDR console (Agilent Technologies, Yarnton, UK) equipped with a head holder, a quadrature volume excitation RF coil with an internal diameter of 72 mm and dual-channel surface receiver coil (Rapid Biomedical, Rimpar, Germany). DTI and MRI volumetric data were acquired together using one diffusion-weighted sequence; volumetric images were then extracted from b=0 scans which were equivalent to T2-weighted images. Following the acquisition of GRE scout images, corrections of animal placement, and manual shimming, we measured thin horizontal diffusion-weighted FSE slices positioned over the telencephalon and brainstem (in-plane resolution 0.4×0.4 mm^2, b=1097 s/mm^2). We acquired images with 10 non-collinear gradient orientations in a half-sphere scheme and two non-weighted images. Total FSE DTI scan time was just under 54 minutes. We acquired T2-weighted FSEMS axial images for positioning of voxel ($3\times3\times4$ mm^3) for localised *in vivo* ^{1}H MRS in the area of the dorsal part of the right hippocampus with the same coil setup. Following the automatic FASTMAP shimming to achieve spectral linewidth of <10 Hz, and water suppression calibration by VAPOR sequence, the MRS was acquired using SPECIAL sequence [5] with outer volume suppression, TE=4.47 ms, 8 blocks of 64 dual-channel acquisitions,and measurements of the unsuppressed water as an internal reference. *In vivo* localised MR spectroscopy took 25 min. We acquired all measurements, including shimming and water suppression calibration, in one uninterrupted session of a total duration of approx. 2 hours.

Data analysis

We performed the DTI reconstruction of data and volumetry using DSI Studio [6], and generated colour-coded, FA, RD, MD and AD maps of diffusion. The diffusion non-weighted images (b=0) were used for the manual *in vivo* volumetry of hippocampi and telencephalon by segmentation viewed on tablet with the help of a sectional brain atlas [7].

We used colour-coded diffusion maps to assess artefacts. Low-quality data and data with low SNR were rejected. The tractographies of both cinguli and forceps maior for each animal were then reconstructed using a deterministic tracking algorithm [8] and topology-informed pruning with two iterations to remove false connections in reconstructed tracts [9]. We deleted repeated tracts. All reconstructed tracts for each animal were visually inspected by the radiologist to search for false connections and to select the best tractographic reconstruction in agreement with the atlas [10]. We cropped the reconstructed tracts to ROIs based on relative position to splenium, which was marked in the previous step individually for each animal, and then we exported the mean values of measured FA, AD, RD, MD in all DTI ROIs.

The second method of DTI data analysis we used was an analysis based on ROIs in the Waxholm Space atlas v4 [11]. Three-dimensional DTI images were registered with atlas (ITK-SNAP), transformed (ANTs) and overlaid with an atlas to enable calculation of mean values

(MRtrix3) of diffusion parameters from previously exported parametric maps in selected ROIs in cingulum, amygdala, basal ganglia, hippocampus, corpus callosum, insula, olfactory bulb, orbitofrontal cortex and white matter tracts.

We corrected the phase and frequency shift of the measured stack of spectra, summed and corrected for eddy currents using non-water-suppressed spectra. Processed *in vivo* ^{1}H MR spectra from the right hippocampus were quantified using LCModel software [12] (Version 6.3-1). A standard 18-metabolite basis set with built-in spline estimation of macromolecule baseline was used to deconvolute spectra in the frequency domain. No correction for T_1 and T_2 relaxation was applied since long TR and short TE were used in the sequence. Metabolite values with Cramér-Rao lower bounds >20 % were excluded from further analysis.

3. Results and Discussion

This study aimed to find an MRI/MRS biomarker with the best validity for the detection of early changes in D-galactose simulated neurodegeneration using an experiment in which MR parameters were measured simultaneously during a single anaesthesia. The reason for using multiple modalities in one measurement session is to ensure constant experimental conditions and limit the effects of anaesthesia on the animal's metabolism [13]. We evaluated hippocampal metabolism (MRS) and structure (volumetry), white matter from a microstructural point of view (DTI) and tracked changes over time to study the neuroprotective action of Huperzine A. Analysis of data from DTI and ^{1}H MRS showed that in our animal model of the ageing brain, we did not notice statistically significant changes in microstructural parameters of white matter functionally connected with the hippocampus. Despite no differences observed in pair-wise comparison, multivariate OPLS-DA analysis (SIMCA, Sartorius) revealed the volume of hippocampus (VIP=1.62), taurine (VIP=1.14) and myo-inositol (VIP=1.05) relative concentrations as significant predictors contributing to the differences between the groups of rats treated with D-galactose (R^2=0.65) (Fig. 2). It is clear, that the D-galactose metabolic model has limitations depending on the application scheme used. [2,14,15]. The effects of Huperzine A, which we expected to have a neuroprotective effect, were confirmed in this experiment, as we administered this drug from the beginning of the experiment. In contrast to our previous study, where we found that the administration of Huperzine A in the D-galactose model is strongly dependent on the application scheme and may even be harmful to already ongoing neurodegeneration [15].

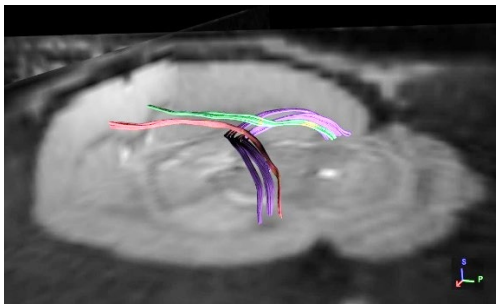

Fig. 1: Rendering of *in vivo* MRI tractography of both cinguli and forceps maior. Top lateral view.

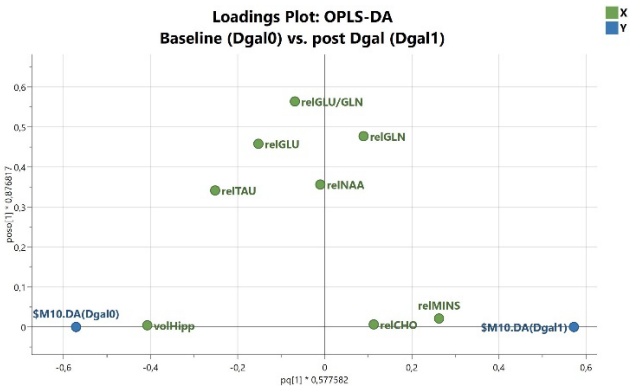

Fig. 2: OPLS-DA loadings plot representing the weights of the relative concentrations of metabolites and hippocampal volume, along the two predictive components derived from OPLS-DA model of measurements in D-galactose group.

ISBN 978-80-972629-6-9

4. Conclusions

We developed MRI/^{1}H MRS protocol for simultaneous *in vivo* measurement of several metabolic, macrostructural and microstructural markers for use in small animal models of brain pathology to ensure unaltered conditions for repeatable non-invasive experiments. For the D-galactose model of "age-related dementia" used in our multimodal experiment, the volumetric and spectroscopic parameters were shown to be the valid "biomarkers" of simulated "neurodegeneration", even with response to the applied huperzine A therapy.

Acknowledgements

This work was financially supported by the Ministry of Education, science, research and sport of the Slovak Republic (grant VEGA 1/0415/16, APVV–21-0299).

References

[1] Holden, H.M., Rayment, I., Thoden, J.B. (2003) Structure and function of enzymes of the Leloir pathway for galactose metabolism. *Journal of Biological Chemistry*, American Society for Biochemistry and Molecular Biology. 278, 43885–8.

[2] Sadigh-Eteghad, S., Majdi, A., McCann, S.K., Mahmoudi, J., Vafaee, M.S., Macleod, M.R. (2017) Correction: D-galactose-induced brain ageing model: A systematic review and meta-analysis on cognitive outcomes and oxidative stress indices. *PloS One*, 12, e0190328.

[3] Song, X.U., Bao, M., Li, D., Li, Y.M. (1999) Advanced glycation in D-galactose induced mouse aging model. *Mechanisms of Ageing and Development*, 108, 239–51.

[4] Hua, X., Lei, M., Zhang, Y., Ding, J., Han, Q., Hu, G. et al. (2007) Long-term D-galactose injection combined with ovariectomy serves as a new rodent model for Alzheimer's disease. *Life Sciences*, Elsevier. 80, 1897–905.

[5] Mlynárik, V., Gambarota, G., Frenkel, H., Gruetter, R. (2006) Localized short-echo-time proton MR spectroscopy with full signal-intensity acquisition. *Magnetic Resonance in Medicine: An Official Journal of the International Society for Magnetic Resonance in Medicine*, Wiley Online Library. 56, 965–70.

[6] Jiang, H., Van Zijl, P.C., Kim, J., Pearlson, G.D., Mori, S. (2006) DtiStudio: resource program for diffusion tensor computation and fiber bundle tracking. *Computer Methods and Programs in Biomedicine*, Elsevier. 81, 106–16.

[7] Paxinos, G., Watson, C. (2007) The Rat Brain in Stereotaxic Coordinates. Elsevier.

[8] Yeh, F.-C., Verstynen, T.D., Wang, Y., Fernández-Miranda, J.C., Tseng, W.-Y.I. (2013) Deterministic diffusion fiber tracking improved by quantitative anisotropy. *PloS One*, Public Library of Science. 8.

[9] Yeh, F.-C., Panesar, S., Barrios, J., Fernandes, D., Abhinav, K., Meola, A. et al. (2019) Automatic removal of false connections in diffusion mri tractography using topology-informed pruning (tip). *Neurotherapeutics*, Springer. 16, 52–8.

[10] Veraart, J., Leergaard, T.B., Antonsen, B.T., Van Hecke, W., Blockx, I., Jeurissen, B. et al. (2011) Population-averaged diffusion tensor imaging atlas of the Sprague Dawley rat brain. *Neuroimage*, Elsevier. 58, 975–83.

[11] Papp, E.A., Leergaard, T.B., Calabrese, E., Johnson, G.A., Bjaalie, J.G. (2014) Waxholm Space atlas of the Sprague Dawley rat brain. *NeuroImage*, 97, 374–86.

[12] Provencher, S.W. (1993) Estimation of metabolite concentrations from localized in vivo proton NMR spectra. *Magnetic Resonance in Medicine*, Wiley Online Library. 30, 672–9.

[13] Xie, Z., Dong, Y., Maeda, U., Moir, R.D., Xia, W., Culley, D.J. et al. (2007) The inhalation anesthetic isoflurane induces a vicious cycle of apoptosis and amyloid β-protein accumulation. *Journal of Neuroscience*, Soc Neuroscience. 27, 1247–54.

[14] Sumbalová, Z., Uličná, O., Kucharská, J., Rausová, Z., Vančová, O., Melicherčík, L. et al. (2022) D-galactose-induced aging in rats–The effect of metformin on bioenergetics of brain, skeletal muscle and liver. *Experimental Gerontology*, Elsevier. 163, 111770.

[15] Melichercik, L., Tvrdik, T., Novakova, K., Nemec, M., Kalinak, M., Baciak, L. et al. (2022) Huperzine aggravated neurochemical and volumetric changes induced by D-galactose in the model of neurodegeneration in rats. *Neurochemistry International*, Elsevier. 158, 105365.

Anti-diabetic Treatment Effect on Early-Stage Neurodegeneration. *In vivo* MRI and MRS Study in Rats.

[1]Marianna Maková, [1]Martin Štosel, [1,2]Tomáš Tvrdík, [2]Ľubomír Melicherčík, [1]Svatava Kašparová

[1]Slovak University of Technology, Faculty of Chemical and Food Technology, Bratislava, Slovak Republic
[2]Department of Radiology, Faculty of Medicine of Comenius University, Slovak Medical University and University Hospital, Bratislava, Slovak Republic
Email: makovamarianna96@gmail.com

Abstract. *While anti-diabetic drugs are known to potentially delay the onset of dementia, little is known about their impact on brain structure and metabolism. This study aims to investigate the structural and neurochemical changes that occur following metformin treatment in a rat model of D-galactose induced brain degeneration. Both MR imaging and spectroscopy methods were used for hippocampal volume evaluation and metabolic profiling, respectively. Our findings confirmed the presence of hippocampal atrophy and respective metabolite changes, including increased myo-inositol/(total creatine), glutamate/(total creatine) and choline/(total creatine) ratios, during the early stages of neurodegeneration. However, metformin administration did not reduce hippocampal shrinkage, and the positive treatment effects were observed only by MR spectroscopy.*

Keywords: In vivo MRI and ^{1}H MRS, Neurodegeneration, Animal Model, D-Galactose, Metformin

1. Introduction

There is a shred of growing evidence demonstrating that people with a high sugar intake are at a greater risk of developing dementia compared to the general population [1]. The previous investigation showed the protective effect of antidiabetic drug metformin in delaying dementia in patients [2], but there is limited data on the neurochemical and structural changes that occur following treatment. Neurodegenerative diseases are characterized by early and progressive loss of selected neuronal populations. It is well known that such diseases can begin years before clinical symptoms appear [3]. Classic examples include the loss of neurons in the hippocampus which controls memory functions [4]. Identifying the location of neuronal damage is crucial for the identification and characterization of the disease. Magnetic resonance spectroscopy (MRS) has been used to measure regional changes in the concentration and ratio of metabolites associated with dementia. Several studies have reported a reduction of N-acetyl aspartate and an increase in myo-Inositol, as well as pronounced loss of volume in the hippocampal area [5]. Some preclinical studies have investigated changes in glutamate, γ-aminobutyric acid (GABA, inhibitory neurotransmitter) and taurine (Tau) in animal models [6].

2 Subject and Methods

Animal model

The experiment involved thirty-two male Wistar rats aged three months, randomly divided into four groups (8 rats in each group). The first group received subcutaneous injections of 0.9% saline (1 mL/rat/day) for 8 weeks (control group). To induce neurodegeneration, the second

group received subcutaneous injections of D-galactose (150 mg/kg/day) daily for the first 3 weeks and then 225 mg/kg/day for the next 5 weeks (D-gal group). The third group received an anti-diabetic drug, metformin (200 mg/kg/day), for six weeks (Met group). The fourth group received both D-galactose (150 mg/kg/day for the first 3 weeks and 225 mg/kg/day for the next 5 weeks) and metformin (200 mg/kg/day) (D-gal + Met group). At the beginning of the experiment and 6 weeks after administration, the animals underwent *in vivo* MR measurements.

In vivo MRI/^{1}H MRS

All *in vivo* MR experiments were performed on 4.7 T horizontal scanner (Agilent, Yarton, UK) equipped with a 600mT/m gradient system. Volume transmit / surface receive RF coil combination (Rapid Biomedical, Germany) was used for signal detection. Fifteen T_2-weighted axial images weres selected to cover the entire brain using a fast spin-echo multi-slice FSEMS sequence (TR 3000 ms, TE 40 ms, 0.5 mm slice thickness, 128x128 matrix) with the field of view (FOV) = 35×35 mm^2. The brain and hippocampal area were manually segmented using ImageJ software. An ultrashort-echo time sequence SPECIAL was used for proton MR spectra acquisition (TR = 3 000 ms, TE = 4.7 ms, eight blocks, and 64 scans, voxel size 3x3x4mm^3) from the dorsal hippocampus. The VAPOR method was used to suppress the water signal. Relative concentrations of metabolites were quantified using both jMRUI and LCModel software.

3 Results

After manual segmentation, brain volumes and hippocampal volumes were calculated by multiplying the sum of hippocampal areas identified on all MR images by the thickness of the slices (0.5 mm). Hippocampal relative volume was calculated as a fraction of hippocampal volume (mm^3) and the whole brain volume (mm^3), which was then multiplied by 100. Statistical analysis was performed using a Student's paired T-test. After 6 weeks, a statistically significant difference in the relative hippocampal volume was observed in the D-gal group (see Table 1). In addition, significant differences in the hippocampal volumes were observed in the D-galactose + Metformin group.

Table 1. Comparison of the relative hippocampal volume of the animal model. The last column of the table represents the p-values of the paired T-tests.

	Mean relative hippocampal volume ± STDEV [%]		**T-test**
	Basal values	**Values after 6 weeks**	
D-galactose group	15.17 ± 1.33	13.72 ± 1.01	**0.01
Metformin group	15.74 ± 1.75	14.59 ± 1.27	0.13
D-galactose + Metformin group	17.37 ± 2.09	13.86 ± 1.05	*0.03

Eight metabolites, including choline (Cho), creatine (Cr), glutamate (Glu), glutamine (Gln), myo-inositol (m-Ins), N-acetylaspartate (NAA), phosphocreatine (PCr) and taurine (Tau) were quantified using both jMRUI and LCModel to obtain their relative metabolite concentrations (related to total creatine, Cr + PCr). Data were analysed using a Student's paired T-test. After 6 weeks of the experiment, a marginal increase in Glu/tCr (jMRUI and LC Model), significant increase (jMRUI) and marginal increase (LC Model) in m-Ins/tCr concentration, and a significant increase in Cho/tCr (only in the LC Model) were observed in the D-gal group. We didn´t observe significant changes in the D-gal + Met group. As no statistical changes were observed in this group, in Figure 1 are presented only the results from the D-gal group.

ISBN 978-80-972629-6-9

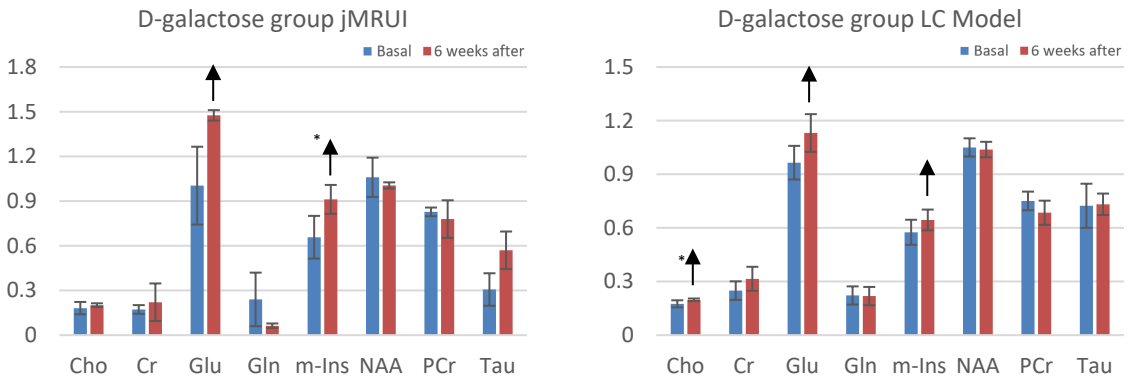

Fig. 1. The relative metabolite concentrations (related to the concentration of tCr) from rat dorsal hippocampus in the D-galactose group analyzed in jMRUI and LCModel. Asterisks + arrows indicate significant changes, and arrows indicate marginal changes in the relative concentrations of selected metabolites.

4 Discussion

The presented animal study was designed to use MRI and localized ^{1}H MRS to non-invasively investigate the structural and metabolic changes in the hippocampus in rats in the early stages of modelled neurodegeneration. In connection with the use of appropriate therapy, we focused on the efficacy of the antidiabetic drug metformin on simulated neurodegeneration in rats using daily D-galactose administration.

The hippocampus is known to show rapid tissue loss and atrophy in Alzheimer´s disease (AD), which is commonly detected as a structural marker in MRI [7]. In this study, relative hippocampal volumes were significantly lower in the D-gal group, indicating atrophy of that hippocampus. The goal of the D-gal + Met group was to find out if metformin, as an antidiabetic agent, has protective effects in the treatment of the early stages of neurodegeneration. Comparing the basal data and post-treatment data (after 6 weeks of D-galactose and metformin administration) showed a significant decrease in the percentage of hippocampal volume. This result indicated that metformin does not have protective effects in the treatment of neurodegeneration.

The concentration of m-Ins, (a marker of neuroglia activity) increases during inflammatory processes in the brain in the early stages of AD [8]. Long-term administration of D-galactose to experimental animals also causes activation of inflammatory processes in the brain and this change was shown in our experiment, as evidenced by the increased m-Ins signal. We also found correlated changes (in both software) in Glu, a major component in the physiology of stress [9]. An increase in Glu is associated with increased anxiety in animal behavior, which is also typical in humans in the early stages of dementia. The increased choline signal in the D-galactose group might represent some degree of myelin damage or glial proliferation. All the above *in vivo* results confirmed the early stages of neurodegeneration, and it was also confirmed in our previous study with *in vivo* ^{31}P MRS (revealed lower intracellular pH and lower inorganic phosphate to ATP).

While AD is often associated with a decrease in NAA, the reduction of NAA content may be related to mitochondrial dysfunction, which was not affected according to our results previously in this study [10]. Our results showed that hippocampal atrophy, i.e. neuronal loss (which was detected from MRI) may not be related to NAA reduction. There were no significant changes in cerebral metabolite concentrations in the treatment group (D-gal + Met group). Spectroscopic analysis showed that metformin was able to modulate elevated levels of mIns and Glu.

ISBN 978-80-972629-6-9

However, hippocampal volume decreased significantly also in the treatment group. These changes were also confirmed in our previous study using *in vivo* ^{31}P MRS to monitor energy metabolism in the rat´s brain. The effect of metformin was also not manifested because pHi remained reduced even in the treatment group [10].

Acknowledgements

This work was financially supported by grants APVV-2/007/22, APVV-21-0299 and VEGA 1/0415/16.

References

[1] Miao, H., Chen, K., Yan, X., & Chen, F. (2021). Sugar in Beverage and the Risk of Incident Dementia, Alzheimer's disease and Stroke: A Prospective Cohort Study. *Journal of Prevention of Alzheimer's Disease*, *8*(2), 188–193.

[2] Liao, W., Xu, J., Li, B., Ruan, Y., Li, T., & Liu, J. (2022). Deciphering the Roles of Metformin in Alzheimer's Disease: A Snapshot. *Frontiers in Pharmacology*, *12*(January), 1–10.

[3] Young, P. N. E., Estarellas, M., Coomans, E., Srikrishna, M., Beaumont, H., Maass, A., Venkataraman, A. V., Lissaman, R., Jiménez, D., Betts, M. J., McGlinchey, E., Berron, D., O'Connor, A., Fox, N. C., Pereira, J. B., Jagust, W., Carter, S. F., Paterson, R. W., & Schöll, M. (2020). Imaging biomarkers in neurodegeneration: Current and future practices. *Alzheimer's Research and Therapy*, *12*(1), 1–17.

[4] Subramaniam, S. (2019). Selective neuronal death in neurodegenerative diseases: The ongoing mystery. *Yale Journal of Biology and Medicine*, *92*(4), 695–705.

[5] McKiernan, E., Su, L., & O'Brien, J. (2023). Magnetic Resonance Spectroscopy in neurodegenerative dementias, prodromal syndromes and at-risk states: a systematic review of the literature. *NMR in Biomedicine*, *March 2022*, 1–13.

[6] Dedeoglu, A., Choi, J. K., Cormier, K., Kowall, N. W., & Jenkins, B. G. (2004). Magnetic resonance spectroscopic analysis of Alzheimer's disease mouse brain that express mutant human APP shows altered neurochemical profile. *Brain Research*, *1012*(1–2), 60–65.

[7] Rao, Y. L., Ganaraja, B., Murlimanju, B. V., Joy, T., Krishnamurthy, A., & Agrawal, A. (2022). Hippocampus and its involvement in Alzheimer's disease: a review. *3 Biotech*, *12*(2), 1–10.

[8] Chen, S. Q., Wang, P. J., Ten, G. J., Zhan, W., Li, M. H., & Zang, F. C. (2009). Role of myo-inositol by magnetic resonance spectroscopy in early diagnosis of Alzheimer's disease in APP/PS1 transgenic mice. *Dementia and Geriatric Cognitive Disorders*, *28*(6), 558–566.

[9] Savic, I. (2020). MRS Shows Regionally Increased Glutamate Levels among Patients with Exhaustion Syndrome Due to Occupational Stress. *Cerebral Cortex*, *30*(6), 3759–3770.

[10] Sumbalová, Z., Uličná, O., Kucharská, J., Rausová, Z., Vančová, O., Melicherčík, Ľ., Tvrdík, T., Nemec, M., & Kašparová, S. (2022). D-galactose-induced aging in rats – The effect of metformin on bioenergetics of brain, skeletal muscle and liver. *Experimental Gerontology*, *163*(March).

Automated Knee Articular Cartilage Segmentation Using Convolutional Neural Network (CNN): Preliminary Results

[1]Andrej Krafcik, [1]Daniel Gogola, [1,2]Pavol Szomolanyi, [2]Siegfried Trattnig

[1]Institute of Measurement Science, Slovak Academy of Sciences, Bratislava, Slovakia,
[2]High Field MR Center, Medical University of Vienna, Vienna, Austria
Email: andrej.krafcik@savba.sk

Abstract. *Automated identification and segmentation of medical imaging data is very desirable. The reason is typically the large size of data and therefore enormous time, which radiologist has to invest in manual segmentation. Therefore, we developed a simplified convolutional neural network (CNN), which could efficiently and automatically segment the knee articular cartilage into multiple classes on a currently available graphical processing unit (GPU). Currently available dataset of ten manually segmented patients MRIs divided into three subsets were used for training, validating and testing our neural network. Therefore our results are only preliminary but fulfill our expectations. Results could be more precise by involvement data augmentation step in training CNN process, which will be realized by our team in the near future. We continually work on the enlargement of our dataset, as well as on the involvement of bigger available datasets from other scientific groups.*

Keywords: Knee Articular Cartilage, MRI, Automated Multi-Class Segmentation, U-Net 3D-Convolutional Neural Network, Artificial Intelligence

1. Introduction

Manual identification and segmentation of cartilage from high-resolution morphological MRI data is time-consuming and subjective inter-variable process of involved radiologists. To automate and objectify this process, is therefore very desirable.

The 3D musculoskeletal morphology data for orthopedic application can be well obtained using 3D double-echo steady-state sequence (3D-DESS), in which contrast is combined features from both the FID-signal of FISP with the Echo-signal of PSIF. Fluid is extremely bright (reflecting T2/T1 weighting) and bone is relatively dark due to T2* dephasing from trabeculae [1].

Recently, many techniques for automated cartilage segmentation have been introduced [2], including the intensity and edge-detection-based approaches, clustering, deformable models, atlas-/graph-based methods, or segmentation scheme that involves automated segmentation of bones from 3D active shape model and further extraction cartilage segmentation at expected bone-cartilage interfaces. Nowadays, a very popular method for automated segmentation of various MRI data is a convolutional neural network (CNN)-based approach, which has the ability to quantify relaxometry and morphology in a single session [3].

The goals of this study were to develop CNN for automated segmentation of human knee articular cartilage 3D MRI data, and to compare the results with a manually segmented mask.

2. Subject and Methods

Dataset

Our primary dataset consists of ten patients. Each underwent an MR examination on a whole body investigational 7 T MR scanner (Magnetom, Siemens Healthineers, Erlangen, Germany) with a dedicated 28-channel knee coil (Quality Electrodynamics, Mayfield Village, OH, USA).

ISBN 978-80-972629-6-9

The 3D-DESS was used to acquire high-resolution MR images for automated cartilage segmentation. Obtained 3D MRI data with resolution $640 \times 640 \times 224$ and one gray-scale channel was manually segmented by a medical student (K. U.) under the supervision of an orthopedic surgeon with extensive experience in musculoskeletal imaging (M. S.). This process is extremely tedious work and for 3D MRI data of each patient took medical student about 8 hours. Each voxel was manually classified to 0-th background class and further 5 classes (lateral and medial femoral cartilage, patellar cartilage, and lateral and medial tibial cartilage) using soft-tool ITK-SNAP 3.8.0 (available online: `http://www.itksnap.org/pmwiki/pmwiki.php`, accessed on 27 January 2023); and further down-sampled to the resolution $128 \times 128 \times 112$. This dataset of patients was further divided into training, validating and testing subsets of patients in the ratio $6 : 2 : 2$. The training and validating subsets were used to train and validate in each epoch of the training process, respectively.

CNN Architecture

Our CNN determined to the segmentation of 3D data comes from a 3D U-net architecture presented by Cicek et al. [4]. In our implementation, it has only two layers in each resolution stage of the analysis and synthesis path, and instead of the MaxPool layer uses down-convolution with strides of two. It uses four resolution stages. Each convolution layer contains one $3 \times 3 \times 3$ kernel convolution with batch normalization (BN) followed by a rectified linear unit (ReLU) activation. In the analysis path for each resolution, a $2 \times 2 \times 2$ kernel down-convolutions with strides of two and without activation is presented. On the other hand, in the synthesis path for each resolution, a $2 \times 2 \times 2$ kernel up-convolutions with strides of two and without activation is presented. Also, shortcut connections from layers of equal resolution in the analysis path provide the essential high-resolution features to the synthesis path by tensor concatenation. In the last layer, a $3 \times 3 \times 3$ kernel convolution reduces the number of output channels to the number of classes, which is 6 in our case, via softmax activation. Each layer has the same padding. The number of channels in the analysis path at each resolution stage doubles in order $32, 64, 128, 256$. In the synthesis path, the order is reversed.

Training

In each training epoch we shuffled the order of the training subset and also shuffled the order of the validation subset. Currently, our source code does not apply any other data augmentation. However, in the near future, data augmentation layers (random crop, rotation, scaling, gray value augmentation, etc.) will be incorporated.

The network output and the ground truth labels are compared using softmax activation with the categorical cross-entropy loss [5]. As a metric for further analysis of training and validation, we used categorical accuracy. For network training, we used an RMSprop gradient descent optimization solver of the TensorFlow 2.7.0 (available online: `https://www.tensorflow.org`, accessed on 27 January 2023) module in Python 3.9.16 (Python Software Foundation 2023, `https://www.python.org`) environment.

3. Results and Discussion

Our CNN had 4 629 846 trainable parameters, ran 500 training epochs on an NVIDIA GeForce RTX 3070 8 GB GPU, which took approximately 24 minutes. The maximal validation metric value was obtained in 141. epoch and the minimal validation loss value in 148. epoch.

A comparison of manual and automated segmentation of two patients from test subset for CNN model with maximal validation metric value (141. epoch) is shown in Fig. 1. There are

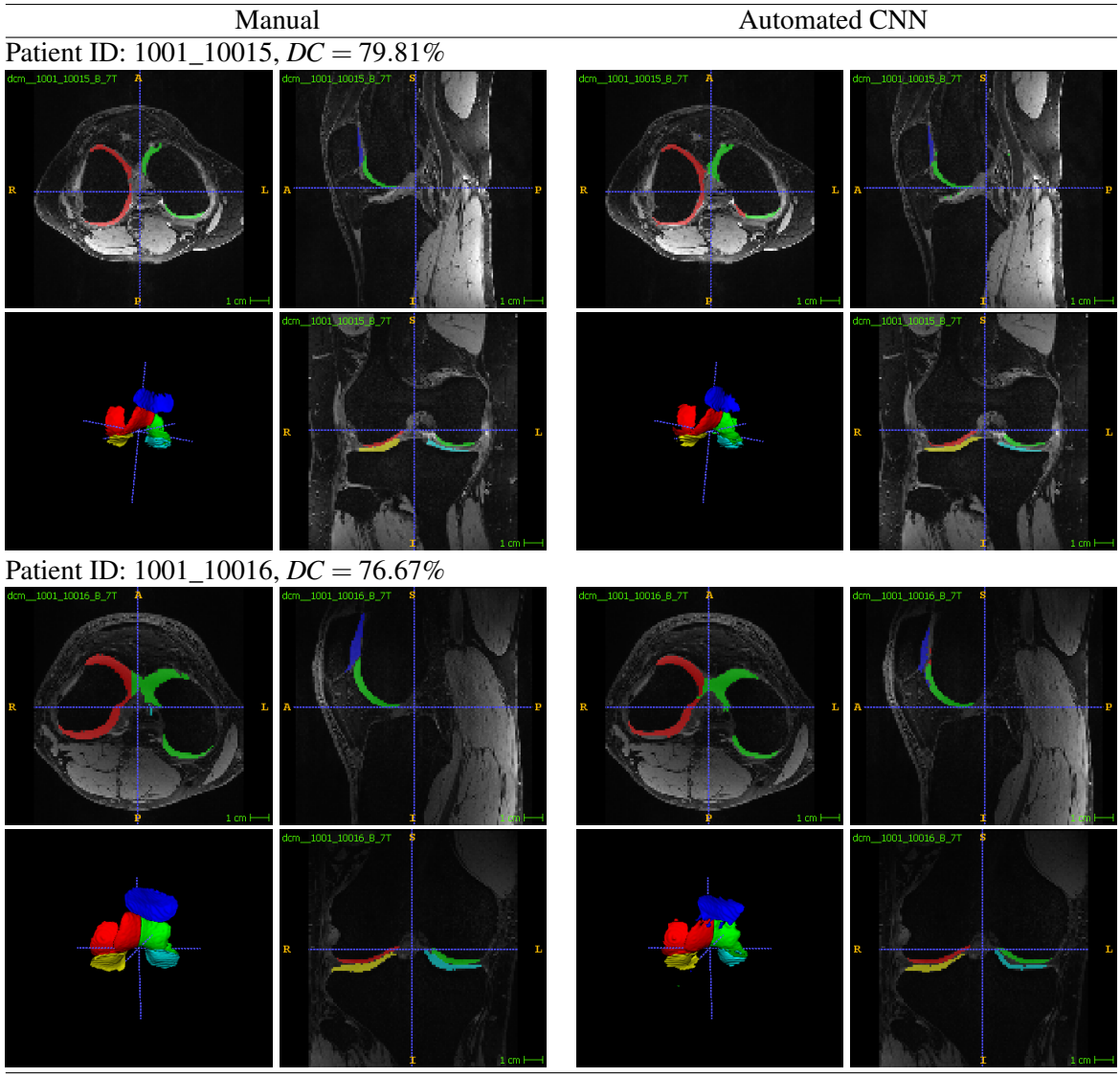

Fig. 1: (Color online.) Comparison of (left) manual and (right) automated CNN knee articular cartilage segmentation of two patients from test subset. Shown in transversal, sagittal, 3D and coronal view. Cartilage segments visualized with different colors: (red) lateral and (green) medial femoral cartilage, (blue) patellar cartilage, and (yellow) lateral and (cyan) medial tibial cartilage.

also presented values of evaluated dice coefficient (*DC*), instead of accuracy. Accuracy takes into account true negatives, which for imbalanced classes in the dataset means that accuracy is a poor metric [6]. For each class index $i = 1,\ldots,5$ binary Dice coefficient is defined as $DC_i = 2|M_i \cap A_i| / (|M_i| + |A_i|)$, where M_i and A_i are manually and automatically obtained segmentation masks of the i-th class, respectively. Also, the overall multi-class Dice coefficient for each patient in test subset was calculated as $DC = 2\sum_{i=1}^{5} |M_i \cap A_i| / \sum_{i=1}^{5} (|M_i| + |A_i|)$ (for results see Table 1). The dice coefficient takes values in the range $[0,1]$, where 1 is obtained for identical segmentation. For two patients in the test subset, we obtained values of *DC* 79.81% and 76.67% (in calculations of dice coefficients, the background class was not included).
The dice coefficient about 80% is an auspicious result. However, presented CNN model and segmented volumetric MRI data are only preliminary, and will be in the near future tuned up with data augmentation layer and adding further convolutional layers in each resolution stage in the CNN architecture, and by extending our primary dataset with new manually segmented knee articular cartilage MRI data. It will require a GPU with bigger memory and more time for our

Table 1: Dice coefficients (*DC*) of segmented knee articular cartilages using CNN.

Cartilage:	lat. femur	med. femur	patella	lat. tibia	med. tibia	overall
Patient ID	DC_1 [%]	DC_2 [%]	DC_3 [%]	DC_4 [%]	DC_5 [%]	DC [%]
1001_10015:	80.06	81.40	73.06	80.78	83.89	79.81
1001_10016:	84.40	84.67	59.44	71.54	68.09	76.67

CNN's training process. Data augmentation is a powerful technique for mitigating overfitting by generating more training data from existing training samples by augmenting the samples via several random transformations such as random crop, random rotation, random scaling, etc. [7]. Therefore, we will augment our small dataset to get a more robust CNN model.
For Dice coefficients of individual classes in Table 1, there are differences that could be relevant for medical issues, depending which segments of articular cartilages are the regions of interest, e.g. in the case of patellar cartilage we obtained worse results in comparison with other segments. We believe that a more robust CNN model could overcome this problem.

4. Conclusions

The CNN model for automated knee articular cartilage segmentation was developed. It was trained on a small dataset of 6 patients, validated on 2 patients and tested on the other 2 patients. Although the input dataset is small, we obtained very promising preliminary results with *DC* about 80% for each patient in the test subset. To improve the results, we would like to involve in the CNN architecture the data augmentation layer and also extend our primary dataset with new manually segmented MRI data, leading to obtaining more robust model.

Acknowledgments

This work was supported by the Slovak Research and Development Agency (APVV-21-0299), and the Slovak Scientific Grant Agency (VEGA 2/0004/23).

References

[1] Thakkar, R. S., et al. (2011). 3T MR imaging of cartilage using 3D dual echo steady state (DESS). *MAGNETON Flash* 3, 33–36.

[2] Juras, V., et al. (2021). Reproducibility of an automated quantitative MRI assessment of low-grade knee articular cartilage lesions. *Cartilage* 13(1_suppl), 646S–657S.

[3] Norman, B., et al. (2018). Use of 2D U-net convolutional neural networks for automated cartilage and meniscus segmentation of knee MR imaging data to determine relaxometry and morphometry. *Radiology* 288(1), 177–185.

[4] Cicek, O., et al. (2016). 3D U-net: Learning dense volumetric segmentation from sparse annotation. *Lect. Notes Comput. Sci.* 9901 LNCS, 424–432.

[5] Gomez, R. (2018). Understanding categorical cross-entropy loss, binary cross-entropy loss, softmax loss, logistic loss, focal loss and all those confusing names. Internet blog. Available online: `https://gombru.github.io/2018/05/23/cross_entropy_loss/`, accessed on 18 April 2023.

[6] Fawcett, T. (2015). The basics of classifier evaluation: Part 1. Silicon Valley Data Science blog. Available online: `https://www.svds.com/the-basics-of-classifier-evaluation-part-1/`, accessed on 18 April 2023.

[7] Chollet, F. (2021). *Deep Learning with Python, Second Edition*. Manning, Shelter Island, NY.

Measurement of Physical Quantities
Posters V

ISBN 978-80-972629-6-9

Velocity and Flow Rate Measurement in a Natural Circulation Helium Loop

Martin Halaj, Marek Mlkvík, Róbert Olšiak, George Sammarah

Slovak University of Technology in Bratislava, Slovakia
Email: martin.halaj@stuba.sk

Abstract. *In nuclear energy power plants, operational safety is of utmost importance. A high-pressure natural circulation loop filled with helium enables the cooling of the residual heat from the reactor. Several operational parameters shall be measured, including measurement of the helium flow velocity and mass flow rate by Pitot tubes. The paper discusses the operational conditions of such measurement, and a suitable design and summarizes uncertainty sources. It also provides a comparison of measured and simulated discharge velocities, which are in a good match, and suitable for intended purposes. Moreover, the measurement results proved the significant impact of the flow type on measured velocities (thus also mass flow), where even the partial inhomogeneities in the helium flow generate the undesired influence on the Pitot tube accuracy. These results are of a preliminary nature and need to be further précised.*

Keywords: Mass Flow Rate, Pitot Tube, ALLEGRO Reactor, Natural Circulation Helium Loop

1. Introduction

In 2010, three Central European research institutions (ÚJV Řež, MTA EK Budapest, and VÚJE Trnava, a.s.) agreed on the construction of the gas-cooled ALLEGRO reactor. It is one of the six fast reactors (GFR) technologies supported at the European level.

An area of increased attention within the GFR framework is operational safety. Even after a successful shutdown, a nuclear reactor generates residual heat for several hours. GFR research is considering several options for the emergency removal of residual heat, one of which is the use of a high-pressure natural circulation circuit filled with helium.

Natural convection loops (NCLs) are a specific type of thermohydraulic circuit, being fully electrically independent by nature, so they are cost-effective, maintenance-free, and highly reliable [1]. Research on this method of heat removal has been continuously studied both theoretically and experimentally, e.g. [2-4], but available experimental results were obtained at low-scale loops in terms of dimensions and power transferred. Therefore, further experiments are still planned.

Fig. 1. Overall view of the helium loop experimental setup. Cold branch on the left, hot branch on the right [5]

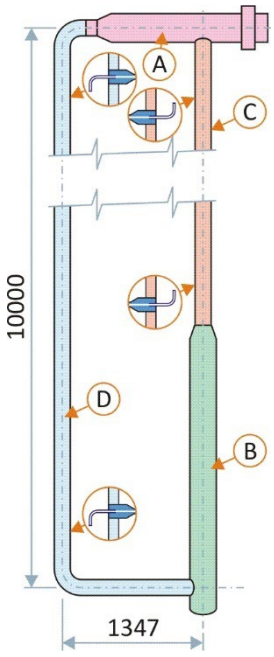

Fig. 2. Scheme of the loop. A - GFR reactor, B - DHR heat exchanger, C - hot branch, D - cold branch (adapted from [5])

ISBN 978-80-972629-6-9

Therefore, a high-pressure and high-temperature helium loop with a cooling design capacity of 250 kW was built at STU in Bratislava in 2015 (see Fig. 1). The operating conditions can reach temperatures of 520 °C and 7 MPa overpressure. Helium is used as the working medium, which is also considered one of the possible coolants in real GFR operation.

2. Measurement of selected process parameters

The basic process parameters (temperatures and pressures) are sampled at four locations around the loop (see Fig. 2). These data allow the values of the working medium state variables to be calculated, including velocity and mass flow rate. Due to the principle of the natural circulation helium loop, all invasive methods (e.g. orifice plates, nozzles, etc.) affect the experiment itself. The optimum solution would be to install non-invasive measuring devices such as ultrasonic flow meters or optical methods (LDA, PIV), the use of which is precluded by the high temperatures and pressures involved in the operation of the device. For the above reasons, it was decided to use Pitot tubes. Fundamental conditions for their use were met except for straight conduit before and after the Pitot tube (see Table 1). There are several reasons for this option, among the most serious being low Reynolds numbers, Re. This is mainly related to the very low-pressure gradients at the Pitot tube pressure taps, which need to be measured at ambient pressures six orders of magnitude higher. The low Re is also related to the problem of pitot tube location in the velocity profile and how the flow rate is calculated from the measured data. In addition to the above, there are deformations of mechanical components during loop operation that can affect the results (see Fig. 3).

Table 1 Fundamental requirements for the Pitot tube use [6]

Condition	What shall be fulfilled	Fulfilled
The length of a straight pipe	20 diameters upstream, 5 diameters downstream of a laminar flow	No
Range of velocities	p is never less than $\frac{2\times10^4}{\rho}\left(\frac{\mu}{\alpha\cdot d_i}\right)^2$	Yes
The ratio of the differential pressure to the absolute value	The ratio shall never exceed the limiting value. For γ = 1.6, the limiting value of $(\Delta p/p)_{max}$ = 0.052	Yes
Dimensional limitations	The ratio of the Pitot tube diameter d to the conduit diameter D shall not exceed 0.02	Yes

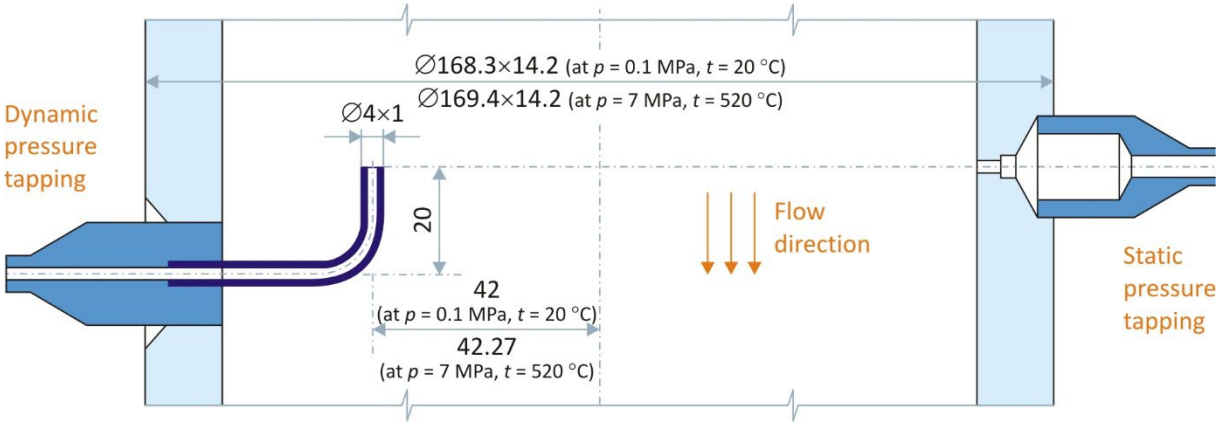

Fig. 3. Changes in geometry of the measuring cross-section due to a changed temperature and pressure (adapted from [5])

ISBN 978-80-972629-6-9

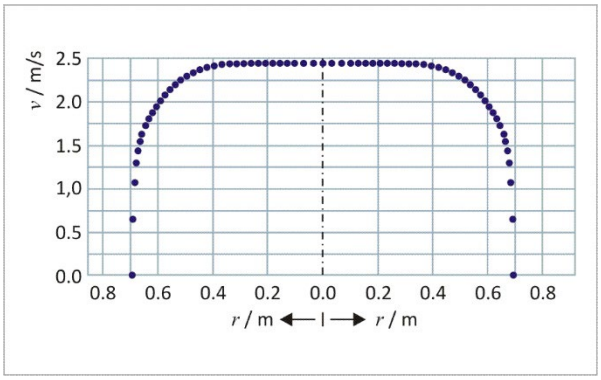

Fig. 4. The simulated velocity profile in a measurement cross-section in a hot line of the helium loop (adapted from [5])

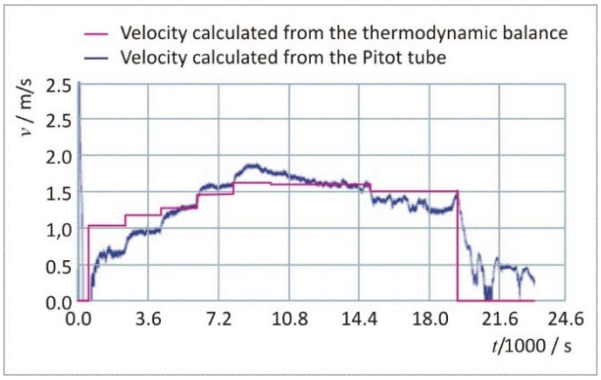

Fig. 5. Comparison of velocities course over time [5]

The local velocity of a fluid in a steady flow without transverse velocity gradient or turbulence at Reynolds number v, based on the internal diameter of the total pressure tapping, greater than 200, is given by formula 1 [6]

$$v = \alpha \cdot (1 - \varepsilon) \sqrt{\frac{2 \cdot \Delta p}{\rho}}, \tag{1}$$

where

$(1 - \varepsilon)$ is a compressibility factor based on the specific heat capacities. For helium at $p = 7$ MP, $(1 - \varepsilon) = 9999998.67 \cdot 10^{-7}$, thus no compressibility correction is required,

ρ is the local density of the fluid, generally related to the temperature and pressure,

Δp is the differential pressure indicated by the Pitot tube,

α is the calibration factor of the Pitot tube, which is usually close to 1.00,

p is the local static pressure (or absolute static pressure).

The mass flow rate q_m is calculated as

$$q_m = \rho \cdot A \cdot \bar{v} = \rho \cdot A \cdot \alpha \cdot (1 - \varepsilon) \sqrt{\frac{2 \cdot \Delta p}{\rho}} = A \cdot \alpha \cdot (1 - \varepsilon) \cdot \sqrt{2 \cdot \rho \cdot \Delta p} \tag{2}$$

where

$\bar{v}$ is the discharge velocity of the flowing medium, having the respective Δp value,

A is the cross-section area of the conduit, for a circular cross-section, $A = \pi \cdot d^2/4$

The discharge velocity can be determined by graphical or numerical integration of the velocity area, respectively by arithmetic methods. All methods require traversing the measuring cross-section by a Pitot tube, measuring the local velocity, thus creating a velocity profile and enabling evaluation of a discharge velocity. Due to the strict requirements for the sealing of the natural circulation helium loop, traversing the Pitot tube is not possible, as its position is fixed by welding and cannot be changed. Therefore, only a simulation of a velocity profile was carried out (see Fig. 4). The position of discharge velocity, and thus a position of a Pitot tube head in a conduit, was determined from a simulated profile (see Fig. 3). Due to a large number of variable parameters, the actually measured velocity differs from that simulated by material balance calculation (see Fig. 5).

ISBN 978-80-972629-6-9

3. Uncertainty sources

Determination of velocity and further the volumetric and mass flow rate by a Pitot tube is a complex task. The whole list of error sources is thoroughly discussed in [6]. They are divided into random and systematic errors, addressing parameters of the measured medium, flow characteristics, Pitot tube design and alignment, and measurement errors of measuring instruments themselves. The major uncertainty sources for the helium loop are connected with unsteady helium flow, the impossibility of measuring a velocity profile, and the shifting of the discharge velocity position within the conduit due to changing helium parameters.

4. Conclusions

The restricted length of the conference paper does not allow a full address of the complexity of the use of the Pitot tube for the measurement of velocity in complicated flow conditions. Those conditions change significantly in terms of helium parameters in different operational modes, changes in the geometry of the measurement cross-section, the impossibility of measuring a velocity profile due to design constrictions, swirls, velocity gradients and other disturbances arising from unsteady flowing conditions. Therefore, the measurement results need to rely on various simulations, estimates and approximations, which increase measurement uncertainty and generate differences between theoretical and measured values. A further investigation has yet to be done, including the use of a Monte Carlo method [7].

Acknowledgements

This paper was created under the support of the Operational Program *Integrated Infrastructure* for the project *Research of physical, technical and material aspects of high-temperature reactors with the potential for hydrogen production*, project code: "ITMS2014+ 313011BUH7", co-financed from the resources of the European Regional Development Fund, as well under the support of the APVV grant agency, project APVV-21-0216 *Advanced mathematical and statistical methods for measurement and metrology*, and the Slovak grant agency KEGA, project No. 016STU-4/2022.

References

[1] Keller, J.B. (1966). Periodic oscillations in a model of thermal convection. *J. Fluid Mech*., 26 (3), 599-606.

[2] Zvirin, Y.(1982). A review of natural circulation loops in pressurized water reactors and other systems. *Nucl. Eng. Des*., 67 (2), 203-225.

[3] Világi, F., Knížat, B., Mlkvik, M., Olšiak, R., Mlynár, P., Ridzoň, F., Urban, F. (2020). Leakage estimation of the high-pressure and high-temperature natural circulation helium loop. *Annals of Nuclear Energy*, 146.

[4] Knížat, B., Vach, M., Mlkvik, M., Mlynár, P., Világi, F., Olšiak, R., Urban, F. (2023). Numerical and Experimental Study of a Large-Scale Natural Circulation Helium Loop. *Applied sciences*, 13(5).

[5] Urban, F., et. al. (2016). Modeling the natural circulation of helium in an experimental helium loop. Research report (in Slovak). STU, 173 pp.

[6] ISO 3966:2020 Measurement of fluid flow in closed conduits — Velocity area method using Pitot static tubes

[7] Nguyen, D.T., Kang, W., Choi, Y.M., Lee, S.H., Choi, Y.M. (2019). Uncertainty Evaluation of Stack Flowrate Measurement with S-Type Pitot Tube by Monte Carlo Method. In *Proc. of Flomeko 2019*. Lisbon, Portugal, pp. 273-277. ISBN: 9781713813095

The Use of Measurement on the Spark Plugs for the Analysis of the Ignition and Injection System

Matej Kucera, Miroslav Gutten, Martin Karman, Marek Nad

Faculty of Electrical Engineering and Information Technology,
University of Zilina, Zilina, Slovakia
Email: matej.kucera@feit.uniza.sk

Abstract. *The article deals with the use of high-voltage measurement on the spark plug for the analysis and detection of faults in the ignition and injection system in the car. It is proposed to use the spark plug as an off-line sensor, on which it is possible to compare real high-voltage waveforms in time during operation with reference waveforms for individual cylinders. In the article, high-voltage waveforms are measured under two extreme conditions, i.e. with on and off injection. Measurements were made using high-voltage probes and a datalogger modified in the LabVIEW program. At the end of the article, these curves are compared, and an error graph is determined for an extreme failure of the injection system for a given cylinder. Within this graph, it is also possible to determine a partial error or failure in the injection system.*

Keywords: Spark Plug, Ignition System, Injection System

1. Introduction

The latest trends in the automotive industry lead to an increase in performance and a reduction in the production of harmful substances contained in exhaust gases, while simultaneously reducing fuel consumption. This is also connected to the huge development in the field of ignition and injection systems of internal combustion engines. Ignition and injection systems are among the most important in the field of engine control. Therefore great emphasis is placed on the diagnosis itself and determining the exact fault [1].

The spark plug can be used as an off-line sensor, on which it is possible to compare the real-time course of high voltage during operation with the reference courses for individual cylinders.

In [2] and [3] the use of waveform analysis on the spark plug for further investigation of electrical and sensor parts of the engine (knocking, pressure regulator, fuel injection, ignition, ...) was mentioned.

The most important element of the fuel system is the fuel injector. Thanks to the monitoring of its operation, it is possible to verify the functionality of the fuel pump, filter, fuel line, fuel tank, and injector itself [4].

The reduced fuel pressure supplied to the injectors and, ultimately, the reduced volume supply of fuel is most often caused by the clogged fuel filter, or damage to the fuel pump and pressure regulator. Such a failure results in a reduction in the car's power and, in worse cases, inactivity of the engine [5].

The spark plug can thus be used as an off-line sensor, on which real high-voltage waveforms can be compared during operation with reference waveforms for individual cylinders. Using the measured two extreme conditions, i.e. with injection on and off, an error graph can be determined for extreme injection system failure for a given cylinder. Within this graph, it is also possible to determine a partial error or failure of the injection system. Using the measurement on the spark plugs, it is possible to understand what is happening in the combustion chamber.

ISBN 978-80-972629-6-9

2. Experimental measurement

Evaluating the failure of the residual estimator not only allows us to detect the failure of components but can also give us information about the degradation of component properties. The best solution for detecting a malfunction and possibly creating a component prognosis is to monitor the progress of the arc burning on the spark plug. By measuring the voltage on the primary or secondary side, we get information about the burning of the arc or possibly about faulty operation in the ignition or injection system.

When analyzing the ignition system, we determined the measurement procedure on the spark plug regarding the effect of its separation distance on the length of the arc burning.

For the measurement, we used an oscilloscope from the Pico Technology brand, which is ideal for measurements directly in vehicles. In most modern vehicles, the new ignition coils are located directly on the spark plugs, which allows us to use a non-intrusive flexible coil on plug (COP) probe. We performed the measurement on two new spark plugs of the same type with different electrode gaps on the same engine to determine the effect of the electrode gap on the measured pattern.

In Fig. 1 we can see two arc burning processes. The blue waveform gives a 0.6 mm spark plug tear and the purple waveform gives a 0.8 mm spark plug tear. From the measured curves, tearing off the spark plugs has a significant effect on the length of the arc burning. The difference between the times is 0.99 ms.

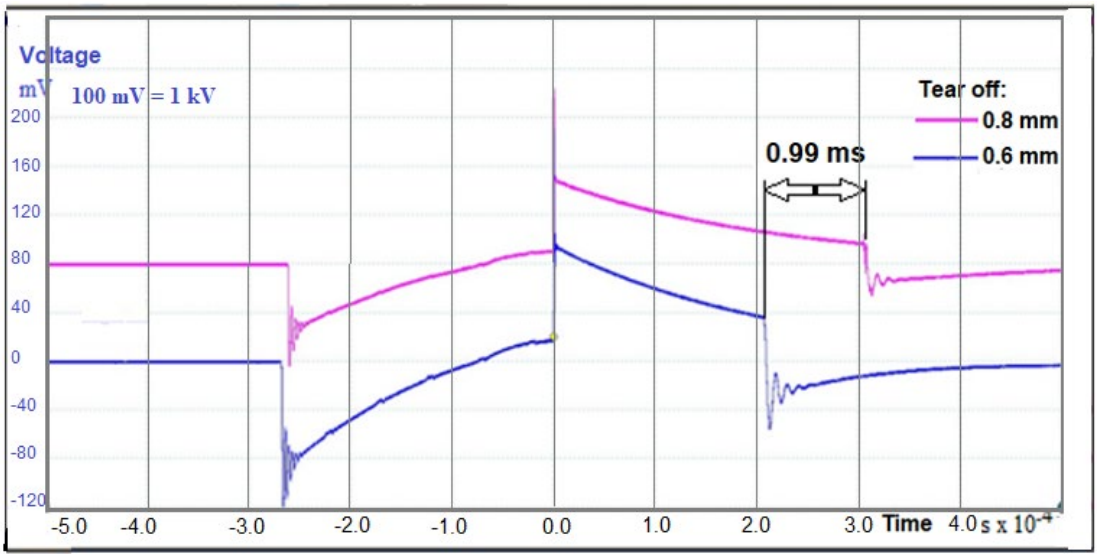

Fig. 1. The effect of tear-off on the arc burning length on the spark plug - from the oscilloscope display

This was a simulated analysis of spark plug ageing. The more the spark plug is worn, the more the distance between the electrodes increases (spark plug tear-off).

Monitoring the voltage characteristic can also provide a lot of information about the condition of the injector and fuel system. Damage to the injector due to long-term operation causes changes that affect the injected amount, and at the same time, the shape of the voltage wave on the spark plug can change.

When analyzing the injection system, we again used the voltage measurement on the spark plug, where we used two extreme cases, i.e. first, the system used a good injection system and then the whole injection system was omitted. For the measurement, we used a modified datalogger with the LabVIEW program, which is ideal for long-term analysis of trends over a longer period of time.

ISBN 978-80-972629-6-9

In Fig. 2 we can see two arc burning processes. The blue waveform is influenced by the operation of the injection system on the voltage curve on the spark plug, and the orange waveform is influenced by the inactivity of the injection system.

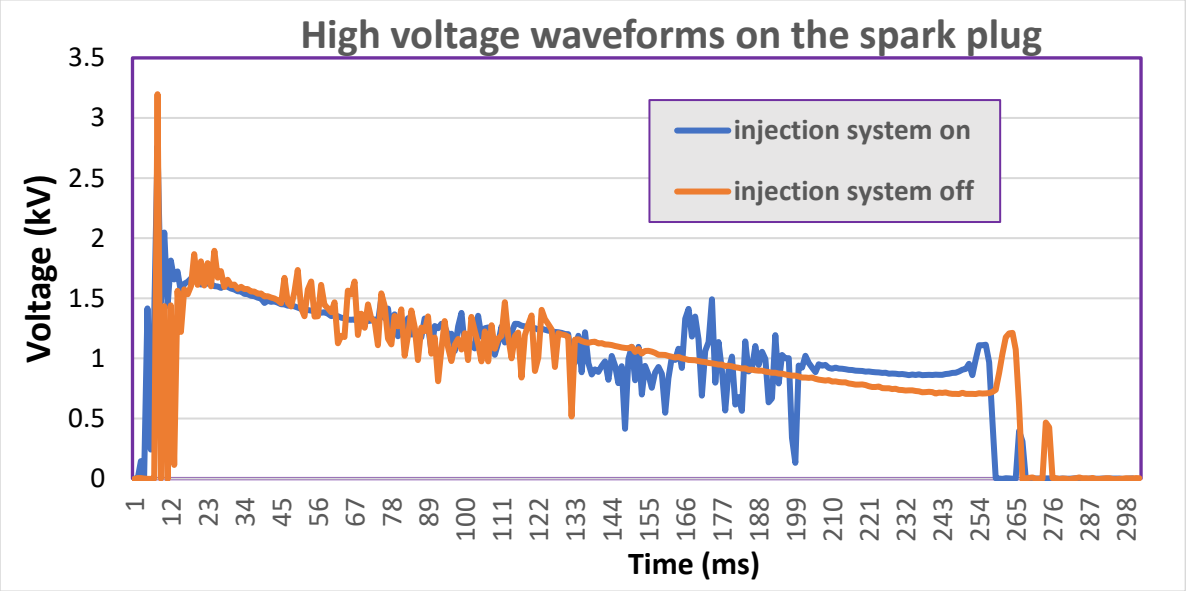

Fig. 2. High voltage waveforms on the spark plug with and without injection system

By comparing the absolute values of the mutual distance measured of both curves by calculation using the Euclidean analysis of the distance of points, we have determined a reference graph that can be used to compare real processes in the ignition system (Fig. 3).

Based on the comparison, it is possible to analyze the condition of the injection system. Thanks to this analysis, we can determine fuel pressure failures, damage to the return spring of the injector, and stopping or slowing down the movement of the injector needle valve.

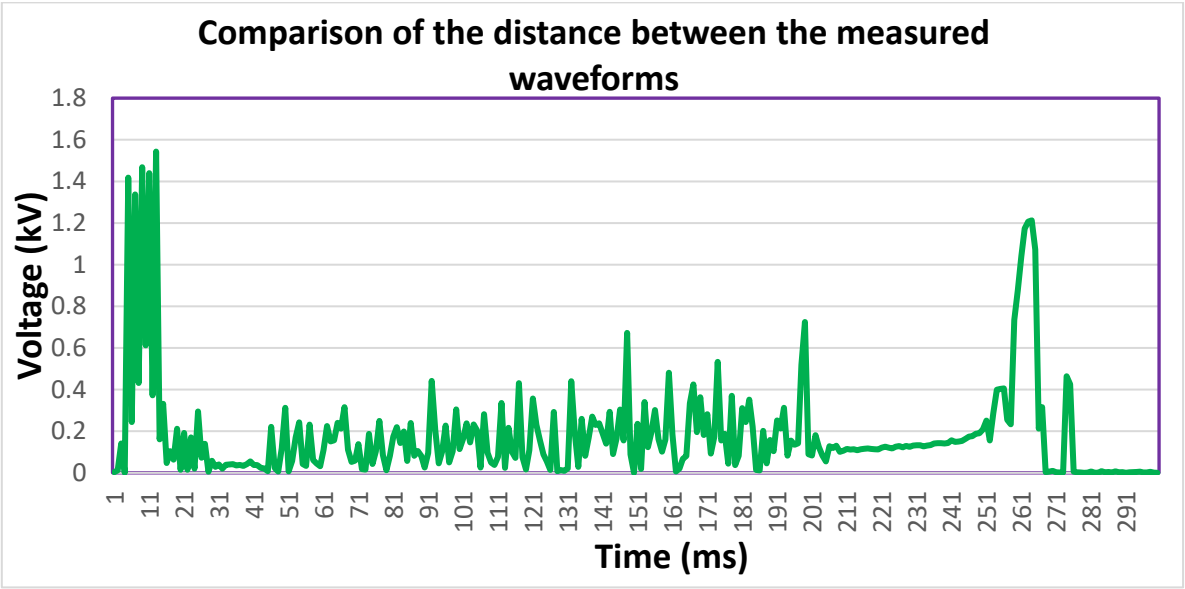

Fig. 3. Comparison of the distance between the measured waveforms on spark plug

An interesting solution for arc burning evaluation is to create a burning history using a recording data logger, as in this case. In this way, it is possible to analyse possible disorders more easily, the manifestation of which is not numerous.

ISBN 978-80-972629-6-9

3. Conclusions

The use of the mentioned measurement method is significant from the point of view of the detection of ageing and its effects on the ignition or injection system in real operation in a car. As for the measurement, it was a comparison of two different measurement systems - a simple digital oscilloscope and a digital measurement system (digital datalogger) created in the LabVIEW program. As can be seen from the analysis of the comparison of the flow from Fig. 3, it is more advantageous to use user-created digital measurement systems that can analyze the measurement more intelligently.

The spark plug was used as an off-line sensor, on which it was possible to compare real high-voltage waveforms with reference waveforms for individual cylinders.

The aim of the first part of the experiment was to find out the differences in the jump voltage on spark plugs with different distances between the electrodes. It was a simulated analysis of spark plug ageing. The more the spark plug is worn, the more the distance between the electrodes increases (tear-off of plug).

Using the measured two extreme conditions, i.e. with the injection on and off, it was possible to determine an error (comparison) graph for a possible extreme failure of the injection system for a given cylinder. Within this graph, it is also possible to determine a partial error or failure of the injection system.

With the help of high-voltage measurement on the spark plugs, other parts in the car can also be analyzed.

Acknowledgements

This work was supported by the Slovak Research and Development Agency under the contract No. APVV-21-0449.

References

[1] Shi, H., Uddeen, K., An, Y., Pei, Y., Johansson, B. (2021). Multiple spark plugs coupled with pressure sensors: A new approach for knock mechanism study on SI engines. *Energy* 227, 120382.

[2] Galloni, E. (2012). Dynamic knock detection and quantification in a spark ignition engine by means of a pressure based method. *Energy Conversion and Management,* 64, 256-262.

[3] Chen, L, et al. (2020). Effect of rapid combustion on engine performance and knocking characteristics under different spark strategy conditions. *Energy*, 192, 116706.

[4] Syrimis, M, Assanis, DN. (2003). Knocking cylinder pressure data characteristics in a spark-ignition engine. *Journal of Engineering for Gas Turbines and Power*. 125 (2), pp. 494-499

[5] Jia, J., Wang, Q., Yu, J., Zheng, Y. (2010). Wideband equivalent circuit model and parameter computation of automotive ignition coil based on finite element analysis. *Application Computational Electromagnetics Society Journal*, 25, 612-619, 2010.

Exploring the Size-of-Source Effect of Transfer Radiation Thermometers by Various Methods

[1]Nasser D. AlDawood, [1]Ebrahem S. AlSbaiy, [1]Nasser M. AlQahtani and [1,2]Khaled M. Ahmed

[1] National Measurement and Calibration Center, Saudi Standards, Metrology and Quality Org. (SASO-NMCC), Riyadh, Saudi Arabia,
[2]National Institute for Standards (NIS), Giza, Egypt
Email: k.abdelftah@saso.gov.sa / khaled55eg@gmail.com

Abstract. *To estimate the proper corrections to temperature values observed while aiming to radiation sources of different sizes, one must be aware of σ, the parameter that assesses the size-of-source effect (SSE) of a radiation thermometer, as a function of the diameter d of a radiation source. Since there is no known mathematical function to relate them, it is difficult to obtain σ as a function of d. The direct method to evaluate σ typically calls for a set of several apertures with increasing diameter. It is desirable to develop methods that produce accurate approximations with fewer apertures to speed up and reduce the cost of evaluating σ. With a constrained number of apertures, we demonstrate in this study an approach for obtaining an approximation to σ as a function of d. Indeed, we explore the SSE in both direct and indirect methods, as well as investigating the non-uniformity of the used source for further future correlation studies. In direct method, we developed the proper equations for calculating σ, and we presented the collected data and show that the SSE function values agree to within 0.08%. In indirect method, the SSE function found to be less than 0.3%.*

Keywords: Radiation thermometers, Size-of-Source Effect (SSE), Calibration, Systematic Error, Uncertainty

1. Introduction

The practice of comparing the unknown radiances from a predetermined target area to reference radiance sources, which may include radiating surfaces of various sizes and shapes, is common in the field of radiation thermometry. In radiation thermometry, it is essential to account for the contributions of the environment since the standards for the errors in temperature measurements are so strict. In addition, the kelvin scale above the freezing point of silver is established using Planck radiance ratios to the freezing point of the Ag-, Au-, or Cu-point blackbodies in the implementation of the International Temperature Scale of 1990 (ITS-90). Due to the need for high emissivities, fixed-point blackbodies sometimes have small, 3mm to 6mm diameter apertures to optimize their temperature uniformities.

SSE is reported as the dependence between the radiation thermometer detector signal and the diameter of a target such as a black body with a spatially uniform radiation source. Geometrically, the detector does not gather radiation from outside the nominal target size established by the field-of-view (FOV). At the target plane, the FOV is dictated by the optics and detector size of the radiation thermometer. In practice, however, due to imperfections in the optics, light scattering inside or outside the instrument, many reflections on important surfaces, and diffraction at the system apertures, the strength of the detector signal is boosted by emission from outside the nominal target size. The wavelength and thermometer field stop size have a significant impact on the SSE [1-4].

The signal of the detector in a radiation thermometer depends on the target size. At certain distances a radiation thermometer has certain nominal target sizes, depending on the field of view defined by the optics [5-6]. Theoretically, we perform the correct measurement if the nominal target of the radiation thermometer is completely filled with the measured target. In practice, this is not possible due to limitations in the optics of a radiation. The SSE is a consequence of radiation scattering on dust particles, reflections between lens surfaces, diffractions and aberrations in the optical system of a radiation

ISBN 978-80-972629-6-9

thermometer [1]. To properly calibrate and determine SSE, we must use a radiation source of uniform spectral radiation with a known diameter. In thermometry there's not one standard way of identifying the SSE of a radiation thermometer. Direct method, indirect method and scanning method are the widely used methods for this task. In this paper, the two main methods are employed, a direct method and an indirect method [3,5].

2. Experimental setups, methods and results

We are conducting several tests to investigate this effect using some of our reference (transfer) radiation thermometers, such as the Heitronics TRT- IV.28 against the blackbody (Isotech, model: R550). Using a spectral range of 8 m to 14 m, we used the direct method to assess the size-of-source-effect (SSE) of a transfer reference thermometer (TRT) in the low temperature mode (see figure 1). For the first investigation experiment (A), the measurements were made at different blackbody temperatures between 50 °C and 250 °C. In the low-temperature range of the SSE measurement, a black body and circular aperture plates with adjustable apertures are used. As blackbody apertures, these plates are positioned in front of the blackbody. These plates were made of 5 mm thick black-painted material with low thermal conductivity to to create a thermal barrier and separate the blackbody from unwanted external radiation and convection. These aperture plates were blackened by paint with emissivity of 0.976 over the wavelength range from 8 μm to 14 μm. The thermometer being tested is coaxially focused on the center of each aperture plate in order to measure the output signal for each plate. Correction is made for the ambient temperature. The TRT signal was acquired with a response time of 3 s for achieving best resolution.

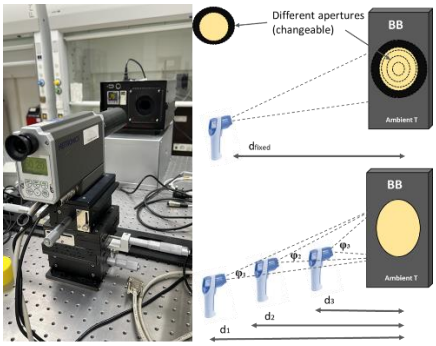

Figure 1. (Left) Photograph of the main setup; (top right) schematic representation of the primary method used in this study for characterizing SSE by comparing measurements made with the same blackbody equipped with various changeable apertures; and (bottom right) schematic representation of the alternative method for characterizing SSE by comparing measurements made with the same blackbody at temperature T, over various distances that correspond to various FOVs (φ_1, φ_2 and φ_3)

A. Direct method for the determination of the SSE

In the direct method a radiation thermometer is focused on a circular aperture placed in front of a stable radiation source, usually the blackbody. Measurements are made with different diameter apertures. The SSE at the radius r is determined as the ratio σS(r) between the signal S(r, L) at the radius r and the signal S(∞, L) at the infinite radius:

$$\sigma_S(r) = S(r, L) / S(\infty, L) \qquad (1)$$

In practice, we cannot realize infinite radius, therefore we measure the SSE as a function of a radius in a limited range from $r_{min} \leq r \leq r_{max}$, where r_{max} usually represents the radius of the blackbody aperture. Thus, we determine the SSE as the ratio of signals at radii r and r_{max}:

$$\sigma S(r, r_{max}) = \sigma S(r) / \sigma S(r_{max}) = S(r, L) / S(r_{max}, L) \qquad (2)$$

We found that the SSE functions observed at various temperatures overlap beautifully when the radiation from the masked area of the aperture plate and its surrounding is taken into account by placing apertures with varied sizes ranging from 10 mm to 50 mm in front of the source. Those measurements shown in figure 2 representing measurements at different blackbody temperatures between 50 °C and 250 °C (RT:

ISBN 978-80-972629-6-9

Heitronics TRT- IV.28 and blackbody: Isotech, model- R550). Results shown are averages of 10 measurements for each aperture diameter with a correction added to each measurement. Emissivity of the TRT is 0.995 and response time 3 ms. The SSE function values agree to within 0.08%.

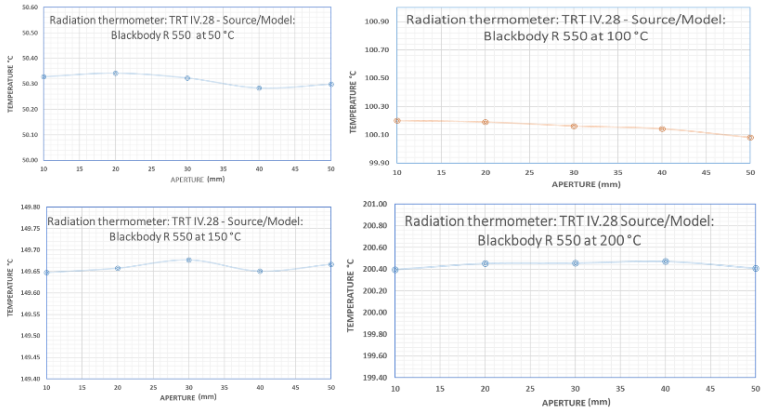

Figure 2. Measurements at different blackbody temperatures between 50 °C and 250 °C with apertures of different diameters (direct method)

B. Indirect method for the determination of the SSE

For the first investigation experiment (B), the SSE measurements of TRT were performed on another setup by employing the indirect method. An integrating sphere (with a diameter of 400 mm) comprising one output port with a diameter of 60 mm was used in measurements. The sphere comprises four incandescent lamps (connected in series) inside. In addition, to minimize specular reflection on outlet port of the sphere, four internal baffles are located at specific locations inside the sphere. The lamps are supplied by a controlled DC current, and are switched on at least one hour before the measurements for establishing the quasi-isothermal condition. Apertures with a diameter of 6, 8, 10, 15, 20, 30, 40 and 50 mm were used to imitate a variable–diameter source. A black spot of 6 mm in diameter was used as a target. The black spot is fixed in the middle of a glass window. In order to exclude the influence of this supporting glass window's transmittance in the SSE measurements, another identical glass window without the spot (a blank glass window) was used in combination with the apertures. The measurements were performed at the distance of 590 mm from the outer surface of the black spot. The transmittance of the spot at the working wavelength band of the thermometers was assessed to be smaller than 0.01%. The SSE was calculated using the following equation:

$$SSE=(S\_spot-S\_dark)/(S\_aperture-S\_dark). \quad (3)$$

Here S_{dark} is the relevant dark signal (voltage), S_{spot} is the signal (voltage) measured when the thermometer is focused on the black spot, and $S_{aperture}$ is the signal (voltage) measured when the aperture is combined with the blank glass window. This measurement is repeated with all apertures of varying diameters. Results of this experiment are presented in figure 3.

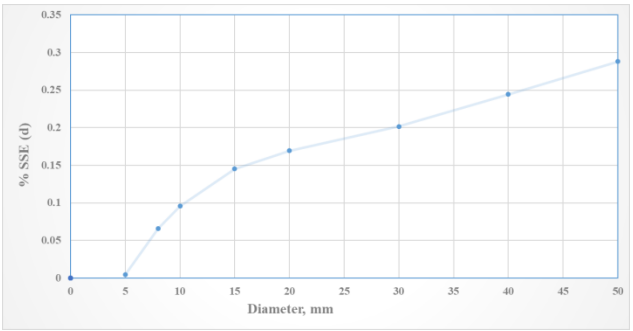

Figure 3. SSE function of the used TRT (indirect method), 6 mm spot at 590 mm distance

C. Further investigation

For further study to explore and correct for the SSE impact, in order to modify the measurement, we investigate the SSE through studying the uniformity profile at the exit aperture of the blackbody. We

ISBN 978-80-972629-6-9

move the TRT in both directions horizontal towards the blackbody (X-axis) and Vertically (Y-axis). The temperature distribution in terms of vertical and horizontal profiles was determined by moving the radiation thermometer in equal distances in both directions by using a 2D translation stage. Figure 4 shows the uniformity of temperature distribution in the Gemini R 550 cavity at set temperatures of 50 °C in both vertical and horizontal directions. We plan to make further measurements by moving over a larger range of distances from the furthest point along the measurement plane toward the source to use a variable-distance (i.e., FOV) approach, as shown in Figure 1 (bottom-right schematic) [from 7].

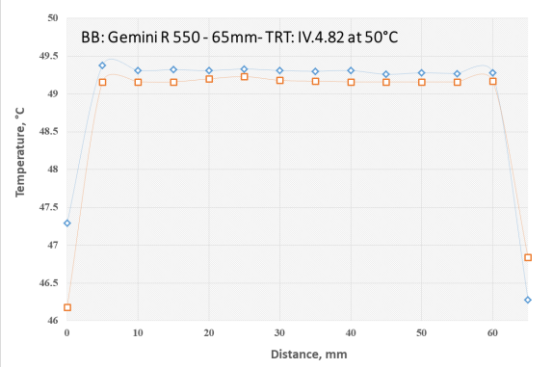

Figure 4. The temperature distribution in terms of vertical and horizontal profiles (x: red, y: blue)

3. Conclusions and future work

By employing blackbodies and apertures with precisely controlled temperatures, the direct method is used to assess the size-of-source effect (SSE) of the TRT. From 50 °C to 250 °C, we measured the SSE for the blackbody temperature. We found that the values of the SSE functions agree to within 0.08%. Applying the indirect method, the SSE function found to be less than 0.3%. Further work was done to assess the uniformity profile of the blackbody by scanning the TRT in two dimensions and relating SSE to the drawn profile is a scheme for future work. For future plan, to further assessment of the SSE, we decide to use both the changing distance (FOV) approach [7] and scanning slit approach [8].

Acknowledgements

Authors thank the Research and Studies Center (RSC) of SASO for considering this work.

References

[1] Yoon H W, Allen D W and Saunders R D. (2005). Methods to reduce the size-of-source effect in radiometers Metrologia 42 89-96

[2] Machin G and Ibrahim M (1999). A size of source effect and temperature uncertainty: II. Low temperature systems Proc. (TEMPMEKO 1999, Delft) Vol 2 pp 687-92

[3] Bloembergen P, Duan Y, Bosma R, Yuan Z (1996). The characterization of radiation thermometers subject to the size-of-source effect Proc. (TEMPMEKO 1996, Torino), 261-266

[4] Gutschwager B, Hollandt J, Jankowski T and Gartner R (2008). A vacuum infrared standard radiation thermometer at the PTB Int J Thermophys 29 330-40

[5] Bloembergen P (1999). On the Correction for the Size-of-Source Effect Corrupted by Background Radiation Proc. (TEMPMEKO 1999, Delft) 607-12

[6] Pusnik I, Grgic G and Drnovsek J (2006). System for the determination of the size-of-source effect of radiation thermometers with the direct reading of temperature Meas. Sci. Technol. 17 1330-6

[7] MSL Technical Guide 26 (2017). Size-of-Source Effect in Infrared Thermometers, Version 2.

[8] E M Vuelban (2013). Determining size-of-source effect using the scanning slit method, Meas. Sci. Technol. 24, 105007.

Experimental Identification of Characteristics of Hall Sensor Arrangement

Tatiana Kelemenová, Miroslav Dovica, Ivana Koláriková, Katarína Paľová, Ondrej Benedik

Technical University of Kosice, Faculty of Mechanical Engineering, Kosice, Slovakia
Email: tatiana.kelemenova@tuke.sk

Abstract. *Sensors based on the principle of the Hall effect are often used to measure the position of objects or their distance from a reference point. In this work, the ability of the selected sensor for the application of distance measurement is assessed. In these applications the measuring range is a few millimeters, and the effort is to develop a measuring system for measuring larger distances.*

Keywords: Sensor, Hall effect, Distance, Measurement

1. Introduction

Sensors based on the principle of the Hall effect are sensitive to a change in the magnetic field, and this change is indicated as a change in the electrical voltage at the output of this sensor. In this case, the change in magnetic flux density is realized by changing the position of the permanent magnet relative to the position of the sensor. From a practical point of view, it is sufficient to place a permanent magnet on an object that is moving, and its distance can then be monitored using this sensor (Fig. 1). The mutual change in the position of the sensor and the permanent magnet can be caused by various non-electric quantities, for example, a change in water level detected by a change in the height of a float or a change in fluid pressure detected as a change in the deformation of the membrane in the measuring chamber of the measuring system or a change in the position of a thermally expanded object during temperature measurement and other applications. In this way, a change in the position of the control lever or a change in the position of the active linear motion system of the actuator can be detected. It is also possible to measure the angular rotation of the detected rotating parts, such as the rotation of the shaft, lever or arm of the device.

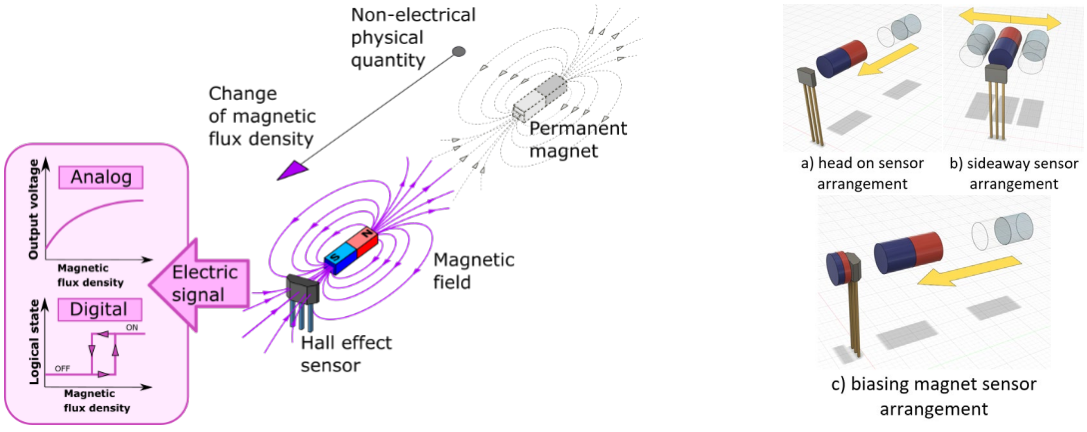

Fig. 1. Hall effect sensor measurement principle (left) and basic configurations of sensor and permanent magnet arrangement (right).

The variety of applications where this sensor can be used is quite large. From an electrical point of view, two types of Hall sensors are available, namely ratiometric sensors, where the change in the output voltage changes continuously according to the change in magnetic flux density or

ISBN 978-80-972629-6-9

distances, and we often refer to these sensors as sensors with an analog output, but it is non-linear, which causes a problem when converting this signal to a distance value. The second electrical variant of the Hall sensor is a binary sensor, which outputs only two values of electric voltage corresponding to the presence/absence of the permanent magnet. This second type is used in applications where we only need information about the presence or absence of a detected object with a permanent magnet. The permanent magnet is thus only used to mark the detected object (Fig. 1). Probably the only disadvantage is the sensitivity of this sensor to other secondary magnetic fields, which result, for example, from the use of electromagnetic actuators or other sources of magnetic fields in the applied system.

The process of activation and influencing the output voltage of the sensor is non-contact, so there is no mechanical wear of the sensor. The sensor housing allows the sensor to be used when immersed in liquids (water, oil) and also used in a chemically aggressive environment. This sensor has a very long service life [1 – 6].

2. Principles of Hall effect sensor arrangement

The active range of the sensor based on this principle depends on the used configuration of the sensor and the permanent magnet (Fig. 1). The movement of the magnet can be realized towards the front of the sensor ("Head-on detection") when the magnetic field of the magnet is oriented perpendicular to the active surface of the sensor (Fig. 1). Another option is lateral movement of the magnet relative to the active surface of the sensor ("Sideways detection"), in which the permanent magnet moves along the active surface of the sensor. The last option is the use of the pre-magnetized state of the sensor, the so-called biasing magnet sensor arrangement, when another permanent magnet is permanently placed near the sensor, which permanently creates a magnetic field of known intensity, and the permanent magnet connected to the detected object creates a change in magnetic flux density, which creates a change in the output voltage to sensor output. To detect the presence of ferromagnetic materials, it is possible to use a sensor based on the principle of the Hall effect in a configuration with a small pre-magnetizing permanent magnet ("biasing magnet") located behind the active surface of the sensor (Fig. 1). The sensor is thus in a constant magnetic field, and any change in the magnetic field caused by the presence of a ferromagnetic object will then be detected by this sensor.

3. Experimental identification of the characteristics of the head on sensor arrangement of the Hall effect sensor

This article documents the experimental investigation of the behavior of this sensor in head-on sensor configurations, when it is possible to create a total of eight different sensor-permanent magnet configurations (Fig. 2 left). These configurations H1 to H8 have a fundamental effect on the operation of the sensor.

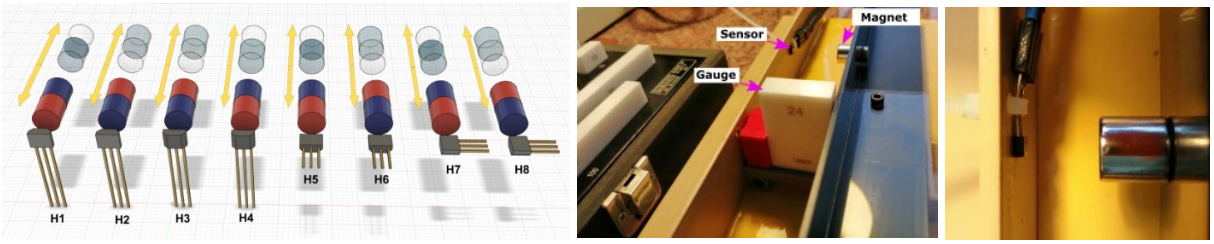

Fig. 2. Head on configuration of the sensor based on the principle of the Hall effect with permanent magnets (left) and a measuring stand for the investigation of the properties of the sensor based on the principle of the Hall effect (right).

ISBN 978-80-972629-6-9

For experimental identification, a measuring stand (Fig. 2 right) was created with the possibility of fine positioning of the permanent magnet relative to the active surface of the sensor. The mutual distance between the magnet and the sensor was set using ceramic parallel length gauges. During this experimental investigation, the hysteresis of the sensor was also monitored when the permanent magnet moved closer and further away from the sensor. The permanent magnet used in the experiments had a cylindrical shape with a diameter of 10 mm and different lengths of NdFeB material with axial anisotropic polarization with remanence 1.25 T and coercive force 907 kA/m.

4. Experimental results and discussion

From the point of view of the largest possible range of distance measurement and the minimal hysteresis of the sensor, the H4 configuration for a permanent magnet with a length of 30 mm was identified as optimal (Fig. 3). The influence of the length of the permanent magnet used was also monitored, where it was shown that the change in the length of the magnet only slightly affects the resulting characteristics of the sensor.

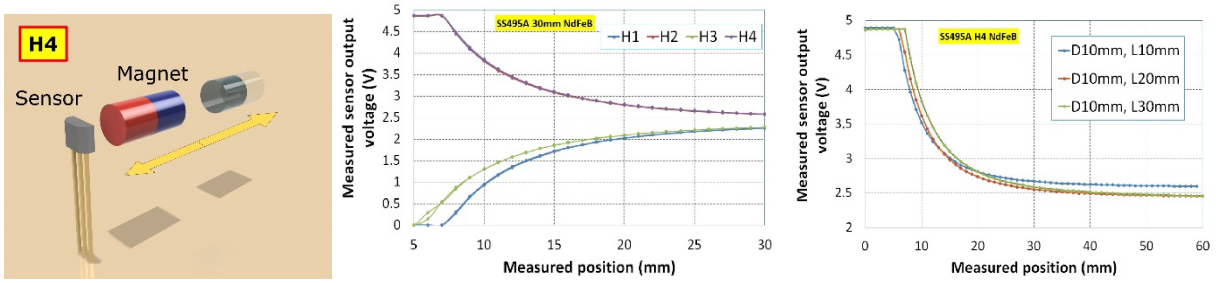

Fig. 3. The most advantageous arrangement of the H4 sensor and permanent magnet (left); dependence of the sensor's output voltage on its position relative to the permanent magnet with the diameter of 10 mm and the length of 30 mm (middle); the effect of different lengths of permanent magnets on the sensor's output voltage (right).

For practical use of this sensor, it is necessary to identify the calibration function of this sensor configuration. This function needs to be determined for each piece of the sensor and magnet due to the high variability of the characteristics observed for different pieces of the sensor and magnet. To determine the uncertainty of the measurement, repeated measurements were carried out and the uncertainty of the measurement was evaluated from them to determine the distance of the permanent magnet relative to the sensor (Fig. 4). Standard measurement uncertainties were determined according to the standard (EAL R2). To assess the stability of the measured distance, the dispersion of the measured data was also monitored using the standard deviation of the series of measurements (Fig. 4).

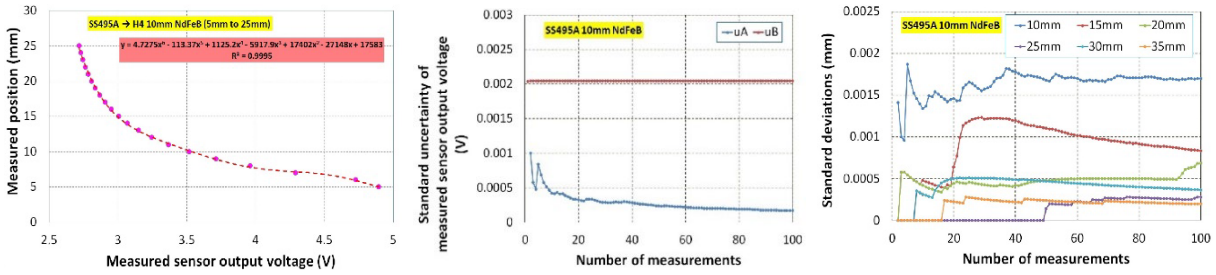

Fig. 4. Approximation of the calibration characteristic using a polynomial function (left); the standard uncertainties of the sensor output voltage measurement (middle); the standard deviations of distance measurement (right).

ISBN 978-80-972629-6-9

The tested sensor configurations enabled a maximum measurement range of only up to 25 mm. For practical use, it would be important to extend the measurement range of this sensor, so the measurement system for larger measurement ranges was designed in this work (Fig. 5). The construction of this measuring system consists of a piston with a permanent magnet, which is inserted into a cylinder with a fixed sensor based on the principle of the Hall effect. For the experiments, bar permanent magnets 10 x 120 mm and 24 x 64 mm were used. The measurement range has increased to 70 mm.

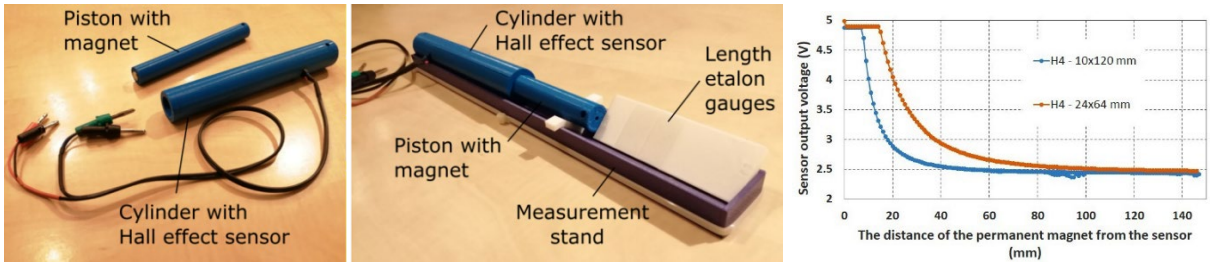

Fig. 5. Prototype of a measuring system with a Hall effect sensor for a larger measurement range (left) and experimental static characteristics of the sensor with different pistons with magnets (right).

5. Conclusions

In this work there were tested different configurations of sensors based on the principle of the Hall effect with permanent magnets of different sizes. The head on sensor configuration provided the best results in terms of measurement range and static characteristic hysteresis. For larger ranges, a measuring system with a guide in the shape of a piston and a cylinder was created.

Acknowledgements

The authors would like to thank the Slovak Grant Agency -project VEGA 1/0168/21 and KEGA 016TUKE-4/2021.

References

[1] Taylor, B.N. and Kuyatt, C.E., (1994). *Guidelines for Evaluating and Expressing the Uncertainty of NIST Measurement Results*, NIST Technical Note 1297.

[2] Taylor, J. R. (1996) *An Introduction to Error Analysis: The Study of Uncertainties in Physical Measurements.* Publisher: University Science Books; 2nd edition (August 1, 1996). Paperback: 327 pages. ISBN-10: 9780935702750.

[3] EA-4/02 1999. (1999) *Expression of the Uncertainty of Measurement in Calibration*. European co-operation Accreditation Publication Reference. December 1999.

[4] JCGM 100 2008 (2008). *Evaluation of measurement data – Guide to the expression of uncertainty in measurement* (ISO/IEC Guide 98-3). First edition September 2008. Available online: http://www.iso.org/sites/JCGM/GUM-JCGM100.htm

[5] JCGM 104 2009. (2009). *Evaluation of measurement data – An introduction to the "Guide to the expression of uncertainty in measurement"* (ISO/IEC Guide 98-1). First edition July 2009. Available online: http://www.bipm.org/en/publications/guides/gum_print.html

[6] JCGM 200. (2008). *International vocabulary of metrology – Basic and general concepts and associated terms* (VIM) 3rd edition (2008 version with minor corrections). © JCGM 2012 Available online: http://www.iso.org/sites/JCGM/VIM-JCGM200.htm

Device for the Sound Quality Measurement of Reeds

Norbert Palsovics, Martin Pustka, Jan Bělík, Pavel Žďárek

VÚTS, a.s., Measurement Department, Liberec, Czech Republic
Email: norbert.palsovics@vuts.cz

Abstract. *The test device was recently developed and realized, which meets the specific requirements for the reproducible sound quality measurement of reeds. The air flow through the reed with a small negative pressure is controlled by means of pressure sensor in the feedback. The device provides an objective assessment of A-weighted sound pressure level, relative harmonic spectrum, inharmonicity, air consumption and average intake pressure. The evaluated values are stored in the database and are available for further processing and comparison. The measurement is controlled and evaluated by means of PC application. The device functionality is verified by a regular use in R&D and production quality activities.*

Keywords: Reed, Test Device, Sound Measurement, Sound Quality

1. Introduction

Reeds in the form of a thin metal strip riveted at one end to a mounting plate (a reed plate) are the main source of the musical sound of accordions and harmonicas. The airflow in the slot between the vibrating strip and the mounting plate generates self-sustained pressure oscillations accompanied by sound emission with strong tonal components [1].

The assessment of basic acoustic parameters such as loudness or tonal spectrum plays an important role in the research and development of high-quality reeds or in the adjustment of production technology. As the commercially available devices for the analysis and tuning of musical instruments do not meet the requirements for sound quality measurement, a new test device based on similar equipment for the objective evaluation of pianos [2] was developed. The sensation of musical sound is subjective and covers many psychoacoustic aspects [3], which have to be expressed by objective parameters. The proposed device provides an objective assessment of reed sound quality by means of several indicators. The parameters of different reed samples can easily be compared.

2. Device description

Basic requirements

The device concept is based on the results of previous measurements and on the general experience with sound quality evaluation [2]. This determines following requirements for the device: The intake negative pressure can be adjusted automatically, with the basic measurement modes being -100 Pa and -400 Pa. The measured quantities are “loudness” in the form of A-weighted sound pressure level [dB], relative frequency harmonic spectrum (up to 10 harmonic components), inharmonicity [cent], air consumption [l/min] and intake pressure [Pa]. The frequency range of reed fundamental tones is from E1 (41.2 Hz) to cis5 (4434.9 Hz). All the measurements should be carried out reproducibly under stable measurement conditions. The sampling frequency must cover the hearing range of 20 Hz to 20 kHz. The simplicity of operation and the clarity of results representation is also required. The device should have reasonably compact dimensions for use in a small laboratory.

ISBN 978-80-972629-6-9

Final design and operation

The CAD model of the test device is shown in Fig. 1. The basic frame is made of duralumin profiles with the worktop and the electrical switchboard cabinet. To stabilize the airflow through the reed, the vacuum air tank with a volume of 0.04 m^3 is located partially under the worktop, with a side vent for connecting the adapter with reed samples. The 3D printed exchangeable adapter for a reed fixture, dimensionally similar to an accordion bridge, is fixed to the side vent using a lever clamp.

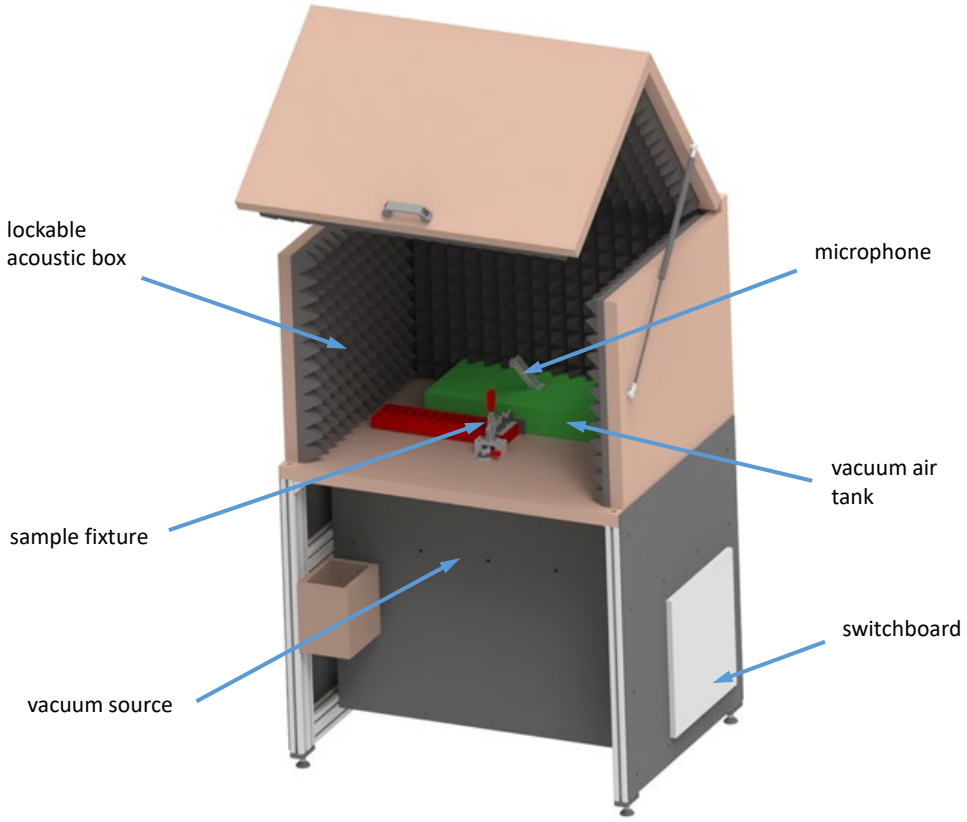

Fig. 1. General view on the measurement device for reeds sound quality measurement.

The worktop is covered by a lockable acoustic box made of MDF boards. The inner walls are equipped with Audiotec S220-070 noise insulation. The box has a volume of 0.27 m^3 and an inner wall surface of 3.46 m^2. The sound field inside the box differs from free-field conditions, so the reed sound emission is distorted in a defined manner. The effective acoustic parameters of the box (transmission loss and sound absorption coefficient) were determined experimentally for the device located in the reverberation chamber. The 1/3-octave spectrum of effective sound absorption coefficient α is shown in Fig. 2. The acoustic field inside the box turned out to be satisfactory for measurement purposes.

The source of a small negative pressure (up to approx. -1 500 Pa) is a hand-held vacuum cleaner powered by 12 V DC. The pressure level in the air tank is controlled by means of motor voltage using a pressure sensor (Cressto TMVG 328 N4H) as a feedback. The digital flow meter Sensirion SFM3000 is a part of the air inlet pipe. The sound pressure in the box is measured by means of 1/2" condenser microphone GRAS 46AE. The microphone is mounted on the console above the reed sample.

The signal measurement, data evaluation and device control are carried out using National Instruments CompactRIO and LabVIEW platforms.

ISBN 978-80-972629-6-9

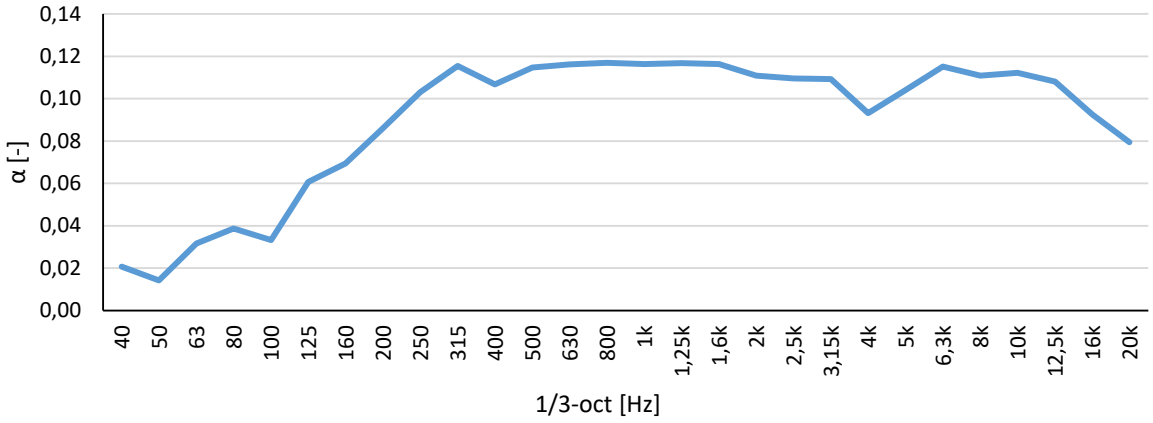

Fig. 2. Effective sound absorption coefficient α of the acoustic box

3. Measurement and evaluation procedure

Regarding the strong tonal character of reed sound emission, a specific evaluation procedure was proposed. The sound emission is characterized by common non-psychoacoustic quantities. All frequency values are compared with the nominal reed frequency f_0 [Hz] (tone pitch), its value is entered manually by the user before measurement.

The reed measurement is controlled and evaluated by means of application running on the PC, which is connected to the device via Ethernet port. The measurement starts after the stabilization of air pressure in the system. Then the time record of sound pressure with a duration of 10 seconds is performed at a sampling frequency of 51.2 kHz. The time record is A-weighted by an input analog filter. From the record, undermentioned acoustic parameters are evaluated.

Overall A-weighted sound pressure level L_{pA} [dB] is determined by means of linear averaging of the time record.

The frequency spectrum of sound pressure with components $\{f_i, A_i\}$ [Hz, Pa] and resolution of 0.1 Hz is calculated from the whole record length using FFT without time window [4]. The fundamental harmonic frequency f_1 (close to the nominal frequency f_0) and its higher components $f_n = n \times f_1$ ($n \leq 10$) are found in the spectrum. To eliminate the influence of the finite measurement time, the spectrum is reduced to harmonic components only. In the vicinity of each harmonic frequency, a band of ±10 Hz (i.e. ±100 lines) is selected, in which the total amplitude of the component is calculated as $\bar{A}_n = \sqrt{\sum_{-100}^{+100} |A_i|^2}$. The amplitudes $\bar{A}_n$ are further normalized with respect to the amplitude of the 1st harmonic as $\bar{\bar{A}}_n = \bar{A}_n / \bar{A}_1$. The components $\{f_n/f_1, \bar{\bar{A}}_n\}$ form the final relative harmonic spectrum of the reed.

Inharmonicity r [cent] is obtained from the relation $r = 1200 \log_2(f_1/f_0)$.

The remaining values of air consumption [l/min] and intake pressure [Pa] are calculated as the average value within the recording time of 10 seconds.

The evaluated values are stored in the XML data file and are available for further processing. The user can gradually create a database of reed measurements and obtain standard data for comparison. The measurement results are continuously displayed in the window of the control application (Fig. 3). In the post-processing, the comparison of parameters of up to ten reeds is possible by means of graphic representation.

ISBN 978-80-972629-6-9

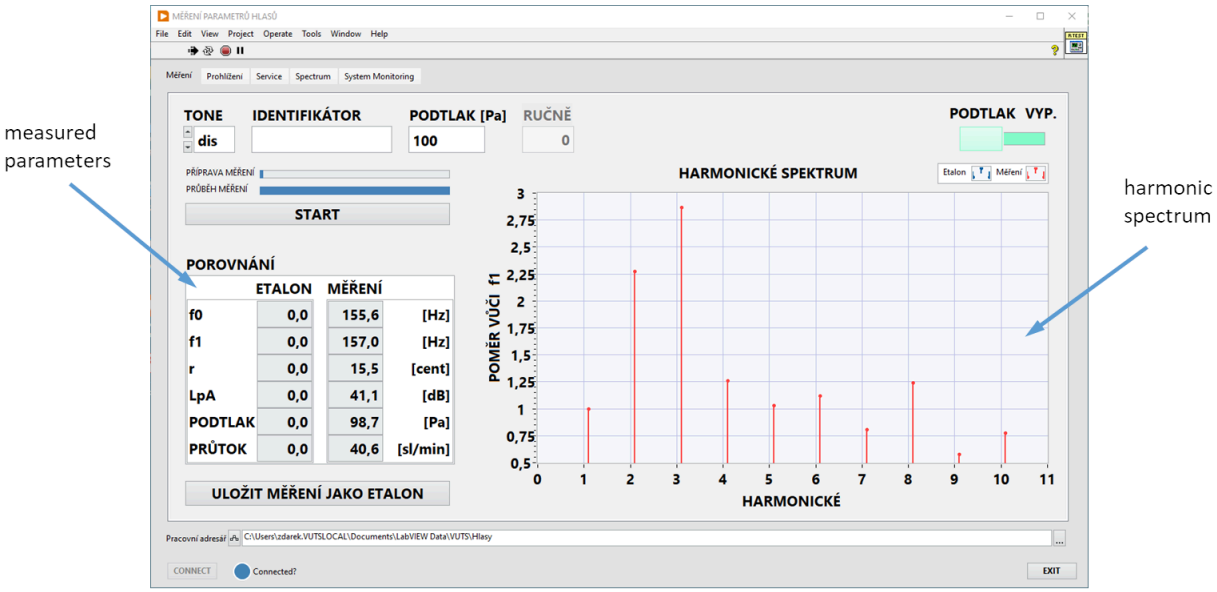

Fig. 3. Default graphic interface of the control application (Czech version only)

4. Conclusions

The test device was recently developed and realized which meets the specific requirements for the sound quality measurement of reeds. This device is regularly used for research and development activities or for production quality monitoring. The measured acoustic parameters are slightly affected by the acoustic box properties, but this influence is invariable and the same for all measurements.

The measurement evaluation can be further enhanced to include the calculation of psychoacoustic parameters as Zwicker loudness or sharpness [5], which better describe the subjective perception of sound. The audibility of reed sound can be assessed objectively by means of the standardized threshold of the hearing curve.

Acknowledgements

This work was supported by the Czech Ministry of Industry and Trade in the framework of the institutional support for long-term conceptual development of research organization - recipient VÚTS, a.s.

References

[1] Ricot, D., Caussé, R., Misdariis, N. (2005). Aerodynamic excitation and sound production of blown-closed free reeds without acoustic coupling: The example of the accordion reed. *The Journal of the Acoustical Society of America*, 117 (4), 2279-2290.

[2] Urbánková, J. (2018). Objective evaluation of upright and grand pianos by measuring play-bench. *ACC Journal*, 24 (1), 43-51.

[3] Terhardt, E. (1978). Psychoacoustic evaluation of musical sounds. *Perception & Psychophysics*, 23, 483-492.

[4] Bracewell, R. N. (2000). *The Fourier transform and its applications*. McGraw Hill.

[5] Fastl, H., Zwicker, E. (2006). *Psychoacoustics: Facts and models*. Springer.

Metrological Aspects of Pollutant Content Monitoring in Water Streams

Pavel Neyezhmakov, Alexander Prokopov, Vladimir Skliarov

National Scientific Centre, Institute of Metrology, Kharkiv, Ukraine
Email: vladimir.skliarov@gmail.com

Abstract. *The procedure of selecting sampling points (or arranging appropriate measurement sensors) for monitoring pollutants in water streams with varying concentrations of pollutant admixtures along the cross-section is substantiated. The requirements for the uncertainty of measurements carried out with the help of sensors or in the process of laboratory analysis of the samples taken have been established.*

Keywords: Pollution Monitoring, Sensors, Sampling, Varying Concentration

1. Introduction

Among the actively developing methods of environmental monitoring, methods of controlling pollutants in water bodies currently occupy an important place. Such methods often use either the results of measurements of pollutant concentrations performed by means of sensors placed on a water body or the results of laboratory analysis of polluted water samples taken in cases when the necessary sensors are not available.

The information obtained from the sensors or by analyzing samples allows one to determine the concentration of pollutants in the control station of the water flow, which must not exceed the maximum allowable concentration.

Unfortunately, the regulatory documents operating in Ukraine do not clearly formulate the rules defining specific sampling sites or installation of sensors. In particular, the documents implementing the main provisions of the European standards of ISO 5667 series, states only that in all cases, you must choose a sampling place, for which you can get a representative sample [1], at the same time in [2] it is noted that the source of errors when taking samples may be the heterogeneous composition of the water body.

In the present work, there is substantiated a strict (from the metrological point of view) procedure for selection of sensor or sampling points for water streams with varying concentrations of pollutant admixtures along the cross-section of the monitoring station. The relations are presented, establishing the requirements for the uncertainty of measurements, carried out with the help of sensors or in the analysis of samples.

2. Subject and Methods

The theoretical basis of the discussed procedure is generally based on the following principles.

Firstly, the pollutant concentration averaged over the cross-section of the flow is expressed through the double integral over the cross-sectional area of the control section with a subintegral function describing the dependence of pollutant concentration on the coordinates in the cross-sectional plane.

Secondly, this integral, with the help of known quadrature formulas, is represented as a function of local values of concentration of pollutants determined at the points, which should correspond to the points of installation of sensors (or sampling). The residual term of the quadrature formula

ISBN 978-80-972629-6-9

used, which is not taken into account when processing the measurement results, determines the methodological component of the uncertainty of the final result of the considered procedure. It must be evaluated in order to establish the conditions under which it can be neglected (not to take into account the above methodological component of the uncertainty in determining the average concentration of contaminants).

3. Results

In order to simplify the description, we present the results for the case of a control section with a shallow flow depth, when the problem is reduced to one-dimensional (there is no dependence of pollution concentration on the depth). In this case, the model of measurement of average pollution concentration Y over the control section can be represented by integral dependence of the following type

$$Y = (x_n - x_0)^{-1} \int_{x_0}^{x_n} f(x)dx\,, \tag{1}$$

where $f(x)$ as the dependence of pollutant concentration on *x*-coordinate, counted across the stream from point x_0 to point x_n, located on the opposite sides of the stream. For the quadrature trapezium formula, for example, formula (1) when dividing the integration interval $x_n - x_0$ into n equal parts by points x_i, where local values of the function $f(x_i)$ are determined, can be presented as $Y = Y_{tr} + R_{tr}$, where in the relation

$$Y_{tr} = \frac{1}{n_{\min}} \left\langle \frac{f(x_{n_{\min}}) - f(x_0)}{2} + \sum_{i=1}^{n_{\min}-1} f(x_i) \right\rangle \tag{2}$$

as *n*, the minimum number of partition sections $n_{\min}$, at which the residual term becomes negligibly small, is used. The value of $n_{\min}$ is determined by numerical experiment, which achieves the necessary closeness of the results obtained using formulas (1) and (2). For the found value of $n_{\min}$, as a model of measurements determining locations of sensors (or sampling) in the control section, the formula (2) is valid. This formula is necessary both for processing the results of measurements and for substantiation of the ratio for the uncertainty u_{Ytr} with which the average concentration of pollutants Y_{tr} is determined along the section of the check station. The resulting value u_{Ytr} must not exceed the limit value $u_{\lim}$, established on the basis of the relevant regulatory documents

$$u_{Ytr} \le u_{\lim}.$$

Based on these considerations are formulated requirements for the uncertainty $u_{f(x)}$ with which it is necessary to determine the local values of contaminant concentrations at sampling points (sensor installation)

$$u_{f(x)} \le u_{\lim} \times n_{\min} \times \sqrt{\frac{2}{2n_{\min} - 1}} \tag{3}$$

If inequality (3) is not fulfilled, it is possible to increase the number $n_{\min}$ to the value necessary for fulfilment of this inequality. Such an increase does not violate the conditions discussed above, the fulfilment of which is necessary to discard the residual term and neglect the corresponding methodological component of uncertainty.

ISBN 978-80-972629-6-9

4. Discussion

The described methodology is also applicable for more complex and cumbersome quadrature relations, including relations that allow considering variants of the non-uniform location of sensors (sampling points) in a control section. NSC "Institute of Metrology" successfully uses this methodology for determining the mean integral refractive index of the air from measurements by temperature, pressure and humidity sensors in the European joint research project named EMPIR 18SIB01 GeoMetre Large-scale dimensional measurements for geodesy. The results obtained within this project (see [3], [4] and the literature cited therein) confirm the high accuracy of the developed methods for representing integral quantities by a set of subintegral value functions on the integration interval in the problems of accounting for the influence of a non-uniform atmosphere on the laser ranging measurement results.

5. Conclusions

For experimental verification of theoretically substantiated recommendations of the present article, known sensors of pollution control in water mediums are applicable. Taking into account the results of such testing, changes in normative documents determining sampling locations (or installation of sensors) for monitoring of pollution in water streams can be recommended.

References

[1] DSTU ISO 5667-10:2005. Water quality. Sampling of water. Part 10. Guidelines for wastewater sampling (ISO 5667-10:1992, IDT) (In Ukraine)

[2] DSTU ISO 5667-14:2005. Water quality. Sampling of water. Part 14: Guidelines for quality assurance of natural water sampling and processing (ISO 5667-14:1992, IDT) (In Ukraine)

[3] Neyezhmakov, P., Kupko, V., T. Panasenko, T., Prokopov, A., Skliarov, V., Shloma, A. (2020). Analysis of accuracy requirements to the meteorological sensors used to compensate for the influence of the Earth's atmosphere in high precision length measurement. *Proceedings of SMSI 2020 Conference.* Nuremberg, Germany. June 2020, 279 –280. https://doi.org/10.5162/SMSI2020/D3.3

[4] Neyezhmakov, P., Prokopov, A., Panasenko, T., Skliarov, V., Shloma, A. (2021). Towards the assessment of the accuracy of measuring the integral characteristics of physical quantities using the sensors of discrete values of these quantities. *Proceedings of SMSI 2021 Conference*. Nuremberg, Germany (digital). May 2021, 310-311, https://doi.org/10.5162/SMSI2021/C9.2

ISBN 978-80-972629-6-9

The Traceability of the Results of Measurement in Additive Manufacturing in Ukraine

[1]Vladimir Skliarov, [1]Valeriy Aschepkov, [2]Kirill Neyezhmakov

[1] National Scientific Centre "Institute of Metrology", Kharkiv, Ukraine,
[2]Kharkiv National University of Radio Electronics Kharkiv, Ukraine
Email: vladimir.skliarov@gmail.com

Abstract. *The national measurement standards from the point of view of traceability of the results of measurement in additive manufacturing in Ukraine are considered in the paper. The metrological characteristics of the national primary measurement standards in the field of ranges geometric measurements which took part in international comparisons within COOMET projects, are presented. The accurate of ranges geometric measurements are the key ones in controlling the quality of additive manufacturing. Accordance to the areas of the technology of additive manufacturing, the ways of improving the national measurement standards of Ukraine for the growing needs of metrology of additive manufacturing are considered.*

Keywords: Nanoscale Range, Additive Manufacturing, Metrological Assurance, Traceability, Modelling, National Measurement Standard.

1. Introduction

Since AM is based on the concept of constructing an object through the sequential application of layers of a material, the main parameter that characterizes the accuracy of constructing an object is the thickness of the layer of material from which the object is constructed, that is, the layer of application.

Thus, the accuracy of 3D printing is the minimum allowable layer height printed by 3D printer. Modern FDM (Fusing Deposition Modelling) 3D printers can provide a thickness of up to 20×10^{-6} m (20 μm). The fusing deposition modelling of the object enables the measurement of roughness parameters Ra, Rz and Rmax of not worse than 50 μm. In addition, an important element of the final stage of AM is to reduce the roughness of the surfaces of the constructed object.

The reduction of roughness of the object is performed using appropriate solvents or laser polishing, which reduces roughness to 1.4μm that can not be achieved by mechanical processing [1-3].

2. The ranges of measurement in additive manufacturing

Analyzing AM technology, it should be noted that almost all technologies have modes of temperature influence on the process of reproduction of the object - sintering, melting, fusing deposition, adhesion, handling of molten metal. Thus, almost all additive manufacturing technologies have corresponding temperature modes of manufacturing, that is, it is important to measure the temperature of the material and the temperature modes in 3D printer case. The range of temperature modes is within the melting and heating up of the materials, it is maintained in the range from 200^0C (for polymers) to 3150^0C (for titanium), in addition, it is important to measure the temperature when the gradual cooling of the object during hardening (corresponding requirements to the cooling time) [4, 5].

Table 1. The ranges of measurement in additive manufacturing.

Section	Range of values of AM characteristics
Minimum permissible height of the printing layer, [μm]	5 to 20
Minimum surface roughness of the object, [μm]	2 to 5
Temperature of additive manufacturing,[^{0}C]	200 to 3150
Laser radiation power, [W]	70 to 15000
Wavelength of laser radiation, [nm]	360 to 1064
Laser beam travel speed, [m/min]	0.2 to 60
Time of effect of laser radiation, [ms]	2 to 6
Viscosityat1000C, centipoise (cP)	1 to 200
Material density, [kg/m3]	1 to 2380
Pressure, [MPa]	10 to 20

3. National measurement standards in the field length

The national measurement standards are the integral part of the national metrological system and provide the reproduction of measurement units and the transfer of their sizes by means of the secondary measurement standards to working measuring instruments, which are exploited in the manufacturing and non-manufacturing spheres.

As of January 1, 2022, there are 81 national measurement standards in Ukraine that provide reproduction, maintenance and transfer of the units of physical quantities. In accordance with the Law of Ukraine “On Metrology and Metrological Activity” [6] and the Program for the Development of the Measurement Standards for 2018-2022 [7], scientific and design work on the creation of the new national measurement standards and secondary measurement standards as well as improving the existing ones in Ukraine is ongoing.

The National Science Center "Institute of Metrology" is the leading organization, as it ensures the unity, reliability and traceability of geometric measurements in Ukraine.

The calibration and measurement capabilities (CMCs) of Ukraine in the field of geometric measurements are provided by 4 national measurement standards National Standard of the length unit for evolvement surfaces and tilt angle of tooth trace, National Standard of the length unit in the field of measurement of deflections from linearity and planarity, National Standard of the length unit from 0,01 mm to 1000 mm, National Standard of the length unit in the field of measurements of the parameters of roughness and 12 secondary measurement standards.

Metrological characteristics of 4 national measurement standards of geometric parameters of NSC “Institute of Metrology” which are responsible for AM are given in Table 2.

ISBN 978-80-972629-6-9

Table 2. National measurement standards in the field length.

Name of the measurement standard	Range of values of metrological characteristics	Expanded uncertainty [μm]
The national primary measurement standard of length unit for the parameters of evolvement surfaces and tilt angle of tooth trace	circle radius - 37 mm to 150 mm tilt angle of tooth trace on its width 10 mm to 160 mm	0.5 μm 0.7 μm
The national primary measurement standard of length unit for deflections from linearity and planarity	0 μm to 10 μm	$2 \cdot 10^{-1}$ μm
The national primary measurement standard of length unit	$1 \cdot 10^{-6}$ m to 1 m	$6 \cdot 10^{-11}$ m
The national primary measurement standard of the length unit for measurements of the parameters of roughness R_{max}, R_z and R_a	0.025 μm to 1.0 μm 1.0 μm to 1600 μm	0.007 μm 0.006 μm

For the national primary measurement standard of length unit, the given expanded uncertainty of 10^{-11} m is the result of interference of laser optical waves – optical frequency beating.

The traceability of geometric measurement results is provided via the results of international comparisons and the availability of CMCs in KCDB (Key Comparisons Date Base) [8].

As of January 2022, 14 international comparisons were performed with COOMET and EURAMET member countries and 28 CMCs were published. This particular group of measurement standards provides the most important parameters of AM – the geometric and spatial dimensions of the object.

4. Conclusion

The national standards of Ukraine, as can be seen from Table 2, fully meet the current requirements to ensure the traceability of measurement results for the above examples of AM.

Promising for further improvement of national standards of Ukraine in the field of geometric measurements is the creation of national standards for measuring Nano ranges of length.

Another promising area of research is the improvement and harmonization of the existing regulatory and legal, regulatory and technical framework for additive production.

Acknowledgements

The authors are grateful to Dr. Volodymyr Kupko and colleagues from Scientific and Research Laboratory of the Length and Size of National Scientific Centre Institute of Metrology for they valuable discussion and suggestions concerning the results international comparisons in the field of nanoscale range and advices when structuring and writing this paper.

References

[1] Sikder, S., Barari, A., Kaji, F., Kishawy, H., "Using Acetone Vapour Treatment to Improve Secondary Finishing Operations in Additive Manufacturing, " Proc. ASPE, 3898, 2 (2014)

[2] Alfieri, V., Argenio, P., Caiazzo, F., Sergi, V., "Reduction of Surface Roughness by Means of Laser Processing over Additive Manufacturing Metal Parts", Materials, 10(1), 30 (2017).

[3] Willenborg, E., [Polishing with Laser Radiation], Kunststoffe international, 97, 6, 37-39 (2007).
[4] Gibson, I., Rosen, D., Stucker, B., [Additive Manufacturing Technologies: Rapid Prototyping to Direct Digital Manufacturing], Springer, New York, 498 (2014).
[5] http://www.matweb.com
[6] Law of Ukraine "On Metrology and Metrological Activity" dated June 5, 2014 No. 1314-VII [Electronic resource]. - Mode of access: http://zakon2.rada.gov.ua/laws/show/1314-18.
[7] “Program for the Development of the Measurement Standards for 2018-2022” No. 1041 of December 28, 2016, [Electronic resource]. - Mode of access: http://zakon2.rada.gov.ua/laws/show/1041-2016-%D0%BF.
[8] https://kcdb.bipm.org/.

Concept of in Situ Metrological Service of Analog-to-Digital Converters for Devices Compatible with the Internet of Things

[1]Xu Aibo, [2]Orest Kochan, [3]Krzysztof Przystupa, [2]Volodymyr Kochan

[1]Wuhan Fiberhome Technical Services Co.,Ltd, Wuhan, China,
[2]School of Computer Science, Hubei University of Technology, Wuhan, China
[3]Department of Automation, Lublin University of Technology, Lublin, Poland
Email: orest.v.kochan@lpnu.ua

Abstract. *The methods for determining error due to nonlinearity of analog-to-digital converters (ADCs) during operation by averaging voltage drops across resistors of the same nominal resistance are summarized. The components of errors of determining the nonlinearity of the ADC are estimated. The properties of the methods were compared, and the best ones were selected for different operating conditions.*

Keywords: Analog-to-Digital Converters, Metrological Service, Voltage Divider

1. Introduction

The laboratory calibration of the analog-to-digital converters (ADC) requires its dismantling, which is highly labourious and costly. Therefore, determination of instantaneous error for the ADC in situ is a relevant problem. The existing metrological service (MS) is laborious because required ADC calibration in a laboratory. The portable devices for MS to determine the ADC error in situ are expensive. There are known methods to determine the additive error of the ADC without standards by shorting the ADC input. To determine the ADC's multiplicative error, a reference voltage source (RVS) is needed, which transfers the value of the voltage reference [1] to the ADC. However, only the monitoring of nonlinearity error allows estimating the net ADC's error. The known methods for determining ADC's nonlinearity using resistor voltage dividers of different nominal resistances and calibrators based on them require accurate resistors [2]. However, they have low metrological reliability. On the other hand, the methods based on averaging the voltage drops across resistors of the same nominal resistance have high metrological reliability [3]. The goal of this article is to generalize the methods for determining ADC's nonlinearity and compare their properties.

2. The Methods of Determining ADC's Nonlinearity

Fig. 1 shows wiring of the ADC ad voltage divider. It consists of resistors of the same nominal resistance $R1...Rn$ in series, and the RVS En ,. The Kirhhof voltage law:

$$En = \sum_{i=1}^{n} U_{Ri} \tag{1}$$

where U_{Ri} are voltage drops across R_i , $i = \overline{1,n}$. the average voltage drop across $\overline{U_{Ri}}$ is

$$\overline{U_{Ri}} = \frac{1}{n} \sum_{i=1}^{n} U_{Ri} \tag{2}$$

Substituting (1) into (2), we get

$$\overline{U_{Ri}} = \frac{1}{n} En \tag{3}$$

ISBN 978-80-972629-6-9

When estimating errors (3), we get

$$\delta_{\overline{URi}} = \delta_n + \delta_{En} \tag{4}$$

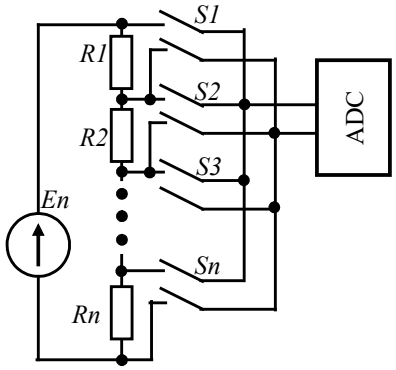

Fig. 1. The basic method for determining ADC nonlinearity

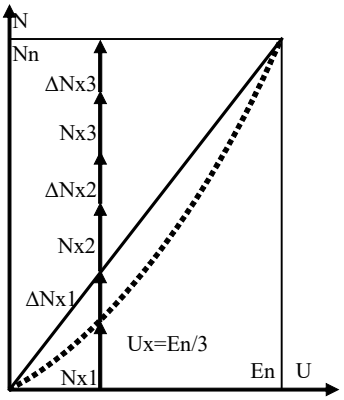

Fig. 2. Determination of ADC's nonlinearity

But n is the number of resistors, therefore $\delta_n = 0$. Thus $\delta_{\overline{URi}} = \delta_{En}$, that is, resistance variations of the divider resistors do not affect the average voltage drop across them. Nyquist noise, created by the divider resistors, affects the error $\delta_{\overline{URi}}$ [3]. For instance, the estimation for the 2.5 V measurement range of ADC, 1 Hz bandwidth (a precision sigma-delta ADC) and $R1 = ... = Rn = 1\ k\Omega$ the noise voltage will not exceed 5 nV, which corresponds to the 29-th bit of ADC. Thus, if one measures the average voltage drop across resistors of the same nominal resistance, the voltage divider becomes an almost ideal measuring transducer. Determining the absolute error of the ADC's nonlinearity for n=3 is illustrated in Fig. 2. The x-axis is the ADC input voltage, and the y-axis shows the code of measurement result. The nominal conversion characteristics (CC) of the ADC is shown by a solid line, the real CC is shown by a dashed line.

From Fig. 2:

$$Nn = Nx1 + \Delta Nx1 + Nx2 + \Delta Nx2 + Nx3 + \Delta Nx3 \tag{5}$$

Since $R1 \approx R2 \approx R3$ we get $Nx1 \approx Nx2 \approx Nx3$. Then for the ADC with continuous CC we can write $\Delta Nx1 \approx \Delta Nx2 \approx \Delta Nx3$. Transforming (5), to $\Delta Nx = \left(Nn - Nx1 - Nx2 - Nx3\right)/3$. Taking into account the results of the measurement of zero $N0$ and reference voltage Nn (this is essential), for $i = \overline{1,n}$, we get the expression as follows

$$\Delta Nx = \left(Nn - N0 - \sum_{i=1}^{n} \left(Nxi - N0\right) \right) / 3 \tag{6}$$

To rise the number of points, we choose n with the maximum number of divisors, e.g. $n = 12$. We determine the nonlinearity at the points $En/12$, $En/6$, $En/4$, $En/3$, $En/2$, i.e. voltage drops across each resistor, resistor pairs, resistor triplets, resistor quadruplets, resistor sextets, respectively. The distribution of the points over the range is shown in Fig. 3 (the basic method). The points are located in the lower half of the range. Therefore, the error in the top part of the range rises. To cope with it a few methods exist. In method 1 the additive, multiplicative and nonlinear (AMN) components of ADC error are determined by the basic method. Then correction of the ADC error for that range. Next measuring voltage drops across half of the divider resistors, switching to two times narrower ADC range of measurements and subsequent calibrating the ADC on this range using the measured voltage drops across divider resistors.

ISBN 978-80-972629-6-9

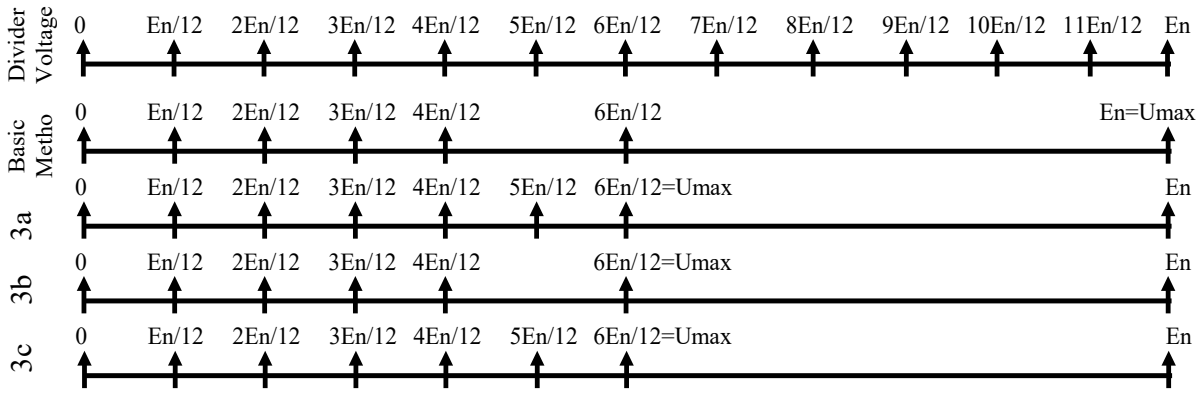

Fig. 3. The distribution of reference points for the considered methods of ADC calibration

The distribution of reference points is uniform (see Fig. 3a), which increases the accuracy. The disadvantage is many additional measurements. Method 2 determines the AMN on a certain range. Then correction of the ADC error for that range. Next measuring the voltage drops across 4 and 6 resistors, switching to two times narrower ADC range and repeat the basic method. The ADC on this range is calibrated using the repeated implementation of the basic method and previously measured voltage drops across 4 and 6 resistors. The distribution of reference points is in Fig. 3b. The advantage is the presence of a calibration point in the range's upper half, the disadvantage is a rise of the error. Method 3 determines the AMN components of the ADC error in a certain range. Then correcting the ADC error for that range. Next measuring the voltage drops across 4, 5 and 6 resistors, starting from the ground, switching to two times narrower ADC range and repeat the basic method. The ADC on this range is calibrated using the results of the repeated implementation of the basic method and previously measured voltage drops across 4, 5 and 6 resistors of the divider. The distribution of reference points is in Fig. 3c. The advantage is the uniformity of the reference points, and the disadvantage is some increase of the error. Method 4 involves determining the AMN components of the ADC error on the range three to four times wider than the required one, switching to the required measurement range and calibration of the ADC using the previously measured voltage drops across the resistors. Method 5 determines the AMN in a certain range. Then correcting the error, measuring voltage drops across all resistors, calculating the total voltage drop across all resistors (in the ascending order) and calibrating the ADC using the calculated total voltage drops across the resistors. We can obtain 11 uniformly distributed calibration points in a range. Method 6 consists of re-switching of the resistors in such a way that at several implementations of the basic method, the voltage drops across individual resistors of the divider appear in the results equally frequently. For instance, there are 4 resistors. We determine the error at the points of *En/4* and *En/2* by the basic method. When determining the error at the point *3En/4* the basic method is used twice. In the first case, the order of turning on the resistors in the divider is *R1, R2, R3, R4* and in the second one - *R1, R3, R2, R4*. So, when calculating the current error we get an equation similar to (6), in which the resistances appear twice, and their errors are mutually compensated. The advantage is a small number of switches and a simple algorithm for measurement data processing.

3 Results of Studies

The influence of the maximum resistance deviation of 1% of the resistors from their mean and the ADC noise on the ADC error was studied by the Monte Carlo method. There were considered 100 random polynomials of the 5-th order, with maximum magnitude of at least 50% of the maximum nonlinearity. AD7714 [3] with the maximum nonlinearity 250 quanta and maximum uniform noise of 8 quanta was used. The results are in Table 1. The least significant bit is denoted as q.

ISBN 978-80-972629-6-9

Table 1. The errors of determining the systematic error of the ADC

	Basic method	Method 1	Method 2	Method 3	Method 4	Method 5	Method 6
# of resistors	12	12	12	12	12	12	4
Number of points	5	5	4	5	3	11	3
Uniformity points	No	Yes	No	Yes	Yes	Yes	Yes
Error due to scattering of resistors' resistance	0.03q	1.6q	0.5q	2.5q	0.5q	0.03q	0.02q
Error due to switch resistances	None	None	None	None	None	None	10q
ADC noise	≈3.5 Qnz	≈3 qNZ	≈4 qNZ	≈2 qNZ	≈qNZ	≈2.5 qNZ	≈qNZ
# of ADC switches	26	26	26	26	26	26	12
Error of leakage of current of switches	1.8q	1.8q	1.8q	1.8q	1.8q	1.8q	q
The total error of the 24-bit ADC	22q	20q	25q	15q	7q	16q	16q
# of measurements	27	32	54	55	25	54	14

The methods 4 and 6 are the most accurate, reducing nonlinearity by 35 and 16 times, respectively, but provide little calibration points. Method 5 provides most of calibration points.

4. Conclusions

The built-in MS system allows significantly increasing the ADC accuracy and metrological reliability [3]. The error is determined mainly by the RVS, so, it is reasonable to specify the errors separately for the ADC alone, and for the RVS. It is necessary to specify the period of replacement of the RVS. The net measurement error is the sum of the errors of the ADC and the calibration voltage source.

References

[1] Webster, J. (1998). The measurement, instrumentation and sensors handbook. CRC press.

[2] Kochan R., Kochan O. (2007). Method of ADC's Nonlinearity Identification. In IEEE International Workshop IDAACS'2007, pp. 14 – 17.

[3] Kochan R. (2012). High precision analog to digital converters with metrological selfcalibration in situ. Lviv. (In Ukrainian).

ISBN 978-80-972629-6-9

Correcting Measurement Error due to Heating by Operating Current of Resistance Temperature Detectors

[1,2]Orest Kochan, [1]Huihui Tian, [1]Jun Su, [3]Krzysztof Przystupa, [2]Roman Kochan, [2]Elvira Dhzumelia, [4]Nataliia Kochan, [2]Ihor Likhnovskyi

[1]Hubei University of Technology, Wuhan 430068, China
[2]Lviv Polytechnic National University, Lviv, Ukraine
[3]Lublin University of Technology, Lublin, Poland
[4]Ivan Franko National University of Lviv, Lviv, Ukraine
Email: orest.v.kochan@lpnu.ua

Abstract. *The assessment of temperature measurement errors by platinum resistance temperature detectors (RTD) was carried out. High measurement accuracy assured with their individual calibration, the voltage divider circuit for measuring resistance, the substitution method and the transitional measure. In this case, error due heating the RTDs by their operating current needs correction. The proposed method of correction of RTD's error due to heating by the operating current decreased this error in two times. The residual error was estimated to be no more than 0.004°C.*

Keywords: Platinum Resistance Temperature Detector, Self Heating, Resistance, Temperature

1. Introduction

Nowadays the conventional platinum resistance temperature detector (PRTD) [1] is the most accurate widely available temperature sensors up to 500 °C [2]. A necessary condition for obtaining high accuracy is the individual calibration to determine individual conversion characteristics (CC) of the PRTD. In this paper we analyze how to achieve high accuracy using the PRTD. When powering the RTD using either a current or a voltage stabilizer with a resistor in series [1] in the four-wire configuration, the lead wires do not increase the measurement error, but accurate measuring instrument is needed. The voltage divider to measure RDT's resistance [3], given in Fig. 1, is the most accurate. The RTD's resistance R_{RTD} is calculated using the measured voltage drops across the RTD U_{RTD} and the reference resistor U_{RN}, whose resistance equals RN [3]

$$R_{RTD} = RN\left(U_{RTD} / U_{RN}\right) \quad . \tag{1}$$

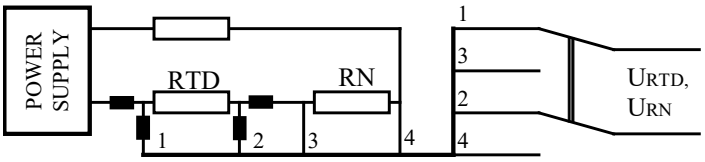

Fig. 1. . Voltage divider circuit to measure RTD's resistance

As can be seen from (1), the error of measuring the RTD's resistance δ_{RTD} is mainly determined by the error of RN. The error of the ratio $\left(U_{RTD} / U_{RN}\right)$ is determined only by the random error of the ADC and its nonlinearity [2]. The resistance of two lead wires (black segments in Fig. 1) affects only the current in the measuring circuit, whose changes are taken into account by (1) when measuring the voltage drop across RN. The other two lead wires (of

the order of tens of Ω) construct a voltage divider with the input resistance of the ADC (of the order of MΩ), that is, their influence is very little. Thus, the error of measuring the RTD's resistance using the circuit shown in Fig. 1 is determined by:

1. the resistor error of RN $\delta_{RN}^{M} \le 0{,}02\%$ $(0{,}05°C)$ and its temperature $\delta_{RN}^{T} \le 0{,}01\%/10°C$ $(0{,}025°C)$ and temporal $\delta_{RN}^{\tau} \le 0{,}008\%/2000h$ $(0{,}02°C)$ instabilities [1, 3];
2. the error of the voltages ratio across the RTD and the reference resistor, is determined by the random error and nonlinearity of the ADC [2]. For the modern precision 24-bit sigma-delta ADC, these errors do not exceed 0.0001% (0.00025° C) and 0.0016% (0.004 °C) respectively. But the RTD's resistance changes within a limited range when measuring the temperature. Thus, the influence of the nonlinearity of the ADC is small (0.002° C);
3. normal mode rejection ratio is $K_{NMR} \ge 60dB$ and common mode rejection ratio is $K_{CMR} \ge 120dB$ for the 24-bit sigma-delta ADC [2]. In laboratory conditions - 0.002° C;
4. error due to the parasitic thermal electromotive forces in the measuring circuit, which, when using reed relays with a thermal equalizer [2], does not exceed 1 μV (0.002° C).

Thus, the net error of resistance measurement using the circuit in Fig. 1 is equivalent to 0.06 °C. According to the analysis above, this error is mainly determined by the errors of the reference resistor RN. The contribution of its error can be reduced when resistance RN is measured using the standard resistor of the 1-st accuracy class. Then $\delta_{RN}^{M} \le 0{,}013\%$ $(0{,}03°C)$. With active thermostating of resistance RN $\delta_{RN}^{T} \le 0{,}001\%/1°C$ $(0{,}0025°C)$. So, the net error of the RTD's resistance measurement is equivalent to 0.035 °C. However, the temperature measurement error includes the error of the RTD itself. This error does not exceed 0.3° C when measuring 0 °C and 0.5 °C when measuring 100 °C. After individual calibration using a standard PRTD of the third category, the measurement error will not exceed 0.1 °C at 0 °C and 0.15 °C at 100 °C. But the figures above do not take into account error due to RTD heating by the operating current (also referred to as error due to selfheating).

The goal of this paper is to correct error due to RTD heating by the operating current by preliminary studies of the individual properties of this error at a certain measurement object.

2. Error due to RTD Heating by the Operating Current

In [1, 3] this error does not exceed $\Delta_{SN}^{ST} \le 0{,}2°C$, if the power dissipated by the conventional PRTD is $P_{SN}^{ST} \le 0{,}01\ W$. The power dissipated by the PRTD depends on the operating current I_{RTD}, the ADC's sensitivity, interference U_{NZ}, and the RTD's sensitivity $S_{RTD} \approx 0{,}4\%/°C$. In [2], the RTD's current I_{RTD} for the minimum error due to selfheating was determined as

$$I_{RTD} = \sqrt[3]{\frac{U_{NZ} P_{SN}^{ST}}{\Delta_{SN}^{ST} R_{RTD}^{2} S_{RTD}}} \tag{2}$$

ISBN 978-80-972629-6-9

By substituting in (2) the values of U_{NZ} from 0.1 to 1000μV, $P_{SN}^{ST} \le 0{,}01\ W$, $\Delta_{SN}^{ST} \le 0{,}2°C$, $R_{RTD} = 100\ \Omega$, $S_{RTD} \approx 0{,}4\%/°C$ we get the values of the current I_{RTD}. Power dissipated by the RTD is $P_{RTD} = I_{RTD}^2 R_{RTD}$. Let's substitute these values of P_{RTD} in the proportion

$$\frac{P_{RTD}}{P_{SN}^{ST}} = \frac{\Delta_{RTD}}{\Delta_{SN}^{ST}} \quad . \tag{3}$$

We get the dependence of error due to selfheating vs random error of the ADC, given in Fig. 2. The higher the noise level of non-rejected interference, the higher error due to selfheating. It should be noted the used method of heating the RTD by the operating current during only the measurement. However, the thermal transien leads to a dynamic error and thermal waves, which complicates control of temperature systems. Therefore, it is reasonable to correct this error.

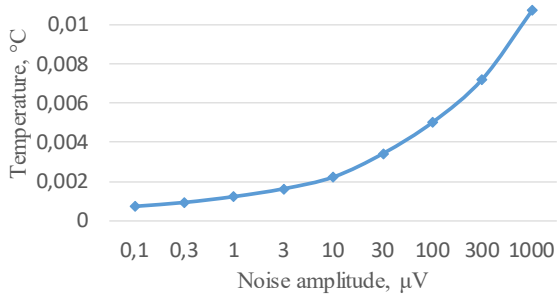

Fig. 2. Temperature of heating versus ADC sensitivity

3. Simple Method for Correcting Error due to RTD's Heating by the Operating Current

Heating of a body can be described by the Newton's law. Its solution is the dependence of temperature versus time, but we are interested in steady state response. So, error due to selfheating Δ_{SN} can be described by the equation that connects it with the power P_{RTD}

$$\Delta_{SN} = F\left(P_{RTD}\right) \quad . \tag{4}$$

In the general (4) is non-linear, due to heat exchange. However, the selfheating does not exceed $\Delta_{SN}^{ST} \le 0{,}2°C$ [3], so we assume (4) to be linear. Then we can write

$$\Delta_{SN} = K \cdot P_{RTD} = K \cdot I_{RTD}^2 \cdot R_{RTD} \quad , \tag{5}$$

where K is the coefficient of heat transfer of RTD. The real temperature of the measurement object T_{MO} can be determined as

$$T_{MO} = T_{RTD} - K \cdot I_{RTD}^2 \cdot R_{RTD} \quad , \tag{6}$$

where T_{RTD} is the temperature measured by the RTD, including its selfheating. There are two unknown variables in (6), such as K and T_{MO}. To find them, it is necessary to measure T_{RTD} using two RTD current values – I_{RTD1} and I_{RTD2}, but due to selfheating, we will compute two values of the measured temperature – T_{MO1} and T_{MO2}. We can neglect the change of R_{RTD} and compose the system of two equations like (6) and find the analytic expression for K

ISBN 978-80-972629-6-9

$$K = \frac{T_{RTD1} - T_{RTD2}}{\left(I_{RTD1}^2 - I_{RTD2}^2\right)R_{RTD}} \quad . \tag{7}$$

The real temperature of the measured object T_{MO} is determined by substituting K to (6). Let us estimate the error of temperature measurement Δ_{MO} after correcting RTD heating. The sources of measurement error are error due to non-linearity of ADC Δ_{NL} and its noise Δ_{NZ}. The error of K calculated by (7), is the higher, the smaller the differences in the numerator and denominator. Therefore, the ratio of currents I_{RTD1} and I_{RTD2} should be as large as possible.

If using a successive-approximation ADC with jumps of 0.0015% (the equivalent to AD7714 [4]), which corresponds to the temperature change of $\Delta T = \delta_{NL} / S_{RTD} \approx 0{,}004°C$. The difference in the numerator (7) for currents $I_{RTD1} = 2\ mA$ and $I_{RTD2} = 0{,}5\ mA$ is $T_{RTD1} - T_{RTD1} \approx 0{,}0075°C$. The abovementioned jumps change the difference in the numerator (7) from $T_{RTD1} - T_{RTD1} - \Delta T \approx 0{,}0035°C$ to $T_{RTD1} - T_{RTD1} + \Delta T \approx 0{,}0115°C$, that is in $0{,}0115°C / 0{,}0035°C \approx 3{,}3$ times. If using in the circuit of Fig. 1 an ADC with a continuous conversion characteristics, e.g. the sigma-delta ADC, such as AD7714 with the integral nonlinearity of $\Delta_{NL} \le 0{,}0015\%$, the error ΔT can be estimated from the proportion

$$\frac{2\Delta_{NL}}{\Delta_{NL}^{RTD}} \approx \frac{T_R}{T_{RTD1} - T_{RTD2}} \quad , \tag{8}$$

where Δ_{NL} – integral nonlinearity of the ADC; U_R – the ADC measurement range; ΔU_{RTD} – change of voltage across the RTD when determining K; Δ_{NL}^{RTD} – manifestation of ADC nonlinearity during determination of K. For the range of 100 °C, from (8) we get $\Delta_{NL}^{RTD} \le 0{,}25 \cdot 10^{-4}\%$, so the numerator of (7) is $\Delta T = \Delta_{NL}^{RTD} / S_{RTD} \approx 6 \cdot 10^{-5}°C$, which is negligible. The estimation of the ADC's nonlinearity in the denominator of (7), is $4 \cdot 10^{-4}°C$.

A greater error of RTD heating by the operating current is caused by ADC noise. According to [4], noise of AD7714 within the range of 320mV does not exceed $U_{NZ} \le 0.1$ μV. The analysis similar to the one given above showed that the numerator of (7) changes by about 3% due to noise. For correcting error due to self-heating, which does not exceed 0,008 °C, it is acceptable. Residual error due to selfheating is 0,0032 °C, so this error is reduced by more than twice. It should be noted errors of resistor RN and RTD virtually do not have any influence.

4. Conclusions

The error correction RTD's heating by the operating current reduces its magnitude by 50% to 0.0032°C. A small error of resistance measurement and a multibit ADC are needed for this.

References

[1] Webster, J. G. (1998). The measurement, instrumentation and sensors handbook. CRC.

[2] Kochan R. (2012). High precision analog to digital converters with metrological selfcalibration in situ. Lviv. (In Ukrainian).

[3] Bychkovskii R. (1978). Contact temperature sensors. Moscow: Metallurgy.

[4] AD7714. Retrieved from https://cutt.ly/75Re81R.

Measurement of Physical Quantities III

ISBN 978-80-972629-6-9

Accurate gravimetric calibration of micro-pipettes using double evaporation trap with temperature correction and uncertainty budget

[1]AbdulKarim A. AlShahrany, [1]Khalid S. AlEnizi and [1,2]Khaled M. Ahmed

[1] National Measurement and Calibration Center, Saudi Standards, Metrology and Quality Org. (SASO-NMCC), Riyadh, Saudi Arabia,
[2]National Institute for Standards (NIS), Giza, Egypt
Email: k.abdelftah@saso.gov.sa / khaled55eg@gmail.com

Abstract. *In disciplines including medicine, chemistry, biology, pharmacy, and genetics, volume measurements are most effectively performed using micropipettes. In order to calibrate micropipettes correctly and calculate uncertainties, laboratories must guarantee that the data produced by this equipment are accurate. The goal of this work is to outline the ideal procedure for calibrating micropipettes, under the specified measurement conditions, down to 1 microliter with sources of errors to be addressed, studied and corrected. Also described is a model for calculating measurement uncertainty. Uncertainty level of 0.02 µL in the calibration level of 1 µL could be achieved.*

Keywords: Volume measurements, micropipette calibration, error analysis, uncertainty

1. Introduction

Volume measurements are most successfully carried out using micropipettes or piston pipettes in fields such as medicine, chemistry, biology, pharmacy, and genetics. Today, pipetting in the microliter range is necessary for almost all chemistry applications. However, although emerging fields like genetics place more expectations on the trustworthiness of the data, new dispensing techniques make tests easier and more automated. Therefore, it's crucial to pay attention to the calibration and uncertainty associated with this kind of equipment [1-3].

A piston pipette's calibration is, in theory, rather straightforward. A quantity of distilled water is delivered via pipette to a vessel for weighing on a balance. The volume of this water is then determined using its weight and density, and it is compared to the volume that was anticipated. Pipette calibration is virtually this easy for pipette contents of 1 mL or greater [4-5].

There are two problems in micropipette calibration, especially in the microliter level (e.g. below 100 microliter). A large amount of the given water from micropipettes, which are piston pipettes with delivered volumes less than 1000 micro-liters, may evaporate before it can be weighed, necessitating the first correction for air buoyancy. Hence, it is advised to use an evaporation trap, which is covered in more detail below, to reduce evaporation. For pipette volumes below roughly 50 µL, the influence of evaporation needs to be decreased in order to obtain the needed accuracy. The rate of evaporation might be evaluated and a correction applied. Accurate weighing of extremely minute amounts of water is necessary for calibrating piston pipettes. To ensure that piston pipettes meet the accuracy standards of [5], they should be calibrated with an expanded uncertainty of less than 1/3rd of the maximum permissible systematic error (MPSE). To verify compliance with the maximum permissible random error, essentially the same capability is needed (MPRE) as per ISO 8655-2. For professional pipette calibration, you need the right balance - A well-balanced combination of Precision, speed and comfort. Precision to meet international regulations, as per international standards.

The goal of this work is to outline the ideal procedure for calibrating micropipettes under the specified measurement conditions. Also to address, study and correct for any error sources throughout the calibration process. A model for uncertainty evaluation as well as concluding the uncertainty budget, with giving an example of calculating the expanded uncertainty in the target range, for instance at 1 microliter level, is presented.

ISBN 978-80-972629-6-9

2. Equipment

The setup comprises a suitable high-accurate microbalance, liquid storage container, an evaporation trap, outer glass shielding box (considered as another trap), a weighing vessel, timing device, climate modules (for recording temperature, humidity and pressure) inside and outside the chamber, a computer and automation software. All those components of the setup are shown in figure 1.

The balances used for pipette calibration are selected to be accurate enough to assess the pipettes' compliance with the MPSE and/or MPRE as necessary. Repeatability is the main source of balance uncertainty. Balance linearity is rarely important and its impact on pipette calibration is easily verified. Balance resolution is a major factor in balance repeatability. The repeatability for a normal balance is one to three times the resolution. For the optimum condition, as per ISO 8655-6: 2022 (Piston-operated volumetric apparatus — Part 6: Gravimetric methods for the determination of measurement error), for the normal volume under test between 1 µL to 20µL, the resolution of the balance should be 0.001 mg.

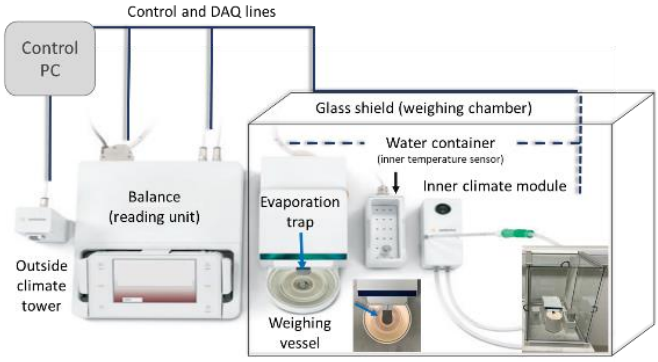

Figure 1. Schematic of the equipment with overlaying real photos for better visibility.

The used electronic balance (Sartorius, model: Cubis MPS6.6S) has readability of 1 µg, weighing range up to 6.1 g, linearity 0.004 mg and standard deviation (resolution) of 0.001 mg. Evaporation trap helps to reduce the influence of evaporation on the pipette calibration. An example of an evaporation trap is shown in Figure 1. The trap works by creating a humid region just above the weighing vessel, which reduces the evaporation of water from the weighing vessel. In addition, we made a special weighing chamber to additionally reduce the evaporation rate. The liquid container is filled with calibration fluid (distilled water), and at its bottom there is a calibrated temperature sensor for measuring liquid's temperature (15-30 °C sensing range). The climate module tower is used to measure the air density, air temperature, relative humidity and atmospheric pressure. A climate ranges are 18-27 °C , 800-1100 hPa , 30-90 % rh. Finally, the automation software provides easy motion control, rapid opening and closing of the evaporation trap for convenient and efficient pipetting with integrated humidity sensor that is used for controlled humidity in the weighing chamber along with white LED light that can be controlled via the software for optimal illumination of the weighing area for better visibility. The software also gives an immediate visual warning if climate data deviates from tolerance values. All the mentioned characteristics of the used software can be considered big advantages of this apparatus.

3. Method

For each pipette, at least three volumes—10%, 50%, and 100% of the nominal volume—are typically tested. It is advised to take ten measurements of each delivered volume. The accuracy and repeatability of the pipette at each volume are then determined using the results, in order to check the compliance with ISO 8655-2:2022. It's crucial to maintain consistency with the calibration measurements' time while calibrating piston pipettes. This is done so that later dummy pipette calibrations (which delivers no water) can be used to accurately estimate the amount of water that is still evaporating from the weighing vessel.

In the beginning, the temperature of the water in the beaker and the ambient temperature should be recorded. The ambient humidity and pressure should be recorded, using the climate module, as well. Then, filling the piston pipette with distilled water, and zeroing the balance. Next steps can be summarized as follows: delivering the volume of water in the pipette in the weighing vessel, following the requirements stated in ISO 8655-series standards, then acquiring the balance reading via the software, refill the pipette and repeat the previous steps. Continue until finishing with taking 10 volumes

ISBN 978-80-972629-6-9

and delivers them in the weighing vessel with recording the balance reading via the software. Record the time for the 10 volumes delivery. For more details, see Section 7 of ISO 8655-6:2022.

Based on references [1-6], the measurement, calculations and uncertainty models could be concluded. For the measurement of volume (distilled water at 20 °C) and modelling associated uncertainty, we use the following equation (1):

$$V_{20} = m \times Z \times Y \tag{1}$$

where, $m = m_2 - m_1 - m_E$

m: weighing value of delivery water (g), m_1: weighing vessel value (g), m_2: weighing value of both water and vessel (g), m_E: weighing value of the quantity of evaporation of water (g), Z: the correction factor takes into account water density and air buoyancy during measurement at the corresponding test temperature, and Y: the thermal expansion correction factor of the pipette.

Z is calculated using the following equation (2):

$$Z = \left(\frac{1}{\rho_w - \rho_a}\right).\left(1 - \frac{\rho_a}{\rho_b}\right) \tag{2}$$

ρ_a: Air density, g/mL

ρ_w: Liquid density, in g/mL, at the calibration temperature t, in ºC

ρ_b: Density of masses used during measurement (substitution) or during calibration of the balance, assumed to be 8,0 g/mL for stainless steel, in g/mL.

Y is calculated using the following equation (3):

$$Y = 1 - \propto_c (t_d - t_{d20}) \tag{3}$$

where, $\propto_c$: thermal expansion coefficient of pipette material (1/ ºC), and t_d: distilled water temperature (ºC)

Density of the pure water is determined as a function of temperature using equation (4) based on Tanaka formula [2] in 0 – 40 ºC range.

$$\rho_w = a_5\left[1 - \frac{(t+a_1)^2.(t+a_2)}{a_3(t+a_4)}\right] \quad \text{(g/mL)} \tag{4}$$

where, a_1: -3.983035 °C, a_2: 301.797 °C, a_3: 522528.9 °C^2, a_4: 69.34881 °C and a_5: 0999974950 g/mL

4. Measurements and uncertainty

In summary, main sources of measurement uncertainty can be stated as follows: (a) thermometer calibration, (b) water temperature measurement, (c) residual evaporation, (d) balance resolution and repeatability, (e) balance linearity, (f) variations in air density, (g) method uncertainty.

We draw the model function for uncertainty as follows, in equation (5):

$$V_{20} = \frac{m}{\rho_b}.\frac{\rho_b - \rho_a}{\rho_w - \rho_a}.[1 - \alpha_c.(t_d - t_{d20})] \tag{5}$$

with, for example, the uncertainty component of temperature drift, can be shown as in equation (6):

$$u(\Delta t) = \frac{\delta_t.\Delta t.m_{avg}}{2.k} \tag{6}$$

Where, δt: Sensitivity temperature drift, Δt: Temperature change during the measurement and m_{avg}: Average weighing value of the delivered water. Other uncertainty components can be evaluated in similar ways and then combined together as combined uncertainty in the overall uncertainty budget as per Guide for Uncertainty in Measurements (GUM). The detailed GUM-based uncertainty models, and its uncertainty budget concluded with the associated expanded uncertainty to be shown elsewhere. Here, in this paper, we only summarize the outcomes of measurements and some representative uncertainty figures.

Table 1 summarizes the results of measurements in the calibration points of 0.5 µL, 1 µL and 10 µL. Measurements made over many days to acquire the optimal data for reproducibility uncertainty estimation, with all possible corrections applied and repeatability tolerances and other measurement conditions and requirements of the relevant standards have been met.

ISBN 978-80-972629-6-9

Summary of uncertainty calculations, as concluded in uncertainty budget (at 1.0 µL calibration as representative point in the range) is shown in table 2. The table presents all components and sources of uncertainty and makes it easier for being understood.

Table 1. Results of measurements at different calibration points (nominal volumes: 0.5, 1.0 and 10.0 µL)

Measurement# / Nominal Volume	1 (µL)	2 (µL)	3 (µL)	Reproducibility uncertainty (µL)	Expanded uncertainty (single measurement) (µL)
0.5 µL	0.4348	0.4644	0.4295	5.43×10^{-3}	**0.02**
1 µL	1.0249	1.0253	1.0504	8.85×10^{-4}	**0.02**
10 µL	9.9108	9.9115	9.9111	1.01×10^{-4}	**0.04**

The detailed discussions of the uncertainty model, evaluation of each component (with the relevant detailed equations), and the steps toward estimating the combined uncertainty at each nominal level, of volume, would be shown elsewhere. Refer to table 2 to see all uncertainty calculations.

Table 2. Uncertainty budget for the calibration at 1 µL

Uncertainty source	Source value of standard uncertainty	Probability Distribution Function (PDF)	Standard uncertainty $u(x_i)$	Sensitivity coefficient c_i	Standard uncertainty contribution $u_i(Y)$ $(c_i\times u(x_i))$
Balance					
calibration (cert.)	0.0002 µg	normal	0.0001 µg	1 nl/µg	0.0001 nl
linearity	4.00 µg	rectangular	2.30 µg	1 nl/µg	2.30 nl
reproducibility	1.00 µg	rectangular	0.60 µg	1 nl/µg	0.60 nl
readability	1.00 µg	rectangular	0.30 µg	1 nl/µg	0.30 nl
temperature drift	0.001 µg	rectangular	0.0003 µg	1 nl/µg	0.0003 nl
correction for evaporation loss	4.50 µg	rectangular	3.0 µg	1 nl/µg	3.00 nl
Water					
temperature	0.01 °C	rectangular	0.0040 °C	0.21 nl $°C^{-1}$	0.001 nl
Air					
temperature	0.10 °C	rectangular	0.043 °C	0.005 nl $°C^{-1}$	0.0002 nl
pressure	0.04 mbar	rectangular	0.02 mbar	0.001 nl $mbar^{-1}$	0.00003 nl
relative humidity	1.45 %	rectangular	0.80 %	0.0001 nl $\%^{-1}$	0.0009 nl
Delivering device					
Thermal expansion coeff.	0.0003 $°C^{-1}$	rectangular	0.0000087 $°C^{-1}$	730.0 nl °C	0.0063 nl
temperature	2.0 °C	rectangular	1.15 °C	0.31 nl $°C^{-1}$	0.35 nl
Combined standard uncertainty					**0.01 µL**
Expanded standard uncertainty; $U(V_{20})$ k=2					**0.02 µL**

5. Conclusions and on-going work

In conclusion, the newly developed method and equipment for calibrating micropipettes in micro-liter range have been tested. Microbalance (0.001 g resolution) and evaporation trap along with customized software have been used. Method comprises careful calibration steps with proper corrections applied. To demonstrate the appropriateness of the method, we calibrate micropipettes at 3 levels in the target range, which shows an excellent reproducibility. Uncertainty model was developed with proper estimations of all uncertainty components presented as a concluded uncertainty budget. Our collected measurement results showed that the used method with the modified apparatus and high-accuracy microbalance gives accurate and reproducible results with relatively low uncertainty in the micro-volume range below 10 microliters. All uncertainty components have been studied carefully and presented in table (2), with further details, which is beyond the scope of this paper, would be shown elsewhere.

Acknowledgements

Authors thanks Research and Studies Center (RSC) of SASO for considering this work.

References

[1] EURAMET Calibration Guide No. 19 (2018): “Guidelines on the Determination of Uncertainty in Gravimetric Volume Calibration”, Version 3.0.

[2] Tanaka, M., Girard, G., Davis, R., Peuto, A. and Bignell, N. (2001). Recommended table for the density of water between 0 °C and 40 °C based on recent experimental reports. Metrologia, 38, 301-309.

[3] Measurement Good Practice Guide No. 69 (2004). “The calibration and Use of Piston Pipettes”, John Blues, Davis Bayliss and Mike Buckley, NPL.

[4] ISO 4787 (2011): Laboratory glassware- Volumetric Instruments – Methods for testing of capacity.

[5] BS EN ISO 8655 (2022): Parts 1 to 6

[6] PD ISO/TR 20461(2000): Determination of uncertainty for volume measurements made using the gravimetric method.

Application of LabVIEW to Determine Characteristics of Two-Terminal Passive Components

[1]Przemysław Otomański, [2]Eligiusz Pawłowski, [3]Anna Szlachta

[1]Poznan University of Technology, Institute of Electrical Engineering and Electronics, Piotrowo street 3A, 60-965 Poznań, Poland
[2]Lublin University of Technology, Faculty of Electrical Engineering and Computer Science, Nadbystrzycka street 38A, 20-618 Lublin, Poland
[3]Rzeszow University of Technology, Department of Metrology and Measurement Systems, W. Pola street 2, Rzeszow, 35-959, Poland

Email: przemyslaw.otomanski@put.poznan.pl

Abstract. *The paper discusses the topic of determining the current-voltage characteristics of two-terminal passive components. A virtual measurement instrument created in the LabVIEW environment using the NI USB-6211 data acquisition device is presented, as well as the results of tests performed for example elements . The described approach can also be applied to other measurement situations, such as for studying the self-heating effect of RTD.*

Keywords: I-V Characteristics Curves, Virtual Instrument, LabVIEW, RTD

1. Introduction

The parameters of two-terminal elements often used in electronic circuits have a significant impact on the correct operation of many technical devices. This paper presents a measurement system, an application to determine the current-voltage characteristics of passive two-terminal elements, and sample test results for several selected objects. The measurement application based on the NI USB 6211 module was carried out in the LabVIEW environment [1].

2. Description of the measurement stand

The laboratory workstation presented in the article consists of the following components: PC with National Instruments LabVIEW environment installed, NI USB-6211 measurement data acquisition module, a high-power DC amplifier, a collection of double-ended linear and nonlinear passive elements. The block diagram of the laboratory workstation for the automatic determination of the DC current-voltage curves of two-terminal linear and nonlinear passive elements is shown in Figure 1.

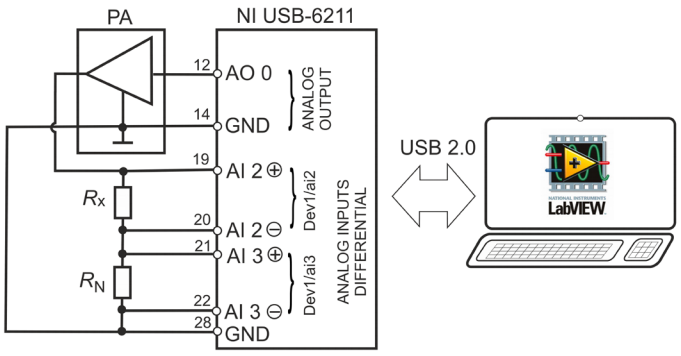

Fig. 1. Block diagram of the laboratory stand for automatic determination of DC current-voltage curves of two-terminal linear and non-linear passive components

The NI USB-6211 measurement data acquisition module is connected to a PC via a USB interface. Basic parameters of tested measurement module are shown in Table 1. The output voltage of the AO 0 DAC (terminal 12) is applied to the input of the power amplifier (PA).The output voltage from the PA supplies the R_x two-terminal device under test and the reference resistor R_N. The test two-terminal R_x and the reference resistor R_N are connected in series between the output of the ground amplifier and the electrical GND of the circuit. The differential analogue inputs AI 2 of the analogue-to-digital converter were used to measure the voltage on the R_x two-terminal test. This measured voltage was connected to AI 2 + (terminal 19) and AI 2 – (terminal 20). Similarly, the differential analogue input AI 3 of the analogue-to-digital converter was used to measure the voltage across the reference resistor R_N. This measured voltage is connected to AI 3 + (terminal 21) and AI 3 – (terminal 22). The amplifier ground is connected to the GND terminals of the DAQ measurement module (terminals 14, 28).

Table 1 shows selected metrological parameters of the NI USB-6211 measurement module used**.**

Table 1. Parameters of tested measurement modules for ±10 V differential range [2].

Model	Resolution	Gain Error	Offset Error	Random Error	Sensitivity
	bits	ppm of Reading	ppm of Range	μV_{rms}	µV
USB 6211	16	75	20	729	91.6

3. Virtual Instrument

Figure 2 shows a block diagram of the developed application. DAQmx libraries were used to support the measurement module. The measurement application controls the D/A converter, whose output voltage is amplified and feeds the circuit of series connection of the reference resistor R_N and the two-terminal R_x under test.

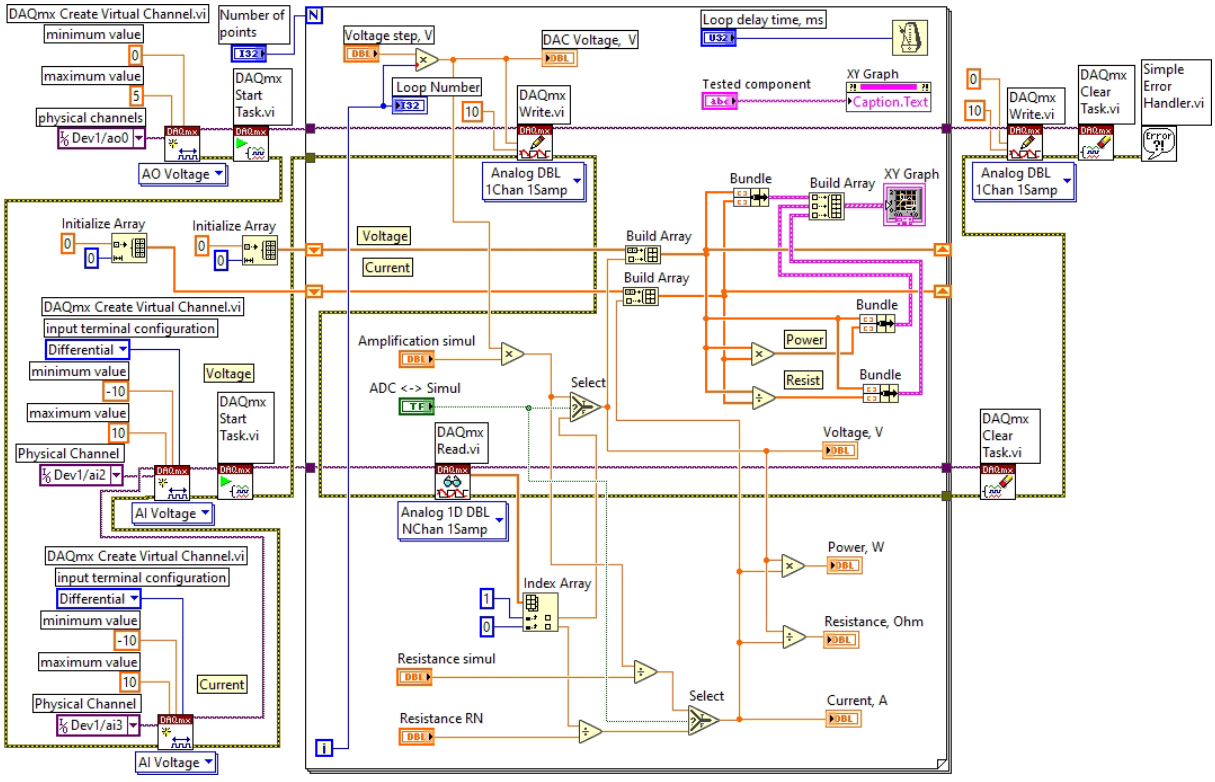

Fig. 2. Block diagram of the application to determine the I–V curve of two-terminal components

Measurements are made in differential mode, alternating between the two channels of the A/D converter. Figure 3 shows the Front Panel of the application, which can operate in simulation or measurement mode. The left side of the programme panel contains fields that allow you to enter data configuring the measurement module and how the measurements are performed. A switch located in the lower left corner allows switching between simulation and measurement modes. The right part contains sample characteristics of current, power, and resistance as a function of voltage.

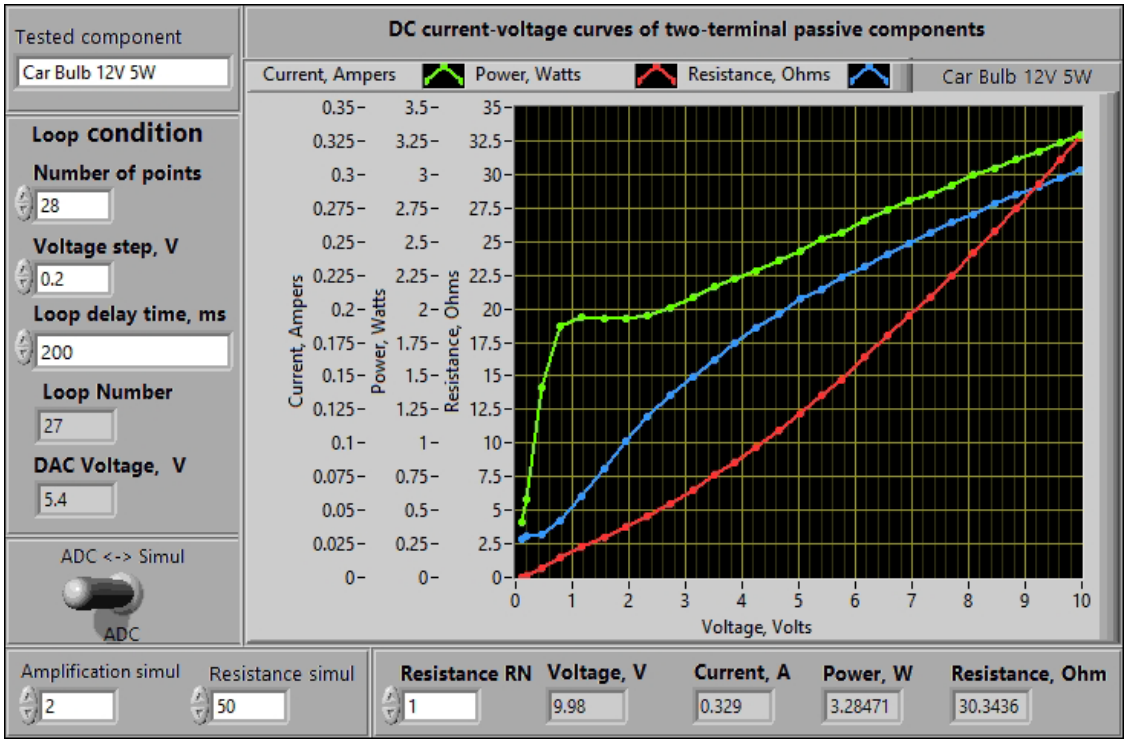

Fig. 3. Front Panel of the application to determine the I–V curve of two-terminal components.

4. Results

The laboratory stand, shown in Figure 1, was used to test selected passive elements. Measurements were made for different values of number of points, voltage step, and loop delay time. For each series of *n* measurements performed, the programme determined the characteristics. The results obtained from the measurements, for selected passive two-terminal elements: Red LED, linear resistor, car bulb 12V/5W and RTD Pt100 sensor are shown as graphs in Figures 4 and 5.

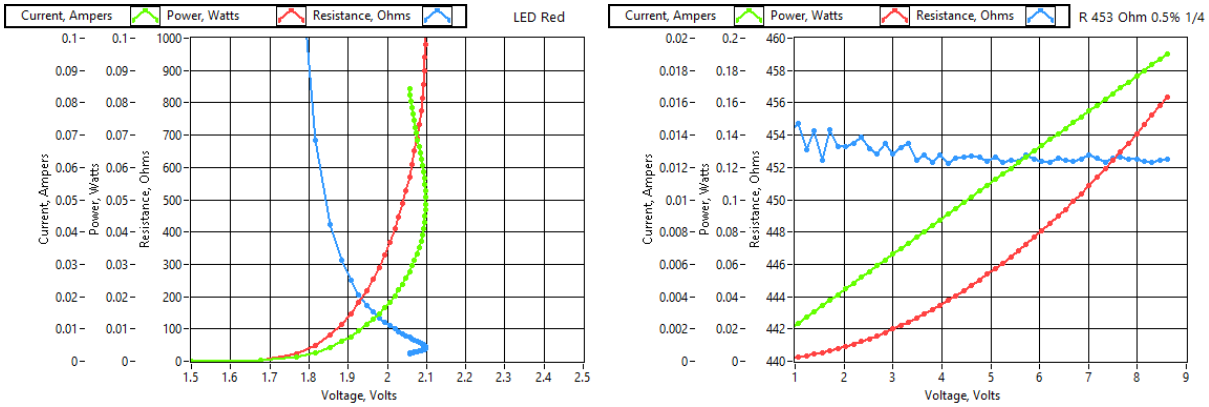

Fig. 4. Exemplary graphs of current, power and resistance of the Red LED and linear resistor 453 Ω.

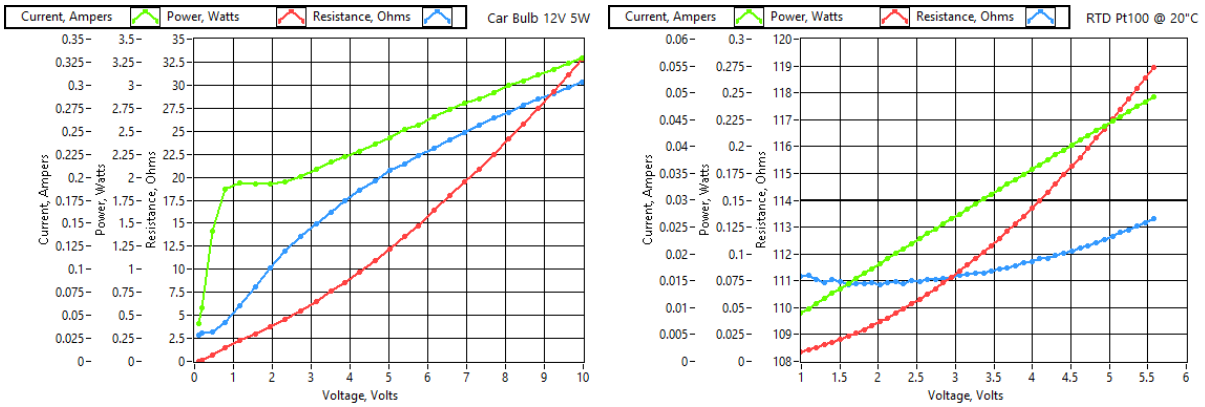

Fig. 5. Exemplary graphs of current, power and resistance of the car bulb 12V/5W and Pt100 sensor.

Analysing the measurement results obtained in the study, presented in the form of characteristics, allows us to formulate a number of conclusions. Loop delay time, in the case of an incandescent bulb, has a significant effect on the shape of the current-voltage characteristics due to the fact of heating of the tested element. On the graph of the current (green line) of the LED for values greater than 50 mA, one can see a decrease in the value of the voltage drop at the junction, as a result of an increase in the temperature of the structure. For the linear resistor, the initial resistance value (blue line) has a relatively large measurement uncertainty. These uncertainties decrease as the measurements approach the end of the measurement range of the NI USB-6211 module [3]. In the case of a tungsten bulb, the shape of the current-voltage characteristics is significantly influenced by the delay time of the measurement loop, due to the fact that the test element heats up. In this case, the measurement duration was 5.5 s (55 points, a delay time of 100 ms). For a different delay time, the bulb shape of the characteristics will change. For the Pt100 sensor, the graph shows the effect of self-heating for currents above 25 mA (the sensor was placed in air).

The measurement results presented in the article should be regarded as exemplary and limited to the tested model of the measurement module and selected passive two-terminal elements. The obtained test results for a broader set of tested two-terminal elements will be presented by the authors during a presentation at the conference. The developed programme can be used to test any passive two-terminal elements using modules that have appropriate drivers running in the LabVIEW environment. This environment is now often used during measurements of many quantities, which is the subject of a number of publications [4]. The authors plan to conduct simulation studies in the future, to verify the parameters of the models used.

References

[1] Sokoloff, L. Applications in LabVIEW; Pearson Prentice Hall: Upper Sadle River, NJ, USA, 2004.

[2] National Instruments. DAQ M Series, NI USB-621x User Manual, Bus-Powered M Series USB, User Guide and specifications 371931F-01; National Instruments: Austin, TX, USA, 2009.

[3] Otomański P., Pawłowski E., Szlachta A. The evaluation of expanded uncertainty of DC voltages in the presence of electromagnetic interferences using the LabVIEW environment, Measurement Science Review, 2021, 21(5), pp. 136 – 141.

[4] M. Saufi N.S., Abdullah N.S.Y., Yaacob M.I.H. Automated measurement system for diode I–V characterization, 2016 6th IEEE International Conference on Control System, Computing and Engineering (ICCSCE), Penang, Malaysia, 2016, pp. 498-501.

Finite Elements and Integro-Differential Methods Are Equivalent for Description of Rotational Dynamics of Spherical Particle During Its Magnetic Alignment

[1]Andrej Krafcik, [2]Peter Babinec, [3]Oliver Strbak, [1]Ivan Frollo

[1]Institute of Measurement Science, Slovak Academy of Sciences, Bratislava, Slovakia,
[2]Faculty of Mathematics, Physics and Informatics, Comenius University, Bratislava, Slovakia,
[3]Biomedical Center Martin, Jessenius Faculty of Medicine in Martin, Comenius University in Bratislava, Martin, Slovakia
Email: andrej.krafcik@savba.sk

Abstract. *Rotational dynamics of spherical micro-particle in a strong external magnetic field and water as a liquid medium during the particle's alignment was numerically modeled using two different descriptive approaches. The first is the solution of the Navier-Stokes equations using the finite element method (FEM). And the second is the solution of an integro-differential equation (IDE) for torques experienced on particle, particularly governing magnetic torque and quasi-steady viscous torque and its history non-local addition due to unsteadiness of particle rotation, inertia, viscosity and friction with the non-Basset kernel, described recently [A. Krafcik et al. Appl. Sci. 11(20) (2021) 9651]. As we have shown, both approaches are in good agreement and fully equivalent for the studied model.*

Keywords: Spherical Particle Rotational Dynamics, Incompressible Navier-Stokes Equations, FEM, Integro-Differential Equation, Non-Basset Kernel Function

1. Introduction

A single spherical magnetic particle in a liquid medium and strong magnetic field experiences magnetic torque, which acts as a governing force during particle rotation. For simplicity, we can assume full magnetic saturation of the particle's magnetic moment and consider only a Brownian rotation of the particle as a whole as the inverse process to the Brownian relaxation. The next addition to the overall torque on particle comes from the viscous effects: In the first, as quasi-steady viscous torque, and in the second unsteady and non-local effects due to fluid inertia and friction, which bring an integro-differential term in the rotational dynamics equation. This integro-differential torque term is an integral of a product of the non-Basset kernel function and the time derivative of angular velocity (introduced in [1] and studied with our group recently in [2]). In comparison, viscous effects on spherical particle, instead of quasi-steady and integro-differential viscous torque can be evaluated directly from the overall moment of viscous forces on the surface of an unsteady rotating spherical particle evaluated numerically using finite element method (FEM) from incompressible Navier-Stokes equations as the first principles.

2. Subject and Methods

Let's consider a quiescent spherical magnetic particle with radius R, mass density ρ_p, and magnetic moment μ_p (fully magnetically saturated) originally oriented in the perpendicular direction to the external homogeneous magnetic flux density $\vec{B}_0$, and water as ambient viscous fluid with mass density ρ, dynamic and kinematic viscosity η and $\nu = \eta/\rho$, respectively. Rotational magnetic alignment of a such particle can be described with the system of differential equations

ISBN 978-80-972629-6-9

and initial conditions:

$$I_p \frac{\mathrm{d}\omega}{\mathrm{d}t} = \mu_p B_0 \sin\varphi + T_\mathrm{v}(t), \qquad \frac{\mathrm{d}\varphi}{\mathrm{d}t} = -\omega, \qquad \varphi(0) = \frac{\pi}{2}\,\mathrm{rad}, \qquad \omega(0) = 0\,\mathrm{rad/s}, \tag{1}$$

where $I_\mathrm{p} = \frac{2}{5} m_\mathrm{p} R^2$, m_p, R, $T_\mathrm{v}(t)$, φ and ω are the particle moment of the inertia, particle mass, particle radius, viscous torque exerted on the particle, alignment angle and angular velocity, respectively. The stochastic Brownian torque was neglected.

FEM model

We come from incompressible Navier-Stokes equations as the first principles: $\rho\left(\frac{\partial \vec{u}}{\partial t} + \vec{u}\cdot\vec{\nabla}\vec{u}\right) = \vec{\nabla}\cdot\vec{\vec{\sigma}}(\vec{u},p)$ and $\vec{\nabla}\cdot\vec{u} = 0$, with initial: $\vec{u}(\vec{r},0) = \vec{0}\,\mathrm{m/s}$, $p(\vec{r},0) = 0\,\mathrm{Pa}$ for $\vec{r}\in\Omega$ and boundary conditions: $\vec{u}(\vec{r},t) = [x,y,0]\times\vec{\omega}(t)$ for $\vec{r}\in\partial\Omega_\mathrm{p}$ (no-slip) and $p(\vec{r},t) = 0\,\mathrm{Pa}$ for $\vec{r}\in\partial\Omega_\mathrm{o}$ (open outer boundary), where $\vec{r} = [x,y,z]$, $\vec{\omega} = [0,0,\omega]$; and $\vec{u}$, p, Ω, $\partial\Omega_\mathrm{p}$ and $\partial\Omega_\mathrm{o}$ are the velocity vector field, pressure scalar field of ambient water medium, spherical computation domain, particle surface inner boundary and outer spherical boundary of the computation domain, respectively. Symbols $\vec{\vec{\sigma}}$ and $\vec{\vec{\varepsilon}}$ defined as $\vec{\vec{\sigma}}(\vec{u},p) = 2\eta\vec{\vec{\varepsilon}}(\vec{u}) - p\vec{\vec{I}}$ and $\vec{\vec{\varepsilon}}(\vec{u}) = \frac{1}{2}[\vec{\nabla}\vec{u} + (\vec{\nabla}\vec{u})^T]$ are the stress tensor and strain-rate tensor, respectively, and $\vec{\vec{I}}$ is the identity tensor.
Finally, the viscous torque exerted by the particle can be expressed as

$$T_\mathrm{v} = \left[\int_{\partial\Omega_\mathrm{p}} \vec{r}_\mathrm{a}\times\left(\vec{\vec{\sigma}}\cdot\vec{n}\right)\mathrm{d}S\right]_z, \tag{2}$$

where the $\partial\Omega_\mathrm{p}$, and $\mathrm{d}S$ are particle surface, and its element with normal vector $\vec{n}$, respectively. Vector $\mathrm{d}\vec{F} \equiv \vec{\vec{\sigma}}\cdot\vec{n}\,\mathrm{d}S$ is an element of fluid viscous force acting on the particle surface element $\mathrm{d}\vec{S} \equiv \vec{n}\,\mathrm{d}S$ with an arm vector $\vec{r}_\mathrm{a} \equiv [x,y,0]$, where x and y fulfill $\vec{r} \equiv [x,y,z] \in \partial\Omega_\mathrm{p}$. Therefore, the cross product in: $\mathrm{d}T_\mathrm{v} \equiv [\mathrm{d}\vec{T}_\mathrm{v}]_z = [\vec{r}_\mathrm{a}\times\mathrm{d}\vec{F}]_z$ is an element of viscous torque felt by the particle.
The Navier-Stokes equations in each time step were solved numerically in PYTHON 3.8.5 (Python Software Foundation 2021, `https://www.python.org`) environment using FENICS 2019.1.0 (FEniCS Project 2021, available online: `https://fenicsproject.org`, accessed on 15 October 2021) module via FEM by modified Chorin's method so-called incremental pressure correction scheme explained in [3].
Governing differential equations (1) for viscous torque (2) were solved numerically using the Euler method in the PYTHON environment.

IDE model

As an alternative approach to express overall viscous torque acting on spherical magnetic particle was used summation of quasi-steady viscous torque and non-local integro-differential viscous torque represented as the integral of the product of non-Basset kernel and angular acceleration over overall history of the particle rotation (introduced in [1])

$$T_\mathrm{v} = \underbrace{-\gamma\omega(t)}_{\text{quasi-steady}} \underbrace{-\frac{\gamma}{3\sqrt{\pi}}\int_{-\infty}^{t} K(t-\tau)\frac{\mathrm{d}\omega(\tau)}{\mathrm{d}\tau}\,\mathrm{d}\tau}_{\text{history acceleration}}, \tag{3}$$

where $\gamma = 8\pi\eta R^3$ is the Stokes viscous coefficient, and $K(\xi) \equiv \frac{1}{\xi} - \sqrt{\pi}\exp\xi^2\operatorname{erfc}\xi$ is non-Basset kernel function with argument $\xi(t-\tau) \equiv \sqrt{\nu(t-\tau)/R^2}$.

ISBN 978-80-972629-6-9

Table 1: Values of parameters used in simulations.

Parameter	Symbol	Value	Unit
Finite time step	h or Δt	10^{-9}, 10^{-10}	s
Magnetic flux density norm	B_0	5.0	T
Water dynamic viscosity	η	10^{-3}	Pa.s
Water mass density	ρ	10^{3}	kg/m^3
MyOne particle diameter	$2R$	10^{-6}	m
MyOne particle mass density	ρ_p	1 792	kg/m^3
MyOne particle magnetic moment[a]	μ_p	2.25×10^{-14}	A.m^2
MyOne particle weight	m_p	$\frac{4}{3}\pi R^3 \rho_\mathrm{p}$	kg
MyOne particle moment of inertia	I_p	$\frac{2}{5} m_\mathrm{p} R^2$	kg.m^2

[a] Calculated as $\mu_p = M_{sp} V_p$, where $M_{sp} = 43 \times 10^3$ A/m and $V_p = \frac{4}{3}\pi R^3$.

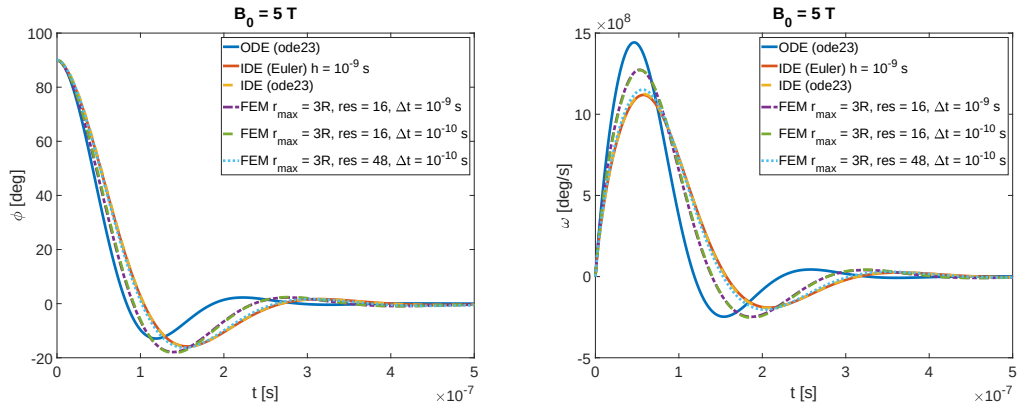

Fig. 1: (Color online.) Magnetic particle alignment model comparison. Time evolution of alignment **(left)** angle and **(right)** angular velocity. Comparison of the ODE (`ode23`), IDE (Euler), IDE (`ode23`) and FEM models (for different spatial resolutions res and sizes of time steps Δt).

Governing differential equations (1) for viscous torque (3) were solved numerically in MATLAB R2020a (MathWorks Inc., Natick, Massachusetts, USA 2020, `https://www.mathworks.com`) environment using Euler method [2] and also with more precise method similar to the variable time step order one quadrature scheme approach introduced in [4] by built-in MATLAB function `ode23` (explicit Runge-Kutta 3(2) pair of Bogacki and Shampine) [5].
Finally, for comparison, an ordinary differential equations (ODEs) model was also simulated using built-in MATLAB `ode23` function. In this case the viscous torque was assumed only as the quasi-steady viscous term.

3. Results and Discussion

The simulations were performed for magnetic particle MyOne one micrometer (ThermoFischer Scientific, Waltham, MA USA, Dynabeads™, MyOne™, available online: `https://www.thermofisher.com/order/catalog/product/65012?SID=srch-srp-65012`, accessed on 31 May 2018) and water as ambient fluid with values of physical parameters specified in Table 1.
Obtained results from simulations are shown in Fig. 1 as the time evolution of angle and angular velocity between the direction of vectors of constant external magnetic flux density and axis of easy magnetization of spherical magnetic particle. There are shown results for different models for comparison. Explicitly for ODE (`ode23`), IDE (Euler), IDE (`ode23`) and FEM model, where r_max and res are the outer boundary radius and spatial resolution of the computational domain in the FEM model, respectively.
As you can see, the ODE model with quasi-steady viscous torque is only approximative, as the

first estimate. By the involvement of viscous non-local integro-differential history acceleration torque, the solution of the IDE model comes closer to the solution of the FEM model. The FEM model for the highest spatial resolution is almost identical with the solved IDE models.
Obtained results for different models are in good agreement. However, it should be noticed that used models are only approximative and limited for several reasons. Our models consider only full magnetic saturation of a particle, as well as only inertia, magnetic torque and viscous torques. Although, Néel rotation of magnetization and stochastic Brownian torque, as well as stochastic noise of magnetic flux density should be considered for a complete description of the studied phenomenon. After that, the stochastic Landau-Lifshitz-Gilbert equation should be considered. Also, mentioned stochastic parameters, instead of Gaussian white noise, could be colored due to unsteadiness and non-locality of overall viscous torque in IDE and FEM models. However, it should be interesting, it is out of the scope of the paper. As shown in [2], stochastic Brownian torque can be neglected in strong magnetic flux density limit.

4. Conclusions

We have studied the rotational dynamics of a single spherical magnetic particle in water as ambient fluid and a strong homogeneous magnetic field—a phenomenon of rotational magnetic alignment of a particle as an inverse process to Brownian relaxation. As computation models, we have numerically simulated the behavior of the studied problem in three different approaches: as the ODE model (inertial, magnetic and quasi-steady viscous torques), the IDE model (same as the ODE model with the addition of unsteady non-local integro-differential viscous torque term), and finally the FEM model (viscous torque as the moment of viscous drag forces on the surface of the spherical particle coming from incompressible Navier-Stokes equations as the first principles). While, the ODE model gave only approximative results, the IDE and FEM models were in good common agreement, and for the highest spatial resolution of the FEM model, the time evolutions of alignment angle and angular velocity were almost identical with those ones of the IDE model. Therefore, it should be concluded that the IDE and the FEM description of studied rotational dynamics are equivalent and can be interchanged or vice versa.

Acknowledgements

This work was supported by the Slovak Research and Development Agency (APVV-19-0032), the Slovak Scientific Grant Agency (VEGA 1/0639/22, 2/0004/23) and the Ministry of Health of the Slovak Republic (2018/11-UKMT-7).

References

[1] Lei, U., Yang, C., Wu, K. (2006). Viscous torque on a sphere under arbitrary rotation. *Appl. Phys. Lett.* 89(18), 181908.

[2] Krafcik, A., Babinec, P., Strbak, O., Frollo, I. (2021). A theoretical analysis of magnetic particle alignment in external magnetic fields affected by viscosity and Brownian motion. *Appl. Sci.* 11(20), 9651.

[3] Langtangen, H. P., Logg, A. (2017). *Solving PDEs in Python*. Springer-Verlag Berlin Heidelberg.

[4] Krafcik, A., Babinec, P., Frollo, I. (2018). Stokes versus Basset: Comparison of forces governing motion of small bodies with high acceleration. *Eur. J. Phys.* 39(3), 035805.

[5] Shampine, L. F., Reichelt, M. W. (1997). The MATLAB ode suite. *SIAM J. Sci. Comput.* 18(1), 1–22.

AUTHORS INDEX

ISBN 978-80-972629-6-9

ISBN 978-80-972629-6-9

ISBN 978-80-972629-6-9

Institute of Measurement Science
Slovak Academy of Sciences
Dúbravská cesta 9
841 04 Bratislava, Slovakia